

Study of the $H \rightarrow ZZ^{(*)} \rightarrow 4\ell$ Decay Channel and Contribution to the Forward Muon Detection with the ATLAS Experiment

by

KALLIOPI IORDANIDOU

*A Dissertation Submitted in Fulfillment of the
Requirements for the Degree of
Doctor of Philosophy in Physics*



*Nuclear and Particle Physics Section
Physics Department
National and Kapodistrian University of Athens*

Advisor: D. Fassouliotis

Athens, January 2015

To all those who inspired me in any way

Contents

Acknowledgments	9
1 Theory Introduction	21
1.1 Introduction	21
1.2 The Standard Model Theory	24
1.2.1 Motion of Scalar and Pseudoscalar Fields	25
1.2.2 Relativistic Wave Equation	25
1.2.3 Symmetries	26
1.2.4 Quantum Electrodynamics (QED)	27
1.2.5 Gauge Fields Lagrangian	28
1.2.6 The Strong Interactions Lagrangian	30
1.2.7 Spontaneous Symmetry Breaking and Goldstone Bosons	31
1.2.8 Local Symmetry Breaking and the Higgs Boson	32
1.3 The SM Higgs Mechanism	33
1.3.1 The Mechanism in the SM	33
1.3.2 The Higgs Particle in the SM	36
1.4 Higgs System Theoretical Constraints	37
1.4.1 Perturbative Unitarity	37
1.4.2 Triviality and Stability Bounds	38
1.4.3 The Fine-Tuning Constraint	41
1.5 Higgs Beyond the Standard Model	42
1.6 Higgs Production at Hadron Colliders	44
1.7 Higgs Searches and Production at the LHC	48
Chapter Bibliography	50
2 LHC Structure, Operation and Experiments	53
2.1 Introduction	53
2.2 The CERN Accelerator Complex	55
2.3 Proton Beams Collisions	58
2.4 The LHC Experiments	59
2.4.1 ATLAS	60

2.4.2	CMS	61
2.4.3	ALICE	63
2.4.4	LHCb	64
2.4.5	TOTEM	66
2.4.6	LHCf	67
2.4.7	MoEDAL	67
	Chapter Bibliography	69
3	Atlas Detector Description	71
3.1	Introduction	71
3.2	The Coordinate System	72
3.3	Performance Requirements	72
3.4	The Inner Detector	73
3.4.1	Pixel Detector	74
3.4.2	The Semiconductor tracker (“SCT”)	75
3.4.3	Transition Radiation Tracker (“TRT”)	77
3.5	The Calorimeters	79
3.5.1	The Liquid Argon (“LAr”) Calorimeter	79
3.5.2	The Tile Calorimeter	82
3.6	The Muon Spectrometer	84
3.6.1	Monitored Drift Tubes (MDT)	86
3.6.2	Cathode Strip Chambers (CSC)	87
3.6.3	Resistive Plate Chambers (RPC)	89
3.6.4	Thin Gap Chambers (TGC)	90
3.6.5	Precision Alignment	92
3.7	The Magnet System	93
3.7.1	The Central Solenoid	93
3.7.2	The Barrel Toroid	94
3.7.3	The EndCap Toroid	96
3.8	The Trigger System	96
3.9	The Data Acquisition System (DAQ) and Controls	99
3.10	Luminosity Determination and Luminosity Detectors	100
3.11	ATLAS Upgrade	102
3.11.1	The Muon Spectrometer Upgrade	103
3.11.2	The Calorimeters Upgrade	106
3.11.3	The Fast Tracker	108
3.11.4	The Forward Physics Upgrade	108
3.11.5	The T/DAQ Upgrade	108
3.12	Summary	110
	Chapter Bibliography	111

4 Cathode Strip Chambers (CSC)	115
4.1 Introduction	115
4.2 Principle of Operation	115
4.3 Signal Formation	118
4.4 Spatial resolution of the CSCs	119
4.5 The Effect of Inclined Tracks and the Lorentz Angle	120
4.6 Timing Resolution	121
4.7 Mechanical Design and Construction	121
4.7.1 Description of the Basic Four-Layer Module	121
4.7.2 Assembly Procedure	122
4.7.3 Support Structure and Alignment of the CSC System	122
4.8 The Readout Complex	124
4.8.1 The On-Detector Electronics	124
4.8.2 The Off-Detector Electronics	127
4.9 Offline Reconstruction	136
4.9.1 Strip Charge Reconstruction	136
4.9.2 Cluster Formation	139
4.9.3 The Segments Reconstruction	144
4.10 CSC Simulation	145
4.11 CSC Operational Conditions During the Run-I	146
4.11.1 2-Samples Data Taking	148
4.11.2 Charge Thresholds	148
4.11.3 Non Applied Busy Reduction Methods	149
4.12 Resolution and Angle Dependence	151
4.13 Alignment Checks	152
4.14 Lorentz Angle Effect Measurement	154
4.15 2 vs 4-Samples Data Taking Performance	155
4.16 CSC Efficiency in the Muon Algorithm	156
4.16.1 The Tag and Probe Method	158
4.17 Performance of Sectors with Problematic Layers	161
4.18 Run-I Performance Summary	162
4.19 25ns Runs	167
4.20 Post-Run-I Chambers Repair	169
4.21 Summary	172
Chapter Bibliography	177
5 Search for $H \rightarrow ZZ^{(*)} \rightarrow 4\ell$ Decays	179
5.1 Introduction	179
5.2 Data Samples	180
5.3 Monte Carlo (MC) samples	180
5.3.1 Signal MC Samples and Cross Sections	180

5.3.2	MC Background Samples	182
5.4	Leptons Definition	185
5.4.1	Electron reconstruction and identification	185
5.4.2	Muon Identification and Reconstruction	187
5.5	Trigger	190
5.6	Events selection	192
5.6.1	Analysis Events Selection	192
5.6.2	FSR recovery	194
5.6.3	Z Mass Constraint	196
5.7	Reducible Background Estimation Methods	196
5.8	Background Discrimination Variables	197
5.8.1	Isolation	198
5.8.2	Impact Parameter Significance	199
5.9	Muon Efficiencies in Background Environments	199
5.10	Muons Reducible Background Estimation	200
5.10.1	The Simultaneous Fit Concept	200
5.10.2	Fit Control Regions	205
5.10.3	MC Closure Test	208
5.10.4	2012 Data Unbinned Simultaneous Fit	209
5.10.5	2012 Data Unbinned Simultaneous Fit Validity	211
5.10.6	2012 Signal Region (SR) Extrapolations	219
5.10.7	2011 Reducible Background Estimations	220
5.11	4ℓ Angular Distributions	225
5.12	Systematic Uncertainties	226
5.13	Higgs Candidates and Background	230
5.14	Summary	233
	Chapter Bibliography	237
6	Study of the $H \rightarrow ZZ^{(*)} \rightarrow 4\ell$ Production Mechanisms	243
6.1	Introduction	243
6.2	Jet Identification and Reconstruction	244
6.3	Definition of Categories	245
6.3.1	VBF-like Section	245
6.3.2	Hadronic VH-like Selection	251
6.3.3	Leptonic VH-like Selection	257
6.3.4	ggF-like Selection	257
6.4	Expected Yields and Signal MC	257
6.5	Reducible Background	259
6.6	Systematic Uncertainties	260
6.7	Higgs Categorized Candidates	263
6.8	Summary	266

Chapter Bibliography	268
7 $H \rightarrow ZZ^{(*)} \rightarrow 4\ell$ Prospect Studies	269
7.1 Introduction	269
7.2 Categories Event Selection	271
7.2.1 $t\bar{t}H, H \rightarrow ZZ^{(*)}$	271
7.2.2 $VH, V = Z \text{ or } W, H \rightarrow ZZ^{(*)}$	272
7.2.3 $VBF, H \rightarrow ZZ^{(*)}$	273
7.2.4 $ggF, H \rightarrow ZZ^{(*)}$	273
7.3 Simulation Procedure	274
7.4 Systematic Uncertainties	274
7.5 $3000 \text{ } fb^{-1}$ Results	276
7.6 Comparison with the Full Analysis at 8 TeV	276
7.7 Study of the VBF Category with Higher Jet Fake Rate	277
7.8 $300 \text{ } fb^{-1}$ Results	279
7.9 Large- η Acceptance Scenario	280
7.10 Run-II Projections	282
7.11 Summary	285
Chapter Bibliography	287
Appendices	289
A RunI MC Samples List	291
A.0.1 Signal Samples	291
A.0.2 ZZ background samples	299
A.0.3 Reducible Background Samples	301
B HL-LHC MC Samples List	307
C Test Fit Distributions	309
List of Figures	319
List of Tables	323

Acknowledgments

I would like to express my gratitude to my advisor D. Fassouliotis who guided me through my studies in particle physics, from the undergraduate level to the Ph.D. His constant support, patience and encouragement were crucial for my academic progress and helped to keep things in perspective.

I would like to deeply thank M. Schernau, who willingly accepted to share his detector and DAQ knowledge with me and devoted significant time for our scientific discussions.

I am honestly grateful to C. Kourkoumelis and V. Polychronakos who gave me the chance to collaborate and be financially supported by the University of Athens and the Brookhaven National Laboratory respectively. Looking further back in time, I would like to thank P. Ioannou who first introduced me to the Athens ATLAS particle physics group.

I would like to thank the SLAC team for the opportunity to be part of the NRC group, specifically M. Huffer, D. Su, R. Bartoldus, R. Claus, N. Garelli, L. Ruckman, C. Young. Also, I would like to thank R. Murillo (ex-UCI) for his inadequate help, not only with the NRC.

I would like to thank my colleagues and especially A. Antonaki, S. Angelidakis, N. Tsirintanis, A. Kourkoumeli, E. Tiouchichine for the professional interaction and friendship.

I would like to thank my family and friends (all around the world) for their long-term support.

Last but not least, I do not forget all those who inspired me in any way ...

Εκτενής Ελληνική Περίληψη

Ένα από τα πρωταρχικά αναπάντητα ερωτήματα της σύγχρονης σωματιδιακής φυσικής αφορά στην προέλευση της μάζας. Στα πλαίσια του Καθιερωμένου Πρότυπου των στοιχειωδών σωματιδίων, το σπάσιμο της ηλεκτρασθενούς συμμετρίας και κατ' επέκταση οι παρατηρούμενες μάζες των φορέων της ασθενούς αλληλεπίδρασης και των σωματιδίων της ύλης, οφείλεται στο μηχανισμό *Higgs*. Άμεση συνέπεια του μηχανισμού *Higgs* είναι η ύπαρξη του μποζονίου *Higgs*, το οποίο αποτελούσε το μοναδικό σωματίδιο του Καθιερωμένου Πρότυπου που δεν είχε ακόμη παρατηρηθεί κατά την έναρξη της εκπόνησης της παρούσας διδακτορικής διατριβής.

Ως εκ τούτου, ένας από τους σημαντικούς στόχους του ερευνητικού προγράμματος του *LHC* (*Large Hadron Collider*) και του ανιχνευτή *ATLAS* στο *CERN* ήταν η ανακάλυψη του μποζονίου *Higgs*. Μια από τις υπογραφές που συνεισέφερε σημαντικά στην ανακάλυψη του μποζονίου *Higgs* ήταν η $H \rightarrow ZZ^{(*)} \rightarrow 4l$, όπου $l = e, \mu$. Η παρούσα διδακτορική διατριβή αφορά στη βελτιστοποίηση και πιστοποίηση με πραγματικά δεδομένα των κριτηρίων επιλογής για την εν λόγω υπογραφή, ενώ ακόμη μελετούνται διεξοδικά οι συνεισφορές υποβάθρου και αναπτύσσονται μέθοδοί για τον υπολογισμό τους από τα πραγματικά δεδομένα. Εν συνεχεία, μελετώνται τα επιπλέον χαρακτηριστικά των υποψήφιων γεγονότων που φωτίζουν τους μηχανισμούς παραγωγής του. Δεδομένου ότι περισσότερα υποψήφια γεγονότα απαιτούνται για να ενταχθεί το *Higgs* σε κάποιο θεωρητικό πρότυπο, η ευαισθησία του καναλιού στα επόμενα χρόνια της λήψης δεδομένων του *LHC* μελετάτε.

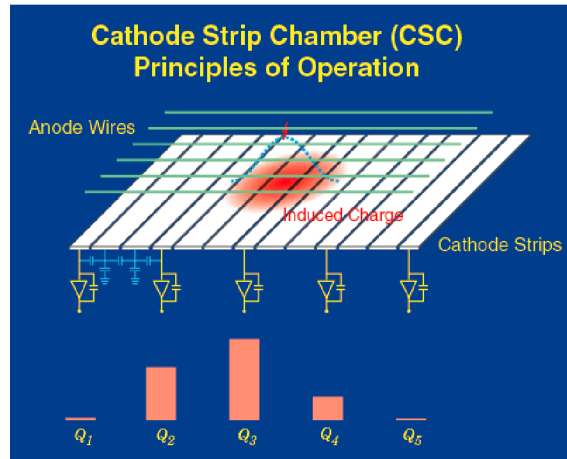
Δεδομένης της ύπαρξης τεσσάρων λεπτονίων στην τελική κατάσταση, προϋπόθεση για την επιτυχή έκβαση της συγκεκριμένης έρευνας αποτέλεσε η μεγιστοποίηση της αποδοχής και απόδοσης στην ανακατασκευή και αναγνώριση των ηλεκτρονίων και των μιονίων. Κατά συνέπεια, ένα σημαντικό ερευνητικό μέρος της διατριβής εστιάζεται στην ανίχνευση των λεπτονίων, και συγκεκριμένα των μιονίων στην εμπρόσθια περιοχή του πειράματος *ATLAS*. Συγκεκριμένα, βελτιώθηκε το λογισμό ανακατασκευής, διεξάχθηκαν μελέτες απόδοσης και υπήρξε μεγάλη συνεισφορά στον τομέα λήψης δεδομένων για τη λειτουργία του ανιχνευτή τόσο στο *Run - I* όσο και από το 2015 και μετέπειτα.

Τα πειραματικά δεδομένα που αναλύθηκαν είναι 4.5 fb^{-1} σε ενέργεια κέντρου μάζας $\sqrt{s} = 7 \text{ TeV}$ και 20.3 fb^{-1} σε $\sqrt{s} = 8 \text{ TeV}$. Τα δεδομένα αυτά καταγράφηκαν τα έτη 2011 και 2012 αντίστοιχα.

0.1 Θάλαμοι Καθοδικών Λωρίδων (CSC)

Οι θάλαμοι καθοδικών λωρίδων είναι εγκατεστημένοι στην πολύ ευπρόσθια περιοχή του πειράματος *ATLAS* ($2.0 \leq \eta \leq 2.7$) και συμβάλλουν στην ανίχνευση μιονίων. Η λειτουργία τους βασίζεται στο προσδιορισμό σήματος από τα πολλαπλά καλώδια που απαρτίζουν τους θαλάμους, όπως παρουσιάζει η Εικόνα 1. Υπάρχουν 16 θάλαμοι σε κάθε πλευρά του ανιχνευτή, διαδοχικά μικροί και μεγάλοι σε μέγεθος, που μερικώς αλληλοκαλύπτονται. Η πληροφορία τους διαβάζεται από μια διαδοχή δύο ηλεκτρικών συστημάτων, όπου τα μεν πρώτα προσάπτονται στους θαλάμους με σκοπό να μεταδώσουν τα δεδομένα στα επόμενα ηλεκτρονικά και τα δε δεύτερα είναι απομακρυσμένα από την περιοχή των θαλάμων και αφαιρούν τη μη χρήσιμη πληροφορία από τα δεδομένα. Τα 'απομακρυσμένα' ηλεκτρονικά αντικαταστάθηκαν πριν το *Run - II* λόγο της περιορισμένης ικανότητας τους να επεξεργαστούν μεγάλο όγκο δεδομένων. Συγκεκριμένα στο *Run - I*, προκειμένου να τρέξει το σύστημα στον όλο και αυξανόμενο ρυθμό σκανδαλισμού χρειάστηκε να μειωθεί ο αριθμός δειγματοληψίας από 4 σε 2 δείγματα και να προσαρμοστούν τα υπόβαθρα δειγματοληψίας.

Σχήμα 1: Αρχή λειτουργίας των Θαλάμων Καθοδικών Λωρίδων (CSC).



Η αναλυτική ανακατασκευή της πληροφορίας για τον προσδιορισμό τροχιών μιονίων στα *CSC* βασίζεται στο προσδιορισμό του φορτίου που εναποτέθηκε σε κάθε λωρίδα, στο σχηματισμό συμπλεγμάτων φορτίου και στο συσχετισμό αυτών στις διάφορες λωρίδες. Μια καινούργια μέθοδος αναπτύχθηκε για την βαθμονόμηση του φορτίου και κατέληξε σε βελτιωμένη ποιότητα τροχιάς με χωρική διακριτική ικανότητα που υπολογίζεται στα $78.6 \pm 0.5 \mu m$.

Η απόδοση της λειτουργίας μελετήθηκε για ολόκληρο το *Run - I*, ξεχωριστά για κάθε περίοδο λήψης δεδομένων με διαφορετικά κριτήρια (Πίνακας 1) και ξεχωριστά για θαλάμους που εμφάνισαν λειτουργικά προβλήματα (Πίνακας 2). Σε κάθε περίπτωση η απόδοση παρέμενε υψηλή.

Πίνακας 1: Πίνακας απόδοσης Θαλάμων Καθοδικών Λωρίδων για κάθε περίοδο λήψης δεδομένων με διαφορετικά κριτήρια.

Επιλογή	Απόδοση (%)			
	4-δείγματα	2-δείγματα	Wrong Latency, $\eta > 50, \phi > 60$ ADCcounts	Correct Latency, $\eta > 40, \phi > 60$ ADCcounts
$> 1 \eta/\text{τροχιά}$	98.947 ± 0.014	98.956 ± 0.014	~ 94	98.744 ± 0.008
$> 1 \phi/\text{τροχιά}$	97.746 ± 0.017	97.729 ± 0.020	~ 87	97.699 ± 0.012
$> 1 \text{ ποιοτικά } \eta/\text{τροχιά}$	91.77 ± 0.04	91.92 ± 0.04	~ 85	90.870 ± 0.023
$Z \text{ Tag\&Probe}$	98.915 ± 0.014	98.873 ± 0.016	~ 98	98.764 ± 0.019

Πίνακας 2: Πίνακας απόδοσης Θαλάμων Καθοδικών Λωρίδων για θαλάμους που εμφάνισαν λειτουργικά προβλήματα.

Επιλογή	Απόδοση (%)		
	$C03, A05, A09$ 1 μη λειτουργικό στρώμα	$C01$ 2 μη λειτουργικά στρώματα	$C05$ Μειωμένη Λειτουργία
$> 1 \eta/\text{τροχιά}$	98.671 ± 0.025	85.30 ± 0.014	89.70 ± 0.04
$> 1 \phi/\text{τροχιά}$	96.96 ± 0.04	91.67 ± 0.14	97.20 ± 0.06
$> 1 \text{ ποιοτικά } \eta/\text{τροχιά}$	89.75 ± 0.08	59.4 ± 0.19	86.40 ± 0.12
$Z \text{ Tag\&Probe}$	98.52 ± 0.04	97.52 ± 0.04	98.71 ± 0.04

0.2 Μελέτη των Διασπάσεων $H \rightarrow ZZ^{(*)} \rightarrow 4\ell$

Το $H \rightarrow ZZ^{(*)} \rightarrow 4\ell$ είναι η καθαρότερη υπογραφή του μποζονίου *Higgs*. Οι διασπάσεις των υποψήφιων γεγονότων ξεκινά με την επιλογή καλής ποιότητας λεπτονίων που σκανδάλισαν το καταγεγραμμένο γεγονός. Ειδικότερα, τα λεπτόνια απαιτείται να δημιουργούν ανά δύο ζεύγη ίδιας γεύσης και αντίθετου φορτίου που να πληρούν περιορισμούς ορίων μαζών, να είναι απομονωμένα και να προέρχονται από τον πρωτεύουσα κορυφή του γεγονότος. Οι πιθανές τελικές καταστάσεις είναι $4e, 2\mu 2e, 2e 2\mu, 4\mu$.

Το υπόβαθρο καθορίζεται από την διάσπαση του δυνητικού Z μποζονίου και ανάλογα χωρίζεται σε υπόβαθρο ηλεκτρονίων ή μιονίων. Συνολικά στο υπόβαθρο συγκαταλέγονται οι εξής διαδικασίες:

- $ZZ^{(*)}/\gamma \rightarrow 4\ell$: Ονομάζεται και αμείωτο υπόβαθρο γιατί έχει την ίδια τοπολογία με το σήμα.
- Μειώσιμο υπόβαθρο: περιλαμβάνει διαδικασίες $Z + \pi\text{ίδακες}$ και $t\bar{t}$ και μπορεί να περιοριστεί με κατάλληλη επιλογή κριτηρίων απομόνωσης λεπτονίων ή περιορισμών που

αφορούν την καρυφή από την οποία προέρχονται τα λεπτόνια.

Το λεγόμενο μειώσιμο υπόβαθρο υπολογίζεται απευθείας από τα πραγματικά δεδομένα ενώ το αμείωτο εκτιμάται από την προσομοίωση. Η διατριβή εστιάστηκε στη μέτρηση του μειώσιμου υποβάθρου μιονίων με χρήση ταυτόχρονης προσαρμογής σε τέσσερις περιοχές ελέγχου. Αυτές οι περιοχές δημιουργούνται από χαλάρωση ή αντιστροφή κριτηρίων στα μιόνια προερχόμενα από το δυνητικό μποζόνιο Z (το επονομαζόμενο δευτερεύον ζεύγος):

- Περιοχή ελέγχου Zbb : σχηματίζεται αντιστρέφοντας το κριτήριο προέλευσης από τον πρωτεύοντα άξονα στο δευτερεύον ζεύγος
- Περιοχή ελέγχου $Zlight$: σχηματίζεται αντιστρέφοντας το κριτήριο απομόνωσης και επιβάλλοντας το κριτήριο προέλευσης από τον πρωτεύοντα άξονα στο δευτερεύον ζεύγος
- Γενική Περιοχή ελέγχου: σχηματίζεται από δευτερεύον ζεύγος ίδιου φορτίου
- Περιοχή ελέγχου $t\bar{t}$: σχηματίζεται από γεγονότα εμ+μ.

Η ταυτόχρονη προσαρμογή στη μάζα του πρώτου ζεύγους (παρουσιάζεται στο Σχήμα 2) υπολογίζει ξεχωριστά τις πηγές υποβάθρου Zbb , $Zlight$ και $t\bar{t}$ σε μια άλλη περιοχή ελέγχου που φτιάχνεται από γεγονότα αντίθετου φορτίου στο δευτερεύον ζεύγος αλλά χωρίς επιβολή κριτηρίων απομόνωσης και προέλευσης από τον πρωτεύοντα άξονα. Η περιοχή αυτή δε συγκαταλέγεται άμεσα στην ταυτόχρονη προσαρμογή λόγο του ότι η περιοχή σήματος είναι μέρος αυτής.

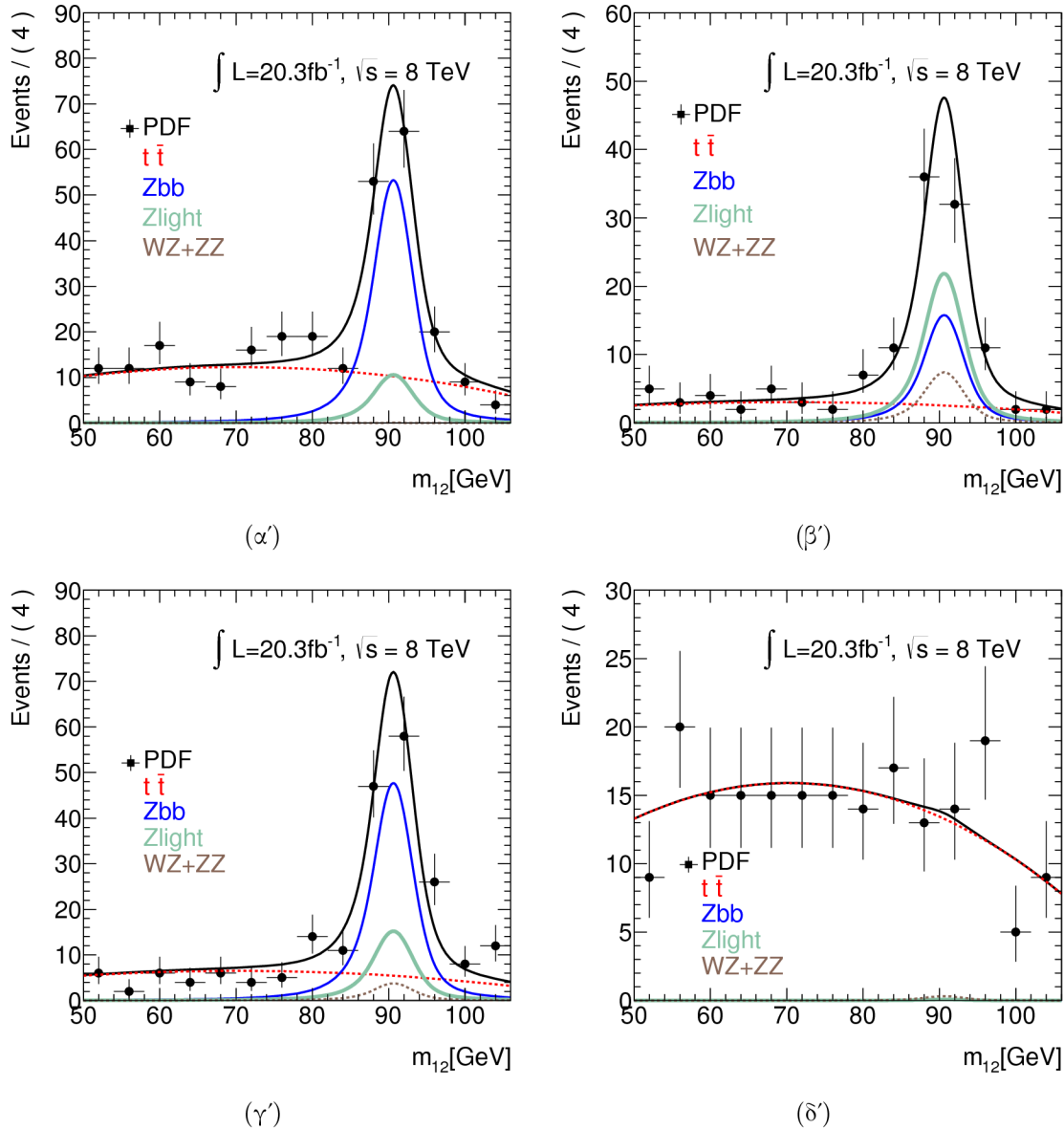
Η συνεισφορά των εκτιμώμενων υποβάθρων στην περιοχή σήματος υπολογίζεται λαμβάνοντας υπόψη την πιθανότητα κάθε τύπου υποβάθρου να πληρεί τα κριτήρια απομόνωσης και προέλευσης από τον πρωτεύοντα άξονα, όπως προβλέπεται από την προσομοίωση. Συγκεντρωτικά τα αποτελέσματα για το $Run - I$ παρουσιάζονται στον Πίνακα 3 και οι μάζες δείχνονται στην Εικόνα 3.

0.3 Μελέτη των Μηχανισμών Παραγωγής του Μποζόνιου $Higgs$

Μετά την ανακάλυψη του $Higgs$ το ενδιαφέρον στράφηκε στη μελέτη των ιδιοτήτων του, μια εκ των οποίων είναι ο μηχανισμός παραγωγής. Αναπτύχθηκαν και εφαρμόστηκαν μέθοδοι για την εύρεση του μηχανισμού παραγωγής του μποζονίου $Higgs$. Θεωρητικά το $Higgs$ θα μπορούσε να παραχθεί από τις παρακάτω διαδικασίες:

- Αλληλεπίδραση διανυσματικών Μποζονίων (VBF): χαρακτηρίζεται από την ύπαρξη δύο πιδάκων ενέργειας που παράγονται σε αντίθετο ημισφαίριο

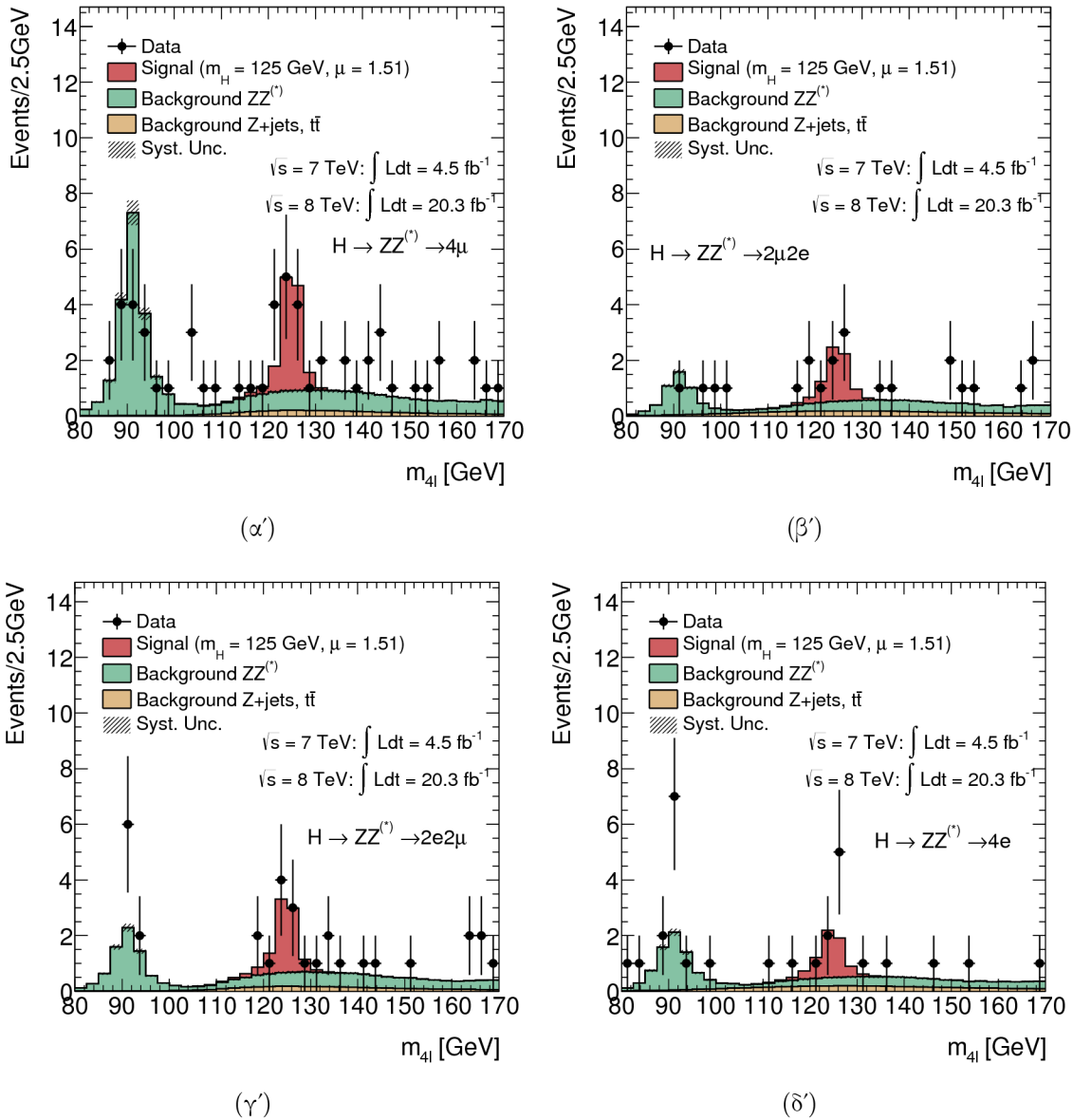
Σχήμα 2: Η ταυτόχρονη προσαρμογή στις τέσσερις περιοχές ελέγχου για τον υπολογισμό των Zbb , $Zlight$ και $t\bar{t}$ υποβάθμων. Οι περιοχές ελέγχου σχηματίζονται ως: (α') αντιστρέφοντας το χριτήριο προέλευσης από τον πρωτεύοντα στο δευτερεύον ζεύγος, (β') αντιστρέφοντας το χριτήριο απομόνωσης και επιβάλλοντας το χριτήριο προέλευσης από τον πρωτεύοντα στο δευτερεύον ζεύγος, (γ') από δευτερεύον ζεύγος ίδιου φορτίου και (δ') από γεγονότα εμπρ.



Πίνακας 3: Αποτελέσματα υπολογιζόμενου σήματος και υπόβαθρου για το κανάλι $H \rightarrow ZZ^{(*)} \rightarrow 4\ell$. Οι θεωρητικές προβλέψεις επίσης παρουσιάζονται.

	$\Sigma_{\text{ήμα}}$	$\Sigma_{\text{ήμα}}$ $\sim 125 \text{ GeV}$	ZZ	$Z + \text{πιδωκες}, t\bar{t}$	S/B	Αναμενόμενα	Παρατηρούμενα
$\sqrt{s} = 7 \text{ TeV}$							
4μ	1.00 ± 0.10	0.91 ± 0.09	0.46 ± 0.02	0.10 ± 0.04	1.7	1.47 ± 0.10	2
$2e2\mu$	0.66 ± 0.06	0.58 ± 0.06	0.32 ± 0.02	0.09 ± 0.03	1.5	0.99 ± 0.07	2
$2\mu2e$	0.50 ± 0.05	0.44 ± 0.04	0.21 ± 0.01	0.36 ± 0.08	0.8	1.01 ± 0.09	1
$4e$	0.46 ± 0.05	0.39 ± 0.04	0.19 ± 0.01	0.40 ± 0.09	0.7	0.98 ± 0.10	1
$\Sigma_{\text{ύνολο}}$	2.62 ± 0.26	2.32 ± 0.23	1.17 ± 0.06	0.96 ± 0.18	1.1	4.45 ± 0.30	6
$\sqrt{s} = 8 \text{ TeV}$							
4μ	5.80 ± 0.57	5.28 ± 0.52	2.36 ± 0.12	0.69 ± 0.13	1.7	8.33 ± 0.6	12
$2e2\mu$	3.92 ± 0.39	3.45 ± 0.34	1.67 ± 0.08	0.60 ± 0.10	1.5	5.72 ± 0.37	7
$2\mu2e$	3.06 ± 0.31	2.71 ± 0.28	1.17 ± 0.07	0.36 ± 0.08	1.8	4.23 ± 0.30	5
$4e$	2.79 ± 0.29	2.38 ± 0.25	1.03 ± 0.07	0.35 ± 0.07	1.7	3.77 ± 0.27	7
$\Sigma_{\text{ύνολο}}$	15.6 ± 1.6	13.8 ± 1.4	6.24 ± 0.34	2.00 ± 0.28	1.7	22.1 ± 1.5	31
$\sqrt{s} = 7 \text{ TeV} \text{ και } \sqrt{s} = 8 \text{ TeV}$							
4μ	6.80 ± 0.67	6.20 ± 0.61	2.82 ± 0.14	0.79 ± 0.13	1.7	9.81 ± 0.64	14
$2e2\mu$	4.58 ± 0.45	4.04 ± 0.40	1.99 ± 0.10	0.69 ± 0.11	1.5	6.72 ± 0.42	9
$2\mu2e$	3.56 ± 0.36	3.15 ± 0.32	1.38 ± 0.08	0.72 ± 0.12	1.5	5.24 ± 0.35	6
$4e$	3.25 ± 0.34	2.77 ± 0.29	1.22 ± 0.08	0.76 ± 0.11	1.4	4.75 ± 0.32	8
$\Sigma_{\text{ύνολο}}$	18.2 ± 1.8	16.2 ± 1.6	7.41 ± 0.40	2.95 ± 0.33	1.6	26.5 ± 1.7	37

Σχήμα 3: Μάζες m_{4l} για τα υποψήφια *Higgs* γεγονότα για $\sqrt{s} = 7$ και 8 TeV , όπου η θεωρητική πρόβλεψη του σήματος είναι αυξημένη κατά 1.51. Οι μάζες αφορούν τα διάφορα λεπτονικά κανάλια (α') 4μ , (β') $2\mu 2e$, (γ') $2e 2\mu$, (δ') $4e$.



Πίνακας 4: Θεωρητικές ενεργές διατομές των διαφόρων μηχανισμών παραγωγής για $\sqrt{s} = 7 \text{ TeV}$ και $\sqrt{s} = 8 \text{ TeV}$.

Παραγωγή	$\sqrt{s} = 7 \text{ TeV}$		$\sqrt{s} = 8 \text{ TeV}$	
	Ενεργός Διατομή [pb]	Ποσοστό [%]	Ενεργός Διατομή [pb]	Ποσοστό [%]
$gg \rightarrow H$	15.1	86.4	19.3	86.4
$qq' \rightarrow Hqq'$	1.22	7.0	1.58	7.1
$q\bar{q} \rightarrow WH$	0.579	3.3	0.705	3.2
$q\bar{q} \rightarrow ZH$	0.335	1.9	0.415	1.9
$q\bar{q}/gg \rightarrow t\bar{t}H$	0.086	0.5	0.13	0.6

- Παραγωγή συσχετισμένη με μποζόνια W ή Z (WH , ZH): ανίχνευση μέσω της διάσπασης των W ή Z , που μπορεί να είναι είτε αδρονική είτε λεπτονική. Στη μεν πρώτη ανιχνεύονται πίδακες ενέργειας συμβατοί με τη μάζα των W ή Z , ενώ στη δε δεύτερη λεπτόνια συμβατά με διασπάσεις W ή Z .
- Παραγωγή συσχετισμένη με ζεύγη $t\bar{t}$ ή $b\bar{b}$ (ttH , bbH): ανιχνεύονται μέσω των ζευγών $t\bar{t}$ ή $b\bar{b}$
- Αλληλεπίδραση γλυκονίων (ggH): όταν καμία από τις παραπάνω παραγωγές δεν ανιχνεύεται.

Λόγω της χαμηλής ενεργού διατομής, όπως φαίνεται από τον Πίνακα 4, για το $Run - I$ οι παραγωγές συσχετισμένες με ζεύγη $t\bar{t}$ ή $b\bar{b}$ δε λαμβάνονται υπόψη στην κατάταξη των υποψήφιων *Higgs* γεγονότων.

Η κατηγοριοποίηση των γεγονότων ξεκινά με την περίπτωση αλληλεπίδρασης διανυσματικών μποζονίων, όπου πίδακες αναλλοίωτης μάζας μεγαλύτερης των 130 GeV διαχωρίζονται με μέθοδο ανάλυσης πολλών μεταβλητών. Αυτές οι μεταβλητές είναι η μάζα των πιδάκων ενέργειας, ο διαχωρισμός τους σε επίπεδο ψευδοωκύτητας, οι εγκάρσιες ορμές και των δύο και η ψευδοωκύτητα του πίδακα με τη μεγαλύτερη ορμή.

Αν το γεγονός δεν είναι συμβατό με αλληλεπίδραση διανυσματικών μποζονίων, τότε μελετάτε η πιθανότητα να προέρχεται από παραγωγή συσχετισμένη με μποζόνια W ή Z που διασπώνται αδρονικά. Σε αυτή την περίπτωση οι πίδακες ενέργειας απαιτείται να έχουν μάζα μικρότερη από 130 GeV ώστε να είναι συμβατοί με τις μάζες των W ή Z . Εν συνεχεία, μια μέθοδος ανάλυσης πολλών μεταβλητών, με τις ίδιες μεταβλητές όπως στην προηγούμενη κατηγορία, εφαρμόζεται.

Αν το γεγονός δεν πέρασε καμία από τις παραπάνω κατηγοριοποίήσεις τότε ερευνάται η πιθανότητα να προέρχεται από παραγωγή συσχετισμένη με μποζόνια W ή Z που διασπώνται λεπτονικά. Το γεγονός πρέπει να έχει τουλάχιστον ένα επιπλέον λεπτόνιο των τεσσάρων

Πίνακας 5: Αποτελέσματα της μελέτης των μηχανισμών παραγωγής.

Κατηγορία	Σήμα				Τπόβαθρο		Συνολικά	Παρατηρούμενα
	$ggF + b\bar{b}H + t\bar{t}H$	VBF	VH –αδρονική	VH –λεπτονική	$ZZ^{(*)}$	$Z + \pi\delta\chi\epsilon$, $t\bar{t}$ Αναμενόμενα		
$120 < m_{4\ell} < 130$ GeV								
VBF	1.18 ± 0.37	0.75 ± 0.04	0.083 ± 0.006	0.013 ± 0.001	0.17 ± 0.03	0.25 ± 0.14	2.4 ± 0.4	3
VH –αδρονική	0.40 ± 0.12	0.034 ± 0.004	0.20 ± 0.01	0.009 ± 0.001	0.09 ± 0.01	0.09 ± 0.04	0.80 ± 0.12	0
VH –λεπτονική	0.013 ± 0.002	< 0.001	< 0.001	0.069 ± 0.004	0.015 ± 0.002	0.016 ± 0.019	0.11 ± 0.02	0
ggF	12.8 ± 1.3	0.57 ± 0.02	0.24 ± 0.01	0.11 ± 0.01	7.1 ± 0.2	2.7 ± 0.4	23.5 ± 1.4	34
$110 < m_{4\ell} < 120$ GeV								
VBF	1.4 ± 0.4	0.82 ± 0.05	0.092 ± 0.007	0.022 ± 0.002	$20. \pm 4.$	1.6 ± 0.9	$24. \pm 4.$	32
VH –αδρονική	0.46 ± 0.14	0.038 ± 0.004	0.23 ± 0.01	0.015 ± 0.001	9.0 ± 1.2	0.6 ± 0.2	10.3 ± 1.2	13
VH –λεπτονική	0.026 ± 0.004	< 0.002	< 0.002	0.15 ± 0.01	0.63 ± 0.04	0.11 ± 0.14	0.92 ± 0.16	1
ggF	14.1 ± 1.5	0.63 ± 0.02	0.27 ± 0.01	0.17 ± 0.01	$351. \pm 12.$	16.6 ± 2.2	$383. \pm 12.$	420

λεπτονίων που πληρεί τις προϋποθέσεις απομόνωσης και προέλευσης από τον πρωτεύον άξονα.

Σε περίπτωση που δεν πληρείται καμία από τις παραπάνω προϋποθέσεις το γεγονός θεωρείται ότι είναι προϊόν αλληλεπίδρασης γλυουνίων.

Από την ανάλυση των δεδομένων του *Run – I* 3 υποψήφια γεγονότα βρέθηκαν για παραγωγή μέσο αλληλεπίδρασης διανυσματικών μποζονίων και η θεωρητική πρόβλεψη είναι 2.4. Όλα τα υπόλοιπα γεγονότα ανήκουν στη παραγωγή μέσω αλληλεπίδρασης γλουονίων, ενώ καμία από τις υπόλοιπες κατηγορίες δεν παρατηρήθηκε. Συνοπτικά τα αποτελέσματα παρουσιάζονται στον Πίνακα 5.

0.4 Πρόβλεψη Μελλοντικής Ευαισθησίας του $H \rightarrow ZZ^{(*)} \rightarrow 4\ell$

Λόγω της μικρής παραγωγής γεγονότων με μποζόνια *Higgs* στην τελική κατάσταση απαιτείται η συλλογή μεγάλου όγκου δεδομένων ώστε να κατανοηθεί πλήρως η φύση του σωματιδίου, συμπεριλαμβανομένων των μηχανισμών παραγωγής. Επομένως, ενδιαφέρον παρουσιάζει η μελέτη της ευαισθησίας του καναλιού στο μελλοντικό πρόγραμμα του *LHC*. Συγκεκριμένα θεωρείται ότι λήψη δεδομένων θα πραγματοποιηθεί σε $\sqrt{s} = 14$ TeV και συνολικά θα συγκεντρωθούν $3000 fb^{-1}$ δεδομένων.

Η κατηγοριοποίηση ξεκινά από τους μηχανισμούς με χαμηλότερη ενεργό διατομή ώστε να αυξηθεί η ευαισθησία τους. Δηλαδή, η σειρά που ακολουθείται είναι $t\bar{t}H$, ZH , WH , VBF και ggF αν δεν ανήκει σε καμία από τις προηγούμενες διαδικασίες. Σε αυτή την περίπτωση η πιθανότητα παραγωγής συσχετισμένη με $t\bar{t}H$ δεν είναι αμελητέα και δεν μπορεί να αγνοηθεί. Η επιλογή γίνεται μέσω κριτηρίων που αποσκοπούν στην ανάδειξη του εκάστοτε μηχανισμού αποφεύγοντας επικάλυψη με άλλους μηχανισμούς.

Τα αποτελέσματα της μελέτης που βασίστηκε σε προσομοίωση συνοψίζονται στον Πίνα-

κα 6. Είναι εμφανές ότι η ανίχνευση του μηχανισμού θα μπορέσει να καθοριστεί με αυτό τον όγκο δεδομένων.

Πίνακας 6: Πρόβλεψη των γεγονότων από τους πιθανούς μηχανισμούς παραγωγής υπόθετοντας μάζα $Higgs m_H = 125 \text{ GeV}$ και 3000 fb^{-1} δεδομένων.

Κατηγορία	ggF	VBF	WH	ZH	ttH	Υπόβαθρο
ttH	3.1 ± 1.0	0.6 ± 0.1	0.6 ± 0.1	1.1 ± 0.2	30 ± 6	0.6 ± 0.2
ZH	0.0	0.0	0.01 ± 0.02	4.4 ± 0.3	1.3 ± 0.3	0.06 ± 0.06
WH	22 ± 7	6.6 ± 0.4	25 ± 2	4.4 ± 0.3	8.8 ± 1.8	13 ± 0.8
VBF	41 ± 14	54 ± 6	0.7 ± 0.1	0.4 ± 0.1	1.0 ± 0.2	4.2 ± 1.5
ggF	3380 ± 650	274 ± 17	77 ± 5	53 ± 3	25 ± 4	2110 ± 50

Επιπλέον με τα παραπάνω μελετήθηκε η περίπτωση αύξησης της κάλυψης μιονικών θαλάμων, εσωτερικού ανιχνευτή και μαγνητών, ώστε τα μιόνια να μπορούν να ανιχνευτούν μέχρι την περιοχή ψευδοωκύτητας $\eta \leq 4.0$. Το σενάριο αυτό δεν περιλαμβάνει καμία αλλαγή στην ανίχνευση ηλεκτρονίων και επομένως επηρεάζει χυρίως το 4μ κανάλι. Τα πιθανά οφέλη παρουσιάζονται στον Πίνακα 7. Είναι εμφανές ότι θα βελτιωθεί σημαντικά η ακρίβεια μέτρησης των ρυθμών παραγωγής του μποζονίου $Higgs$ με τους υπο μελέτη μηχανισμούς, σε αυτό το σενάριο, αλλά η μελέτη των ιδιοτήτων του $Higgs$ δεν επωφελείται σημαντικά λόγω της μεγάλης αύξησης του υποβάθρου.

Πίνακας 7: Πρόβλεψη των 4μ γεγονότων από τους πιθανούς μηχανισμούς παραγωγής υπόθετοντας μάζα $Higgs m_H = 125 \text{ GeV}$, 3000 fb^{-1} δεδομένων και επέκταση την περιοχής ανίχνευσης μιονίων.

	Προσομοιωμένα Σήματα					
	ggF	VBF	WH	ZH	ttH	Υπόβαθρο
$\eta < 2.7$	3439	335	104	64	66	2126
$\eta < 4.0$	3765	361	116	72	68	2493
Σταθμισμένο Όφελος	9.49%	7.88%	11.92%	11.88%	3.81%	17.30%
Πραγματικό Όφελος	12.04%	9.85%	15.97%	15.46%	4.31%	26.86%

1

1

2

Theory Introduction

3 1.1 Introduction

4 The Standard Model, the theory attempting to describe the particle physics, is
5 briefly introduced in this chapter, mainly focused on the Higgs mechanism. Start-
6 ing from the electroweak theory, the spontaneous symmetry breaking mechanism and
7 the Goldstone bosons are explained. After the short theoretical introduction, the pro-
8 duction phenomenology of the Higgs boson at hadron colliders and the sensitivity of
9 observing it are explored. Both theoretical and experimental constraints on the Higgs
10 boson mass are also presented.

11 The theory decomposes the complexity of the elementary particles of the ordinary
12 matter and the interactions taking place between them to two group of particles, the
13 quarks and the leptons, and a set of four force carriers [1], schematically shown in
14 Figure 1.1.

15 Leptons are spin- $\frac{1}{2}$ particles which do not take part in the strong interactions. They
16 compose three generations formed by the integer charged lepton and the relevant neu-
17 trino [2]. Besides the charge, leptons have also different masses. Individually, they are
18 denoted as $e, \mu, \tau, \nu_e, \nu_\mu, \nu_\tau$ or collectively by ℓ [3]. Their basic properties are summa-
19 rized in table 1.1.

20 The quarks (q) are fractionally charged spin- $\frac{1}{2}$ strongly interacting particles which
21 are known to form the composites collectively called hadrons. Two categories of hadrons
22 are known, the mesons and the baryons. Mesons are made up from a quark and an

Figure 1.1: Schematic view of the building blocks of the ordinary matter, the quarks and the leptons, along with the force carriers [1].

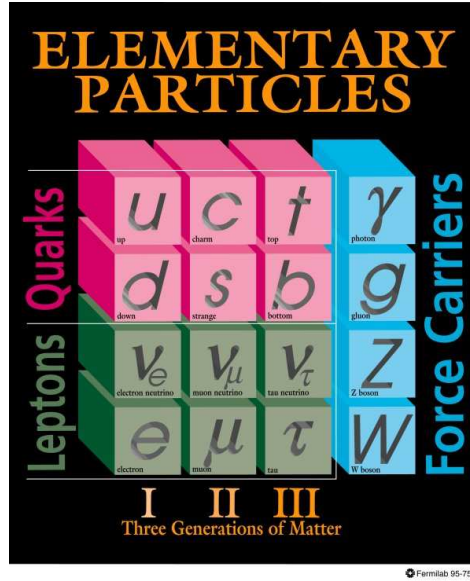


Table 1.1: Summary of the lepton types along with their basic properties, charge, mass and mean life time [2].

Lepton	Charge	Mass	Mean Life
e	-1	$0.510998928 \pm 0.000000011$ MeV	$> 4.6 \times 10^{26}$ years
μ	-1	$105.6583715 \pm 0.0000035$ MeV	$(2.1969811 \pm 0.0000022) \times 10^{-6}$ s
τ	-1	1776.82 ± 0.16 MeV	$(290.6 \pm 1.0) \times 10^{15}$ s
ν_e	0	< 225 eV (95% CL)	$> 15.4 \times \text{mass}$ s (90% CL)
ν_μ	0	< 0.19 MeV (90% CL)	$> 15.4 \times \text{mass}$ s (90% CL)
ν_τ	0	< 18.2 MeV (95% CL)	$> 15.4 \times \text{mass}$ s (90% CL)

Table 1.2: Quark quantum numbers: charge Q , baryon number B , strangeness S , charm c , bottomness b , and topness t [4].

name	symbol	Q	B	S	c	b	t
up	u	$\frac{2}{3}$	$\frac{1}{3}$	0	0	0	0
down	d	$-\frac{1}{3}$	$-\frac{1}{3}$	0	0	0	0
strange	s	$-\frac{1}{3}$	$-\frac{1}{3}$	-1	0	0	0
charm	c	$\frac{2}{3}$	$\frac{1}{3}$	0	1	0	0
bottom	b	$-\frac{1}{3}$	$-\frac{1}{3}$	0	0	-1	0
top	t	$-\frac{1}{3}$	$\frac{1}{3}$	0	0	0	1

23 antiquark ($q\bar{q}$), consequently have integer spin, and are described by the Bose Statistics.
24 Baryons are a combination of three quarks (qqq), have half-integer spin and obey the
25 Fermi statistics. There are six different types of quarks, known as flavors: up (u),
26 down (d), strange (s), charm (c), bottom (b), and top (t); their properties are given
27 in Table 1.2. The antiquarks have opposite signs of electric charge, baryon number,
28 strangeness, charm, bottomness, and topness. The quarks carry "color" which enables
29 them to interact strongly with one another [4]. Each quark flavor can have three
30 colors usually designated red, green and blue and the antiquarks are colored antired,
31 antigreen and antiblue respectively. The composites the quarks create, are made up
32 of three quarks one of each color (baryons) or consist of a quark-antiquark pair of a
33 particular color and its anticolor (mesons). Both baryons and mesons are thus colorless
34 or white. Because the color is different for each quark, it serves to distinguish them
35 and allows the exclusion principle to hold.

36 Quarks and leptons are called fermions and interact via the four known basic forces
37 – gravitational, electromagnetic, strong, and weak – that can be characterized on the
38 basis of the following four criteria [4]: the types of particles that experience the force,
39 the relative strength of the force, the range over which the force is effective, and the
40 nature of the particles that mediate the force. The force carriers are the gauge bosons:
41 the electromagnetic force is carried by the spin-1 photon, the strong force is mediated
42 with the eight massless spin-1 gluons, the W^\pm and Z^0 spin-1 bosons transmit the weak
43 force, while no gravitational mediator has been observed yet. A comparison of the
44 approximate relative force strengths is given in Table 1.3. Gravity, on a nuclear scale,
45 is the weakest of the four forces and its effect at the particle level can nearly always be
46 ignored [4].

47 The electromagnetic and the weak interactions are unified after identifying them as
48 two different manifestations of a more fundamental (single) interaction, the electroweak
49 interaction. The so called "Glashow–Weinberg–Salam electroweak theory" [5, 6, 7] has
50 had many notable successes [8], culminating in the discovery of the predicted W^\pm and Z^0

Table 1.3: Relative strength of the four forces for two protons inside a nucleus [4].

Type	Relative Strength	Field Particle
Strong	1	gluons (g)
Electromagnetic	10^{-2}	photon (γ)
Weak	10^{-6}	W^\pm, Z^0 bosons
Gravitational	10^{-38}	graviton

51 bosons ($m_W = (80.385 \pm 0.015)$ GeV and $m_Z = (91.1876 \pm 0.0021)$ GeV) [2]. However,
52 the favored electroweak symmetry breaking mechanism indicated broken symmetries
53 and generated questions about the nature of the symmetry breaking.

54 1.2 The Standard Model Theory

55 The Standard Model is the theory that provides a unified framework to describe the
56 electromagnetic, weak and strong interactions between quarks and leptons [9, 10]. These
57 interactions are understood as due to the exchange of spin-1 bosons between the spin-
58 $\frac{1}{2}$ particles that make up matter [3]. In the Standard Model, the electroweak theory,
59 which is a Yang–Mills theory based on the symmetry group $SU(2)_L \times U(1)_Y$ [3, 10],
60 is combined with the strong interactions, an $SU(3)_C$ group based on a QCD gauge
61 theory [10].

62 The $SU(3)_C$ symmetry [11] is associated with the eight gluons ($8G_{\mu\nu}^\alpha$), the $SU(2)_L$
63 is associated with the W^\pm and Z^0 bosons ($3W_{\mu\nu}^\alpha$) and the factor $U(1)_Y$ with the photon
64 ($B_{\mu\nu}$) [3]. The conserved quantities, indicated as subscripts in the $SU(2)_L \times U(1)_Y \times SU(3)_C$
65 symmetry, are the isospin, hypercharge and color respectively. The model, before in-
66 troducing the electroweak symmetry breaking mechanism, has two kinds of fields:

- 67 • The matter fields for the three generations of left-handed and right-handed chiral
68 quarks and leptons [10, 8].
- 69 • The gauge fields corresponding to the spin-1 bosons that mediate the interactions

70 In the next sections the theoretical prerequisites and framework are briefly developed
71 in several steps. It has to be noted that the Gravity is not included in the SM theory.

1.2.1 Motion of Scalar and Pseudoscalar Fields

From the classical mechanics, it is known that the dynamics of a system can be summarized by the Lagrangian:

$$\mathcal{L} = \frac{1}{2} \partial_\mu \phi \partial^\mu \phi - \frac{1}{2} m^2 \phi^2 \quad (1.1)$$

and the relevant motion is described by the Euler-Lagrange equation:

$$\partial_\mu (\partial_\mu \phi \mathcal{L}) - \partial_\phi \mathcal{L} = 0. \quad (1.2)$$

By substituting the Lagrangian 1.1 into the Euler-Lagrange equation 1.2:

$$\partial_\mu \partial^\mu \phi + m^2 \phi \equiv (\square^2 + m^2) \phi = 0 \quad (1.3)$$

the result is the so called Klein-Gordon equation which describes the motion of scalar and Pseudoscalar fields.

1.2.2 Relativistic Wave Equation

The Hamiltonian of a system has the general form of:

$$H\psi = (\alpha \cdot \mathbf{P} + \beta m)\psi \quad (1.4)$$

where the α and β are determined by energy and momentum relations that a free particle must fulfill.

By multiplying the equation 1.4 by H , it transforms to:

$$\begin{aligned} H^2\psi &= (\alpha_i P_i + \beta m)(\alpha_j P_j + \beta m)\psi \\ &= (\alpha_i^2 P_i^2 + (\alpha_i \alpha_j + \alpha_j \alpha_i)P_i P_j + (\alpha_i \beta + \beta \alpha_i)P_i m + \beta^2 m^2)\psi. \end{aligned} \quad (1.5)$$

Taking into account that α and β all anti-commute with each other and $\alpha_1^2 = \alpha_2^2 = \alpha_3^2 = \beta^2 = 1$ [8], equation 1.5 transforms to:

$$H^2\psi = (\mathbf{P}^2 + m^2)\psi. \quad (1.6)$$

The lowest dimensionality matrices satisfying the above requirements are the 4×4 Dirac-Pauli matrices [8]:

$$\alpha = \begin{pmatrix} 0 & \boldsymbol{\sigma} \\ \boldsymbol{\sigma} & 0 \end{pmatrix} \quad \text{and} \quad \beta = \begin{pmatrix} \mathbf{I} & 0 \\ 0 & \mathbf{I} \end{pmatrix} \quad (1.7)$$

⁸⁸ where the I matrix denotes the unit 2×2 matrix and σ the Pauli matrices:

$$\sigma_1 = \begin{pmatrix} 0 & 1 \\ 1 & 0 \end{pmatrix}, \sigma_2 = \begin{pmatrix} 0 & -i \\ i & 0 \end{pmatrix}, \sigma_3 = \begin{pmatrix} 1 & 0 \\ 0 & -1 \end{pmatrix}. \quad (1.8)$$

⁸⁹ By replacing terms in equation 1.4 and multiplying by β , the equation transforms to
⁹⁰ the covariant form of the Dirac's equation:

$$\begin{aligned} i\beta\partial_t\psi &= -i\beta\alpha \cdot \vec{\nabla}\psi + m\psi \Leftrightarrow \\ &\Leftrightarrow (i\gamma^\mu\partial_\mu - m)\psi = 0. \end{aligned} \quad (1.9)$$

⁹¹ In the above equation the Dirac γ -matrices have been introduced ($\gamma^\mu \equiv (\beta, \beta\alpha)$).

⁹² The Dirac's Lagrangian should be reproduced by the Euler-Lagrange equation 1.2
⁹³ for independent fields such as the ψ and $\bar{\psi}$. A Lagrangian describing the behavior of
⁹⁴ spin- $\frac{1}{2}$ relativistic particle of mass m can be written as [4]:

$$\mathcal{L}_{\text{Dirac}} = \bar{\psi}(i\gamma^\mu\partial_\mu - m)\psi. \quad (1.10)$$

⁹⁵ 1.2.3 Symmetries

⁹⁶ The symmetries in physical systems are described by Noether's theorem [12] and
⁹⁷ are associated with conserved quantities equal in number with the number of symme-
⁹⁸ tries. For example, the invariance under rotations is related to the angular momentum
⁹⁹ conservation. Mathematically, a conserved quantity, also called current, follows the
¹⁰⁰ equation:

$$\partial_\mu J^\mu = 0. \quad (1.11)$$

¹⁰¹ The existence of a current implies that there must be a “charge” which acts as the
¹⁰² generator of the symmetry group.

¹⁰³ The interpretation of Noether's theorem in the particle physics case relates the glu-
¹⁰⁴ ons ($8G_{\mu\nu}^\alpha$), the W^\pm and Z^0 bosons and the photon (γ) to the fundamental interactions
¹⁰⁵ described by the symmetry groups of $SU(3)_C$, $SU(2)_L$, and $U(1)_Y$ respectively.

¹⁰⁶ The unitary Abelian group $U(1)$ is the simplest example of a local symmetry. The
¹⁰⁷ term local or internal stands for space-time invariant symmetries and it describes trans-
¹⁰⁸ formations such as the ensemble of wave function phase

$$\Psi \rightarrow e^{i\alpha}\Psi \quad (1.12)$$

$$\bar{\Psi} \rightarrow e^{-i\alpha}\bar{\Psi} \quad (1.13)$$

¹⁰⁹ where α can run continuously over real numbers.

¹¹⁰ To find the conserved current, the invariance of the Lagrangian \mathcal{L} under the in-
¹¹¹ finitesimal $U(1)$ transformations $\Psi \rightarrow (1 + i\alpha)\Psi$ needs to be studied [4]:

$$\begin{aligned}\delta\mathcal{L} &= \partial_\psi\mathcal{L} \delta\psi + \partial_{\partial_\mu\psi}\mathcal{L} \delta(\partial_\mu\psi) + \delta\bar{\psi} \partial_{\bar{\psi}}\mathcal{L} + \delta(\partial_\mu\bar{\psi}) \partial_{\partial_\mu\bar{\psi}}\mathcal{L} \\ &= \partial_\psi\mathcal{L} (i\alpha\psi) + \partial_{\partial_\mu\psi}\mathcal{L} (i\alpha\partial_\mu\psi) + \dots \\ &= i\alpha [\partial_\psi\mathcal{L} - \partial_\mu(\partial_{\partial_\mu\psi}\mathcal{L})] \psi + i\alpha\partial_\mu(\partial_{\partial_\mu\psi}\mathcal{L}) \psi + \dots \\ &= 0.\end{aligned}\tag{1.14}$$

¹¹² The term in the square brackets corresponds to the Euler-Lagrange equation and van-
¹¹³ ishes and the equation 1.14 reduced to the form of:

$$\partial_\mu \left[-\frac{i}{2} (\partial_{\partial_\mu\psi}\mathcal{L} \psi - \bar{\psi} \partial_{\partial_\mu\bar{\psi}}\mathcal{L}) \right] = 0.\tag{1.15}$$

¹¹⁴ The Lagrangian of a relativistic particle with spin- $\frac{1}{2}$ can be described by Dirac's La-
¹¹⁵ grangian 1.10 and thus, by replacing in the equation 1.15:

$$\partial_\mu [\bar{\psi} \gamma^\mu \psi] = 0.\tag{1.16}$$

¹¹⁶ It follows that the charge $Q \equiv \int d^3x J^0$ must be a conserved quantity.

¹¹⁷ 1.2.4 Quantum Electrodynamics (QED)

¹¹⁸ A generalization of the previous section phase transformation 1.12 that includes also
¹¹⁹ the local phase transformations is [4]:

$$\psi \rightarrow \psi' \equiv e^{i\alpha(x)} \psi.\tag{1.17}$$

¹²⁰ Possible ψ replacement in the Dirac's Lagrangian will break the invariance due to the
¹²¹ derivative of $\partial_\mu\alpha(x)$, with an additional phase change that corresponds to:

$$\delta\mathcal{L}_{\text{Dirac}} = \bar{\psi} i\gamma^\mu [i\partial_\mu\alpha(x)] \psi.\tag{1.18}$$

¹²² The invariance can be restored only if a modified derivative is inserted $\partial_\mu \rightarrow D_\mu \equiv$
¹²³ $\partial_\mu + ieA_\mu$ and $D_\mu\psi \rightarrow e^{i\alpha(x)}D_\mu\psi$, then:

$$\begin{aligned}\mathcal{L}_{\text{Dirac}} &= \bar{\psi} (i\cancel{D} - m) \psi \\ &= \bar{\psi} (i\cancel{D} - m) \psi - e\bar{\psi} \cancel{A}(x) \psi.\end{aligned}\tag{1.19}$$

¹²⁴ The Lagrangian under the transformations, given that $\psi \rightarrow \psi'$ and $A \rightarrow A'$, is:

$$\begin{aligned}\mathcal{L}'_{\text{Dirac}} &= \bar{\psi}' (i\cancel{D} - m) \psi' - e\bar{\psi}' \cancel{A}' \psi' \\ &= \bar{\psi} (i\cancel{D} - m) \psi - e\bar{\psi} [\cancel{D}\alpha(x)] \psi - e\bar{\psi} \cancel{A}' \psi.\end{aligned}\tag{1.20}$$

¹²⁵ The condition $\mathcal{L} = \mathcal{L}'$ is achieved $A(x)$ is a vector potential:

$$A'_\mu(x) = A_\mu(x) - \frac{1}{e} \partial_\mu \alpha(x). \quad (1.21)$$

¹²⁶ In other words a gauge field introduced A_μ , which does not change the electromagnetic field strength $F_{\mu\nu}$, that couples to fermions of charge e in exactly the same way as the ¹²⁷ photon field [4].

¹²⁹ The complete Lagrangian that describes the QED should also contain the kinematic ¹³⁰ term (known from the Maxwell equations):

$$\mathcal{L} = -\frac{1}{4} F_{\mu\nu} F^{\mu\nu} + \bar{\psi}(i\cancel{\partial} - m)\psi - e\bar{\psi}\cancel{A}\psi. \quad (1.22)$$

¹³¹ Local phase changes described by the equation 1.17 forms an Abelian $U(1)$ group of ¹³² transformations and consequently the QED is an Abelian gauge theory [11].

¹³³ 1.2.5 Gauge Fields Lagrangian

¹³⁴ A field composed of two complex scalar fields $\Phi_A = \phi_1 + i\phi_2$ and $\Phi_B = \phi_3 + i\phi_4$ can ¹³⁵ be expressed as [13]:

$$\Phi = \begin{pmatrix} \Phi_A \\ \Phi_B \end{pmatrix}. \quad (1.23)$$

¹³⁶ If the Lagrangian density of this field, which is a set of four real fields, is required to ¹³⁷ be invariant under the a $U(1) \times SU(2)$ transformation, this would be:

$$\Phi \rightarrow \Phi' = e^{-i\theta} \mathbf{U} \Phi \quad (1.24)$$

¹³⁸ where $e^{-i\theta}$ is an element of the group $U(1)$ as seen in section 1.2.4 and \mathbf{U} is an element ¹³⁹ of the group $SU(2)$, so that $\mathbf{U}\mathbf{U}^\dagger = \mathbf{U}^\dagger\mathbf{U} = 1$.

¹⁴⁰ The simplest Lagrangian that could obey such symmetry is :

$$\mathcal{L} = \partial_\mu \Phi^\dagger \partial^\mu \Phi - m^2 \Phi^\dagger \Phi \quad (1.25)$$

¹⁴¹ where the terms

$$\begin{aligned} \Phi^\dagger \Phi &= \Phi_A^* \Phi_A + \Phi_B^* \Phi_B = \phi_1^2 + \phi_2^2 + \phi_3^2 + \phi_4^2 \\ \partial_\mu \Phi^\dagger \partial^\mu \Phi &= \partial_\mu \phi_1 \partial^\mu \phi_1 + \partial_\mu \phi_2 \partial^\mu \phi_2 + \partial_\mu \phi_3 \partial^\mu \phi_3 + \partial_\mu \phi_4 \partial^\mu \phi_4 \end{aligned} \quad (1.26)$$

¹⁴² and the fields describes a set of four independent fields with the same mass m .

¹⁴³ The fields must be invariant under the $U(1)$ transformation which can be written
¹⁴⁴ as:

$$\Phi \rightarrow \Phi' = e^{-i\theta}\Phi = e^{-i\theta I}\Phi \quad (1.27)$$

¹⁴⁵ where I is the unit matrix $\begin{pmatrix} 1 & 0 \\ 0 & 1 \end{pmatrix}$. In order for this symmetry to become a local
¹⁴⁶ symmetry we must introduce a vector field $B_\mu(x)I$, with the transformation law:

$$B_\mu(x) \rightarrow B'_\mu(x) = B_\mu(x) + (2/g_i)\partial_\mu\theta \quad (1.28)$$

¹⁴⁷ and make the replacement:

$$i\partial_\mu \rightarrow i\partial_\mu - (g_i/2)B_\mu \quad (1.29)$$

¹⁴⁸ where g_i is a dimensionless parameter of the theory and the factor 2 follows convention.

¹⁴⁹ An element of $SU(2)$ can be written in the form of:

$$\mathbf{U} = e^{i\alpha^k \sigma^k} \quad (1.30)$$

¹⁵⁰ where α^k are three real numbers and σ^k are the Pauli matrices 1.7, generators of the
¹⁵¹ $SU(2)$ group. A global $SU(2)$ symmetry can be made into a local $SU(2)$ symmetry by
¹⁵² making the group element dependent on space and time coordinates $\mathbf{U} = \mathbf{U}(x)$ and
¹⁵³ introducing a vector gauge field:

$$\mathbf{W}_\mu(x) = W_\mu^k(x)\sigma^k$$

¹⁵⁴

$$\mathbf{W}_\mu(x) \rightarrow \mathbf{W}'_\mu(x) = \mathbf{U}(x)\mathbf{W}_\mu(x)\mathbf{U}^\dagger(x) + (2i/g_2)(\partial_\mu\mathbf{U}(x))\mathbf{U}^\dagger(x) \quad (1.31)$$

¹⁵⁵ which is a generalization of equation 1.28.

¹⁵⁶ By defining:

$$D_\mu\Phi = [\partial_\mu + (ig_1/2)B_\mu + (ig_2/2)\mathbf{W}_\mu]\Phi \quad (1.32)$$

¹⁵⁷ and thus given equation 1.27:

$$D'_\mu\Phi' = [\partial_\mu + (ig_1/2)B'_\mu + (ig_2/2)\mathbf{W}'_\mu]\Phi' = e^{-i\theta}\mathbf{U}D_\mu\Phi \quad (1.33)$$

¹⁵⁸ the Lagrangian 1.25 can be written as:

$$\mathcal{L} = (D_\mu\Phi)^\dagger D_\mu\Phi - V\Phi^\dagger\Phi. \quad (1.34)$$

¹⁵⁹ The field strength tensors can be expressed as:

¹⁶⁰

$$B_{\mu\nu} = \partial_\mu B_\nu - \partial_\nu B_\mu$$

$$\mathbf{W}_{\mu\nu} = [\partial_\mu + (ig_2/2)\mathbf{W}_\mu]\mathbf{W}_\nu - [\partial_\nu + (ig_2/2)\mathbf{W}_\nu]\mathbf{W}_\mu \quad (1.35)$$

¹⁶¹ and the total contribution to the Lagrangian density associated with these gauge fields
¹⁶² is:

$$\mathcal{L} = -\frac{1}{4}B_{\mu\nu}B^{\mu\nu} - \frac{1}{8}Tr(\mathbf{W}_{\mu\nu}\mathbf{W}^{\mu\nu}). \quad (1.36)$$

¹⁶³ 1.2.6 The Strong Interactions Lagrangian

¹⁶⁴ Similarly to the electromagnetic and weak interactions, the strong interactions can
¹⁶⁵ be described by a gauge theory known as Quantum Chromodynamics (QCD) [13].
¹⁶⁶ Each quark can be described by three fields named after the colors red, green, blue that
¹⁶⁷ quarks carry and associated to the triplet:

$$\mathbf{u} = \begin{pmatrix} u_r \\ u_g \\ u_b \end{pmatrix} \quad (1.37)$$

¹⁶⁸ where u_r , u_g , u_b are the Dirac spinors. The theory is invariant under a local $SU(3)$
¹⁶⁹ transformation of the form $\mathbf{q} \rightarrow \mathbf{q}' = \mathbf{U}\mathbf{q}$, where \mathbf{q} is any quark triplet and \mathbf{U} is any
¹⁷⁰ space and time element of the $SU(3)$ group. A 3×3 matrix gauge field G_μ is introduced
¹⁷¹ (as an analogue of the matrix field \mathbf{W}_μ of the electroweak theory):

$$\mathbf{G}_\mu \rightarrow \mathbf{G}'_\mu = \mathbf{U}\mathbf{G}_\mu\mathbf{U}^\dagger + \frac{i}{g}(\partial_\mu\mathbf{U})\mathbf{U}^\dagger. \quad (1.38)$$

¹⁷² Where $(\partial_\mu + ig\mathbf{G}_\mu)\mathbf{q} \equiv D_\mu\mathbf{q}$ and under a local $SU(3)$ transformation:

$$D'_\mu\mathbf{q}' = (\partial_\mu + ig\mathbf{G}'_\mu)\mathbf{q}' = \mathbf{U}D_\mu\mathbf{q}. \quad (1.39)$$

¹⁷³ The parameter g that appears in these equations is the strong coupling constant.
¹⁷⁴ \mathbf{G}_μ is taken to be Hermitian and traceless, just like \mathbf{W}_μ in the electroweak theory,
¹⁷⁵ and it is expressed as:

$$\mathbf{G}_\mu = \frac{1}{2} \sum_{\alpha=1}^8 G_\mu^\alpha \lambda_\alpha \quad (1.40)$$

¹⁷⁶ where the fraction $\frac{1}{2}$ is conventional and the $G_\mu^\alpha(x)$ are eight real independent gluon
¹⁷⁷ gauge fields. The Yang-Mills constructor, similarly to the electroweak case, is:

$$\mathbf{G}_{\mu\nu} = \partial_\mu\mathbf{G}_\nu - \partial_\nu\mathbf{G}_\mu + ig(\mathbf{G}_\mu\mathbf{G}_\nu - \mathbf{G}_\nu\mathbf{G}_\mu). \quad (1.41)$$

¹⁷⁸ The gluon Lagrangian density is taken to be:

$$\mathcal{L}_{gluon} = \frac{1}{2}Tr [\mathbf{G}_{\mu\nu}\mathbf{G}^{\mu\nu}]. \quad (1.42)$$

¹⁷⁹ By expanding the $\mathbf{G}_{\mu\nu}$ in terms of each components, using Equation 1.40:

$$\mathbf{G}_{\mu\nu} = \frac{1}{2} \sum_{\alpha=1}^8 G_{\mu\nu}^\alpha \lambda_\alpha. \quad (1.43)$$

¹⁸⁰ Hence the trace is $Tr [\lambda_\alpha \lambda_\beta] = 2\delta_{\alpha\beta}$ and the Equation 1.42 becomes:

$$\mathcal{L}_{gluon} = \frac{1}{4} \sum_{\alpha=1}^8 G_{\mu\nu}^\alpha G_\alpha^{\mu\nu}. \quad (1.44)$$

¹⁸¹ The total strong Lagrangian density is:

$$\mathcal{L}_{strong} = \mathcal{L}_{gluon} + \mathcal{L}_{quark} \quad (1.45)$$

¹⁸² where the \mathcal{L}_{quark} is taken from the QED and specifically from the Equation 1.20:

$$\mathcal{L}_{quark} = \sum_{f=1}^6 [\bar{\mathbf{q}}_f i\gamma^\mu (\partial_\mu + ig\mathbf{G}_\mu) \mathbf{q}_f - m_f \bar{\mathbf{q}}_f \mathbf{q}_f]. \quad (1.46)$$

¹⁸³ 1.2.7 Spontaneous Symmetry Breaking and Goldstone Bosons

¹⁸⁴ The simplest Lagrangian 1.25, considered for the estimation of the gauge fields
¹⁸⁵ Lagrangian, contributes to the energy only with the term $m^2 \Phi^\dagger \Phi$ if Φ is independent
¹⁸⁶ of time and space [13]. Given that m^2 is positive, the minimum is achieved when
¹⁸⁷ $\phi_1 = \phi_2 = 0$. The Lagrangian density, obtained by changing the sign in front of the
¹⁸⁸ m^2 , is thus unstable and specifically the potential energy density is unbounded below.

¹⁸⁹ The stability can be restored by introducing a term $(m^2/2\phi_0^2)(\Phi^\dagger \Phi)^2$, where ϕ_0 is
¹⁹⁰ a real parameter. The new minimum, given a constant Φ , is obtained on the circle
¹⁹¹ defined by $|\Phi| = \phi_0$ and therefore the vacuum states are infinite. Under the $U(1)$
¹⁹² symmetry 1.17:

$$\phi'_1 = \phi_1 \cos\theta + \phi_2 \sin\theta \quad (1.47)$$

$$\phi'_2 = -\phi_1 \sin\theta + \phi_2 \cos\theta. \quad (1.48)$$

¹⁹³ If the vacuum state is taken to be $(\phi_0, 0)$, the $SU(1)$ symmetry breaks. This is an
¹⁹⁴ example of *Spontaneous Symmetry Breaking*.

¹⁹⁵ Expanding around this ground state $(\phi_0, 0)$, $\Phi = \phi_0 + (1/\sqrt{2})(x + i\psi)$, the Lagrangian
¹⁹⁶ density becomes:

$$\mathcal{L} = \frac{1}{2} \partial_\mu x \partial^\mu x + \frac{1}{2} \partial_\mu \psi \partial^\mu \psi - \frac{m^2}{2\phi_0^2} \left[\sqrt{2}\phi_0 x + \frac{x^2}{2} + \frac{\psi^2}{2} \right]^2 \quad (1.49)$$

¹⁹⁷ where

$$\frac{1}{2} \partial_\mu x \partial^\mu x + \frac{1}{2} \partial_\mu \psi \partial^\mu \psi - m^2 x^2 \equiv \mathcal{L}_{free}. \quad (1.50)$$

198 After breaking the $U(1)$ symmetry, the \mathcal{L}_{free} term is interpreted as the free particle field,
 199 which is dominant for classical fields and small oscillations, and the rest corresponds to
 200 interactions between the free particles and higher order corrections to their motion.

201 The term $-m^2 x^2$ in 1.50, represents a scalar spin-zero particle of mass $\sqrt{2}m$, which in
 202 the case of the ψ field there is no such term, consequently the particle is massless. These
 203 massless particles, arise from the global symmetry breaking and are called *Goldstone*
 204 *bosons* [14].

205 1.2.8 Local Symmetry Breaking and the Higgs Boson

206 To generalize, the $U(1)$ transformation is considered to be of the form $\Phi \rightarrow \Phi' =$
 207 $e^{-iq\theta}\Phi$, where $\theta = \theta(x)$ is space-time dependent [13]. This requires the introduction of
 208 a massless gauge field A_μ , such that:

$$\mathcal{L} = [(\partial_\mu - iqA_\mu)\Phi^\dagger] [(\partial^\mu + iqA^\mu)\Phi] - \frac{1}{4}F_{\mu\nu}F^{\mu\nu} - V(\Phi^\dagger\Phi) \quad (1.51)$$

209 where $F_{\mu\nu} = \partial_\mu A_\nu - \partial_\nu A_\mu$ and $V(\Phi^\dagger\Phi) = \frac{m^2}{2\phi_0^2} [\Phi^\dagger\Phi - \phi_0^2]^2$.

210 \mathcal{L} is invariant under the local gauge transformation:

$$\Phi(x) \rightarrow \Phi'(x) = e^{-iq\theta}\Phi(x), \quad A_\mu(x) \rightarrow A'_\mu(x) = A_\mu(x) + \partial_\mu\theta(x). \quad (1.52)$$

211 The minimum energy is obtained when the fields A_μ vanishes and Φ is constant,
 212 defined by the circle $|\Phi| = \phi_0$. If the $\Phi'(x)$ is real, the symmetry breaks, since we are no
 213 longer free to make further gauge transformations. Substituting $\Phi'(x) = \phi_0 + h(x)/\sqrt{2}$,
 214 where $h(x)$ is real, gives:

$$\begin{aligned} \mathcal{L} = & \left[(\partial_\mu - iqA'_\mu)(\phi_0 + h(x)/\sqrt{2}) \right] \left[(\partial^\mu + iqA'^\mu)(\phi_0 + h(x)/\sqrt{2}) \right] \\ & - \frac{1}{4}F'_{\mu\nu}F'^{\mu\nu} - \frac{m^2}{2\phi_0^2} \left[\sqrt{2}\phi_0h + \frac{h^2}{2} \right]^2. \end{aligned} \quad (1.53)$$

215 The Lagrangian is again separated to two term $\mathcal{L} = \mathcal{L}_{free} + \mathcal{L}_{int}$:

$$\mathcal{L}_{free} = \frac{1}{2}\partial_\mu h\partial^\mu h - m^2h^2 - \frac{1}{4}F_{\mu\nu}F^{\mu\nu} + q^2\phi_0^2A_\mu A^\mu, \quad (1.54)$$

$$\mathcal{L}_{int} = q^2A_\mu A^\mu \left(\sqrt{2}\phi_0h + \frac{h^2}{2} \right) - \frac{m^2h^2}{2\phi_0^2} \left(\sqrt{2}\phi_0h + \frac{h^2}{4} \right). \quad (1.55)$$

216 In the \mathcal{L}_{int} a single scalar field $h(x)$ is described corresponding to a spinless boson
 217 of mass $\sqrt{2}m$ and a vector field A_μ , corresponding to a vector boson of mass $\sqrt{2}q\phi_0$
 218 with three independent components.

219 The mechanism for introducing mass is called the **Higgs mechanism** [15, 16] and
 220 the particle corresponding to the $h(x)$ field is called the **Higgs boson**. As a consequence
 221 of local symmetry breaking the gauge field acquires a mass, and the massless spin-zero
 222 Goldstone boson that appeared in the global symmetry breaking 1.2.7 is replaced by
 223 the longitudinal polarized state of this massive spin one boson.

224 In the Glashow-Weinberg-Salam electroweak theory, the masses of the W^\pm and Z
 225 particles arise as a result of symmetry breaking. The resulting theory can be renormal-
 226 ized.

227 1.3 The SM Higgs Mechanism

228 In the standard non-Abelian case of the SM, the theory should reproduce the mass
 229 of three gauge bosons W^\pm and Z , the γ should remain massless and the QED must stay
 230 an exact symmetry [10]. In order to generate masses, the gauge symmetry must break
 231 in some way, however the fully symmetric Lagrangian is needed to preserve renormal-
 232 ization [17].

233 The Lagrangian should follow the general form:

$$\mathcal{L} = \partial_\mu \phi^\dagger \partial^\mu \phi - V(\phi) \quad (1.56)$$

234 and the potential is chosen to be of the form:

$$V(\phi) = \mu^2 \phi^\dagger \phi + h(\phi^\dagger \phi)^2. \quad (1.57)$$

235 In order to have a ground state the potential must be bounded from below, i.e. $h > 0$.
 236 Whereas for the μ^2 there are two possibilities, graphically shown in Figure 1.2:

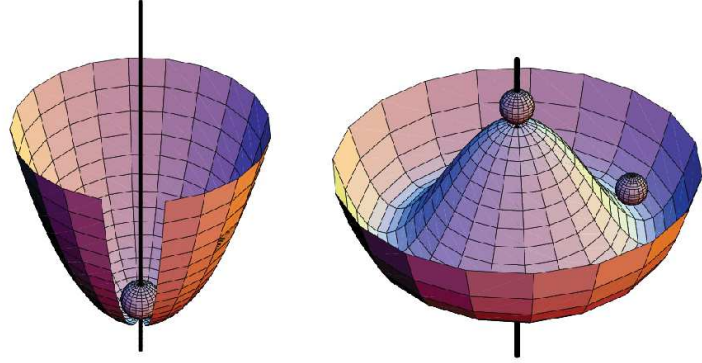
- 237 1. $\mu^2 > 0$: the potential has only one minimum ($\phi = 0$) and it describes a massive
 238 scalar particle with mass μ and coupling \sqrt{h}
- 239 2. $\mu^2 < 0$: the minimum is obtained for the ϕ_0 value, $|\phi_0| = \sqrt{\frac{-\mu^2}{2h}} \equiv \frac{v}{\sqrt{2}} > 0$, for
 240 which the potential is $V(\phi_0) = -\frac{h}{4}v^4$. v is called the *vacuum expectation value*.

241 1.3.1 The Mechanism in the SM

242 For the case of $\mu^2 < 0$, the simplest choice is a complex $SU(2)$ doublet of scalar
 243 fields ϕ :

$$\phi(x) \equiv \begin{pmatrix} \phi^+(x) \\ \phi^0(x) \end{pmatrix}, \quad Y_\phi = +1 \quad (1.58)$$

Figure 1.2: Graphical representation of the potential 1.57 for $\mu^2 \geq 0$ (left) and $\mu^2 < 0$ (right) [18].



7

²⁴⁴ for which there is a finite set of degenerate states with minimum energy satisfying:

$$|\lesssim 0|\phi^0|0\gtrsim| = \sqrt{\frac{-\mu^2}{2h}} \equiv \frac{v}{\sqrt{2}} \quad (1.59)$$

²⁴⁵ as the previously chosen potential. Rewriting the field Φ as an expansion around the v
²⁴⁶ of the $\theta_i(x)$ fields and $H(x)$, where $i = 1, 2, 3$, at the first order:

$$\Phi(x) = \begin{pmatrix} \theta_2 + i\theta_1 \\ \frac{1}{\sqrt{2}}(v + H) - i\theta_3 \end{pmatrix} = e^{i\theta_a(x)\tau^a(x)/v} \begin{pmatrix} 0 \\ \frac{1}{\sqrt{2}}(v + H(x)) \end{pmatrix}. \quad (1.60)$$

²⁴⁷ A gauge transformation of this field leads to:

$$\Phi(x) \rightarrow e^{-i\theta_a(x)\tau^a(x)} \Phi(x) = \frac{1}{\sqrt{2}} \begin{pmatrix} 0 \\ v + H(x) \end{pmatrix} \quad (1.61)$$

²⁴⁸ and after the full expansion of terms $|D_\mu \Phi|^2$ as in the Equation 1.34 result to:

$$\begin{aligned} |D_\mu \Phi|^2 &= \left| \left(\partial_\mu - ig_2 \frac{\tau_a}{2} W_\mu^a - ig_1 \frac{1}{2} B_\mu \right) \Phi \right|^2 \\ &= \frac{1}{2} \left| \begin{pmatrix} \partial_\mu - \frac{i}{2}(g_2 W_\mu^3 + g_1 B_\mu) & -\frac{ig_2}{2}(W_\mu^1 - iW_\mu^2) \\ -\frac{ig_2}{2}(W_\mu^1 + iW_\mu^2) & \partial_\mu + \frac{i}{2}(g_2 W_\mu^3 - g_1 B_\mu) \end{pmatrix} \begin{pmatrix} 0 \\ v + H \end{pmatrix} \right|^2 \\ &= \frac{1}{2}(\partial_\mu H)^2 + \frac{1}{8}g_2^2(v + H)^2|W_\mu^1 + iW_\mu^2|^2 + \frac{1}{8}(v + H)^2|g_2 W_\mu^3 - g_1 B_\mu|^2 \end{aligned} \quad (1.62)$$

²⁴⁹ In the above equation, the following fields can be defined:

$$W^\pm = \frac{1}{\sqrt{2}}(W_\mu^1 \mp iW_\mu^2), \quad Z_\mu = \frac{g_2 W_\mu^3 - g_1 B_\mu}{\sqrt{g_2^2 + g_1^2}}, \quad A_\mu = \frac{g_2 W_\mu^3 + g_1 B_\mu}{\sqrt{g_2^2 + g_1^2}} \quad (1.63)$$

²⁵⁰ where A_μ is orthogonal to the Z_μ . In this interpretation, the W^\pm , Z have acquired ²⁵¹ masses while the photon remained massless:

$$M_W = \frac{1}{2}v g_2, \quad M_Z = \frac{1}{2}v \sqrt{g_2^2 + g_1^2}, \quad M_A = 0. \quad (1.64)$$

²⁵² The achievement is that by the spontaneous breaking of the symmetry $SU(2)_L \times U(1)_Y \rightarrow U(1)_Q$, ²⁵³ three Goldstone bosons have been absorbed by the W^\pm and Z bosons to form their ²⁵⁴ longitudinal components and to get their masses. Since the $U(1)_Q$ symmetry is still ²⁵⁵ unbroken, the photon which is its generator, remains massless.

²⁵⁶ In a similar manner, using the same scalar field Φ and the isodoublet $\tilde{\Phi} = i\tau_2 \Phi^*$, ²⁵⁷ which has hypercharge $Y = -1$, the fermion masses can be generated. The $SU(2)_L \times U(1)_Y$ ²⁵⁸ invariant Yukawa Lagrangian is introduced:

$$\mathcal{L}_F = -\lambda_e \bar{L} \Phi e_R - \lambda_d \bar{Q} \Phi d_R - \lambda_u \bar{Q} \tilde{\Phi} u_R + h.c. \quad (1.65)$$

²⁵⁹ Taking the electron as an example, one obtains:

$$\begin{aligned} \mathcal{L}_F &= -\frac{1}{\sqrt{2}}\lambda_e (\bar{\nu}_e, \bar{e}_L) \begin{pmatrix} 0 \\ v + H \end{pmatrix} e_R + \dots \\ &= -\frac{1}{\sqrt{2}}\lambda_e (v + H) \bar{e}_L e_R + \dots \end{aligned} \quad (1.66)$$

²⁶⁰ The constant term in front of $\bar{f}_L f_R$ is identified as the fermion mass:

$$m_e = \frac{\lambda_e v}{\sqrt{2}}, \quad m_u = \frac{\lambda_u v}{\sqrt{2}}, \quad m_d = \frac{\lambda_d v}{\sqrt{2}}. \quad (1.67)$$

²⁶¹ The scalar Lagrangian 1.56 is written as:

$$\mathcal{L} = (D_\mu \phi)^\dagger D^\mu \phi - \mu^2 \phi^\dagger \phi + h(\phi^\dagger \phi)^2 \quad (h > 0, \mu^2 < 0) \quad (1.68)$$

²⁶² and it must be invariant under the $SU(2) \times U(1)$ transformations. If the scalar doublet ²⁶³ is parametrized in the general form of:

$$\phi(x) = e^{i\frac{\sigma_2}{2}\theta^i(x)} \frac{1}{\sqrt{2}} \begin{pmatrix} 0 \\ v + H(x) \end{pmatrix} \quad (1.69)$$

²⁶⁴ The kinematic term of the Lagrangian 1.68 for $\theta^i(x) = 0$, takes the form:

$$\begin{aligned} (D_\mu \phi)^\dagger D^\mu \phi &= \left[\left(\partial^\mu + igW^\mu + ig' \frac{1}{2} B^\mu \right) \phi \right]^\dagger \left(\partial^\mu + igW^\mu + ig' \frac{1}{2} B^\mu \right) \phi \\ &= \frac{1}{2} \partial_\mu H \partial^\mu H + (v + H)^2 \left(\frac{g^2}{2} W_\mu^\dagger W^\mu + \frac{g^2}{8\cos^2\theta_W} Z_\mu Z^\mu \right) \end{aligned} \quad (1.70)$$

265 Through this procedure masses are generated for the W^\pm and Z bosons, while the
 266 photon remained massless:

$$M_Z \cos\theta_W = M_W = \frac{1}{2}vg. \quad (1.71)$$

267 **1.3.2 The Higgs Particle in the SM**

268 Finally, the Higgs itself is studied through the kinetic part of the field, $\frac{1}{2}(\partial_\mu H)^2$, of
 269 the Lagrangian 1.71 and the potential 1.57:

$$V = \frac{\mu^2}{2}(0, v + H) \begin{pmatrix} 0 \\ v + H \end{pmatrix} + \frac{\lambda}{4} \left| (0, v + H) \begin{pmatrix} 0 \\ v + H \end{pmatrix} \right|^2. \quad (1.72)$$

270 Using the relation $v^2 = -\mu^2/\lambda$:

$$V = -\frac{1}{2}\lambda v^2 (v + H)^2 + \frac{1}{4}\lambda(v + H)^4 \quad (1.73)$$

271 and resulting to the Lagrangian containing the Higgs field H :

$$\begin{aligned} \mathcal{L}_H &= \frac{1}{2}(\partial_\mu H)(\partial^\mu H) - V \\ &= \frac{1}{2}(\partial^\mu H)^2 - \lambda v^2 H^2 - \lambda v H^3 - \frac{\lambda}{4} H^4 \end{aligned} \quad (1.74)$$

272 where $M_H^2 = 2\lambda v^2 = -2\mu^2$ is simply the Higgs boson mass and the Feynman rules are
 273 given by:

$$g_{H^3} = (3!)i\lambda v = 3i \frac{M_H^2}{v}, \quad g_{H^4} = (4!)i \frac{\lambda}{4} = 3i \frac{M_H^2}{v^2}. \quad (1.75)$$

274 The Higgs boson couplings to gauge bosons and fermions almost derived previously,
 275 when the masses of these particles were calculated:

$$\mathcal{L}_{M_V} \sim M_V^2 \left(1 + \frac{H}{v}\right)^2, \quad \mathcal{L}_{m_f} \sim -m_f \left(1 + \frac{H}{v}\right) \quad (1.76)$$

276 along with the Higgs boson couplings to gauge bosons and fermions:

$$g_{Hff} = i \frac{m_f}{v}, \quad g_{HVV} = -2i \frac{M_V^2}{v}, \quad g_{HHVV} = -2i \frac{M_V^2}{v^2}. \quad (1.77)$$

²⁷⁷ In the previous, the vacuum expectation value v is fixed in terms of the W boson mass
²⁷⁸ M_W or the Fermi constant G_μ determined from muon decay:

$$M_W = \frac{1}{2}g_2 v = \left(\frac{\sqrt{2}g^2}{8G_\mu} \right)^{1/2} \Rightarrow v = \frac{1}{(\sqrt{2}G_\mu)^{1/2}} \simeq 246 \text{ GeV.} \quad (1.78)$$

²⁷⁹ The Higgs couplings to fermions, massive gauge bosons as well as the self-couplings,
²⁸⁰ are given in Figure 1.3 using both v and G_μ .

²⁸¹ The Higgs boson propagator is given, in momentum space, by:

$$\Delta_{HH}(q^2) = \frac{i}{q^2 - M_H^2 + i\epsilon} \quad (1.79)$$

²⁸² 1.4 Higgs System Theoretical Constraints

²⁸³ The Higgs mechanism has various theoretical constraints which are derived from
²⁸⁴ assumptions on the energy range in which the SM is valid before perturbation theory
²⁸⁵ breaks down and new phenomena should emerge [10]. These include constraints from
²⁸⁶ unitarity in scattering amplitudes, perturbativity of the Higgs self-coupling, stability
²⁸⁷ of the electroweak vacuum and fine-tuning, as summarized below.

²⁸⁸ 1.4.1 Perturbative Unitarity

²⁸⁹ In processes involving the W_L and Z_L bosons, given that the interactions of the lon-
²⁹⁰ gitudinal components grow with momenta, this would eventually lead to cross sections
²⁹¹ which increase with the energy which would then violate unitarity at some stage [10].
²⁹² The limit to preserve the unitarity condition if estimated to be:

$$M_H \sim 870 \text{ GeV.} \quad (1.80)$$

²⁹³ Imposing similar criteria on the $Z_L Z_L$, HH and $Z_L H$ the unitarity constraints the
²⁹⁴ Higgs mass below:

$$M_H \sim 710 \text{ GeV.} \quad (1.81)$$

²⁹⁵ Thus, in the SM, if the Higgs boson mass exceeds values of $\mathcal{O}(700 \text{ GeV})$, unitarity
²⁹⁶ will be violated unless new phenomena appear and restore it.

297 The perturbation has also to be taken into account in the decays of the Higgs boson
 298 to gauge bosons. Using the equivalence theorem and the Lagrangian, the partial decay
 299 width of the Higgs boson into two longitudinal Z bosons can be written as:

$$\Gamma(H \rightarrow ZZ) = \left(\frac{1}{2M_H} \right) \left(\frac{2! M_H^2}{2v} \right)^2 \frac{1}{2} \left(\frac{1}{8\pi} \right) \rightarrow \frac{M_H^3}{32\pi v^2}. \quad (1.82)$$

300 For the decay $H \rightarrow WW$, one needs to remove the statistical factor to account for both
 301 W^\pm states:

$$\Gamma(H \rightarrow W^+W^-) \simeq 2\Gamma(H \rightarrow ZZ). \quad (1.83)$$

302 This means that for high Higgs masses the width becomes comparable to the mass and
 303 hence the Higgs cannot be considered as a “real” resonance anymore. The expected
 304 width of the Higgs boson is presented in Figure 1.4 and especially in the region \sim
 305 125 GeV, where the Higgs mass is observed, the expectation is below 10^{-2} GeV.

306 1.4.2 Triviality and Stability Bounds

307 The variation of the quartic Higgs coupling with the energy scale Q is described by
 308 the Renormalization Group Equation [10]:

$$\frac{d}{dQ^2} \lambda(Q^2) = \frac{3}{4\pi^2} \lambda^2(Q^2) + \text{higher orders} \quad (1.84)$$

309 Choosing the natural reference energy point to be the electroweak symmetry breaking
 310 scale, $Q_0 = v$, the solution is:

$$\lambda(Q^2) = \lambda(v^2) \left[1 - \frac{3}{4\pi^2} \lambda(v^2) \log \frac{Q^2}{v^2} \right]^{-1}. \quad (1.85)$$

311 If the energy is much smaller than the electroweak breaking scale, $Q^2 \ll v^2$, the quartic
 312 coupling becomes extremely small and eventually vanishes, $\lambda(Q^2) \sim \lambda(v^2)/\log(\infty) \rightarrow$
 313 0_+ . In this case the theory is said to be *trivial*, i.e. non interacting since the coupling
 314 is zero. In the opposite limit, where the energy is much smaller than the weak scale,
 315 the quartic coupling becomes infinite. The energy where this happens is called *Landau*
 316 *pole* and is equal to:

$$\Lambda_C = v \exp \left(\frac{4\pi^2}{3\lambda} \right) = v \exp \left(\frac{4\pi^2 v^2}{M_H^2} \right). \quad (1.86)$$

Figure 1.3: The Higgs boson couplings to fermions and gauge bosons and the Higgs self-couplings in the SM. The normalization factors of the Feynman rules are also displayed [10].

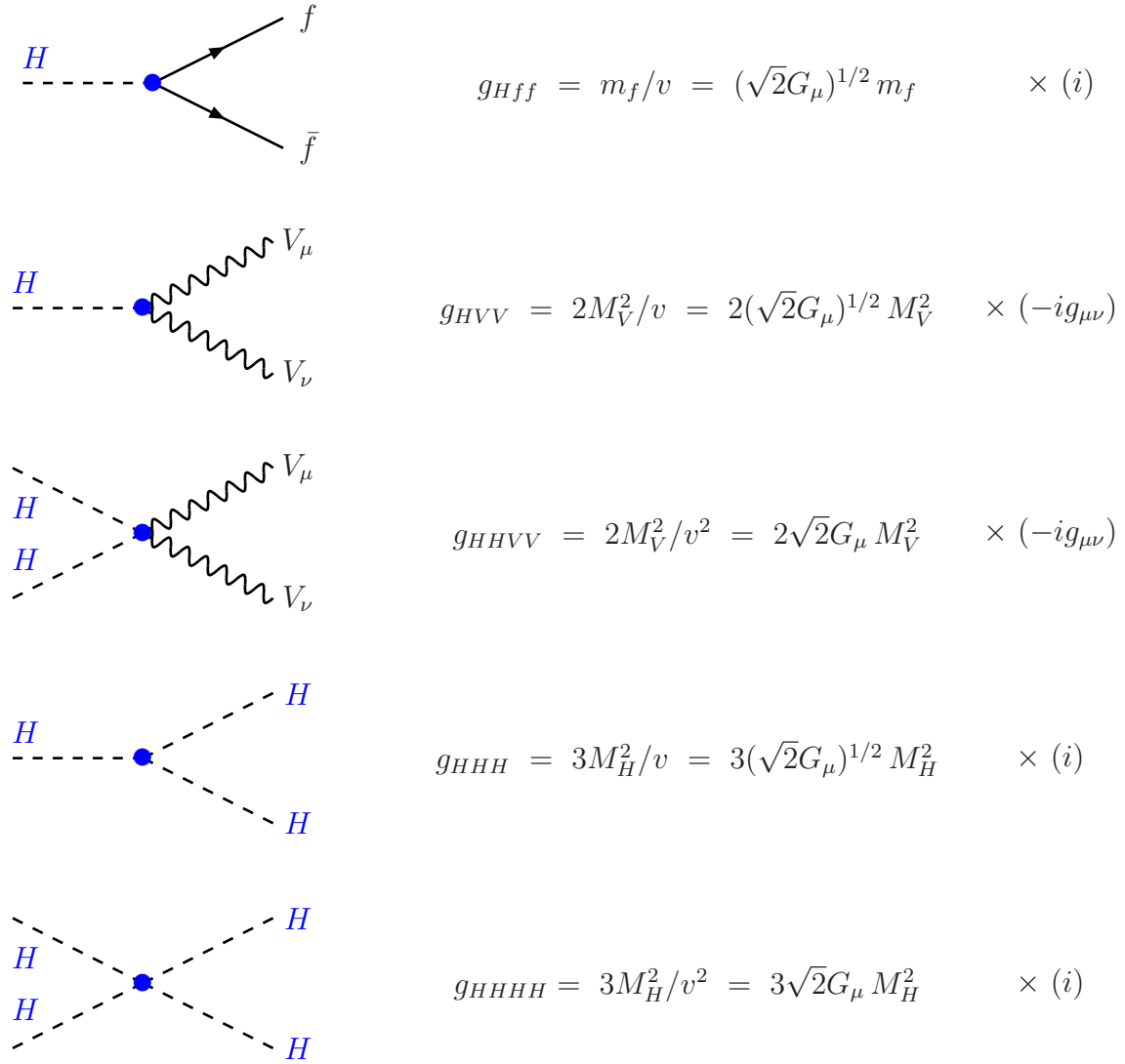
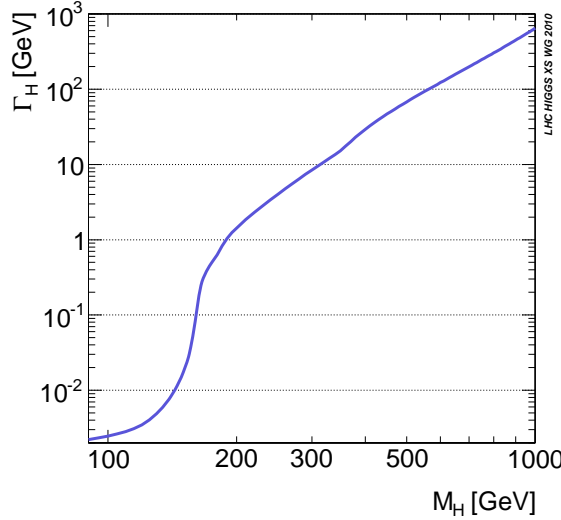


Figure 1.4: Standard model Higgs boson expected total width [19].



317 In order for the theory to remain perturbative at all scales a cut-off energy of Λ_c
 318 should be defined. From simulations of gauge theories on the lattice, where the non-
 319 perturbative effects are properly taken into account, it turns out that the rigorous
 320 bound is $M_H < 640$ GeV.

The one-loop renormalization group equation 1.84 for the quartic coupling, including the fermion and gauge boson contributions, becomes:

$$\begin{aligned} \frac{d\lambda}{d\log Q^2} &\simeq \frac{1}{16\pi^2} \left[12\lambda^2 + 6\lambda\lambda_t^2 - 3\lambda_t^4 - \frac{3}{2}\lambda(3g_2^2 + g_1^2) + \frac{3}{16}(2g_2^4 + (g_2^2 + g_1^2)^2) \right] \quad (1.87) \\ &\simeq \frac{1}{16\pi^2} \left[12\lambda^2 - 12\frac{m_t^4}{v^4} + \frac{3}{16}(2g_2^4 + (g_2^2 + g_1^2)^2) \right] \quad (\lambda \ll \lambda_t, g_1, g_2) \end{aligned}$$

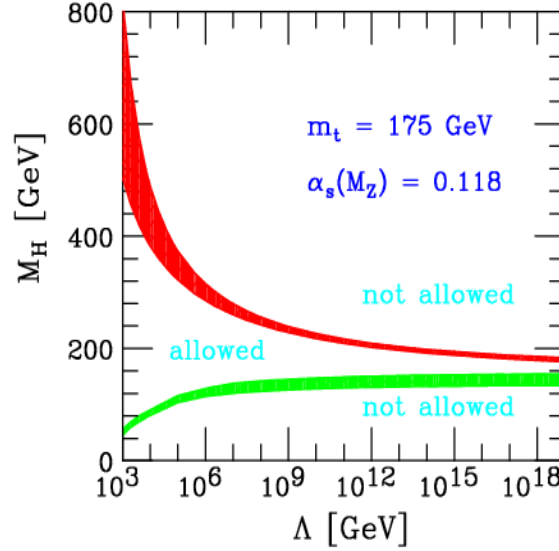
321 where the top quark Yukawa coupling is given by $\lambda_t = \sqrt{2}m_t/v$. Taking the weak scale
 322 as a reference point, the solution is:

$$\lambda(Q^2) = \lambda(v^2) + \frac{1}{16\pi^2} \left[-12\frac{m_t^4}{v^4} + \frac{3}{16}(2g_2^4 + (g_2^2 + g_1^2)^2) \right] \log \frac{Q^2}{v^2}. \quad (1.88)$$

323 If the coupling λ is too small, the top quark contribution can be dominant and could
 324 drive it to a negative value $\lambda(Q^2) < 0$, leading to a scalar potential $V(Q^2) < V(v)$.
 325 Therefore vacuum is not stable anymore since it has no minimum. The stability argument
 326 requires a lower bound in order to have a scalar potential:

$$M_H^2 > \frac{v^2}{8\pi^2} \left[-12\frac{m_t^4}{v^4} + \frac{3}{16}(2g_2^4 + (g_2^2 + g_1^2)^2) \right] \log \frac{Q^2}{v^2}. \quad (1.89)$$

Figure 1.5: The triviality (upper) bound and the vacuum stability (lower) bound on the Higgs boson mass as a function of the cutoff scale Λ_c . The allowed region lies between the bands and the colored bands illustrate the impact of various uncertainties [10].



³²⁷ The constraints on the Higgs boson mass depend on the cut-off Λ_C :

$$\begin{aligned} \Lambda_C \sim 10^3 \text{ GeV} &\Rightarrow M_H \gtrsim 70 \text{ GeV} \\ \Lambda_C \sim 10^{16} \text{ GeV} &\Rightarrow M_H \gtrsim 130 \text{ GeV}. \end{aligned} \quad (1.90)$$

³²⁸ Collectively, the limits imposed are the triviality (upper) bound and the vacuum sta-
³²⁹ bility (lower) bound of the Higgs mass as a function of the cut-off scale Λ_c , given the
³³⁰ top quark mass $m_t = 175 \pm 6$ GeV and $\alpha_s = 0.118 \pm 0.002$, also shown in Figure 1.5.

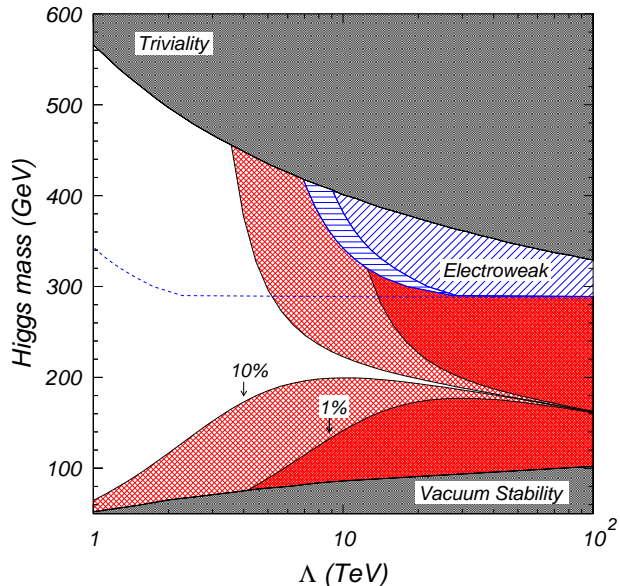
³³¹ 1.4.3 The Fine-Tuning Constraint

³³² A last theoretical constraint comes from the fine-tuning problem originating from
³³³ the radiative corrections to the Higgs boson mass [10]. Cutting off the loop integral
³³⁴ momenta at a scale Λ , and keeping only the dominant contribution in this scale, one
³³⁵ obtains:

$$M_H^2 = (M_H^0)^2 + \frac{3\Lambda^2}{8\pi^2 v^2} [M_H^2 + 2M_W^2 + M_Z^2 - 4m_t^2] \quad (1.91)$$

³³⁶ where M_H^0 is the bare mass contained in the unrenormalized Lagrangian.

Figure 1.6: Constraints from various theoretical bounds are presented [10]. The dark (light) hatched region marked “1%” (“10%”) represents fine-tunings of greater than 1 part in 100 (10). The constraints from triviality, stability and electroweak precision data are also shown. The white region is consistent with all the constraints.



If the cut-off Λ_c is very large, for instance of the order of the Grand Unification scale $\sim 10^{16}$ GeV, one needs a very fine arrangement of 16 digits between the bare Higgs mass and the radiative corrections to have a physical Higgs boson mass in the range of the electroweak symmetry breaking scale, $M_H \sim 100$ GeV to 1 TeV, as is required for the consistency of the SM. This is the naturalness of fine-tuning problem. The acceptable mass regions are presented in Figure 1.6.

343 1.5 Higgs Beyond the Standard Model

344 Despite the success of the SM to describe particle physics processes, there are several
345 aspects where it does not provide satisfactory answers. Among these issues, the most
346 important are:

- Gravity is not contained in the SM theory
- Gauge coupling unification is not provided

- 349 • Neutrino masses are not included
- 350 • SM has no proper candidate for Dark Matter
- 351 • The Higgs sector suffers from the instability of the value of the Higgs boson
352 mass when radiative corrections are included in presence of a physical cut-off that
353 is placed at energies far above the electroweak scale (the so called **Hierarchy
354 problem**).

355 The existence of one new symmetry, or more, relating fermions and bosons is the
356 most popular proposal to solve the hierarchy problem of the SM Higgs sector [20]. This
357 new symmetry is called **Supersymmetry (SUSY)** and generically acts as:

$$\begin{aligned} Q|\text{boson}\rangle &= |\text{fermion}\rangle \\ Q|\text{fermion}\rangle &= |\text{boson}\rangle. \end{aligned} \tag{1.92}$$

358 This is interpreted as SUSY particles partners (*sparticles*) to the SM particles that
359 share quantum numbers but differ by 1/2 unit in their spin. Exact SUSY requires mass
360 degeneracy between particles and sparticles, however in a realistic model SUSY must
361 be broken, since the SUSY partners with such masses have not been observed. These
362 SUSY-breaking models can be classified in two big groups:

- 363 • Unconstrained Models: A general parametrization of all possible SUSY-breaking
364 terms is implemented. The simplest and most popular of these models is the
365 Minimal Supersymmetric Standard Model (MSSM).
- 366 • Constrained Models: Specific assumptions on the scenario that achieves the sponta-
367 neous SUSY breaking is assumed. There are different kinds of models according
368 to the origin of the SUSY breaking and the way it is transmitted from the so-called
369 “Hidden sector” to the “Visible sector”, e.g. Gravity-mediated, Gauge-mediated,
370 Anomaly-mediated, etc.

371 The MSSM and other SUSY models have an extra symmetry, called the “R-parity”,
372 that implies the conservation of a new multiplicative quantum number defined for each
373 particle as:

$$P_R = (-1)^{3(B-L)+2s} \tag{1.93}$$

374 where B , L and s are the baryon number, the lepton number and the spin of the particle
375 respectively. All the SM-particles have even R-parity, $P_R = +1$, whereas the superpart-
376 ners have odd R-parity, $P_R = -1$. This symmetry has very important consequences
377 for Dark Matter Physics, since it provides a natural particle candidate for explaining
378 the Dark Matter: the lightest SUSY particle (LSP), that due to the R-parity is stable.

379 Since the LSP is neutral and uncolored, it leaves no traces in collider detectors and,
 380 therefore, the typical SUSY signatures are events with missing energy.

381 In supersymmetric extensions of the SM, at least two Higgs doublet fields are re-
 382 quired for a consistent electroweak symmetry breaking and in the minimal model, the
 383 MSSM, the Higgs sector is extended to contain five Higgs bosons: two CP-even h and
 384 H , a CP-odd A and two charged Higgs H^\pm particles [21]. Besides the four masses, two
 385 more parameters enter the MSSM Higgs sector: a mixing angle α in the neutral CP-
 386 even sector and the ratio of the vacuum expectation values of the two Higgs fields $\tan\beta$.
 387 Only two free parameters are needed at tree-level: one Higgs mass, usually chosen to
 388 be M_A and $\tan\beta$ which is expected to lie in the range $1 \lesssim \tan\beta \lesssim m_t/m_b$. In addition,
 389 while the masses of the heavy neutral and charged H, A, H^\pm particles are expected to
 390 range from M_Z to the SUSY breaking scale $M_S = \mathcal{O}(1 \text{ TeV})$, the mass of the lightest
 391 Higgs boson h is bounded from above, $M_h \leq M_Z$ at tree-level. This relation is altered
 392 by large radiative corrections, the leading part of which grow as the fourth power of m_t
 393 and logarithmically with the SUSY scale or common squark mass M_S ; the mixing (or
 394 trilinear coupling) in the stop sector A_t plays also an important role. The upper bound
 395 on M_h is then shifted to $M_h^{\max} \sim 110\text{--}135 \text{ GeV}$ depending on these parameters.

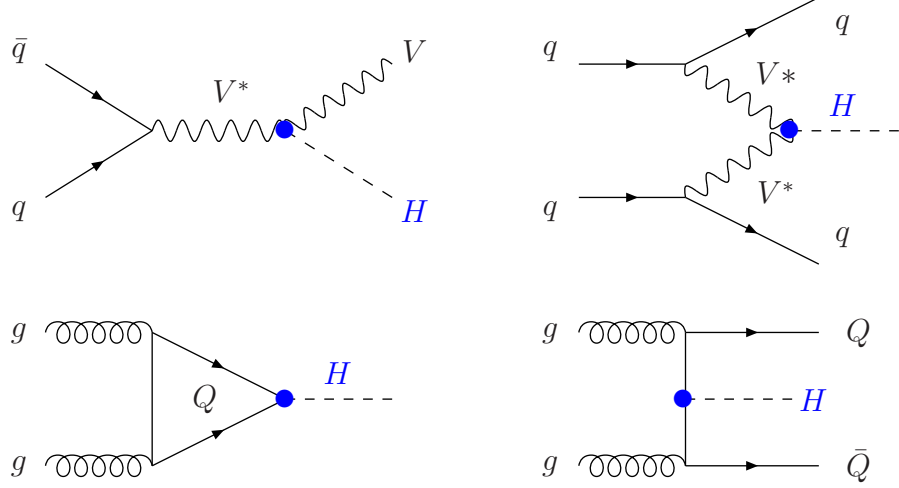
396 1.6 Higgs Production at Hadron Colliders

397 In the Standard Model, the main production mechanisms for the Higgs boson at
 398 hadron colliders make use of the fact that the Higgs boson couples preferentially to the
 399 heavy particles, that is the massive W and Z vector bosons, the top quark and, to a
 400 lesser extent, the bottom quark [10]. The four main production processes, the Feynman
 401 diagrams of which are displayed in Figure 1.7, are thus: the associated production with
 402 W/Z bosons, the weak vector boson fusion processes, the gluon–gluon fusion mechanism
 403 and the associated Higgs production with heavy top or bottom quarks:

- 404 • Associated production with W/Z (WH/ZH): $q\bar{q} \rightarrow V + H$
- 405 • Vector Boson Fusion (VBF): $qq \rightarrow V^*V^* \rightarrow qq + H$
- 406 • Gluon-Gluon Fusion (ggF): $gg \rightarrow H$
- 407 • Associated production with heavy quarks (bbH,ttH): $gg, q\bar{q} \rightarrow Q\bar{Q} + H$

408 The production cross sections of the different mechanisms as a function of the Higgs
 409 mass are presented in Figure 1.8. The cross sections are shown for the Run-I center of
 410 mass energies (7 and 8 TeV) and the maximum possible energy of the LHC (14 TeV).
 411 The missing VH and ttH cross sections for $M_H > 300 \text{ GeV}$ are due to the very small

Figure 1.7: The dominant SM Higgs boson production mechanisms in hadronic collisions.



⁴¹² estimated cross sections. Analytically, the theoretical cross sections around the observed
⁴¹³ Higgs mass at $\sqrt{s} = 7, 8, 13, 14$ TeV are presented in Table 1.4 for all the production
⁴¹⁴ mechanisms. Once again the missing estimations are due to very small expected cross
⁴¹⁵ sections.

⁴¹⁶ There are also several mechanisms for the pair production of the Higgs particles:

$$\text{Higgs Pair Production : } pp \rightarrow HH + X \quad (1.94)$$

⁴¹⁷ and the relevant sub-processes are the $gg \rightarrow HH$ mechanism, which proceeds through
⁴¹⁸ heavy top and bottom quark loops, the associated double production with massive gauge
⁴¹⁹ bosons, $q\bar{q} \rightarrow HHV$, and the vector boson fusion mechanisms $q\bar{q} \rightarrow V^*V^* \rightarrow HHq\bar{q}$.
⁴²⁰ However, because of the suppression by the additional electroweak couplings, they have
⁴²¹ much smaller production cross sections than the single Higgs production mechanisms
⁴²² listed above.

⁴²³ Also suppressed are processes where the Higgs is produced in association with one,
⁴²⁴ two or three hard jets in gluon-gluon fusion, the associated Higgs production with
⁴²⁵ gauge boson pairs, the production with a vector boson and two jets. Other produc-
⁴²⁶ tion processes exist, but have even smaller production cross sections (e.g. diffractive
⁴²⁷ processes).

Figure 1.8: Standard Model Higgs boson mechanisms production cross sections at $\sqrt{s} = 7$ (a) and $\sqrt{s} = 8$ TeV (b) as a function of the Higgs mass [19]. (c) shows the total cross sections for $\sqrt{s} = 7, 8, 14$ TeV. The missing VH and tth cross sections for $M_H > 300$ GeV are due to the very small estimated cross sections.

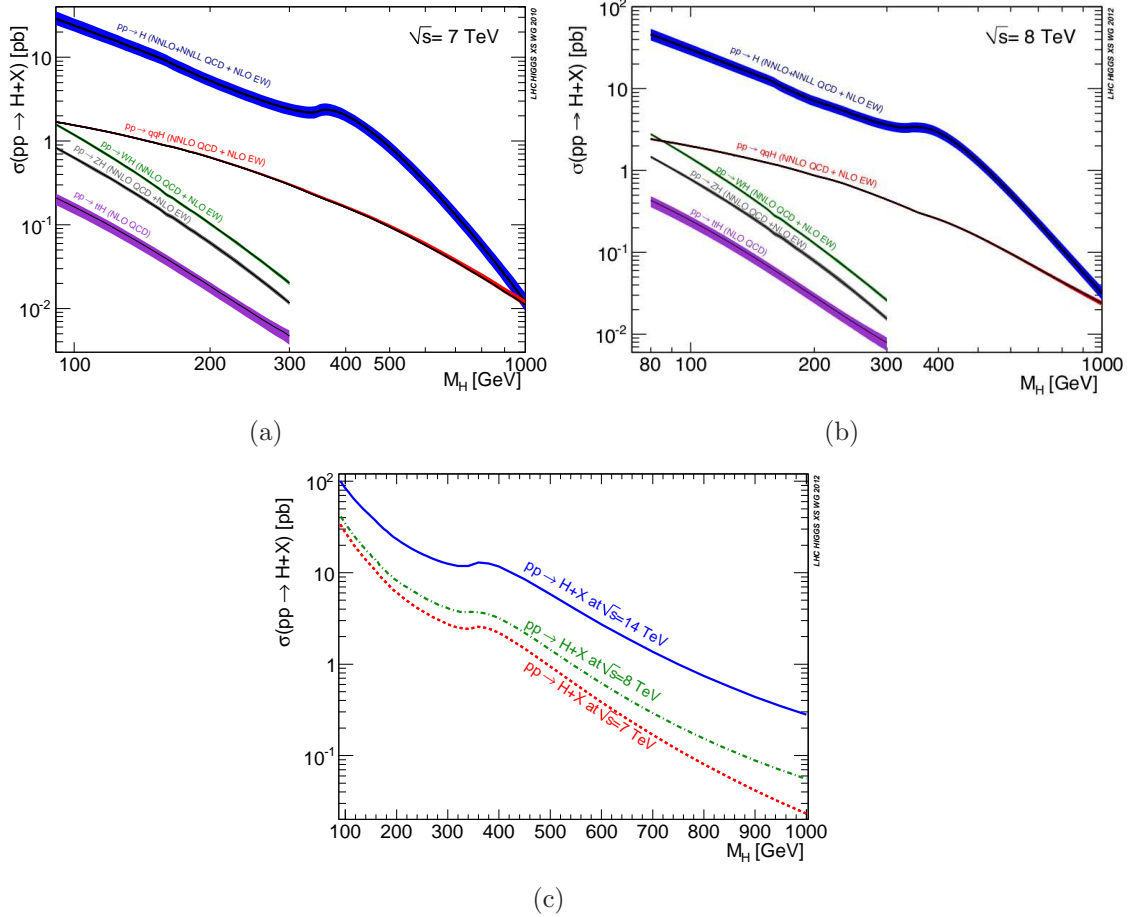
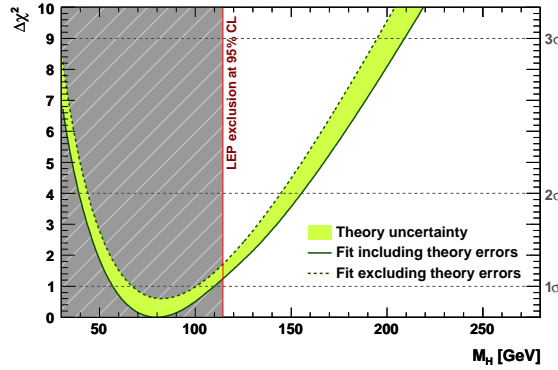


Table 1.4: SM Higgs production cross sections through ggF , VBF , WH , ZH , bbH (where available) and ttH processes at $\sqrt{s} = 7, 8, 13, 14$ TeV [19] around the around Higgs mass.

m_H (GeV)	ggF σ (pb)	VBF σ (pb)	WH σ (pb)	ZH σ (pb)	bbH σ (pb)	ttH σ (pb)
$\sqrt{s} = 7$ TeV						
125.0	15.13	1.222	0.5785	0.3351	-	0.08632
125.5	15.01	1.219	0.5703	0.3309	-	0.08528
126.0	14.89	1.211	0.5629	0.3267	-	0.08426
$\sqrt{s} = 8$ TeV						
125.0	19.27	1.578	0.7046	0.4153	0.2035	0.1293
125.5	19.12	1.573	0.6951	0.4102	0.2008	0.1277
126.0	18.97	1.568	0.6860	0.4050	0.1979	0.1262
$\sqrt{s} = 13$ TeV						
125.0	43.92	3.748	1.380	0.8696	0.5116	0.5085
125.5	43.62	3.727	1.362	0.8594	0.5053	0.5027
126.0	43.31	3.703	1.345	0.8501	0.4969	0.4966
$\sqrt{s} = 14$ TeV						
125.0	49.47	4.233	1.522	0.9690	0.5805	0.6113
125.5	49.13	4.220	1.502	0.9574	0.5739	0.6043
126.0	48.80	4.206	1.485	0.9465	0.5673	0.5969

Figure 1.9: $\Delta\chi^2$ as a function of m_H , where the solid (dashed) lines give the results when including (ignoring) theoretical errors [23].



428 1.7 Higgs Searches and Production at the LHC

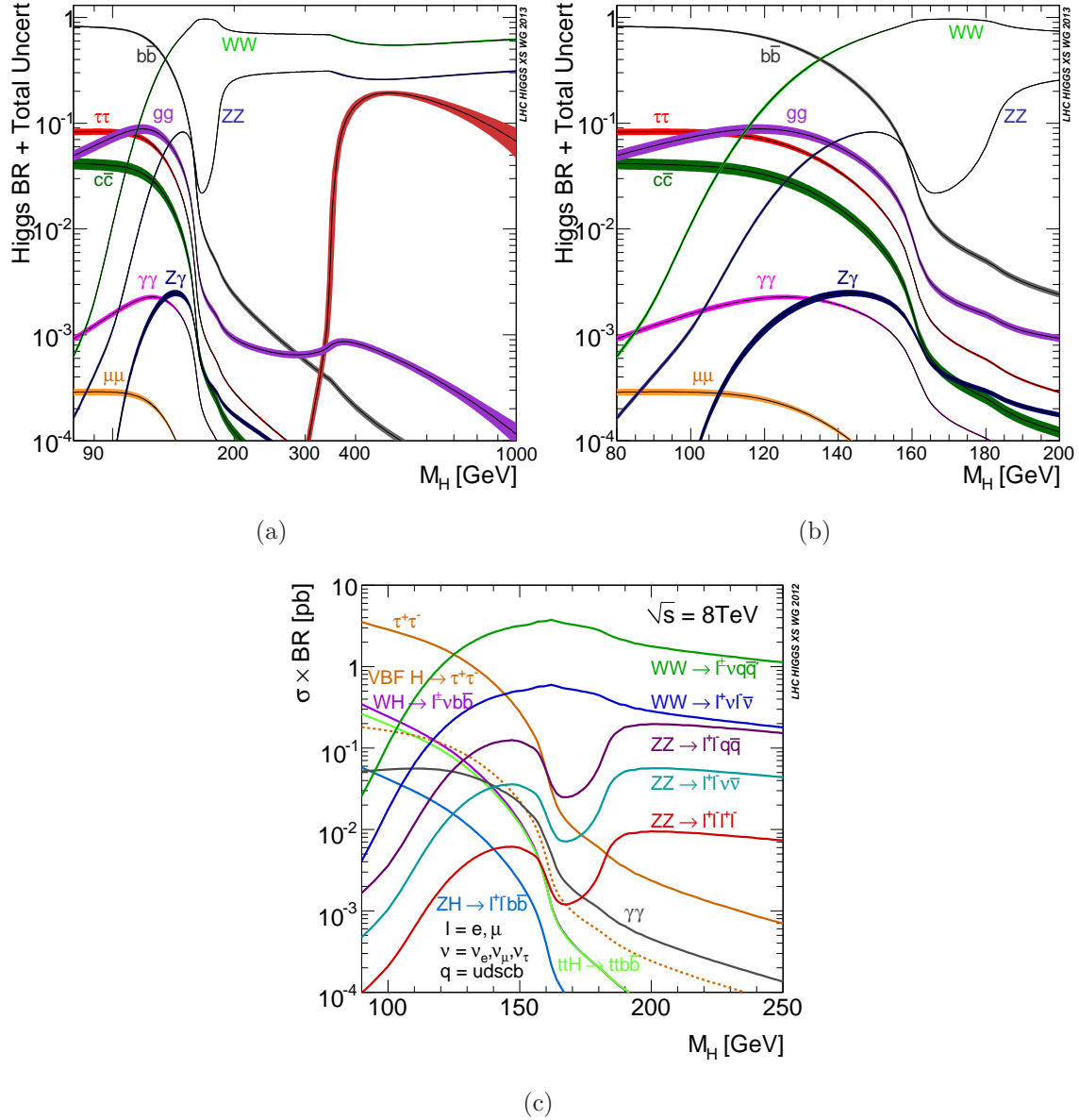
429 The very low mass region, below ~ 110 GeV, was excluded by the Large Electron-
 430 Positron Collider (LEP) experiments [22] before the LHC era and hence the LHC studies
 431 are focused in the mass region above 100 GeV. Figure 1.9 shows the $\Delta\chi^2$ profile versus
 432 the m_H obtained using the Gfitter [23] and the LEP excluded region appears in grey.
 433 In the low mass region, the sensitivity is as:

- 434 • $ZZ \rightarrow 4\ell$: less sensitive but cleanest
- 435 • $\gamma\gamma$: is very clean
- 436 • $WW \rightarrow \ell\ell\nu\nu$: very sensitive and less accurate, no mass reconstruction is possible
 437 due to the presence of two neutrinos
- 438 • $\tau\tau$: needs distinctive production features to reduce background, e.g. VBF
- 439 • bb : huge backgrounds from QCD
- 440 • Rest Channels: the background dominates at low center of mass (\sqrt{s}) energies

441 In the high mass region the $WW \rightarrow \ell^\pm\nu q\bar{q}$, $WW \rightarrow \ell^+\nu\ell^-\bar{\nu}$, $ZZ \rightarrow \ell^+\ell^-q\bar{q}$ and
 442 $ZZ \rightarrow \ell^+\ell^-\nu\bar{\nu}$ dominate.

443 Figures 1.10 present the Higgs channel production branching ratios at $\sqrt{s} = 8$ TeV
 444 as a function of the Higgs mass [19]. In the entire possible mass range and separately in
 445 the low mass region. The expected significance of the Higgs discovery had been studied
 446 prior to the data taking period and the discovery potential found to be significant [24].

Figure 1.10: Standard model Higgs boson decay branching ratios ((a), (b)) and branching ratios to specific channels (c) at $\sqrt{s} = 8$ TeV [19].



447 Chapter Bibliography

448 [1] Fermi National Laboratory, The science of matter, space and time,
 449 <http://www.fnal.gov/pub/inquiring/matter/madeof>.

450 [2] J. Beringer et al., Review of Particle Physics (RPP), *Phys.Rev.*, D86:010001, 2012.

451 [3] C.P. Burgess and G.D. Moore, The standard model: A primer, *Cambridge, UK: Cambridge Univ. Pr. (2007) 542 p.*

452

453 [4] Luis Anchordoqui and Francis Halzen, Lessons in particle physics, 2009,
 454 arXiv:0906.1271.

455 [5] S.L. Glashow, Partial Symmetries of Weak Interactions, *Nucl.Phys.*, 22:579–588,
 456 1961.

457 [6] Steven Weinberg, A Model of Leptons, *Phys.Rev.Lett.*, 19:1264–1266, 1967.

458 [7] Abdus Salam, Weak and Electromagnetic Interactions, *Conf.Proc.*, C680519:367–
 459 377, 1968.

460 [8] F. Halzen and Alan D. Martin, Quarks and Leptons: An Introductory Course in
 461 Modern Particle Physics, *New York, Usa: Wiley (1984) 396 p.*

462 [9] D.H. Perkins, Introduction to high energy physics, *Reading, USA: Addison-Wesley*
 463 *(1972) 353 p.* 1982.

464 [10] Abdelhak Djouadi, The Anatomy of electro-weak symmetry breaking. I: The Higgs
 465 boson in the standard model, *Phys.Rept.*, 457:1–216, 2008, arXiv:hep-ph/0503172.

466 [11] Predrag Cvitanovic, Group theory: Birdtracks, Lie's and exceptional groups,
 467 *Princeton, USA: Univ. Pr. (2008) 273 p.*

468 [12] Emmy Noether and M. A. Tavel, Invariant variation problems, 1918,
 469 arXiv:physics/0503066.

470 [13] W.N. Cottingham and D.A. Greenwood, An introduction to the standard model
 471 of particle physics, 2007.

472 [14] J. Goldstone, Field Theories with Superconductor Solutions, *Nuovo Cim.*, 19:154–
 473 164, 1961.

474 [15] Peter W. Higgs, Broken symmetries, massless particles and gauge fields, *Phys.Lett.*,
 475 12:132–133, 1964.

476 [16] F. Englert and R. Brout, Broken Symmetry and the Mass of Gauge Vector Mesons,
477 *Phys. Rev. Lett.*, 13:321–323, 1964.

478 [17] Antonio Pich, The Standard model of electroweak interactions, 2007,
479 arXiv:0705.4264.

480 [18] Jean Iliopoulos, Introduction to the STANDARD MODEL of the Electro-Weak
481 Interactions, *2012 CERN Summer School of Particle Physics, Angers* :, France,
482 2012, arXiv:1305.6779.

483 [19] S. Heinemeyer et al., Handbook of LHC Higgs Cross Sections: 3. Higgs Properties,
484 2013, arXiv:1307.1347.

485 [20] Maria Herrero, The Higgs System in and Beyond the Standard Model, 2014,
486 arXiv:1401.7270.

487 [21] Abdelhak Djouadi, Higgs Physics: Theory, *Pramana*, 79:513–539, 2012, 1203.4199.

488 [22] R. Barate et al., Search for the standard model Higgs boson at LEP, *Phys. Lett.*,
489 B565:61–75, 2003, hep-ex/0306033.

490 [23] Henning Flacher, Martin Goebel, Johannes Haller, Andreas Hocker, Klaus Monig,
491 et al., Revisiting the Global Electroweak Fit of the Standard Model and Beyond
492 with Gfitter, *Eur. Phys. J.*, C60:543–583, 2009, arXiv:0811.0009.

493 [24] G. Aad et al., Expected Performance of the ATLAS Experiment - Detector, Trigger
494 and Physics, 2009, 0901.0512.

495 [25] Michael E. Peskin and Daniel V. Schroeder, An Introduction to quantum field
496 theory, *Reading, USA: Addison-Wesley (1995) 842 p.*

497 [26] J. Beringer et al., Review of Particle Physics (RPP), *Phys. Rev.*, D86:010001, 2012.

498 [27] John F. Gunion, Howard E. Haber, Gordon L. Kane, and Sally Dawson, The Higgs
499 Hunter’s Guide, *Front. Phys.*, 80:1–448, 2000.

500 [28] James D. Wells, Lectures on Higgs Boson Physics in the Standard Model and
501 Beyond, 2009, arXiv:0909.4541.

502 [29] Riccardo Barbieri, Ten lectures on the electroweak interactions, arXiv:0706.0684v1.

503 [30] Scott Willenbrock, Symmetries of the standard model, pages 3–38, 2004,
504 arXiv:hep-ph/0410370.

505 [31] S. Heinemeyer, Higgs and Electroweak Physics, pages 37–67, 2009,
506 arXiv:0912.0361.

507 [32] S.F. Novaes, Standard model: An Introduction, 1999, arXiv:hep-ph/0001283.

508 [33] Gautam Bhattacharyya, A Pedagogical Review of Electroweak Symmetry Breaking
509 Scenarios, *Rept. Prog. Phys.*, 74:026201, 2011, arXiv:0910.5095.

2

510

511 LHC Structure, Operation and Experiments

512 2.1 Introduction

513 The Large Hadron Collider (LHC), currently the most powerful particle accelerator
514 [1], is designed to collide two counter rotating beams of protons or heavy ions [2]. The
515 accelerator sits in a circular tunnel of 27 km in circumference [2], between 50 and 175 m
516 under the surface, crossing the Swiss and French borders on the outskirts of Geneva
517 (Figure 2.1). During the Run-I period (2010 - 2013) proton-proton collisions took place
518 at energies of 3.5 and 4.0 TeV per beam and in the Run-II (2015 - 2018) the center of
519 mass energy is foreseen to reach 13 TeV. The capabilities of the collider's technology
520 reach the 14 TeV limit. The beams collision points, as appear in Figure 2.2, are the
521 places where the detectors of the experiments are located. Descriptions of the largest
522 LHC experiments are provided later on this section.

523 The name of the LHC describes its basic properties [1]:

524 • **Large** : The size of an accelerator is related to the maximum obtainable energy
525 and therefore the radius of the tunnel is an essential element of the design

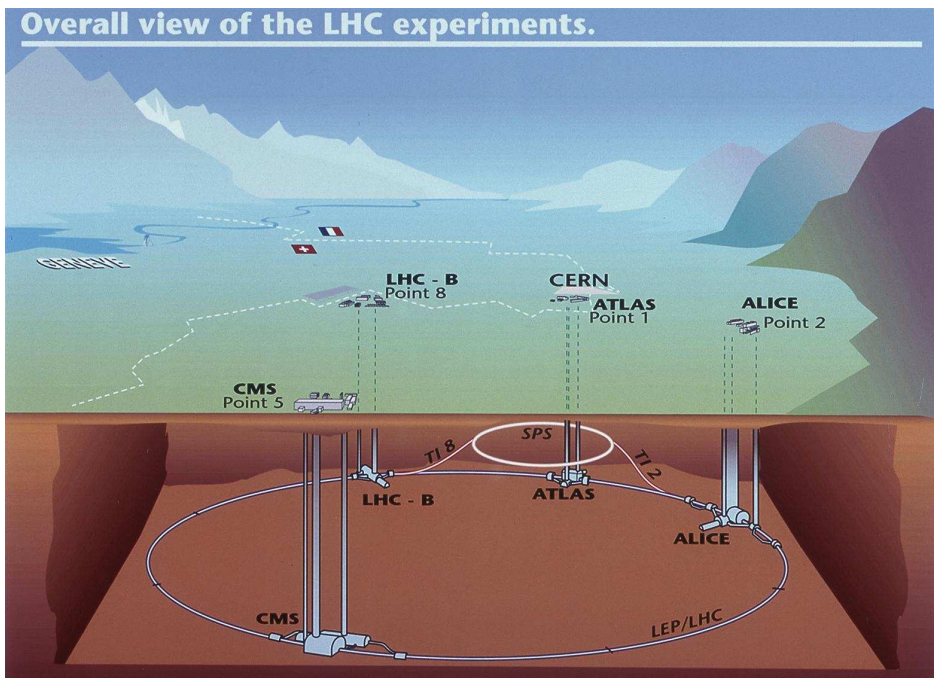
526 • **Hadron** : The LHC accelerates hadrons, either protons or lead ions, using both
527 radio-frequency cavities and dipole magnetic fields in order to generate them and
528 keep them in orbit

529 • **Collider** : Counter circulate beams collide and the energy of the collision is the
530 sum of the energies of the two beams.

Figure 2.1: Schematic view of the LHC size crossing the Swiss and French borders on the outskirts of Geneva [1].



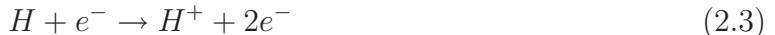
Figure 2.2: Schematic view of the LHC beam collision points where the experiments are located, specifically the ATLAS, CMS, ALICE and LHC-B sectors can be seen. [3].



531 The advantage of circular over linear accelerators is that the ring topology allows
 532 continuous acceleration, as the particle can transit several times [2]. Another advantage
 533 is that circular accelerators require relatively smaller size than a linear accelerator of
 534 comparable power. The beams move around the LHC ring inside a continuous vacuum
 535 guided by superconducting magnets that are cooled to 1.9 K by a huge cryogenics
 536 system and can be stored at high energies for hours. Even though in the next paragraphs
 537 the properties of the colliding mechanism are briefly explained, Table 2.1 presents the
 538 most important parameters of the LHC design.

539 2.2 The CERN Accelerator Complex

540 The proton beam origin that is accelerated, is the result of a chemical reaction
 541 chain [1], analytically:



544 This reactions take place when hydrogen gas is injected into a metal cylinder shown
 545 in Picture 2.3, called *Duoplasmatron* [1]. That leads to break down of the gas into its
 546 constituents protons and electrons. The protons, with energies that can reach 100 keV,
 547 then enter the accelerator complex, which is a succession of machines that increasingly
 548 accelerate to higher energies [4], as the diagram 2.4 shows. The beam is accelerated
 549 gradually as injected through the machines sequence, until it reaches the LHC. The start
 550 is the Radio Frequency Quadrupole (QRF), an accelerating component where four vanes
 551 (electrodes) provide a quadrupole RF field that both speeds up to 750 keV and focuses
 552 the beam [1]. From the quadrupole, the particles are sent to the linear accelerator
 553 (LINAC2). The LINAC2 tank is a multi-chamber resonant cavity tuned to a specific
 554 frequency which creates potential differences in the cavities that accelerate the particle
 555 up to 50 MeV [1]. Protons cross the LINAC2 and reach the 157 m circumference
 556 circular accelerator Proton Synchrotron Booster (PSB) in a few microseconds.

557 A distance of 80 m intercedes between the LINAC2 and the PSB, where twenty
 558 quadrupole magnets focus the beam along the line and two bending and eight steering
 559 magnets direct the beam. Afterwards, the PS Booster accelerates the beam to 1.4 GeV
 560 in 530 ms and injects it in the 628 m circumference circular accelerator Proton Syn-
 561 chrotron (PS) in less than 1 μ s [1]. The PS is responsible to feed the Super Proton
 562 Synchrotron (SPS) with beam of 25 GeV energy [5] in bunches with the appropriate

Table 2.1: Important parameters of the LHC design [1].

LHC parameters	
Circumference	26659 <i>m</i>
Dipole operating temperature	1.9 <i>K</i>
Number of arcs (2450 <i>m</i> long)	8
Number of lattice cells per arc	23
Number of straight sections (545 <i>m</i> long)	8
Main RF System	400.8 <i>MHz</i>
Number of magnets (dipoles, quadrupoles ... dodecapoles)	9300
Number of dipoles	1232
Number of quadrupoles	858
Number of RF cavities	8/ beam
Nominal energy (protons)	7 <i>TeV</i>
Momentum at collision	7 <i>TeV/c</i>
Momentum at injection	450 <i>GeV/c</i>
Nominal energy (ions)	2.76 <i>TeV/nucleon</i>
Peak magnetic dipole field	8.33 <i>T</i>
Current in main dipole	11800 <i>A</i>
Energy density of the LHC magnets	500 <i>kJ/m</i>
Main dipole coil inner diameter	56 <i>mm</i>
Distance between aperture axes (1.9 <i>K</i>)	194.00 <i>mm</i>
Distance between aperture axes (293 <i>K</i>)	194.52 <i>mm</i>
Main Dipole Length	14.3 <i>m</i>
Horizontal force at 8.33 <i>T</i> (inner and outer layer)	1.7 <i>MN/m</i>
Maximum current with NO resistance (1.9 <i>Ke</i> , 8.33 <i>T</i>)	17000 <i>A</i>
Maximum current with NO resistance (1.9 <i>Ke</i> , 0 <i>T</i>)	50000 <i>A</i>
Number de strands per cable	36
Bending radius	2803.95 <i>m</i>
Minimum distance between bunches	~ 7 <i>m</i>
Bunch spacing	25 <i>ns</i>
Design Luminosity	$10^{34} \text{ cm}^{-2} \cdot \text{s}^{-1}$
Number of bunches / proton beam	2808
Number of protons / bunch (at start)	$1.15 \cdot 10^{11}$
Circulating current / beam	0.54 <i>A</i>
Number of turns / second	11245
Stored beam energy	360 <i>MJ</i>
Stored energy in magnets	11 <i>GJ</i>
Beam lifetime	10 <i>h</i>
Average crossing rate	31.6 <i>MHz</i>
Number of collisions / second	600 <i>millions</i>
Radiated Power / beam (synchrotron radiation)	~ 6 <i>KW</i>
Total crossing angle (collision point)	300 μrad
Emittance ϵ_n	3.75 μrad
Amplitude Function β	0.55 <i>m</i>

Figure 2.3: The proton beam originates from hydrogen gas injected into a metal cylinder, surrounded by an electric field [1]. The Figure presents the metal cylinder, also called Duoplasmatron.

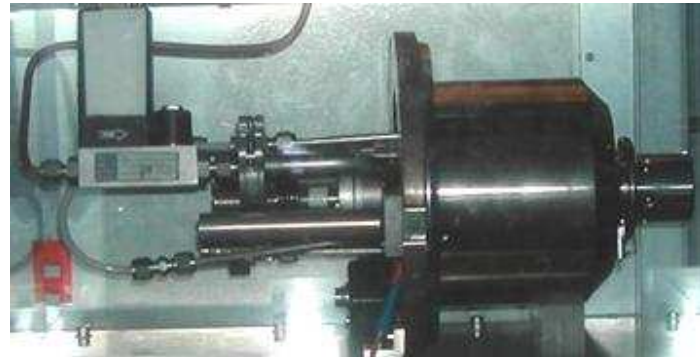
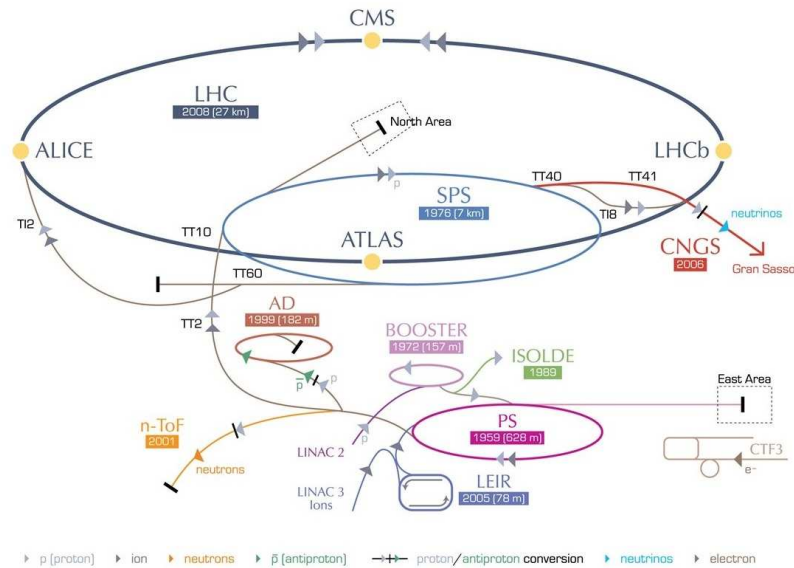


Figure 2.4: Schematic view of the different machines succession through which the proton beams gradually accelerated until they reach their final energy at the LHC [5].



563 spacing. During the Run-I period the bunch spacing was 50 ns and it is expected to
 564 be half during the Run-II operation. The SPS is the final step before the beam trans-
 565 fered to the LHC with an energy of 450 GeV both in clockwise and counter-clockwise
 566 directions after a filling time of 4.20 *minutes* per LHC ring. In the LHC, the beams
 567 circulate until they ramp to high energy and can be stored up to 10 *hours*, this is the
 568 so called "beam lifetime".

569 The higher the density of the stored particles is, the lower the beam lifetime is.
 570 Coulomb scattering of charged particles traveling together causes an exchange of mo-
 571 mentum between the transverse and longitudinal directions. Due to relativistic effects,
 572 the momentum transferred from the transverse to the longitudinal direction is enhanced
 573 by the relativistic factor γ . For stored beam, particles are lost (Touschek effect) if their
 574 longitudinal momentum deviation exceeds the RF bucket or the momentum aperture
 575 determined by the lattice.

576 After the dump of the beam, the dipole magnets are ramped down to 0.54 T.
 577 Meanwhile beam injection is repeated before the magnets are ramped up again to 8.3 T
 578 for another cycle of high energy collisions.

579 2.3 Proton Beams Collisions

580 The beams after the acceleration to the desired energy, e.g. 7, 8, 14 TeV, collide at
 581 the four collision points of the LHC while circulated in the beam lines. Between each
 582 consecutive bunch there is 7.5 m distance, which makes

$$26659 \text{ m} / 7.5 \text{ m} \approx 3550 \text{ bunches} \quad (2.4)$$

583 given the LHC circumference of 27km [1].

584 To get a correct sequence of bunches injected into the ring and to be able to insert
 585 new bunches when non-useful ones are extracted it is necessary to allow enough space
 586 for that. The effective number of bunches per beam is 2808. Each bunch has $1.15 \cdot 10^{11}$
 587 protons (1 cm³ of hydrogen gas has $\sim 10^{19}$ protons). Each bunch gets squeezed down
 588 (using magnetics lenses) to $16 \times 16 \mu\text{m}$ at an interaction point, where collisions take
 589 place [6]. The occupied volume for each proton in the interaction point is:

$$(74800 \times 16 \times 16) / (1.15 \cdot 10^{11}) \sim 10^{-4} \mu\text{m}^3. \quad (2.5)$$

590 That is much bigger than an atom, so a collision is still rare. The probability of one
 591 particular proton in a bunch colliding with a particular proton in the opposite bunch
 592 depends roughly on the proton size (d^2 with $d \sim 1 \text{ fm}$) and the cross-sectional size
 593 of the bunch (σ^2 , with $\sigma = 16 \mu\text{m}$) in the interaction point [1]. The exact relation is

594 described by the equation:

$$Probability = \frac{d_{proton}^2}{\sigma^2} = 4 \cdot 10^{-21}. \quad (2.6)$$

595 A sufficient number of interactions in every crossing is achieved with $N = 1.15 \cdot 10^{11}$
 596 protons/bunch, since the number of interactions per crossing is given by:

$$Probability \times N^2 \approx 50. \quad (2.7)$$

597 Taking into account that a fraction of $\sim 50\%$ are inelastic scatterings that give rise
 598 to particles at sufficient high angles with respect to the beam axis. Therefore, there
 599 are about 20 "effective" collisions at every crossing. With 11245 crosses per second and
 600 considering the number of bunches to be equal to the effective ($= 2808$), the average
 601 crossing rate is estimated to be:

$$11245 \times 2808 = 31.6 \text{ million crosses}. \quad (2.8)$$

602 The collisions per second can be calculated by multiplying the average crossing rate
 603 with the collision probability:

$$(31.6 \cdot 10^6 \text{ crosses/s}) \times (20 \text{ collisions/cross}) = 600 \text{ k collision/s}. \quad (2.9)$$

604 Considering 3550 bunches and the 11245 crossings per second the frequency is \sim
 605 40 MHz .

606 2.4 The LHC Experiments

607 As previously mentioned, the LHC ring hosts collision points, where the ATLAS,
 608 CMS, ALICE and LHCb experiments are located. The two large experiments, AT-
 609 LAS and CMS, are based on general-purpose detectors and are designed to investigate
 610 the largest range of physics possible. Having two independently designed detectors is
 611 vital for cross-confirmation of any new discoveries made. The rest medium-sized experi-
 612 ments, ALICE and LHCb, have specialized detectors for analyzing the LHC collisions in
 613 relation to specific phenomena [1]. Two other experiments, the LHCf and the TOTEM,
 614 are located very close to the ATLAS and CMS facilities respectively and designed to
 615 focus on "forward particles" (protons or heavy ions). The term forward particles refers
 616 to particles that do not meet head-on. In December 2009, the CERN Research Board
 617 approved another experiment called "MoEDAL" (the Monopole and Exotics Detector
 618 at the LHC) for the research of very specific exotic particles.

619 The detectors principle is to identify the products of the collisions of the proton
 620 beams, based on simple properties:

- 621 • *Charged Particles, electrons, protons and muons, leave traces through ionization*
- 622 • *Electrons are light particle (0.51 MeV) compared to protons (938.27 MeV) and*
623 *therefore lose energy quicker (in the calorimeters), while protons penetrate deeper*
624 *into the detector*
- 625 • *Photon traces in the electromagnetic calorimeters are the result of their decay*
626 *into an electron-positron pair*
- 627 • *Neutral hadrons transfer their energy to protons*
- 628 • *Muons leave traces in the trackers, pass through the calorimeters loosing a small*
629 *amount of their energy and reach the outer layers of the detectors, the muon*
630 *chambers*
- 631 • *Neutrinos do not interact with the detector, but can be identified using the missing*
632 *energy of each event*
- 633 • *The trajectories of charged particle are bent by the magnetic fields and the radius*
634 *of the curvature is used to calculate their momentum.*

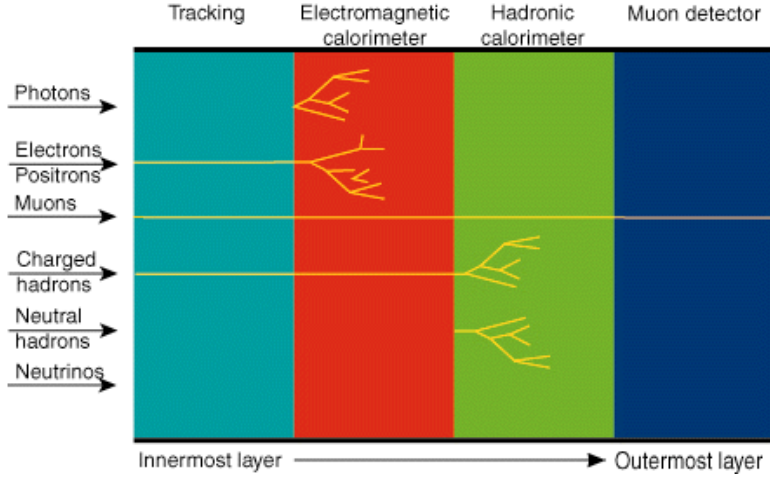
635 The above interactions are summarized in the Figure 2.5 for each particle passing
636 through the different detector components. Heavy collision products, such as the Z or
637 W^\pm bosons, are short-lived and decay into lighter particles which are detectable. The
638 complexity of the detectors arises from the ability to built a system able to identify fast
639 enough particles within a harsh background, reading the useful information out reliably
640 and reconstructing it accurately.

641 In the next paragraphs brief descriptions of the LHC experiments is given.

642 2.4.1 ATLAS

643 ATLAS acronym means “A Toroidal LHC ApparatuS” describing the world’s largest
644 general purpose particle detector, measuring 46 m long, 25 m high, 25 m wide, weight-
645 ing 7000 tons and consisting of 100 million sensors [1]. It records sets of measurements
646 on the particles created in collisions - their paths, energies, and their identities [7].
647 This is accomplished through six different detecting subsystems, shown in Figure 2.6,
648 that identify particles and measure their momentum and energy. The inner layer of
649 the ATLAS is the tracker, which consists of a silicon pixel, a silicon micro-strip and a
650 transition radiation gas detector. The next technology, outer from the tracker is the
651 Liquid Argonne Calorimeter (“LAr”), consisting of a barrel and forward calorimeter.
652 The ATLAS has another calorimeter technology, the Tile Calorimeter, made from plas-
653 tic scintillator tiles to detect hadrons in the barrel region. The Muon spectrometer

Figure 2.5: Particles interactions as passing through the different layers of a detector [1]. The figure represents the basic principles of the particle identification.



654 is based on four different technologies, the Cathode Strip Chambers (“CSC”) and the
 655 Monitored Drift Tubes (“MDT”) are used for the precision tracking and the Thin Gap
 656 Chambers (“TGC”) and the Resistive Plate Chambers (“RPC”) provide the trigger.
 657 The coverage of the muon spectrometer extends to the very forward region where there
 658 is no tracker coverage, with the ability to provide muon track reconstruction. Another
 659 vital element is the huge magnet system, combination of toroidal and solenoid magnets,
 660 that bends the paths of charged particles for the momentum measurement [8]. In the
 661 next chapter, a detailed description of the ATLAS detector is given.

662 2.4.2 CMS

663 The Compact Muon Solenoid (“CMS”) is the other of the two general-purpose LHC
 664 experiments [9]. Although it has the same scientific goals as the ATLAS experiment,
 665 it uses different technical solutions and design of its detector magnet system to achieve
 666 these [1]. The CMS detector is built around a huge solenoid magnet as shown in Fig-
 667 ure 2.7. This takes the form of a cylindrical coil of superconducting cable that generates
 668 a magnetic field of 4 T. The main volume of the CMS detector is a multi-layered cylin-
 669 der, 21 m long, 15 m wide and 15 m high, weighing 12500 tons. The innermost layer
 670 is a silicon-based particle tracker, surrounded by a scintillating crystal electromagnetic
 671 calorimeter which is itself surrounded with a sampling hadronic calorimeter. Both fit
 672 inside a central superconducting solenoid magnet, 13 m long and 6 m in diameter, that
 673 bends charged particles to allow their momentum measurements. Outside the magnet,
 674 are the large muon detectors, which are inside the return yoke of the magnet.

Figure 2.6: Figure of the ATLAS detector [3] showing the constituting subsystems, i.e. Inner Detector, Electromagnetic - Forward - Hadronic Calorimeters, Muon Spectrometer, Toroid and Solenoid Magnets.

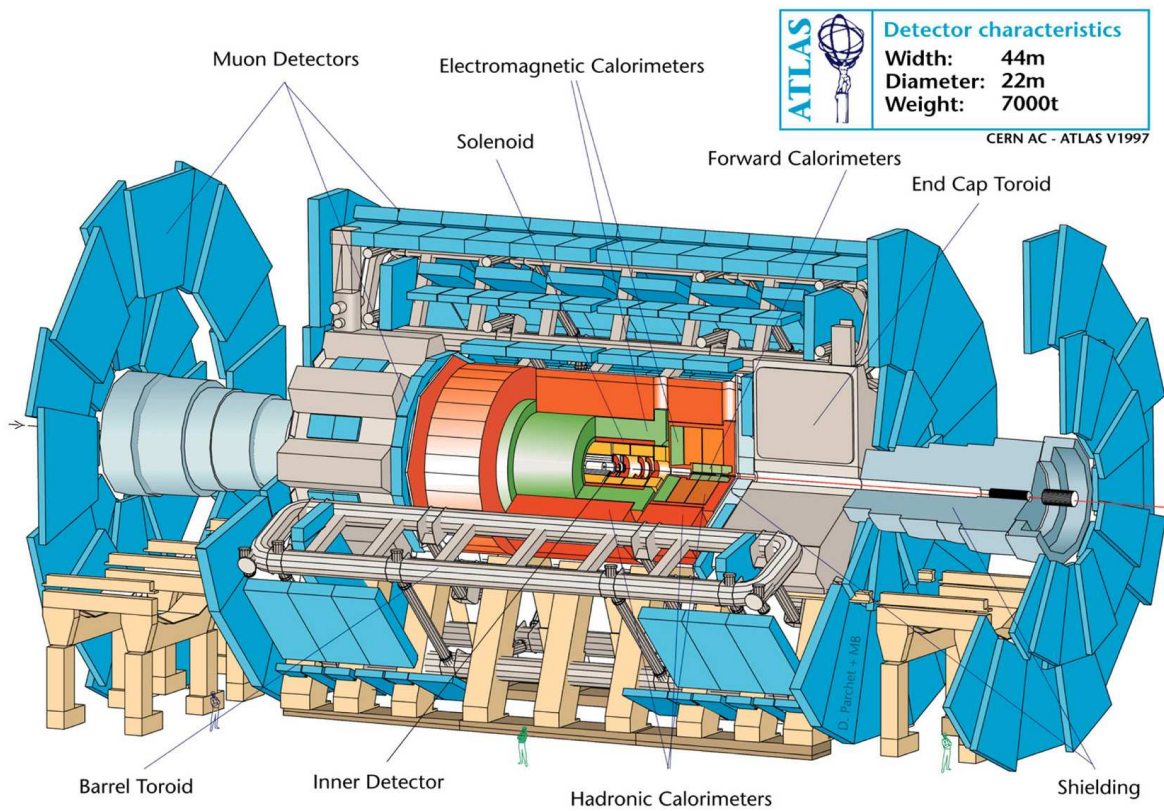
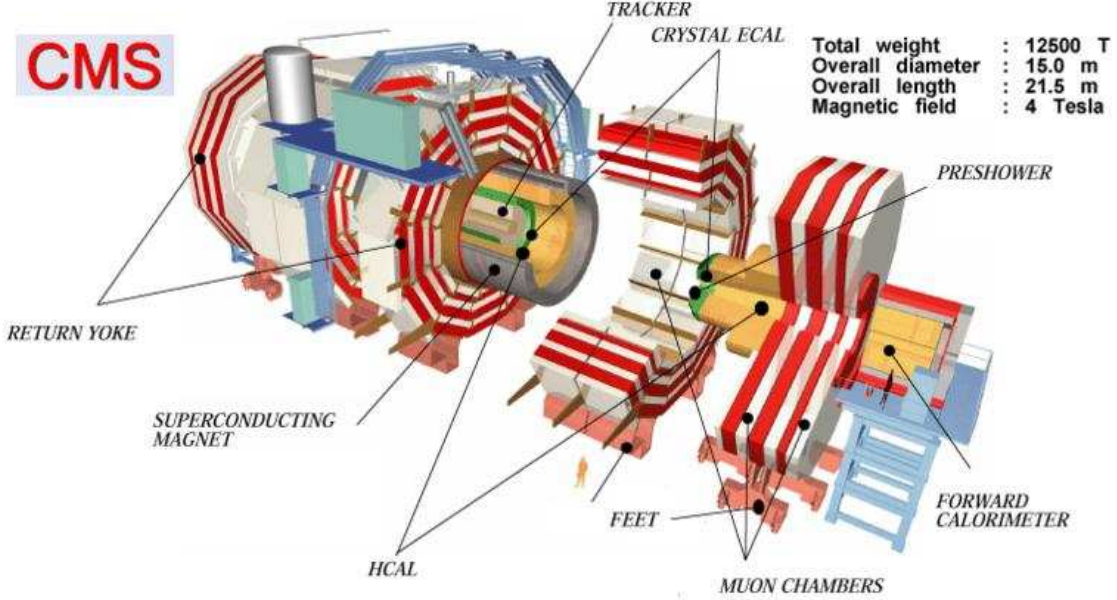


Figure 2.7: The Compact Muon Solenoid (“CMS”) detector schematic view [1]. The different components are marked on the Figure.



2.4.3 ALICE

ALICE (A Large Ion Collider Experiment) designed to study relativistic heavy ion interactions and the physics of strongly interacting matter at extreme densities where the formation of a new phase of matter, the quark-gluon plasma, is expected [10]. The heavy ions, specifically lead ions, are produced from a highly purified lead sample heated to a temperature of about 550°C. The lead vapor is ionized by an electron current, which produces many different charged states with a maximum around Pb^{27+} . These ions are selected and accelerated to 4.2 MeV/nucleon before passing through a carbon foil, which strips most of them to Pb^{54+} . The Pb^{54+} beam is accumulated, then accelerated to 72 MeV/nucleon in the Low Energy Ion Ring (“LEIR”), which transfers them to the PS. The PS accelerates the beam to 5.9 GeV/nucleon and sends it to the SPS after first passing it through a second foil where it is fully stripped to Pb^{82+} . The SPS accelerates it to 177 GeV/u then sends it to the LHC, which accelerates it to 2.76 TeV/u.

The detector consists of two main components: the central part composed of detectors dedicated to the study of hadronic signals and electrons, and the forward muon spectrometer dedicated to the study of quarkonia behavior in dense matter. The central part is embedded in a large solenoid magnet with a weak field (full current of 6000 A and magnetic field of 670 mT). The innermost part of the detector is the tracking

694 system, which consists of the inner tracking system (“ITS”) and the outer tracking
 695 system (“TPC”). TPC is a time projection chamber, a cylindrical device filled with gas
 696 and incorporating uniform electric and magnetic fields, ideal for separating, tracking,
 697 and identifying thousands of charged particles in a dense environment. A schematic
 698 representation of the ALICE detector is given in Figure 2.8.

699 **2.4.4 LHCb**

700 The LHCb detector (Large Hadron Collider beauty experiment) is a 21 m long, 10 m
 701 high and 13 m wide detector specializes in investigating the CP violation and other rare
 702 phenomena in decays of hadrons with heavy flavors, in particular B-mesons [12]. The
 703 interest in CP violation comes not only from the elementary particle physics but also
 704 from the cosmology, in an attempt to explain the dominance of matter over antimatter
 705 observed in the universe. B-mesons are most likely to emerge from collisions close to
 706 the beam direction, so the LHCb detector is designed to catch low-angle particles. The
 707 VErtex LOcator (“VELO”) is mounted closest to collision point subdetector of the
 708 LHCb and uses silicon detector elements to pick out the short-live B-mesons [13]. The
 709 products of the B-meson decay, π^\pm , K^0 and protons, can be detected from the two
 710 RICH (Ring Imaging Cherenkov) detectors by measuring the cones of the Cherenkov
 711 radiation. Precision tracking is provided by the silicon tracker and the gas-filled straw
 712 tubes of the outer tracker. The detector also consists of electromagnetic and hadron
 713 calorimeters for the energy measurement, as well as a muon system in the far end of
 714 the detector, as shown in Figure 2.9. A sophisticated feature of the LHCb is that the
 715 tracking detectors are movable close to the path of the beams circling in the LHC in
 716 order to catch the b-hadrons from the abundance of different types of hadrons created
 717 by the LHC.

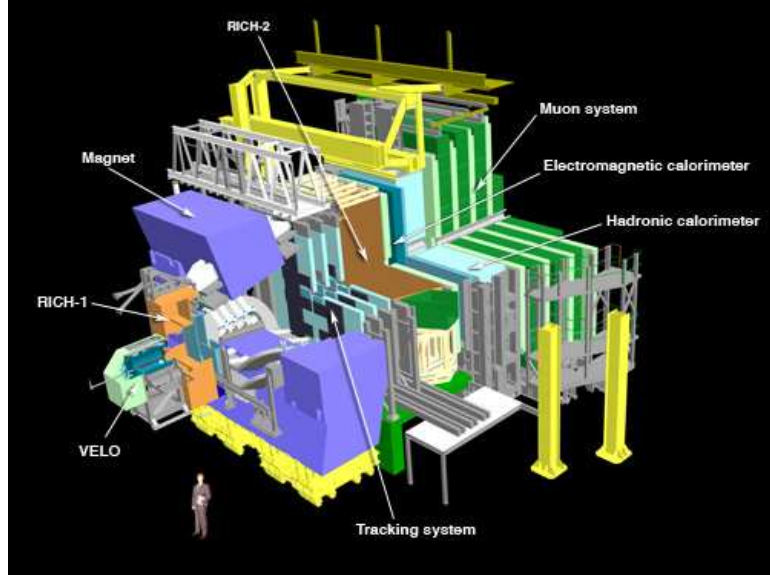
718 **2.4.5 TOTEM**

719 The TOTEM (Total Cross Section, Elastic Scattering and Diffraction Dissociation)
 720 experiment aims to measure the total p-p cross-section and study elastic and diffrac-
 721 tive scattering at the LHC [1]. The hosting point of the TOTEM detectors is near
 722 the protons collision point in the center of the CMS detector. The experiment mea-
 723 sures particles scattering at very small angles from the LHC’s proton-proton collisions,
 724 allowing the study of physical processes such as how the shape and size of a proton
 725 varies with energy, unable to be measured by any other of the LHC experiments. It
 726 includes detectors housed in specially designed vacuum chambers called “Roman pots”
 727 connected to the beam pipes in the LHC. There are eight Roman pots, placed in pairs

Figure 2.8: ALICE detector designed for the study of relativistic heavy ion collisions [11].



Figure 2.9: The LHCb detector designed to explore the CP violation and other rare phenomena in decays of hadrons with heavy flavors, in particular B-mesons [13].

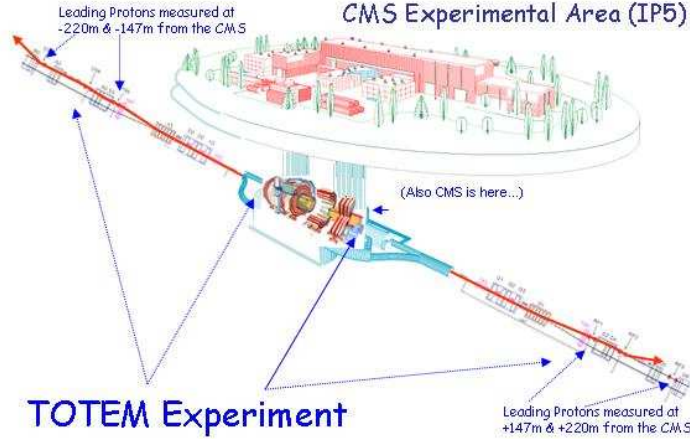


at four locations on either side of the collision point of the CMS experiment, including micro-strip silicon detectors used to detect protons [14]. Although the experiment is scientifically independent from other, TOTEM complements the results from the CMS detector and from other LHC experiments. The 20 tons TOTEM detector, in addition to the 8 Roman pots, is made up of gas-electron-multiplier (“GEM”) detectors and cathode strip chambers that measures the jets of forward-going particles that emerge from collisions when the protons break apart [15]. The experiment, schematically presented in Figure 2.10, spans over 440 m and the main detector is 5 m high and 5 m wide.

2.4.6 LHCf

The LHC forward experiment (“LHCf”) is placed on either sides of the ATLAS experiment for accurately measuring the number and energy of neutral pions and other forward particles in the ATLAS collisions [1]. The aim of the LHCf experiment is the study of the neutral-particle production cross sections in the very forward region of proton-proton and nucleus-nucleus interactions. The study is essential for the understanding of the development of atmospheric showers induced by very high energy cosmic rays hitting the Earth atmosphere. Studying how collisions inside the LHC cause similar cascades of particles to those of cosmic rays, it will help to interpret and calibrate

Figure 2.10: The Total Cross Section, Elastic Scattering and Diffraction Dissociation experiment (“TOTEM”) extended at both sides of the CMS detector [16].

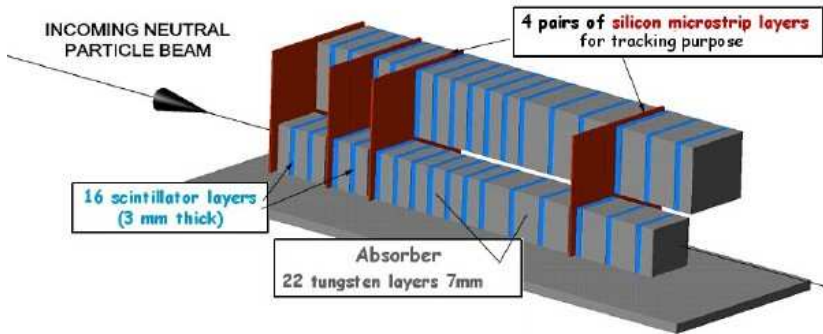


746 large-scale cosmic-ray experiments that can cover thousands of kilometers. The LHCf
 747 detector, presented in Figure 2.11, consists of two electromagnetic calorimeters made
 748 of tungsten plates, plastic scintillator and position sensitive sensors, installed at zero
 749 degree collision angle ± 140 m from the ATLAS interaction point inside the “TAN” [17].
 750 The TANs (Target Neutral Absorber) are massive zero degree neutral absorbers where
 751 charged particles transit from a single common beam tube to two separate beam tubes
 752 joining to the arcs of LHC.

753 2.4.7 MoEDAL

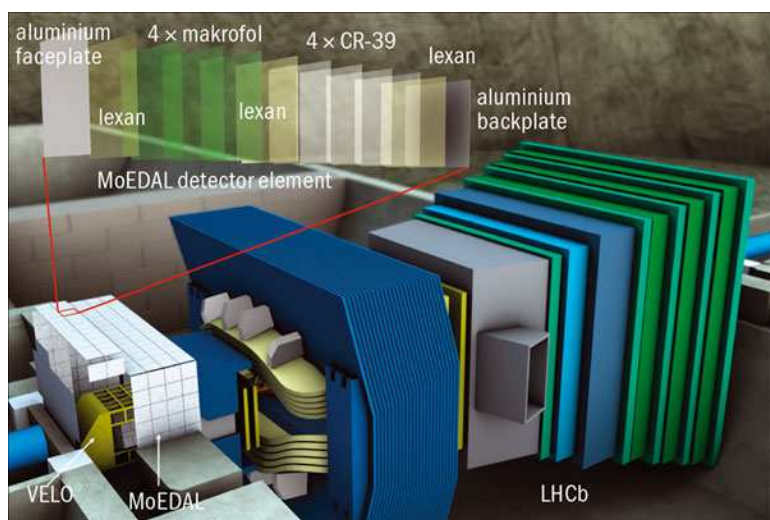
754 The search strategy for exotics planned for the main LHC detectors can be ex-
 755 tended with dedicated experimental designs to enhance, in a complementary way, the
 756 physics reach of the LHC [18]. The MoEDAL (Monopole and Exotics Detector at the
 757 LHC) project is such an experiment. The prime motivation is to directly search for the
 758 Magnetic Monopole or Dyon and other highly ionizing Stable or pseudo-stable Massive
 759 Particles (“SMPs”) at the LHC. The magnetic monopoles can be detected through the
 760 electromagnetic interaction between the magnetic charge and the macroscopic quantum
 761 state of a superconducting loop [19]. The Nuclear Track Detectors (“NTD”), shown in
 762 Figure 2.12, will be able to record the tracks of highly ionizing particles with electro-
 763 magnetic charges greater than 206 e. The detection of even one magnetic monopole
 764 that fully penetrated a NTD stack is expected to be distinctive. Another important
 765 area of physics beyond the Standard Model that can be addressed is the existence of
 766 SMPs with single electrical charge which provides a second category of a particle that

Figure 2.11: The LHCf simply consists of two calorimeters to accurately study the number and energy of neutral pions and other forward particles in the ATLAS collisions [1].



767 is heavily ionizing by virtue of its small speed. The third class of SMP which could be
 768 accessed by MoEDAL has multiple electric charge such as the black hole remnant, or
 769 long-lived doubly charged Higgs bosons. SMPs with magnetic charge, single or multiple
 770 electric charge and with Z/β ($\beta = v/c$) as low as five can, in principle, be detected by
 771 the CR39 nuclear track detectors, putting them within the physics reach of MoEDAL.

Figure 2.12: Schematic view of the MoEDAL Nuclear Track Detectors (“NTD”) to enhance the exploration of the exotic searches [1].



772 Chapter Bibliography

773 [1] X. C. Vidal, R. Cid, and M. Rey, Taking a closer look at LHC,
774 <http://www.lhc-closer.es>.

775 [2]

776 [3] ATLAS Collaboration, The ATLAS experiment portal, <http://www.atlas.ch/>.

777 [4] C. Lefevre, LHC: the guide, Feb 2009, <https://cds.cern.ch/record/1165534>.

778 [5] Christiane Lefevre, The cern accelerator complex, Dec 2008,
779 <https://cds.cern.ch/record/1260465>.

780 [6] Lyndon Evans, The Large Hadron Collider: A marvel technology, *Lausanne,*
781 *Switzerland: EPFL (2009) 251 p*, 2009.

782 [7] CERN, ATLAS: Detector and physics performance technical design report. Volume
783 1, 1999.

784 [8] ATLAS Collaboration, ATLAS: Detector and physics performance technical design
785 report. Volume 2, 1999.

786 [9] G.L. Bayatian et al., CMS physics: Technical design report, 2006.

787 [10] ALICE: Technical proposal for a large ion collider experiment at the CERN LHC,
788 1995.

789 [11] Berkeley Lab News Center, A flow of heavy-ion results from the LHC,
790 <http://newscenter.lbl.gov/2010/12/08/heavy-ion-results-lhc/>.

791 [12] *LHCb : Technical Proposal*, Tech. Proposal. CERN, Geneva, CERN-LHCC-98-004,
792 LHCC-P-4.

793 [13] LHCb Collaboration, The large hadron collider beauty experiment,
794 <http://lhcb-public.web.cern.ch/lhcb-public/en/Detector/Detector-en.html>.

795 [14] TOTEM Collaboration, The TOTEM experiment,
796 <http://home.web.cern.ch/about/experiments/totem>.

797 [15] G. Anelli et al., The TOTEM experiment at the CERN Large Hadron Collider,
798 *JINST*, 3:S08007, 2008.

799 [16] TOTEM Collaboration, Overall view of the totem experiment, BUL Collection -
800 BUL-PHO-2009-080, Aug 2009.

801 [17] O. Adriani et al., The LHCf detector at the CERN Large Hadron Collider, *JINST*,
802 3:S08006, 2008.

803 [18] MoEDAL Collaboration, The MoEDAL experiment, <http://moedal.web.cern.ch/>.

804 [19] James L. Pinfold, Searching for the magnetic monopole and other highly ionizing
805 particles at accelerators using nuclear track detectors, *Radiat. Meas.*, 44:834–839,
806 2009.

807 [20] Maximilien Brice, First lhc magnets installed at lhc, Apr 2005,
808 <https://cds.cern.ch/record/834351>.

809 [21] Lund University, Particle physics - ALICE website, <http://www.hep.lu.se/alice/>.

810 [22] James Pinfold et al., Technical Design Report of the MoEDAL Experiment, 2009.

811 [23] Oliver S. Bruning, P. Collier, P. Lebrun, S. Myers, R. Ostojic, et al., LHC Design
812 Report. 1. The LHC Main Ring, *CERN-2004-003-V-1, CERN-2004-003*, 2004.

813 [24] The LHC experiments, <http://public.web.cern.ch/public/en/lhc>.

3

814

Atlas Detector Description

815

816 3.1 Introduction

817 The ATLAS (A Toroidal LHC Apparatus) experiment is a general-purpose detector
818 at the LHC, whose design was guided by the need to accommodate the wide spectrum
819 of possible physics signatures [1]. The major remit of the ATLAS experiment is the
820 exploration of the TeV mass scale where ground-breaking discoveries are expected, such
821 as the discovery of the Higgs boson. The electroweak symmetry breaking is only one
822 focus of the investigation, as research is also conducted for all kinds of physics beyond
823 the Standard Model.

824 The design and construction of the ATLAS detector is briefly introduced in this
825 chapter. Summaries of the key aspects and functionalities of each component are re-
826 ported and their future upgrades are also discussed. Upgrades are expected during
827 the long shutdown periods referred to as "Phase Upgrades". The Phase-0 is the era
828 between the Run-I and Run-II, the Phase-I is the long shutdown after the Run-II and
829 later another one will follow in order to transit to the high luminosity LHC scenario
830 (HL-LHC).

3.2 The Coordinate System

The origin of the ATLAS coordinate system is defined as the nominal interaction point in the center of the detector [2]. The z-axis runs parallel to the beam line in counterclockwise direction. Half of the detector that corresponds to positive values of z is referred to as side A and the other half as side C. The x-axis points to the center of the LHC ring and the y-axis points upwards to the surface, resulting in a right-handed orientation. The xy-plane is referred to as the transverse plane. The ATLAS detector has a global cylindrical structure, where each subdetector consists of concentric layers around the beam axis, the barrel component, and two EndCaps formed by disks perpendicular to the z-axis on each side of the interaction point. A coordinate system closely related to cylindrical coordinates is convenient. The radial distance is given by $R = \sqrt{x^2 + y^2}$. The azimuthal angle $\phi \in [-\pi, \pi]$ is the angle with the positive x-axis and increases in clockwise direction when looking down the positive z-axis. The polar angle $\theta \in [0, \pi]$ is defined as the angle with the positive z-axis, albeit generally replaced by the pseudorapidity η , which is given by

$$\eta = -\ln(\tan \frac{\theta}{2}) \quad (3.1)$$

The preference for this quantity is motivated by the particle flux being roughly constant as a function of η . A direction (η, ϕ) is assigned to the reconstructed final state objects and the opening angle between two of them is denoted ΔR :

$$\Delta R = \sqrt{(\Delta\eta)^2 + (\Delta\phi)^2} \quad (3.2)$$

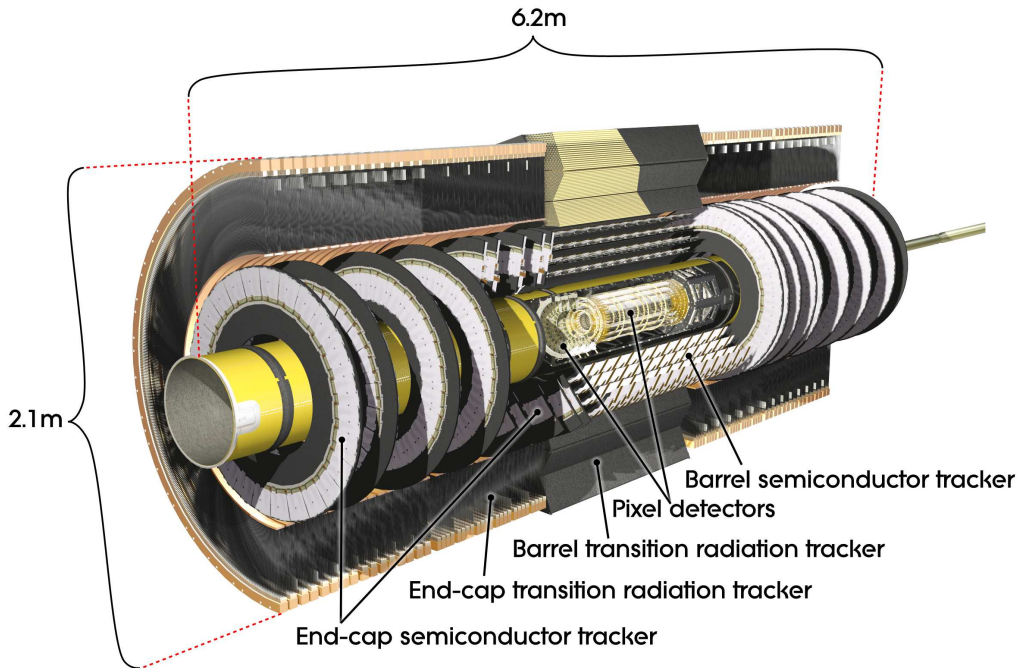
3.3 Performance Requirements

The performance requirements for the design of the ATLAS detector are based on the processes that may be observed at this new energy scale, such as the production of the Higgs boson, SUSY particles or any kind of Beyond the SM physics. The extensive variety of objects to be detected, the broad energy range of particles to be measured, the high radiation conditions and the high collision rate impose strict requirements on the detectors precision, speed, performance, radiation hardness, efficiency and acceptance. An additional challenge is the instantaneous selection of collisions to be stored, which is taken care of by the trigger system.

3.4 The Inner Detector

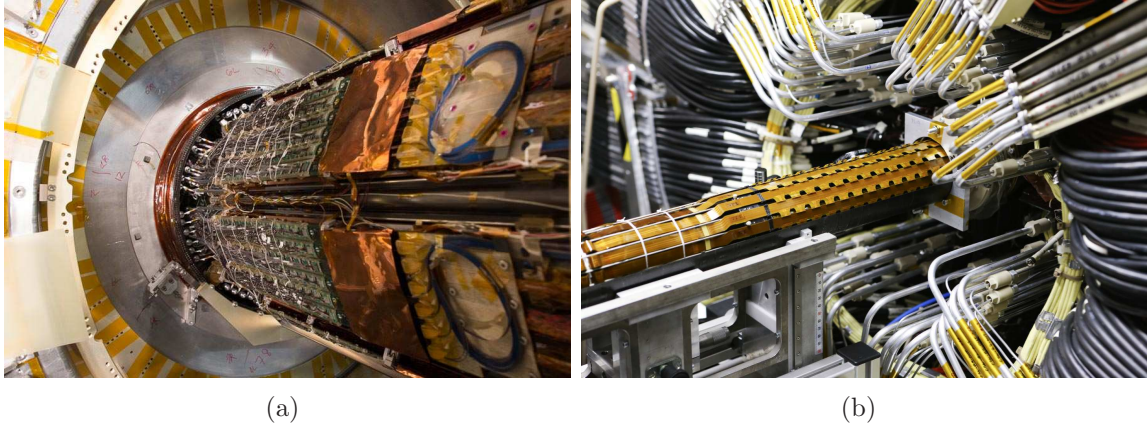
The ATLAS inner detector is designed to cope with 10^3 charged particle tracks for every beam collision every 25 ns ¹ at the design luminosity of the LHC [1]. A powerful magnetic field causes the particle carrying electric charge tracks to bend, and the curvatures of these tracks allow the momentum and electric charge of each particle to be determined. Concentric layers of high precision tracking detectors are used to record the tracks as they fly away from the interaction point. The inner detector is the first detector layer, very close to the collision point, as seen in Figure 3.1, where the radiation levels are intense, fluxes are up to 10^5 particles per mm^2 per sec, making radiation hardness a top priority for detector and readout electronics. At the same time, the amount of material in the Inner Detector must be minimized to avoid obstructing the particle trajectories ($< 0.1\text{ mm}$ [3]). In the next subsections, the different technologies that the ATLAS uses for tracking are briefly described along with the central solenoid that provides the necessary magnetic field.

Figure 3.1: Inner detector schematic where the different technologies that it apart (Pixel, Silicon and Transition Radiation Tracker) are visible [2].



¹Design value. During the Run-I period it was 50 ns .

Figure 3.2: The B-layer of the inner detector replaced after the Run-I [6]. Figure (a) taken during the extraction which followed by the installation of a new module (IBL) (Figure (b)) as preparation for the Run-II [5]. Due to the high levels of radiation the lifetime of the module is three years of operations [4].



3.4.1 Pixel Detector

The pixel detector system provides critical tracking information for pattern recognition near the collision point and largely determines the ability of the Inner Detector to find secondary vertices [4]. The pixel system provides three or more space points over the complete acceptance of the Inner Detector, $|\eta| < 2.5$. The innermost pixel layer is called B-layer and located as close as possible to the interaction point to provide the optimal impact parameter resolution. The Insertable B-layer (IBL) operated for the Run-I and replaced for the Run-II, Figure 3.2 shows the extraction followed by the installation of the IBL as preparation for the Run-II [5]. The two other barrel layers and the disk layers are located at radii greater than about 10 cm, for which the useful lifetime is expected to be about seven years at the design luminosity. Four disk layers on either side of the interaction point are required to provide full coverage for $|\eta| < 2.5$.

The layout and parameters of the pixel detector system are determined by performance requirements and by the desired lifetime of the system in the intense radiation environment near the collision point. The detector system is composed of modular units. Read out integrated circuits are mounted on a detector substrate to form barrel and disk modules. The detector substrate is silicon, and the current baseline design is an n^+ in n -bulk sensor. The read out integrated circuits are mounted on the silicon sensor using bump bonding techniques. An additional integrated circuit for control and clock distribution and data compression is mounted on each module, and flexible cables connect each module to data transmission/control circuitry located within the detector volume. Optical fibers or twisted pair cables are used to transmit data to and from the pixel system to read out drivers located outside the ATLAS detector. There are about

895 1500 identical barrel modules and about 1000 identical disk modules in the system. The
 896 barrel modules are mounted on supporting structures (staves) that are also identical
 897 throughout the system. Similarly, the disk modules are located on identical support
 898 sectors that are joined to form disks. The resulting mechanical structure is very stable
 899 and provides the cooling capability to maintain the silicon temperature at $\leq -6^{\circ}\text{C}$ even
 900 with the large heat load from the electronics and other sources.

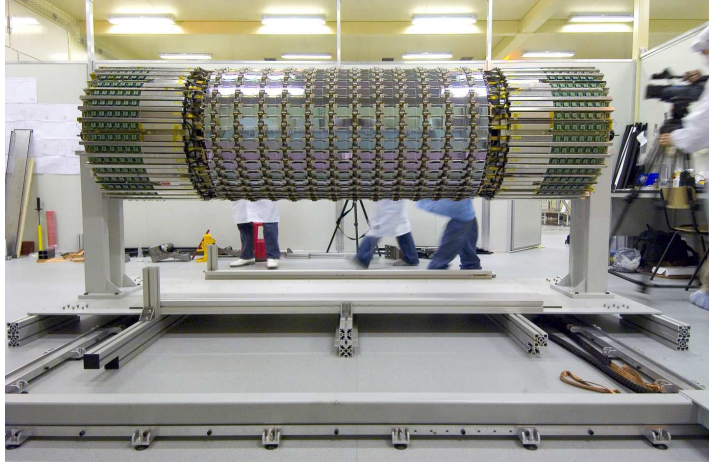
901 Specifically, a Pixel sensor is a $16.4 \times 60.8 \text{ mm}$ wafer of silicon with 46080 pixels,
 902 50 microns each. A Pixel module comprises an un-packaged flip-chip assembly of 16
 903 front-end chips bump bonded to a sensor substrate. There are 1744 modules in the
 904 Pixel Detector for nearly 80 million channels in a cylinder 1.4 m long, 0.5 m in dia-
 905 meter centered on the interaction point. The barrel part of the pixel detector consists of
 906 the 3 cylindrical layers with the radial positions of 50.5 mm, 88.5 mm and 122.5 mm
 907 respectively. These three barrel layers are made of identical staves inclined with az-
 908 imuthal angle of 20 degrees. There are 22, 38 and 52 staves in each of these layers
 909 respectively. Each stave is composed of 13 pixel modules. In the module there are
 910 16 front-end (FE) chips and one Module Control Chip (MCC). One FE chip contains
 911 160 rows and 18 columns of pixel cells, i.e. 2880 pixels per FE chip or 46080 pixels
 912 per module. There are three disks on each side of the forward regions. One disk is
 913 made of 8 sectors, with 6 modules in each sector. Disk modules are identical to the
 914 barrel modules, except the connecting cables. The front-end chips are a major heat
 915 source (0.8 W/cm^2) dissipating more than 15 kW into the detector volume. This heat
 916 is taken out via integrated cooling channels in the detector support elements: Staves
 917 in the barrel region and Sectors in the forward region.

918 3.4.2 The Semiconductor tracker (“SCT”)

919 The Semiconductor Tracker (“SCT”) designed to provide four precision measure-
 920 ments per track in the intermediate radial range, contributing to the measurement of
 921 momentum, impact parameter and vertex position, as well as providing good pattern
 922 recognition by the use of high granularity [7]. The system is an order of magnitude
 923 larger in surface area than any silicon micro-strip detector of previous generations and
 924 faces high radiation levels.

925 The barrel SCT, shown in Figure 3.3 before the installation, uses four layers of silicon
 926 micro-strip detectors to provide precision points in the R , ϕ and z coordinates, using
 927 small angle stereo to obtain the z measurement. Each silicon detector is $6.36 \times 6.40 \text{ cm}^2$
 928 with 768 readout strips each with $80 \mu\text{m}$ pitch. Each module consists of four detectors.
 929 On each side of the module, two detectors are wire-bonded together to form 12.8 cm
 930 long strips. Two such detector pairs are then glued together back-to-back at a 40 mrad
 931 angle, separated by a heat transport plate, and the electronics are mounted above

Figure 3.3: The Barrel Semiconductor Tracker (“SCT”) [8]. The high-precision and high-efficiency semiconductor detector elements near to the collision point distinguish individual tracks from the hundreds produced in each collision [3].



932 the detectors on a hybrid. The readout chain consists of a front-end amplifier and
 933 discriminator, followed by a binary pipeline which stores the hits above threshold until
 934 the first level trigger decision. The forward modules are very similar in construction
 935 but use tapered strips, with one set aligned radially. Forward modules are made with
 936 both 12 and 7 cm lengths.

937 The detector contains $61\ m^2$ of silicon detectors, with 6.2 million readout channels.
 938 The spatial resolution is $16\ \mu m$ in $R\phi$ and $580\ \mu m$ in z . Tracks can be distinguished if
 939 they are separated by more than $200\ \mu m$.

940 The barrel modules are mounted on local supports which allow units of six modules
 941 to be tested together before mounting on carbon-fibre cylinders which carry the cooling
 942 system; the four complete barrels at radii of 300, 373, 447 and 520 mm are then linked
 943 together. The forward modules are mounted in up to three rings onto nine wheels,
 944 which are interconnected by a space-frame. The radial range of each disk is adapted
 945 to limit the coverage to $|\eta| \leq 2.5$ by equipping each one with the minimum number of
 946 rings, and by using 6 cm long modules where appropriate.

947 The system requires a very high stability, cold operation of the detectors, and the
 948 evacuation of the heat generated by the electronics and the detector leakage current.
 949 The structure is therefore designed with materials with as low a coefficient of ther-
 950 mal expansion as possible. The cooling is a bi-phase system using ice suspended in
 951 a methanol-water mixture (“binary ice”) to achieve low thermal gradients across the
 952 detector. The detector and its front-end electronics are expected to be operational for
 953 10 years, given the irradiation levels [7].

954 3.4.3 Transition Radiation Tracker (“TRT”)

955 The Transition Radiation Tracker (“TRT”), partially presented in Figure 3.4, is
 956 based on the use of straw detectors, which can operate at the very high rates needed
 957 by virtue of their small diameter and the isolation of the sense wires within individual
 958 gas envelopes [7]. Electron identification capability is added by employing xenon gas
 959 to detect transition-radiation photons created in a radiator between the straws. This
 960 technique is intrinsically radiation hard, and allows a large number of measurements,
 961 typically 36, to be made on every track at modest cost. However, the detector must
 962 cope with a large occupancy and high counting rates at the LHC design luminosity.

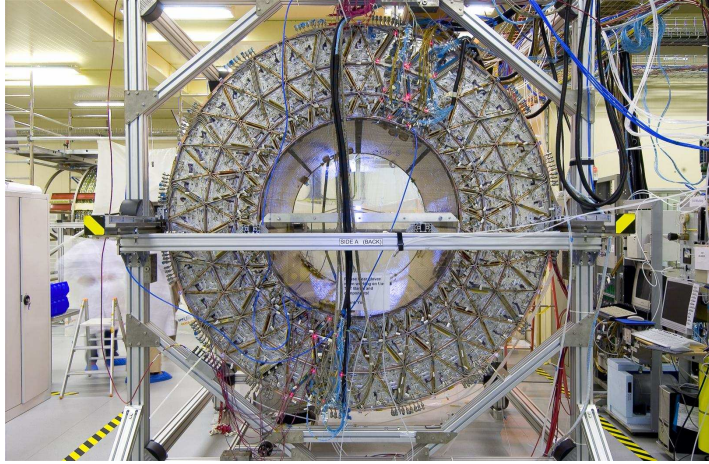
963 Each straw is 4 mm in diameter, giving a fast response and good mechanical prop-
 964 erties for a maximum straw length of 150 cm . The barrel contains about 50000 straws,
 965 each divided in two at the center in order to reduce the occupancy and read out at
 966 each end. The EndCaps contain 320000 radial straws, with the readout at the outer
 967 radius. The total number of electronic channels is 420000. Each channel provides a
 968 drift-time measurement, giving a spatial resolution of $170\text{ }\mu\text{m}$ per straw, and two in-
 969 dependent thresholds. These allow the detector to discriminate between tracking hits,
 970 which pass the lower threshold, and transition-radiation hits, which pass the higher.
 971 The discrimination is needed for the particles identification.

972 The barrel section is built of individual modules with between 329 and 793 axial
 973 straws each, covering the radial range from 56 to 107 cm . The modularity was chosen
 974 as a compromise between the ease of construction and maintenance, and the additional
 975 structural elements involved. The first six radial layers are inactive over the central
 976 80 cm of their length, in order to reduce their occupancy, while providing extra coverage
 977 of the crack between the barrel and EndCap sections.

978 Each of the two EndCaps consists of 18 wheels. The 14 wheels nearest the interaction
 979 point cover the radial range from 64 to 103 cm , while the last four wheels extend to an
 980 inner radius of 48 cm in order to maintain a constant number of crossed straws over
 981 the full acceptance. To avoid an unnecessary increase in the number of crossed straws
 982 at medium rapidity, wheels 7 to 14 have half as many straws per cm in z as the other
 983 wheels.

984 A primary challenge of the design is to obtain good performance at high occupancy
 985 and high counting rate. In the barrel, the rate of hits above the lower threshold varies
 986 with radius from 6 to 18 MHz , while in the EndCaps the rate varies with z from 7 to
 987 19 MHz . The maximum rate of hits above the higher TR-threshold is 1 MHz . Within
 988 a single drift-time bin, the occupancy is about one third of that in the entire straw
 989 active time window. A fast, low-noise preamplifier-shaper circuit with active baseline
 990 restoration has been developed to process the signals, using a radiation hard bipolar
 991 process. Position accuracies of about $170\text{ }\mu\text{m}$ have been achieved in tests at average
 992 straw counting rates of about 12 MHz . At these rates, only about 70% of the straws
 993 give correct drift time measurements because of shadowing effects, but the large number

Figure 3.4: View of the TRT before the installation [9]. Made from hundreds of thousands of narrow, gas-filled “straws”, each with a high-voltage wire running along its axis. Charged particles passing through the straw ionize the gas producing electrical pulses. The timing of these pulses allows the positions of the particles to be measured with a precision of 0.15 mm . Special materials are embedded between the straw tubes to cause electrons to produce X-rays when they pass through them, essential to distinguish electrons produced in collisions from heavier particles such as pions [3].



994 of straws per track guarantees a measurement accuracy of better than $50\text{ }\mu\text{m}$ averaged
 995 over all straws at the LHC design luminosity, including errors from alignment.

996 A good pattern recognition performance is assured by the continuous tracking.
 997 Within the radial space available, the straw spacing has been optimized for tracking
 998 at the expense of electron identification, which would be improved by a greater path
 999 length through the radiator material and fewer active straws. The distribution of the
 1000 straws over the maximum possible path length also enhances the pattern recognition
 1001 performance. The TRT contributes to the accuracy of the momentum measurement in
 1002 the Inner Detector by providing a set of measurements roughly equivalent to a single
 1003 point of $50\text{ }\mu\text{m}$ precision. It aids the pattern recognition by the addition of around 36
 1004 hits per track, and allows a simple and fast level-2 track trigger to be implemented.
 1005 It allows the Inner Detector to reconstruct V^0 s which are especially interesting in CP-
 1006 violating B decays. In addition it provides additional discrimination between electrons
 1007 and hadrons, with a pion rejection varying with η between a factor of 15 and 200 at
 1008 90% electron efficiency.

3.5 The Calorimeters

Surrounding the Inner Detector are the Calorimeters, which measure the energies of charged and neutral particles of the interaction [3]. The so-called “sampling calorimeters” consist of many layers of dense plates, which absorb incident particles and transform their energies into “showers” of lower energy particles. Between the absorber plates are thin layers of liquid argon or scintillating plastic which sample the energies of the particle showers and produce proportional signals. The calorimeters are designed to trigger on and to provide precision measurements of the energy of electrons, photons, jets, and missing E_T [10].

In order to explore the full physics potential of the LHC, the ATLAS electromagnetic (“EM”) calorimeter must be able to identify efficiently electrons and photons within a large energy range (5 GeV to 5 TeV), and to measure their energies with a linearity better than 0.5% [2]. One of the key ingredients for the description of the detector performance is the amount and position of the upstream material. At larger radii, where most of the calorimeter weight is located, and where the radiation levels are low, a less expensive iron-scintillator hadronic “Tile Calorimeter” is used.

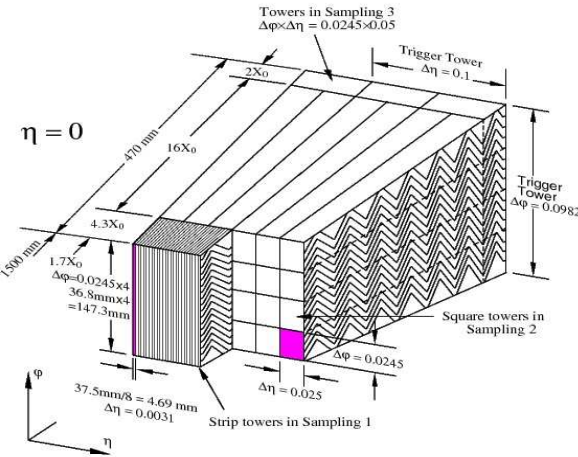
The following paragraphs describe the calorimeter technologies used in the ATLAS experiment.

3.5.1 The Liquid Argon (“LAr”) Calorimeter

The Liquid Argon sampling calorimeter technique with ”accordion-shaped” electrodes, as shown in Figure 3.5, is used for all electromagnetic calorimetry covering the pseudorapidity interval of $|\eta| < 3.2$ [10]. The Liquid Argon technique is also used for hadronic calorimetry from $1.4 < |\eta| < 4.8$. In order to operate a cryogenic system is needed. It includes the system for cooling down and warming up the cryostats and the detectors by circulation of helium. In routine operation, the cooling of the cryostats is achieved using liquid nitrogen produced in a closed loop by a liquefier located in the cryogenics cavern. This equipment has to maintain the temperature of liquid argon in the cryostats constant at approximately 89.3 K and the purity below 2 ppm of oxygen equivalent.

The Barrel EM Calorimeter, presented in Figure 3.6, has a cryostat of 6.8 m long, with an outer radius of 2.25 m, and an inner cavity radius of 1.15 m. Both the inner and the outer shells are in aluminum alloy, with vacuum insulation. The superconducting solenoid uses the same insulation vacuum as the liquid argon vessel. The total thickness of the bare solenoid is 44 mm, amounts to $0.63 X_0$ and is supported by the warm flange of the inner shell. Inside the liquid argon vessel, the calorimeter consists of two identical half-barrels, with a gap of a few millimeters in between. Because of

Figure 3.5: Sketch of the accordion geometry structure of the EM calorimeter [10] which provides uniform response in all directions. It consists of closely-spaced absorber layers of stainless steel-clad lead with liquid argon as the sampling material. Particle showers produce ions in the liquid argon which are seen as electric pulses by segmented electrodes.

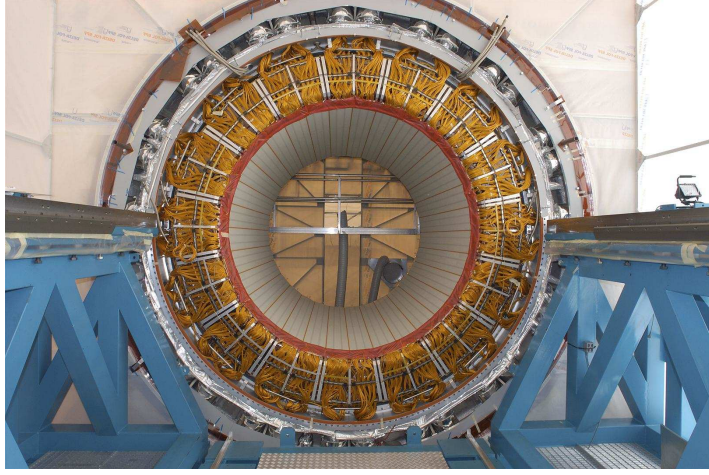


1045 the accordion shape, each half-barrel appears continuous in azimuth. Each half-barrel
 1046 consists of 1024 lead-stainless-steel converters with copper-polyimide multilayer read-
 1047 out boards in between. Fully pointing readout cells are defined in η and in azimuth by
 1048 grouping together four (for the central towers) adjacent boards. Connections are made
 1049 at the front and back face of the calorimeter using motherboards, which also carry the
 1050 calibrating element (one resistor per readout and calibration signals are routed through
 1051 cold-to-warm feedthroughs located at each end of the cryostat. Electronics boxes con-
 1052 taining the readout elements, including the ADCs, are located on each feedthrough,
 1053 and provide electrical continuity of the ground so as to form a single Faraday cage out
 1054 of which come the digital signals.

1055 In the EndCaps, the amplitude of the accordion waves scales with the radius. Given
 1056 the practical limitations in fabricating the absorber plates, which are arranged like the
 1057 spokes of a wheel, the ratio of inner to outer radius of a given plate is limited to about
 1058 three. As a consequence each EndCap EM wheel consists of two concentric wheels, the
 1059 large one spanning the pseudorapidity interval from 1.4 to 2.5, and the small one from
 1060 2.5 to 3.2. There are 768 plates in the large wheel (3 consecutive planes are grouped
 1061 together to form a readout cell of 0.025 in ϕ) and 256 in the small wheel.

1062 The amount of material, the way it is distributed in space and the presence of
 1063 a magnetic field combine to necessitate a presampler to correct for the energy lost in
 1064 front of the calorimeter. The barrel (EndCap) presampler feature, a 1 cm (5 mm) liquid
 1065 argon active layer instrumented with electrodes roughly perpendicular (parallel) to the

Figure 3.6: View of the LAr Barrel EM calorimeter [11] after the cabling and insertion.



beam axis. In the transition region between barrel and EndCap, around $|\eta| = 1.4$, a scintillator layer, between the two cryostats, is used to recover mainly the jet energy measurement. This also helps for electrons and photons. Beyond a pseudorapidity of 1.8, the presampler is no longer necessary given the more limited amount of dead material and the higher energy of particles for a given p_T . In order to avoid creating a gap in the electromagnetic calorimetry coverage the electromagnetic EndCap wheels have to be as close as possible to the barrel modules. To satisfy this requirement, the gap between the two cryostats (95 mm), and the EndCap presampler, which is of minimum thickness, is encased in a notch of the cryostat cold wall. This takes advantage of the fact that at this radius the mechanical stresses in the EndCap cryostat cold wall are not too large.

The hadronic EndCap calorimeter (“HEC”), is a liquid argon (LAr) sampling calorimeter with copper-plate absorbers, designed to provide coverage for hadronic showers in the range $1.5 < |\eta| < 3.2$. The HEC detector elements are located in the EndCap cryostats at both ends of the ATLAS tracking volume. They share the cryostats with the EM and the forward calorimeter (“FCAL”). The HEC sits behind the EM and FCAL is completely shadowed by it. The boundary between the HEC and the is on a cylinder of radius 0.475 m. Thus the η boundary between the two detectors varies as a function of z . This technology was selected as it allows a simple mechanical design to be produced that is radiation resistant and covers the required area in a cost-effective way. The gaps between the copper plates are instrumented with a readout structure. This structure optimizes the signal-to-noise ratio while reducing the high-voltage requirement and ionization pile-up, and limiting the effect of failure modes such as high-voltage sparks and shorts. The signals are amplified and summed employing the concept of “active pads”: the signals from two consecutive pads are fed into a separate

1091 amplifier mounted on the outer radius of the HEC. The use of cryogenic preamplifiers
 1092 provides the optimum signal-to-noise ratio for the HEC. An important aspect of the
 1093 HEC is its ability to detect muons, and to measure any radiative energy loss.

1094 The FCAL provides electromagnetic and hadronic calorimetry coverage in the range
 1095 $3.2 < |\eta| < 4.9$. The FCAL is a liquid argon ionization device integrated into the End-
 1096 Cap cryostat so as to minimize the effects of the transition in the region $|\eta| \sim 3.2$.
 1097 The three modules of the FCAL are positioned within the forward tube structure of
 1098 the EndCap cryostat. A fourth module, a passive shielding plug, is also contained
 1099 within the forward tube. The FCAL is composed of three modules; the electromagnetic
 1100 (FCAL1) and two hadronic modules (FCAL2 and FCAL3). The FCAL1 module is of
 1101 copper composition and the hadronic modules of tungsten and sintered tungsten alloy.
 1102 All three modules have the same nominal outer dimensions (450 mm in z , 455 mm
 1103 outer radius) and have a centered beam hole of different radius for each module. Struc-
 1104 turally, the FCAL modules are quite simple, consisting of single absorber matrix bodies
 1105 carrying an array of tube electrodes in holes in the matrix bodies. Mechanical stress
 1106 considerations are, therefore, largely reduced to questions of tube electrode integrity
 1107 near module bearing points. The modules are supported by contact between their outer
 1108 circumferences and the inner surface of the cryostat's forward tube. The basic electrode
 1109 cell used in the FCAL is a tubular electrode with the tube axis parallel to the beam
 1110 line. The electrode is composed of a rod held within a tube to form an exceptionally
 1111 thin cylindrical shell liquid argon gap between them. Unit cell dimensions have been
 1112 optimized for physics performance. The tube electrode signals are summed at the mod-
 1113 ule face to form readout cells. Cell signals are carried on miniature (1 mm diameter)
 1114 polyimide-copper coaxial cables which run rearward in cable troughs on the module
 1115 outer surfaces. These cables then emerge from the forward tube via notches in the rear
 1116 face of the forward tube. A shielding plug is located behind the FCAL modules in the
 1117 forward tube. This shielding plug acts to provide shielding for the most forward muon
 1118 chambers and is not instrumented. The FCAL is designed to detect jets with an E_T
 1119 resolution of $\sigma(E_T)/E_T < 10\%$ for $E_T > 100$ GeV [10]. This requires the FCAL energy
 1120 resolution to be $\sigma(E)/E < 7\%$ and the jet angle resolution to be $\sigma(q)/q < 7\%$ typically.
 1121 At the highest $|\eta|$, it is the angular resolution which dominates.

1122 3.5.2 The Tile Calorimeter

1123 The Tile Calorimeter is a large hadronic sampling calorimeter which makes use of
 1124 steel as the absorber material and scintillating plates read out by wavelength shifting
 1125 (“WLS”) fibres as the active medium [12], to sample the emitted light when charged
 1126 particles pass through it. A characteristic feature of its design is the orientation of the
 1127 scintillating tiles which are placed in planes perpendicular to the colliding beams and

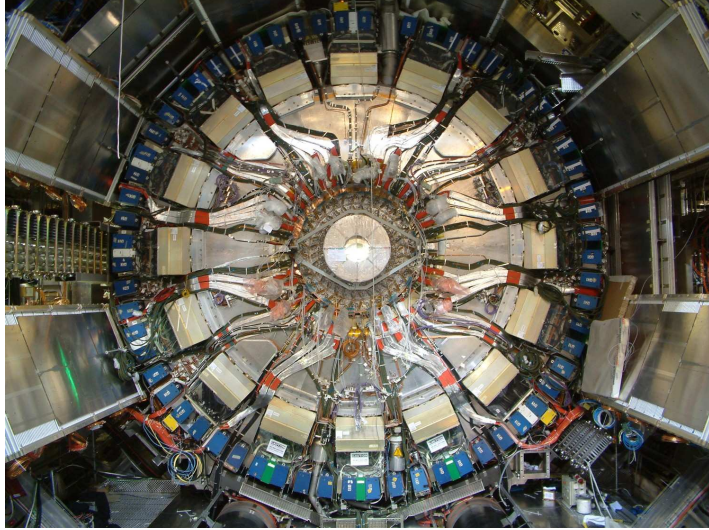
1128 are staggered in depth. A good sampling homogeneity is obtained when the calorimeter
 1129 is placed behind an electromagnetic compartment and a coil equivalent to a total of
 1130 about two interaction lengths (λ) of material.

1131 The absorber structure is a laminate of steel plates of various dimensions, connected
 1132 to a massive structural element referred to as a girder. Simplicity has been the guide-
 1133 line for the light collection scheme used as well: fibres are coupled radially to the tiles
 1134 along the outside faces of each module. The laminated structure of the absorber al-
 1135 lows for channels in which the fibres run. The use of fibre readout allows to define a
 1136 tridimensional cell readout, creating a projective geometry for triggering and energy
 1137 reconstruction. A compact electronics readout is housed in the girder of each module.
 1138 Finally, the readout of the two sides of each of the scintillating tiles into two separate
 1139 photomultipliers (PMTs) guarantees a sufficient light yield.

1140 The Tile Calorimeter consists of one barrel, shown in Figure 3.7, and two extended
 1141 barrel hadron parts. The barrel calorimeter consists of a cylindrical structure with
 1142 inner and outer radius of 2280 and 4230 mm respectively. The barrel part is 5640 mm
 1143 in length along the beam axis, while each of the extended barrel cylinders is 2910 mm
 1144 long. Each detector cylinder is built of 64 independent wedges along the azimuthal
 1145 direction. Between the barrel and the extended barrels there is a gap of about 600 mm,
 1146 which is needed for the Inner Detector and the Liquid Argon cables, electronics and
 1147 services. The barrel covers the region $-1.0 < |\eta| < 1.0$, and the extended barrels cover
 1148 the region $0.8 < |\eta| < 1.7$. Part of the gap contains an extension of the extended
 1149 barrel: the Intermediate Tile Calorimeter (ITC), which is a structure stepped in order
 1150 to maximize the volume of active material in this region, while still leaving room for
 1151 the services and cables. The ITC consists of a calorimeter plug between the region
 1152 $0.8 < |\eta| < 1.0$, and, due to severe space constraints, only scintillator between $1.0 < |\eta| < 1.6$. The scintillators in the region $1.0 < |\eta| < 1.2$ are called gap scintillators, and
 1154 the scintillators between $1.2 < |\eta| < 1.6$ are called crack scintillators. The latter extend
 1155 down to the region in between the barrel and the EndCap cryostats, while the plug and
 1156 the gap scintillators primarily provide hadronic shower sampling, the crack scintillator
 1157 plays a critical role in sampling electromagnetic showers, where the normal sampling is
 1158 compromised by the dead material of the cryostat walls and the inner detector cables.

1159 The main function of the Tile Calorimeter is to contribute to the energy reconstruc-
 1160 tion of the jets produced in the pp interactions and, with the addition of the EndCap
 1161 and forward calorimeters, to provide a good p_T^{miss} measurement. The large center of
 1162 mass energy requires good performance over an extremely large dynamic range extend-
 1163 ing from a few GeV up to several TeV. To resolve events over a background of 21
 1164 minimum bias events per bunch crossing a fast detector response with fine granularity
 1165 is required. High radiation resistance is needed to cope with the high particle fluxes
 1166 expected at the design luminosity over a period of 10 years of operation. The guidelines
 1167 for the design of this device are derived from the required overall physics performance
 1168 which call for an intrinsic resolution for jets of $\Delta E/E = \frac{50\%}{\sqrt{E}} \oplus 3\%$ for $|\eta| < 3.0$ with a

Figure 3.7: The Tile Calorimeter Central Barrel assembly and installation [13]. Particle showers are sampled by tiles of scintillating plastic which emit light when charged particles pass through them [3]. The light pulses are carried by optical fibres to photomultiplier tubes behind the calorimeter and converted to electric signals.



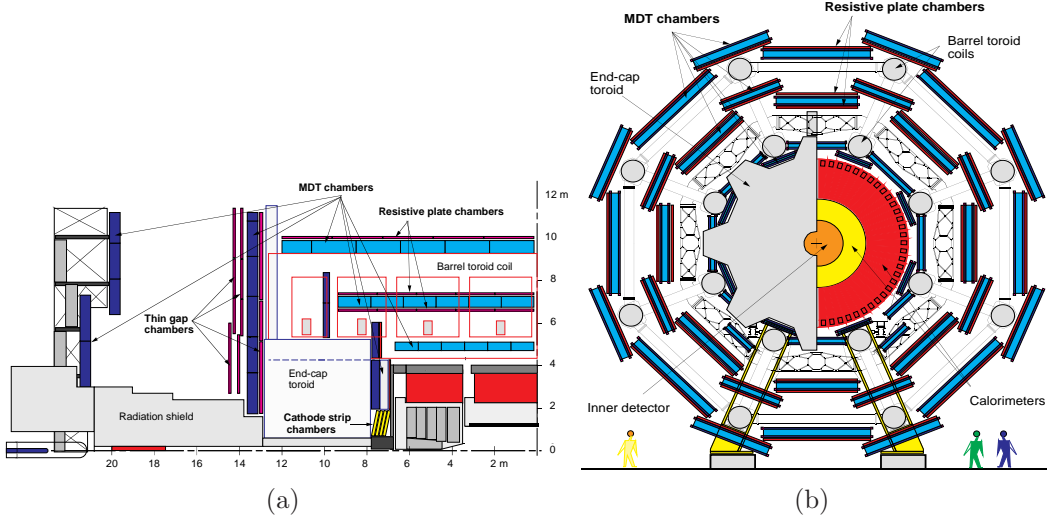
₁₁₆₉ segmentation of $\Delta\eta \times \Delta\phi = 0.1 \times 0.1$.

₁₁₇₀ 3.6 The Muon Spectrometer

₁₁₇₁ The ATLAS muon spectrometer, based on the magnetic deflection of muon tracks
₁₁₇₂ in a system of three large superconducting air-core toroid magnets instrumented with
₁₁₇₃ separate-function trigger and high-precision tracking chambers, deigned to exploit the
₁₁₇₄ potential of the most promising and robust signatures of physics at the LHC [14].
₁₁₇₅ Figure 3.8 shows a side view of one quadrant of the spectrometer and its transverse
₁₁₇₆ view.

₁₁₇₇ In the pseudorapidity range $|\eta| \leq 1.0$, magnetic bending is provided by a large
₁₁₇₈ barrel magnet constructed from eight coils surrounding the hadron calorimeter. For
₁₁₇₉ $1.4 \leq |\eta| \leq 2.7$, muon tracks are bent in two smaller EndCap magnets inserted into
₁₁₈₀ both ends of the barrel toroid. In the interval $1.0 \leq |\eta| \leq 1.4$ referred to as transition
₁₁₈₁ region, magnetic deflection is provided by a combination of barrel and EndCap fields.
₁₁₈₂ This magnet configuration provides a field that is mostly orthogonal to the muon tra-
₁₁₈₃ jectories, while minimizing the degradation of resolution due to multiple scattering. In
₁₁₈₄ the barrel region, tracks are measured in chambers arranged in three cylindrical layers
₁₁₈₅ (stations) around the beam axis; in the transition and EndCap regions, the chambers

Figure 3.8: (a) is the side view of one quadrant of the muon spectrometer and the transverse view is presented in Figure (b). The muon spectrometer measures the trajectories of muons as they bent by a system of large superconducting magnet coils [3]. This allows their momenta and electric charge to be precisely determined.

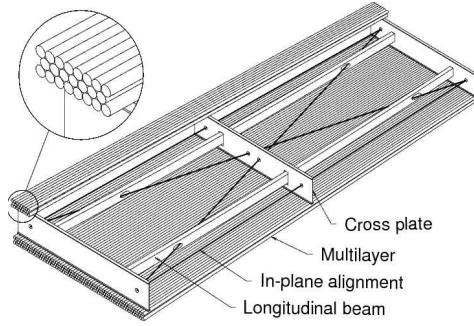


1186 are installed vertically, also in three stations. Over most of the pseudorapidity range,
 1187 a precision measurement of the track coordinates in the principal bending direction of
 1188 the magnetic field is provided by Monitored Drift Tubes (MDT). At large pseudora-
 1189 pidities and close to the interaction point, Cathode Strip Chambers (CSC) with higher
 1190 granularity are used to sustain the demanding rate and background conditions. Optical
 1191 alignment systems have been designed to meet the stringent requirements on the me-
 1192 chanical accuracy and the survey of the precision chambers. The trigger system covers
 1193 the pseudorapidity range $|\eta| \leq 2.4$. Resistive Plate Chambers (RPC) are used in the
 1194 barrel and Thin Gap Chambers (TGC) in the EndCap region. Both types of trigger
 1195 chambers also provide a second-coordinate measurement of track coordinates orthogo-
 1196 nal to the precision measurement, in a direction approximately parallel to the magnetic
 1197 field lines. The second-coordinate capability of the trigger chambers is designed to
 1198 match the acceptance of the precision chambers.

1199 The muon spectrometer designed for a momentum resolution $\Delta p_T/p_T < 10^4 p/\text{GeV}$
 1200 for $p_T > 300 \text{ GeV}$; at smaller momenta, the resolution is limited to a few per cent by
 1201 multiple scattering in the magnet and detector structures, and by energy loss fluctu-
 1202 ations in the calorimeters. To achieve this resolution by a three-point measurement,
 1203 with the size and bending power of the ATLAS toroids, each point must be measured
 1204 with an accuracy better than $50 \mu\text{m}$.

1205 In the next paragraphs, details for the four different technologies of the muon spec-
 1206 trometer, MDT, CSC, RPC and TGC, are provided [14].

Figure 3.9: Schematic drawing of a rectangular MDT chamber constructed from multilayers of three monolayers each, for installation in the barrel spectrometer [14]. The chambers for the EndCap are of trapezoidal shape, but are of similar design otherwise. The ionized tracks of muons passing through these tubes produce electrical pulses in the wires [3].



3.6.1 Monitored Drift Tubes (MDT)

Aluminum tubes of 30 mm diameter and $400\text{ }\mu\text{m}$ wall thickness, with a $50\text{ }\mu\text{m}$ diameter central WRe wire, form the detection element of the MDT chambers, shown in Figure 3.9. The tubes operate with a non-flammable $91\%\text{Ar} - 5\%\text{CH}_4 - 4\%\text{N}_2$ mixture at 3 bars absolute pressure. The envisaged working point provides for a highly linear spacetime relation with a maximum drift time of 500 ns , a small Lorentz angle, and good aging properties due to small gas amplification. The single-wire resolution is typically $80\text{ }\mu\text{m}$, except very close to the anode wire.

The tubes are produced by extrusion from a hard aluminum alloy and are closed by endplugs, which provide accurate positioning of the anode wires, wire tension, gas tightness, and electrical and gas connections. The tube lengths vary from 70 cm to 630 cm . To improve the resolution of a chamber beyond the single-wire limit and to achieve adequate redundancy for pattern recognition, the MDT chambers are constructed from 2×4 monolayers of drift tubes for the inner and 2×3 monolayers for the middle and outer stations. The tubes are arranged in multilayers of three or four monolayers, respectively, on either side of a rigid support structure. The support structures (spacer frames) provide for accurate positioning of the drift tubes with respect to each other, and for mechanical integrity under effects of temperature and gravity; for the barrel chambers which are not mounted in a vertical plane, they are designed to bend the drift tubes slightly in order to match them to the gravitational sag of the wires. The spacer frames also support most of the components of the alignment system.

The structural components of the spacer frames are three cross-plates, to which the drift tube multilayers are attached, and two long beams connecting the cross-plates. The frames constructed to a moderate mechanical accuracy of $\pm 0.5\text{ mm}$ only and

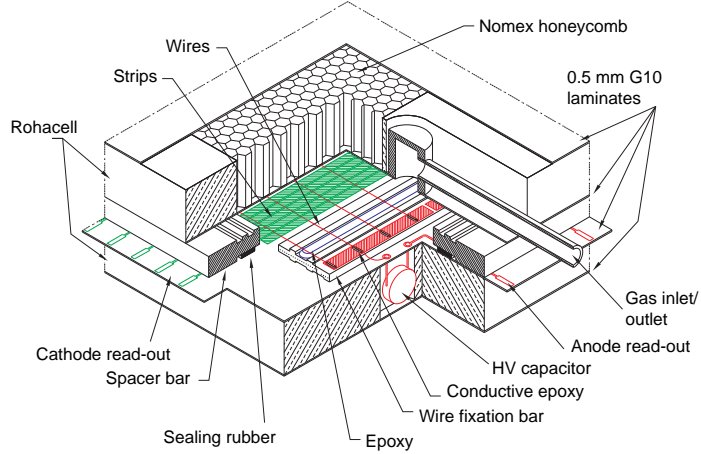
1231 mechanical deformations are monitored by an in-plane optical system; hence the name
1232 monitored drift tube chambers.

1233 Each drift tube is read out at one end by a low-impedance current sensitive pream-
1234 plifier, with a threshold five times above the noise level. The preamplifier is followed
1235 by a differential amplifier, a shaping amplifier and a discriminator. The output of the
1236 shaping amplifier is also connected to a simple ADC, such that the charge-integrated
1237 signal can be used to correct the drift time measurement for time slewing. Eight am-
1238 plifier/shaper/discriminator (ASD) readout channels are packaged, together with the
1239 ADCs, in a single custom-built integrated circuit. Signals from three ASD chips are fed
1240 into $24 - \text{channel}$ time to digital converters (TDC) which measure the drift time with
1241 300 ps RMS resolution. A phase calibration system serves to correct for time offsets
1242 between different MDT channels. The ASDs and TDCs are mounted on the chambers
1243 by means of simple printed circuit boards. In response to a level-1 trigger, the TDC
1244 data are transferred over fast serial links to readout drivers housed in VME (Versa
1245 Module Europa) crates in the experimental area.

1246 3.6.2 Cathode Strip Chambers (CSC)

1247 The CSCs are multiwire proportional chambers with cathode strip readout and
1248 with a symmetric cell in which the anode-cathode spacing is equal to the anode wire
1249 pitch [14]. The precision coordinate is obtained by measuring the charge induced on the
1250 segmented cathode by the avalanche formed on the anode wire. Good spatial resolution
1251 is achieved by segmentation of the readout cathode and by charge interpolation between
1252 neighboring strips. The cathode strips for the precision measurement are oriented
1253 orthogonal to the anode wires. Other important characteristics are the small electron
1254 drift times ($\leq 45 \text{ ns}$), good time resolution (7 ns) [15], good two-track resolution,
1255 and low neutron sensitivity. A measurement of the transverse coordinate is obtained
1256 from orthogonal strips, i.e. oriented parallel to the anode wires, which form the second
1257 cathode of the chamber. The spatial resolution of CSCs is sensitive to the inclination
1258 of tracks and the Lorentz angle. To minimize degradations of the resolution, chambers
1259 installed in a tilted position such that infinite-momentum tracks originating from the
1260 interaction point are normal to the chamber surface. The CSCs are arranged in $2 \times$
1261 4 layers. The design utilizes low-mass construction materials to minimize multiple
1262 scattering and detector weight. A four-layer multilayer is formed by five flat, rigid
1263 panels, each of which is made of Nomex honeycomb and two thin copper-clad FR4
1264 laminates forming the cathodes. The panel frames are made of machined rohacell.
1265 Precision machined FR4 strips glued on the panels provide the 2.5 mm step for the $W - Re$
1266 anode wires 30 μm in diameter. A cutout view of one gap is shown in Figure 3.10.
1267 In each of the four gaps, the position sensing cathode strips are lithographically etched.

Figure 3.10: Cutout view of a single CSC layer showing the construction details [14]. The CSC are characterized by small drift times and therefore are ideal for the forward region where the radiation backgrounds are high.



1268 The five panels are precisely positioned with respect to each other with the aid of
 1269 locating pins. Signals from the cathode strips are transferred via ribbon cable jumpers
 1270 to the electronic readout boards located on the outer panels. The whole assembly is
 1271 rigid enough so that no in-plane alignment system is necessary.

1272 The gas is a non-flammable mixture of 80% Ar , 20% CO_2 [15]. The fact that it
 1273 contains no hydrogen, combined with the small gap width, explains the low sensitivity
 1274 to neutron background. In general, the CSC performance is less sensitive to variations
 1275 of the gas parameters than that of the MDTs.

1276 The front-end section of the strip readout electronics consists of a charge-sensitive
 1277 preamplifier that drives a pulse shaping amplifier. Sixteen channels of preamplifier and
 1278 shaper are packaged in a complementary metaloxidesemiconductor (CMOS) integrated
 1279 circuit mounted on an on-detector readout card. This chip is followed by analog storage
 1280 of the peak cathode pulse-height during the Level-1 trigger latency. Upon a Level-1
 1281 trigger, the analog data are multiplexed into a 10-bit ADC. Since the precision coor-
 1282 dinate is obtained from charge interpolation, the spatial resolution obtained depends
 1283 critically on the relative gain of neighboring cathode strips and readout channels.

3.6.3 Resistive Plate Chambers (RPC)

The RPC is a gaseous detector providing a typical spacetime resolution of $1\text{ cm} \times 1\text{ ns}$ with digital readout [14]. The basic RPC unit is a narrow gas gap formed by two parallel resistive bakelite plates, separated by insulating spacers (Figure 3.11). The primary ionization electrons are multiplied into avalanches by a high, uniform electric field of typically 4.5 kV/mm . Amplification in avalanche mode produces pulses of typically 0.5 pC . The candidate gas mixture is based on tetrafluoroethane ($C_2H_2F_4$), a non-flammable and environmentally safe gas that allows for a relatively low operating voltage. The signal is read out via capacitive coupling by metal strips on both sides of the detector. A trigger chamber is made from two rectangular detector layers, each one read out by two orthogonal series of pick-up strips: the η strips are parallel to the MDT wires and provide the bending view of the trigger detector; the ϕ strips, orthogonal to the MDT wires, provide the second-coordinate measurement which is also required for the offline pattern recognition.

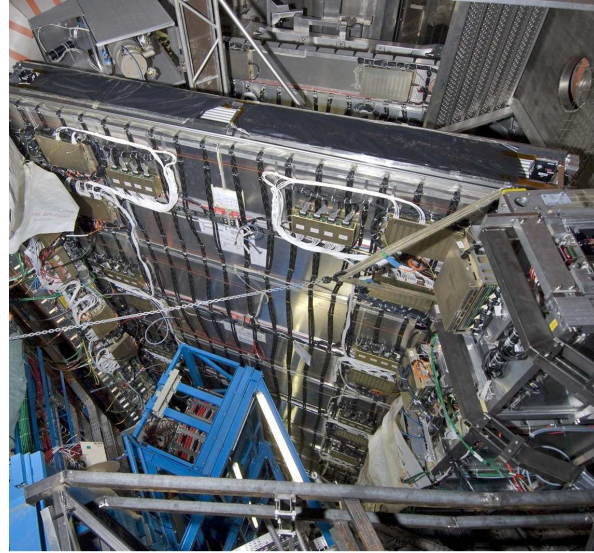
RPCs have a simple mechanical structure, use no wires and are therefore simple to manufacture. The 2 mm thick Bakelite plates are separated by polycarbonate spacers of 2 mm thickness which define the size of the gas gap. The spacers are glued on both plates at 10 cm intervals. A 7 mm wide frame of the same material and thickness as the spacers is used to seal the gas gap at all four edges. The outside surfaces of the resistive plates are coated with thin layers of graphite paint which are connected to the high voltage supply. These graphite electrodes are separated from the pick-up strips by $200\text{ }\mu\text{m}$ thick insulating films which are glued on both graphite layers. The readout strips are arranged with a pitch varying from 30.0 to 39.5 mm .

Each chamber is made from two detector layers and four readout strip panels. These elements are rigidly held together by two support panels which provide the required mechanical stiffness of the chambers. The panels are made of polystyrene sandwiched between two aluminum sheets. One panel is flat, 50 mm thick, with 0.5 mm thick aluminium coatings; the other panel is 10 mm thick with 0.3 mm coatings and is preloaded with a 1 cm sagitta. The two panels are rigidly connected by 2 mm thick aluminium profiles, such that the preloaded support panel provides uniform pressure over the whole surface of an RPC module.

The RPCs are operated with a gas mixture of 97% tetrafluoroethane ($C_2H_2F_4$) and 3% isobutane (C_4H_{10}), with a total volume of 18 m^3 . As for the precision chambers, the gas is stored, mixed and purified on the surface and the distribution system is installed underground.

To preserve the excellent intrinsic time resolution of the RPCs, the readout strips are optimized for good transmission properties and are terminated at both ends to avoid signal reflections. The front-end electronics are based on a three-stage voltage amplifier followed by a variable-threshold comparator. The amplifier frequency response is optimized for the typical time structure of RPC avalanches. Eight amplifier-comparator

Figure 3.11: Installation of RPC Muon chambers in the ATLAS cavern (July 2007) [16].



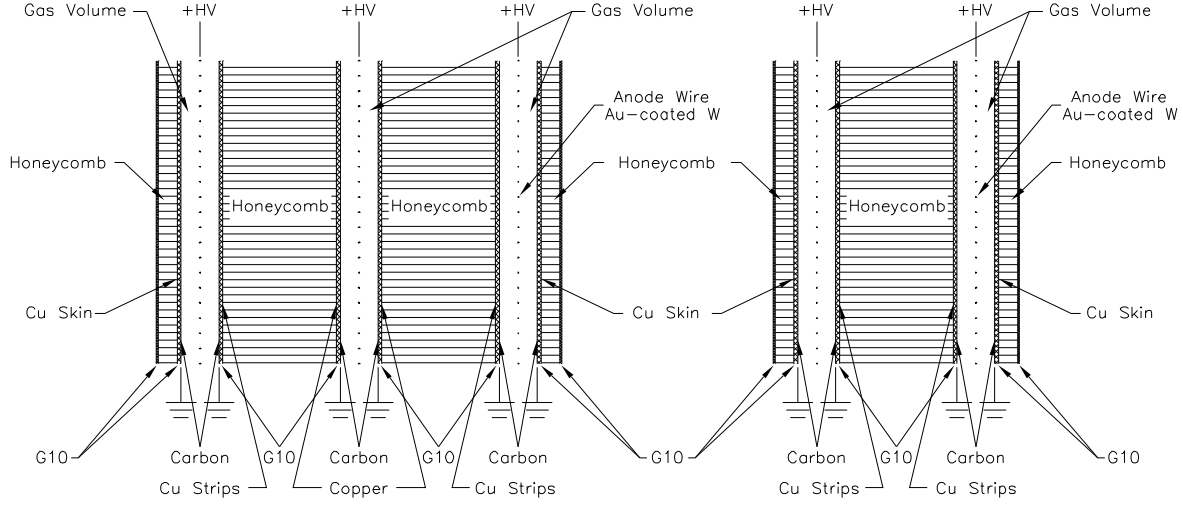
¹³²⁴ channels are implemented in a VLSI chip in GaAs technology. The chips are mounted
¹³²⁵ on printed circuit boards attached to the edges of the readout panels.

¹³²⁶ 3.6.4 Thin Gap Chambers (TGC)

¹³²⁷ Thin gap chambers are designed in a way similar to multiwire proportional chambers,
¹³²⁸ with the difference that the anode wire pitch is larger than the cathode-anode
¹³²⁹ distance [14]. Signals from the anode wires, arranged parallel to the MDT wires, pro-
¹³³⁰ vide the trigger information together with readout strips arranged orthogonal to the
¹³³¹ wires. The readout strips also serve to measure the second coordinate. Using a highly
¹³³² quenching gas mixture of 55% CO_2 and 45% n – pentane (n – C_5H_{12}), with a total
¹³³³ volume of 16 m^3 , this type of cell geometry permits operation in saturated mode, with
¹³³⁴ a number of advantages:

- ¹³³⁵ • small sensitivity to mechanical deformations - important for the economical design
¹³³⁶ of large-area chambers
- ¹³³⁷ • small dependence of the pulse height on the incident angle, up to angles of 40°
- ¹³³⁸ • nearly Gaussian pulse height distribution with small Landau tails and no streamer
¹³³⁹ formation.

Figure 3.12: Schematic cross-section of a triplet (left) and of a doublet of TGCs, where the width of the gas gap is shown enlarged [14]. These detectors, along with the RPC, provide fast information on muon tracks to enable online selection of events containing muons [3].



1340 The main dimensional characteristics of the chambers are a cathode-cathode dis-
 1341 tance (gas gap) of 2.8 mm , a wire pitch of 1.8 mm , and a wire diameter of $50\text{ }\mu\text{m}$.
 1342 The operating high voltage foreseen is 3.1 kV . The electric field configuration and the
 1343 small wire distance provide for a short drift time and thus a good time resolution. As
 1344 the angle increases, the tracks pass closer to the wire, thus reducing the maximum
 1345 drift distance and improving the time resolution. In the ATLAS chamber layout, all
 1346 muons passing through TGCs with transverse momenta above the required threshold
 1347 have incident angles greater than 10° . Aging properties of the chambers have been
 1348 investigated in detail and were found to be fully adequate for the expected operating
 1349 conditions at the LHC, with a large safety margin.

1350 TGCs are constructed in doublets and in triplets. The seven layers in the middle
 1351 station are arranged in one triplet and two doublets; one doublet is used for the inner
 1352 station, which only serves to measure the second coordinate. The anode plane is sand-
 1353 wiced between two cathode planes made of 1.6 mm $G-10$ plates on which the graphite
 1354 cathode is deposited. On the back side of the cathode plates facing the center plane
 1355 of the chamber, etched copper strips provide the readout of the azimuthal coordinate.
 1356 The TGC layers are separated by 20 mm thick paper honeycomb panels which provide
 1357 a rigid mechanical structure for the chambers (Figure 3.12). On the outside, the gas
 1358 pressure is sustained by 5 mm thick paper honeycomb panels. These are covered in
 1359 turn by 0.5 mm $G-10$ plates.

1360 The used gas mixture is highly flammable and requires adequate safety precautions.
 1361 As in the other gas systems, the gas is stored, mixed, and purified on the surface and
 1362 the distribution system is installed underground. *n* – *pentane* has a low vapor pressure
 1363 and is liquid at room temperature and atmospheric pressure.

1364 To form a trigger signal, several anode wires are grouped together and fed to a
 1365 common readout channel. The number of wires per group varies between 4 and 20,
 1366 depending on the desired granularity as a function of pseudorapidity. The grouped
 1367 signals are fed into a low-impedance two-stage amplifier. The combination of chamber
 1368 and amplifier yields a rise-time of the amplifier output into the discriminator of 1020 ns.
 1369 Four amplifier-discriminator (ASD) circuits are integrated into one chip; four ASD chips
 1370 are grouped in turn on an amplifier-discriminator printed circuit board attached to
 1371 the edges of the chambers, thus providing the readout of 16 channels. By appropriate
 1372 adjustment of the threshold, the same ASD chips can be used for wire and strip readout.

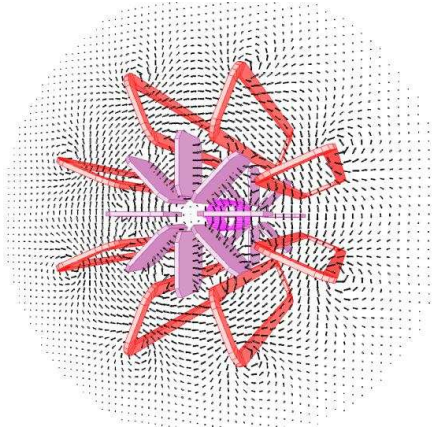
1373 3.6.5 Precision Alignment

1374 The requirements on the momentum resolution of the spectrometer call for an accuracy
 1375 of the relative positioning of chambers traversed by a muon track that matches the
 1376 intrinsic resolution and the mechanical tolerances of the precision chambers [14]. Over
 1377 the large global dimensions of the spectrometer, however, it is not possible to stabilize
 1378 the dimensions and positions of the chamber at the 30 μm level. Therefore, chamber
 1379 deformations and positions are constantly monitored by means of optical alignment
 1380 systems and displacements up to about 1 cm are corrected for in the offline analysis.

1381 All alignment systems are based on optical straightness monitors. Owing to geometrical
 1382 constraints, different schemes are used to monitor chamber positions in the
 1383 barrel, in the EndCap and the deformations of large chambers, the so called in-plane
 1384 alignment. Chambers in the small sectors are aligned with particle tracks, exploiting
 1385 the overlap with chambers in the large sectors. Alignment with tracks also serve to
 1386 cross-calibrate the optical survey of the large sectors.

1387 Very high accuracy is required only for the positioning of chambers within a projective tower.
 1388 The accuracy required for the relative positioning of different towers to obtain
 1389 adequate mass resolutions for multimuon final states is in the millimeter range.
 1390 This accuracy is easily achieved by the initial positioning and survey of chambers at
 1391 installation time. The relative alignment of muon spectrometer, calorimeters and inner
 1392 detector relies on high-momentum muon trajectories.

Figure 3.13: A schematic view of the magnetic field.



3.7 The Magnet System

An essential part of the ATLAS detector is the magnet systems which provides the bending power required for the momentum measurements of charged particles [17]. ATLAS selected the arrangement of a central solenoid serving the inner tracker with magnetic field, surrounded by a system of 3 large scale air-core toroids, generating the magnetic field for the muon spectrometer.

The superconducting magnets, named Barrel Toroid, EndCap Toroid and Central Solenoid, along with the power system, control, cryogenics and the refrigeration plant compose the magnet system. The overall dimension is 26 m long and 20 m in diameter.

A schematic view of the magnetic field is depicted in Figure 3.13.

3.7.1 The Central Solenoid

The Central Solenoid (Figure 3.14) designed to provide an axial magnetic field of 2 T at the center of the tracking volume [18]. It is located in front of the EM calorimeter and therefore the material must be kept minimal for the best calorimeter performance. The technology of a superconducting magnet using indirectly cooled aluminium stabilized superconductor was chosen to achieve the highest possible field with minimum thickness. In order to minimize the material, the vacuum vessels of the Solenoid and of the LAr calorimeter combined into one, eliminating two vacuum walls.

An important safety aspect of the design is the quench protection and recovery, which requires 4 hours recovery time. Except from that, operational factors are set from the alignment, which must be known within $\pm 1 \text{ cm}$ along the beam axis and considering that the coil moves in the cryostat vacuum vessel when it is cooled and shrinks by 2 cm

Figure 3.14: The Central Solenoid before the installation [19]. The 4 *tonne* coil contains 10 *km* of superconducting cable which is cooled with liquid helium [3]. The nominal current is 8 *kA* during normal operation.



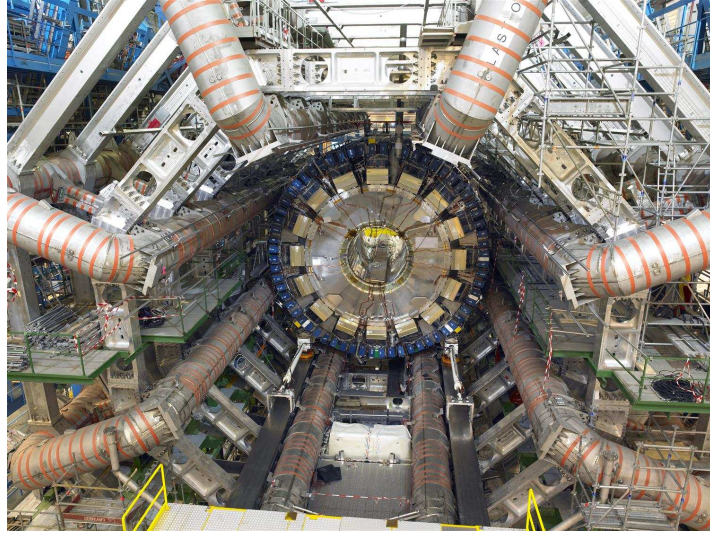
¹⁴¹⁵ while the radius changes by 0.5 *cm* and the radiation exposition (reaches 0.5 *kGy/year*).

¹⁴¹⁶ 3.7.2 The Barrel Toroid

¹⁴¹⁷ The Barrel Toroid (BT) consists of eight flat coils, shown in Figure 3.15, in a race-
¹⁴¹⁸ track configuration, assembled radially and symmetrically around the beam axis [20].
¹⁴¹⁹ Each coil contains its own individual cryostat and is supported internally to its vacuum
¹⁴²⁰ vessel by means of distributed sets of cold-to-warm rods and struts. The only opening
¹⁴²¹ in the cryostat are communication ports where electrical and cryogenic lines can be
¹⁴²² brought out for external connections.

¹⁴²³ The assembly of coils in the toroid configuration requires a very strong and rigid
¹⁴²⁴ mechanical structure for supporting both the weights and the magnetic forces. The main
¹⁴²⁵ magnetic forces are directed symmetrically and radically towards the beam axis. Each
¹⁴²⁶ coil is submitted to a total radial force of 1100 *tonnes*. The force is transferred from the
¹⁴²⁷ cold mass to the warm structure by means of titanium rods attached to solid fixtures
¹⁴²⁸ distributed at 8 locations along the length of the inner leg of the cryostat. The fixtures
¹⁴²⁹ themselves are linked between adjacent coils by warm voussoirs, which all together
¹⁴³⁰ constitute 8 solid rings working in compression under the combined radial forces. The
¹⁴³¹ above suspension rods work in tension, at a high stress of 400 *MPa*, and are articulated
¹⁴³² in order to accommodate the coil thermal contraction. In addition, cryogenic stops,
¹⁴³³ near the rods, provide lateral bracing against out-of-plane forces, mainly due to the
¹⁴³⁴ weight and to eventual magnetic unbalance. For the same purpose, the outer legs of

Figure 3.15: A view of the toroid barrel magnets [19]. The ATLAS detector uses an unusually large system of air-core toroids arranged outside the calorimeter volumes to provide a large-volume magnetic field [3].



1435 the cryostats are braced by warm structures, concentric to the inner voussoirs internally
 1436 by similar stops.

1437 The complete toroid is also supported off the ground by a limited number of legs,
 1438 which are incorporated in the general support structure of the ATLAS detector, namely
 1439 called the “CERN feet”. This structure has also to support the weight of the muon
 1440 chambers, around 500 tonnes.

1441 The indirect cooling eliminates the need for complex and bulky helium vessels and
 1442 is particularly appropriate for the ATLAS coil configuration. Indirect cooling requires
 1443 a monolithic coil structure made of high thermal conductivity materials and designed
 1444 with low levels of stress and strain in order to prevent internal mechanical disturbances.
 1445 This is achieved by the use of a massive aluminium stabilized conductor, impregnated in
 1446 a rigid alu-alloy structure, and of adequately distributed cooling loops.

1447 The operating current, rated below 65% of the critical current along the load line,
 1448 provides a temperature margin of 2 K above the operating temperature of 4.5 K,
 1449 corresponding to an enthalpy margin of about 4000 J/m³. The coil cooling is achieved
 1450 by a set of pipes welded in grooves running along the coil casings and fed in parallel
 1451 with 2 – phase helium² circulated in forced flow by means of cold pumps.

²Refers to helium 3He and 4He .

3.7.3 The EndCap Toroid

The design of the EndCap Toroid constrained by the geometry of the experiment and the requirement to produce a high magnetic field across a radial span [21]. The system can be retracted from the operating position to allow access to the central parts of the ATLAS detector. Other constraints of the operation are to transfer the axial force to the Barrel Toroid, support about 100 *tonnes* of shielding at the inner bore, support the BEE muon chambers on the vacuum vessel to enhance the muon spectrometer performance in the critical region between the barrel and the EndCap Toroids and provision the alignment paths for muons detectors alignment through the vessel. One of the two ATLAS EndCap toroid is shown in Figure 3.16 between the Large Muon wheel and close to the Barrel Toroids.

The toroidal fields are generated by 8 superconducting coils, mounted as a single cold mass unit in a large cryostat. The coils are fabricated using aluminium alloy center and side plates to react to the internal coil forces. The cold mass is mounted in a single large cryostat which consists of a large aluminium alloy vacuum vessel, super-insulation, radiation shields and cold mass supports. The cryostat performs a number of mechanical force transfer functions in addition to its thermal isolation requirements (transfer of cold mass loads to the rail system within the ATLAS and transfer of axial forces to the Barrel Toroid).

3.8 The Trigger System

The trigger system during the Run-I had three distinct levels: L1, L2, and the event filter. Each trigger level refines the decisions made at the previous level and, where necessary, applies additional selection criteria [22]. The data acquisition system (DAQ) receives and buffers the event data from the detector-specific readout electronics, at the L1 trigger accept rate, over 1600 point-to-point readout links. The first level uses a limited amount of the total detector information to make a decision in less than 2.5 *ms*, reducing the rate to about 75 *kHz*. The two higher levels access more detector information for a final rate of up to 200 *Hz* with an event size of approximately 1.3 *Mbyte*. The trigger flow is schematically presented in Figure 3.17.

The L1 trigger searches for high transverse-momentum muons, electrons, photons, jets, and τ -leptons decaying into hadrons, as well as large missing and total transverse energy. Its selection is based on information from a subset of detectors. High transverse-momentum muons are identified using trigger chambers in the barrel and EndCap regions of the spectrometer. Calorimeter selections are based on reduced-granularity information from all the calorimeters. Results from the L1 muon and calorimeter triggers are processed by the central trigger processor, which implements a trigger menu

Figure 3.16: One of the two EndCap Toroids, siting between the Large Muon wheel and close to the Barrel Toroids [19]. It is movable detector part in order to allow access to the detector inner parts and designed to transfer the axial force to the Barrel Toroid [21].

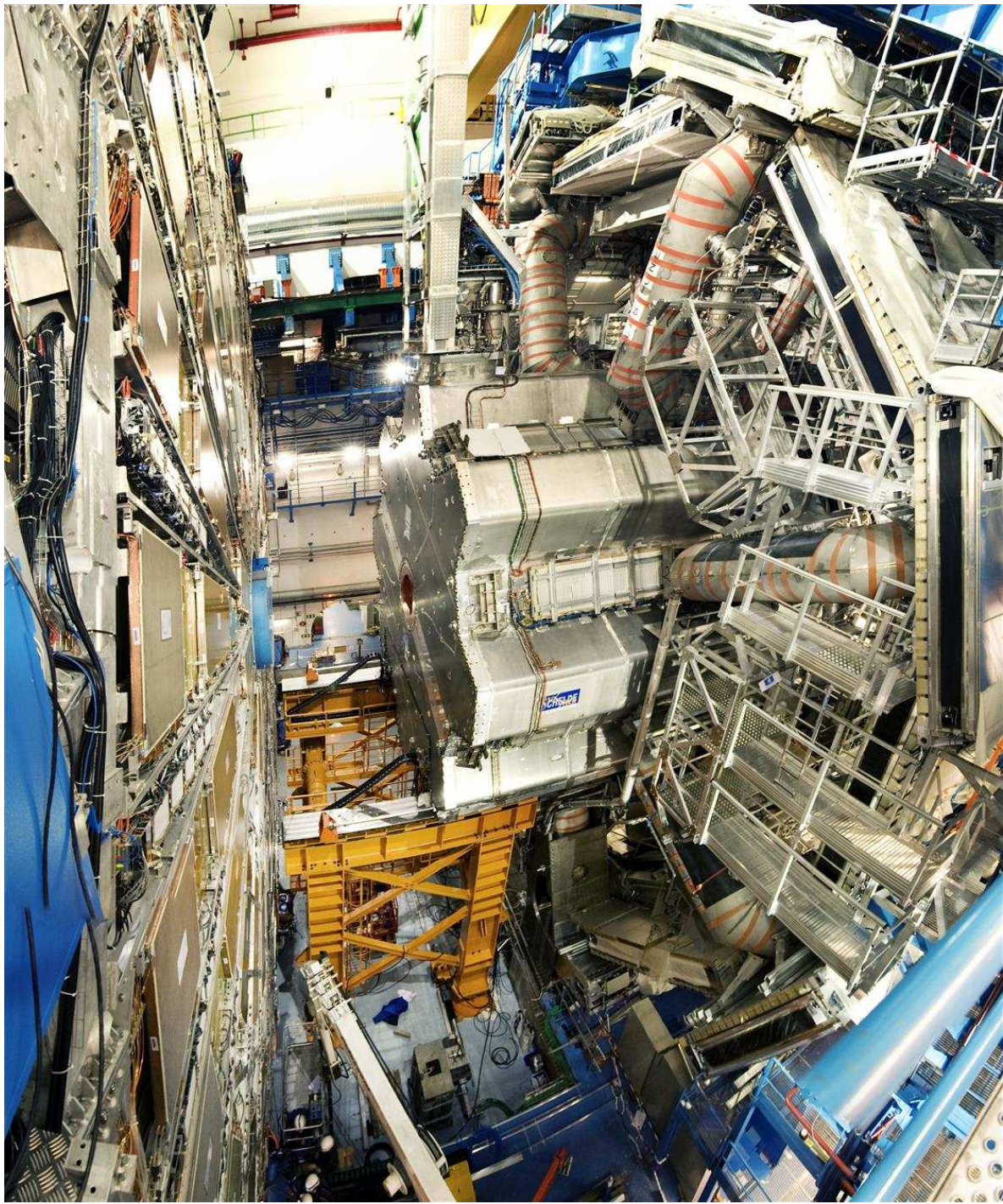
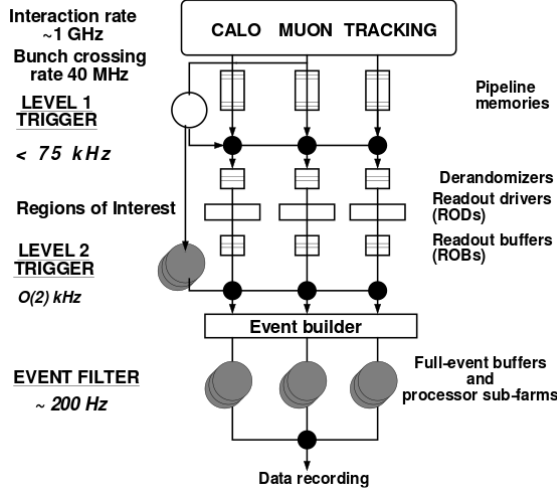


Figure 3.17: Sketch of the ATLAS triggering and DAQ (T/DAQ) system [23]. The places where the HLT and thus the HLT Steering is deployed (L2/EF) are marked in grey.



made up of combinations of trigger selections. Pre-scaling of trigger menu items is also available, allowing optimal use of the bandwidth as luminosity and background conditions change. Events passing the L1 trigger selection are transferred to the next stages of the detector-specific electronics and subsequently to the data acquisition via point-to-point links.

In each event, the L1 trigger also defines one or more Regions-of-Interest (RoIs), i.e. the geographical coordinates in η and ϕ , of those regions within the detector where its selection process has identified interesting features. The RoI data include information on the type of feature identified and the criteria passed, e.g. a threshold. This information is subsequently used by the high-level trigger.

The L2 selection is seeded by the RoI information provided by the L1 trigger over a dedicated data path. L2 selections use, at full granularity and precision, all the available detector data within the RoIs (approximately 2% of the total event data). The L2 menus are designed to reduce the trigger rate to approximately 3.5 kHz , with an event processing time of about 40 ms , averaged over all events.

The final stage of the event selection is carried out by the event filter (EF), which reduces the event rate to roughly 200 Hz . Its selections are implemented using offline analysis procedures within an average event processing time of the order of 4 s . The L2 and EF are also called High Level Triggers (HLT).

In the Run-II, the trigger organization will include the first level trigger and the combination of L2 and the EF will be the final level, called High Level Trigger (HLT). The purpose of the upgrade is to add robustness and flexibility to the selection and

1510 the conveyance of the physics data, simplify the maintenance of the infrastructure,
1511 exploit new technologies and, overall, make ATLAS data-taking capable of dealing
1512 with increasing event rates [24].

1513 3.9 The Data Acquisition System (DAQ) and Con- 1514 trols

1515 The Readout Drivers (RODs) of each sub-detector uses standardized blocks which
1516 subject to common requirements [22]. After an event is accepted by the L1 trigger, the
1517 data from the pipe-lines are transferred off the detector to the RODs. Digitized signals
1518 are formatted as raw data prior to being transferred to the DAQ system. The RODs
1519 follow some general ATLAS rules, including the definition of the data format of the
1520 event, the error detection/recovery mechanisms to be implemented, and the physical
1521 interface for the data transmission to the DAQ system.

1522 The first stage of the DAQ, the readout system, receives and temporarily stores the
1523 data in local buffers. It is subsequently solicited by the L2 trigger for the event data
1524 associated to RoIs. Those events selected by the L2 trigger are then transferred to the
1525 event-building system and subsequently to the event filter for final selection. Events
1526 selected by the event filter are moved to permanent storage at the CERN computer
1527 center. In addition to the movement of data, the data acquisition also provides for the
1528 configuration, control and monitoring of the hardware and software components which
1529 together provide the data-taking functionality.

1530 The Detector Control System (DCS) permits the coherent and safe operation of the
1531 ATLAS detector hardware, and serves as a homogeneous interface to all sub-detectors
1532 and to the technical infrastructure of the experiment. It controls, continuously monitors
1533 and archives the operational parameters, signals any abnormal behavior to the opera-
1534 tor, and allows automatic or manual corrective actions to be taken. Typical examples
1535 are high- and low-voltage systems for detector and electronics, gas and cooling sys-
1536 tems, magnetic field, temperatures, and humidity. The DCS also enables bi-directional
1537 communication with the data acquisition system in order to synchronize the state of
1538 the detector with data-taking. It also handles the communication between the sub-
1539 detectors and other systems which are controlled independently, such as the CERN
1540 technical services, the ATLAS magnets, and the detector safety system.

1541 3.10 Luminosity Determination and Luminosity De- 1542 tectors

1543 This section provides a description of the detector subsystems and the algorithms
 1544 used for luminosity measurements [25]. An accurate measurement of the delivered lumi-
 1545 nosity is a key component of the ATLAS physics program. For cross-section measure-
 1546 ments, the uncertainty on the delivered luminosity is often one of the major systematic
 1547 uncertainties. Searches and discoveries of new physical phenomena rely on accurate in-
 1548 formation about the delivered luminosity to evaluate background levels and determine
 1549 sensitivity to the signatures of new phenomena.

1550 3.10.0.1 The Luminosity Detectors

1551 In the early 2010 data taking, MBTS (Minimum Bias Trigger Scintillators), which
 1552 belong to the category of segmented scintillator counters, were primarily used for lu-
 1553 minosity measurements, since they provide efficient triggers at low instantaneous lumi-
 1554 nosity ($\mathcal{L} < 10^{33} \text{ cm}^{-2} \text{ s}^{-1}$). Located at $z = \pm 365 \text{ cm}$ from the nominal interaction
 1555 point (IP) and covering a rapidity range $2.09 < |\eta| < 3.84$, the main purpose of the
 1556 MBTS system was to provide a trigger on minimum collision activity during a pp bunch
 1557 crossing. Light emitted by the scintillators is collected by wavelength-shifting optical
 1558 fibers and guided to photomultiplier tubes. The MBTS signals, after being shaped and
 1559 amplified, are fed into leading-edge discriminators and sent to the trigger system.

1560 The Beam Conditions Monitor (BCM), started partially to operate in late 2010.
 1561 It consists of four small diamond sensors, approximately 1 cm^2 in cross-section each,
 1562 arranged around the beampipe in a cross pattern on each side of the IP, at a distance
 1563 of $z = \pm 184 \text{ cm}$. The BCM is a fast device originally designed to monitor background
 1564 levels and issue beam-abort requests when beam losses start to risk damaging the Inner
 1565 Detector. The fast readout of the BCM also provides a bunch-by-bunch luminosity
 1566 signal at $|\eta| = 4.2$ with a time resolution of $\sim 0.7 \text{ ns}$. The horizontal and vertical pairs of
 1567 BCM detectors are read out separately, leading to two luminosity measurements labeled
 1568 BCMH and BCMV respectively. Because the acceptances, thresholds, and data paths
 1569 may all have small differences between BCMH and BCMV, these two measurements are
 1570 treated as being made by independent devices for calibration and monitoring purposes,
 1571 although the overall response of the two devices is expected to be very similar. In the
 1572 2010 data, only the BCMH readout was available for luminosity measurements, while
 1573 both BCMH and BCMV became available in 2011.

1574 Another detector technology specifically designed to measure the luminosity is the
 1575 Cherenkov detector named LUCID. Sixteen mechanically polished aluminium tubes
 1576 filled with C_4F_{10} gas surround the beampipe on each side of the IP at a distance of
 1577 17 m , covering the pseudorapidity range $5.6 < |\eta| < 6.0$. The Cherenkov photons cre-

1578 ated by charged particles in the gas are reflected by the tube walls until they reach photo-
 1579 tomultiplier tubes (PMTs) situated at the back end of the tubes. Additional Cherenkov
 1580 photons are produced in the quartz window separating the aluminium tubes from the
 1581 PMTs. The Cherenkov light created in the gas typically produces 6070 photoelectrons
 1582 per incident charged particle, while the quartz window adds another 40 photoelectrons
 1583 to the signal. If one of the LUCID PMTs produces a signal over a preset threshold
 1584 (equivalent to 15 photoelectrons), a hit is recorded for that tube in that bunch cross-
 1585 ing. The LUCID hit pattern is processed by a custom-built electronics card which
 1586 contains Field Programmable Gate Arrays (FPGAs). This card can be programmed
 1587 with different luminosity algorithms, and provides separate luminosity measurements
 1588 for each LHC bunch crossing.

1589 Both BCM and LUCID are fast detectors with electronics capable of making sta-
 1590 tistically precise luminosity measurements separately for each bunch crossing within
 1591 the LHC fill pattern with no deadtime. These FPGA-based front-end electronics run
 1592 autonomously from the main data acquisition system, and in particular are not affected
 1593 by any deadtime imposed by the Central Trigger Processor (CTP).

1594 The Inner Detector, already briefly introduced, is useful for the luminosity mea-
 1595 surements by detecting the primary vertices produced in inelastic pp collisions. The
 1596 vertex data and the MBTS data are components of the events read out through the
 1597 data acquisition system, and so must be corrected for deadtime imposed by the CTP in
 1598 order to measure the delivered luminosity. Since not every inelastic collision event can
 1599 be read out through the data acquisition system, the bunch crossings are sampled with
 1600 a random or minimum bias trigger. While the triggered events uniformly sample every
 1601 bunch crossing, the trigger bandwidth devoted to random or minimum bias triggers is
 1602 not large enough to measure the luminosity separately for each bunch pair in a given
 1603 LHC fill pattern during normal physics operations. For special running conditions such
 1604 as the Van der Meer (VdM) scans, where calibration is performed using dedicated beam
 1605 separation scans, a custom trigger with partial event readout was introduced in 2011
 1606 to record enough events to allow bunch-by-bunch luminosity measurements from the
 1607 Inner Detector vertex data.

1608 In addition to the detectors listed above, further luminosity-sensitive methods have
 1609 been developed which use components of the ATLAS calorimeter system. These tech-
 1610 niques do not identify particular events, but rather measure average particle rates over
 1611 longer time scales. The Tile Calorimeter (TileCal) provides a signal proportional to the
 1612 total luminosity summed over all the colliding bunches present at a given time. Simi-
 1613 larly, the currents provided by the FCal high-voltage system are directly proportional
 1614 to the average rate of particles interacting in a given FCal sector.

1615 **3.10.0.2 The Luminosity Algorithms**

1616 This section describes the algorithms used by the luminosity-sensitive detectors to
 1617 measure the visible interaction rate per bunch crossing (μ_{vis}). ATLAS primarily uses
 1618 event counting algorithms to measure luminosity, where a bunch crossing is said to con-
 1619 tain an event if the criteria for a given algorithm to observe one or more interactions are
 1620 satisfied. The two main algorithm types being used are EventOR (inclusive counting)
 1621 and EventAND (coincidence counting). Additional algorithms have been developed us-
 1622 ing hit counting and average particle rate counting, which provide a cross-check of the
 1623 linearity of the event counting techniques.

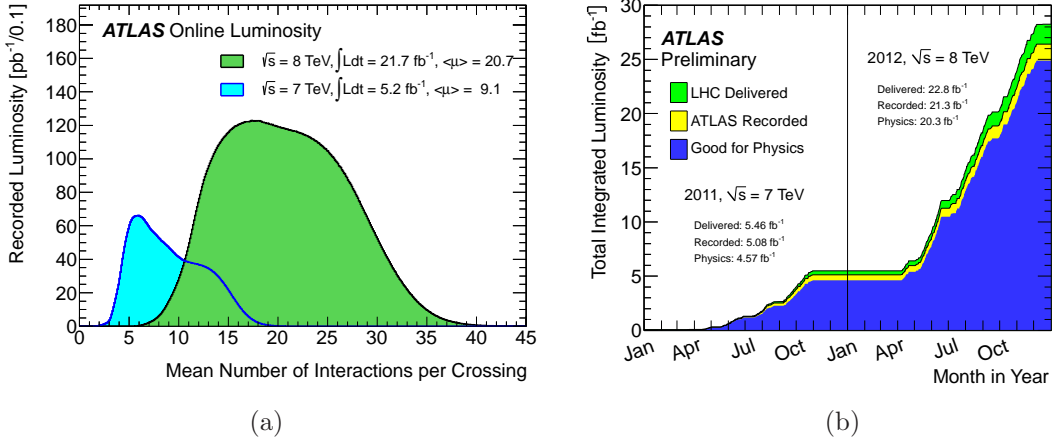
1624 Figure 3.18 presented the number of interactions per crossing and the total in-
 1625 tegrated luminosity and data quality in 2011 and 2012 [26]. The mean number of
 1626 interactions per crossing corresponds the mean of the Poisson distribution on the num-
 1627 ber of interactions per crossing calculated for each bunch. It is calculated from the
 1628 instantaneous per bunch luminosity as $\mu = L_{bunch} \times \sigma_{inel}/f_r$, where L_{bunch} is the per
 1629 bunch instantaneous luminosity, σ_{inel} is the inelastic cross section which considered to
 1630 be 71.5 mb for 7 TeV collisions and 73.0 mb for 8 TeV collisions and f_r is the LHC
 1631 revolution frequency. The delivered luminosity accounts for the luminosity delivered
 1632 from the start of stable beams until the LHC requests ATLAS to put the detector in
 1633 a safe standby mode to allow a beam dump or beam studies. The recorded luminos-
 1634 ity reflects the data acquisition inefficiency, as well as the inefficiency of the so called
 1635 "warm start": when the stable beam flag is raised, the tracking detectors undergo a
 1636 ramp of the high-voltage and, for the pixel system, turning on the preamplifiers.

1637 **3.11 ATLAS Upgrade**

1638 A long shutdown (LS2) is being planned in 2018 to integrate the Linac4 into the
 1639 injector complex, to increase the energy of the PS Booster to reduce the beam emittance,
 1640 and to upgrade the collider collimation system. When data taking resumes in 2019
 1641 (Phase-I), the peak luminosity is expected to reach $2 - 3 \times 10^{34} \text{ cm}^{-2} \text{s}^{-1}$ corresponding
 1642 to 55 to 80 interactions per crossing (pile-up³) with 25 ns bunch spacing, well beyond
 1643 the initial design goals [27]. ATLAS Phase-I upgrades will enable the experiment to
 1644 exploit the physics opportunities afforded by the upgrades to the accelerator complex.
 1645 In particular, Phase-I will allow collection of an integrated luminosity of $300 - 400 \text{ fb}^{-1}$,
 1646 extending the reach for discovery of new physics and the ability to study new phenomena
 1647 and states. Furthermore, these upgrades are designed to be fully compatible with the
 1648 physics program of the high luminosity (HL-LHC), where the instantaneous luminosity

³The high luminosity conditions at the LHC cause extra jets from other softer proton interactions in the same event, these are called "pile-up".

Figure 3.18: (a) shows the luminosity-weighted distribution of the mean number of interactions per crossing, the integrated luminosities and the mean μ values are given in the figures [26]. (b) presents the cumulative luminosity versus time delivered (green), recorded by ATLAS (yellow), and certified to be good quality data (blue) during stable beams and for pp collisions at 7 and 8 TeV center-of-mass energy in 2011 and 2012.



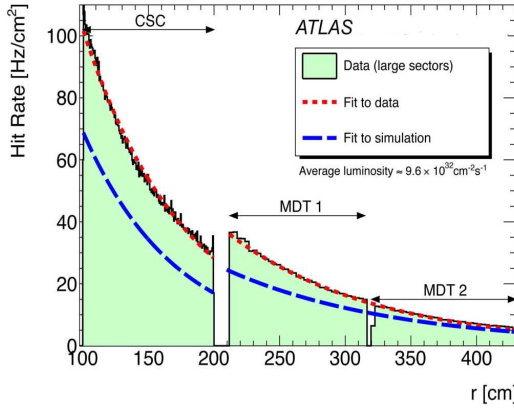
1649 should reach $5 - 7 \times 10^{34} \text{ cm}^{-2} \text{s}^{-1}$ for a total integrated luminosity of 3000 fb^{-1} (Phase-II).

1651 The interactions per bunch crossing (μ) during the Phase-I are estimated to be 55.
 1652 Despite that, it is prudent to plan at this stage an additional safety factor of about
 1653 30%, equivalent to an instantaneous luminosity of $3 \times 10^{34} \text{ cm}^{-2} \text{s}^{-1}$ and μ up to 80.
 1654 The associated integrated luminosity is then 400 fb^{-1} . When estimating the total doses
 1655 and particle fluences to qualify the electronics for the necessary radiation hardness, a
 1656 further safety factor of 2 should be applied to take into account the uncertainties on the
 1657 simulation predictions. Furthermore, any component installed in Phase-I needs to be
 1658 fully operational in ATLAS also through Phase-II, requiring therefore to be compatible
 1659 with $7 \times 10^{34} \text{ cm}^{-2} \text{s}^{-1}$, μ 200, and 3000 fb^{-1} of integrated luminosity. How the inner
 1660 detectors, the calorimeters, the muon spectrometer and the relevant triggers perform
 1661 under conditions after LS2, is described in the next paragraphs. Detector occupancy,
 1662 detector resolution, trigger rates and trigger thresholds are discussed in detail, starting
 1663 from the knowledge acquired from the current operations and data taking.

1664 3.11.1 The Muon Spectrometer Upgrade

1665 The expected rate in the EndCap region, and in particular in the first muon station
 1666 (small wheel), exceeds the existing detector capability and compromises the muon track-

Figure 3.19: Measured hit rate of cavern background using the MDT and CSC detectors [28]. The discontinuity at $R = 210$ cm is caused by the different sensitivity of the MDTs and CSCs to cavern background particles [27], which indicates possible dependency of the background hit rate on the detector technology. Old simulation studies also appear on the plot.

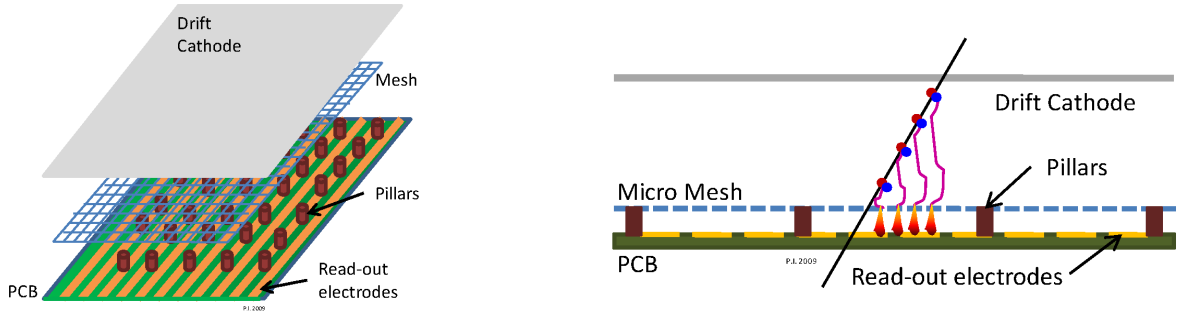


ing performance [27]. The small wheel was designed to be operational and to maintain its performance up to the condition of the nominal LHC luminosity, $1 \times 10^{34} \text{ cm}^{-2} \text{ s}^{-1}$, including a safety factor of 5 with respect to the cavern background level estimated at the time of designing the detector. However, the actual background level has been found to be higher than these original estimates, partially due to shielding which was modified during the Run-I, e.g. a shielding gap in the barrel region lead to higher background in the BI chambers. More recent FLUGG simulations agree much better with the hit rate measurements (presented in Figure 3.19), providing a more reliable estimate of the expectations for future operation, but the safety margins are significantly reduced.

Sharpening the Level-1 threshold is necessary for the data taking in Phase-I and beyond. The Level-1 trigger upgrade addresses both the suppression of the fake triggers and improvement of the p_T resolution. Presently, the Level-1 muon trigger in the EndCap is operating as follows. A track segment is identified first using hits on the 7 layers in the TGC. Then, the p_T is determined from the deviation of the segment angle from the direction pointing towards the nominal interaction point (IP) position (assuming that the track produced at the IP). As a result of the assumption, there is unexpectedly high rates of fake triggers in the EndCap region. This may be removed by requiring a corresponding activity in the small wheel. Studies have been made to see how well such approach works using collision data by emulating the small wheel segments in an upgraded detector using data from the existing detectors (CSC, MDT, TGC). The L1MU20 ⁴ rate is reduced by about one order of magnitude compared to

⁴L1 muon trigger with p_T threshold of 20 GeV

Figure 3.20: Sketch of the layout and operating principle of a MM detector [29].

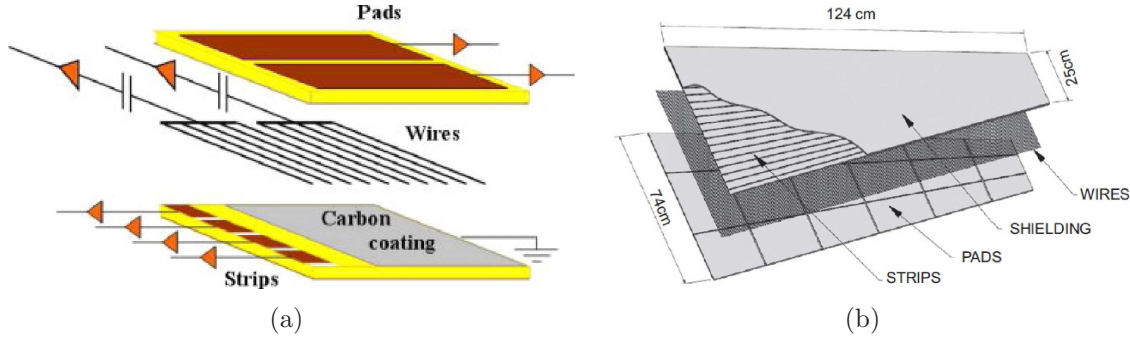


1688 the initial rate and the efficiency of high p_T muons is 95%. The detector technologies
 1689 chosen to replace the existing small wheel are the Micromegas and sTGCs [29].

1690 3.11.1.1 The MicroMegas Detectors

1691 The micromegas, “micro mesh gaseous structure” (MM), technology permits the
 1692 construction of thin wireless gaseous particle detectors [29]. MM detectors consist of a
 1693 planar (drift) electrode, a gas gap of a few millimeters thickness acting as conversion and
 1694 drift region, and a thin metallic mesh at typically 100-150 μm distance from the readout
 1695 electrode, creating the amplification region. A sketch of the MM operating principle
 1696 is shown in Figure 3.20. The HV potentials are chosen such that the electric field in
 1697 the drift region is a few hundred V/cm , and 40-50 kV/cm in the amplification region.
 1698 Charged particles traversing the drift space ionize the gas; the electrons liberated by
 1699 the ionization process drift towards the mesh. With an electric field in the amplification
 1700 region 50-100 times stronger than the drift field, the mesh is transparent to more than
 1701 95% of the electrons. The electron avalanche takes place in the thin amplification region,
 1702 immediately above the readout electrode. The drift of the electrons in the conversion
 1703 gap is a relatively slow process; depending on the drift gas, the drift distance, and
 1704 the drift field it typically takes several tens of nanoseconds. On the other hand the
 1705 amplification process happens in a fraction of a nanosecond, resulting in a fast pulse
 1706 of electrons on the readout strip. The ions that are produced in the avalanche process
 1707 move, in the opposite direction of the electrons, back to the amplification mesh. Most
 1708 of the ions are produced in the last avalanche step and therefore close to the readout
 1709 strip. Given the relatively low drift velocity of the ions, it takes them about 100 ns to
 1710 reach the mesh, still very fast compared to other detectors. It is the fast evacuation
 1711 of the positive ions which makes the MM particularly suited to operate at very high
 1712 particle fluxes.

Figure 3.21: The sTGC internal structure sketch [29].



3.11.1.2 The sTGC Detectors

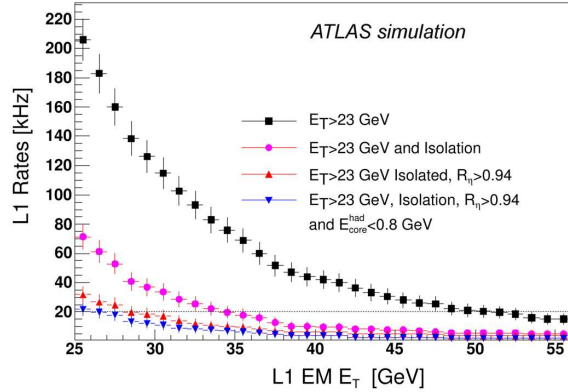
The basic Small strip Thin Gap Chamber (sTGC) structure is shown in Figure 3.21. It consists of a grid of $50 \mu\text{m}$ gold-plated tungsten wires, sandwiched between two cathode planes [29]. The cathode planes are made of a graphite-epoxy mixture with a typical surface resistivity of $100 \text{ k}\Omega$ sprayed on a thick $G - 10$ plane, behind which there are on one side strips (that run perpendicular to the wires) and on the other pads (covering large rectangular surfaces), on a thick PCB with the shielding ground on the opposite side. The strips are much smaller than the TGC pitch, hence the name Small TGC for this technology.

The TGC system, used in the present ATLAS muon EndCap trigger system, has passed a long phase of R&D and testing. The basic detector design for the NSW has two quadruplets 35 cm apart in z . Each quadruplet contains four TGCs, each TGC with pad, wire and strip readout. The pads are used to produce a 3-out-of-4 coincidence to identify muon tracks roughly pointing to the interaction point. They are also used to define which strips are to be readout to obtain a precise measurement in the bending coordinate, for the online muon candidate selection. The azimuthal coordinate, where only about 10 mm precision is needed, is obtained from grouping wires together. The charge of all strips, pads and wires are readout for offline track reconstruction.

3.11.2 The Calorimeters Upgrade

Higher transverse granularity and depth information is required by the Level-1 trigger system to reduce the rates and improve resolution for several trigger objects as Figure 3.22 shows [27]. Rejection factors of about $3 - 5$ for low p_T jets faking electrons can be achieved by implementing shower shape algorithms using the 2nd sampling layer of the EM calorimeters. Furthermore, studies of discriminant variables using the 3rd sampling layer of the EM and the hadronic Tile Calorimeter layers are in progress and

Figure 3.22: Expected Level-1 rates for different algorithms and conditions calculated from Monte Carlo simulations with the current Level-1 trigger system [28]. The pileup corresponds to $\mu = 46$ with a bunch spacing of 25 ns [27].



1738 could potentially lead to substantial improvements of the resolution of τ s, jets and more
 1739 importantly, missing E_T (MET) triggers.

1740 This additional information will require a partial upgrade of the calorimeter front-
 1741 end readout architecture, part of the input stage of the Level-1 calorimeter trigger and
 1742 the interfaces among the two systems. The upgrade plan for Phase-I is part of a more
 1743 general staged program to be implemented over the next decade for the entire HL-
 1744 LHC lifetime: the ultimate goal is a free-running digital architecture of all individual
 1745 LAr and Tile calorimeter channels. The proposed architecture will be validated by an
 1746 in-beam system test planned for installation in ATLAS during the Phase-0 shutdown.
 1747 The system will be run seamlessly within ATLAS during the Run-II. It is aimed at
 1748 improving the granularity in one $\Delta\eta \times \Delta\phi = 0.4 \times 0.4$ slice of the LAr and Tile barrel
 1749 calorimeters, matching the size of the current L1Calo electron algorithm window. Two
 1750 trigger Tower Builder Boards and four new Tile drawers with digitization of data at
 1751 the front-end will be installed in order to test the digital trigger path and hardware
 1752 implementations of novel single-object triggers.

1753 For the Phase-I, an intermediate stage will be applied. It combines analog and
 1754 digital trigger readout, fully compatible with the present analog transmission of the
 1755 trigger primitives but with a digital readout path that contains many of the elements
 1756 required by the final upgrade.

1757 For the LAr calorimeters, this will be implemented by means of new Tower Builder
 1758 Boards (sTBBs) that are modified by adding a digital readout path. This provides the
 1759 trigger with finer granularity data in depth and in η .

1760 The full digital readout of the Tile calorimeter is planned for Phase-II. For Phase-I,
 1761 an upgrade based on using the "D-cell outputs" (the outermost layer of TileCal) that
 1762 are already available is being considered, if it can be motivated by simulations results.

1763 3.11.3 The Fast Tracker

1764 The FastTracKer (FTK) [27], is a pipelined electronics system that rapidly finds
 1765 and fits tracks in the inner-detector silicon layers for every event that passes the Level-1
 1766 trigger. Its goal is global track reconstruction with near offline resolution at a maximum
 1767 Level-1 rate of 10^5 events per second and a latency per event of less than $100\ \mu\text{s}$. This
 1768 can be compared with the time to carry out full track reconstruction in the Level-2
 1769 processors which is estimated to be several hundred milliseconds at Phase-I luminosity.
 1770 FTK uses 11 silicon layers over the full rapidity range covered by the barrel and the
 1771 disks. It receives a copy of the pixel and silicon strip (SCT) data at full speed as it
 1772 moves from the RODs to the ROSs following a Level-1 trigger, and after processing
 1773 it provides the helix parameters and χ^2 of all tracks with p_T above a minimum value,
 1774 typically 1 GeV. The Level-2 processors can request the track information in a Region
 1775 of Interest or the entire detector.

1776 FTK has been designed as a highly parallel system that is segmented into η and
 1777 ϕ towers, each with its own pattern recognition hardware and track fitters, and the
 1778 installation milestone target is the Long Shutdown starting at 2018.

1779 3.11.4 The Forward Physics Upgrade

1780 ATLAS considers to install a Forward Proton (AFP) detector in order to detect
 1781 protons at 206 and 214 m on both side of the ATLAS experiment at very small scattering
 1782 angles [27]. The physics motivation is to identify and record events with leading intact
 1783 protons emerging from diffractive collisions occurring in ATLAS, for both “exploratory”
 1784 physics, e.g. anomalous couplings between W/Z bosons and γ , and QCD physics in
 1785 new kinematical domain. These studies could not be performed using the other ATLAS
 1786 forward detectors.

1787 The AFP detector will consist of three parts: movable beam pipe, silicon position
 1788 detectors and quartz timing detectors. The movable beam line specializes in the mea-
 1789 surement of scattered protons, the silicon tracker in combination with the LHC dipole
 1790 and quadrupole magnets forms a powerful momentum spectrometer and the quartz
 1791 detector will provide a fast timing system.

1792 3.11.5 The T/DAQ Upgrade

1793 As mentioned in the previous paragraphs, the replacement of the Small wheel and
 1794 the partial replacement of the LAr on-detector electronics will impose changes to the
 1795 L1 Muon and Calorimeter triggers. On top of that, upgrades to the Level-1 trigger

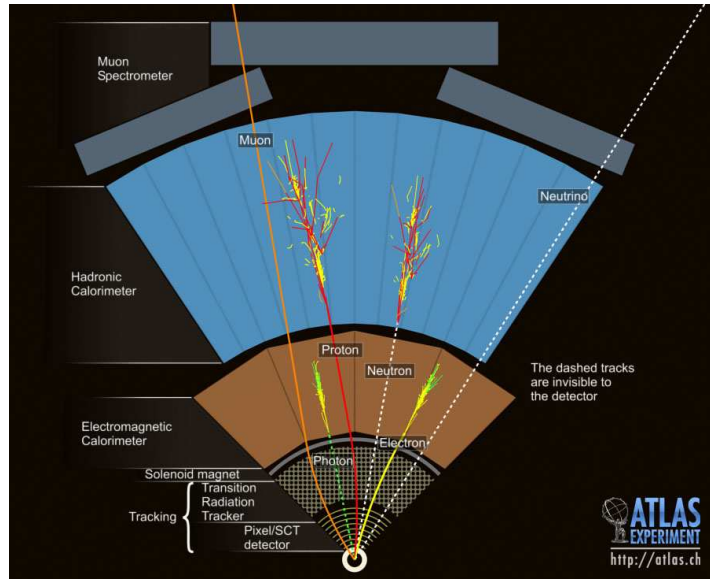
1796 electronics are expected to improve performance at higher pile-up and provide increased
1797 trigger flexibility without major architectural changes to the current detector readout
1798 and data acquisition [27].

1799 Following the L1 trigger changes, the HLT needs to adapt the selection software
1800 for higher luminosity. The HLT steering software will be upgraded to provide greater
1801 flexibility, to optimize the event processing, to minimize average execution times and
1802 prevent excessive times in the case of events with many RoIs. The HLT tracking code
1803 will be upgraded to limit the rise of algorithm execution times as events become more
1804 complex due to the higher levels of pile-up and cavern background, affecting the muon
1805 detectors, as the luminosity increases. In addition to minimizing the average per-event
1806 processing time, it is important to prevent very long execution times which would
1807 otherwise cause time-outs. The HLT muon code must be adapted for the new small
1808 muon wheels and the ID tracking must be adapted for the insertable B-layer and to
1809 use FTK information. The FTK will provide initial track parameter information which
1810 can be used to guide (seed) the HLT tracking that will add TRT information and refine
1811 and refit the tracks.

1812 The current DAQ/HLT architecture is expected to meet the needs of the experiment
1813 with respect to Level-1 rate and bandwidth. However, a new version of the readout
1814 link (RoL), whose current implementation runs at 160/200 *Mbytes/s*, may be needed to
1815 provide increased bandwidth for new detectors. The physics demands of ATLAS have
1816 pushed the operation of the ROS a factor of two beyond its original design specifica-
1817 tion. The performance is currently network bandwidth limited (2 *Gbits/s*). This limit
1818 constrains some Level-2 trigger chains and in order to remove this limitation and re-
1819 establish some of the operational headroom originally provided in the system, the data
1820 flow network will be upgraded to a 10 *Gbits/s* Ethernet connection at the ROS and,
1821 via link aggregation, 100 *Gbits/s* Ethernet connections to a central core. This upgrade
1822 would also allow the rate at which events are built to be increased. A sub-component of
1823 the ROS is the ROBIN, a PCI-X card. By the Phase-I shutdown, it is anticipated that
1824 PCI-X slots will no longer be deployed in sufficient numbers on commercially available
1825 computers, having been replaced by PCI-express. The ROBIN will be re-designed and
1826 re-implemented to follow this technological trend and support readout links of higher
1827 speeds than the current.

1828 By the end of Phase-I operations, the custom VMEbus electronics implementing the
1829 Region of Interest Builder (RoIB) will have been in operation for sixteen years. Two
1830 upgrade paths are currently being investigated. The first aims to exploit the contin-
1831 ued advances in server technology. It is expected to be able to implement the RoIB
1832 functionality in one or more servers housing one or more custom mezzanine cards that
1833 handle the small data packets arriving at up to 100 *kHz* from the Level-1 system. This
1834 will remove or reduce the dependency on custom electronics and introduce additional
1835 operational flexibility into the system. The alternative of re-implementing the RoIB in
1836 modular electronics will also be investigated as a back-up solution.

Figure 3.23: Schematic view of the signatures the different physics objects leave in the detector. The ATLAS detector layout is consider for the graph.



1837 Other upgrades to the ATLAS detector imply the deployment of additional DAQ/HLT
 1838 hardware. Additional RoLs and ROSs (including ROBINS) will be deployed to readout
 1839 the new small wheels and the upgraded LAr electronics.

1840 The deployed software will have become obsolete and in some cases no longer meet
 1841 the requirements on the DAQ/HLT system, which will necessitate its upgrade.

1842 3.12 Summary

1843 In this chapter, the technologies on which the ATLAS detector is based are exten-
 1844 sively described. The combination of the information from the tracking detectors, the
 1845 calorimeters and the muon chambers leads to the identification of physics objects as
 1846 Figure 3.23 shows. The triggering and the data acquisition are of high importance for
 1847 fruitful and efficient data taking, especially in harsh pile-up conditions. At the end of
 1848 this chapter the future plans for the detector upgrade are presented.

1849 Chapter Bibliography

1850 [1] G. Aad et al., Expected Performance of the ATLAS Experiment - Detector, Trigger
1851 and Physics, 2009, 0901.0512.

1852 [2] CERN, ATLAS: Detector and physics performance technical design report. Volume
1853 1, 1999.

1854 [3] ATLAS Collaboration, Technical challenges of atlas,
1855 http://atlas.ch/atlas_brochures/atlas_brochures_pdf/atlas_tech_full.pdf.

1856 [4] Norbert Wermes and G Hallewel, *ATLAS pixel detector: Technical Design Re-*
1857 *port*, Technical Design Report ATLAS. CERN, Geneva, ATLAS-TDR-11, CERN-
1858 LHCC-98-013.

1859 [5] Maximilien Brice, Re-insertion of the pixel detector, CERN-HI-1312311.

1860 [6] Atlas Collaboration, Atlas interior 2013, <http://www.atlas.ch/photos/atlas-interior.html>.

1861 [7] ATLAS inner detector: Technical design report. Vol. 1, 1997, CERN-LHCC-97-16,
1862 ATLAS-TDR-4.

1863 [8] ATLAS Collaboration, ATLAS SCT public twiki page,
1864 <https://twiki.cern.ch/twiki/pub/Atlas/SctWiki>.

1865 [9] Maximilien Brice, ATLAS experiment - view of the inner detector ATLAS TRT,
1866 Sep 2005, <http://cds.cern.ch/record/889555>.

1867 [10] ATLAS liquid argon calorimeter: Technical design report, 1996,
1868 CERN-LHCC-96-41.

1869 [11] ATLAS Collaboration, Liquid Argon Barrel ATLAS Photos,
1870 <http://www.atlas.ch/photos/calorimeters-lar-barrel.html>.

1871 [12] ATLAS Tile calorimeter: Technical design report, 1996, CERN-LHCC-96-42.

1872 [13] ATLAS Collaboration, Combined Barrel ATLAS Photos,
1873 <http://www.atlas.ch/photos/calorimeters-combined-barrel.html>.

1874 [14] ATLAS muon spectrometer: Technical design report, 1997, CERN-LHCC-97-22,
1875 ATLAS-TDR-10.

1876 [15] T. Argyropoulos, K. A. Assamagan, B. H. Benedict, V. Chernyatin, E. Cheu,
1877 et al., Cathode strip chambers in ATLAS: Installation, commissioning and in situ
1878 performance, *IEEE Trans.Nucl.Sci.*, 56:1568–1574, 2009.

1879 [16] ATLAS Collaboration, RPC ATLAS Photos,
 1880 <http://www.atlas.ch/photos/muons-rpc.html>.

1881 [17] CERN, *ATLAS magnet system: Technical Design Report, 1*, Technical Design
 1882 Report ATLAS. CERN, Geneva, 1997, ATLAS-TDR-6, CERN-LHCC-97-018.

1883 [18] CERN, *ATLAS central solenoid: Technical Design Report*, Technical Design Re-
 1884 port ATLAS. CERN, Geneva, ATLAS-TDR-9, CERN-LHCC-97-021.

1885 [19] ATLAS Collaboration, Magnets ATLAS Photos,
 1886 <http://www.atlas.ch/photos/magnets.html>.

1887 [20] J P Badiou, J Beltramelli, J M Baze, and J Belorgey, *ATLAS barrel toroid:*
 1888 *Technical Design Report*, Technical Design Report ATLAS. CERN, Geneva, 1997,
 1889 ATLAS-TDR-7, CERN-LHCC-97-019.

1890 [21] CERN, *ATLAS end-cap toroids: Technical Design Report*, Technical Design Re-
 1891 port ATLAS. CERN, Geneva, 1997, ATLAS-TDR-8, CERN-LHCC-97-020, Elec-
 1892 tronic version not available.

1893 [22] P.J. Clark, The ATLAS detector simulation, *Nucl.Phys.Proc.Suppl.*, 215:85–88,
 1894 2011.

1895 [23] N. Berger, T. Bold, T. Eifert, G. Fischer, S. George, et al., The ATLAS high level
 1896 trigger steering, *J.Phys.Conf.Ser.*, 119:022013, 2008.

1897 [24] A Krasznahorkay, The evolution of the Trigger and Data Acquisition System in
 1898 the ATLAS experiment, Technical Report ATL-DAQ-PROC-2013-018, CERN,
 1899 Geneva, Sep 2013.

1900 [25] Georges Aad et al., Improved luminosity determination in pp collisions at \sqrt{s}
 1901 = 7 TeV using the ATLAS detector at the LHC, *Eur.Phys.J.*, C73:2518, 2013,
 1902 1302.4393.

1903 [26] ATLAS Collaboration, ATLAS Luminosity Public Results Twiki,
 1904 <https://twiki.cern.ch/twiki/bin/view/AtlasPublic/LuminosityPublicResults>.

1905 [27] Letter of Intent for the Phase-I Upgrade of the ATLAS Experiment, Technical
 1906 Report CERN-LHCC-2011-012, LHCC-I-020, CERN, Geneva, Nov 2011.

1907 [28] ATLAS Collaboration, ATLAS public results,
 1908 <https://twiki.cern.ch/twiki/bin/view/AtlasPublic/WebHome>.

1909 [29] S. Gadomski, Updated impact parameter resolutions of the ATLAS Inner Detector,
 1910 2000, ATL-INDET-2000-020, ATL-COM-INDET-2000-026, CERN-ATL-INDET-
 1911 2000-020.

1912 [30] Georges Aad et al., Measurement of the muon reconstruction performance of
1913 the ATLAS detector using 2011 and 2012 LHC proton-proton collision data,
1914 *Eur.Phys.J.*, C74(11):3130, 2014, 1407.3935.

1915 [31] Georges Aad et al., Electron and photon energy calibration with the ATLAS
1916 detector using LHC Run 1 data, *Eur.Phys.J.*, C74(10):3071, 2014, 1407.5063.

1917 [32] X. C. Vidal, R. Cid, and G. M. Rey, Taking a closer look at LHC,
1918 <http://www.lhc-closer.es>.

1919 [33] CERN, ATLAS: Detector and physics performance technical design report. Volume
1920 2, 1999.

1921 [34] M Capeans, G Darbo, K Einsweiller, M Elsing, T Flick, M Garcia-Sciveres,
1922 C Gemme, H Pernegger, O Rohne, and R Vuillermet, ATLAS Insertable B-Layer
1923 Technical Design Report, Technical Report CERN-LHCC-2010-013, ATLAS-TDR-
1924 19, CERN, Geneva, Sep 2010.

1925 [35] ATLAS inner detector: Technical design report. Vol. 2, 1997, CERN-LHCC-97-17.

1926 [36] A. Artamonov, D. Bailey, G. Belanger, M. Cadabeschi, T.Y. Chen, et al., The
1927 ATLAS forward calorimeters, *JINST*, 3:P02010, 2008.

1928 [37] J.C. Barriere, F. Bauer, M. Fontaine, A. Formica, V. Gautard, et al., The align-
1929 ment system of the ATLAS barrel muon spectrometer, 2008.

1930 [38] S Aefsky, C Amelung, J Bensinger, C Blocker, A Dushkin, M Gardner, K Hashemi,
1931 E Henry, B Kaplan, M Ketchum, P Keselman, U Landgraf, A Ostapchuk, J E
1932 Rothberg, A Schricker, N Skvorodnev, and H Wellenstein, The Optical Alignment
1933 System of the ATLAS Muon Spectrometer Endcaps, *J. Instrum.*, 3:P11005. 49 p,
1934 Feb 2008, ATL-MUON-PUB-2008-003, ATL-COM-MUON-2008-005.

1935 [39] R (SLAC) Bartoldus, C (Marseille CPPM) Bee, D (CERN) Francis, N (RAL)
1936 Gee, S (London RHBNC) George, R (Michigan SU) Hauser, R (RAL) Middleton,
1937 T (CERN) Pauly, O (KEK) Sasaki, D (Oregon) Strom, R (Roma I) Vari, and
1938 S (Roma I) Veneziano, Technical Design Report for the Phase-I Upgrade of the
1939 ATLAS TDAQ System, Technical Report CERN-LHCC-2013-018, ATLAS-TDR-
1940 023, CERN, Geneva, Sep 2013, Final version presented to December 2013 LHCC.

1941 [40] dE/dx measurement in the ATLAS Pixel Detector and its use for particle identi-
1942 fication, Technical report, CERN, Geneva, Mar 2011, ATLAS-CONF-2011-016.

1943 [41] Basic ATLAS TRT performance studies of Run 1, Technical report, CERN,
1944 Geneva, Mar 2014, ATL-INDET-PUB-2014-001.

¹⁹⁴⁵ [42] Georges Aad et al., Monitoring and data quality assessment of the ATLAS liquid
¹⁹⁴⁶ argon calorimeter, *JINST*, 9:P07024, 2014, 1405.3768.

¹⁹⁴⁷ [43] Georges Aad et al., Performance of the ATLAS muon trigger in pp collisions at
¹⁹⁴⁸ $\sqrt{s} = 8$ TeV, 2014, 1408.3179.

4

1949

1950

Cathode Strip Chambers (CSC)

4.1 Introduction

1951 In this chapter, the performance and operational properties of the Cathode Strip
1952 Chambers (CSC) are studied. Starting from the basic construction properties, the
1953 readout of the chambers is described. The on-detector electronics send the collected
1954 information to the off-detector for enhanced processing and signal allocation. The major
1955 operational problem during the Run-I was the deadtime caused by the off-detector
1956 system. A variety of methods were applied to resolve the problem and a new system
1957 was designed for the Run-II.

1958 The reconstruction software is explained in all steps until the required CSC muon
1959 signal is extracted and performance summaries are also given in this chapter. The
1960 resolution and the alignment of the detector are explored, given their importance on
1961 the muon quality.

1962 At the end, the repair of chambers and their functionality is reported.

4.2 Principle of Operation

1963 The CSC, introduced in Section 3.6.2, are well suited to meet the requirements for
1964 the precision measurement of muons in ATLAS [1]. Precision tracking at the inner-

most station (Small Wheel) in the high pseudorapidity regions, $2.04 \leq |\eta| \leq 2.70$, is performed by 16 four-layered Cathode Strip Chambers on each EndCap [2]. These are multi-wire proportional chambers with segmented cathodes providing excellent spatial resolution and high counting rate capability. The second cathode of each layer is coarsely segmented, providing the transverse coordinate [2]. The sensitivity to neutrons is low, $\epsilon_n < 10^{-4}$, due to the small gas volume and the lack of hydrogen in the operating gas. Photon sensitivity is also small, $\epsilon_\gamma \sim 1\%$ for $E_\gamma = 1 \text{ MeV}$. The rather large chamber dimension and high operating pressure, however, make them unsuitable for use in areas where high ($> 200 \text{ Hz/cm}^2$) counting rates are expected [1].

Following the overall ATLAS geometry, there are two chamber versions, Large and Small, which differ slightly in the active area [2]. These are installed alternately and overlap partially to seamlessly cover the 27% of the Muon Spectrometer's pseudorapidity acceptance. The large chambers of one out of the two small wheels are presented in Figure 4.1. Multiple measurements of the same track are provided, since every chamber consists of four identical layers each with 192 precision and 48 transverse coordinate strips, which are lithographically etched for highest precision. The precision strips have a readout pitch of 5.308 and 5.556 mm for the Large and Small chambers respectively. The basic operation and design parameters are presented in Table 4.1.

Table 4.1: Basic CSC Operation Parameters [2].

Number of chambers	2×16	
Number of layers / chamber	4	
Layers separation	25 mm	
Inclination angle	11.6°	
Gas mixture	$Ar/C0_2$ (80% : 20%)	
Wire material	$W - Re$ (97% : 3%)	
Operating voltage / gain	$1900 \text{ V} / 10^4$	
Anode - cathode distance	2.5 mm	
Anode wire pitch	2.5 mm	
	Small	Large
Number of wires / layers	250	420
Number of η readout strips	192	192
η readout strip pitch (mm)	5.566	5.308
Number of ϕ readout strips	48	48
ϕ readout strip pitch (mm)	12.922	21.004
Active area (m^2) / chamber	0.50	0.78
Gas volume (l) / chamber	10.0	15.5
Chamber total weight (kg)	70	92

Figure 4.1: One of the two ATLAS Small Wheels in the assembly building before the installation [3]. In the inner radius the eight CSC large chambers are visible and partially overlapping from the backside (not visible) with the eight small chambers.

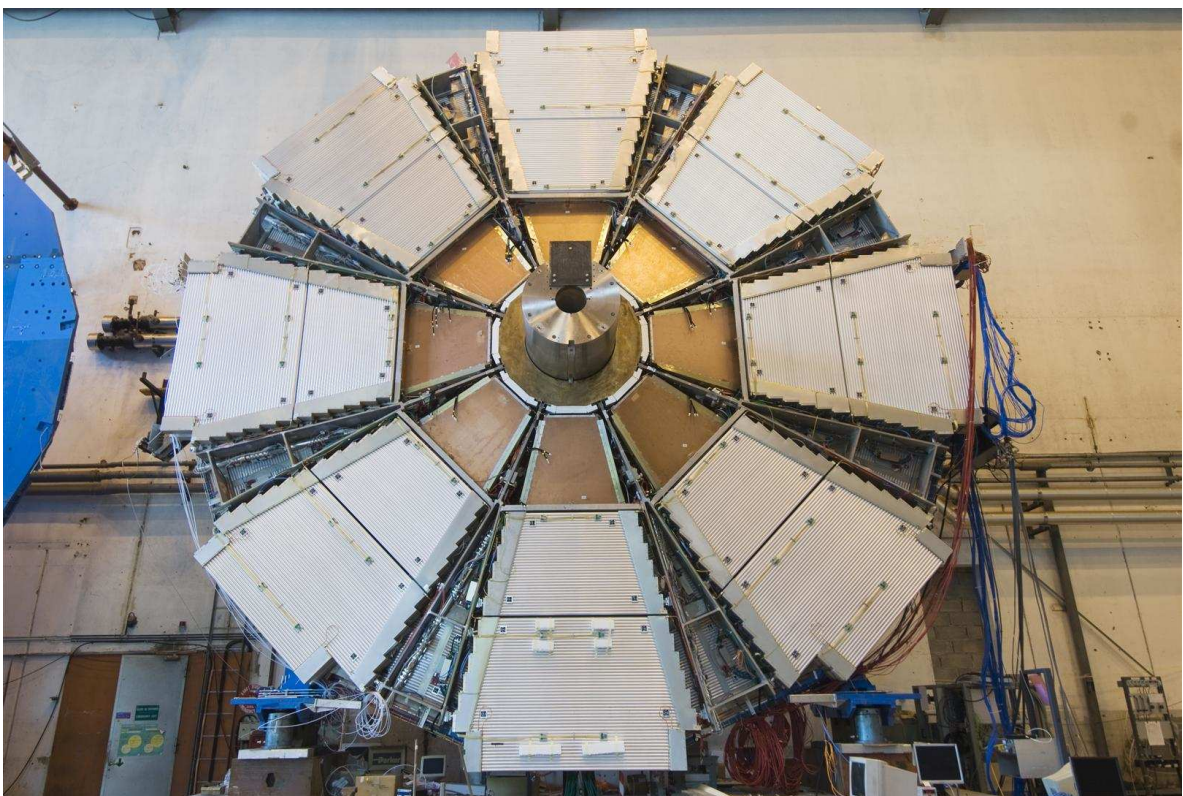
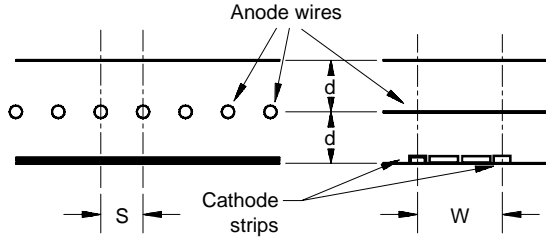


Figure 4.2: Schematic diagram of the cathode strip chamber (side view) [2].



1985 The gas used is a mixture of Ar/CO_2 which comply the characteristics of high drift
 1986 velocity, low Lorentz angle and is non-flammable. Despite the fact that a high drift
 1987 velocity is needed to ensure that the bunch-crossing identification can be performed
 1988 [1], for the position measurement, variations of the drift velocity or non-uniform drift
 1989 velocities as a function of E/p are inconsequential to the performance. For the same
 1990 reason, the CSC operation is immune to modest variations of temperature and pressure.
 1991 Similarly, variations in the absolute gas gain do not, to first order, affect the CSC
 1992 operation since a relative charge measurement in adjacent strips is involved.

1993 4.3 Signal Formation

1994 The CSCs are multiwire proportional chambers with a symmetric cell in which the
 1995 anode-cathode spacing (d) is equal to the anode wire pitch (S), which has been fixed at
 1996 2.5 mm, as schematically shown in Figures 4.2,4.3. In a typical multiwire proportional
 1997 chamber the anode wires are read out limiting the spatial resolution to an R.M.S. of
 1998 $S/\sqrt{12}$ [2]. In a CSC the precision coordinate is obtained by measuring the charge
 1999 induced on the segmented cathode by the avalanche formed on the anode wire. The
 2000 induced charge distribution as a function of the variable $\lambda = x/d$, where x is the
 2001 precision coordinate (transversely to the strips), is given by:

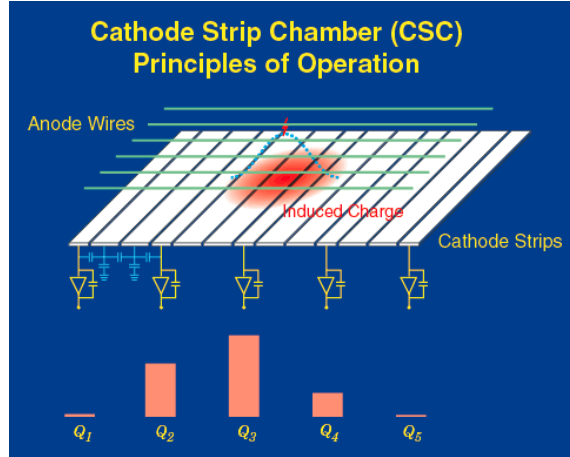
$$\Gamma(\lambda) = K_1 \frac{1 - \tanh^2 K_2 \lambda}{1 + K_3 \tanh^2 K_2 \lambda} \quad (4.1)$$

2002 where the constants K_2 , K_3 are related by the empirical formula:

$$K_2 = \frac{\pi}{2} \left(1 - \frac{1}{2} K_3^{1/2} \right). \quad (4.2)$$

2003
 2004 Using the equation 4.2 and the constraint that the total charge induced on one cath-
 2005 ode equals half the avalanche charge, Equation 4.1 can be reduced to a one-parameter

Figure 4.3: The principle of operation is illustrated in the diagram, this particular cathode geometry is called "Two Intermediate Strips", which improves the position linearity using capacitive charge division [4, 5].



2006 expression. The optimum cathode readout pitch W is determined by the width of the
 2007 induced charge and the desire to keep the number of readout channels to a minimum
 2008 while maintaining a linear response.

2009 Optimal capacitive coupling requires that the inter-strip capacitance (C_1) be much
 2010 larger than the capacitance of a strip to ground, (C_2). Specifically for the ATLAS
 2011 CSC design $C_1/C_2 \approx 10$ [1]. Since the preamplifier noise is dominated by the input
 2012 capacitance an additional advantage from the use of two intermediate strips (graphically
 2013 presented in Figure 4.3) is a reduction by a factor between two and three of the inter-
 2014 node capacitance. Further optimization of the linearity can be accomplished by making
 2015 the width of the intermediate strip slightly larger than that of the readout strips. It
 2016 is necessary to provide a high resistance path to ground to maintain the intermediate
 2017 strips at the proper DC potential. A thin strip of resistive epoxy (conductivity $6 M\Omega$
 2018 per square) is silk screened on the tips of the strips at the end of the cathode opposite
 2019 to the amplifiers.

2020 4.4 Spatial resolution of the CSCs

2021 In a CSC the precision coordinate is obtained by a relative measurement of charges
 2022 induced by the avalanche on adjacent cathode strips. Therefore modest (< 20%) vari-
 2023 ations in the chamber's gas gain do not affect the spatial resolution [1]. For this reason
 2024 the CSC performance is immune to variations in temperature and pressure commonly

2025 encountered in the experimental hall. Since no precision time measurement is involved,
 2026 the CSC operation is insensitive to the drift properties of the operating gas. A modest
 2027 34 ns R.M.S. time resolution is sufficient to determine the bunch crossing with high
 2028 efficiency.

2029 The primary factor limiting the CSC spatial resolution is the electronic noise of the
 2030 preamplifier. The precision in the determination of the center of gravity of the induced
 2031 charge depends linearly on the signal-to-noise ratio. Eventually other factors, such as
 2032 uncertainty in electronic gain, calibration and geometrical cathode distortions, set the
 2033 limit for this technique at about 30 μm . A design consideration of the readout amplifier
 2034 is an electronic noise level such that the chamber can be operated with a total anode
 2035 charge of about 1 pC per minimum ionizing particle at the target spatial resolution.

2036 Assuming that the projection of the avalanche position on the cathode strip plane
 2037 is at a point $x = 0$. The position of the center of gravity is given by the ratio of the
 2038 first and second moments of the charge distribution on the strip plane

$$x_{cg} = \frac{\sum_{i=1}^N x_i q_i}{\sum_{i=1}^N q_i} \quad (4.3)$$

2039 where $x_i = iW$ and W is the pitch of the cathode readout. If the charges q_i are the
 2040 measured with an R.M.S. error of σ then the uncertainty in x_{cg} is:

$$\sigma_{cg} = \frac{\sigma}{Q} \sqrt{2 \sum_i x_i^2} \quad (4.4)$$

2041 or

$$\sigma_{cg} = \frac{\sigma}{Q} \sqrt{2W^2 + 2(4W^2) + 2(9W^2) + \dots} \quad (4.5)$$

2042 Therefore, the resolution depends on the number of strips used. The optimum lies
 2043 between three and five strips, as estimated from Monte Carlo studies. The resolution
 2044 deteriorates rapidly for one or two (due to lack of information), while it increases slowly
 2045 when more than five strips are used because the electronic noise of more channels is
 2046 added in quadrature.

2047 4.5 The Effect of Inclined Tracks and the Lorentz 2048 Angle

2049 The second most significant contribution to the spatial resolution of the CSC is
 2050 the effect of the inclined tracks and the Lorentz angle. The charge interpolation is

2051 optimum when the avalanche is formed on a single point along the wire. A finite
2052 spatial extent of the anode charge results in a resolution degradation [1]. Such non-
2053 local charge deposition can be caused by a number of factors such as delta electrons,
2054 inclined tracks, and a Lorentz force along the anode wire in the presence of a magnetic
2055 field which is not collinear with the electric field of the chambers. It should be noted,
2056 however, that the Lorentz effect in the CSC does not result in a systematic shift of the
2057 measured coordinate. It does not, therefore, require a correction. In fact, no correction
2058 is possible. Simply the resolution degrades because of the spread of the charge along the
2059 wire. The effect of the inclined tracks is minimized by tilting the chamber by an angle
2060 of 11.59° so that, on the average, the tracks are normal to the plane of the chambers [1].

2061 4.6 Timing Resolution

2062 The maximum drift distance of the ionization electrons for a track traversing a cham-
2063 ber exactly between two anode wires is 1.25 mm . With a drift velocity of $60\text{ }\mu\text{m/ns}$,
2064 typical of the chosen operating gas, the maximum drift time is about 30 ns [1]. A time
2065 of arrival distribution has been measured to have an R.M.S. of about 7 ns . It exhibits,
2066 however, significant tails due to very low drift fields in the boundary of two adjacent
2067 cells. In any case, this resolution is not sufficient to permit efficient tagging of the
2068 bunch crossing of a given muon traversing the chamber. For this reason, the following
2069 technique is used to determine the bunch crossing. The earliest time of arrival in a
2070 four-plane multilayer is determined by connecting the four signals from these planes in
2071 an OR circuit. Test beam measurements of the timing obtained with such an arrange-
2072 ment show a timing resolution of 3.6 ns R.M.S. with a symmetric, nearly Gaussian,
2073 distribution.

2074 4.7 Mechanical Design and Construction

2075 4.7.1 Description of the Basic Four-Layer Module

2076 The CSC design utilizes low-mass construction materials to minimize multiple scat-
2077 tering and detector weight [1]. A four-layer multilayer is formed by five flat, rigid panels,
2078 each of which is made of an 18.75 mm thick sheet of nomex honeycomb (hexcel) and
2079 two 0.5 mm thick copper-clad FR4 laminates, the $17\text{ }\mu\text{m}$ thick copper cladding form-
2080 ing the cathodes. The panel frames are made of machined rohacell, a closed-cell, high
2081 stiffness lightweight foam. Precision machined FR4 strips glued on the panels provide
2082 the step for the anode wire plane. The anode wires are made of gold-plated tungsten

2083 with 3% rhenium and have a diameter of $30 \mu m$. The high voltage (HV) distribution
 2084 system and all the passive components are encapsulated in the rohacell frames. A
 2085 rubber gasket between two adjacent planes provides the gas seal for the assembly. No
 2086 components under high voltage are outside the seal, thus minimizing the risk of high
 2087 voltage breakdowns. These panels weigh approximately $1 kg/m^2$.

2088 In each of the four gaps, the position-sensing cathode strips are lithographically
 2089 etched. One of the cathodes has precision strips, parallel to the corresponding MDT
 2090 anode wires. The second cathode is segmented in coarser strips parallel to the CSC
 2091 wires. They provide the transverse coordinate and bunch crossing timing. The five
 2092 panels are precisely positioned with respect to each other with the aid of locating pins.
 2093 The outer copper-clad laminates of each module form an electromagnetic shield for the
 2094 detector. A cutout view of one gap formed by two panels has been already presented in
 2095 Figure 3.10. Signals from the cathode strips are transferred via ribbon cable jumpers
 2096 to the electronic readout boards located on the chamber edges. The whole assembly is
 2097 rigid enough so that no in-plane alignment system is necessary.

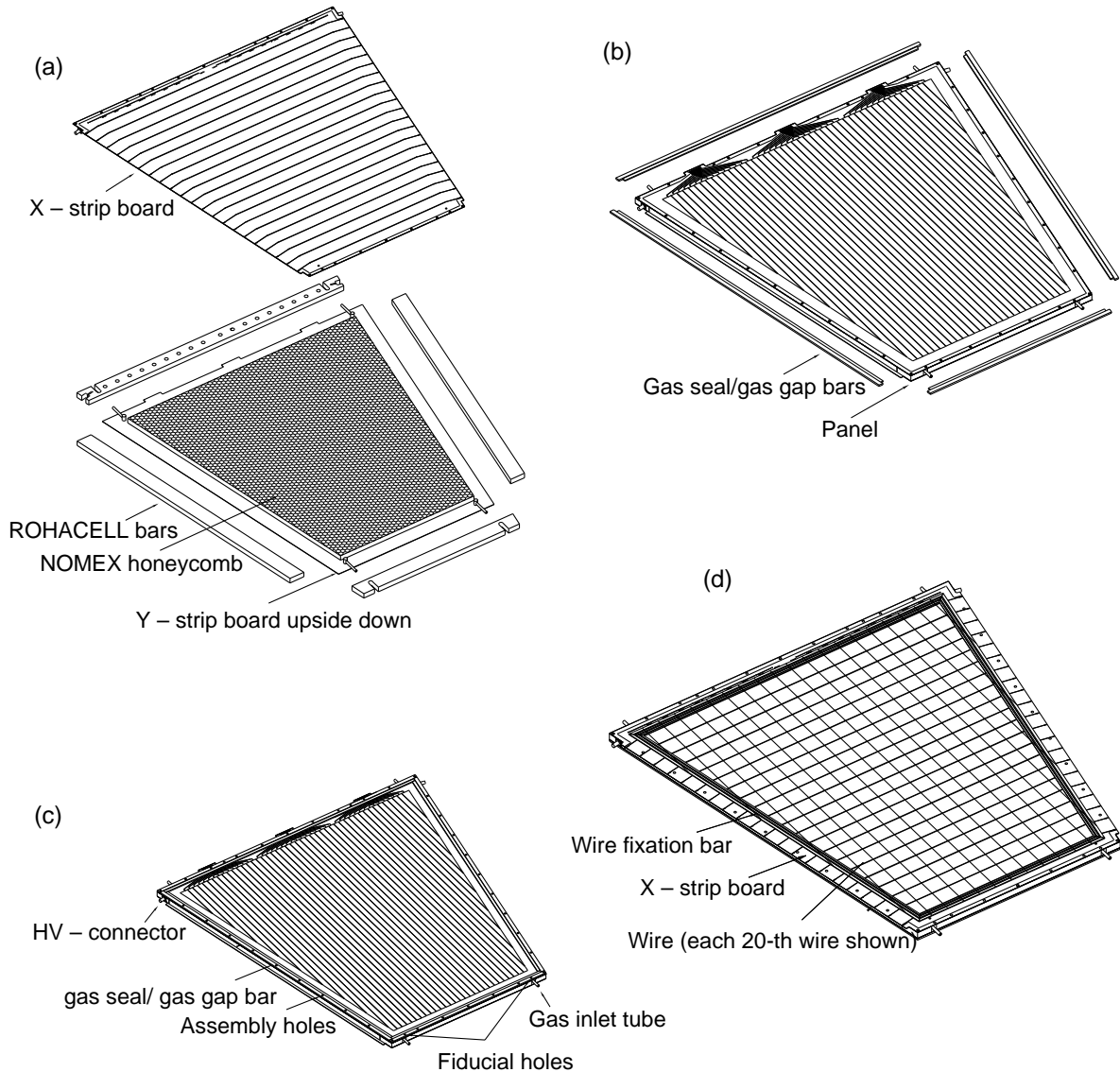
2098 4.7.2 Assembly Procedure

2099 Key elements in the construction of the cathode strip chambers are the lithographi-
 2100 cally segmented precision cathodes. These cathodes are produced in industry using
 2101 standard lithographic techniques. The design of the cathodes is done using printed
 2102 circuit layout tools and incorporates, in the perimeter of the boards, the necessary
 2103 circuitry for the signal routing and HV distribution and filtering. The design is then
 2104 electronically transmitted to an industrial firm for the photo-plotting of the artwork
 2105 and the etching of the boards. The rest of the assembly procedure is schematically
 2106 shown in Figure 4.4.

2107 4.7.3 Support Structure and Alignment of the CSC System

2108 The sixteen chambers in each EndCap are mounted on a rigid support structure,
 2109 as seen in Figure 4.1 in the form of a wheel, inclined in order to reduce the resolution
 2110 degradation due to inclined tracks [1]. The support structure is aligned, as a unit,
 2111 within the EndCap global alignment system and no individual chamber alignment is
 2112 needed.

Figure 4.4: The chamber assembly sequence [1].



2113 4.8 The Readout Complex

2114 The severe radiation levels where the CSC chambers operate imposes the minimum
 2115 of the electronics to be located on the detector [6]. The on-detector electronics amplifies
 2116 and shapes the cathode strip signals, and stores the analog pulse height information
 2117 during the first-level trigger latency. When a trigger is received, four consecutive time
 2118 samples are digitized and transmitted via fiber-optic links to the off-detector electronics.
 2119 Sampling and digitization are performed on-detector but are controlled by the off-
 2120 detector electronics.

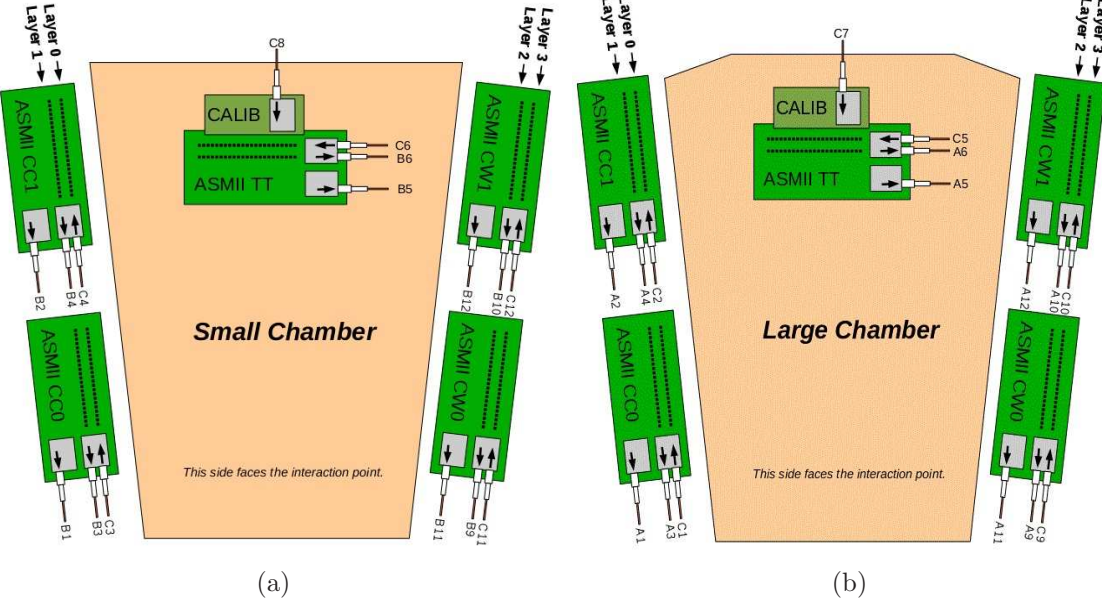
2121 The off-detector electronics operated during Run-I and replaced with new ones for
 2122 the Run-II, due to limitations of the former to operate beyond 70 kHz . The hardware of
 2123 the two systems is based on different technologies but the processing of the information
 2124 is similar. It contains the sparsification stage, during which hits below the threshold and
 2125 hits not associated with the current bunch crossing are suppressed. The rejection stage
 2126 identifies hits possibly belonging to tracks by removing isolated background hits. The
 2127 remaining data are formatted and sent to the ATLAS Trigger/DAQ System (TDAQ)
 2128 for further processing.

2129 4.8.1 The On-Detector Electronics

2130 The CSC on-detector electronics consists of two layers of amplifier-storage module
 2131 (ASM) boards [6]. Each strip is connected to a preamplifier and shaper circuit, imple-
 2132 mented as a radiation-tolerant custom ASIC, which forms a bipolar pulse with a 70 ns
 2133 peaking time to mitigate pile-up effects. The shaped pulses are sampled every 50 ns ,
 2134 and the analog pulse height information is stored in a custom radiation tolerant CMOS
 2135 switched capacitor array (SCA) for the duration of the first-level trigger latency, which
 2136 for the CSCs is estimated to reach 188 bunch crossings in the worst case scenario. The
 2137 SCA provides an effective pipeline depth of 288 bunch crossings. Following a trigger,
 2138 those cells of the SCAs specified by the ROD are time multiplexed and digitized using
 2139 12 – bit Analog Devices AD9042 ADCs. Custom ASICs multiplex the data from 16
 2140 ADCs to two G-Link serializers configured to operate with 16 – bit input words at
 2141 40 MHz single frame rate.

2142 Eight preamplifier/shaper ICs supporting a total of 96 channels reside on a printed
 2143 circuit board (ASM-I). Two ASM-I boards piggyback on one ASM-II which contains
 2144 the 16 SCAs, ADCs, multiplexors serving 192 channels total, and two fiber optic G-
 2145 Link transmitters. A total of five such ASM-I/ASM-II combinations are needed to read
 2146 out one chamber, four for the precision coordinate strips and one for the transverse
 2147 coordinate strips from all four layers. Four ASM-I/ASM-II configurations are attached
 2148 to the narrow edge of the chamber and share a common Faraday cage and cooling

Figure 4.5: CSC fiber connections for the small (Figure (a)) and large (Figure (b)) chambers [7].



2149 fixture. The transverse strip ASM-I/ASM-II package is attached to the broad side of
 2150 the chamber, together with circuitry for injecting a pulse onto the wires of each layer
 2151 for calibration purposes.

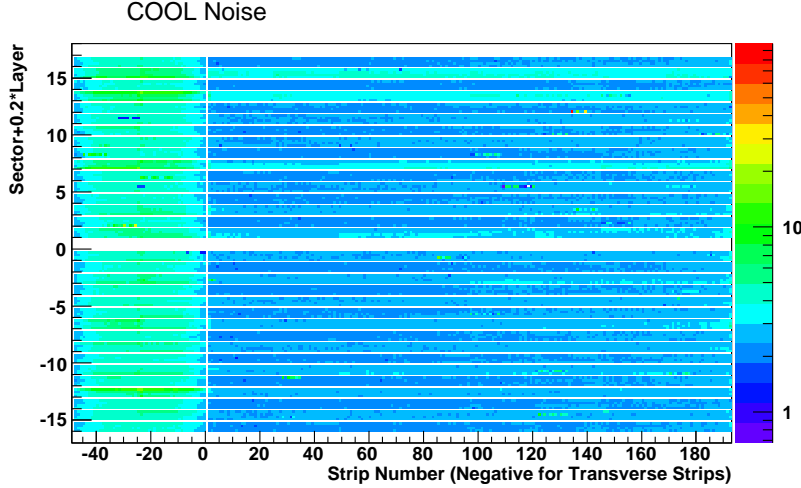
2152 Each of the on detector electronic package is connected to the off detector electronics
 2153 by two data fibers and one control fiber. The data fiber transmits the detector infor-
 2154 mation, whereas the control fiber is used for the protocol establishment between the on
 2155 and off electronics for the control of the latter. The connections for each chamber type
 2156 are presented in Figure 4.5. It has to be noted that each fiber bundle contains twelve
 2157 fibers, two of which are used as spares.

2158 4.8.1.1 Calibration

2159 The calibration of the on-detector electronics is done by a pulser [8], which practi-
 2160 cally provides a fast voltage step. Control is delivered by a fiber optic link from the
 2161 off-detector electronics and deserialized by a "G-Link" receiver. The deserialized data
 2162 directly feeds the pulse drivers, attenuator level select lines, and analog switches. The
 2163 pulse drivers are gated out and the analog switches ground the output when the G-Link
 2164 Rx receives fill frames or is unlocked to prevent spurious pulses. The comparison of
 2165 known input and the measured output is used as a calibration constant.

2166 The calibration procedure also includes daily pedestal runs. These runs are taken
 2167 during the operations period and the procedure is to record the electronics noise when

Figure 4.6: Pedestal noise pattern used for the Run-I operations. Side C sectors appear with negative numbers as well as the ϕ channels [9].



2168 the chamber HV is off (no gas amplification). When a pedestal is taken, a histogram is
 2169 filled with ADC values and the pedestal is defined as the mean of the Gaussian distribu-
 2170 tion. The thresholds for the data acquisition are set to a few σ from the pedestal value
 2171 of each channel and the pedestal values itself are used to define the charge measurement
 2172 uncertainty, as is discussed later.

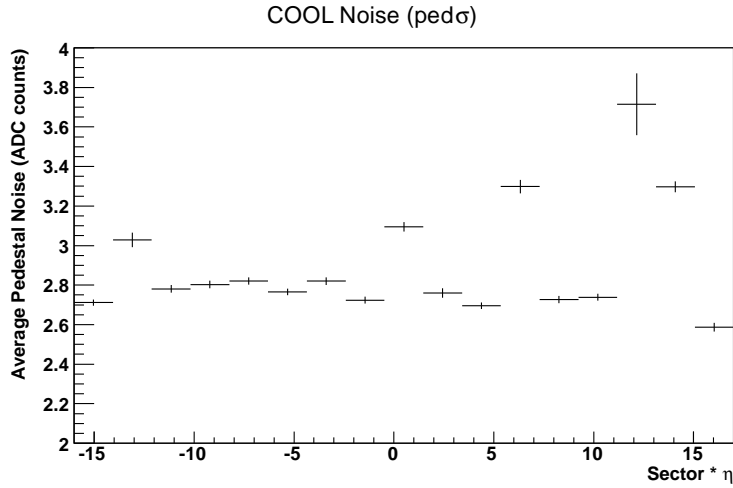
2173 A typical pedestal pattern, the one used for the Run-I operations, is presented in
 2174 Figure 4.6. Side C sectors appear with negative numbers as well as the ϕ channels.
 2175 All the pedestal runs taken, were analyzed and no significant variation found in the
 2176 three years of operations, which proves the pedestal stability. The deviations from the
 2177 database pattern (Figure 4.7) recorded are within the uncertainties and consequently
 2178 the database pattern remain unchanged.

2179 Apart from the pedestal, other calibration constants are monitored and these are
 2180 the peaking time, the time of the maximum of each channel relative to the first sample
 2181 which might show variation between groups of 12 channels up to 10 ns, dead and hot
 2182 channels are kept for the accurate offline reconstruction, gain constants, defined as
 2183 the amplifier's sensitivity in ADC counts per fC for each channel, the linearity and
 2184 saturation points, which describe deviations from the ideal proportionality between the
 2185 pulser amplitude and the measured amplitude.

2186 Especially for the problematic channels, detailed studies conducted periodically to
 2187 reveal possible degradation, based on occupancy histograms of hits on muon tracks
 2188 (excluding the dead layers¹). Figure 4.8 shows the map of the dead channels in the

¹As will be discussed later, the HV failures in layers was the main source of channels dis-
 functionality.

Figure 4.7: The average pedestal noise for each sector shows small deviation with respect to the database pattern used for the operations [9]. The differences are within the uncertainties, are considered marginal and prove the pedestal stability.



2189 beginning of the 2012 data taking, where dead channels appear with no entries and
2190 hot channels have relatively high entries. Overall, the problematic precision channels
2191 corresponded to 3.6% and the transverse ones to 4.3%. By the end of 2012 the only
2192 degradation was coming from the two dead layers of one sector, which resulted to 5.0% η
2193 channels and 5.9% ϕ dead channels.

2194 In the long shutdown of 2013 – 2015 the dead layers were repaired and the expected
2195 numbers of problematic channels is predicted to be 1.1% and 2.0% for the η and ϕ
2196 respectively, though new studies based on actual data need to be conducted at the
2197 beginning of the Run-II.

2198 4.8.2 The Off-Detector Electronics

2199 Signals associated with a particle trajectory must be correlated with adjacent strips
2200 and time [6]. The consecutive time samples retrieved from each strip provide pulse
2201 shape information. An example is shown in Figure 4.9 for four samples. The effective
2202 trigger latency is adjusted so that the second and third sample are closest to the peak
2203 of the positive lobe. Receipt of a first-level trigger automatically leads to readout of
2204 the four or two samples associated with the event.

2205 Signal below a predefined threshold, either the pedestal value of the channel or
2206 a user-defined threshold², are rejected and calibration constants are applied to the

²The higher than the pedestal thresholds could be imposed due to stuck bit or dead channels or

Figure 4.8: Dead and hot channels showing as zero entries bins and relatively high entries bins respectively. The study based on the exclusion of dead layers and the histograms with the occupancy of hits on muon tracks separately for the η (Figure (a)) and ϕ (Figure (b)) channels in the beginning of 2012. At the end of the Run-I operations the only degradation was due to additional dead layers.

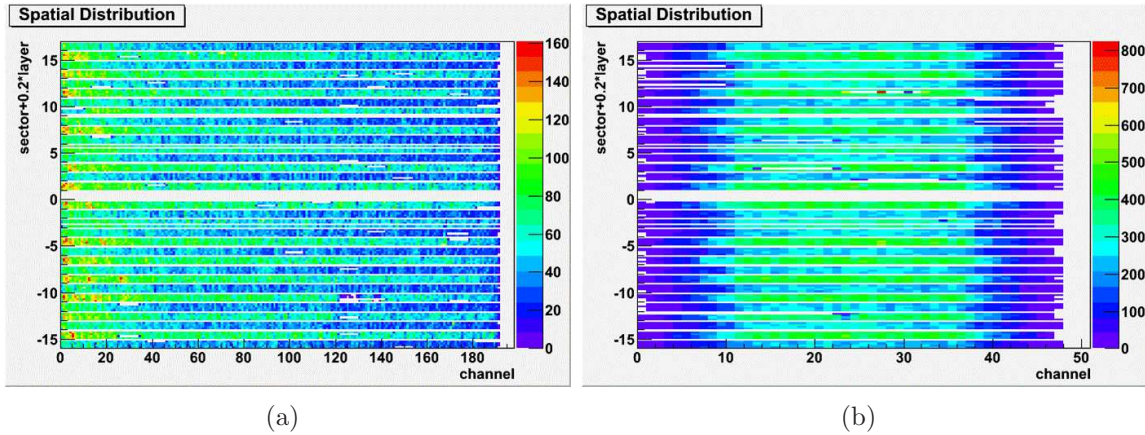


Figure 4.9: CSC pulse shape, with sampling times (of arbitrary latency) indicated by dashed lines [6].

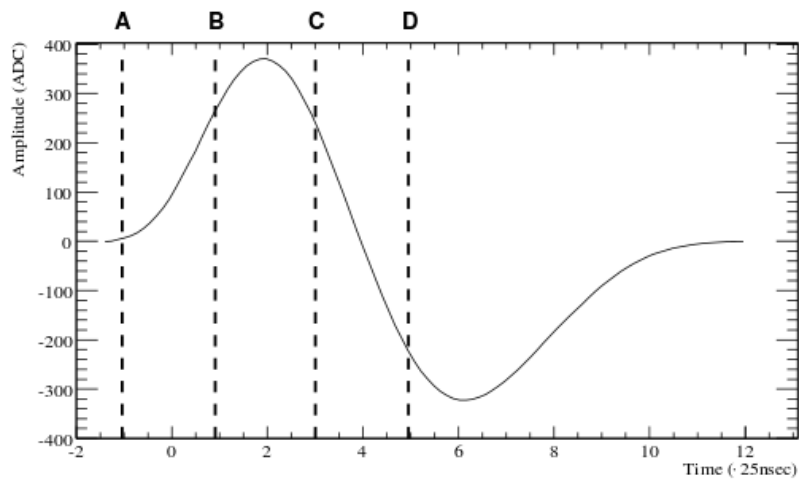
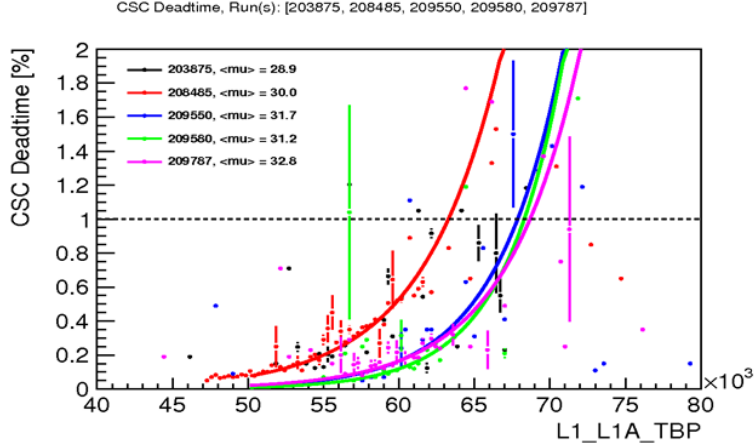


Figure 4.10: CSC dead-time, during the Run-I, as a function of the trigger rate during physics runs [11]. Special handling methods invented to allow the operation within the allowed by the experiment 2% dead-time. The curves corresponds to different data taking conditions that is discussed later.



rest. The next step is to identify the clusters by finding groups of contiguous hit channels [10], taking into account that stuck bit channels can create spurious clusters and dead channels can split a cluster in two. The cluster identification is performed via a parabola interpolation and the peaking time is also determined. Overlapping clusters are not a concern during the data taking and the offline reconstruction deals with them.

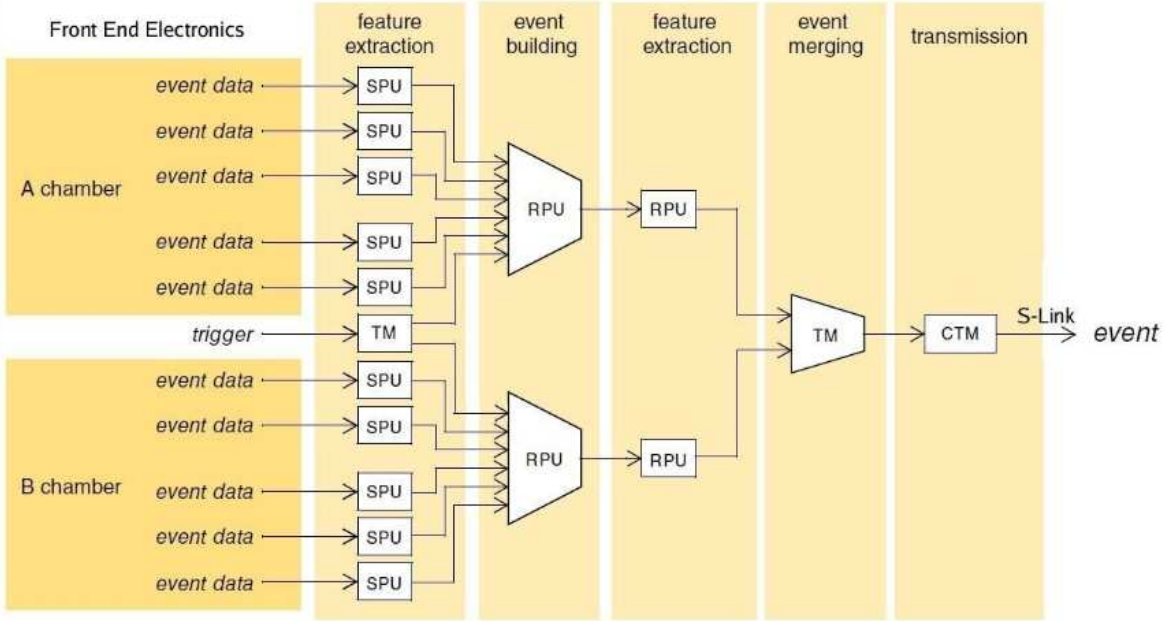
Except from the nominal data taking acquisition the off-detector electronics control the pulser used for the on-detector electronics calibration, reported in Section 4.8.1.

Between the Run-I and the Run-II the off-detector electronics had to be replaced due to limitations of the initial design. As Figure 4.10 shows, the system could not sustain high trigger rates and the corresponding occupancy [11]. Even from the Run-I period special busy handling methods had to be invented to anticipate the trigger rates and allow running below the maximum allowed dead-time of 2% by the ATLAS experiment. This methods is analyzed in detail in this chapter, focused on the studies performed to evaluate the physics impact on each one of them and the actual impact, after the application, is also be reported.

The description of the off-detector readout technologies are briefly discussed in the next paragraphs. Both of them, as well as the rest of the ATLAS detectors, are configured through the “Object Kernel Support (OKS)” database [12].

data suppression strategy (to be discussed later).

Figure 4.11: CSC readout information flow schema [11].



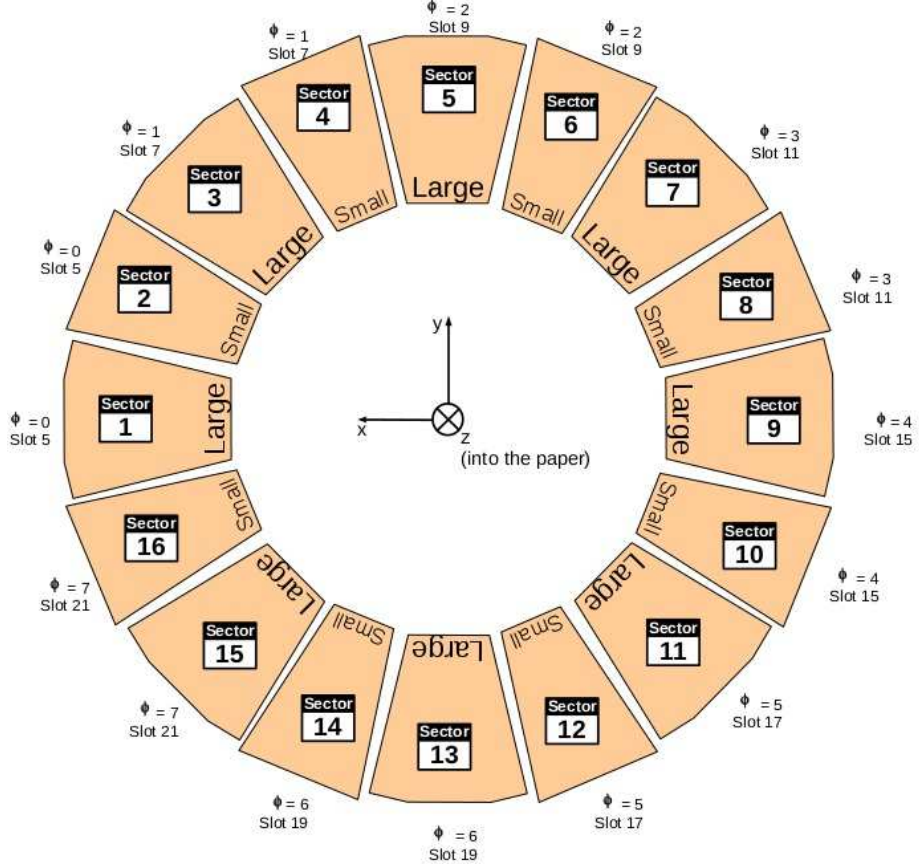
4.8.2.1 The Run-I off-Detector Electronics

The Run-I off-detector electronics consists of 16 readout drivers (RODs), each coupled with a transition module (CTM) [6]. Each ROD/CTM pair handles the incoming data of two chambers, i.e. from 10 ASM-II boards as shown in Figure 4.11. It also controls the ASM-II, in particular the readout of the SCA when a trigger has been received.

The CTM provides three major functions: the logic to monitor, control and receive data from the FEE of its corresponding chambers; the logic and buffering to respond appropriately to trigger requests; and a single fiber-optic transmitter, referred to as the Read-Out Link (ROL), used to send event data to the ATLAS Trigger and Data Acquisition (TDAQ) system [11]. The responsibilities of each ROD are twofold: setting up, controlling and monitoring the on-detector electronics and the CTM; and extracting data from the chambers and sending the resulting event to the ROL.

The CSC ROD is a 9U VME board encapsulating thirteen 300 MHz digital signal processors (DSPs) and 40 Xilinx Spartan II field programmable gate arrays (FPGAs). Ten such units are used as Sparsification Processing Units (SPU) and two as Rejection Processing Units (RPU). Each ROD has two identical halves, known as side A and side B, one for each serving chamber. The naming schema for identifying the chambers, starts by defining the wheel, "A" or "C" side, followed by the chamber number, e.g. A12. The sectors are numbered on the wheel so that the closest to the ground chamber

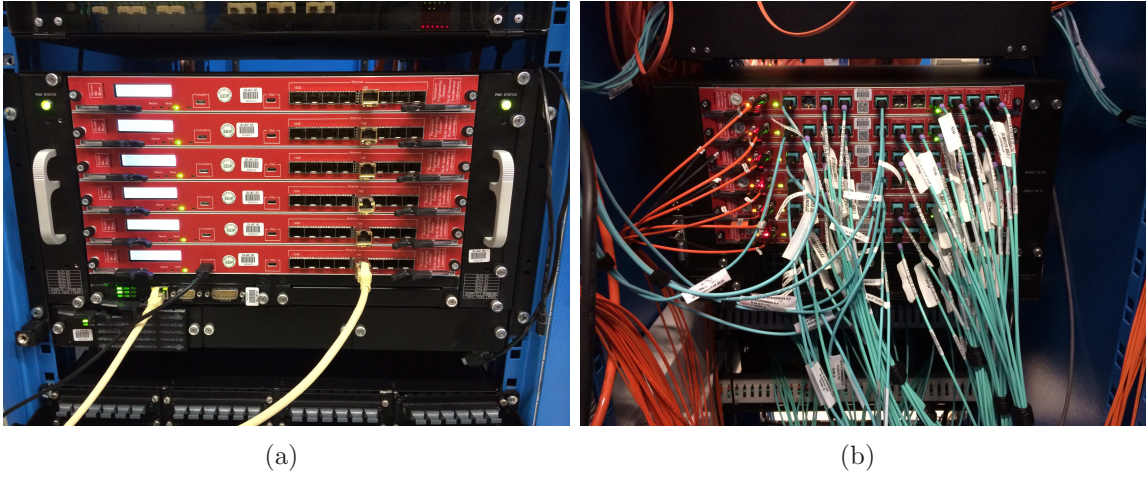
Figure 4.12: Number assignment of the CSC chambers for the EndCap A as viewed from the interaction point or EndCap C as seen from outside [7].



2245 is the number "13" and the sequence, as seen from the interaction point, is clockwise
 2246 and counterclockwise for the side "A" and "C" respectively. The small chambers have
 2247 even numbers whereas the large chambers have odd. The convention is to measure the
 2248 layers of each chamber starting from the IP and pointing to the outside, usually starting
 2249 from "0". The chamber number assignments are schematically presented in Figure 4.12
 2250 along with the slot numbers that the corresponding board is housed.

2251 Each crate houses also a Timing Interface Module (TIM), a Local Trigger Processor
 2252 (LTP) and a ROD crate controller (RCC). The RCC functions as the crates VME bus
 2253 master and executes ATLAS specified run control software, used to orchestrate and
 2254 monitor the behavior of the RODs operating as one component of the ATLAS TDAQ
 2255 system.

Figure 4.13: The Run-II readout system is based on boards hosted on an ATCA crate. The front view is shown in Figure (a) and the back view in Figure (b) where the RTM are hosted and the fibers are connected.



2256 4.8.2.2 The Run-II Off-Detector Electronics

2257 The new off-detector electronics are based on the Reconfigurable Cluster Element
 2258 (RCE), a $6 - slot$ ATCA (Advanced TeleCommunication Architecture) shelf which hosts
 2259 the boards and is equivalent to the VME crate and a LINUX server to adapt and host
 2260 the TDAQ software [13].

2261 The shelf hosts the front boards and the corresponding Rear Transition Modules
 2262 (RTM), shown in Figure 4.13. A key component of the ATCA is the shelf manager
 2263 which provides Ethernet access and controls, monitors and maintains the safety of the
 2264 infrastructure (i.e. temperature, fan speed, power).

2265 The front board, also called Cluster-On-Board (COB), is the carrier of the RCE
 2266 and hosts the firmware and software. The connection of the various components of
 2267 the COB is succeeded with high speed communication paths. Each COB has a Real
 2268 Transition Module (RTM) which provides a useful extension of the front board for
 2269 the input/output (I/O) interface (e.g S-Link, G-Link) and increases the useful foot-
 2270 prints. Every board contains one Data Transport Module (DTM) bay and four Data
 2271 Processing Modules (DPM) bays. The DTM holds a mezzanine board which contains
 2272 one RCE and interacts with the self manager via interconnections. The DPM acquires
 2273 and processes data originating from the RTM with use of a number of RCEs. The
 2274 RCE itself, the computational element, is a bundled set of hardware, firmware and soft-
 2275 ware (FPGA+processor+DSP, using the System-On-Chip technology, both running on
 2276 ZYNQ). It contains soft (programmable) and hard (resources) silicon (hence the name
 2277 "Cluster Element"). The fact that it is highly parallel and inhomogeneous, because
 2278 data are carried over a variety of media employing various inhomogeneous protocols,

2279 makes its performance significant.

2280 The system is composed of six COBs, four of them acting as Front-End and two
2281 as Back-End (Formatters). The corresponding RTMs serve the CSC chambers and the
2282 RoL (16 channels) respectively. With the new readout, 8 chambers are read by one
2283 board whereas the new system needs 6 boards to read the same number of chambers.

2284 The new system is a plug compatible replacement of the Run-I system and this
2285 means that no modification is needed either on the on-detector electronics. The re-
2286 quirements that is satisfies are the same as for the old system: interacts with the
2287 on-detector electronics to lock the fibers, control the pulser, set the number of samples,
2288 the sampling frequency and the latency, receives and processes trigger and timing sig-
2289 nals with the ability to re-synchronize, performs the feature extraction, monitors and
2290 asserts busy, sends the data to the ROS, handles the TDAQ control and monitoring
2291 (including functionalities that the old system did not support, e.g. stopless recovery
2292 and TTC restart) and the infrastructure is remotely controlled.

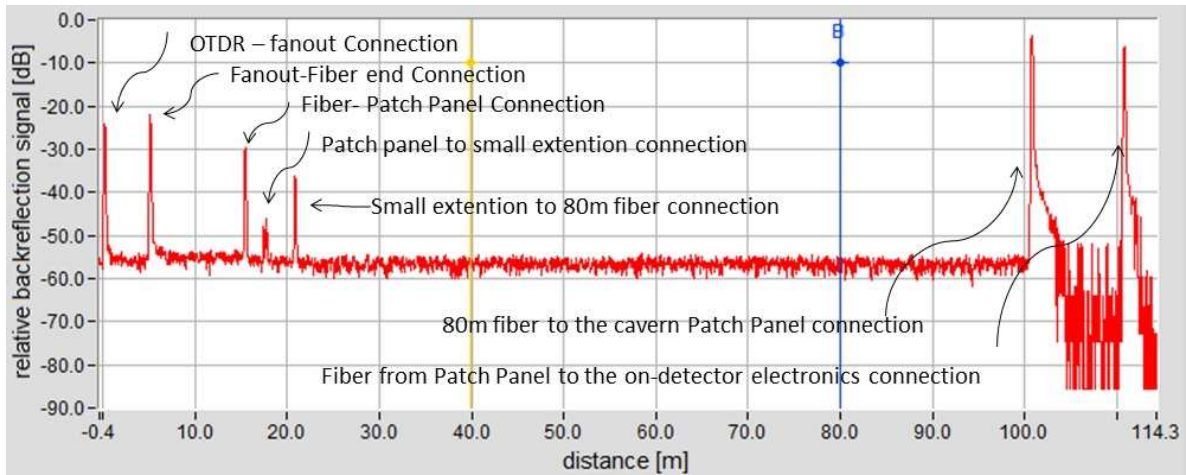
2293 To make the use of the old readout possible while the new system was under devel-
2294 opment, a patch panel installed to allow reverting between the two system in a simple
2295 way. After the installation, even though the additional fibers added only a few meters
2296 to overall fiber path, the system was re-evaluated to measure the attenuation losses
2297 and the length of the fibers by two independent methods. One of them used an OTDR
2298 machine (Optical Time Domain Reflectometer), connected to one end of the fibers (be-
2299 fore the off-detector electronics) and extracted the scattered or reflected light after the
2300 injection of an optical pulse. A typical distribution of the OTDR output, for the CSC
2301 fibers, is presented in Figure 4.14. The peaks are connections and from the left to
2302 right these are: fan-out connection with the CSC fibers, fibers up to the patch panel,
2303 two connections of the 30 cm fibers on the patch panel, patch panel connection with
2304 the small fiber extension, extension connection with the 80 m long fiber that goes to
2305 the cavern, 80 m fiber connection with the cavern patch panel, fiber connection from
2306 the cavern patch panel to the on-detector electronics. The comparison of the signal
2307 intensity at the beginning and the end of the fibers path is the signal loss. The second
2308 method used, is more direct compared to the previous one but applicable only to the
2309 detector fibers and not the control fibers. It was performed by plugging a light receiver
2310 before the on-detector electronics and measuring the light that the ASMs send to the
2311 off-detector electronics when operated at nominal low voltage (LV). The method could
2312 not be used to measure the control fiber losses because in this case the optical signal is
2313 send from the off-detector electronics to the on-detector electronics and not vice versa.
2314 The light measurements for all sectors are summarized in Table 4.2. Both methods
2315 shown marginal losses, except from a few cases which were resolved by replacing the
2316 fibers.

Table 4.2: Measurements of the data transmission light (in dBm) at the end of the fiber paths before the on detector electronics. The fibers with numbers “7” and “8” are not included in the table because they are not used.

Side A											
Sector	Fiber-1	Fiber-2	Fiber-3	Fiber-4	Fiber-5	Fiber-6	Fiber-9	Fiber-10	Fiber-11	Fiber-12	
A01	-8.96	-7.97	-8.85	-10.1	-8.22	-7.9	-9.45	-10.31	-9.14	-8.56	
A02	-7.98	-8.87	-8.22	-8.02	-7.71	-10.41	-6.91	-9.46	-6.71	-8.35	
A03	-8.35	-18.22	-7.94	-7.86	-8.06	-7.44	-7.65	-9.97	-7.5	-8.72	
A04	-11.6	-7.18	-8.12	-8.54	-7.63	-8.23	-9.11	-9.27	-7.6	-7.65	
A05	-8.64	-7.86	-6.8	-10.41	-7.92	-8.81	-8.26	-9.68	-7.65	-8.54	
A06	-9.58	-8.64	-7.2	-8.79	-8.85	-7.53	-7.19	-7.88	-9.18	-8.17	
A07	-8.85	-10.44	-7.91	-8.49	-7.9	-8.08	-8.21	-8.28	-8.36	-10.13	
A08	-8.27	-8.39	-7.88	-7.37	-9.04	-9.08	-8.6	-8.24	-13.94	-8.51	
A09	-7.62	-7.90	-7.07	-8.30	-8.43	-8.35	-7.66	-8.41	-7.27	-8.79	
A010	-9.03	-7.02	-7.78	-8.00	-7.82	-9.04	-6.60	-7.41	-6.96	-7.71	
A011	-7.40	-8.24	-7.73	-8.91	-8.95	-10.72	-7.73	-7.49	-7.05	-7.48	
A012	-9.02	-9.49	-8.43	-8.10	-8.61	-8.56	-7.09	-9.10	-8.01	-8.02	
A013	-7.68	-8.74	-8.22	-9.03	-9.88	-8.30	-8.09	-8.35	-6.86	-7.53	
A014	-8.80	-9.03	-10.06	-9.09	-9.13	-8.23	-7.61	-9.77	-10.25	-9.44	
A015	-8.12	-8.54	-8.69	-10.13	-13.31	-10.06	-8.51	-9.88	-14.89	-8.82	
A016	-9.15	-8.06	-7.20	-9.21	-8.02	-7.96	-7.46	-8.29	-7.40	-8.28	

Side C											
Sector	Fiber-1	Fiber-2	Fiber-3	Fiber-4	Fiber-5	Fiber-6	Fiber-9	Fiber-10	Fiber-11	Fiber-12	
C01	-7.86	-8.64	-6.63	-7.86	-8.69	-7.59	-8.53	-9.5	-7.94	-8.47	
C02	-7.39	-8.32	-7.03	-7.98	-9.44	-6.83	-7.26	-7.72	-7.53	-8.60	
C03	-10.09	-7.33	-6.93	-8.32	-8.81	-7.37	-8.34	-8.65	-8.15	-9.19	
C04	-7.34	-8.99	-7.53	-9.12	-7.92	-8.23	-8.06	-7.65	-6.87	-8.58	
C05	-7.59	-7.63	-7.36	-7.02	-8.78	-8.11	-7.53	-11.03	-8.35	-7.90	
C06	-9.33	-7.07	-6.97	-11.79	-7.29	-7.59	-7.63	-8.06	-8.43	-7.83	
C07	-9.14	-7.46	-7.35	-7.95	-7.85	-7.34	-7.62	-8.13	-6.83	-7.29	
C08	-7.10	-8.56	-16.23	-9.45	-8.30	-7.45	-7.44	-7.81	-7.20	-8.51	
C09	-9.09	-7.90	-7.03	-10.08	-9.22	-7.65	-7.29	-12.06	-7.59	-7.41	
C10	-11.38	-9.05	-8.38	-9.05	-8.85	-10.24	-12.81	-8.99	-8.53	-9.33	
C11	-9.17	-9.51	-9.15	-9.27	-9.00	-9.52	-8.06	-11.64	-10.51	-9.85	
C12	-9.62	-10.33	-8.54	-9.70	-10.15	-12.3	-9.61	-9.99	-10.33	-10.24	
C13	-9.01	-9.02	-9.02	-9.35	-12.52	-9.92	-9.03	-16.11	-9.34	-11.18	
C14	-9.21	-8.04	-8.59	-8.09	-7.75	-6.75	-7.88	-9.45	-12.01	-8.38	
C15	-7.56	-7.31	-7.84	-7.53	-8.87	-7.24	-7.88	-9.25	-8.12	-8.06	
C16	-6.61	-7.28	-6.89	-7.36	-7.50	-7.65	-8.24	-7.56	-9.01	-8.42	

Figure 4.14: An example output of the OTDR (Optical Time Domain Reflectometer) measurements performed on the CSC fibers, to measure pulse losses and attenuation. The peaks are connections and from the left to right these are: fan-out connection with CSC fibers, fibers up to the patch panel, two connections with the 30 cm fibers on the patch panel, patch panel connection with the small fiber extension, extension connection with the 80 m long fiber that goes to the cavern, 80 m fiber connection with the cavern patch panel, fiber connection from the cavern patch panel to the on-detector electronics.



²³¹⁷ 4.8.2.3 The Trigger and Timing (TTC) Unit

²³¹⁸ The trigger and timing crate (TTC), as Figure 4.15 shows, is the same for the Run-I
²³¹⁹ and Run-II electronics and contains the modules for the control of the timing and trigger
²³²⁰ signals. The modules in the crate consist of the SBC (Single Computer Board), the LTPi
²³²¹ (Local Trigger Processor interface), two LTPs (Local Trigger Processors), two TTCvis
²³²² and one TTCex module. The local trigger processor contains a pattern generator, that
²³²³ can generate all TTC trigger signals. This generator can run in continuous mode or
²³²⁴ in single-shot operation. The TTCvi module passes on the signals from the LTP and
²³²⁵ adds the Bunch Counter Reset (BCR) signals.

²³²⁶ The busy modules propagate the busy signal from the readout electronics to ATLAS.
²³²⁷ Once a detector component raise busy the so called “Simple Deadtime” increases and
²³²⁸ trigger the raise of the so called “Complex Deadtime”. The latter causes a global
²³²⁹ deadtime rise to avoid mix of the various readout information between different events.
²³³⁰ The maximum allowed busy by the ATLAS experiment is 2%. If it is exceeded then
²³³¹ an automatic procedure removes the part that creates the busy (the action is called
²³³² “Stopless Removal”). The electronics that will be used for the Run-II allow removal
²³³³ of the CSC detector components with better granularity compared to the old system,

Figure 4.15: The trigger and timing unit (TTC), which is the same for the Run-I and the Run-II. The modules are responsible for the synchronization of the system with the rest ATLAS components and the trigger handling.



2334 where the entire detector side had to be removed.

2335 The new readout electronics also allow the so called “TTC Restart”, which is not
 2336 possible with the old system. This allows the re-synchronization of a detector part with
 2337 ATLAS in the case where it is lost.

2338 To avoid deadtime originating from the readout links (RoLs), the Run-I 16 readout
 2339 links were used for the data transmission from the off detector electronics to the ATLAS
 2340 Readout System (ROS). For Run-II, the RoLs are doubled and replaced by the so called
 2341 “3rd generation” ones. This means that each RoL serves one chamber instead of two.
 2342 The two ROSes, each one reads out a detector side, were also replaced by modern
 2343 machines with bigger capabilities. These changes were motivated by the amount of the
 2344 predicted data volume that is expected to be transferred during the Run-II.

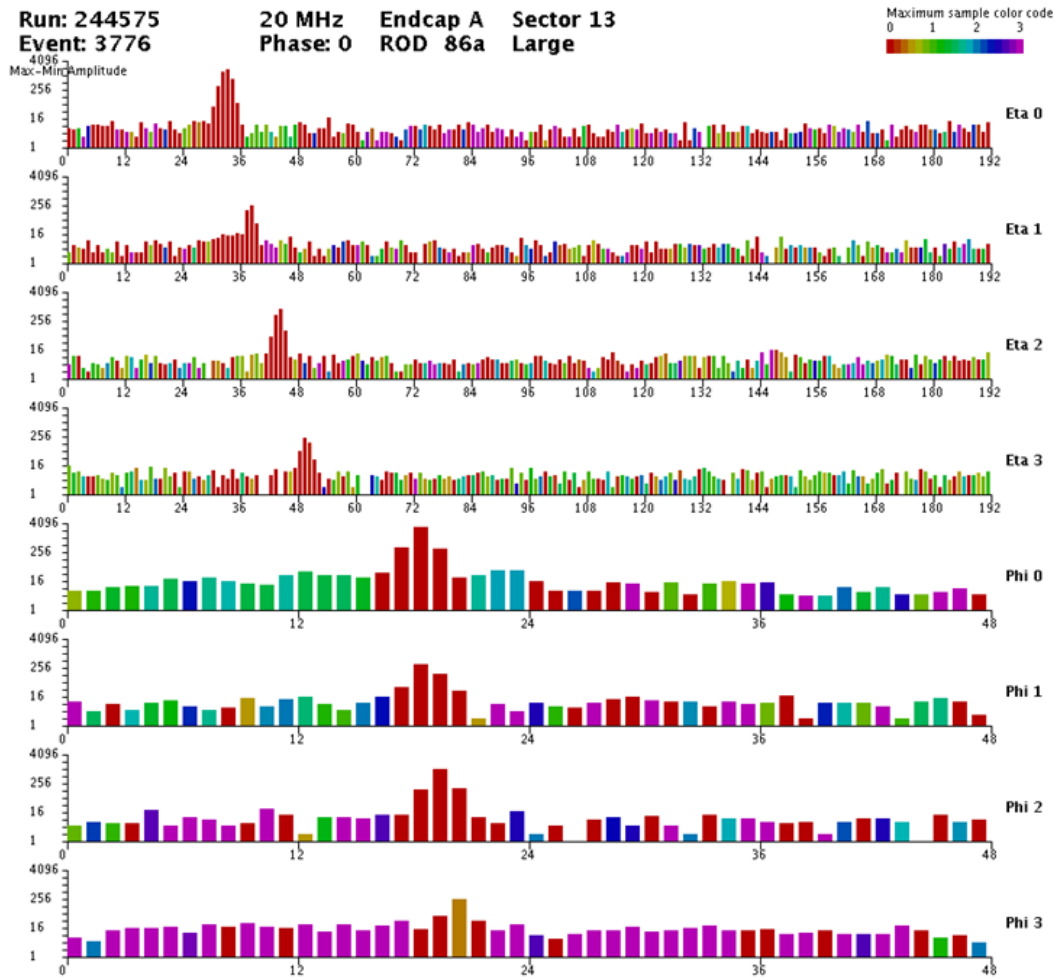
2345 The system is in place for the Run-II and an event display showing a cosmic track on
 2346 top of the pedestal noise is shown in Figure 4.16. The pedestal had not been subtracted
 2347 from this run for testing reasons.

2348 4.9 Offline Reconstruction

2349 4.9.1 Strip Charge Reconstruction

2350 The offline reconstruction starts by defining the charge of each strip. This is done by
 2351 performing a parabolic interpolation between the samples, in the case of four samples,
 2352 and calculating the peaking time as the time of the largest sample corrected by the

Figure 4.16: Cosmic track passing through the CSC recorded with the new readout complex. The pedestal had not been subtracted from this run for testing reasons.

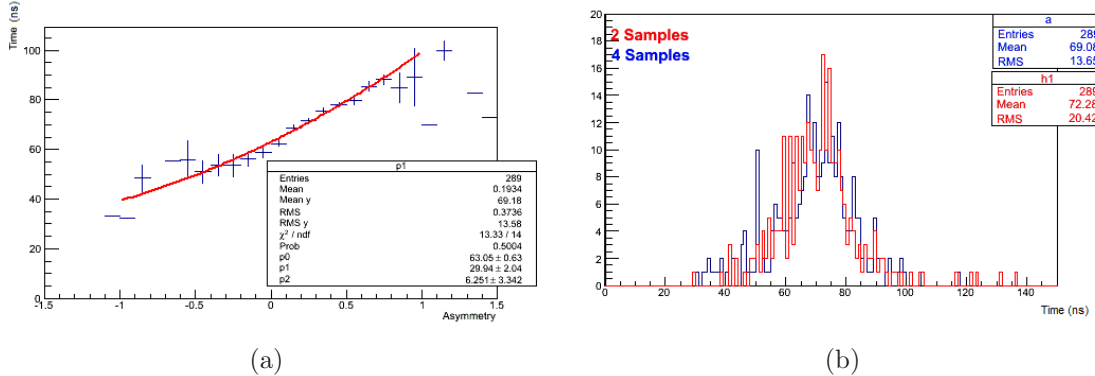


2353 "time offset" estimated from the interpolation. In case of two samples data taking,
 2354 the parabolic interpolation is not possible. In this case, the charge is the result of a
 2355 linear interpolation and the time information can be retrieved by making use of the
 2356 "asymmetry", defined as:

$$\text{Asymmetry} = \frac{\text{Time}_{1\text{st Sample}} - \text{Time}_{2\text{nd Sample}}}{\text{Time}_{1\text{st Sample}} + \text{Time}_{2\text{nd Sample}}}. \quad (4.6)$$

2357 From a 4 – *samples* recorded run, the time as a function of the asymmetry of the 2nd
 2358 and the 3rd samples (middle samples, i.e. in Figure 4.9 the "B" and "C" samples) found
 2359 to follow a 2nd order polynomial, as shown in Figure 4.17. The time reconstruction using
 2360 this formula provides a very close result to time reconstruction using the 4 – *samples*
 2361 information, also shown in Figure 4.17. The time information is very important for
 2362 beam halo and cavern background studies.

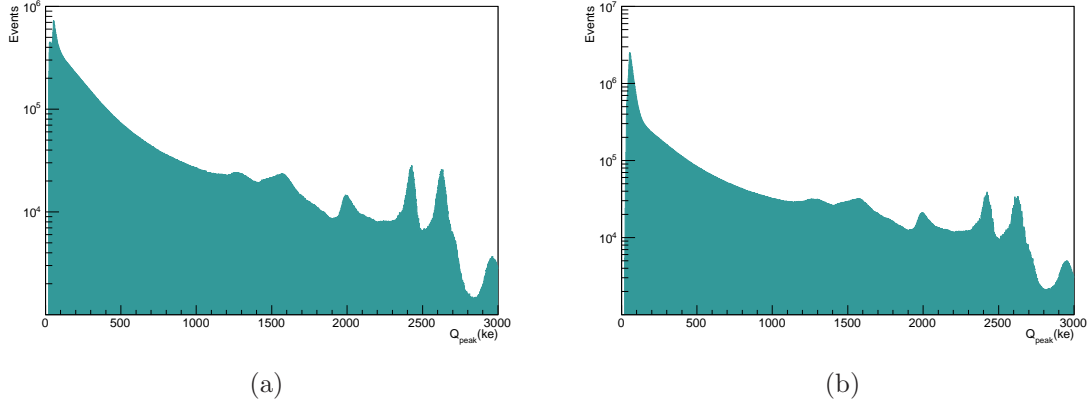
Figure 4.17: Study for the time reconstruction of data recorded with 2 – *samples*, based on a 4 – *samples* recorded run using the 2nd and the 3rd sample (Figure 4.9). Figure (a) shows the time vs the asymmetry, defined as in Equation 4.6. The distribution is fitted with a 2nd order polynomial and the obtained formula used to reconstruct the time. Figure (b) shows the comparison of the time as reconstructed using the asymmetry, denoted as "2 Samples", and the nominal "4 Samples" reconstruction.



2363 The hit is kept only if the charge exceeds the noise level and the channel does not
 2364 belong to the known problematic channels, e.g. dead channels. The threshold of the
 2365 offline reconstruction is set to (*pedestal* + 2(*f001* – *pedestal*)), even though in some
 2366 data taking periods the online charge threshold exceeded the offline threshold as it is
 2367 discussed later.

2368 At this reconstruction levels, the charges of the η and ϕ strips are presented in
 2369 Figure 4.18 for 4 – *samples* data. 2 – *samples* data are extensively studied in a following
 2370 section (4.11.1).

Figure 4.18: The charge distributions of each strip that exceeds the thresholds separately for η (a) and ϕ (b) hits in logarithmic scale. This charge deposition, formed from 4 – *samples* data, includes background hits and muon tracks. The tails of the distributions are formed by the saturation peaks.



4.9.2 Cluster Formation

The next step is the clustering, during which hits of neighboring channels are combined to reconstruct the charge deposition left by particles crossing the detector layers. The process is different for the precision (η) and the transverse (ϕ) layers due to the different pitches. The size of the pitch defines how extensive the charge deposition of a charged particle is, hence it imposes different approaches for the clusters identification.

4.9.2.1 The η Clustering

The η strips clustering algorithm was modified during the Run-I (specifically, in the end of the 2011 data taking) in order to provide more accurate position reconstruction based on a calibration directly obtained from real data (the previous calibration had been obtained from the Monte Carlo (MC)).

The process starts by identifying the highest channel charge among the lowest neighboring and forming the charge ratios:

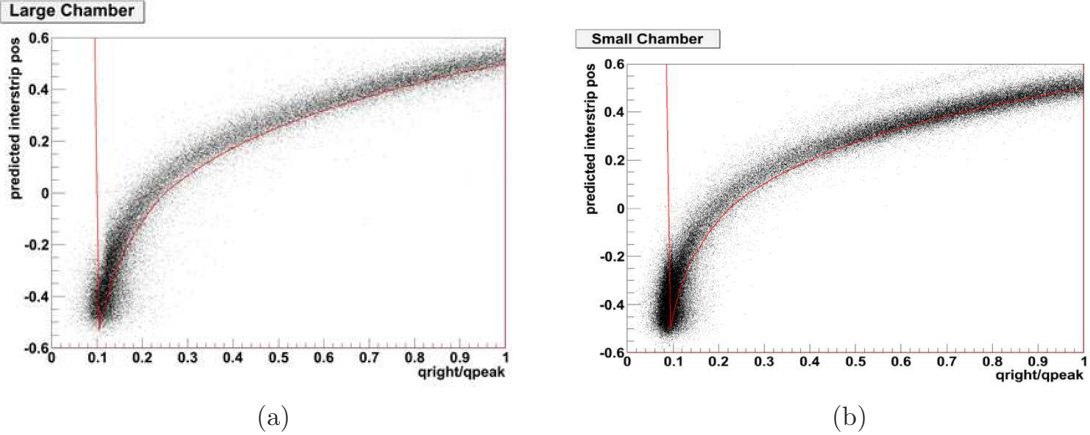
$$Q_{RAT1} = Q_{left}/Q_{peak} \quad (4.7)$$

2384

$$Q_{RAT2} = Q_{right}/Q_{peak} \quad (4.8)$$

2385 where Q_{left} and Q_{right} are the left and the right channels respectively to the one with
2386 the highest charge (Q_{peak}). The initial Run-I reconstruction applied a correction to this

Figure 4.19: Interstrip position as a function of the charge ratio, separately for large (a) and small (b) chambers due to different pitches. The distributions, which are made from data, are the inputs of the "S-Curve" calibration. The red line indicates the old calibration.



2387 ratios based on the simulation, whereas later a more sophisticated method invented.
 2388 The interstrip position³, defined as:

$$\text{Interstrip Position } x = \frac{\text{Position (mm)}}{\text{Pitch}} + 96 - \text{ChannelNumber} \quad (4.9)$$

2389 plotted as a function of the charge ratios, is shown in Figure 4.19, separately for the
 2390 large and small chambers due to the different pitches. The distributions are fitted with
 2391 a hyperbolic tangent and a correction is applied based on the inverse of the function:

$$x = \frac{\operatorname{atanh} \left(\frac{Q_{RAT} - a}{b} \right)}{c} + x_0 \quad (4.10)$$

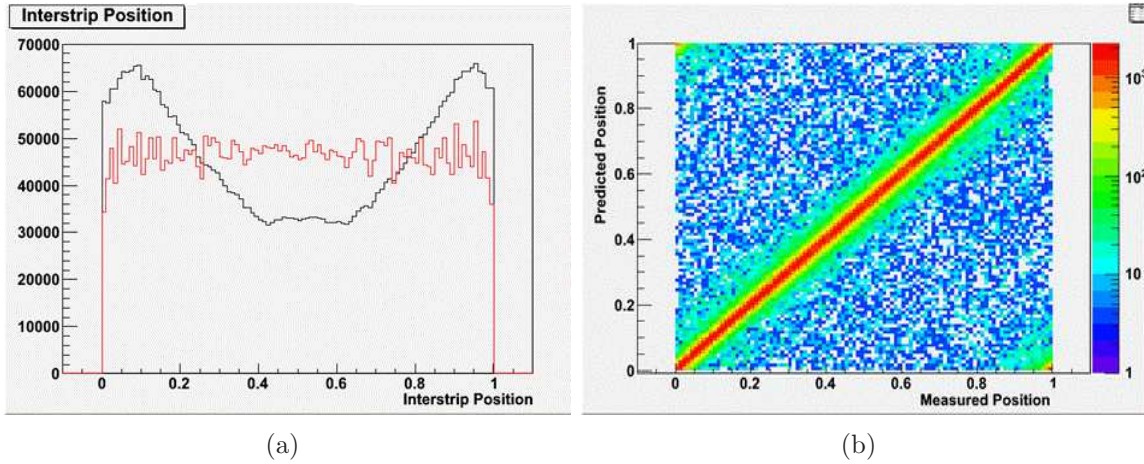
2392 where a , b , c , x_0 are parameters estimated from the fit. The method is called the
 2393 "S-Curve" calibration and the performance results are shown later on this section.

2394 The position corresponds to the weighted average between the charge ratios and
 2395 the uncertainty is estimated from the error propagation in this formula. The interstrip
 2396 positions from the improved and original calibrations are presented in Figure 4.20. For
 2397 a sufficient number of data, the position within the strip is flat, as expected, for the
 2398 new calibration.

2399 The inconsistency, i.e. large asymmetry, between the two charge ratios (Equations
 2400 4.7 and 4.8), along with the information of the width (in strips) of the clusters, define the
 2401 quality of the hit. Based on this, each cluster is categorized to be either a clean cluster

³There are 192 channels, and the number 96 corresponds to half of the channels number.

Figure 4.20: Interstrip position (Figure (a)) for the improved (red) and old (black) calibration. As expected, for the new calibration the distribution is flat for a large number of measurements. Additional check performed by taking advantage of the other layers information and performing a line fit to estimate the position in the given layer. The result shows good agreement between the measured and the predicted position within the strip (Figure (b)).



2402 precisely fitted (unspoiled) or a spoiled hit. The spoiled category includes clusters that
 2403 are on the edge of the plane, have multiple peaks, are too narrow (less than three
 2404 strips), too wide, skewed, show inconsistency between the charge ratios, the parabolic
 2405 interpolation failed in the peak charge or the left and/or the right strips are saturated.
 2406 The most common spoiled reason is the inconsistency between the charge ratios, which
 2407 appeared more frequently in the initial reconstruction, as Figure 4.21 presents, and
 2408 corrected by the improved reconstruction. Figure 4.22 shows the η charge with and
 2409 without the spoil requirement. The flag of too wide clusters is removed because the
 2410 width is amplitude dependent.

2411 4.9.2.2 The ϕ Clustering

2412 The non-precision transverse ϕ hits form clusters using the strip with the highest
 2413 charge and the two adjacent strips (left and right). The position of the cluster is simply
 2414 the mean of the strip with the highest charge. By definition, ϕ clusters are three strips
 2415 wide, whereas the η clusters usually have three strips as Figure 4.23 shows.

2416 Figure 4.24 shows the clusters charge, defined as the sum of the charge of the strips
 2417 that form the cluster, separately for the η and ϕ strips.

Figure 4.21: Unspoiled hits (1st bin) and spoiled hits (the rest bins) percentages between the old and the new reconstruction. The spoiled bins correspond to: 2nd non- η hits, 3rd on edge of the plane, 4th has multiple peaks, 5th too narrow, 6th too wide, 7th skewed, 8th show inconsistency between the charge ratios, 9th parabolic interpolation failed in the peak charge, 10th the left and/or the right strips are saturated. The most common spoiled category is due to the inconsistency of the charges, which was improved with the new reconstruction.

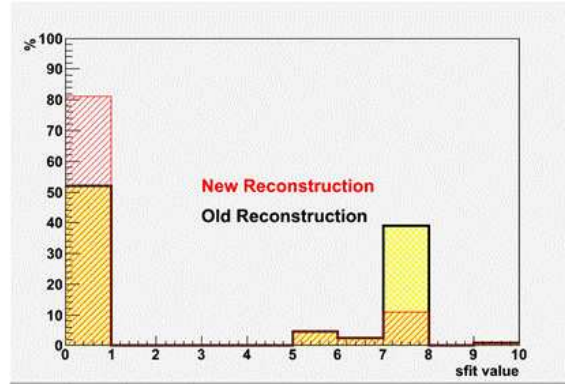


Figure 4.22: Precision charge for unspoiled hits (a) and spoiled hits (b) from 4-*samples* data. The saturation is included in the spoil flags and hence the saturation peaks, at the end of the distribution, appear in (b).

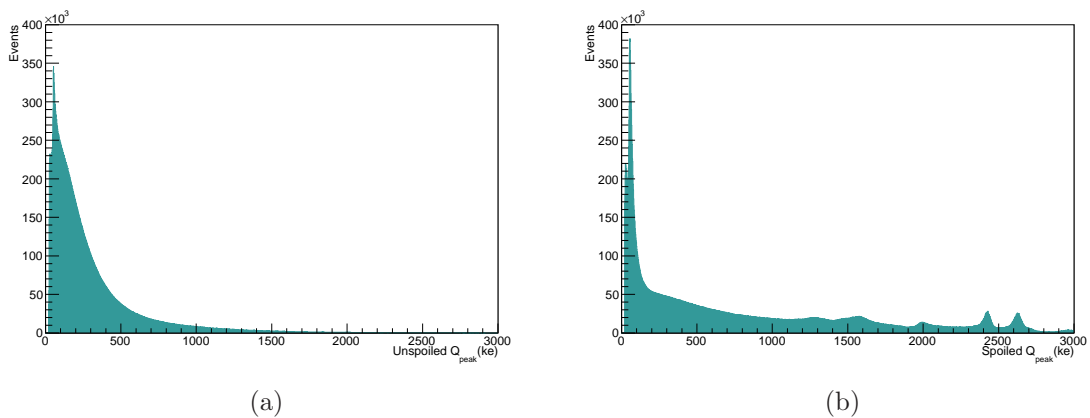


Figure 4.23: Precision cluster width measured in strips. The usual width case is clusters of three strips. Non-precision clusters have three strips by definition due to the largest strip pitch.

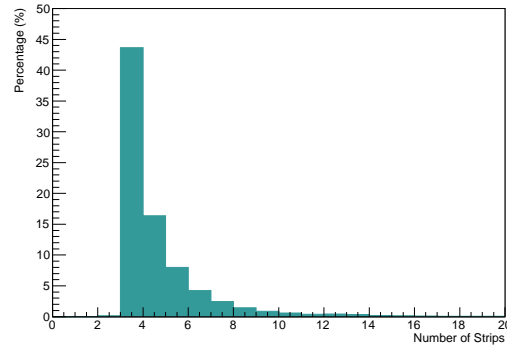


Figure 4.24: Cluster charge distributions, defined as the sum of the strips charge that forms the cluster, separately for precision (a) and non precision (b) strips from 4 – *samples* data.

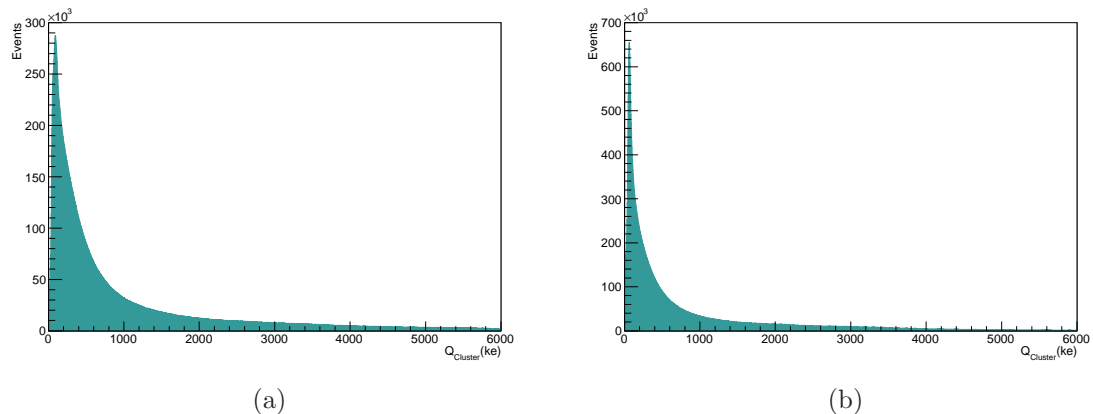
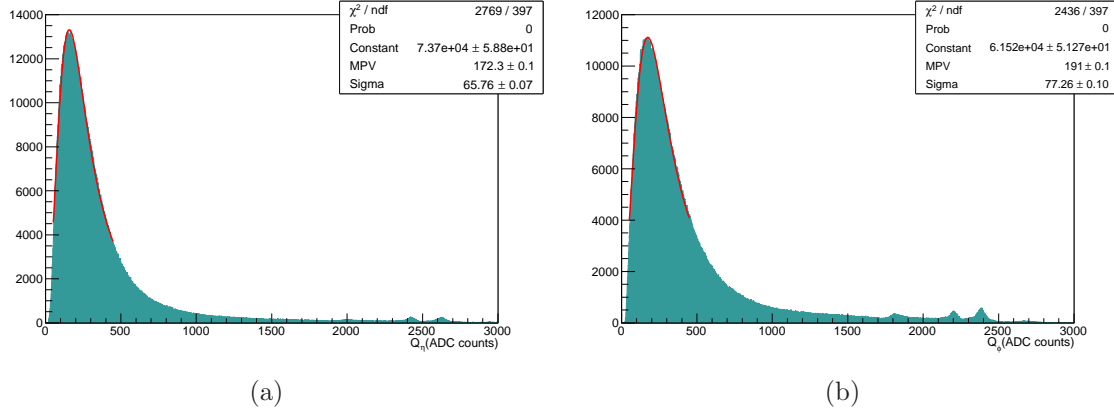


Figure 4.25: Peak strip charge distributions separately for precision (a) and non precision strips (b) from 4 – *samples* data. The clusters were preselected to belong to segments and the shapes are different compared to Figure 4.18 without the preselection requirement. The fit parameters of the Landau distributions are presented and as expected the MPV value is higher for the ϕ hits because of the largest strip pitch.



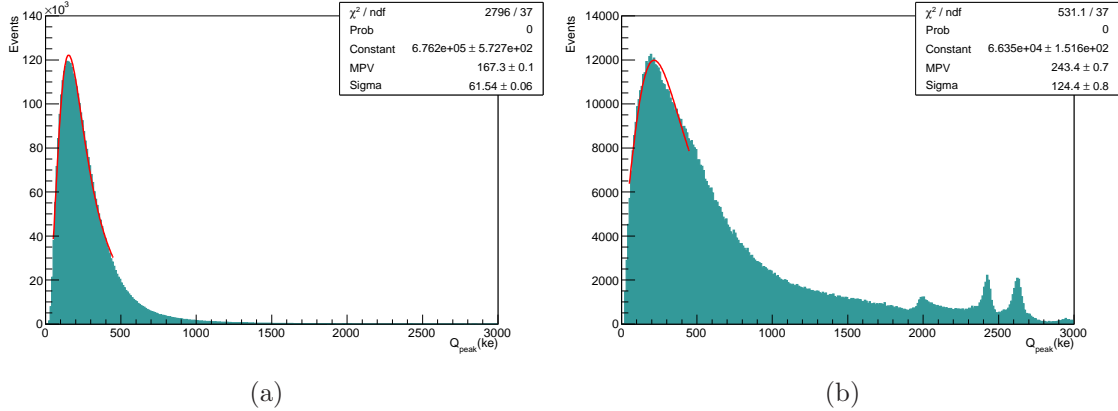
4.9.3 The Segments Reconstruction

After the cluster finding, clusters from different layers are associated in space and time to reconstruct the particle track within the CSC detector, to form the "segment". There are two possible segment combinations, called the $2d$ and $4d$ segments. The former measures the position and direction for one orientation, either η or ϕ , and the latter provide a complete measurement of both coordinates and directions.

The cluster charge distribution, for clusters that are part of segments, is presented in Figure 4.25. The peak shape is clearer compared to the single clusters distributions, already presented (Figure 4.18), because these clusters are part of tracks. The peaks are modeled by Landau distributions and the fitting parameters are also presented on the same Figure. The effect on the η charge distribution of the spoil requirement when the cluster is part of a segment is presented in Figure 4.26 fitted with a Landau.

The CSC reconstruction is finished after the segments formation. The reconstructed information is combined with the information from other detector technologies, i.e. inner detector or other muon detectors, to form muons. During the Run-I period two muon algorithms existed, the STACO (SStatistical COmbination of the different vectors) and the MUID (algorithm which refits the combined tracks starting from the ID track and then adding the muon measurements) [14]. For the upcoming Run-II, these two algorithms will be replaced by the unified "Muon" or "3rd" chain, which performs muon identification by a chain of algorithms starting from the pattern recognition inside the Muon Spectrometer and ending with the final definition of the muon object using

Figure 4.26: η peak charge distributions on segments when are required to be unspoiled (a) and spoiled (b) for 4 – *samples* data. The peaks are fitted with Landaus and the parameters appear on the Figures.



2439 information from all detectors.

2440 The tracks passing through the CSC detector have the momentum profile shown in
 2441 Figure 4.27. The peak in the low region is normally excluded in track-related analysis,
 2442 since it is the result of background processes.

2443 4.10 CSC Simulation

2444 The MC production starts from the so called "Generation" stage, during which the
 2445 interaction of two protons is simulated producing a list of particles. The final state
 2446 products of the interaction are propagated through the detector using *GEANT4*, this
 2447 step is called "Propagation". Afterwards, the first detector specific stage follows, the
 2448 "Digitization".

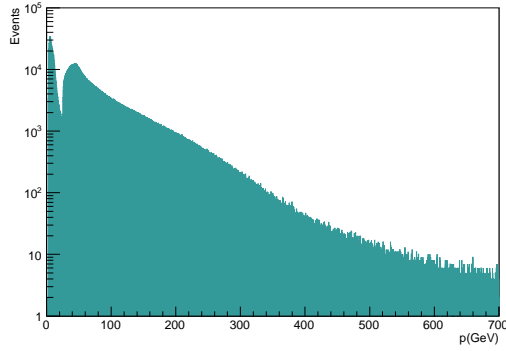
2449 Specifically for the CSCs, the digitization is performed for each hit and defines how
 2450 a cluster is created. For the production of more accurate MC, when the reconstruction
 2451 improved, new "Charge Sharing Profiles" were created. This means, that data distri-
 2452 butions of $Q_{peak}/(Q_{left} + Q_{right} + Q_{peak})$ as a function of the interstrip position were
 2453 created, as shown in Figure 4.28. Then, the distributions are fitted by the functions:

$$f(x) = \frac{Q}{1 + ax^2 + bx^4} \quad (4.11)$$

2454 separately for the large and small chambers due to different pitches. The obtained
 2455 formula is used for the digitization.

2456 The reconstruction, as described for the data in Section 4.9, follows the digitization.

Figure 4.27: Momentum distribution of tracks going through the high η region where the CSC detectors are located. In muon analysis good tracks selection includes a cut of $p > 50$ GeV to reject background processes, which form the low region peak.



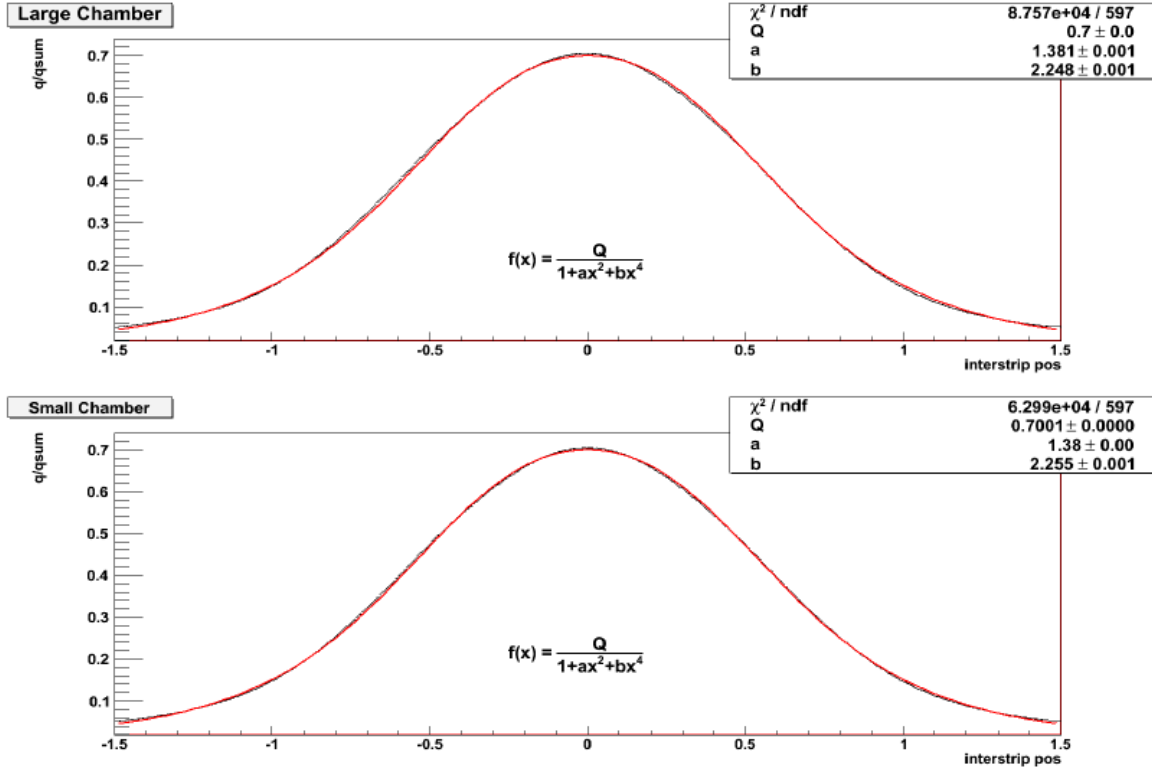
2457 4.11 CSC Operational Conditions During the Run- 2458 I

2459 The overall CSC operation during the ATLAS Run-I period was smooth, without
2460 significant data acquisition losses or operational problems. The hardware limitation of
2461 the off-detector electronics was a serious concern during the entire Run-I. Concerning
2462 the detector operation, before the 2012 data taking, the year that the majority of Run-I
2463 data were collected (20.3fb^{-1}), and the operating rate was high, the only problems were
2464 the HV failure in three layers in different chambers ($C03$, $A05$, $A09$). In June 2012,
2465 $C05L1$ showed less occupancy in the half plane and in August 2012 one chamber showed
2466 failure in two consecutive layers ($C01$). In a following section the physics impact of this
2467 malfunctions is investigated in details.

2468 In 2010 data taking, the off-detector electronics charge threshold corresponded to the
2469 ($\text{pedestal} + 3.1(f001 - \text{pedestal})$) noise of each channel and in 2011 raised to ($\text{pedestal} +$
2470 $5.1(f001 - \text{pedestal})$). The motivation was both physics and mostly the deadtime
2471 increase. The former was based on the fact that physics objects leave higher charge
2472 signatures (as can be concluded from Figures 4.18 and 4.25) and the latter was caused
2473 by the hardware limitation of the off-detector electronics.

2474 In 2012, when the trigger rate increased even more, the first step taken in the direc-
2475 tion of decreasing the input occupancy was to raise the charge thresholds to 40 ADC
2476 counts (1 ADC count = 1100 e) at the RODs level or above the noise level in case it
2477 was higher. Typical charge distributions of the η and ϕ peak charges when the cluster
2478 belongs to segment, have already been presented in Figure 4.25. The applied thresh-
2479 old modification in the beginning of 2012 suppressed further hits coming mainly from
2480 background processes, cross talk and echos and deteriorated the efficiency by less than

Figure 4.28: Fitted data distributions of the charge ratios as a function of the interstrip position, defined as in Equation 4.9. The obtained formulas are used to produce charge, at the digitization level, given the interstrip position.



2481 0.7%.

2482 The rate continued to increase gradually, during 2012, until it reached $\sim 70 \text{ kHz}$ and
 2483 a number of possible temporary solutions explored, tested and some of them applied in
 2484 order to compensate the high rates and allow the operation under the conditions that
 2485 the experiment required. All the introduced methods aimed to reduce the data volume
 2486 and/or the cluster volume. Before the application of each method a careful evaluation
 2487 of the advantages and the disadvantages was conducted. In the next paragraphs the
 2488 deadtime reduction methods are explored in chronological order.

2489 4.11.1 2-Samples Data Taking

2490 When the deadtime started becoming non negligible ⁴ a drastic solution was applied.
 2491 The RODs sampling changed from four samples to two samples. The outer samples,
 2492 i.e. "A" and "D" in Figure 4.9, were discarded and the latency settings were modified
 2493 so that the pulse peak is between the two inner samples. In addition to the sampling
 2494 changes, fiber extensions were installed and perplexed the latency choice. A wrong
 2495 value was chosen and but it was corrected after a few runs.

2496 The sampling method itself did not affect the efficiency though it required different
 2497 reconstruction handling as previously mentioned in Section 4.9. The performance is
 2498 discussed in Section 4.15 and it slightly deteriorated due to the non accurate hit charge
 2499 and peaking time reconstruction.

2500 The modified two sample reconstruction helped to restore the timing measurement
 2501 lost by the application of this method.

2502 4.11.2 Charge Thresholds

2503 In the end of August 2012, the deadtime had to be further reduced to anticipate
 2504 the gradually increasing trigger rate. At this point the charge threshold was increased
 2505 to lower the data volume. A detailed study was performed in advance to evaluate the
 2506 physics impact. Because of the different shapes of the η and ϕ distributions, as shown
 2507 in Figure 4.25, and the early peaking of the precision - η charge, from the beginning
 2508 different thresholds were considered.

2509 Clusters that are part of tracks were studied for the calculation of the efficiency losses
 2510 with higher thresholds. The number of the CSC hits on track is presented analytically
 2511 in Table 4.3 for different thresholds and also in Figure 4.29 as a percentage. The study
 2512 was performed using runs taken with low thresholds and at the reconstruction level
 2513 they were increased to the values reported in the Table.

2514 Based on the above Table, the decision taken to raise the thresholds to 50 and
 2515 60 *ADC* counts for the η and ϕ hits respectively. The performance prediction was
 2516 confirmed by the observations after the deployment of this data taking schema.

2517 In parallel, ROD monitors were deployed to unveil the actual source of busy within
 2518 the ROD. Figures 4.30 show the sources of busy during a typical run separately for
 2519 large and small chambers. As expected, the large chambers contribute to the busy
 2520 more compared to the small, due to higher data volume, but the majority of the dead-
 2521 time was a result of the ϕ channels processing. The ϕ channels per layer are 48 and are
 2522 processed together for all the layers (in total $4 \times 48 = 192$ channels) by one processing

⁴The maximum acceptable dead-time by the experiment is 2%. When a sub-detector's dead-time increases the complex dead-time also increases.

Table 4.3: Percentage of CSC hits on track for different charge thresholds. The study was performed using runs taken with low thresholds and at the reconstruction level they were increased.

Threshold	$N = 0$ (%)		$N = 1$ (%)		$N = 2$ (%)		$N = 3$ (%)		$N = 4$ (%)	
	η	ϕ								
20 ke	0.24	0.04	0.03	0.04	0.2	0.7	19.19	22.12	80.33	77.1
45 ke	0.24	0.04	0.04	0.05	0.55	1.05	20.69	23.04	78.47	75.82
50 ke	0.24	0.04	0.05	0.06	0.83	1.23	21.71	23.55	77.18	75.11
55 ke	0.24	0.04	0.06	0.09	1.15	1.47	22.96	24.23	75.59	74.18
60 ke	0.24	0.04	0.1	0.1	1.6	1.86	24.45	24.95	73.62	73.04
70 ke	0.25	0.04	0.2	0.2	2.9	2.76	27.85	26.76	68.8	70.24
75 ke	0.25	0.04	0.26	0.28	3.86	3.34	29.59	27.81	66.04	68.54
85 ke	0.26	0.05	0.49	0.45	6.03	4.8	33.12	30.11	60.1	64.58
90 ke	0.26	0.06	0.71	0.6	7.22	5.72	34.87	31.08	56.93	62.54

unit. For each η layer, one unit is assigned for the processing (192 channels). This means that eventually the ϕ unit processes the exact same number of channels as each of the η processing units, however the ϕ unit was busier than the rest. The problem was considered to originate from some sort of trafficking during the data transmission. The assumption was enhanced by the fact that the readout links showed relatively high busy.

The evaluation of the busy monitors led soon to the decision to revert the η threshold back to 40 ADC counts and left the ϕ threshold unchanged to 60 ADC counts. As had been predicted, the busy did not increase with this choice and the efficiency was partially restored.

4.11.3 Non Applied Busy Reduction Methods

Other methods were also considered and evaluated because of the rather exponential increase of the busy at ~ 70 kHZ , as Figure 4.10 shows. Despite that, eventually there was no need for any of these methods to be applied. The most important of them included higher ϕ thresholds (with the losses reported in Table 4.3) different or not for the large and small chambers, use only the peak strip for the ϕ hits⁵, reduced time

⁵The ϕ strips are wider than the η and the charge is mostly deposited at the peak strip. Along with the fact that the transverse coordinate is the non-precision one, no major efficiency discrepancies predicted. The study showed that the probability of having ≥ 2 ϕ hits on track is $97.5 \pm 0.5\%$ whereas

Figure 4.29: η (a) and ϕ (b) percentage of hits on tracks as a function of the charge thresholds. The study was performed using runs taken with low thresholds and at the reconstruction level they were increased.

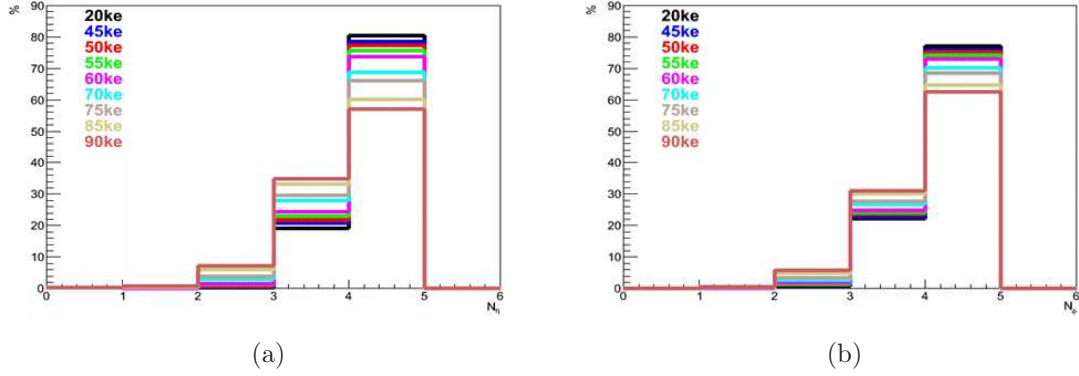


Figure 4.30: Large (a) and small (b) chambers busy source monitoring (in arbitrary units). The bin assignments are: the first 4 bins correspond to the processing units of the η channels of the 4 layers consecutively, the 5th is the unit that processes all the ϕ channels, the 6th bin corresponds to the RPU, the 7th to the stream caring the trigger information summary and the last one is the readout link. The large chambers contributed to busy more, due to higher data volume, but the majority of the dead-time was a result of the ϕ channels processing.

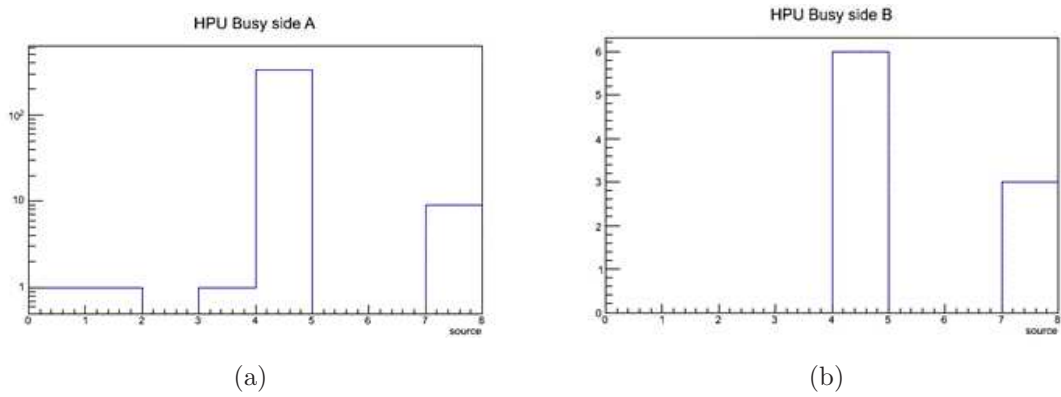
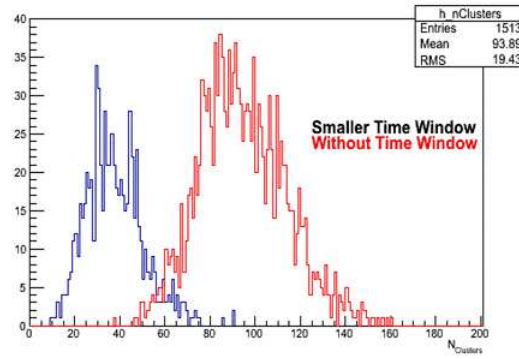


Figure 4.31: Investigation of the impact of the reduced time window in order to reduce the busy. The number of clusters are reported for a sample taken with the nominal time-window and then reprocessed offline with reduced time range. The major physics impact of this method would be the loss of hits primarily originate from beam halo and other cavern background processes. The method was never applied in the data taking, except from one test run which showed that the processing time due to the time calculation was a significant busy factor.



2539 windows (expected to reduce the cluster volume, as Figure 4.31 shows, and cut all hits
 2540 essential for beam halo and cavern background studied).

2541 All these method implemented in the software and the OKS configuration was up-
 2542 dated to include them. The actual application would only require a parameter change
 2543 in the database.

2544 4.12 Resolution and Angle Dependence

2545 An indication of the good performance is the track resolution. The $3 - point$ resid-
 2546 uals, defined as:

$$R_1 = x_1 - \frac{1}{2}(x_0 + x_2) \quad (4.12)$$

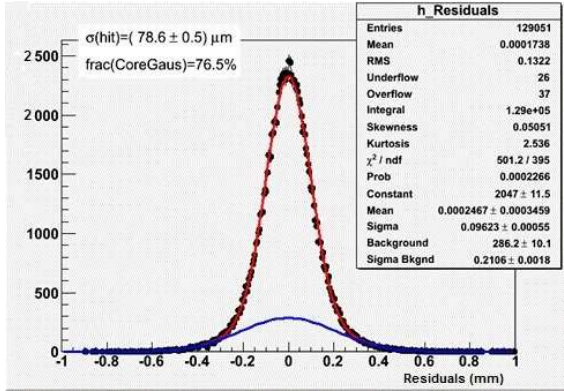
$$R_2 = x_2 - \frac{1}{2}(x_1 + x_3)$$

2547 are formed from the middle layers, i.e. "1" and "2", and the adjacent outer, i.e. either
 2548 "0" and "2" or "1" and "3" respectively⁶, are used to predict the hit position. The

by using the neighboring strips is $97.68 \pm 0.17\%$.

⁶The measuring of the layers starts from 0.

Figure 4.32: The residuals distribution, defined as in Equation 4.13, fitted with a double Gaussian to account for both the signal (red line) and the background (blue line). The resolution is estimated to be $78.6 \mu\text{m}$ for *4 – samples* runs.



resolution is estimated by fitting the residuals distribution, shown in Figure 4.32, with a double-Gaussian, one for the signal and one for the cavern background. The resolution is obtained by multiplying the width of the inner Gaussian by a factor of $\sqrt{\frac{2}{3}}$ to account for the error propagation in the residual. In the case of *4 – samples* the resolution is measured to be $78.6 \mu\text{m}$.

The resolution is not similar for inclined and perpendicular tracks, but depends on the segment angle shown in Figure 4.33. Figure 4.34 shows the resolution as a function of the incident angle. The curve follows the formula $\sqrt{p_0^2 + (p_1 \times \tan\theta)^2}$, where p_0 is the resolution for tracks with perpendicular incidence and the p_1 term describes the resolution degradation for larger angles, experimentally measured to be:

$$p_0 = 73.4 \pm 0.3 \quad (4.13)$$

$$p_1 = 954 \pm 34.$$

4.13 Alignment Checks

The mean value of the residuals is a clear indication of the alignment of the system (discussed in Section 4.7.3). Figure 4.35 shows the mean values, theoretically expected to be 0.00, for each sector with the final alignment values for Run-I. The deviations observed are too small and this indicates how well the wheels are aligned. The analysis is based on the 2012 data and the final alignment constants for the Run-I.

Except from this detector specific alignment checks, regular checks of the alignment

Figure 4.33: The segment angle for the tracks passing through the CSC detector. The resolution is different for perpendicular and inclined tracks, but the observed positive and negative asymmetry is due to lower efficiency of sectors with dead layers.

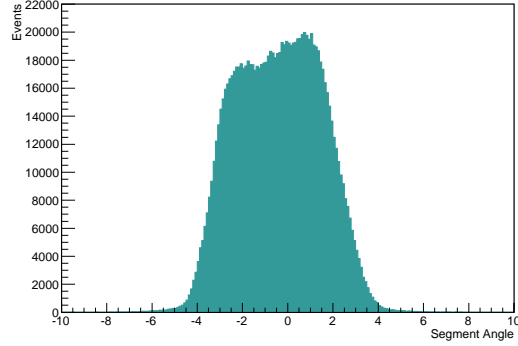


Figure 4.34: The resolution as a function of the incident angle. The curve follows the function $\sqrt{p_0^2 + (p_1 \times \tan\theta)^2}$, where $p_0 = (73.4 \pm 0.3) \mu m$ is the resolution for tracks with perpendicular incidence and the $p_1 = (954 \pm 34)$ term describes the resolution degradation for larger angles.

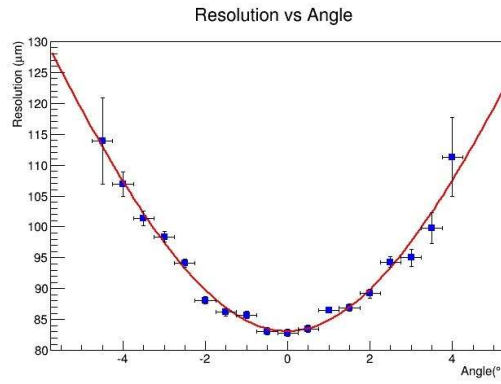
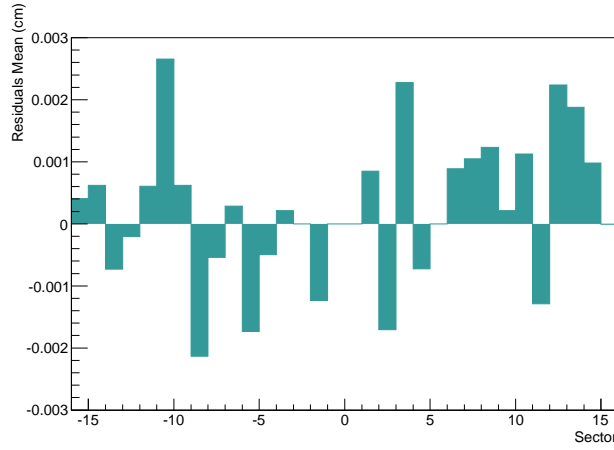


Figure 4.35: Plot of the residuals mean (in cm) for each sector, which proves the good alignment of the wheels given the small deviation from the expected value of 0.00. The analysis performed on 2012 data with the final alignment constants for the Run-I. Sectors with dead layers were not included since the *3 – point* residuals formation was not possible.



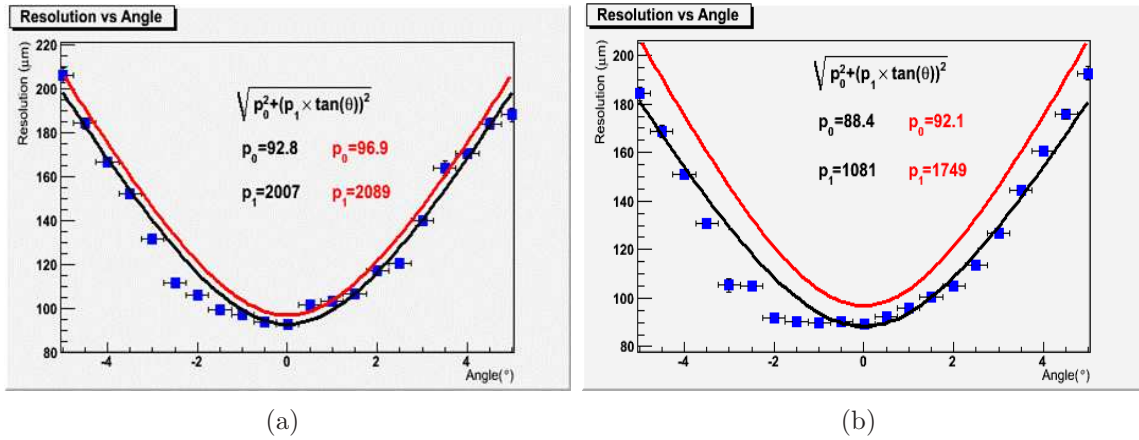
2566 are performed for the muons to measure the misalignment not only between the muon
 2567 detectors but between the inner detector and the muon spectrometer.

2568 4.14 Lorentz Angle Effect Measurement

2569 In 2011, a few runs were recorded with stable beams and the toroids and solenoids
 2570 magnets switched off. The motivation was various studies for the different detector
 2571 components.

2572 The resolution analysis of the inclined tracks of these runs and the comparison
 2573 with the runs taken with nominal magnets operation, provides a measurement of the
 2574 effect of the Lorentz force on the charged tracks. Specifically, the resolution is slightly
 2575 decreased as Figure 4.36 shows. The run reconstructed with the initial Run-I method
 2576 and is compared to a run similarly reconstructed, hence the resolution is different from
 2577 previously reported value.

Figure 4.36: In 2011, a few runs were recorded with stable beams and without magnetic field. The runs reconstructed with the initial Run-I method and compared to a similarly reconstructed run (red line). The resolution dependence on the incident track angle is studied separately for the large (a) and small (b) chambers, following the method presented in Section 4.12. As expected smaller resolution values are estimated.



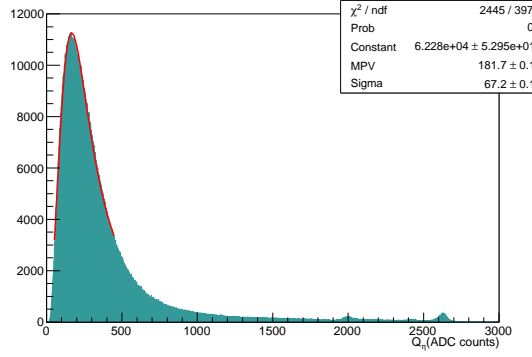
4.15 2 vs 4-Samples Data Taking Performance

The 2 – *samples* data taking, applied to reduce the data volume, even though is expected not to reduce the hit-finding efficiency, it deteriorates slightly the accuracy of the reconstruction reconstruct the time and the charge of the hits (as introduced in Section 4.9).

Figure 4.37 presents the fitted reconstructed η peak charge, for clusters belonging to segments, in order to be compared to Figure 4.25. The MPV value, of the fitted Landau, is different between the 2 – *samples* and 4 – *samples*. This charge difference is reflected also in the unspoiled fraction, which is increased to 85% with respect the 4 – *samples* value of 80%. The source is the decrease of the "inconsistency" between the charge ratios, apparently related to the charge reconstruction. The η position reconstruction is therefore affected, in contrast to the ϕ clusters position which position is defined as the middle of the peak strip.

These changes are also reflected in the residuals and the resolution as shown in Figure 4.38. In the case of 4 – *samples* the resolution is measured to be 78.6 μm and in the case of 2 – *samples* is increased to 84.1 μm . The outliers in the residual distributions, another indication of the performance, is also increased from 0.05 % to

Figure 4.37: The η charge distribution, for clusters on segments with $2 - samples$ data taking, fitted with Landau. The MPV is shifted compared to $4 - samples$ to higher values, consequently the position reconstruction is affected, as well as the spoil fraction.



2595 0.13% respectively. The pulls, defined from the error propagation in the residuals:

$$\begin{aligned}\delta R_1 &= \sqrt{\delta x_1^2 + 0.25(\delta x_0^2 + \delta x_2^2)} \\ \delta R_2 &= \sqrt{\delta x_2^2 + 0.25(\delta x_1^2 + \delta x_3^2)}\end{aligned}\quad (4.14)$$

2596 also deviate slightly more from the expected value of 1.000 when migrated to the $2 -$
 2597 $samples$ data taking. The fitted with a Gaussian pulls distributions are presented in
 2598 Figure 4.39 and the estimated means are $\sigma = 1.044$ and $\sigma = 1.064$ for the $4 -$ and
 2599 $2 - samples$ respectively. The $2 - samples$ data taking was crucial for the operation
 2600 of the system and the efficiency deterioration was considered acceptable, otherwise the
 2601 operation would have been impossible.

2602 4.16 CSC Efficiency in the Muon Algorithm

2603 In this section the CSC efficiency in the STACO muon algorithm [14] is investigated
 2604 using the tag and probe method. In the beginning, the muon spectrometer reconstruc-
 2605 tion efficiency is extracted in the high η region, where the CSC detectors are located,
 2606 and then the efficiency of the CSC segments, when a STACO muon exists, is estimated.

Figure 4.38: The residuals distribution for $2-samples$ data, defined as in Equation 4.13, fitted with a double Gaussian to account for both the signal (red line) and the background (blue line). The resolution is estimated to be $78.6 \mu m$ for the $4-samples$ runs (in Section 4.12) and for the $2-samples$ is $84.1 \mu m$. The outliers correspond to 0.05 % and 0.13% respectively. The differences are attributed to the non-accurate charge reconstruction when two of the four samples are not recorded.

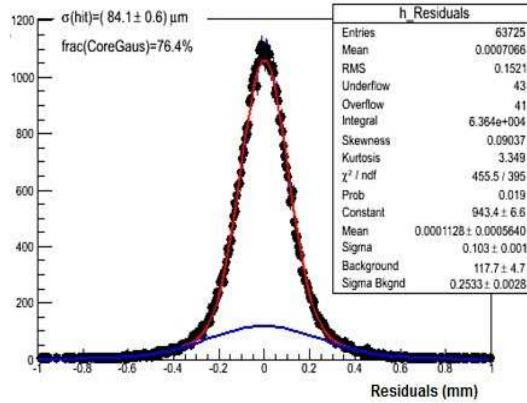


Figure 4.39: The pulls distributions, defined as in Equation 4.15, are fitted with a Gaussian. The measured pulls are $\sigma = 1.044$ and $\sigma = 1.064$ for the $4-samples$ (a) and $2-samples$ (b) respectively. The deviation from the expected zero value is due to the less accurate reconstruction.

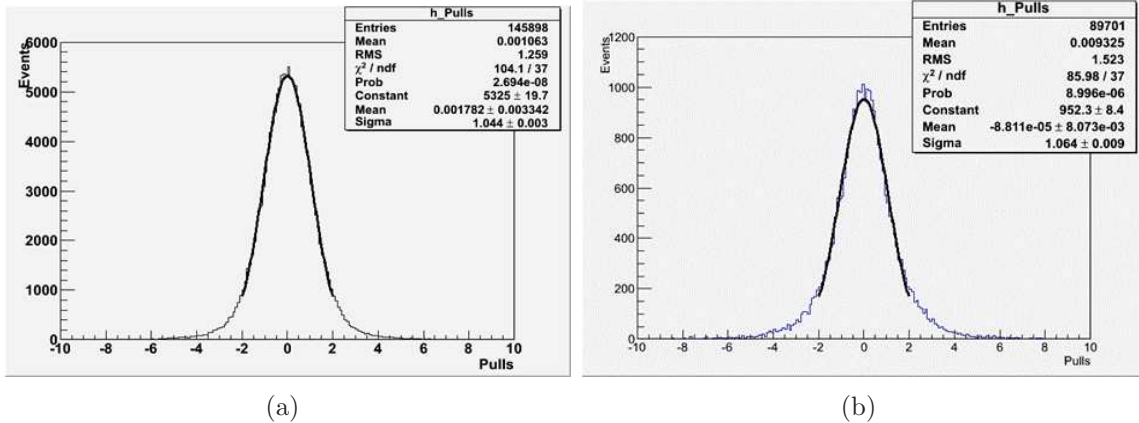
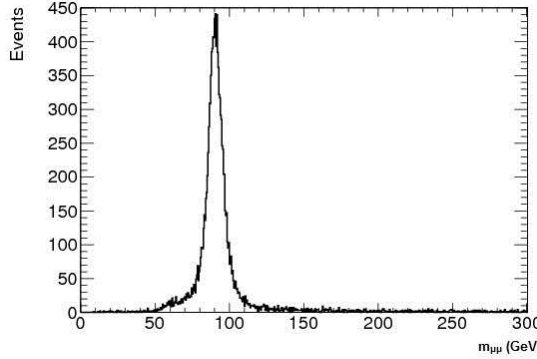


Figure 4.40: Mass distribution formed by the tag muon and the probe charged track for a subset of the Run-I data. The Z -resonance can be seen above a constant background.



4.16.1 The Tag and Probe Method

The tag and probe method relies on the preparation of an unbiased sample of physics objects and uses a well-known resonance or PDF for a data-driven efficiency estimation. Specifically, the $Z \rightarrow \mu^+ \mu^-$ decays are used in this section. The "tag" muon is selected using tight selection (for fake rate elimination) and the "probe" muon selection is looser. The so called "passing probe" has stricter criteria than the probe, but looser compared to the tag. The ratio of the passing probes over probes is defined as the efficiency of the technique:

$$Efficiency = \frac{N_{Passing\ Probes}}{N_{Probes}}. \quad (4.15)$$

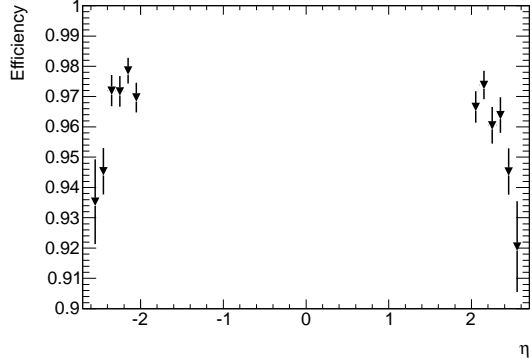
The tag muon is a combined (both ID and MS information) or segment tagged (ID and partial MS information), with $p_T > 20$ GeV, satisfying a number of inner detector criteria, B-Layer/SCT/Pixel hits and a successful TRT extension. Isolation criteria, both track based and calorimeter based, are also applied. The probe object is an inner detector opposite charged track, going through the CSC region ($2.0 < \eta < 2.7$), with $p_T > 20$ GeV. The tag and probe objects form the Z mass above a constant background, shown in Figure 4.40. A mass cut, $|m - m_Z| < 15$ GeV is applied to suppress non Z -resonant events. The passing probe is associated with the probe inner detector track by requiring $\Delta R < 0.1$ between them. All the selection criteria are summarized in Table 4.4.

The efficiencies in η bins are presented in Figure 4.41 and they are relatively high. The error bars correspond to the binomial errors and no systematic uncertainty is included. Further investigation follows for better understanding of the inefficiency concerning only the CSC segments and hits information. It has to be noted that the CSC detectors are only 1/3 of the muon spectrometer stations in the forward region.

Table 4.4: Selection criteria for the tag and probe objects used for the efficiency extraction of the STACO muon algorithm in the high η region.

Object Type	Selection
Tag	Combined or Segment Tagged Muon $p_T > 20$ GeV $N_{B-Layer\ Hits} > 0$ when B - Layer Hit expected $N_{Pixel\ Hits} + N_{Crossed\ Dead\ Pixel\ Sensors} > 1$ $N_{SCT\ Hits} + N_{Crossed\ Dead\ SCT\ Sensors} \geq 6$ $N_{Pixel\ Holes} + N_{SCT\ Holes} < 3$ $n_{TRT}^{hits} = \text{number of TRT hits}$, $n_{TRT}^{outliers} = \text{number of TRT outliers}$ $n = n_{TRT}^{hits} + n_{TRT}^{outliers}$ $ \eta < 1.9 : n > 5 \text{ and } n_{TRT}^{outliers} > 0.9n$ $ \eta \geq 1.9 : n > 5 \text{ and } n_{TRT}^{outliers} > 0.9n$ $\Sigma p_T/p_T < 0.15 (\Delta R = 20)$ $\Sigma E_T/E_T < 0.30 (\Delta R = 20)$
Probe	Opposite Charged Inner Detector Track in the CSC region $p_T > 20$ GeV
Tag & Probe	$ m - m_Z < 15$ GeV
Passing Probe	Muon Associated to the Probe Track ($\Delta R < 0.1$)

Figure 4.41: Efficiency of the STACO muon algorithm as estimated from the tag and probe method. Results are provided for the high η region where the CSC detectors are located. The estimated efficiency depends on all the muon technologies in the region where the probe object passes.



2630 The classification of the CSC segments conditions is the following in the inefficiency
 2631 cases:

2632 • 33.6% segment with 4 unspoiled hits
 2633 • 33.7% segment with 3 unspoiled hits⁷
 2634 • 13.4% segment with <3 unspoiled hits
 2635 • 19.3% segments with no track association.

2636 The tag and probe estimated efficiency depends on all the muon technologies in the
 2637 region where the probe object passes. To optimize the result for the CSC detectors
 2638 another tag and probe method is used. The CSC reconstruction contributes to the
 2639 muon object reconstruction with segments. These segments are formed from the layer
 2640 hits, which might be unspoiled hits or not. The CSC segment efficiency is estimated
 2641 using the same tag selection as previously and now the probe is required to be a STACO
 2642 muon passing through the CSC region. The efficiency is estimated as the number of
 2643 muons related to a CSC segment divided by the number of probe muons. Table 4.5
 2644 presents analytically the selection. The resulting efficiencies are shown in Figure 4.42.
 2645 The overall efficiency is $(98.85 \pm 0.10)\%$ and the variations between sectors or the
 2646 different η, ϕ regions are small.

⁷The cases of less than four unspoiled hits can be partially explained from the dead layers and the stuck bit channels.

Table 4.5: Selection criteria for the tag and probe objects used for the CSC segment efficiency extraction in the STACO muon algorithm.

Object Type	Selection
Tag	Combined or Segment Tagged Muon $p_T > 20 \text{ GeV}$ $N_{B-Layer \text{ Hits}} > 0$ when B - Layer Hit expected $N_{Pixel \text{ Hits}} + N_{Crossed \text{ Dead Pixel Sensors}} > 1$ $N_{SCT \text{ Hits}} + N_{Crossed \text{ Dead SCT Sensors}} \geq 6$ $N_{Pixel \text{ Holes}} + N_{SCT \text{ Holes}} < 3$ $n_{TRT}^{hits} = \text{number of TRT hits}$, $n_{TRT}^{outliers} = \text{number of TRT outliers}$ $n = n_{TRT}^{hits} + n_{TRT}^{outliers}$ $ \eta < 1.9 : n > 5 \text{ and } n_{TRT}^{outliers} > 0.9n$ $ \eta \geq 1.9 : n > 5 \text{ and } n_{TRT}^{outliers} > 0.9n$ $\Sigma p_T/p_T < 0.15 (\Delta R = 20)$ $\Sigma E_T/E_T < 0.30 (\Delta R = 20)$
Probe	Opposite Charged STACO Muon passing through the CSC region $p_T > 20 \text{ GeV}$
Tag & Probe	$ m - m_Z < 15 \text{ GeV}$
Passing Probe	STACO Muon with Associated CSC Segment

4.17 Performance of Sectors with Problematic Layers

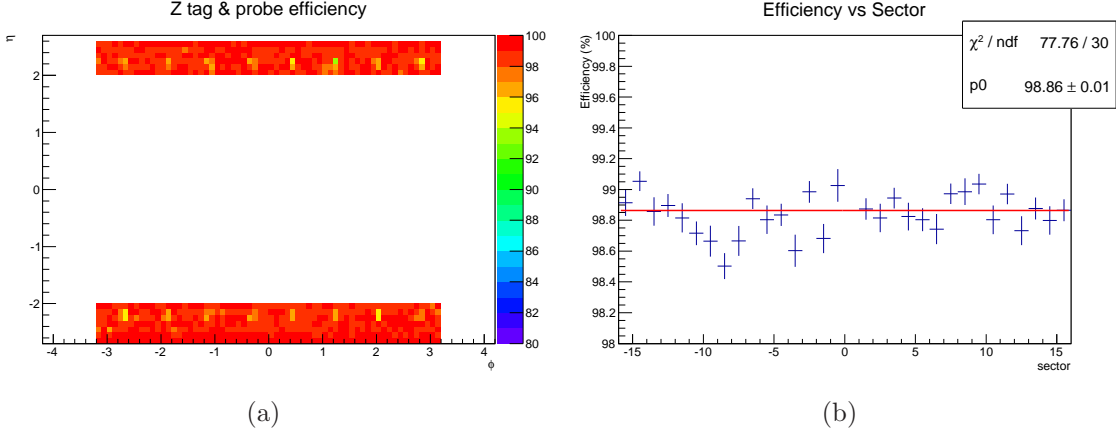
During the Run-I, sectors $A05$, $A09$, $C03$ lost one layer because of HV failure (before 2012) and in the middle of 2012 $C01$ lost two consecutive layers. In addition, the second layer of chamber $C05$ showed less occupancy, starting from the middle of 2012, and this is also be investigated in this section.

The performance of sectors already presented with the tag and probe method in Figures 4.42, including those with dead layers. Since the muon algorithms are robust against the detector efficiency and can work with a few hits on each subsystem, no significant loss is observed. Even though, in terms of detector performance, specifically in the case of $C01$ the real loss is visible in the segment angle determination.

Using a data sample taken when the $C01$ was fully operated, a study conducted to simulate the loss of the two outer layers. Pseudo-segments are defined by using the first two layers, simply by requiring the same event clusters within 5 strips apart⁸. This

⁸Assuming that clusters part of the same track cannot be more strips apart given the layers distance and the pitch

Figure 4.42: CSC segment efficiencies in the STACO muon algorithm using the tag and probe method. Overall, the efficiency as a function of the passing probe muon in the η - ϕ range (a) and the sectors efficiencies (b) are presented. Partial cause of the inefficiency cases are TGC holes. The study performed with the 2012 data.



2661 segments are compared to the real segments found by the nominal segment algorithm.
 2662 The fake rate, defined as:

$$\text{Fake Rate} = \frac{\text{Pseudo - segments unassociated with real segments}}{\text{Total pseudo - segments}} \quad (4.16)$$

2663 was estimated to be 3.6% and the probability of not finding a pseudo-segment when
 2664 a real segment exists is negligible ($\sim 0.01\%$). Despite the low fake rate, further investi-
 2665 gation was performed for possible fake reduction. Specifically, the association of the
 2666 clusters charges was used to reveal possible patterns. As Figure 4.43 shows, no corre-
 2667 lation could be revealed. The real cost of the loss of the two layers is in the segment
 2668 angle, the estimated pseudo-segment angle shows non-marginal deviation from the real
 2669 angle (Figure 4.44).

2670 Except from the dead layers, C05 showed less occupancy in half of one plane (Figure
 2671 4.45) and the analysis showed that the hit finding efficiency deteriorated as Table 4.6
 2672 reports. The cause is probably a failure in the HV distribution line. This assumption is
 2673 supported by the evidence that when the occupancy reduction occurred, the HV value
 2674 on this layer was less than expected (Figure 4.45).

2675 4.18 Run-I Performance Summary

2676 Table 4.7 summarizes the efficiency during the Run-I operations for fully operating
 2677 sectors, i.e. without dead layers. The time intervals are defined as the eras with the

Figure 4.43: Possible correlation of the fake rate with the cluster charges investigated for the C01 pseudo-segments after the two dead layers appeared. No pattern is visible. Figures show the charge of the inner layers separately for true (a) and for fake pseudo-segments (b). Sector C01 study of the segment identification, after the loss of the two outer layers, estimated to have a fake rate of 0.036.

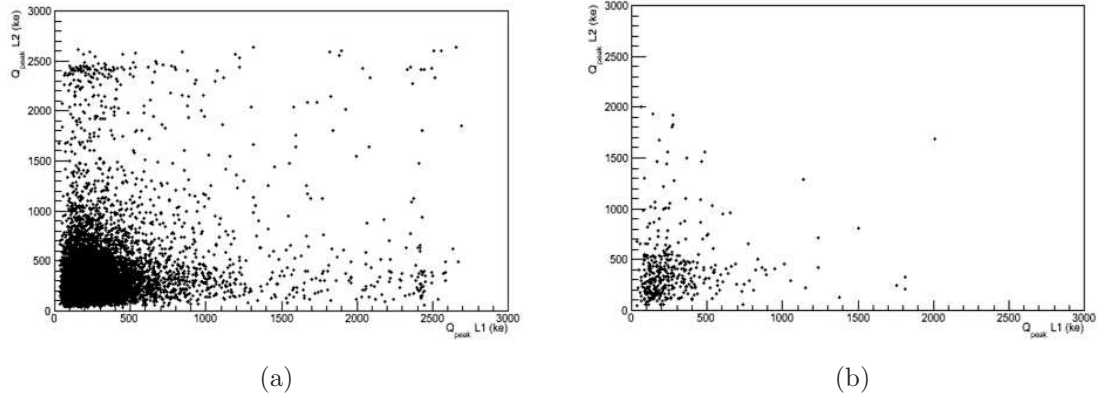


Figure 4.44: $C01$ pseudo-segments angle difference from the real angle. The loss of the two layers is visible at this estimation.

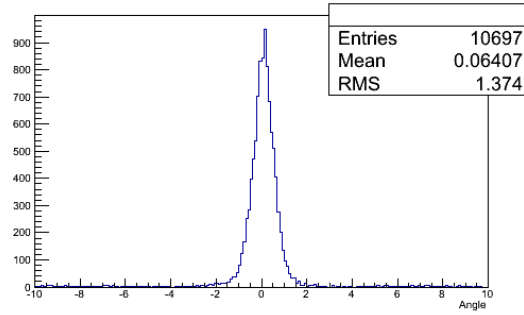


Figure 4.45: $C05L1$ shows less occupancy than expected (red line). The problem is associated with lower current drawn from this plane.

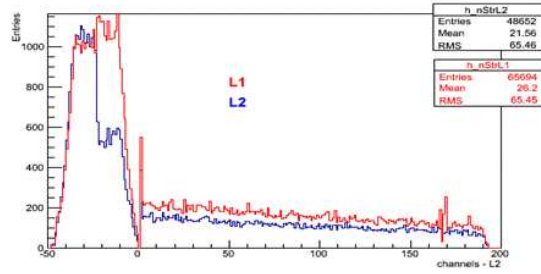


Figure 4.46: $C05L1$ less occupancy associated with the lower current drawn in the middle of the data taking (June 13th, 2012). The source is probably due to a failure in the HV distribution line. The image is a screen shot from the DCS viewer.

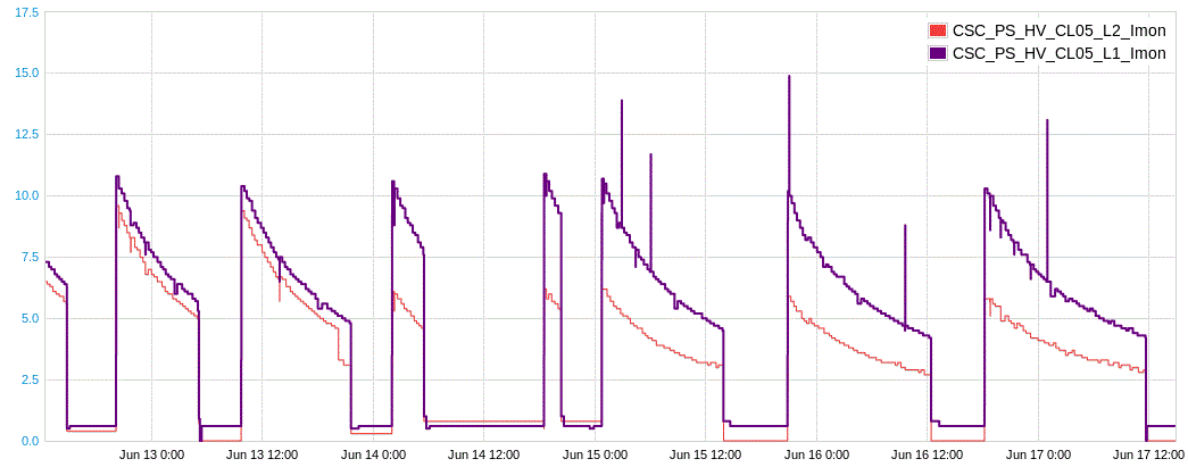


Table 4.6: The Table summarizes the performance of $C05L1$ after found to show less occupancy in half of the plane. For comparison reasons other sectors are presented.

Hits on Tracks	$C05$	Rest Sectors without dead layers
$> 1 \eta$	94.0 ± 0.3	98.77 ± 0.12
$> 1 \phi$	93.5 ± 0.3	97.68 ± 0.17
$> 1 \text{ } Unspoiled \eta$	85.6 ± 0.4	91.4 ± 0.3

2678 same data acquisition conditions. These are in chronological order: the $4 - samples$
 2679 data taking, the $2 - samples$ data taking with wrong latency settings and increased
 2680 thresholds ($\eta > 50$ and $\phi > 60$ ADC counts) and correct latency with restored η
 2681 thresholds (40 ADC counts). Schematically the inefficiency of all runs included in the
 2682 “Good Runs List” [15] (GRL, in total 474 runs) are presented in Figure 4.47. The
 2683 performance, excluding the runs taken with wrong latency settings, was overall stable
 2684 and high.

Table 4.7: Summary Table of the Run-I performance in eras with the same data acquisition conditions for fully operating sectors. Run to run deviations observed only for runs taken with wrong latency settings. The quoted uncertainties are statistical only.

Selection	Efficiency (%)			
	$4 - samples$	$2 - samples$	Wrong Latency, $\eta > 50, \phi > 60$ ADC counts	Correct Latency, $\eta > 40, \phi > 60$ ADC counts
$> 1 \eta$ on track	98.947 ± 0.014	98.956 ± 0.014	~ 94	98.744 ± 0.008
$> 1 \phi$ on track	97.746 ± 0.017	97.729 ± 0.020	~ 87	97.699 ± 0.012
$> 1 \text{ } Unspoiled \eta$ on track	91.77 ± 0.04	91.92 ± 0.04	~ 85	90.870 ± 0.023
$Z \text{ Tag\&Probe}$	98.915 ± 0.014	98.873 ± 0.016	~ 98	98.764 ± 0.019

2685 The efficiency of sectors with malfunctions was studied separately since they do
 2686 not reflect the general performance. The results of the study are summarized in the
 2687 Table 4.8 for the time period starting from the appearance of the problem and excluding
 2688 the time period with the wrong latency settings. The efficiency is very close to the
 2689 efficiency of the rest sectors reported in Table 4.7.

Figure 4.47: The fraction of tracks with less than 2η (a) and less than 2ϕ hits are presented for all runs in the good runs lists of the Run-I for fully operating sectors. The x-axis are the runs (in total 474 runs) in chronological order. Excluding the period where the latency set wrongly, motivated by the installation of fiber extensions and sampling changing, the inefficiency was low and stable over time. This is a strong indication of the robust detector performance.

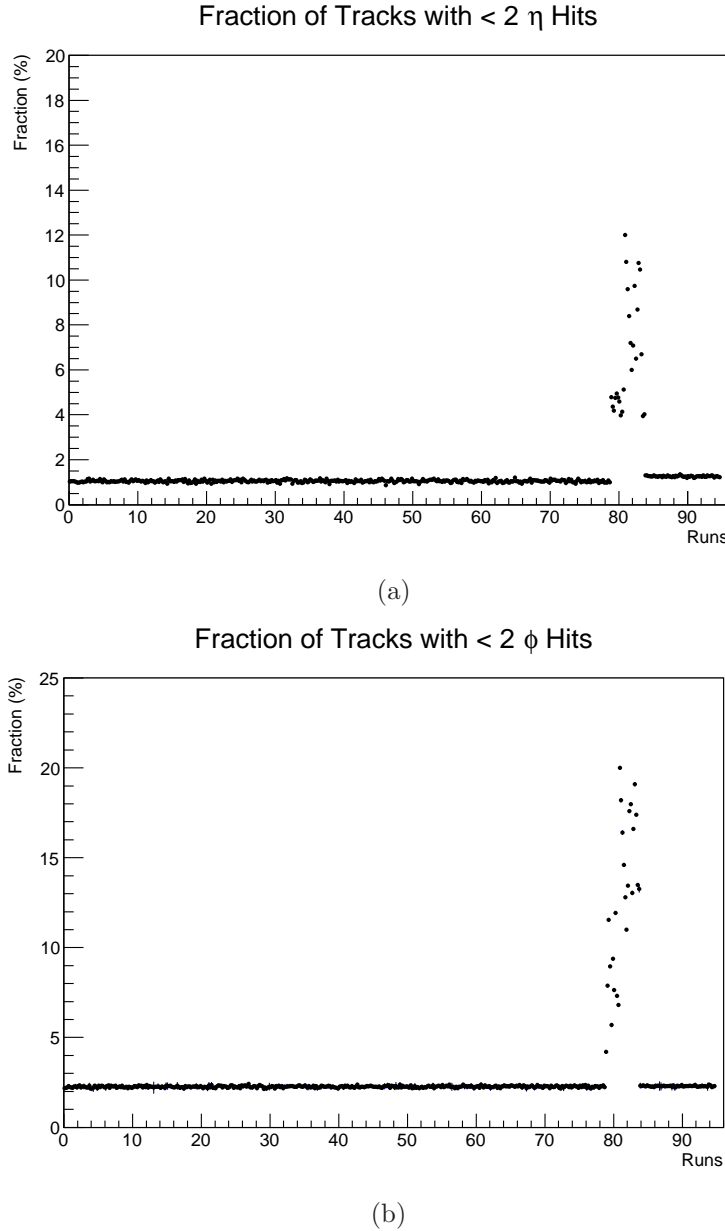


Table 4.8: Summary Table of the Run-I performance for sectors with malfunctions starting from the appearance of the problem and excluding the period with wrong latency settings. The efficiencies are comparable with the fully working chambers, reported in Table 4.7.

Selection	Efficiency (%)		
	<i>C03, A05, A09</i> 1 dead layer	<i>C01</i> 2 dead layers	<i>C05</i> Less occupancy
$> 1 \eta$ on track	98.671 ± 0.025	85.30 ± 0.014	89.70 ± 0.04
$> 1 \phi$ on track	96.96 ± 0.04	91.67 ± 0.14	97.20 ± 0.06
> 1 <i>Unspoiled</i> η on track	89.75 ± 0.08	59.4 ± 0.19	86.40 ± 0.12
<i>Z Tag&Probe</i>	98.52 ± 0.04	97.52 ± 0.04	98.71 ± 0.04

4.19 25ns Runs

At the end of the 2012 data taking, runs with 25 ns bunch spacing, instead of the 50 ns , recorded with $2 - samples$. The reason was to conduct a preliminary study of the detectors operation and be better prepared for the Run-II, during which the bunch spacing will be decreased. The specific conditions of the recorded three runs are summarized in Table 4.9. The run was analyzed in multiple levels. Figure 4.48 presents the occupancies for relatively low and high charges and for comparison the 50 ns occupancies are presented. The 50 ns run was chosen to have roughly the same instantaneous luminosity in order to have the same pile up conditions.

Table 4.9: Summary of the exact conditions of the 25 ns runs recorded in 2012 at $\sqrt{s} = 8\text{ TeV}$ center of mass energy.

Run	Trains	Colliding Bunches	Peak Instantaneous Luminosity ($cm^{-2} s^{-1}$)	ATLAS Delivered Luminosity (pb^{-1})	Lumi Blocks	Recorded Events (Hz)
216399	2	48	5.83×10^{32}	10.942	1095	357.5
216419	3	48	3.44×10^{32}	2.174	271	479.0
	3	42				
216432	3	48	1.70×10^{32}	0.876	435	158.5
	1	42				

The offline analysis of the precision charge shows certain differences in the peaks positions when no further requirement is imposed. As Figure 4.37 shows, the peak shapes are different. Despite that, when the cluster on segment requirement is imposed

Figure 4.48: Comparison of the occupancies of 25 ns bunch spacing data with 50 ns as recorded from the online monitor. The latter data run chosen to have similar pile up conditions in order to be comparable. Figure (a) shows the 25 ns data with $Q_{peak} < 100\text{ ke}$, (b) the 50 ns with $Q_{peak} < 100\text{ ke}$, (c) shows the 25 ns with $Q_{peak} > 100\text{ ke}$ and (d) the 50 ns with $Q_{peak} > 100\text{ ke}$ cases. The negative channels correspond to the ϕ channels, whereas as the positive are the η .

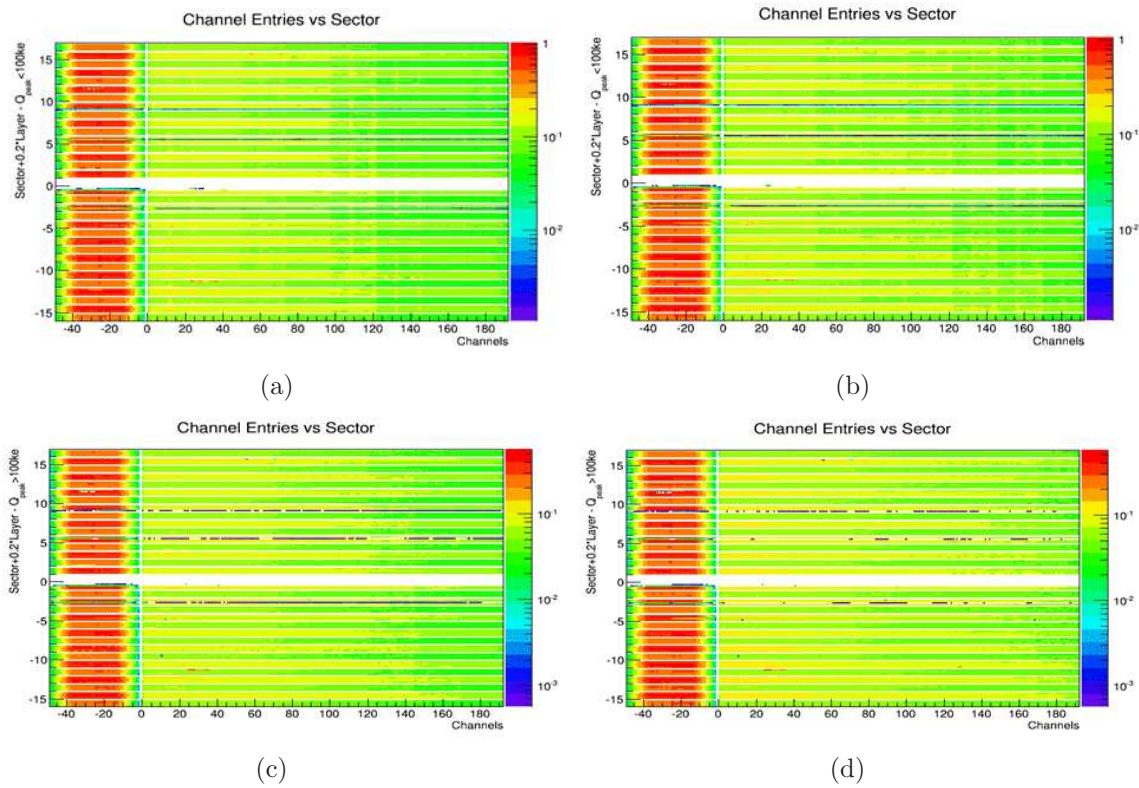
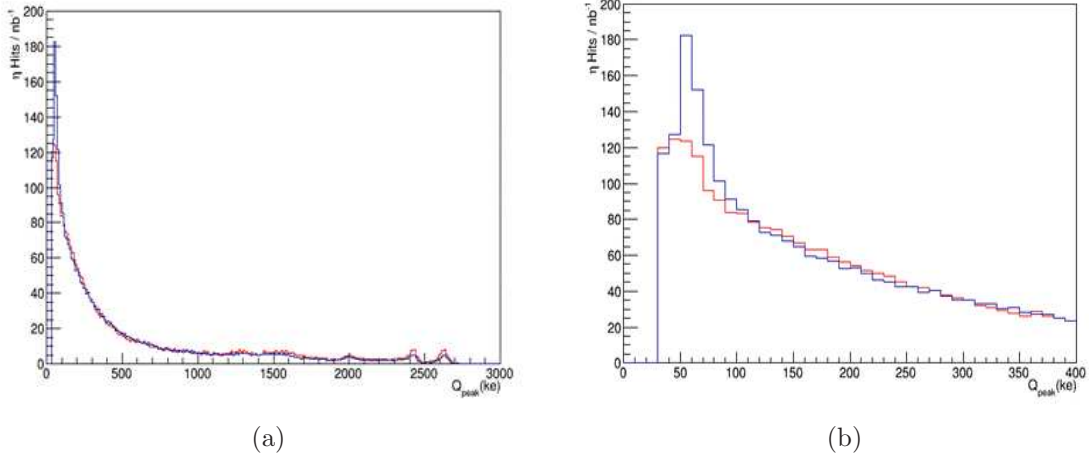


Figure 4.49: Comparison of the 25 ns data η charge (red line) with the 50 ns (blue line). Figure (b) is the zoomed Figure (a). The shapes are different but restored when clusters on segments are required (see Figure 4.37), which indicates different background composition.



(Figure 4.50, a Landau MPV value of $(172 \pm 36)\text{ ke}$) is found similar to the 50 ns value of $(181.7 \pm 0.1)\text{ ke}$ (Figure 4.37, which indicates different background composition. The peaking time of the small hits is further investigated and reveals that the 50 ns excess contamination concentrates around 0 ns (Figure 4.51). The overall time distributions do not look significantly different though (Figure 4.52).

The unspoiled hits on segments are also higher for the 25 ns , which is probably due to the smaller contamination with small amplitude hits, as Figure 4.53 presents. Despite that, the resolution slightly degraded to $(87.9 \pm 0.6)\text{ }\mu\text{m}$ (the residuals are presented in Figure 4.54) with the respect to the measured $2 - \text{samples}$ resolution (Figure 4.38) of $(84.1 \pm 0.6)\text{ }\mu\text{m}$.

The findings are used for precision 25 ns simulation production.

4.20 Post-Run-I Chambers Repair

During the Long Shutdown (LS1), between the Run-I and Run-II, the sectors with dead layers were repaired. Initially, the plan was to repair only the side C broken sectors, because only that wheel was lifted to the surface for the Insertable B-Layer replacement (mentioned in Section 3.4.1). However, the design of a new chamber extraction tool, schematically presented in Figure 4.55, made possible the side A chambers repair, owing to the small required space, which was enough to fit the space between the Barrel MDT

Figure 4.50: η charge on segments for 25 ns data fitted with a Landau distribution. The MPV is estimated to be $(172 \pm 36) \text{ ke}$ and is well compared to the $(181.7 \pm 0.1) \text{ ke}$ (see Figure 4.37) obtained with the 50 ns data.

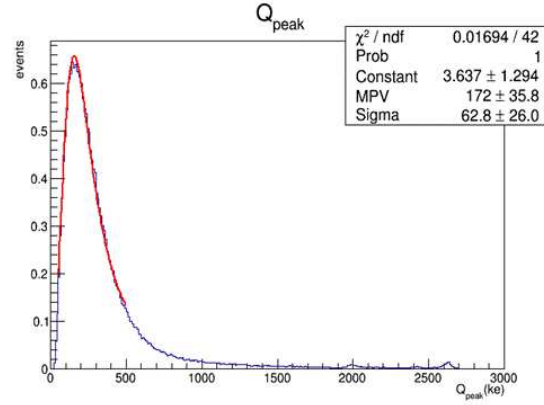


Figure 4.51: The peaking time (ns) of hits is presented as a function of the peak charge amplitude (ke) separately for 25 ns (a) and 50 ns (b) data. The hits excess in the case of 50 ns data is concentrated around 0 ns.

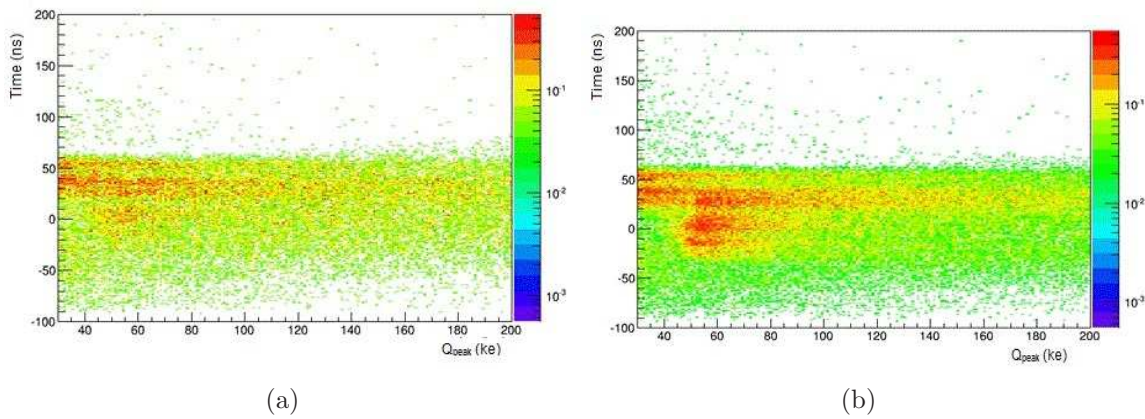


Figure 4.52: The peaking time of hits is presented for 25 ns (red line) and 50 ns (blue line).

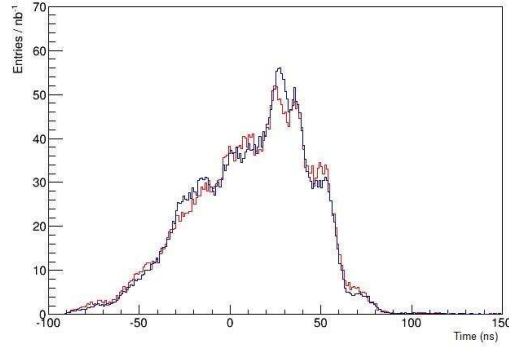


Figure 4.53: The unspoiled hits on segments for 25 ns (red line) and 50 ns (blue line) data. Due to the smaller contamination with small amplitude hits, the unspoiled fraction is higher for the 25 ns data.

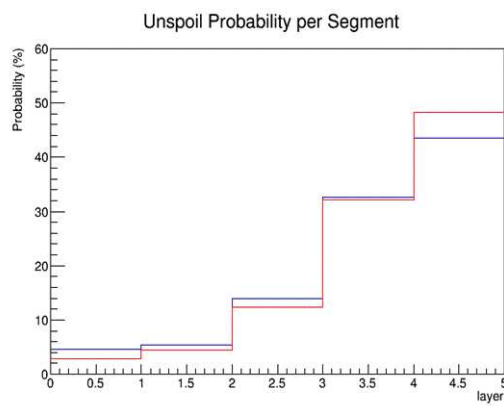
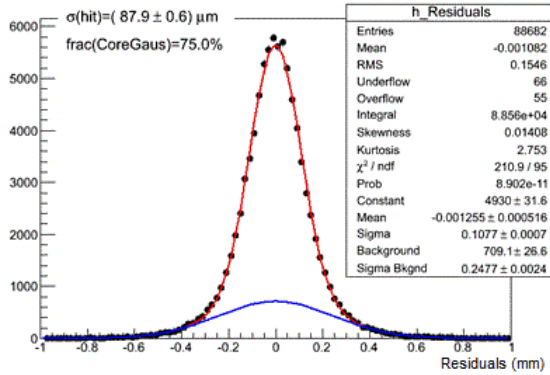


Figure 4.54: The residuals of 25 ns data fitted to give a resolution of $(87.9 \pm 0.6) \mu\text{m}$, slightly higher than the 2 – samples resolution of $(84.1 \pm 0.6) \mu\text{m}$ (4.38).



2720 and the EndCap Toroid.

2721 The chambers extracted were the *C*01, *C*03, *A*05 and *A*09 which had at least one
 2722 dead layer. The sector's *C*05 problem of less occupancy in half of one plane was not
 2723 repair. The assumption is that the problem is due to partial HV distribution failure,
 2724 but lack of absolute determination of the cause led to the decision of not extracting the
 2725 chamber.

2726 After the dismounting from the wheel, the chambers were moved to the laboratory
 2727 (Figure 4.56) where the surrounding copper shield, the on-detector electronics, the
 2728 cooling system and the gas were removed. The dead cables showed as curled, were
 2729 replaced and all the pieces put back together. The chambers in the laboratory run
 2730 on HV for one night and the DAQ tests showed no significant change of the pedestal
 2731 pattern which indicates the good operational level. Finally, the chambers were installed
 2732 on the wheel and further commissioning tests were followed to verify the functionality
 2733 of the chambers. The pedestal differences from the database values were not significant,
 2734 as shown in Figure 4.57 and this strongly proves the success of the repairs.

2735 4.21 Summary

2736 In this chapter, the CSC operations and performance during the Run-I presented.
 2737 Despite the problems occurred, caused by the dead layers and mainly by the limitation
 2738 of the readout electronics, the efficiency remained high. The official ATLAS reports,
 2739 presented in Figure 4.58, shows that the overall deadtime originating from the CSC
 2740 was marginal compared to other subsystems [17] and the online data quality was 100%
 2741 during the 2012 [18], i.e. the year that the majority of the Run-I data recorded.

Figure 4.55: Schematic view of the chamber removal tool used for the chambers extraction [16]. Due to the small required space the dismount of chambers from the cavern became possible.

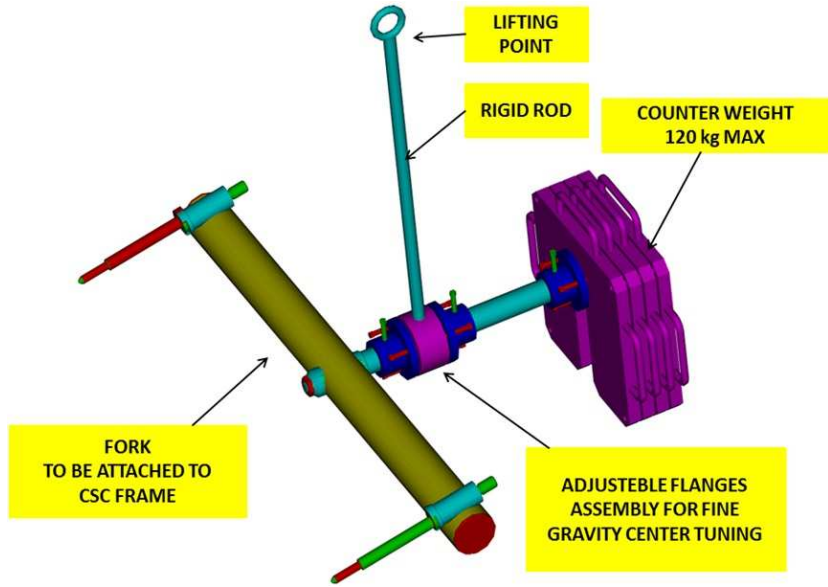


Figure 4.56: Pictures taken during the repair of the chambers. (a) shows the extraction of a broken chamber from the Wheel C (on the surface), (b) shows a chamber in the laboratory with the copper protection removed as well as the on-detector electronics (sitting on the planes), the colling system and the gas, (c) shows the layer with the damaged wire at the time of its removal (too delicate wires to be seen on the Picture) and (d) shows the chamber after the repair when the DAQ test took place. The final step was the installation and connection of the service on the wheel and another DAQ test for the absolute verification of the successful installation and repair.

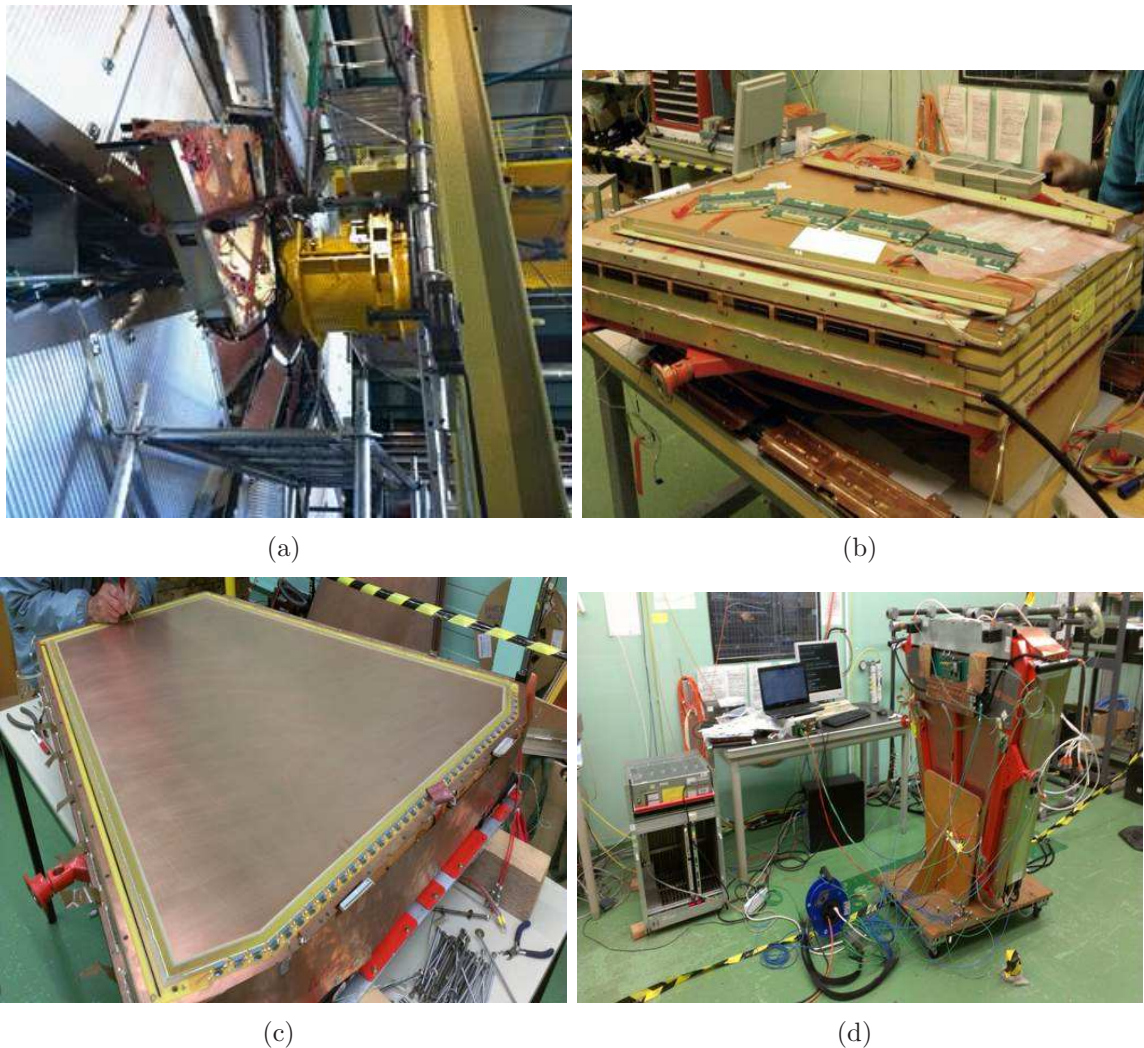


Figure 4.57: Pedestal runs deviations from the database values of Run-I for the repaired sectors after the installation for each channel (the ϕ channels are denoted with negative numbers). No significant change, above the uncertainty value, is observed.

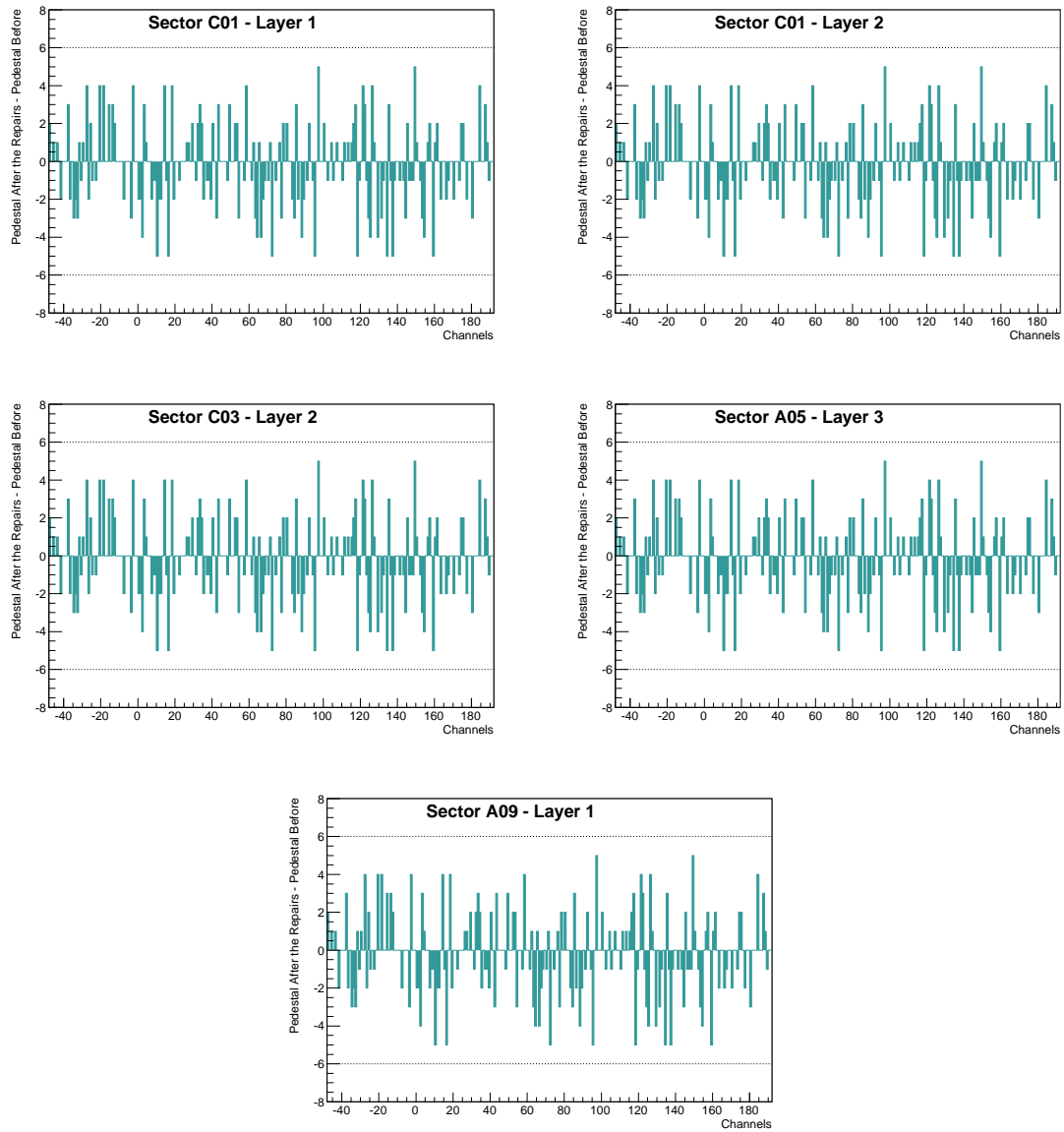
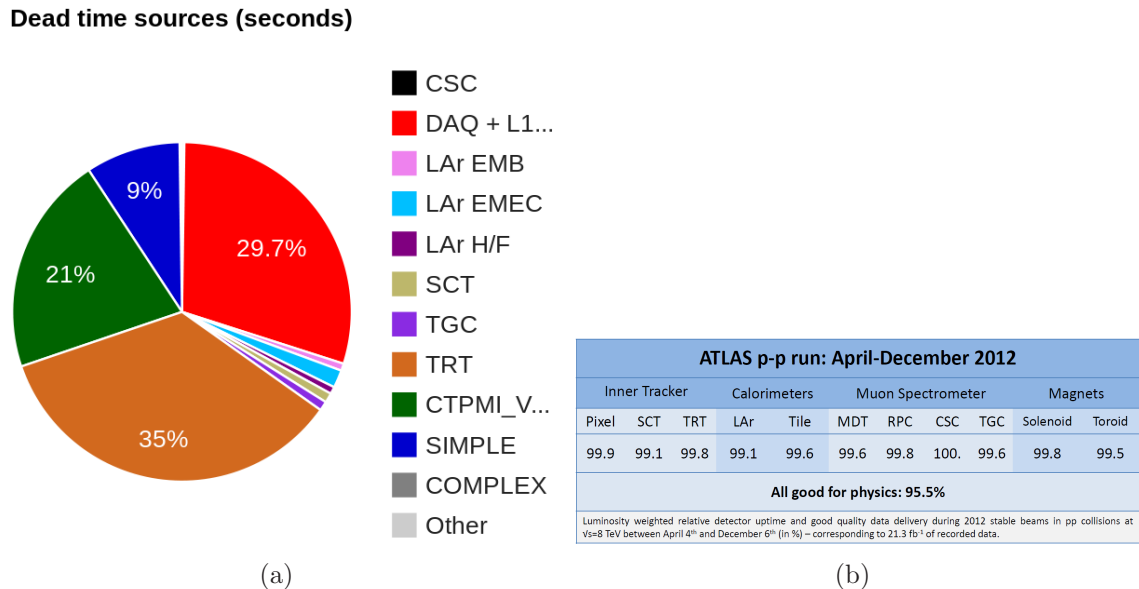


Figure 4.58: ATLAS official reports for the deadtime [17] and the online data quality efficiency [18]. Figure (a) shows that the deadtime caused by the CSC was marginal (8.1 *seconds*, 0.2%) compared to other subsystems and Figure (b) presents the luminosity weighted relative fraction of good quality data delivery by the various ATLAS subsystems during LHC fills with stable beams in pp collisions at $\sqrt{s} = 8$ TeV. Runs between April 4th and December 6th, corresponding to a recorded integrated luminosity of 21.3 fb^{-1} , are accounted. The CSC had 100% efficiency.



2742 Chapter Bibliography

2743 [1] ATLAS Collaboration, ATLAS muon spectrometer: Technical design report, 1997,
2744 CERN-LHCC-97-22, ATLAS-TDR-10.

2745 [2] T. Argyropoulos, K. A. Assamagan, B. H. Benedict, V. Chernyatin, E. Cheu,
2746 et al., Cathode strip chambers in ATLAS: Installation, commissioning and in situ
2747 performance, *IEEE Trans.Nucl.Sci.*, 56:1568–1574, 2009.

2748 [3] ATLAS Collaboration, Csc atlas photos, <http://www.atlas.ch/photos/muons-csc.html>.

2749 [4] Brookhaven National Laboratory Instrumentation Division, Cathode strip cham-
2750 bers, <http://www.inst.bnl.gov/programs/gasnobleddet/hepnp/csc.shtml>.

2751 [5] E Mathieson, Induced charge distributions in proportional detectors,
2752 <http://www.inst.bnl.gov/programs/gasnobleddet/publications/Mathieson%27sBook.pdf>.

2753 [6] I. Gough Eschrich, Readout electronics of the ATLAS muon cathode strip cham-
2754 bers, pages 247–250, 2008.

2755 [7] M. Schernau, CSC website, <http://positron.ps.uci.edu/~schernau>.

2756 [8] ATLAS Collaboration, CSC pulser calibration website,
2757 https://twiki.cern.ch/twiki/pub/Atlas/Pulser/CSC_Pulser_H.pdf.

2758 [9] ATLAS Collaboration, CSC calibration monitoring website,
2759 <https://atlas-csc-calib.web.cern.ch>.

2760 [10] D. L. Hawkins, ATLAS particle detector CSC ROD software design and imple-
2761 mentation, and, Addition of K physics to chi-squared analysis of FDQM.

2762 [11] R. Murillo, M. Huffer, R. Claus, R. Herbst, A. Lankford, et al., Software design of
2763 the ATLAS Muon Cathode Strip Chamber ROD, *J.Phys.Conf.Ser.*, 396:012031,
2764 2012.

2765 [12] I. Soloviev, User’s Guide Tools Manual, OKS Documentation, 2002, ATLAS DAQ
2766 Technical Note: 033.

2767 [13] SLAC, Muon CSC readout upgrade, <https://confluence.slac.stanford.edu/display/Atlas>.

2768 [14] ATLAS Collaboration, Muon Performance in Minimum Bias pp Collision Data at
2769 $\sqrt{s} = 7$ TeV with ATLAS, 2010.

2770 [15] ATLAS Collaboration, Data quality information public results,
2771 <https://twiki.cern.ch/twiki/bin/view/AtlasPublic/RunStatsPublicResults2010>.

2772 [16] A. Gordeev (BNL), Graphics and design of the CSC Removal Tool.

2773 [17] ATLAS Collaboration, ATLAS daq efficiency summary,
2774 https://atlasdaq.cern.ch/daq_eff_summary.

2775 [18] ATLAS Collaboration, Data quality information for 2010 and 2011 data,
2776 <https://twiki.cern.ch/twiki/bin/view/AtlasPublic/RunStatsPublicResults2010>.

2777 [19] G. C. Smith, J. Fischer, and V. Radeka, Capacitive Charge Division in Centroid
2778 Finding Cathode Readouts in MWPCs, *IEEE Trans.Nucl.Sci.*, 35:409–413, 1988.

2779 [20] E Mathieson and G C Smith, Reduction in Non-Linearity in Position-Sensitive
2780 MWPCs, *IEEE Trans.Nucl.Sci.*, 36:305–310, 1989.

2781 [21] J. Dailing, N. Drego, D. Hawkins, A. Lankford, Y. Li, et al., Performance and
2782 radiation tolerance of the ATLAS CSC on-chamber electronics, pages 196–200,
2783 2000.

2784 [22] J. Dailing, N. Drego, A. Gordeev, V. Grachev, D. Hawkins, et al., Off-detector
2785 electronics for a high-rate CSC detector, *IEEE Trans.Nucl.Sci.*, 51:461–464, 2004.

2786 [23] UCL, ATLAS TIM website, <http://www.hep.ucl.ac.uk/atlas/sct/tim/tim-muons.shtml>.

5

2787

2788

Search for $H \rightarrow ZZ^{(*)} \rightarrow 4\ell$ Decays

2789 5.1 Introduction

2790 The decay channel $H \rightarrow ZZ^{(*)} \rightarrow 4\ell$, where $\ell = e, \mu$, is one of the experimen-
2791 tally cleanest signatures for the search of the Standard Model Higgs boson. The
2792 main backgrounds to the $H \rightarrow ZZ^{(*)} \rightarrow 4\ell$ search at the LHC are the irreducible
2793 $ZZ^{(*)}/\gamma^* \rightarrow 4\ell$, while the reducible backgrounds are mainly $Z + QQ$ (Q=b or c quark),
2794 $t\bar{t}$, and $Z + light\, jets$ with one or more "fake" leptons in the final state.

2795 For the high mass region, $m_H \geq 160$ GeV, the two on-shell Z bosons from the
2796 Higgs decay allow for a selection which strongly suppresses the reducible backgrounds
2797 leaving only the irreducible $ZZ^{(*)} \rightarrow 4\ell$ component. At low Higgs masses, where one of
2798 the decay bosons is off-shell, contributions from $Z + jets$ and $t\bar{t}$ can be significant and
2799 tighter cuts are therefore applied to reduce these backgrounds to a level safely below
2800 the $ZZ^{(*)}$ continuum.

2801 Previous direct searches for the Higgs boson performed at the CERN Large Electron-
2802 Positron Collider (LEP) excluded at 95% confidence level (CL) the production of a SM
2803 Higgs boson with mass, m_H , less than 114.4 GeV [1]. The searches at the Fermilab
2804 Tevatron $p\bar{p}$ collider have excluded at 95% CL the region between $156 < m_H < 177$ GeV
2805 [2]. At the LHC, results from data collected in 2010 extended the search in the region
2806 between $200 < m_H < 600$ GeV by excluding a Higgs boson with cross section larger
2807 than 5 – 20 times the SM prediction [3].

2808 This analysis presents a general, model independent, search for Higgs candidate

Table 5.1: Luminosity collected during the 2011 and 2012 data taking [4], the data taking conditions and the data quality are also presented [5].

Year	Energy (\sqrt{s})	Peak luminosity	Pile-up ($< \mu >$)	Integrated luminosity	Data taking efficiency	Data quality efficiency
2011	7 TeV	$3.65 \times 10^{33} cm^{-2}s^{-1}$	9.1	$4.5 fb^{-1}$	$\sim 96.5\%$	$\sim 89.9\%$
2012	8 TeV	$7.73 \times 10^{33} cm^{-2}s^{-1}$	20.3	$20.3 fb^{-1}$	$\sim 95.5\%$	$\sim 95.3\%$

2809 events and background measurements, with focus on the muons background, using
 2810 data collected from the ATLAS experiment in 2011 and 2012. The available data were
 2811 analyzed per year of data taking due to different center of mass energies (\sqrt{s}), 7 TeV
 2812 for 2011 and 8 TeV for 2012.

2813 Several control regions are constructed by relaxing or inverting cuts applied for the
 2814 Higgs search and then are fitted simultaneously to extract the background contribution.
 2815 Estimations in the signal region are based on transfer factors. Hence, the efficiency of
 2816 the leptons in background environments is also studied, as an important factor of the
 2817 search. Comparisons between real data and Monte Carlo expectations are performed
 2818 in each of the analysis steps. Multiple cross checks are also presented to guaranty the
 2819 validity of the result.

2820 5.2 Data Samples

2821 The data, collected during the 2011 and 2012 years, are subjected to quality require-
 2822 ments and are rejected when recorded during periods when either the LHC declared
 2823 unstable beams or the relevant ATLAS detector components were not operating nomi-
 2824 nally. The events surviving this quality requirements are said to belong to the "Good
 2825 Runs List". The resulting integrated luminosity is $\mathcal{L} = 4.5 fb^{-1}$ for $\sqrt{s} = 7$ TeV and
 2826 $\mathcal{L} = 20.3 fb^{-1}$ for $\sqrt{s} = 8$ TeV, respectively, for all the final states. Details about the
 2827 data taking conditions [4] and efficiencies [5] are presented in Table 5.1.

2828 5.3 Monte Carlo (MC) samples

2829 5.3.1 Signal MC Samples and Cross Sections

2830 The $H \rightarrow ZZ^{(*)} \rightarrow 4\ell$ signal is modeled using the POWHEG Monte Carlo (MC)
 2831 event generator [6, 7], which calculates separately the gluon-gluon fusion and vector-

2832 boson fusion production mechanisms with matrix elements up to next-to-leading or-
 2833 der (NLO). The Higgs boson transverse momentum (p_T) spectrum in the gluons fu-
 2834 sion process is re-weighted to follow the calculation of Reference [8], which includes
 2835 QCD corrections up to NLO and QCD soft-gluon re-summations up to next-to-next-
 2836 to-leading logarithm (NNLL). POWHEG is interfaced to PYTHIA8.1 [9] for showering
 2837 and hadronization, which in turn is interfaced to PHOTOS [10] for quantum electro-
 2838 dynamics (QED) radiative corrections in the final state. PYTHIA is used to simulate
 2839 the production of a Higgs boson in association with a W or a Z boson as well as the
 2840 associated production with a top quark pair.

2841 The Higgs boson production cross sections and decay branching ratios, as well as
 2842 their uncertainties, are taken from References [11, 12]. The cross sections for the glu-
 2843 ons fusion process have been calculated to next-to-leading order (NLO) [13, 14, 15] and
 2844 next-to-next-to-leading order (NNLO) [16, 17, 18] in QCD. In addition, QCD soft-gluon
 2845 resummations calculated in the next-to-next-to-leading logarithm (NNLL) approxima-
 2846 tion are applied for the gluons fusion process [19]. NLO electroweak (EW) radiative
 2847 corrections are also applied [20, 21]. These results are compiled in References [22, 23, 24]
 2848 assuming factorization between QCD and EW corrections.

2849 The cross sections for the vector-boson fusion process are calculated with full NLO
 2850 QCD and EW corrections [25, 26, 27], and approximate NNLO QCD corrections are
 2851 available [28]. The cross sections for the associated WH/ZH production processes are
 2852 calculated at NLO [29] and at NNLO [30] in QCD, and NLO EW radiative correc-
 2853 tions [31] are applied. The small contribution from the associated production with a $t\bar{t}$
 2854 pair ($q\bar{q}/gg \rightarrow t\bar{t}H$, denoted $t\bar{t}H$) is now taken into account in the analysis. The cross
 2855 sections for the $t\bar{t}H$ process are estimated up to NLO QCD [32, 33, 34, 35, 36].

2856 The Higgs boson decay branching ratio [37] to the four-leptons final state is predicted
 2857 by PROPHECY4F [38, 39], which includes the complete NLO QCD+EW corrections,
 2858 the interference effects between identical final-state fermions, and the leading two-loop
 2859 heavy Higgs boson corrections to the four-fermion width. Table 5.2 gives the production
 2860 cross sections and branching ratios for $H \rightarrow ZZ^{(*)} \rightarrow 4\ell$ which are used to normalize
 2861 the signal MC samples for several Higgs boson masses.

2862 The QCD scale uncertainties for $m_H = 125$ GeV amount to $^{+7}_{-8}\%$ for the gluons
 2863 fusion process and $\pm 1\%$ for the vector-boson fusion and associated WH/ZH production
 2864 processes. The mass-dependent uncertainty in the production cross section due to
 2865 uncertainties in the parton distribution function (PDF) and α_s are $\pm 8\%$ for gluon-
 2866 initiated processes and $\pm 4\%$ for quark-initiated processes, estimated in the mass range
 2867 around 125 GeV by following the prescription in Reference [40] and by using the PDF
 2868 sets of CTEQ [41], MSTW [42] and NNPDF [43]. The PDF uncertainties are assumed
 2869 to be 100% correlated for processes with identical initial states, regardless of their being
 2870 signal or background [40, 44, 41, 42, 43].

Table 5.2: Higgs boson production cross sections for gluons fusion, vector-boson fusion and associated production with a W or Z boson in pp collisions at \sqrt{s} of 7 TeV and 8 TeV [11]. The quoted uncertainties correspond to the total theoretical systematic uncertainties. The production cross section for the associated production with a W or Z boson is negligibly small for $m_H > 300$ GeV. The decay branching ratio for $H \rightarrow ZZ^{(*)} \rightarrow 4\ell$, with $\ell = e$ or μ , is reported in the last column [11].

m_H [GeV]	$\sigma(gg \rightarrow H)$ [pb]	$\sigma(qq' \rightarrow Hqq')$ [pb]	$\sigma(q\bar{q} \rightarrow WH)$ [pb]	$\sigma(q\bar{q} \rightarrow ZH)$ [pb]	$\sigma(gg \rightarrow Htt')$ [pb]	$\text{BR}(H \rightarrow ZZ^{(*)} \rightarrow 4\ell)$ [10^{-3}]
$\sqrt{s} = 7 \text{ Tev}$						
123	15.6 ± 1.6	1.25 ± 0.03	0.61 ± 0.02	0.35 ± 0.01	0.09 ± 0.01	0.103 ± 0.005
125	15.1 ± 1.6	1.22 ± 0.03	0.58 ± 0.02	0.34 ± 0.01	0.09 ± 0.01	0.125 ± 0.005
127	14.7 ± 1.5	1.20 ± 0.03	0.55 ± 0.02	0.32 ± 0.01	0.08 ± 0.01	0.148 ± 0.006
$\sqrt{s} = 8 \text{ Tev}$						
123	19.9 ± 2.1	$1.61^{+0.04}_{-0.05}$	0.74 ± 0.02	0.44 ± 0.02	$0.14^{+0.01}_{-0.02}$	0.103 ± 0.005
125	19.3 ± 2.0	1.58 ± 0.04	0.70 ± 0.02	0.42 ± 0.02	$0.13^{+0.01}_{-0.02}$	0.125 ± 0.005
127	18.7 ± 1.9	1.55 ± 0.04	0.67 ± 0.02	0.40 ± 0.02	$0.13^{+0.01}_{-0.02}$	0.148 ± 0.006

5.3.2 MC Background Samples

The $ZZ^{(*)}$ continuum background is modeled using POWHEG [45] for quark-antiquark annihilation and GG2ZZ [46] for gluon fusion. The mass-dependent PDF and α_s scale uncertainties are parametrized as recommended in Reference [12]. The QCD scale uncertainty has a $\pm 5\%$ effect on the expected $ZZ^{(*)}$ background at 125 GeV, and the effect due to the PDF and α_s uncertainties is $\pm 4\%$ ($\pm 8\%$) at 125 GeV for quark-initiated (gluon-initiated) processes.

The $Z +$ jets production is modeled using ALPGEN [47] interfaced to PYTHIA for hadronization and showering and is divided into two sources: $Z +$ light jets, which includes $Zc\bar{c}$ in the massless c -quark approximation, $Zb\bar{b}$ from parton showers, and $Zb\bar{b}$ using matrix element calculations that take into account the b -quark mass. The MLM [48] matching scheme is used to remove any double counting of identical jets produced via the matrix element calculation and the parton shower, but this scheme is not implemented for b -jets. Therefore, $b\bar{b}$ pairs with separation $\Delta R = \sqrt{(\Delta\phi)^2 + (\Delta\eta)^2} > 0.4$ between the b -quarks are taken from the matrix-element calculation, whereas for $\Delta R < 0.4$ the parton-shower $b\bar{b}$ pairs are used. In this search the $Z +$ jets background is normalized using control samples from data. For comparisons with simulation, the QCD NNLO FEWZ [49, 50] and MCFM [51] cross section calculations are used for inclusive Z boson and $Zb\bar{b}$ production, respectively.

The $t\bar{t}$ background is modeled using POWHEG interfaced to PYTHIA for parton

shower hadronization, to PHOTOS for quantum electrodynamics (QED) radiative corrections and TAUOLA [52, 53] for the simulation of τ lepton decays.

SHERPA [54] is used for the WZ production simulation.

Generated events are fully simulated using the ATLAS detector simulation [55] within the GEANT4 framework [56]. The simulation of the additional pp interactions (pileup) is done in a separate step in the simulation chain, during digitization. Here minimum bias events, which were previously simulated, are superimposed on the simulated signal event. The distribution of the number of pileup events reproduces the bunch structure and the average number of interactions of the run periods.

The cross sections and background samples used for the data comparison are summarized in Table 5.3. The corresponding Feynman diagrams of the processes are presented in Figure 5.1. All the MC samples used for this analysis are summarized in the Appendix A analytically.

Figure 5.1: Production mechanisms of the ZZ , $Zb\bar{b}$ and $t\bar{t}$ backgrounds of the $H \rightarrow ZZ^{(*)} \rightarrow 4\ell$.

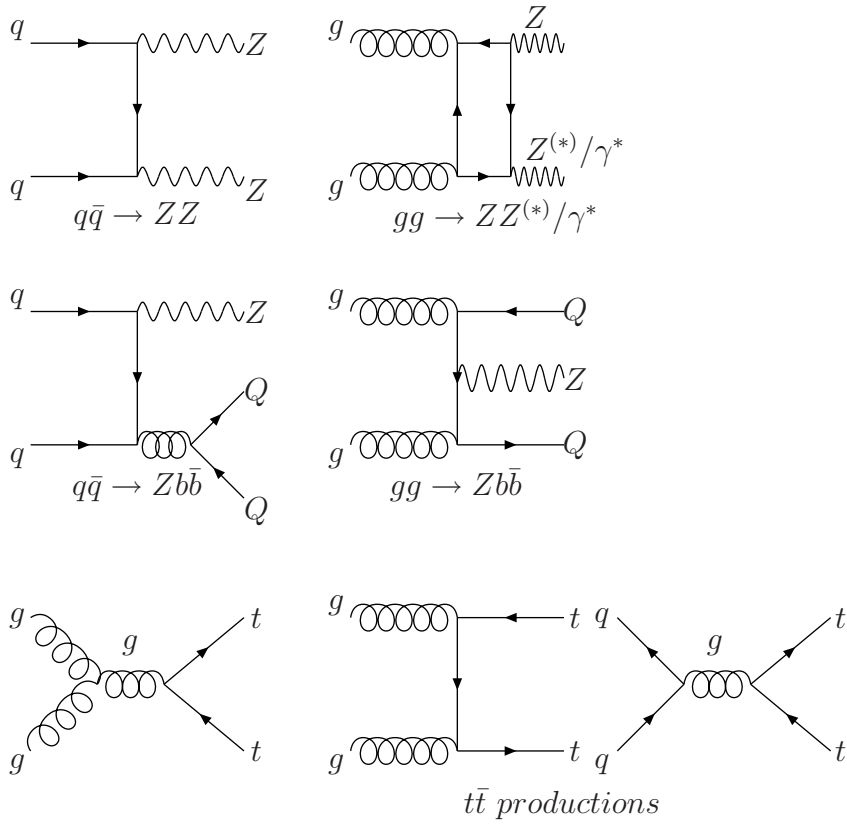


Table 5.3: Higgs backgrounds cross sections in pp collisions at \sqrt{s} of 7 TeV and 8 TeV and the generated MC events.

Background Sample	$\sqrt{s} = 7$ TeV			$\sqrt{s} = 8$ TeV		
	Cross Section (pb)	k-factor	Events	Cross Section (pb)	k-factor	Events
$Z(\rightarrow \mu^+ \mu^-) bb$ 3 ℓ filter Np0	646.234	1.6	249899	837.906	1.6	499897
$Z(\rightarrow \mu^+ \mu^-) bb$ 3 ℓ filter Np1	328.405	1.6	148000	438.495	1.6	297899
$Z(\rightarrow \mu^+ \mu^-) bb$ 3 ℓ filter Np2	116.831	1.6	91500	159.779	1.6	169499
$Z(\rightarrow e^+ e^-) bb$ 3 ℓ filter Np0	645.316	1.6	249998	834.997	1.6	499995
$Z(\rightarrow e^+ e^-) bb$ 3 ℓ filter Np1	328.759	1.6	148000	437.617	1.6	297998
$Z(\rightarrow e^+ e^-) bb$ 3 ℓ filter Np2	116.276	1.6	91000	158.952	1.6	169499
$Z(\rightarrow \mu^+ \mu^-) bb$ 4 ℓ filter Np0	29.820	1.6	1194396	38.533	1.6	2488592
$Z(\rightarrow \mu^+ \mu^-) bb$ 4 ℓ filter Np1	21.159	1.6	678199	28.081	1.6	1383294
$Z(\rightarrow \mu^+ \mu^-) bb$ 4 ℓ filter Np2	9.886	1.6	241296	13.592	1.6	479518
$Z(\rightarrow e^+ e^-) bb$ 4 ℓ filter Np0	29.620	1.6	1195393	38.146	1.6	2488990
$Z(\rightarrow e^+ e^-) bb$ 4 ℓ filter Np1	21.033	1.6	678599	27.905	1.6	1453390
$Z(\rightarrow e^+ e^-) bb$ 4 ℓ filter Np2	9.786	1.6	241076	13.520	1.6	479018
$Z(\rightarrow \mu^+ \mu^-)$ Np0	712000	1.23	6615230	718910	1.18	12907286
$Z(\rightarrow \mu^+ \mu^-)$ Np1	155000	1.23	1334296	175810	1.18	6533889
$Z(\rightarrow \mu^+ \mu^-)$ Np2	48800	1.23	1999941	58805	1.18	3580483
$Z(\rightarrow \mu^+ \mu^-)$ Np3	14200	1.23	549896	15589	1.18	204799
$Z(\rightarrow \mu^+ \mu^-)$ Np4	3770	1.23	150000	3907	1.18	129800
$Z(\rightarrow \mu^+ \mu^-)$ Np5	1120	1.23	50000	1193	1.18	239200
$Z(\rightarrow e^+ e^-)$ Np0	712000	1.23	6618284	718890	1.18	12908972
$Z(\rightarrow e^+ e^-)$ Np1	155000	1.23	1334897	75600	1.18	7029177
$Z(\rightarrow e^+ e^-)$ Np2	48800	1.23	2004195	58849	1.18	3580989
$Z(\rightarrow e^+ e^-)$ Np3	14200	1.23	549949	15560	1.18	1004994
$Z(\rightarrow e^+ e^-)$ Np4	3770	1.23	149948	3932	1.18	428597
$Z(\rightarrow e^+ e^-)$ Np5	1120	1.23	50000	1199	1.18	239700
$t\bar{t}$	80070	1.203	9984443	252890	0.105	37909974
WZ	11485	1.00	999896	9757*0.274	1.06	5998980
$ZZ^* \rightarrow 4\mu$	46.6	1.00	100000	69.75	1.00	1081496
$ZZ^* \rightarrow 4e$	46.6	1.00	100000	69.75	1.00	1081496
$ZZ^* \rightarrow 2e2\mu$	99.1	1.00	199900.	145.37	1.00	1599696
$gg \rightarrow ZZ^* \rightarrow 4\mu$	0.43	1.00	65000	0.6725	1.00	90000
$gg \rightarrow ZZ^* \rightarrow 4e$	0.43	1.00	65000	0.6725	1.00	90000
$gg \rightarrow ZZ^* \rightarrow 2e2\mu$	0.86	1.00	65000	1.345	1.00	90000

5.4 Leptons Definition

Leptons identification and reconstruction are of particular importance for the $H \rightarrow ZZ^{(*)} \rightarrow 4\ell$ channel. In this section, the algorithms are briefly described and the baseline electron/muon selection for the analysis is defined.

5.4.1 Electron reconstruction and identification

Electron candidates are required to have a well-reconstructed ID track pointing to an electromagnetic calorimeter cluster [57]. The cluster longitudinal and transverse shower profiles are required to be consistent with those expected for the electromagnetic showers. Tracks associated with electromagnetic clusters are fitted using a Gaussian-Sum Filter [58], which allows for bremsstrahlung energy losses to be taken into account.

The electron identification is based on requirements on variables that provide good separation between isolated electrons and hadronic jets faking electrons. In the central region of $|\eta| < 2.47$, variables describing the longitudinal and transverse shapes of the electromagnetic showers in the calorimeters, the properties of the tracks in the inner detector, e.g. number of b-layer and silicon hits, signal in the TRT, or change in the momentum from the beginning to the end of the track from bremsstrahlung, as well as the matching between tracks and energy clusters are used to discriminate against the different background sources.

5.4.1.1 Electron Identification and Reconstruction in the 2011

For the 2011 dataset, the identification criteria for central-electron candidates are implemented based on rectangular cuts on the calorimeter, tracking, as well as on combined track-cluster variables [59]. These requirements are optimized in 10 detector-motivated cluster- η bins and 11 E_T bins (from 5 to 80 GeV), in order to provide good separation between signal (isolated) electrons and background from hadrons faking electrons, non-isolated electrons (e.g. from semi-leptonic decays of heavy-flavors quarks), and electrons from photon conversions.

For the 2011 analysis the selection criteria are designed for general physics-analysis use and the menu is called "loose++". It corresponds to an intermediate menu between the loose and medium working points. Shower shape variables in both the first and the second layers of the EM calorimeter are used and cuts are applied on the fraction of the energy deposited in the hadronic and the electromagnetic calorimeters. Requirements on the quality of the electron track and track-cluster matching are also applied.

2936 **5.4.1.2 Electron Identification and Reconstruction in the 2012**

2937 For the 2012 dataset a multivariate analysis (MVA) technique [60] is employed to
 2938 define the electron identification, since it allows for simultaneous evaluation of several
 2939 properties when making a selection decision [59]. Out of the different MVA techniques,
 2940 the maximum Likelihood (LH) approach has been chosen for the electron identification
 2941 because of its simple construction.

2942 The electron LH makes use of signal and background probability density functions
 2943 (PDFs) of the discriminating variables. Based on these PDFs, an overall probability is
 2944 calculated for the object to be signal or background-like. The signal and background
 2945 probabilities for a given electron are combined into a discriminant on which a cut is
 2946 applied:

$$d_{\mathcal{L}} = \frac{\mathcal{L}_S}{\mathcal{L}_S + \mathcal{L}_B}, \quad \mathcal{L}_S(\vec{x}) = \prod_{i=1}^n P_{s,i}(x_i) \quad (5.1)$$

2947 where \vec{x} is the vector of variable values and $P_{s,i}(x_i)$ is the value of the signal probability
 2948 density function of the i^{th} variable evaluated at x_i . In the same way, $P_{b,i}(x_i)$ refers to
 2949 the background probability function. The choice of the cut value on the discriminant
 2950 determines the signal efficiency/background rejection of the Likelihood working point.

2951 Signal and background PDFs used for the electron LH Particle Identification (PID)
 2952 are obtained from data. The variables counting the hits on the track are not used as
 2953 PDFs in the LH, but are left as simple cuts, since every electron should have a high
 2954 quality track to allow for a robust 4-vector measurement. The LH menu cuts on the
 2955 LH discriminant called Loose-LH has been chosen to define the electron identification
 2956 of this analysis out of the three possible working points namely loose, medium, tight.

2957 **5.4.1.3 Electrons E-p Combination**

2958 In order to improve the energy resolution of low E_T electrons and electrons in prob-
 2959 lematic regions of the electromagnetic calorimeter, such as the crack region of the EM
 2960 calorimeter in $1.37 < |\eta| < 1.52$, where its response tends to be poorer, a combi-
 2961 nation of the track momentum and the cluster energy is performed [59]. Specifically, the com-
 2962 bination is applied to electrons with $E_T < 30$ GeV and $\eta < 1.52$, which have consistent
 2963 Inner Detector and cluster energy measurements, as judged by the ratio:

$$\text{Significance } (E_{\text{Cluster}} - p_{\text{Track}}) = \frac{|E_T^{\text{Cluster}} - E_T^{\text{Track}}|}{\sqrt{\sigma_{E_T^{\text{Cluster}}}^2 + \sigma_{E_T^{\text{Track}}}^2}} < 5. \quad (5.2)$$

2964 The combination method employs a maximum likelihood fit of E_T^{Track} and E_T^{Cluster} ,
 2965 using probability density functions (PDFs) which are generated by fitting the $E_T^{\text{Track}}/E_T^{\text{Truth}}$
 2966 and $E_T^{\text{Cluster}}/E_T^{\text{Truth}}$ distributions with a Crystal Ball in order to take into account both

Table 5.4: Electron selection criteria for 2011 and 2012 analysis.

Electron Selection	
Menu	Loose++ (2011), Loose-LH (2012)
Kinematics	$E_T > 7 \text{ GeV}$
$ \eta $ Region	< 2.47
Improved Resolution	E-p Combination

2967 the Gaussian core resolution and the tails of the distributions. The events used to build
 2968 the PDFs come from single e^\pm Monte Carlo samples with flat E_T spectra on $7 < E_T <$
 2969 80 GeV, with all constituent electrons required to have Significance ($E_{\text{Cluster}} - E_{\text{Track}} <$
 2970 5).

2971 Electrons are placed into categories according to their E_T and $|\eta|$ along with their ap-
 2972 proximate bremsstrahlung loss (quantified as $|\Delta E_{\text{Track}}|/E_{\text{Track}}$ between the momentum
 2973 at the perigee and the momentum at the last track measurement), with separate distri-
 2974 butions of $\mathcal{F}_1\left(\frac{E_T^{\text{Track}}}{x}\right)$ and $\mathcal{F}_2\left(\frac{E_T^{\text{Cluster}}}{x}\right)$ for each category, where $x = (E_T^{\text{Track}} + E_T^{\text{Cluster}})/2$.
 2975 The product:

$$- \log \left[\mathcal{F}_1\left(\frac{E_T^{\text{Track}}}{x}\right) \cdot \mathcal{F}_2\left(\frac{E_T^{\text{Cluster}}}{x}\right) \right] \quad (5.3)$$

2976 is minimized with respect to the variable x , yielding the combined transverse momen-
 2977 tum for a given electron, as well as its error. Any electrons which do not meet the
 2978 requirements on E_T , $|\eta|$, and significance($E_{\text{Cluster}} - E_{\text{Track}}$) instead have their four mo-
 2979 ments built using the default cluster energy and the track direction.

2980 The likelihood combination method shows the greatest potential for improvement
 2981 in cases of low E_T electrons, and electrons in the central $|\eta|$ region of the detector. For
 2982 electrons in the forward region ($1.37 < |\eta| < 2.5$), or those with high E_T the cluster-
 2983 based transverse momentum is used. For the $H \rightarrow ZZ^{(*)} \rightarrow 4\ell$ case the improvement
 2984 of the E-p combination is seen in the $4e$ and $2\mu 2e$ channels and corresponds to an
 2985 approximate reduction of 4% and 3.5% respectively in the width of the $m_{4\ell}$ distribution.

2986 The electron criteria are summarized in Table 5.4 for both 2011 and 2012 analysis
 2987 selection.

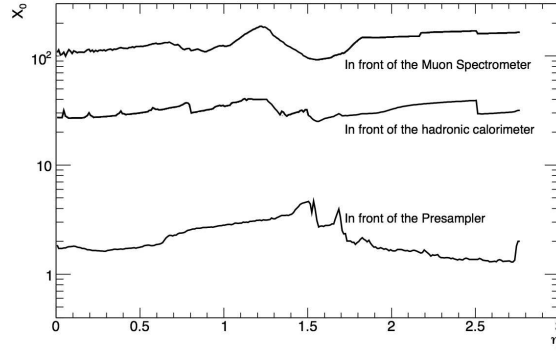
2988 5.4.2 Muon Identification and Reconstruction

2989 In the ATLAS four kind of muon candidates are distinguished depending on the way
 2990 they are reconstructed: *standalone muons*, *combined muons*, *segment tagged muons*,
 2991 and *calorimeter tagged muons* [61].

- *Standalone muons* (SA): This reconstruction is based entirely on the muon spectrometer information, independently of the inner detector. It is initiated locally in a muon chamber by a search for straight line track segments in the bending plane. A minimum of two track segments in different muon stations are combined to form a muon track candidate using three - dimensional tracking in the magnetic field. The track parameters are obtained from the muon spectrometer track fit and are extrapolated to the interaction point taking into account both multiple scattering and energy loss in the calorimeters. These muons are used in the $|\eta| > 2.5$ region outside the ID coverage, to increase the overall analysis acceptance.
- *Combined muons* (CB): The trajectory measured by the ID is associated with a previously defined Standalone muon, by performing a χ^2 -test, defined by the difference between the respective track parameters weighted by their combined covariance matrices. The parameters are evaluated at the point of the closest approach to the beam axis. The track parameters are derived from a χ^2 fit on the two tracks or the refit of the ID and MS hits associated with the track.
- *Segment tagged muons* (ST): A track in the ID is identified as a muon if the trajectory extrapolated to the MS can be associated with track segments in the precision muon chambers. If a segment is sufficiently close to the predicted track position, then the inner detector track is tagged as corresponding to a muon. ST muons adopt the measured parameters of the associated ID track.
- *Calorimeter tagged muons* (Calo Muons): A trajectory in the ID is identified as a muon if the associated energy depositions in the calorimeters are compatible with the hypothesis of a minimum ionizing particle. Their use in the analysis is to cover the region of $|\eta| < 0.1$, which is not equipped with muon chambers, and only if $p_T > 15$ GeV, since the calorimeter muon identification algorithm is optimized for muons with $p_T > 15$ GeV. The material thickness traversed by the muons is over 100 radiation lengths (X_0), as presented in Figure 5.2. By passing through this material, muons undergo electromagnetic interactions which result in a partial loss of their energy. Since over 80% of this material is in the instrumented areas of the calorimeters, the energy loss can be measured.

In the first years of the LHC operation, ATLAS used two reconstruction algorithms [63], the STACO and MUID, as already discussed in Section 4.9, following different pattern recognition strategies. In this analysis the STACO algorithm is used. Between the years of 2011 and 2012 data taking, the changes in the muon reconstruction do not concern the algorithmic part of the STACO but were a mixture of software and hardware updates, the list of which is given below:

Figure 5.2: Material distribution before the Muon Spectrometer in ATLAS as a function of η . The material is expressed in radiation lengths (X_0) [62].



- *Inclusion of EE chambers:* During the Christmas shutdown of 2011, the staged Extended EndCap chambers in the η region between 1.1 and 1.3 namely the *EE* chambers have been installed and commissioned. More specifically the totality of the *EE* chambers in side C and 3 out of 16 sectors in side A have been installed, resulting in an improved reconstruction efficiency in the transition region between the barrel and the EndCap ($\eta \approx -1.2$), as they allow for a three-point momentum measurement in this region.
- *Improved reconstruction in the CSC chambers:* As already discussed in Section 4.9, the reconstruction of the Cathode Strip Chambers that equip the Muon Spectrometer in the $|\eta| > 2.0$ has been considerably improved as described in Chapter 4, resulting in an overall improvement of the momentum resolution in this region.
- *Inner Detector hit requirements:* The ID hit quality requirements of the muon tracks of all categories (except SA tracks) have been slightly modified. This allowed to remove some inconsistency with respect to the calorimeter muon selection, to fix a problem in the 2012 data of the Pixel sensor status not propagated to the offline reconstruction and to remove non-uniformity of the ID efficiency as a function of η .
- *ID, MS alignment improvement:* Improved alignment constants were provided during the 2012 reprocessing for both the ID and the MS system.

The list of the ID hit requirements that the combined, segment tagged and calo muons are required to fulfill is given in Table 5.5. The standalone muons do not have an ID track, consequently there are no ID requirements, but they are required

Table 5.5: List of the Inner Detector hit requirements for combined, segment tagged and calo muons for the 2011 and 2012 datasets.

ID Hit Requirements 2011	
ID Si hit requirement	Expect B-layer hit = false or Number of B-layer hits ≥ 1
	No. of Pixel hits + No. of crossed inactive Pixel sensors > 1
	No. of SCT hits + No. of crossed inactive SCT sensors > 5
	No. of Pixel holes + No. of SCT holes < 3
TRT hit requirements: $ \eta < 1.9$	Hits + Outliers > 5 & $Outliers < 0.9(Hits + outliers)$
TRT hit requirements: $ \eta \geq 1.9$	if (Hits + Outliers > 5): $Outliers < 0.9(Hits + outliers)$
ID Hit requirements 2012	
ID Si hit requirement	No. of Pixel hits + No. of crossed inactive Pixel sensors > 0
	No. of SCT hits + No. of crossed inactive SCT sensors > 4
	No. of Pixel holes + No. of SCT holes < 3
TRT hit requirements: $0.1 < \eta \leq 1.9$	Hits + Outliers > 5 & $Outliers < 0.9(Hits + outliers)$

Table 5.6: Muon selection Criteria in both 2011 and 2012.

2011 and 2012 Muon Selection	
ID cuts	as in Table 5.5
CB,ST	$p_T > 6$ GeV, $ \eta < 2.7$
Kinematics	Calo Muons $p_T > 15$ GeV, $ \eta < 0.1$
	SA $p_T > 6$ GeV, $2.5 < \eta < 2.7$
Overlap	Reject Calo if $DR_{Calo-STACO} < 0.1$
Removal	Reject SA if $DR_{SA-ST} < 0.1$
	Allow maximum one Calo muon or SA

3052 to be identified by all three available muon stations. The muons selection criteria are
 3053 summarized in Table 5.6.

3054 5.5 Trigger

3055 The trigger signatures for the online selection of four-lepton events are single and
 3056 di-lepton triggers. Due to the higher instantaneous luminosity and pile-up levels of
 3057 the 2012 data-taking, both single- and di-lepton trigger thresholds have been raised,
 3058 and isolation cuts have been introduced for single lepton triggers. A summary of the
 3059 triggers that are used in the 2011 analysis is shown in Table 5.7 and the corresponding
 3060 2012 triggers are shown in Table 5.8. The "i" in the name denotes that the trigger item

3061 is required to be isolated. The isolation cut is applied at the Event Filter level only
 3062 and requires the sum of the p_T of tracks (with $p_T > 1$ GeV) in a cone of size $\Delta R < 0.2$
 3063 around the lepton track, to be less than 10% of the lepton p_T . The same trigger criteria
 3064 applied also on MC to achieve the same level of efficiency with the data.

3065 In the four-lepton event selection it is required that either one of the leptons matches
 3066 the single-lepton trigger, or that two leptons match the di-lepton trigger, even though
 3067 the requirement of trigger matching has a negligible impact on the total event selection
 3068 efficiency.

3069 The trigger efficiency with respect to the 2012 offline analysis requirements for a
 3070 simulated Higgs signal (gluon-fusion with $m_H = 130$ GeV) is estimated to be:

- 3071 • 4μ : 97.6%
- 3072 • $2e2\mu/2\mu2e$: 97.3%
- 3073 • $4e$: 99.7%

Table 5.7: Summary of the triggers used during the 2011 data taking. In each data taking period, the OR of single and di-lepton triggers is used to select each signature. The naming convention is explained in the text.

Single-lepton triggers				
Period	B-I	J	K	L-M
4μ	EF_mu18_MG	EF_mu18_MG_medium	EF_mu18_MG_medium	EF_mu18_MG_medium
$4e$	EF_e20_medium	EF_e20_medium	EF_e22_medium	EF_e22vh_medium1
$2e2\mu$			4μ OR $4e$	
Di-lepton triggers				
Period	B-I	J	K	L-M
4μ	EF_2mu10_loose	EF_2mu10_loose	EF_2mu10_loose	EF_2mu10_loose
$4e$	EF_2e12_medium	EF_2e12_medium	EF_2e12T_medium	EF_2e12Tvh_medium
$2e2\mu$		4μ OR $4e$ OR EF_e10_medium_mu6		

3074 The trigger efficiency in data and MC is measured using tag and probe methods [64]
 3075 based on $Z \rightarrow \mu^+\mu^-$ and $Z \rightarrow e^+e^-$ events. The efficiency is computed in bins of the
 3076 phase space $\epsilon_i = (p_{T_i}, \eta_i, \phi_i)$ and is defined for p_T values above the trigger threshold.
 3077 Differences between trigger efficiency in data and MC is accounted for re-weighting MC
 3078 events according to the single-lepton efficiency computed in phase-space bins η_i of all
 3079 the reconstructed leptons in the event. The trigger efficiency scale factor for the single
 3080 lepton triggers is computed as:

$$SF_{trigger} = \frac{[1 - \Pi_i(1 - \epsilon(\eta_i))]_{Data}}{[1 - \Pi_i(1 - \epsilon(\eta_i))]_{MC}}. \quad (5.4)$$

3081 No correction is applied for the dilepton triggers.

Table 5.8: Summary of the triggers used during the 2012 data taking for the four analysis channels. When multiple chains are indicated, it is intended that the OR among them is requested. The naming convention is explained in the text.

Channel	Single-lepton	Di-lepton
4e	e24vhi_medium1, e60_medium1	2e12Tvh_loose1, 2e12Tvh_loose1_L2StarB(data only)
4 μ	mu24i_tight, mu36_tight	2mu13, mu18_mu8_EFFS
2e2 μ	4 μ OR 4e OR e12Tvh_medium1_mu8 OR e24vhi_loose1_mu8	

5.6 Events selection

5.6.1 Analysis Events Selection

The analysis starts by pre-selecting leptons as described in Section 5.4. The standard selection of primary vertexes is used in this analysis, meaning that the vertex selected as the primary one is the vertex with the largest p_T sum in the event. Since the four leptons emerge from the primary vertex, the lepton tracks must have distances $|\Delta z_0| < 10$ mm from the primary vertex along the proton beam pipe. To reduce the cosmic background an additional cut on the transverse impact parameter is required ($|\Delta d_0| < 1$ mm).

The event selection criteria (consisting of lepton quality, kinematic, isolation and impact parameter significance cuts) are presented in Table 5.9. The candidate quadruplet is formed by selecting two opposite sign, same flavor di-lepton pairs in an event. Muons are required to have $p_T > 6$ GeV and $|\eta| < 2.7$, while electrons are required to have $E_T > 7$ GeV and $|\eta| < 2.47$. In each quadruplet the p_T thresholds for the three leading leptons are 20, 15 and 10 GeV. The four leptons of the quadruplets are required to be well separated, $\Delta R = \sqrt{\Delta\eta^2 + \Delta\phi^2} > 0.10$ for same flavor leptons and $\Delta R > 0.20$ for different flavor leptons.

The di-lepton of the quadruplet with a mass m_{12} closest to the nominal Z boson mass is called the leading di-lepton, while the second di-lepton of the quadruplet with a mass m_{34} is the sub-leading one. For each event there is a mass window requirement applied to the invariant mass of each of the two di-leptons. The cut values are chosen event-by-event using the reconstructed four-leptons invariant mass, resulting in a single mass spectrum for each background regardless of the hypothesized Higgs mass. m_{12} is required to be between 50 and 106 GeV, m_{34} is required to exceed a threshold, $m_{threshold}$, which varies as a function of the four-leptons invariant mass, $m_{4\ell}$, and it should always be below 115 GeV. The value of $m_{threshold}$ is 12 GeV for $m_{4\ell} < 140$ GeV, rises linearly to 50 GeV with $m_{4\ell}$ in the interval $m_{4\ell} \in [140 \text{ GeV}, 190 \text{ GeV}]$ and stays at 50 GeV for $m_{4\ell} > 190$ GeV. Table 5.10 summarizes the m_{34} cut values. In the case that more than one quadruplet survive the kinematic selection, the one with m_{12} closest the m_Z mass is retained, if multiple quadruplets have the same m_{12} the one with the highest m_{34} is

Table 5.9: Summary of the $H \rightarrow ZZ^{(*)} \rightarrow 4\ell$ candidate selection requirements. The two lepton pairs are denoted as m_{12} and m_{34} . The choice of the threshold value $m_{threshold}$ for m_{34} can be found in Table 5.10.

Kinematic Selection	Require at least one quadruplet of leptons consisting of two pairs of same-flavor (SF) opposite-charge (OS) leptons fulfilling the following requirements: p_T thresholds for three leading leptons in the quadruplet 20, 15 and 10 GeV Select best quadruplet to be the one with the leading dilepton mass being the one closer to the Z mass and the second mass closer to the Z one, to be the subleading one. Leading di-lepton mass requirement $50 \text{ GeV} < m_{12} < 106 \text{ GeV}$ Sub-leading di-lepton mass requirement $m_{threshold} < m_{34} < 115 \text{ GeV}$ Remove quadruplet if alternative same-flavor opposite-charge di-lepton gives $m_{\ell\ell} < 5 \text{ GeV}$ $\Delta R(\ell, \ell') > 0.10(0.20)$ for all same (different) flavor leptons in the quadruplet.
Isolation	Isolation cut applied on all leptons of the quadruplet Contribution from the other leptons of the quadruplet is subtracted Lepton track isolation ($\Delta R = 0.20$): $\Sigma p_T/p_T < 0.15$ Electron calorimeter isolation ($\Delta R = 0.20$): $\Sigma E_T/E_T < 0.20$ Muon calorimeter isolation ($\Delta R = 0.20$): $\Sigma E_T/E_T < 0.30$ Standalone muons calorimeter isolation ($\Delta R = 0.20$): $\Sigma E_T/E_T < 0.15$
Impact Parameter	Apply impact parameter significance cut to all leptons of the quadruplet.
Significance	For electrons : $d_0/\sigma_{d_0} < 6.5$ For muons : $d_0/\sigma_{d_0} < 3.5$

Table 5.10: The m_{34} mass cut depends on the $m_{4\ell}$ value. For the intermediate values the cuts increase linearly.

$m_{4\ell}$ GeV	< 140	140	190	> 190
m_{34} cut GeV	12	12	50	50

³¹¹¹ selected.

³¹¹² The normalized track isolation discriminant is defined as the sum of the transverse
³¹¹³ momenta of tracks, Σp_T , inside a cone of $\Delta R < 0.2$ around the lepton, excluding the
³¹¹⁴ lepton track, divided by the lepton p_T . The tracks are considered in the sum are of
³¹¹⁵ good quality; i.e. they have at least four hits in the pixel and silicon strip detectors
³¹¹⁶ ("silicon hits") and $p_T > 1 \text{ GeV}$ for muons, and at least nine silicon hits, one hit in
³¹¹⁷ the innermost pixel layer (the b -layer) and $p_T > 0.4 \text{ GeV}$ for electrons. Each lepton is
³¹¹⁸ required to have normalized track isolation smaller than 0.15.

³¹¹⁹ The normalized calorimetric isolation discriminant for muons is defined as the sum
³¹²⁰ of the calorimeter cells, ΣE_T , inside an isolation cone of 0.20 around the muon, after
³¹²¹ having subtracted the muon ionization energy which is calculated as the sum of cells in
³¹²² a much smaller cone around the muon, divided by the muon p_T . In the case of electrons,

3123 the normalized calorimetric isolation is computed as the sum of the topological cluster
 3124 transverse energies inside a cone of 0.2 around the electron cluster divided by the
 3125 electron E_T , the cells corresponding to the core of the electron cluster are excluded
 3126 from the sum. Muons are required to have a normalized calorimetric isolation of less
 3127 than 0.30, while for electrons the corresponding value is 0.20. For both the track-
 3128 and calorimeter-based isolation any contributions arising from other leptons of the
 3129 quadruplet are subtracted. For the track isolation the contribution from any other
 3130 lepton in the quadruplet within $\Delta R < 0.2$ is subtracted. For the calorimetric isolation,
 3131 the contribution of any electron in the quadruplet within $\Delta R < 0.18$ is subtracted. The
 3132 impact parameter significance, d_0/σ_{d0} , is required to be lower than 3.5 for muons and
 3133 6.5 for electrons. The electron impact parameter is affected by bremsstrahlung and is
 3134 thus broader. The final discrimination variable is the mass of the leptons quadruplet.

3135 5.6.2 FSR recovery

3136 $H \rightarrow ZZ^{(*)} \rightarrow 4\ell$ decays include low E_T photon Final State Radiation (FSR) [65].
 3137 The QED process of radiative photon production in Z decays is well modeled by the MC.
 3138 Some of the FSR photons can be identified in the detector as incorporated directly into
 3139 the four lepton measurement. This can recover events which have their reconstructed
 3140 four lepton mass moved out of the signal region.

3141 FSR recovery is allowed only for one photon per event and can be added to the
 3142 leading Z for $m_{4\ell} < 190$ GeV or any of the two Z s above this threshold. The candidate
 3143 FSR photons, nominally calibrated, in case they are collinear within a cone of $\Delta R <$
 3144 0.05 around a muon, 400 MeV of energy is removed from the photon measured energy
 3145 to account for the average contribution from muon ionization. Collinear FSR search is
 3146 performed only for muons. The photon candidates are obtained from any of the two
 3147 different objects:

- 3148 • 3 \times 5 clusters seeded by clusters satisfying the requirements:
 - 3149 – cluster transverse energy between $1.5 \text{ GeV} < E_T < 3.5 \text{ GeV}$,
 - 3150 – the cone between the cluster and the muon $\Delta R_{\text{cluster},\mu} = \sqrt{\Delta\eta^2 + \Delta\phi^2} <$
 3151 0.08,
 - 3152 – the fraction of the cluster energy deposited in the front sampling of the
 3153 calorimeter over the total energy (f_1) > 0.2 .
- 3154 • Standard photons or electrons satisfying the requirements:
 - 3155 – cluster transverse energy $E_T > 3.5 \text{ GeV}$

- 3156 – the cone between the cluster and the muon $\Delta R_{\text{cluster},\mu} = \sqrt{\Delta\eta^2 + \Delta\phi^2} <$
- 3157 0.15,
- 3158 – the fraction of the cluster energy deposited in the front sampling of the
- 3159 calorimeter over the total energy (f_1) > 0.1 .

3160 If more than one cluster are found in the cone, then the one with the highest E_T
 3161 is selected. The cut on the fraction f_1 is effective only in low energies ($E_T < 15$ GeV)
 3162 where a large fraction of the EM energy is deposited in the front sampling and helps in
 3163 discriminating against background induced by the muon itself via ionization at energies
 3164 where the muon energy loss Landau tail is still significant (i.e. cluster energies up to
 3165 3 GeV).

3166 The non collinear search is performed for both electrons and muons. Candidates
 3167 are required to satisfy the following requirements :

- 3168 • the FSR photon candidate to pass the tight identification criteria,
- 3169 • the cone between the cluster and the lepton $\Delta R_{\text{cluster},\ell} = \sqrt{\Delta\eta^2 + \Delta\phi^2} > 0.15$,
- 3170 • the transverse energy of the cluster $E_T > 10$ GeV,
- 3171 • the FSR photon candidate to be isolated $E_T^{\text{cone}40} < 4$ GeV

3172 In this analysis the FSR photon addition is applied on the events that pass all
 3173 selections. FSR photons are searched for all lepton candidates of the final quadruplet
 3174 but at maximum one FSR photon candidate is added to the 4ℓ system. The FSR
 3175 correction is applied only to the on-shell Z . Priority is given to collinear photons
 3176 associated to the leading $Z \rightarrow \mu^+\mu^-$. The correction is applied if $66 < m_{\mu\mu} < 89$ GeV
 3177 and the $m_{\mu\mu\gamma} < 100$ GeV. In the case the collinear search has failed then the non
 3178 collinear FSR photon with the highest E_T , if found, is added provided it satisfies the
 3179 following requirements:

- 3180 • $m_{4\ell} \leq 190$ GeV, $m_{ll} < 81$ GeV and $m_{ll\gamma} < 100$ GeV \rightarrow the on-shell Z is corrected
- 3181 • $m_{4\ell} > 190$ GeV, $m_{ll} < 81$ GeV and $m_{ll\gamma} < 100$ GeV \rightarrow the pair with the $m_{ll\gamma}$
 3182 closest to the Z pole is corrected since both Z s are on shell.

3183 The lower cut on E_T reduces the hadronic background (mainly due to π^0 decays),
 3184 whereas the upper cut on the M_{ll} is applied in both cases in order to reduce the Initial
 3185 State Radiation (ISR), the π^0 and muon ionization backgrounds for a very small loss
 3186 of efficiency of a few percent. FSR photons correspond to events with m_{ll} below the Z
 3187 pole mass while the ISR photons, π^0 's and muon ionization clusters do not.

3188 The effect of the FSR recovery in $Z \rightarrow \mu^+\mu^-$ events recovers 70% of the collinear
 3189 FSR photons, whereas the non-collinear FSR selection has an efficiency of $\approx 60\%$ and a
 3190 purity of $\geq 95\%$ [65]. Similarly, the addition of FSR in $Z \rightarrow e^+e^-$ significantly improves
 3191 the tails and the bulk of the mass resolution.

5.6.3 Z Mass Constraint

In the $H \rightarrow ZZ^{(*)} \rightarrow 4\ell$, the first lepton pair is predominately produced in a decay of an on-shell Z boson and hence allows for the improvement of the di-lepton mass resolution exploiting the Z line shape given the knowledge of the lepton momentum measurement uncertainties. The probability of observing a Z boson having a true mass m_{12}^{true} and decaying to two leptons with true 4-momenta, $\mathbf{p}_{1,2}^{true}$, while measuring the 4-momenta $\mathbf{p}_{1,2}^{rec}$ is given by the product:

$$L(\mathbf{p}_1^{true}, \mathbf{p}_2^{true}, \mathbf{p}_1^{rec}, \mathbf{p}_2^{rec}) = B(\mathbf{p}_1^{true}, \mathbf{p}_2^{true}) \cdot R_1(\mathbf{p}_1^{true}, \mathbf{p}_1^{rec}) \cdot R_2(\mathbf{p}_2^{true}, \mathbf{p}_2^{rec}), \quad (5.5)$$

where B is the probability density function (PDF) of the Z line shape at generator level and the PDFs $R_{1,2}$ of the energy or momentum response functions for the two leading leptons.

The m_{12}^{true} , in the case that the lepton energies are much higher than the lepton mass, is given by:

$$(m_{12}^{true})^2 = 2 \cdot E_1^{true} E_2^{true} (1 - \cos \theta) \quad (5.6)$$

where $E_{1,2}^{true}$ denotes the true lepton energies and θ the opening angle between the two decay leptons depending on the true lepton angles $\eta_{1,2}^{true}$ and $\phi_{1,2}^{true}$. The lepton angles are measured very precisely such that the values $\eta_{1,2}^{rec}$ and $\phi_{1,2}^{rec}$ effectively correspond to $\eta_{1,2}^{true}$ and $\phi_{1,2}^{true}$, respectively. Therefore, the lepton response functions are essentially PDFs of the true energies for certain measurement of the lepton 4-momenta:

$$R_{1,2}(\mathbf{p}_{1,2}^{true}, \mathbf{p}_{1,2}^{rec}) = R_{1,2}(E_{1,2}^{true} | \mathbf{p}_{1,2}^{rec}). \quad (5.7)$$

In summary, the only uncertainty comes from the measured lepton energies, $E_{1,2}^{true}$.

The likelihood (L), defined in Equation 5.5, is maximized for a given event over the true lepton energies, to give the maximum likely 4-momenta, $\mathbf{p}_{1,2}^{ml}$. B is modeled with a relativistic Breit-Wigner function, $\mathcal{F}_{BW}(m_{12}^{true} | m_Z, \Gamma_Z)$, with mean and width parameters set to the Z boson mass (m_Z) and natural width (Γ_Z) respectively. Furthermore, the single lepton response functions are approximated by a Gaussian distribution, $\mathcal{F}_G(E_{1,2}^{true} | E_{1,2}, \sigma_{1,2})$, with mean set to the measured lepton energies ($E_{1,2}$) and variance ($\sigma_{1,2}^2$, lepton momentum resolution squared obtained from simulation).

The improvement for all channels from the Z mass constrained fit is $\sim 15\%$ in the mass resolution.

5.7 Reducible Background Estimation Methods

The backgrounds in the $H \rightarrow ZZ^{(*)} \rightarrow 4\ell$ analysis are the $ZZ^{(*)}$ SM production, which has exactly the same topology as the signal and is therefore referred to as the

irreducible background, and the reducible ones from $Z + jets$ (comprised of both the heavy and light flavor jets) and top quark pairs ($t\bar{t}$). The $ZZ^{(*)}$ background has good quality and isolated leptons in the final state. Its normalization and shape is fine-tuned from the data fit in the low mass region where the single Z resonant appears and the high mass region formed by the spectrum of the two on-shell Z s. For the estimation of the reducible background processes, which originate from fake or non-isolated leptons, data-driven methods using control regions are used. The WZ production contribution is also taken into account as it is predicted from the MC.

The background methods are divided into two subcategories, the so called "muons" and "electrons" backgrounds. The final states of $Z + \mu\mu$ and $Z + ee$ are strongly dependent on the muons and electrons, that form the secondary pair since the on-shell Z is a clean signature, and therefore are studied separately. $Z + \mu\mu$ states accept significant contribution from $Zb\bar{b}$ mostly and smaller contributions come from $t\bar{t}$ and $Zlight$, whereas the dominant background in the $Z + ee$ are Z bosons accompanied by jets misidentified as electrons.

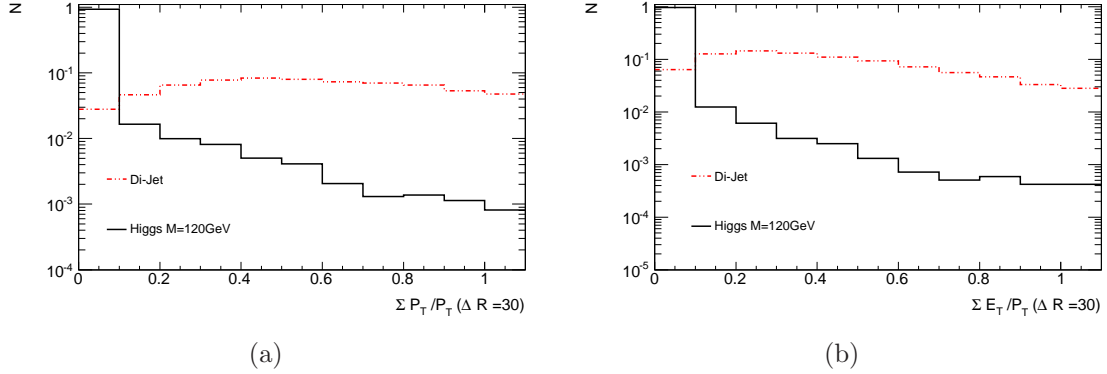
The following section describes the data-driven reducible background estimation concept, primarily focused on the muons background. The general procedure is as follows:

- The background composition and shapes are studied in special control regions (CR) constructed by relaxing or inverting selection and/or lepton identification requirements on the secondary pair only. The selection of the leading pair follows the nominal Higgs selection, described in Section 5.6. The higher statistics in the control regions, enriched in the reducible background, permit several distributions to be compared between data and simulation.
- An unbinned simultaneous fit is performed on the control regions for the extraction of the reducible background, which treats the backgrounds globally and allows the minimization of the statistical uncertainty.
- The expected background in the signal region (SR) is computed by extrapolating the background from the control region using the so-called transfer factors. These factors are determined from the per event efficiency of a given background in a control region with respect to the signal region from the MC.

5.8 Background Discrimination Variables

In order to reduce $Z + jets$ and $t\bar{t}$ below a safety level, isolation and impact parameter criteria are used, as described in Section 5.6. These criteria are also called additional lepton selection [62]. In this section they are extensively discussed since

Figure 5.3: (a) Track - based and (b) calorimeter-based isolation distributions in cone $\Delta R = 0.3$ for muons originating from Higgs decays and jets ($m_H = 120$ GeV). The isolation cuts at low values of the relative isolation variable suppress the background. The cut values are chosen to be < 0.15 and < 0.30 for the relative track- and calorimeter-based isolation respectively.



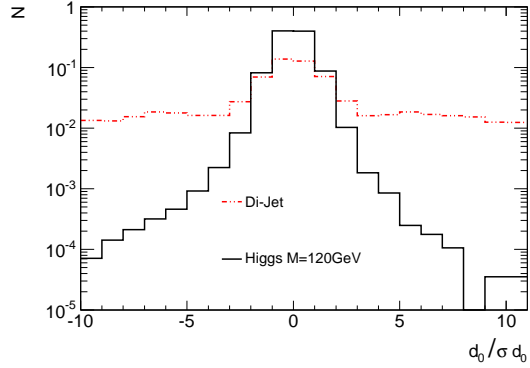
3257 they are essential for measuring the background. Focus is given on muons since the
 3258 presented background method is applied to the 4μ and $2e2\mu$ final states.

3259 5.8.1 Isolation

3260 Muons that originate from light quark jets, from $Z + light\ Jets$ decays, populate in
 3261 general the low p_T spectrum and are characterized by relatively large difference between
 3262 the transverse momenta measured in the inner detector and the muon spectrometer.
 3263 Consequently, such muons are not isolated. Muons coming from either heavy hadrons
 3264 or fakes are expected to be in jet environment and therefore they tent not to be isolated.
 3265 As opposed to these, the prompt muons from W or Z boson decays have on average
 3266 just the opposite properties except that they originate from the interaction point.

3267 The imposal of calorimetric and track isolation, especially on muons, reduces drastically
 3268 the reducible backgrounds, including the "fake" muons of the $Z+jets$ background.
 3269 As an example the distributions of the isolation variables used in this analysis for muons
 3270 originating from Higgs decays as well as muons originating from jets are shown in Figure
 3271 5.3. The isolation distributions of $H \rightarrow ZZ^{(*)} \rightarrow 4\ell$ ($m_H = 120$ GeV) and a dijet
 3272 sample are presented. It can be observed that the signal peaks at zero whereas the
 3273 backgrounds extends to higher values.

Figure 5.4: $d_0/\sigma d_0$ significance distribution of muons from Higgs decays and muons from jets. The application of this cut (specifically $-3.5 < d_0/\sigma d_0 < 3.5$) leads to background rejection.



5.8.2 Impact Parameter Significance

Due to the appreciable life time of the b -hadrons, some of the leptons from the $Zb\bar{b}$ and $t\bar{t}$ processes are expected to originate from displaced vertexes, which can be used for further rejection of the reducible backgrounds. The impact parameter significance, defined as the impact parameter of the lepton normalized to its measurement error, is required not to exceed 3.5 for muons. In Figure 5.4, where the distributions of a $H \rightarrow ZZ^{(*)} \rightarrow 4\ell$ ($m_H = 120$ GeV) and a dijet sample are presented, it is visible how this requirement rejects the background [62].

5.9 Muon Efficiencies in Background Environments

From the previous Section 5.8 it is clear that the additional lepton selection plays an important role on the discrimination of the Higgs and $ZZ^{(*)}$ candidates against the reducible background. This section presents the efficiency extraction of background-like muons, performed in a control region (CR) which allows quantitative comparisons for the additional muons in the $Z + \mu$ final state. Table 5.11 summarizes the selection, which includes a Z candidate decaying either to muons or electrons, isolated and passing impact parameter criteria, with p_T thresholds of 20 and 15 GeV and the mass window is strictly set within 15 GeV from the nominal Z mass. The muon accompanying the Z is required to pass only the muon pre-selection criteria.

Figure 5.5 presents the muon additional selection variables and the p_T spectrum after the selection of Table 5.11 for the 2011 and Figure 5.6 for the 2012 data. For combined muons, Figure 5.7 shows the difference of the transverse momentum as measured in the

Table 5.11: Summary of the $Z + \mu$ selection for the study of the muon additional selection (isolation and impact parameter significance) efficiencies.

Z Candidate Selection	
Leptons	e or μ
p_T Thresholds	20, 15 GeV
Mass Cut	$ m_{\ell\ell} - m_Z < 15$ GeV
Additional Selection	Imposed
Overlap Removal	$DR > 0.1$
Additional Muon	
Overlap Removal	$DR > 0.1$ Same Flavor (SF), $DR > 0.2$ Opposite Flavor (OF)
J/ Ψ Veto	$m_{\mu^+\mu^-} > 5$ GeV

3295 inner detector and the muon spectrometer. The structure at high $(p_{T_{ID}} - p_{T_{MS}})/p_{T_{ID}}$
3296 from fake leptons (i.e. muons from π and K decays) is well described by the simulation.

3297 The $Z + \mu$ efficiencies after the additional selection cuts, separately and combined
3298 for the two possible Z decays, are presented in Table 5.12. As expected, no difference
3299 is observed between the $Z \rightarrow e^+e^- + \mu$ and $Z \rightarrow \mu^+\mu^- + \mu$ channels. The overall
3300 discrepancy between data and MC is small and is attributed squared as a systematic
3301 uncertainty in the $Z + \mu\mu$ final state.

3302 5.10 Muons Reducible Background Estimation

3303 5.10.1 The Simultaneous Fit Concept

3304 The muons background estimation is based on an unbinned maximum likelihood fit,
3305 which is performed simultaneously to four orthogonal control regions in order to achieve
3306 a better statistical uncertainty and global handling of the three reducible background
3307 sources, $Zb\bar{b}$, $Zlight$ and $t\bar{t}$. The fit is performed on the leading di-lepton mass (m_{12})
3308 distribution, since it allows separation of the Z component from the $t\bar{t}$ due to the
3309 on-shell Z peak of the former, of both the 4μ and $2e2\mu$ channels.

3310 The four CRs used for the fit are chosen to be non-overlapping to both each other
3311 and the SR. The fit aim is to estimate the background contribution in a fifth CR, which
3312 is formed by opposite sign secondary muon pairs, $Z + \mu^+\mu^-$, without isolation and
3313 impact parameter criteria on them. This control region is referred to as "OS CR" or
3314 "reference CR". The reference CR contains also the SR and that is the reason why

Figure 5.5: Properties of the muons accompanying a Z candidate before the application of the isolation and impact parameter selection using the 2011 data: (a) p_T spectrum, (b) normalized track-based isolation, (c) normalized calorimeter-based isolation and (d) $d_0/\sigma d_0$.

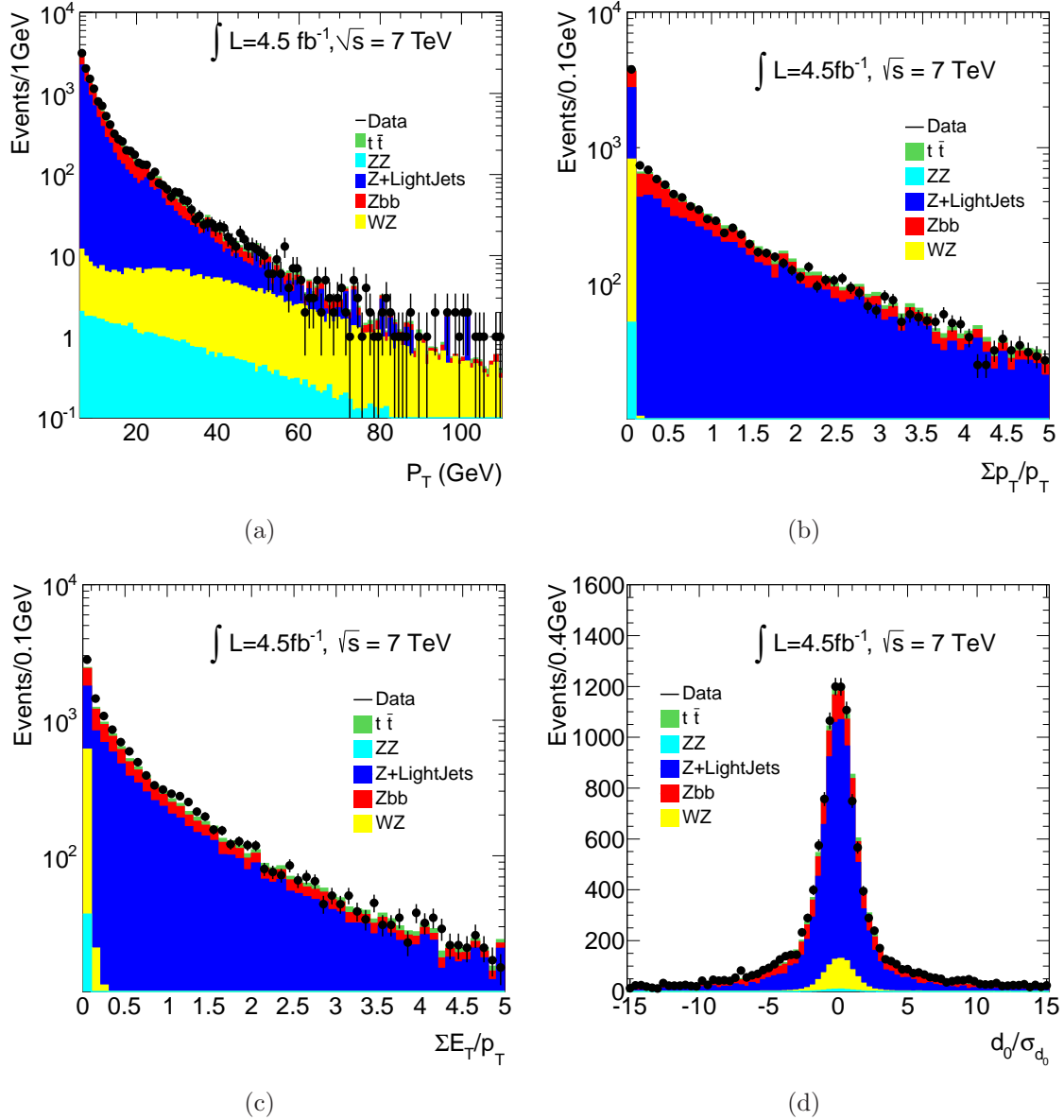


Figure 5.6: Properties of the muons accompanying a Z candidate before the application of the isolation and impact parameter selection using the 2012 data: (a) p_T spectrum, (b) normalized track-based isolation, (c) normalized calorimeter-based isolation and (d) $d_0/\sigma d_0$.

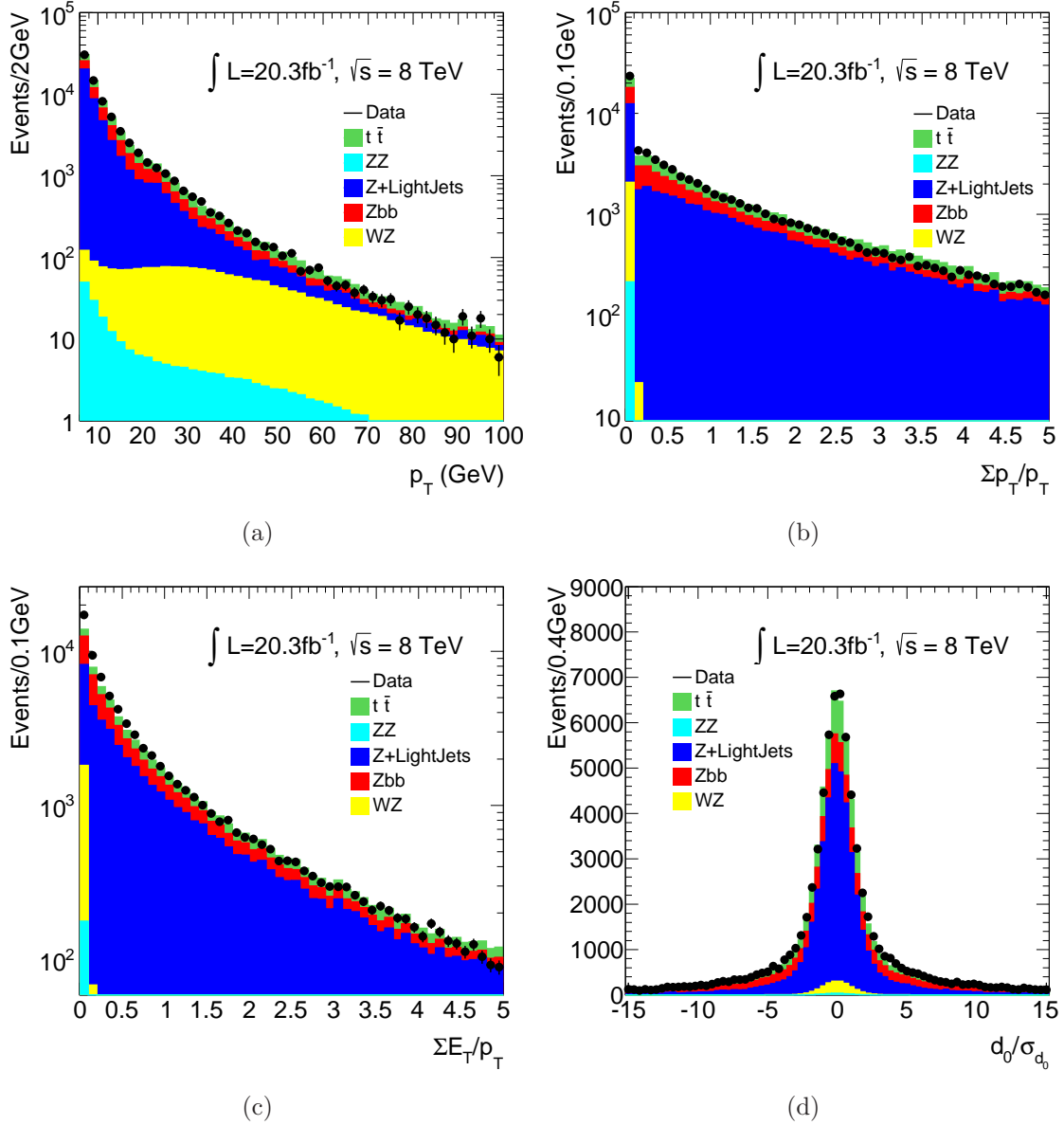


Figure 5.7: The 2011 (a) and 2012 (b) distributions of the difference between ID and MS transverse momentum estimates normalized to the ID measurement, $(p_{T_{ID}} - p_{T_{MS}})/p_{T_{ID}}$, for combined muons accompanying a $Z \rightarrow \ell^+\ell^-$ candidate. This control plot for the background estimate demonstrates that the π/K in-flight decays are well-described by the simulation.

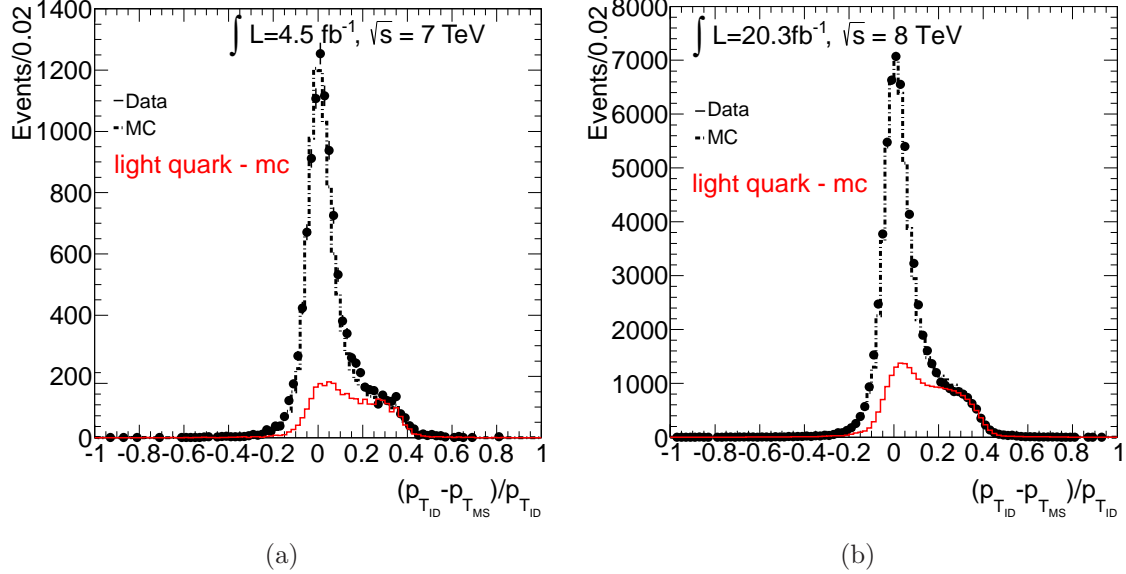


Table 5.12: 2011 and 2012 efficiencies of muons accompanying a Z candidate. The combined and separate efficiencies according to the possible Z decays are reported. As expected, no difference is observed between the $Z \rightarrow e^+e^- + \mu$ and $Z \rightarrow \mu^+\mu^- + \mu$ channels.

Selection	Data (%)	MC (%)
2011		
$Z \rightarrow \mu^+\mu^- + \mu$	20.1 ± 0.5	18.9 ± 0.4
$Z \rightarrow e^+e^- + \mu$	19.6 ± 0.5	18.0 ± 0.4
$Z \rightarrow \ell^+\ell^- + \mu$	19.6 ± 0.3	18.5 ± 0.3
2012		
$Z \rightarrow \mu^+\mu^- + \mu$	19.71 ± 0.19	19.32 ± 0.15
$Z \rightarrow e^+e^- + \mu$	19.04 ± 0.21	18.79 ± 0.17
$Z \rightarrow \ell^+\ell^- + \mu$	19.38 ± 0.14	19.07 ± 0.09

it cannot be included directly in the fit. However, indirectly is used in the model describing each CR as:

$$\begin{aligned}
 PDF_{CR} = & N_{t\bar{t}} \cdot f_{t\bar{t}} \cdot M_{t\bar{t}} & (t\bar{t}) \\
 & + N_{Zb\bar{b}} \cdot f_{Zb\bar{b}} \cdot M_{Zb\bar{b}} & (Zb\bar{b}) \\
 & + N_{Zlight} \cdot f_{Zlight} \cdot M_{Zlight} & (Zlight) \\
 & + N_{ZZ+WZ} \cdot f_{ZZ+WZ} \cdot M_{ZZ+WZ} & (ZZ + WZ)
 \end{aligned} \tag{5.8}$$

where:

- N_x : is the number of the x -background events in the OS CR,
- f_x : is the ratio of the x -background between the under study CR and the OS CR (estimated from the MC),
- M_x : is the shape model of the x -background.

It should be noted that despite the small ZZ and WZ contribution in the control regions used for the fit, due to the inverted cuts, the remaining contributions are included for accuracy in the fit unified and fixed to the values estimated from the MC.

The m_{12} shapes, included in the Equation 5.8, for the backgrounds are:

- $t\bar{t}$ background: is modeled by a 2^{nd} order Chebychev polynomial (parameters c_0 , c_1)
- $Zb\bar{b}$, $Zlight$ and $WZ + ZZ$ backgrounds: are modeled by a convolution of a Crystal Ball with a Breit-Wigner (parameters μ , α , η , σ and m_Z). The same shape parameters are used for the $Zb\bar{b}$, $Zlight$ and $WZ + ZZ$ models¹, given that there is no physics motivation for them to be different, and the same shapes are considered in the different CR with only the number of events left to be estimated from the fit.

The four CR are described by one separate model each of the Form 5.8. For better handling of the uncertainties, the ratios and shape parameters are promoted to nuisance parameters with Gaussian constraints. The m_{12} data distributions are fitted with the minimization requirement. *MINOS* errors are enabled to obtain better estimation of asymmetric errors and to change the *MINUIT* verbosity level to its lowest possible value [66].

At the end, the reference CR fit estimations are extrapolated to the SR with use of transfer factors. Transfer factors are estimated from the MC and correspond to the efficiency of a reference CR event to pass the additional selection, i.e. isolation and $d_0/\sigma d_0$ criteria, and be detected in the SR.

¹Later in this Chapter a check is performed with different parameters and the result is almost identical.

5.10.2 Fit Control Regions

The control regions used for the fit are selected such that there is no contamination from the Higgs signal and as little as possible contamination from the irreducible $ZZ^{(*)}$. Below a brief description of the four control regions is given:

(1) Inverted $d_0/\sigma d_0$ CR

The standard four-lepton analysis selection is applied on the leading dilepton, whereas the subleading dilepton pair has the impact parameter significance selection inverted for at least one lepton in the pair and no isolation selection is applied. This control region is enhanced primarily in $Zb\bar{b}$ and secondarily in $t\bar{t}$ since leptons from b-quark mesons are characterized by large d_0 significance.

(2) Inverted Isolation CR

The standard four-lepton analysis selection is applied on the leading dilepton and the subleading dilepton pair passes the standard impact parameter significance selection and at least one lepton in the pair fails the isolation selection. Relative to the previous CR, this control region aims to enhance the $Zlight$ jet component (π/K in-flight decays) over the $Zb\bar{b}$ component by requiring the impact parameter significance selection. These two background processes are described by the same model and would be consequently highly correlated.

(3) Same Sign (SS) CR

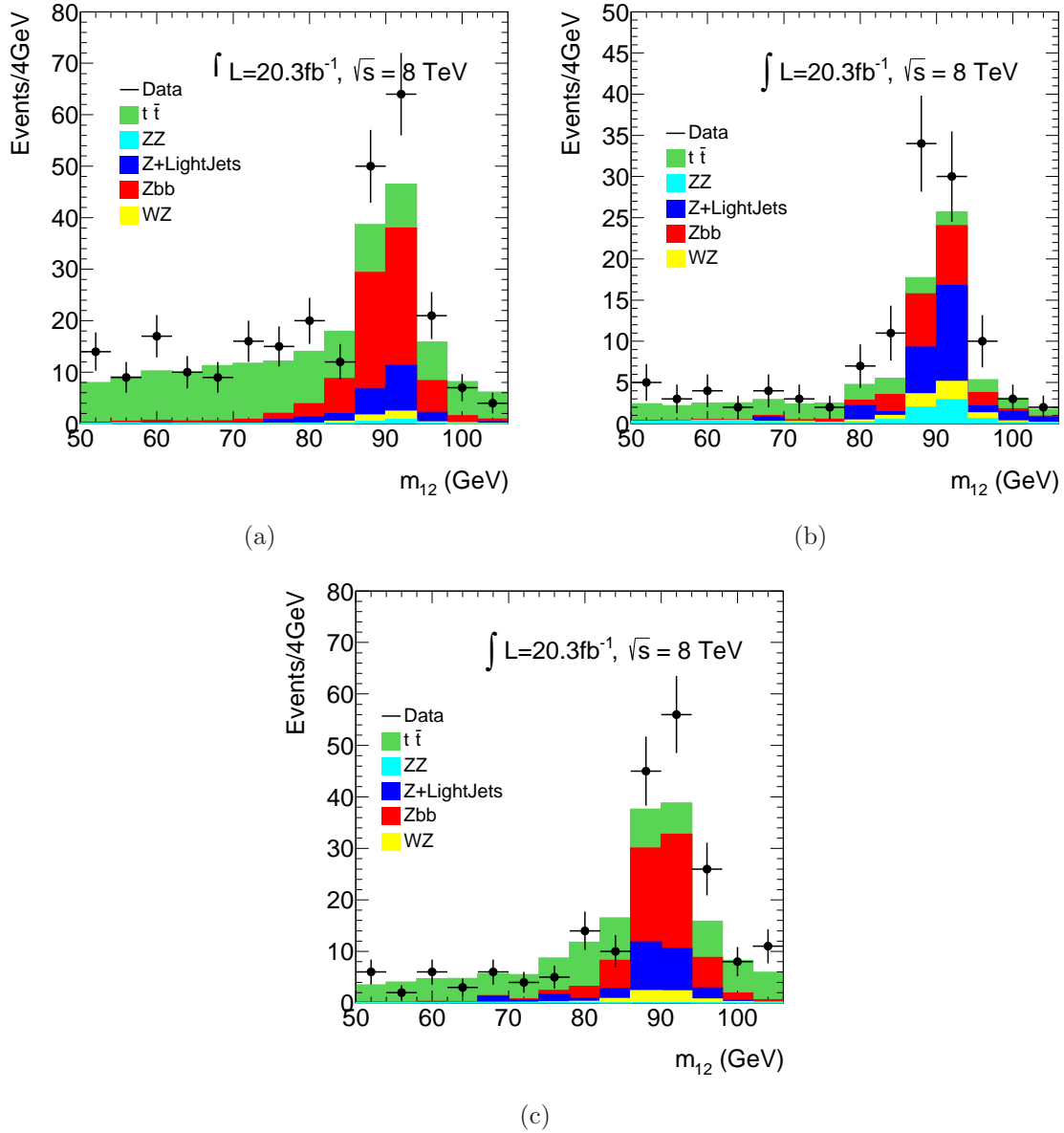
The standard four-lepton analysis selection is applied on the leading dilepton and the subleading dilepton has neither the impact parameter significance nor the isolation selection applied while the leptons are required to have same charge. This same sign control region is not dominated by a specific background; all the reducible backgrounds have a significant contribution.

(4) $e\mu + \mu\mu$ CR

This is a $t\bar{t}$ targeted CR and the decays to $e\mu + \mu\mu$ are expected to be as many as the sum of the $4\mu + 2e2\mu$. The events of this control region are opposite-charge different-flavor leading dileptons which must satisfy the standard four-lepton analysis selection. The subleading dilepton has neither the impact parameter significance nor the isolation selection applied, while both same and opposite charge leptons are accepted to increase statistics. Events with a Z boson decaying to a pair of electrons or muons are vetoed in this CR, by vetoing events where any combination of same flavor opposite sign leptons have an invariant mass in the region 50–106 GeV.

In Figure 5.8 the m_{12} distributions of the inverted $d_0/\sigma d_0$, inverted isolation and SS CRs are presented for data and MC simulation, where MC contributions are normalized to the theoretical cross sections. A visible discrepancy is reported which leads to the need of a data-driven based estimation of the background.

Figure 5.8: The m_{12} distributions for the 2012 data and MC simulation, normalized to the theoretical cross sections, are presented for the inverted $d_0/\sigma d_0$ CR (a), inverted isolation CR (b) and the SS CR (c). An excess is observed to the data with respect to the theoretical expectations.



3381 The $e\mu + \mu\mu$ CR is dominated by $t\bar{t}$ events, however a check for possible contributions
 3382 from QCD is performed. The QCD CR is formed by same sign leading $e\mu$ events
 3383 ($e^\pm\mu^\pm + \mu$ or $e^\pm\mu^\pm + \mu\mu$). In this CR any difference between data and the known
 3384 MC ($t\bar{t}$, diboson and Z) is attributed to QCD and $W + jets$ and a "QCD factor" is
 3385 estimated from the formula:

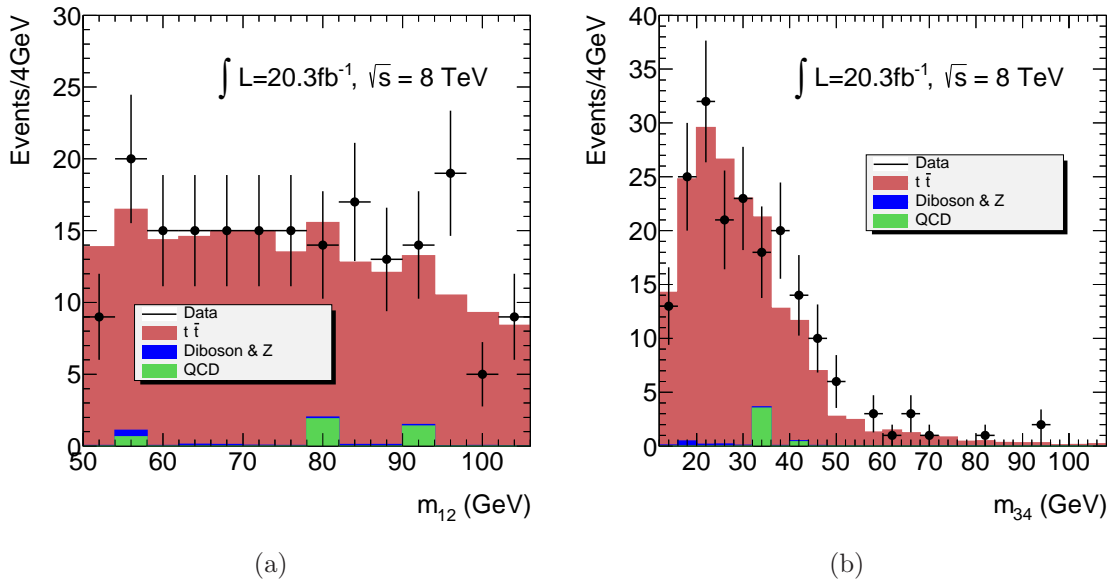
$$f_{QCD} = (Data - Known\ MC)_{e^\pm\mu^\mp + \mu} / (Data - Known\ MC)_{e^\pm\mu^\pm + \mu}. \quad (5.9)$$

3386 The 3ℓ final state is used since it allows quantitative comparisons. In the 4ℓ final state
 3387 of $e^\pm\mu^\mp + \mu\mu$, the QCD is estimated by:

$$N_{QCD}^{e^\pm\mu^\mp + \mu\mu} = f_{QCD} \times N^{e^\pm\mu^\pm + \mu\mu} \quad (5.10)$$

3388 and the shape is considered to be the shape of the $e^\pm\mu^\pm + \mu\mu$ events. The m_{12} and m_{34}
 3389 distributions of the $e^\pm\mu^\mp + \mu\mu$ CR are presented in Figure 5.9. The QCD estimated
 3390 events correspond to 3.0 ± 2.1 and 2.5 ± 1.7 in the OS and SS secondary pair final states
 3391 respectively. This contribution will not be taken into account for the simultaneous fit,
 3392 because it is very small, the uncertainty is significant and the shape is based on the
 3393 observed events.

Figure 5.9: (a) m_{12} and (b) m_{34} mass distributions of $e^\pm\mu^\mp + \mu\mu$ events, where both
 OS and SS secondary pairs are considered. The comparison is performed between data
 and $t\bar{t}$, diboson, Z MC and the measured QCD.



3394 For the four presented control regions, the MC contributions of the background
 3395 sources normalized to the theoretical cross sections are quoted in Table 5.13. The

Table 5.13: 2012 MC estimated contributions of the reducible background sources normalized to the theoretical cross sections in the four fit CRs.

Background	$inv - d_0/\sigma d_0$ CR	$inv - iso$ CR	SS CR	$e\mu + \mu\mu$ CR
Zbb	70.5 ± 0.6	19.5 ± 0.3	47.0 ± 0.7	0.4 ± 1.9
$Zlight$	20 ± 3	29 ± 3	26 ± 3	0.0 ± 1.3
$t\bar{t}$	124.6 ± 1.3	25.2 ± 0.6	80.6 ± 1.1	159.6 ± 1.6

Table 5.14: MC estimated ratios for the reducible background of the fit CR with respect to the OS CR at $\sqrt{s} = 8$ TeV, following the naming convention $f_x = CR_x/CR_{OS}$. The uncertainties correspond to the MC statistical errors. These fractions are used by the fit, as the Equation 5.8 describes, after being promoted to nuisance parameters for better handling of the uncertainties.

Background	f_{inv-d0}	$f_{inv-iso}$	f_{SS}	$f_{e\mu+\mu\mu}$
Zbb	0.751 ± 0.010	0.209 ± 0.005	0.653 ± 0.012	0.0005 ± 0.0003
$Zlight$	0.44 ± 0.09	0.52 ± 0.09	0.59 ± 0.10	0.000 ± 0.003
$t\bar{t}$	0.828 ± 0.012	0.167 ± 0.004	0.539 ± 0.009	1.201 ± 0.023

relevant ratios of each background type in each CR with respect to the OS CR are presented in Table 5.14, as estimated from the simulation. The uncertainties are the MC statistical uncertainties. These fractions are used for modeling each CR after being promoted to nuisance parameters.

5.10.3 MC Closure Test

To validate the fit method, the consistency of the results and to extract the shape parameters a closure test is performed on MC events. Inputs from Zbb , $Zlight$ and $t\bar{t}$ ² simulated events feed the four CR and an unbinned simultaneous fit is performed. Each control region is fitted by the model described by the Equation 5.8, since the values of the fractions reported in Table 5.14 are treated as nuisance parameters and the shape parameters are set free. The test is performed on 2012 MC since the amount of events allows more accurate quantitative comparisons.

The fitted distributions are presented in Figure 5.10 and the reducible background estimations in the OS CR are presented in Table 5.15. The results are in agreement with the expected values and hence the method is proved to work. The shape param-

²For the $t\bar{t}$ MC the generator MC@NLO is used.

Table 5.15: Closure test of the simultaneous fit method using MC inputs at $\sqrt{s} = 8$ TeV. The reducible background events in the OS CR as predicted from the MC and estimated from the fit shows no discrepancy. This proves the validity of the method.

Reducible Background	MC prediction	MC Fit estimation
Zbb	93.5 ± 0.7	94.1 ± 0.8
$Zlight$	43 ± 5	43.7 ± 1.1
$t\bar{t}$	106.1 ± 1.9	107.5 ± 0.9

Table 5.16: Shape parameters for the Chebychev polynomials (c_0, c_1) and the Crystal Ball convoluted with a Breit-Wigner ($\mu, \alpha, \eta, \sigma$ and m_Z) as estimated from the MC closure test fit. The parameters are used for the data fit with Gaussian constraints in their uncertainties.

Shape Parameter	MC fit estimated value
c_0	-0.230 ± 0.020
c_1	-0.182 ± 0.011
μ	-0.32 ± 0.22
α	1.35 ± 0.07
η	4 ± 3
σ	1.69 ± 0.28
m_Z	91.0 ± 0.3

³⁴¹¹eters estimated from the fit are presented in Table 5.16 and are used later in the data
³⁴¹²simultaneous fit with Gaussian constraints within their uncertainties.

³⁴¹³ 5.10.4 2012 Data Unbinned Simultaneous Fit

³⁴¹⁴ Since the fit validity and consistency is proved from the MC closure test, the method
³⁴¹⁵ can be safely applied on the data. Each control region is fitted by the model described
³⁴¹⁶ by the Equation 5.8. As fractions, the values reported in Table 5.14 are used and the
³⁴¹⁷ shape parameters are taken from the MC (Table 5.16). Both are promoted to nuisance
³⁴¹⁸ parameters with Gaussian constraints in their uncertainties for better error handling.

³⁴¹⁹ Figure 5.11 shows the simultaneous fit PDFs as well as the separate background
³⁴²⁰ components for the four CRs in the data as estimated from the fit. The number of
³⁴²¹ events in the reference CR are presented in Table 5.17 for both the fit results and

Figure 5.10: Closure test of the simultaneous fit method using MC inputs at $\sqrt{s} = 8$ TeV. The data m_{12} distributions are presented after the unbinned simultaneous fit in the control regions of inverted $d_0/\sigma d_0$ (a), inverted isolation and passing $d_0/\sigma d_0$ (b), SS (c) and $e\mu + \mu\mu$ (d).

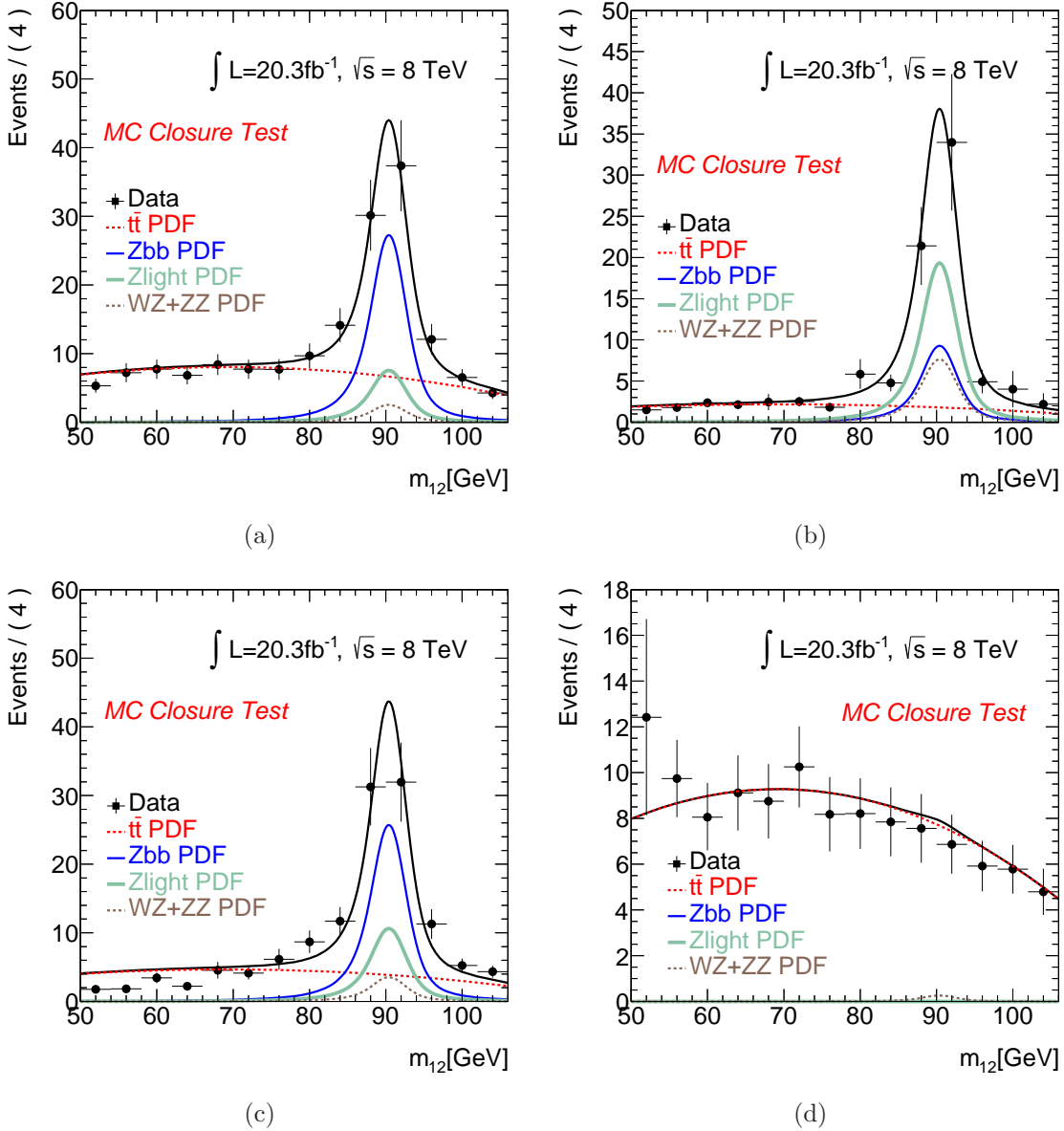


Table 5.17: Estimations of the reducible background contributions made from the 2012 data simultaneous fit in the OS CR and the relevant MC expectations. The difference between the two is quoted as "scaling". The presented uncertainties are the statistical uncertainties estimated from the fit and the MC available statistics respectively.

Reducible Background	MC prediction	Fit estimation	Scaling
$Zb\bar{b}$	93.5 ± 0.7	139 ± 16	1.49 ± 0.17
$Zlight$	43 ± 5	46 ± 9	1.07 ± 0.24
$t\bar{t}$	150.6 ± 1.5	181 ± 11	1.20 ± 0.07

Table 5.18: Correlation values of the $Zb\bar{b}$, $Zlight$ and $t\bar{t}$ with each other as estimated from the simultaneous fit of the 2012 data.

Reducible Background	$Zb\bar{b}$	$t\bar{t}$	$Zlight$
$Zb\bar{b}$	1.000	-0.506	0.028
$t\bar{t}$	-0.506	1.000	-0.020
$Zlight$	0.028	-0.020	1.000

³⁴²² the MC expectations. The corresponding ratio called "scaling" also appears on the
³⁴²³ Table. The correlation matrix of the fit parameters is presented in Figure 5.12 and
³⁴²⁴ the corresponding pulls are presented in Figure 5.13. The pulls are defined as $(p_{fit} -$
³⁴²⁵ $p_{nominal})/\delta p_{nominal}$, where the "nominal" values correspond to the pre-fit values, and
³⁴²⁶ are expected to be distributed around 0.00. The pull error bars correspond to the ratio
³⁴²⁷ of the estimated fit uncertainty divided by the pre-fit assigned uncertainty. Table 5.18
³⁴²⁸ presents the correlation of the parameters of interest, i.e. the OS CR events of $Zb\bar{b}$,
³⁴²⁹ $Zlight$ and $t\bar{t}$, with each other.

³⁴³⁰ The m_{12} , m_{34} and $m_{4\ell}$ masses in the reference OS CR are presented in Figure 5.14,
³⁴³¹ where the reducible backgrounds are scaled to the fit estimation and the ZZ and WZ
³⁴³² are taken from the MC. The exact numbers of each background are mentioned on the
³⁴³³ legends. The Higgs signal contribution is not included.

³⁴³⁴ 5.10.5 2012 Data Unbinned Simultaneous Fit Validity

³⁴³⁵ Even though, the method of the simultaneous fit is validated and proved to work on
³⁴³⁶ the MC, as described in Section 5.10.3, a number of other sanity checks are performed
³⁴³⁷ to further ensure the validity of the results. This includes the following cross checks

Figure 5.11: The 2012 data m_{12} distributions are presented after the unbinned simultaneous fit in the control regions of inverted $d_0/\sigma d_0$ (a), inverted isolation (b), SS (c) and $e\mu + \mu\mu$ (d). The WZ and ZZ contamination is fixed to the MC estimation and the rest of the background results estimated from the fit.

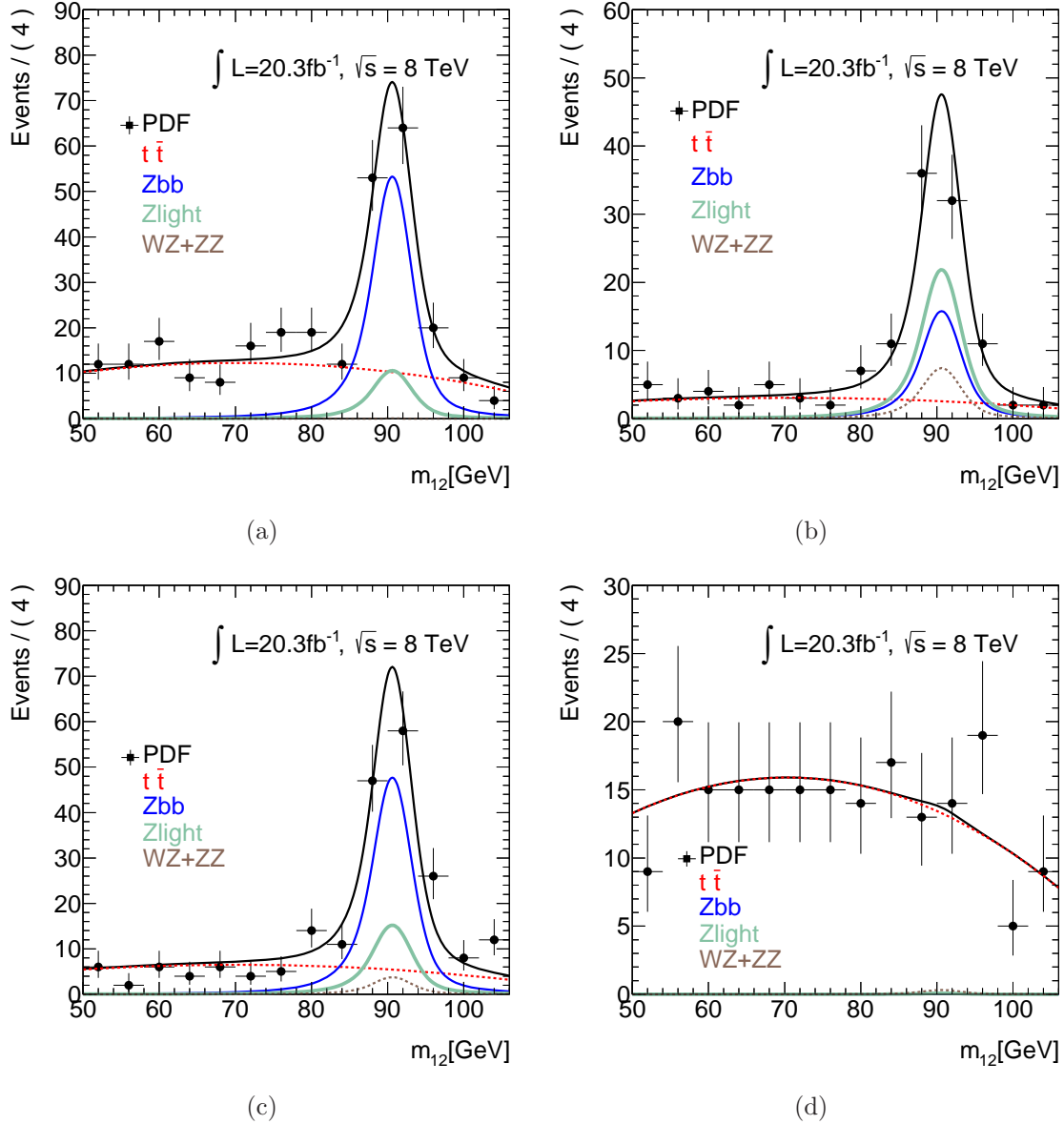


Figure 5.12: Correlation matrix of the parameters used for the 2012 data simultaneous fit. The parameters in the matrix include the shape parameters, the fractions of each control region with respect to the reference OS CR following the naming convention "frac_(Process)_ (Control Region)" and the estimated reducible backgrounds in the reference CR.

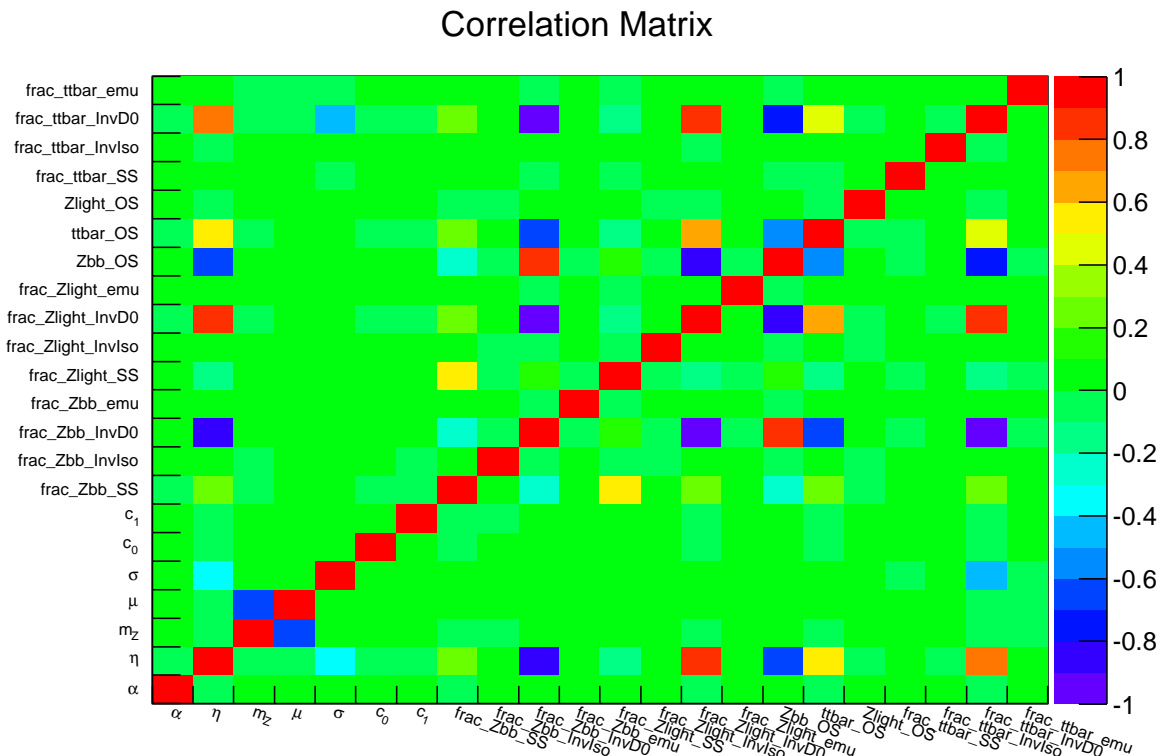


Figure 5.13: 2012 fit parameters pull distributions defined as $(p_{fit} - p_{nominal})/\delta p_{nominal}$ centering around 0.00 as expected. The "nominal" values correspond to the pre-fit values. The parameters include the shape parameters described in the text and the fractions of each control region with respect to the reference OS CR following the naming convention "Fraction_(Process)_ (Control Region)". The pull error bars correspond to the ratio of the estimated fit uncertainty divided by the pre-fit assigned uncertainty.

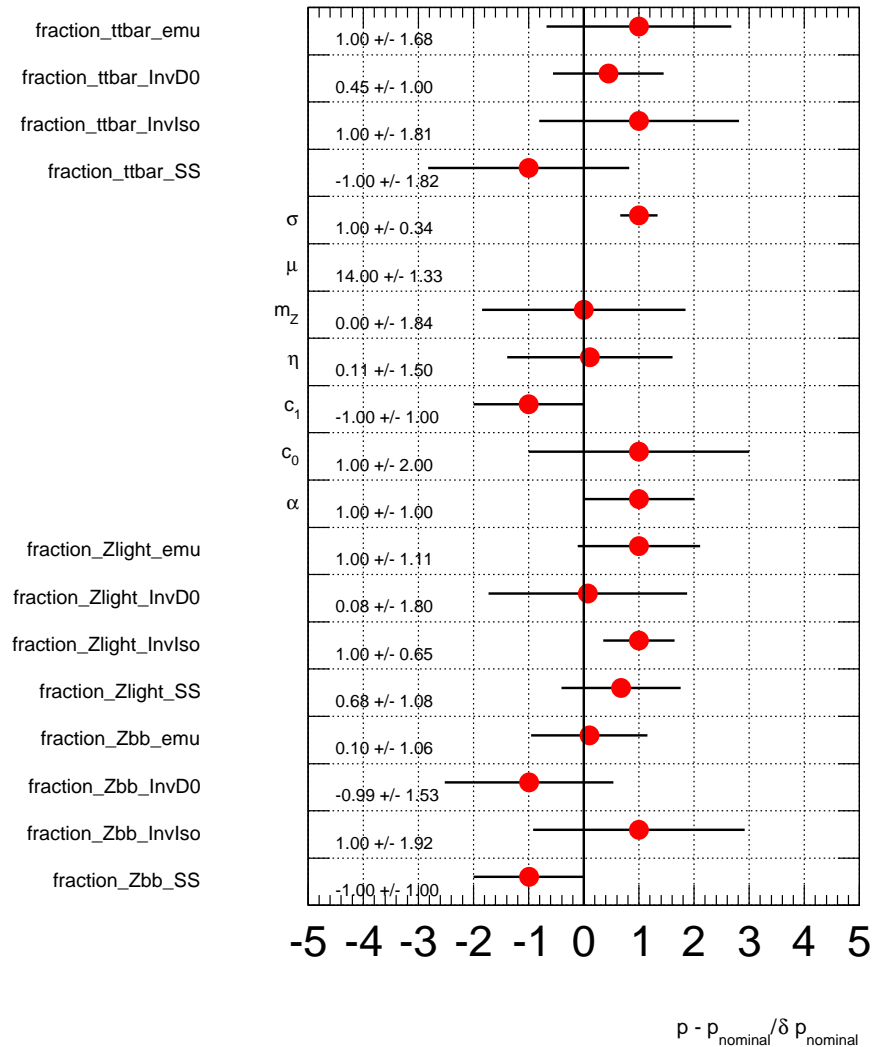


Figure 5.14: 2012 $Z + \mu^+\mu^-$ event distributions in data and the expected backgrounds. The reducible backgrounds contributions come from the fit while the ZZ and WZ are taken from the MC. The Higgs signal contamination is not shown. The m_{12} (a), m_{34} (b) and $m_{4\ell}$ (c) are presented.

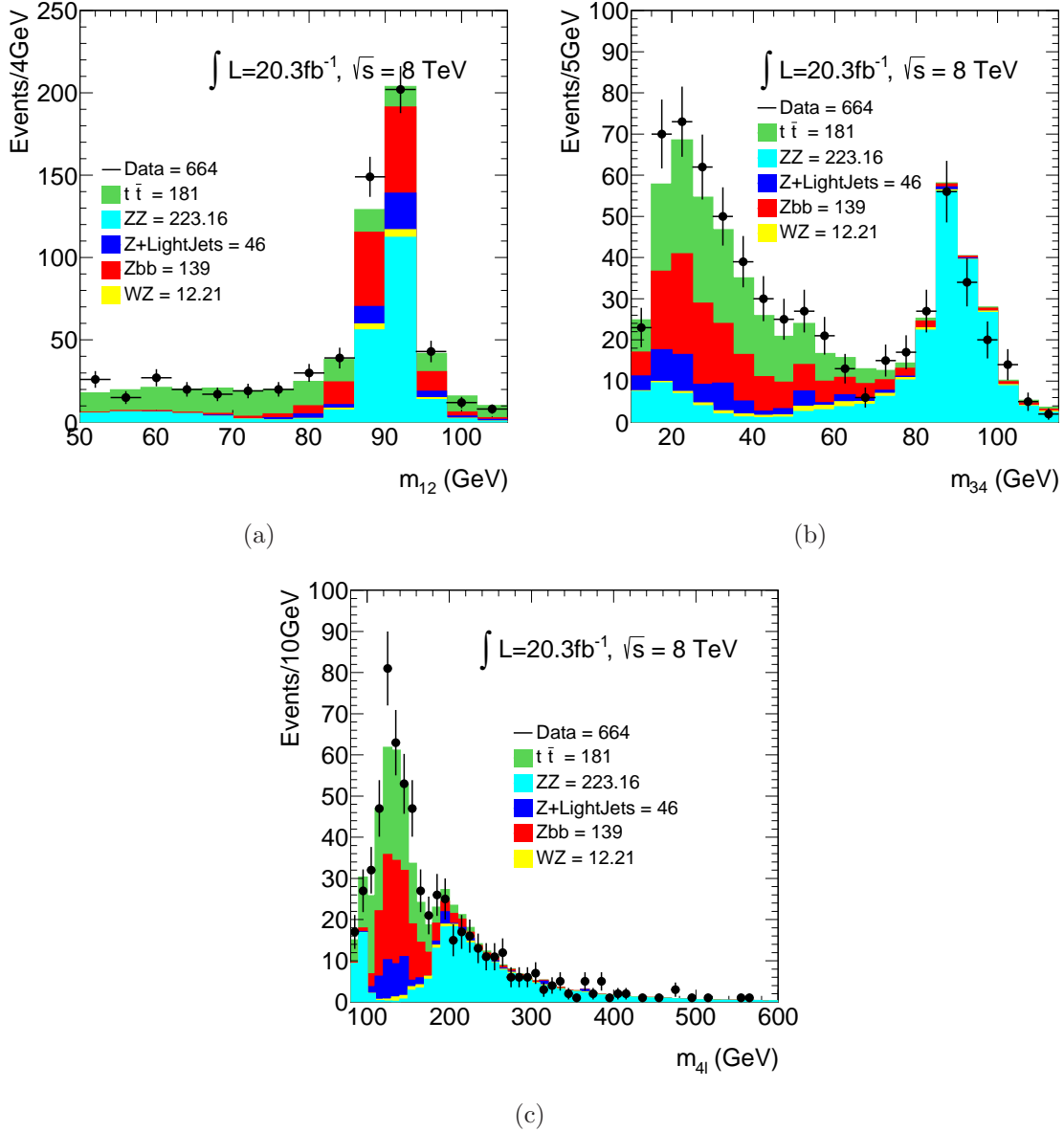


Table 5.19: Fit estimated results for the OS CR from the nominal fit method and by un-constraining the shape parameters for testing reasons. The test is performed on the 2012 data because of the higher statistics.

Reducible Background	Test Fit	Nominal Fit estimation
Zbb	137 ± 15	139 ± 16
$Zlight$	46 ± 9	46 ± 9
$t\bar{t}$	183 ± 11	181 ± 11

Table 5.20: Fit estimated results for the OS CR from the nominal fit method and by reducing the fractions uncertainties to 0.1 of each value for testing reasons. The test is performed on the 2012 data because of the higher statistics.

Reducible Background	Test Fit	Nominal Fit estimation
Zbb	137 ± 14	139 ± 16
$Zlight$	46 ± 7	46 ± 9
$t\bar{t}$	185 ± 10	181 ± 11

³⁴³⁸ (for which the fitted distributions are located in the Appendix C):

³⁴³⁹ (1) Shape Parameters Effect

³⁴⁴⁰ In this check, the shape parameters are set essentially free to fluctuate rather than
³⁴⁴¹ being constrained in the MC values. Table 5.19 shows the estimated Zbb , $Zlight$
³⁴⁴² and $t\bar{t}$ contributions and for comparison the values that the nominal fit method esti-
³⁴⁴³ mates are presented. The results are compatible within the statistical uncertainties
³⁴⁴⁴ and no unexpected shape is observed in the fitted CR (Figure C.1).

³⁴⁴⁵ (2) Fractions Uncertainties Effect

³⁴⁴⁶ The fractions uncertainties are set to 0.1 of each value and the fit is performed
³⁴⁴⁷ without other modifications. No significant discrepancy is observed within the un-
³⁴⁴⁸ certainties as the Table 5.20 and the Figures C.2 show.

³⁴⁴⁹ In another test the uncertainties are doubled, Table 5.21 and Figure C.3 show the
³⁴⁵⁰ results, once again no discrepancy with the nominal results is observed.

³⁴⁵¹ (3) $Zjets$ and $t\bar{t}$ Fit

³⁴⁵² The fit in this case is performed without trying to separate the heavy and light
³⁴⁵³ flavor of the $Zjets$, in all the rest the fit is similar to the nominal method. The
³⁴⁵⁴ results are reported in Table 5.22 and the fitted masses are shown in Figure C.4.
³⁴⁵⁵ No significant discrepancy from the nominal method is observed.

Table 5.21: Fit estimated results for the OS CR from the nominal fit method and by doubling the fractions uncertainties for testing reasons. The test is performed on the 2012 data because of the higher statistics.

Reducible Background	Test Fit	Nominal Fit estimation
Zbb	136 ± 19	139 ± 16
$Zlight$	46 ± 14	46 ± 9
$t\bar{t}$	175 ± 11	181 ± 11

Table 5.22: Fit estimated results for the OS CR from the nominal fit method where the Zbb and the $Zlight$ have been merged and the fit is performed for the $Zjets$ and $t\bar{t}$ estimation for testing reasons. The test is performed on the 2012 data because of the higher statistics.

Reducible Background	Test Fit	Nominal Fit estimation
$Zjets$	189 ± 16	185 ± 18
$t\bar{t}$	180 ± 11	181 ± 11

3456 (4) Individual CR Fits

3457 The individual CRs are fitted for the extraction of each background component.
 3458 The shape parameters are fixed to the values of the simultaneous fit, in order to
 3459 avoid the tail mismodeling, and the Zbb and $Zlight$ are treated as $ZJets$ since it is
 3460 impossible to distinguish their identical shapes from one CR. The results are pre-
 3461 sented in Table 5.23 and are in well agreement with the simultaneous fit estimations
 3462 withing the statistical uncertainties.

3463 (5) $t\bar{t}$ Cross Checks

3464 The $e\mu + \mu\mu$ results can be used to estimate the 4μ and $2e2\mu$ $t\bar{t}$ results using
 3465 the formulas:

$$N_{t\bar{t} \text{ estimated}}^{4\mu} = N_{data}^{e\mu+\mu\mu} \times N_{MC}^{\frac{4\mu}{e\mu+\mu\mu}} \quad (5.11)$$

$$N_{t\bar{t} \text{ estimated}}^{2e2\mu} = N_{data}^{e\mu+\mu\mu} \times N_{MC}^{\frac{2e2\mu}{e\mu+\mu\mu}} \quad (5.12)$$

3466 For this estimation only $e\mu + \mu^+\mu^-$ events with OS secondary pairs are considered,
 3467 given that the result of the estimation has to be the expected reference OS events.
 3468 The data $e\mu + \mu^+\mu^-$ are found to be 101 ± 10 . From the MC samples, the ratios of

Figure 5.15: The data m_{12} distributions are presented after the individual fit of each CR. No separation between light and heavy jets made, given that their same shape does not allow it. The CRs of the inverted $d_0/\sigma d_0$ (a), inverted isolation and nominal $d_0/\sigma d_0$ (b), SS (c) and $e\mu + \mu\mu$ (d) are presented. The test proves no significant deviation with the nominal results.

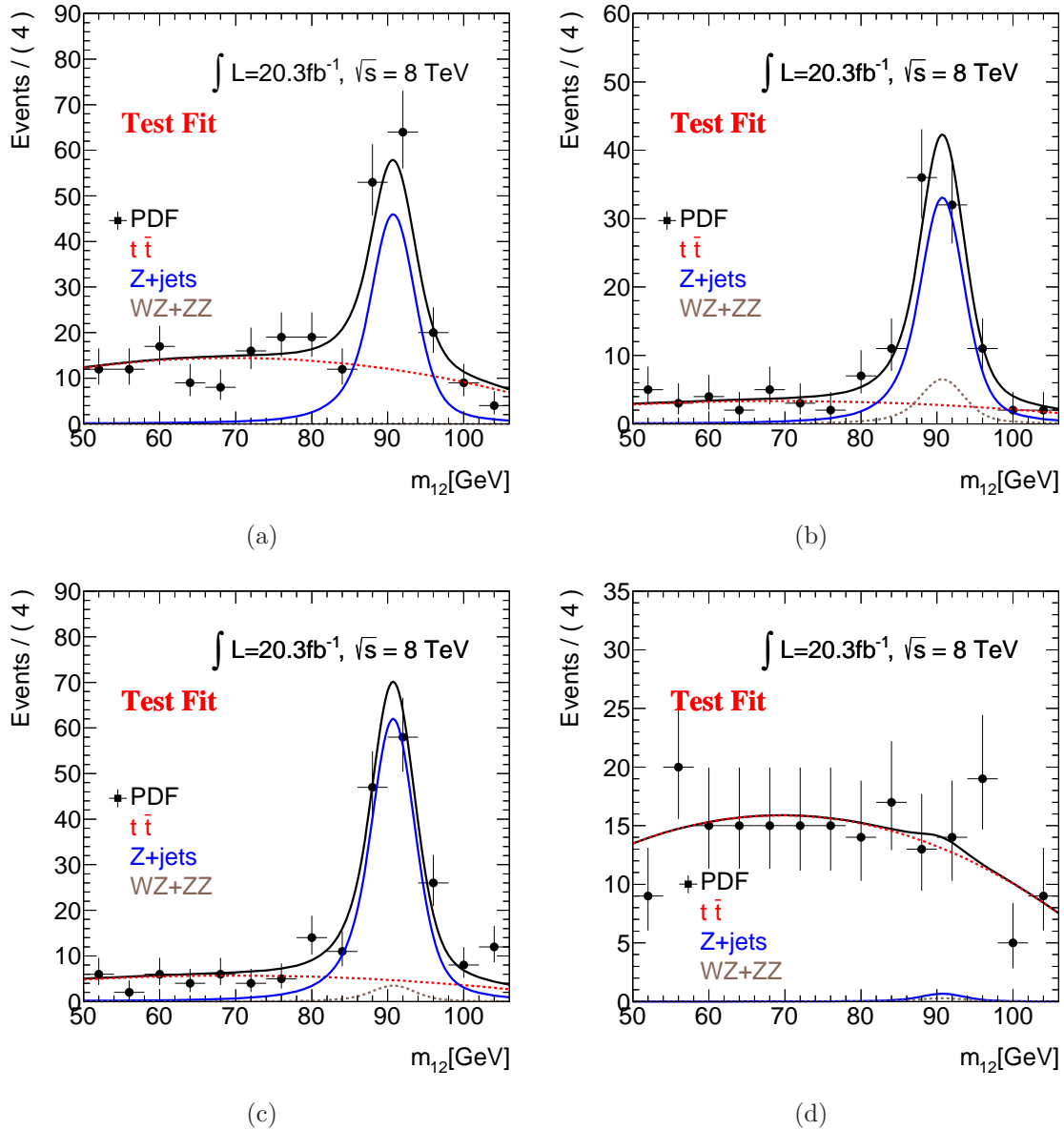


Table 5.23: Individual CR fit results of the Z *Jets* (including heavy and light jets) and $t\bar{t}$ background is performed as a sanity check of the simultaneous fit results for the 2012. In the case of $e\mu + \mu\mu$ CR the Z *Jets* component cannot be extracted because of its small contamination.

Control Region	$Z + Jets$	$t\bar{t}$
Inverted $d_0/\sigma d_0$	186 ± 29	181 ± 18
Inverted Isolation	194 ± 24	189 ± 26
SS	198 ± 23	155 ± 25
$e\mu + \mu\mu$	meaningless	184 ± 21
Simultaneous Fit	185 ± 18	181 ± 11

Table 5.24: $t\bar{t}$ cross checks made from the $e\mu + \mu^+\mu^-$ CR and are compared to the fit results in the reference CR. No systematic uncertainties are included.

$t\bar{t}$	Individual CR	Nominal Simultaneous Fit
Estimations in the Reference CR	166 ± 6	181 ± 11

the reference over the $t\bar{t}$ enriched CR are calculated as:

$$N_{MC}^{\frac{4\mu}{e\mu+\mu\mu}} = 0.840 \pm 0.016 \quad (5.13)$$

$$(5.14)$$

$$N_{MC}^{\frac{2e2\mu}{e\mu+\mu\mu}} = 0.798 \pm 0.015$$

The $t\bar{t}$ reference OS estimations are presented in Table 5.24 for both the 4μ and the $2e2\mu$ channels. In the same Table the nominal fit estimations are given for comparison.

5.10.6 2012 Signal Region (SR) Extrapolations

The results of the fit, reported in Table 5.17, can be extrapolated to the SR by multiplying with the probability of each background type to fulfill the additional selection, i.e. isolation and $d_0/\sigma d_0$ criteria. The so called "transfer factor" (T.F.) is calculated from the relevant MC samples and is presented in Table 5.25. The quoted uncertainties correspond to the statistical MC uncertainties and the systematic uncertainties which originate from the efficiency difference of the additional selection observed in the 3ℓ

Table 5.25: Efficiencies for each background type to fulfill the isolation and impact parameter criteria, calculated from $\sqrt{s} = 8$ TeV MC samples. The uncertainties correspond to the statistical MC errors and the systematic uncertainty from the efficiency difference of the additional selection observed in the 3ℓ final state (Section 5.9) between data and MC.

Reducible Background	Transfer Factor (%)
Zbb	3.10 ± 0.19
$Zlight$	3.0 ± 1.8
$t\bar{t}$	0.55 ± 0.09

final state (Section 5.9) between data and MC (1.6%). During the fit, only the Zbb uncertainty for the case of inverted isolation was included (4%). This is considered to be the only source of systematic uncertainties during the fitting procedure, given that the final estimation is dominated by the statistical uncertainties and the transfer factor error.

The final reducible backgrounds estimations in the signal region are estimated based on the formula:

$$N_x^{SR} = N_x \times T.F._x \quad (5.15)$$

where the N_x is the x -background estimated from the fit events in the OS CR (Table 5.17) and the corresponding transfer factors are the $T.F._x$. The results correspond to the sum of the $Z \rightarrow e^+e^- + \mu^+\mu^-$ and $Z \rightarrow \mu^+\mu^- + \mu^+\mu^-$ final states, also denoted as $2e2\mu$ and 4μ respectively. In order to split those, a multiplication with the ratios of $2e2\mu/(2e2\mu + 4\mu)$ or $4\mu/(2e2\mu + 4\mu)$ is needed, i.e.:

$$N_x^{SR} = N_x \times T.F._x \times \frac{4\mu \text{ OR } 2e2\mu}{2e2\mu + 4\mu} \quad (5.16)$$

The final estimations for the 2012 data are given in Table 5.26. The fit uncertainty is assigned as the statistical error and the transfer factor uncertainty with the channel splitting uncertainty ($2e2\mu/(2e2\mu + 4\mu)$ or $4\mu/(2e2\mu + 4\mu)$ error) as the systematic uncertainty of the method.

5.10.7 2011 Reducible Background Estimations

The method followed for the 2012 $Z + \mu\mu$ background estimation at $\sqrt{s} = 8$ TeV is applied in a similar way to the 2011 data. The method is fully validated in the

Table 5.26: Reducible background estimated contamination in the SR for the 2012 data, based on the formula 5.16. The fit uncertainty is assigned as the statistical error and the transfer factor uncertainty with the channel splitting uncertainty ($2e2\mu/(2e2\mu+4\mu)$ or $4\mu/(2e2\mu+4\mu)$ error) as the systematic uncertainty of the method.

$\sqrt{s} = 8$ TeV		
Reducible Background	4μ	$2e2\mu$
Z_{jets}	$3.11 \pm 0.46(\text{stat}) \pm 0.43(\text{syst})$	$2.58 \pm 0.39(\text{stat}) \pm 0.43(\text{syst})$
$t\bar{t}$	$0.51 \pm 0.03(\text{stat}) \pm 0.09(\text{syst})$	$0.48 \pm 0.03(\text{stat}) \pm 0.08(\text{syst})$
WZ MC expectation	0.42 ± 0.07	0.44 ± 0.06
Z_{jets} decomposition		
$Zb\bar{b}$	$2.30 \pm 0.26(\text{stat}) \pm 0.14(\text{syst})$	$2.01 \pm 0.23(\text{stat}) \pm 0.13(\text{syst})$
$Zlight$	$0.81 \pm 0.38(\text{stat}) \pm 0.41(\text{syst})$	$0.57 \pm 0.31(\text{stat}) \pm 0.41(\text{syst})$

³⁴⁹⁹ 2012 data (Section 5.10.5) and no further cross check is necessary. The data are fitted
³⁵⁰⁰ simultaneously with each CR modeling taken from Equation 5.8. The fractions between
³⁵⁰¹ the CR are extracted from the 2011 MC at $\sqrt{s} = 7$ TeV and are presented in Table 5.27.

³⁵⁰² Figure 5.16 shows the simultaneous fit results in the four CRs. The number of events
³⁵⁰³ in the OS CR are presented in Table 5.28 for both the expectations from MC and the
³⁵⁰⁴ fit results. Their difference is also reported.

³⁵⁰⁵ The m_{12} , m_{34} and $m_{4\ell}$ masses in the reference OS CR are presented in Figure 5.17,
³⁵⁰⁶ where the irreducible backgrounds are scaled to the fit estimation and the ZZ and WZ
³⁵⁰⁷ are taken from the MC. The exact numbers of each background are mentioned on the
³⁵⁰⁸ legends of the Figures. The Higgs signal contribution is not included.

Table 5.27: MC estimated ratios for the reducible background of the fit CRs with respect to the OS CR at $\sqrt{s} = 7$ TeV, following the naming convention $f_x = CR_x/CR_{OS}$. The uncertainties correspond to the MC statistical errors. This fractions are used by the fit, as Equation 5.8 describes, after being promoted to nuisance parameters for better handling of the uncertainties.

Background	f_{inv-d0}	$f_{inv-iso}$	f_{SS}	$f_{e\mu+\mu\mu}$
$Zb\bar{b}$	0.76 ± 0.10	0.231 ± 0.005	0.699 ± 0.012	0.0000 ± 0.0003
$Z + light$	0.49 ± 0.19	0.48 ± 0.16	0.89 ± 0.23	0.0000 ± 0.0029
$t\bar{t}$	0.79 ± 0.05	0.206 ± 0.022	0.89 ± 0.05	1.13 ± 0.04

Figure 5.16: The 2011 data m_{12} distributions are presented after the unbinned simultaneous fit in the control regions of inverted $d_0/\sigma d_0$ (a), inverted isolation and nominal $d_0/\sigma d_0$ (b), SS (c) and $e\mu + \mu\mu$ (d). The WZ and ZZ contamination is fixed to the MC estimations and the rest of the background results are estimated using the nominal fit.

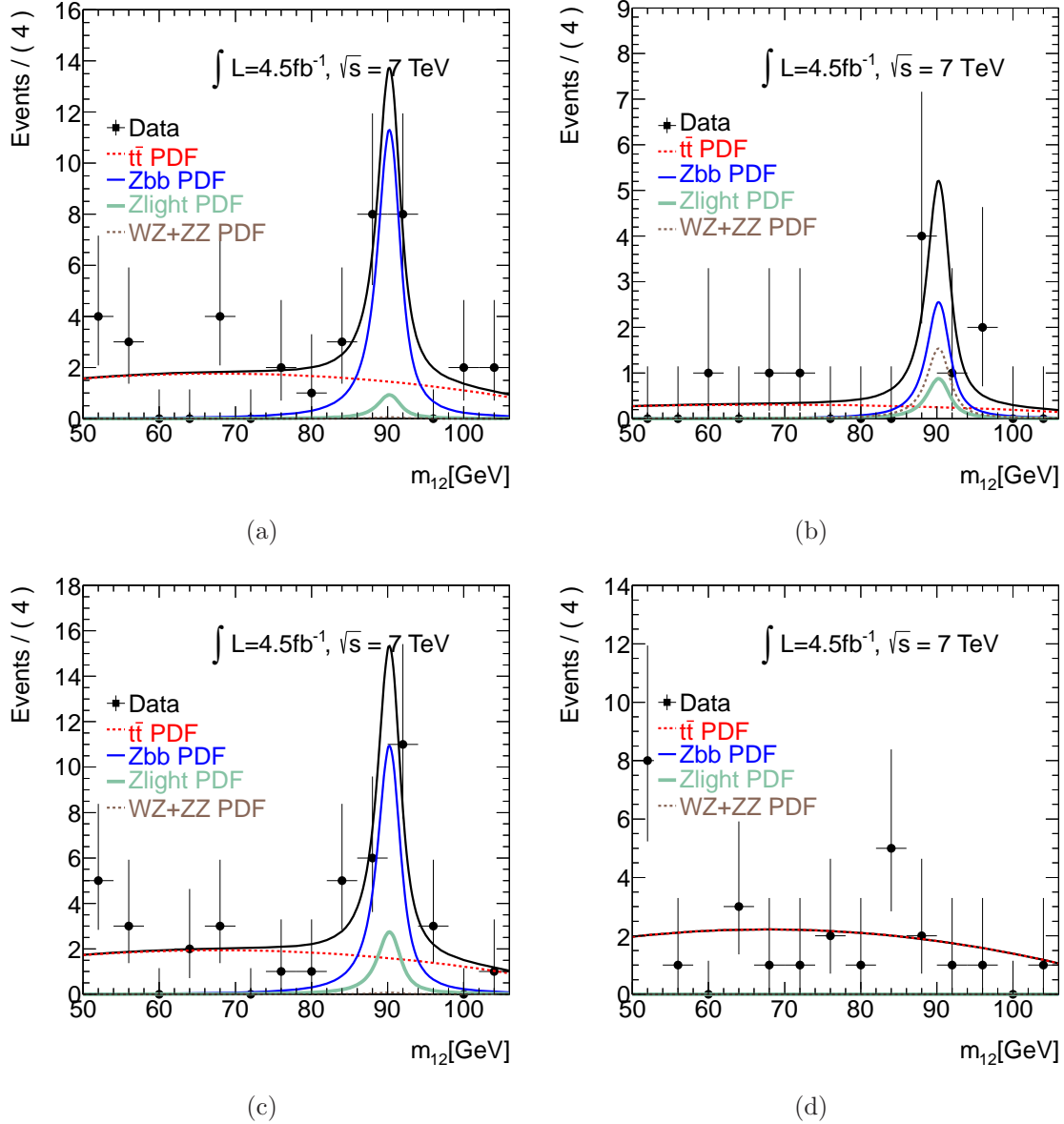


Figure 5.17: 2011 $Z + \mu^+\mu^-$ event distributions in data and the expected backgrounds in the reference CR. The reducible backgrounds contributions come using the nominal fit while the ZZ and WZ are taken from the MC. The Higgs signal contamination is not shown. The m_{12} (a), m_{34} (b) and m_{4l} (c) are presented.

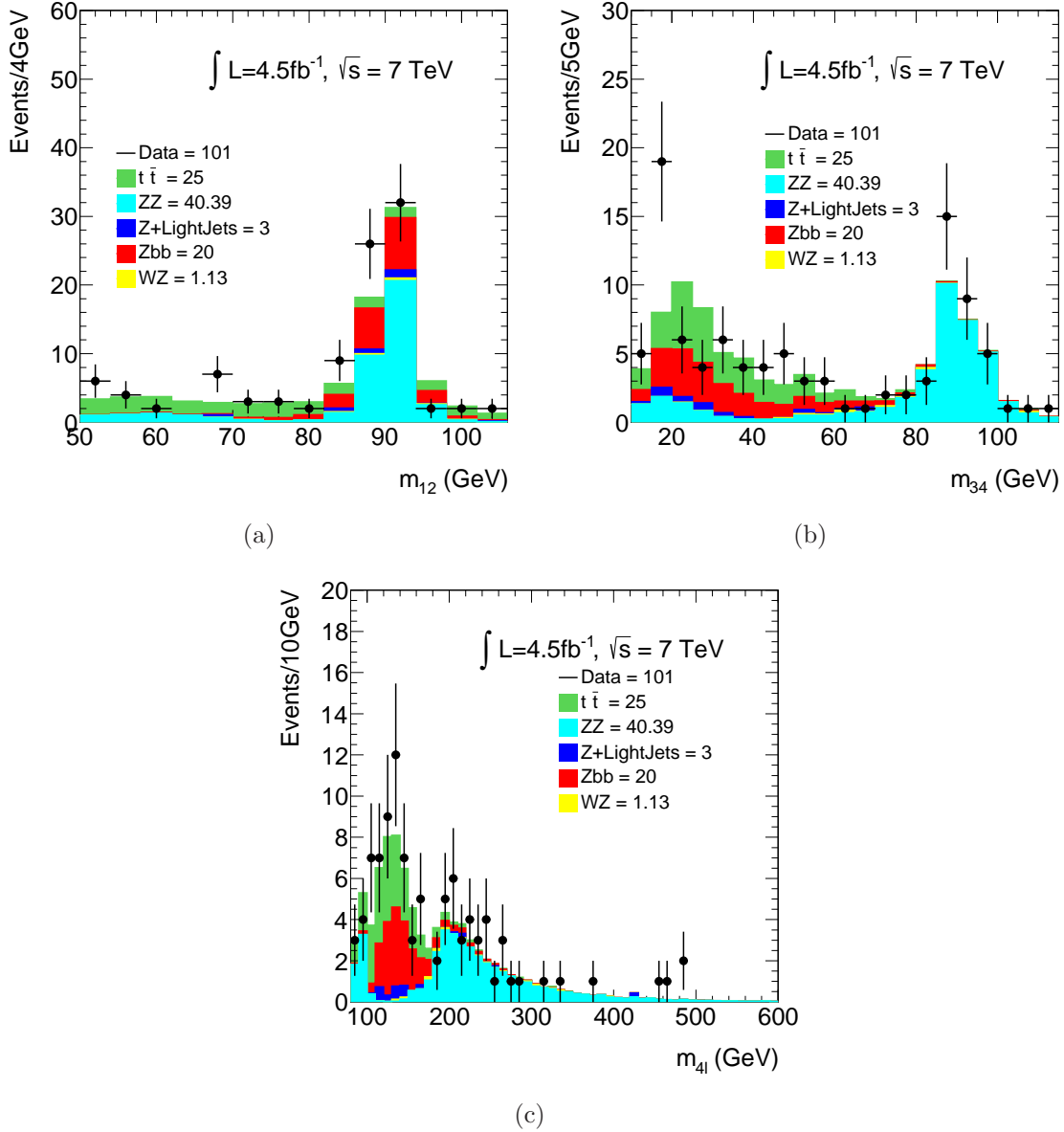


Table 5.28: Estimations of the reducible background contributions made from the 2011 data simultaneous fit in the OS CR and the relevant MC expectations. The difference between the two is quoted as "scaling". The presented uncertainties are the statistical uncertainties estimated from the fit and the MC available statistics accordingly.

Reducible Background	MC prediction	Fit estimation	Scaling
$Zb\bar{b}$	15.1 ± 0.06	20 ± 12	1.3 ± 0.8
$Zlight$	3.9 ± 0.9	3 ± 4	0.8 ± 1.0
$t\bar{t}$	22.4 ± 1.0	25 ± 5	1.14 ± 0.23

Table 5.29: Per-event efficiencies for each background type at $\sqrt{s} = 7$ TeV to fulfill the isolation and impact parameter criteria. The $t\bar{t}$ transfer factor is taken from the 2012 MC because of the inadequate statistical precision of the MC samples used in the 2011 analysis. The uncertainties correspond to the statistical MC error and the systematic efficiency difference of the additional selection observed in the 3ℓ final state (Section 5.9) between data and MC.

Reducible Background	Transfer Factor %
$Zb\bar{b}$	3.2 ± 0.3
$Zlight$	3.4 ± 1.9
$t\bar{t}$	0.55 ± 0.11

3509 The fit results of Table 5.28 are extrapolated to the SR using formula 5.16. The
 3510 transfer factors are quoted in Table 5.29 and are estimated from the $\sqrt{s} = 7$ TeV
 3511 MC except from the $t\bar{t}$ transfer factor which is taken from the 2012 MC because of
 3512 the inadequate statistical precision of the MC samples used in the 2011 analysis. The
 3513 motivation for this is the agreement between the heavy flavor extrapolation in the
 3514 $Zb\bar{b}$ sample of the 7 TeV and the 8 TeV samples using the same generator (ALPGEN
 3515 HERWIG). The quoted uncertainties correspond to the statistical MC uncertainties
 3516 and the systematic uncertainty comes from the squared efficiency difference of the
 3517 additional selection that is observed in the 3ℓ final state (Section 5.9) between data and
 3518 MC (5.0%).

3519 The final reducible backgrounds estimations in the SR are given in Table 5.30 based
 3520 on the extrapolation formula 5.16. The fit uncertainty is assigned as the statistical error
 3521 and the transfer factor uncertainty with the channel splitting uncertainty, $2e2\mu/(2e2\mu +$
 3522 $4\mu)$ or $4\mu/(2e2\mu + 4\mu)$ error, as the systematic uncertainty of the method.

Table 5.30: Reducible background estimated contamination in the SR for the 2011 data, based on the formula 5.16. The fit uncertainty is assigned as the statistical error and the transfer factor uncertainty with the channel splitting uncertainty ($2e2\mu/(2e2\mu+4\mu)$ or $4\mu/(2e2\mu+4\mu)$ error) as the systematic uncertainty of the method.

$\sqrt{s} = 7$ TeV		
Reducible Background	4μ	$2e2\mu$
Z_{jets}	$0.42 \pm 0.21(\text{stat}) \pm 0.08(\text{syst})$	$0.29 \pm 0.14(\text{stat}) \pm 0.05(\text{syst})$
$t\bar{t}$	$0.081 \pm 0.016(\text{stat}) \pm 0.021(\text{syst})$	$0.056 \pm 0.011(\text{stat}) \pm 0.015(\text{syst})$
WZ MC expectation	0.08 ± 0.05	0.19 ± 0.10
Z_{jets} decomposition		
$Zb\bar{b}$	$0.36 \pm 0.19(\text{stat}) \pm 0.07(\text{syst})$	$0.25 \pm 0.13(\text{stat}) \pm 0.05(\text{syst})$
$Zlight$	$0.06 \pm 0.08(\text{stat}) \pm 0.04(\text{syst})$	$0.04 \pm 0.06(\text{stat}) \pm 0.02(\text{syst})$

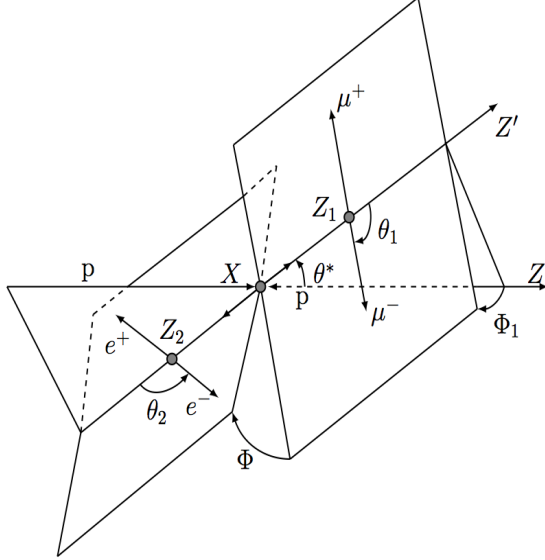
5.11 4ℓ Angular Distributions

When the $ZZ^{(*)}$ system decays to the four leptons, the angles of Figure 5.18 appear. These angles are the observables for the Higgs Spin and Parity analysis and therefore this background measurement was used to control the contribution of the reducible backgrounds to the distributions of these angles. The production and decay angles are defined in the following way:

- θ_1, θ_2 : are the angles between negative final state leptons and the direction of flight of their respective Z -bosons. The 4-vectors of the leptons are calculated in the rest frame of the corresponding Z -bosons.
- ϕ is the angle between the decay planes of the four final state leptons expressed in the rest frame of the four-leptons system
- ϕ_1 is the angle defined between the decay plane of the first lepton pair and a plane defined by the vector of Z_1 in the rest frame of the four-leptons system and the positive direction of the collision axis.
- θ^* is the production angle of Z_1 defined in the rest frame of the four-lepton system.

The angular distributions in the reference OS CR of the 4μ and $2e2\mu$ channels are presented in Figures 5.19 and 5.20 for the 2011 and the 2012 data respectively. The reducible background is normalized to the estimations of the previously presented data

Figure 5.18: Graphical display of production and decay angles in the $X \rightarrow ZZ^{(*)} \rightarrow 4\ell$ decay. These angles are the observables used for the Spin and Parity analysis.



3541 driven methods (Section 5.10), the irreducible background is taken from the MC and
 3542 no signal MC is included. These estimations are the inputs for the determination of
 3543 the Spin/CP of the Higgs boson.

3544 5.12 Systematic Uncertainties

3545 For the $H \rightarrow ZZ^{(*)} \rightarrow 4\ell$ decay modes involving electrons, the electron energy scale
 3546 uncertainty which is determined from $Z \rightarrow ee$ and $J/\psi \rightarrow ee$ decays, is propagated
 3547 as a function of the pseudorapidity and the transverse energy of the electrons. The
 3548 precision of the energy scale is better than 0.1% for $|\eta| < 1.2$ and $1.8 < |\eta| < 2.47$, and
 3549 a few per mille for $1.2 < |\eta| < 1.8$ [59]. The uncertainties on the measured Higgs boson
 3550 mass due to the electron energy scale uncertainties are $\pm 0.04\%$, $\pm 0.025\%$ and $\pm 0.04\%$
 3551 for the $4e$, $2e2\mu$ and $2\mu2e$ final states, respectively.

3552 Similarly, for the $H \rightarrow ZZ^{(*)} \rightarrow 4\ell$ decay modes involving muons, the various
 3553 components of the systematic uncertainty on the muon momentum scale are determined
 3554 using large samples of $J/\psi \rightarrow \mu\mu$ and $Z \rightarrow \mu\mu$ decays and are validated using $\Upsilon \rightarrow$
 3555 $\mu\mu$, $J/\psi \rightarrow \mu\mu$ and $Z \rightarrow \mu\mu$ decays. In the muon transverse momentum range of
 3556 6 – 100 GeV, the systematic uncertainties on the scales are about $\pm 0.04\%$ in the barrel
 3557 region and reach $\pm 0.2\%$ in the region $|\eta| > 2$ [61]. The uncertainties on the measured
 3558 Higgs boson mass due to the muon energy scale uncertainties are estimated to be

Figure 5.19: Angular distributions for the 4μ and $2e2\mu$ reference OS CR events at $\sqrt{s} = 7$ TeV: (a) θ_1 , (b) θ_2 , (c) ϕ , (d) ϕ_1 and (e) θ^* . The reducible background is normalized to the estimations made using the nominal fit, the irreducible background is taken from the MC and no signal MC is included.

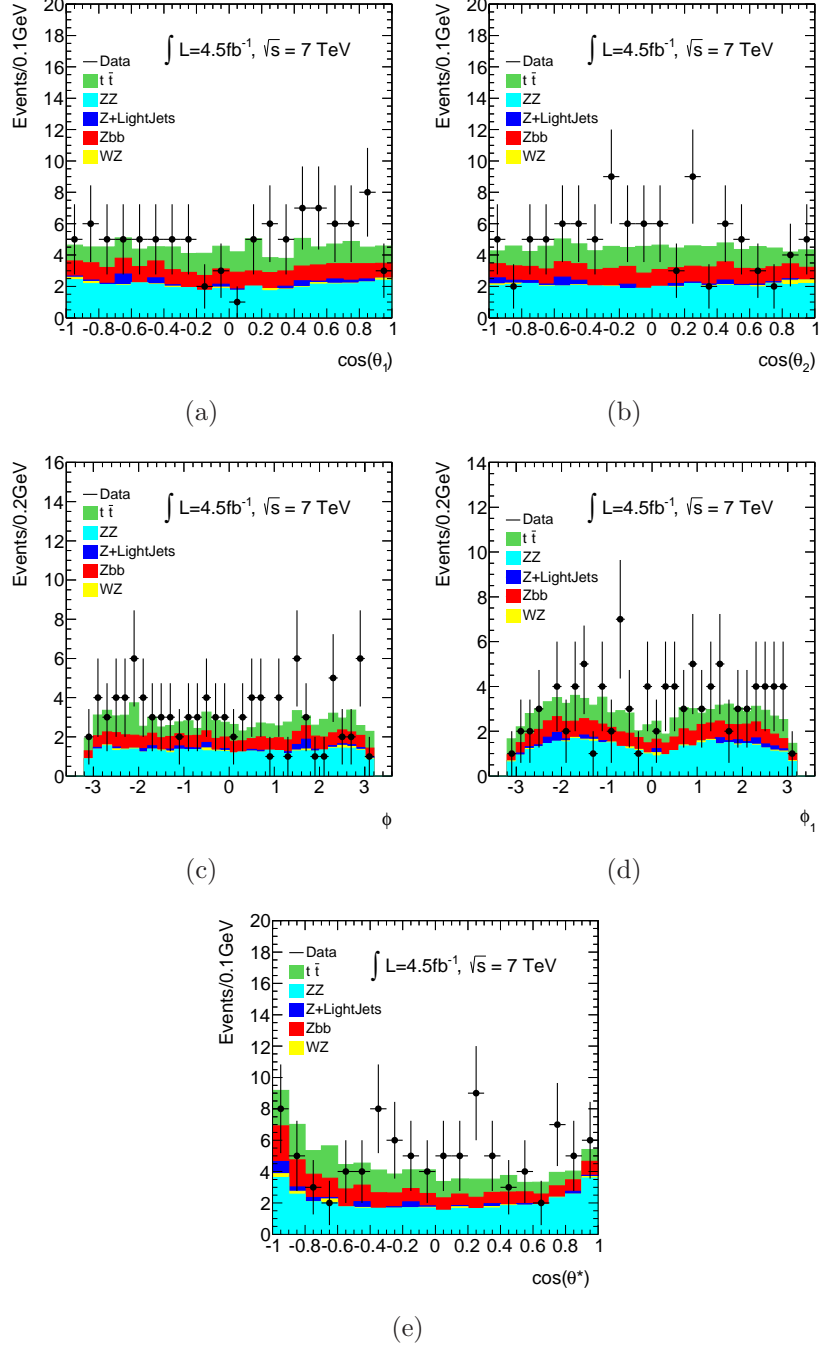
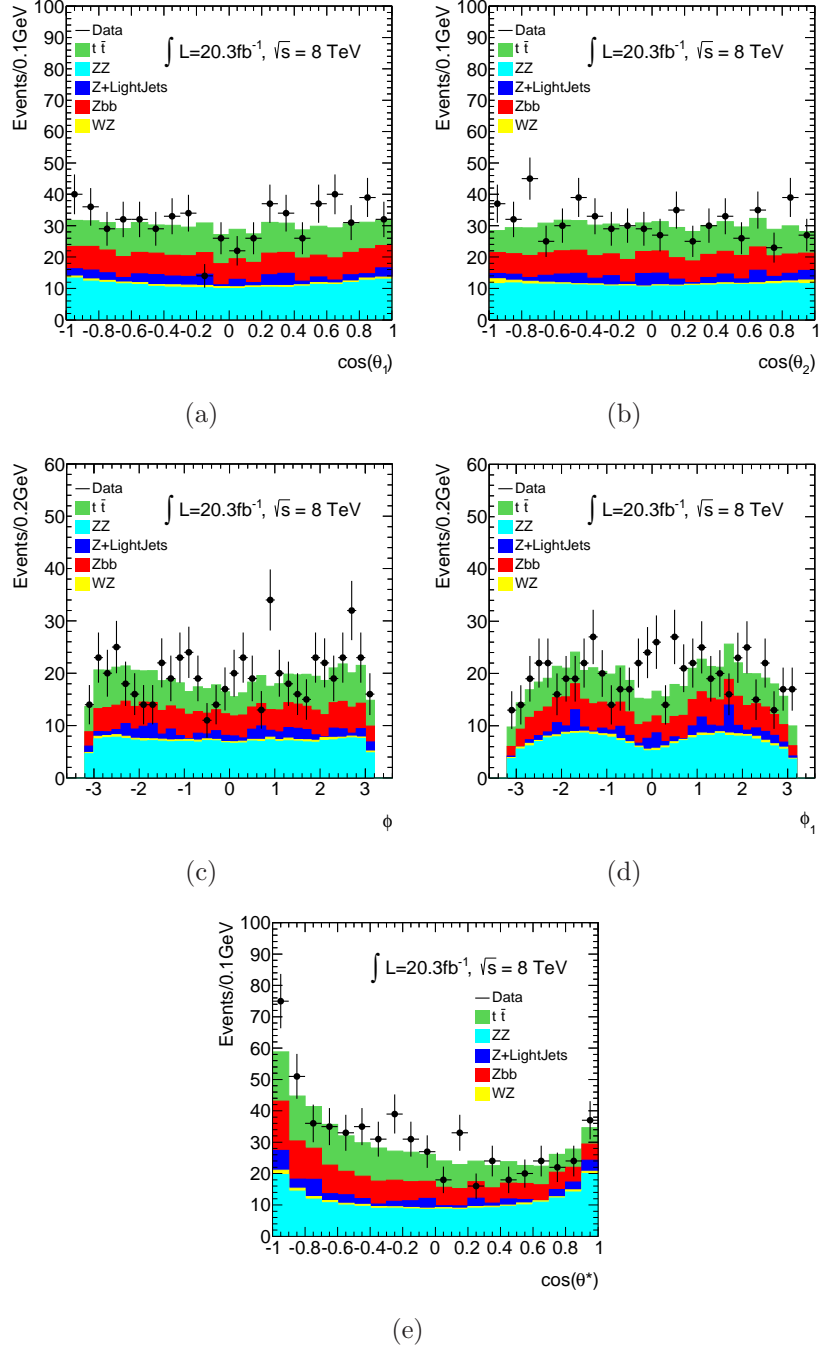


Figure 5.20: Angular distributions for the 4μ and $2e2\mu$ reference OS CR events at $\sqrt{s} = 8$ TeV: (a) θ_1 , (b) θ_2 , (c) ϕ , (d) ϕ_1 and (e) θ^* . The reducible background is normalized to the estimations made using the nominal fit, the irreducible background is taken from the MC and no signal MC is included.



$\pm 0.04\%$, $\pm 0.015\%$ and $\pm 0.02\%$ for the 4μ , $2e2\mu$ and $2\mu2e$ final states, respectively.

Uncertainties on the measured Higgs boson mass related to the background contamination and final-state QED radiation modeling are negligible compared to the other sources described above.

The weighted contributions to the uncertainty in the mass measurement, when all the final states are combined, are $\pm 0.01\%$ for the electron energy scale uncertainty and $\pm 0.03\%$ for the muon momentum scale uncertainty. The large impact of the muon momentum scale uncertainty is due to the fact that the muons final states have more significant weight in the combined mass.

The efficiencies to trigger, reconstruct and identify electrons and muons are studied using $Z \rightarrow \ell\ell$ and $J/\psi \rightarrow \ell\ell$ decays [67, 57, 68, 61]. The expected impact from the simulation of the associated systematic uncertainties on the signal yield are presented in Table 5.31. The impact is presented for the individual final states and for all channels combined.

A small additional uncertainty on the isolation and impact parameter selection efficiency is applied for electrons with E_T below 15 GeV. The effect of the isolation and impact parameter uncertainties on the signal strength is given in Table 5.31. The corresponding uncertainty for muons is found to be negligible. The background uncertainties, as estimated from the data driven methods, are also presented in Table 5.31. Additionally the three most important theoretical uncertainties are given in the same Table. Uncertainties on the predicted Higgs boson p_T spectrum due to those on the PDFs and higher-order corrections are estimated to affect the signal strength by less than $\pm 1\%$. The systematic uncertainty of the ZZ background rate is around $\pm 4\%$ for $m_{4\ell} = 125$ GeV and increases for higher masses, averaging to around $\pm 6\%$ for the ZZ production above 110 GeV.

The overall uncertainty on the integrated luminosity for the complete 2011 data set is $\pm 1.8\%$ [69]. The uncertainty on the integrated luminosity for the 2012 data set is $\pm 2.8\%$; this uncertainty is derived following the methodology used for the 2011 data set, from a preliminary calibration of the luminosity scale with beam-separation scans performed in November 2012.

5.13 Higgs Candidates and Background

The selection described in Section 5.6 is applied for the allocation of Higgs candidates in the four possible decay channels (4μ , $2e2\mu$, $2\mu2e$, $4e$). This analysis, along with the previously presented muons background measurement, was a major contribution in the discovery of the Higgs boson, officially announced in summer 2012. The analysis was performed on the Run-I data corresponding to 20.3 fb^{-1} at $\sqrt{s} = 8 \text{ TeV}$ and 4.5 fb^{-1} at $\sqrt{s} = 7 \text{ TeV}$ and the results are presented in the following paragraphs.

Table 5.31: The expected impact of the systematic uncertainties on the signal yield, derived from the simulation for $m_H = 125$ GeV, are summarized for each of the four final states for the combined $\sqrt{s} = 7$ TeV and $\sqrt{s} = 8$ TeV data. The missing fields of the table do not contribute significantly and therefore are omitted.

Source of uncertainty	4μ	$2e2\mu$	$2\mu2e$	$4e$	combined
Electron reconstruction and identification efficiencies	–	1.7%	3.3%	4.4%	1.6%
Electron isolation and impact parameter selection	–	0.07%	1.1%	1.2%	0.5%
Electron trigger efficiency	–	0.21%	0.05%	0.21%	<0.2%
$\ell\ell + ee$ backgrounds	–	–	3.4%	3.4%	1.3%
Muon reconstruction and identification efficiencies	1.9%	1.1%	0.8%	–	1.5%
Muon trigger efficiency	0.6%	0.03%	0.6%	–	0.2%
$\ell\ell + \mu\mu$ backgrounds	1.6%	1.6%	–	–	1.2%
QCD scale uncertainty					6.5%
PDF, α_s uncertainty					6.0%
$H \rightarrow ZZ^{(*)}$ branching ratio uncertainty					4.0%

3596 In total 428 candidate events are selected by the analysis (with $m_{4\ell} > 100$ GeV),
 3597 137 4μ , 212 $2e2\mu$ and 79 $4e$ events, in the 2012 data and 83 candidate events, 34 4μ ,
 3598 31 $2e2\mu$ and 18 $4e$ events in the 2011 data. Table 5.32 presents the results of the
 3599 separate channels in the "Low" and "High" mass regions, defined as $m_{4\ell} < 160$ GeV
 3600 and $m_{4\ell} \geq 160$ GeV respectively, the estimated background and the signal expectations
 3601 normalized to the theoretical cross sections for $\sqrt{s} = 7$ TeV. Table 5.33 presents the
 3602 similar results for the 2012 data at $\sqrt{s} = 8$ TeV. The $m_{4\ell}$ mass distributions are
 3603 presented in Figure 5.21. The corresponding primary and secondary mass distributions
 3604 are shown in Figure 5.22. In all these Figures, the systematic uncertainty associated to
 3605 the total background contribution is represented by the hatched areas.

3606 Especially around the region of the Higgs boson (~ 125 GeV) the observations
 3607 are compared to the expected background and the theoretical signal expectations in
 3608 Table 5.34. It has to be noted that in this region only 2 events were found with non-
 3609 collinear FSR correction.

3610 In the low mass region, where the reducible background contributes, the separate
 3611 mass distributions for each channel, 4μ , $2e2\mu$, $2\mu2e$ and $4e$, are presented for the com-
 3612 bined 2012 and 2011 data in Figure 5.23.

3613 5.14 Summary

3614 The final Run-I analysis for the study of the final state $H \rightarrow ZZ^{(*)} \rightarrow 4\ell$ is pre-
 3615 sented. The analysis is performed using pp collision data corresponding to integrated

Table 5.32: The observed number of events and the final estimate for the expected background, separated into "Low mass" ($m_{4\ell} < 160$ GeV) and "High mass" ($m_{4\ell} \geq 160$ GeV) regions, are presented for the $\sqrt{s} = 7$ TeV data. The expected signal events are also shown for a Higgs boson of 125 GeV mass hypothesis.

	4 μ		2e2 μ + 2 μ 2e		4e	
	Low mass	High mass	Low mass	High mass	Low mass	High mass
$ZZ(*)$	5.27 \pm 0.26	16.98 \pm 1.26	4.39 \pm 0.24	25.71 \pm 1.91	2.02 \pm 0.13	9.85 \pm 0.77
Z , $Zb\bar{b}$, and $t\bar{t}$	0.43 \pm 0.19	0.17 \pm 0.07	2.32 \pm 0.57	1.16 \pm 0.28	2.16 \pm 0.45	1.13 \pm 0.24
Total Background	5.70 \pm 0.32	17.15 \pm 1.26	6.71 \pm 0.64	26.87 \pm 1.94	4.18 \pm 0.47	10.98 \pm 0.81
Data	11	23	7	24	4	14
$m_H = 125$ GeV	1.00 \pm 0.10		1.16 \pm 0.11		0.46 \pm 0.05	

Table 5.33: The observed number of events and the final estimate for the expected background, separated into "Low mass" ($m_{4\ell} < 160$ GeV) and "High mass" ($m_{4\ell} \geq 160$ GeV) regions, are presented for the $\sqrt{s} = 8$ TeV data. The expected signal events are also shown for a Higgs boson mass hypothesis.

	4 μ		2e2 μ + 2 μ 2e		4e	
	Low mass	High mass	Low mass	High mass	Low mass	High mass
$ZZ(*)$	27.58 \pm 1.37	95.00 \pm 7.06	23.43 \pm 1.28	145.25 \pm 10.85	11.20 \pm 0.74	56.42 \pm 4.44
Z , $Zb\bar{b}$, and $t\bar{t}$	2.90 \pm 0.53	1.14 \pm 0.21	4.44 \pm 0.87	1.98 \pm 0.40	1.89 \pm 0.40	0.99 \pm 0.21
Total Background	30.49 \pm 1.47	96.13 \pm 7.07	27.86 \pm 1.55	147.23 \pm 10.85	13.10 \pm 0.84	57.41 \pm 4.44
Data	42.00	95.00	38.00	174.00	23.00	56.00
$m_H = 125$ GeV	5.80 \pm 0.57		6.99 \pm 0.70		2.79 \pm 0.29	

Figure 5.21: $m_{4\ell}$ distributions of the selected candidates compared to the background expectation and the theoretical Higgs signal expectation for $m_H = 125$ GeV scaled by 1.51. (a) is the low mass region at $\sqrt{s} = 7$ TeV, (b) is the full mass region at $\sqrt{s} = 7$ TeV, (c) is the low mass region at $\sqrt{s} = 8$ TeV, (d) is the full mass region at $\sqrt{s} = 8$ TeV, (e) is the high mass region of the combined dataset and (f) is the full mass region of the combined dataset.

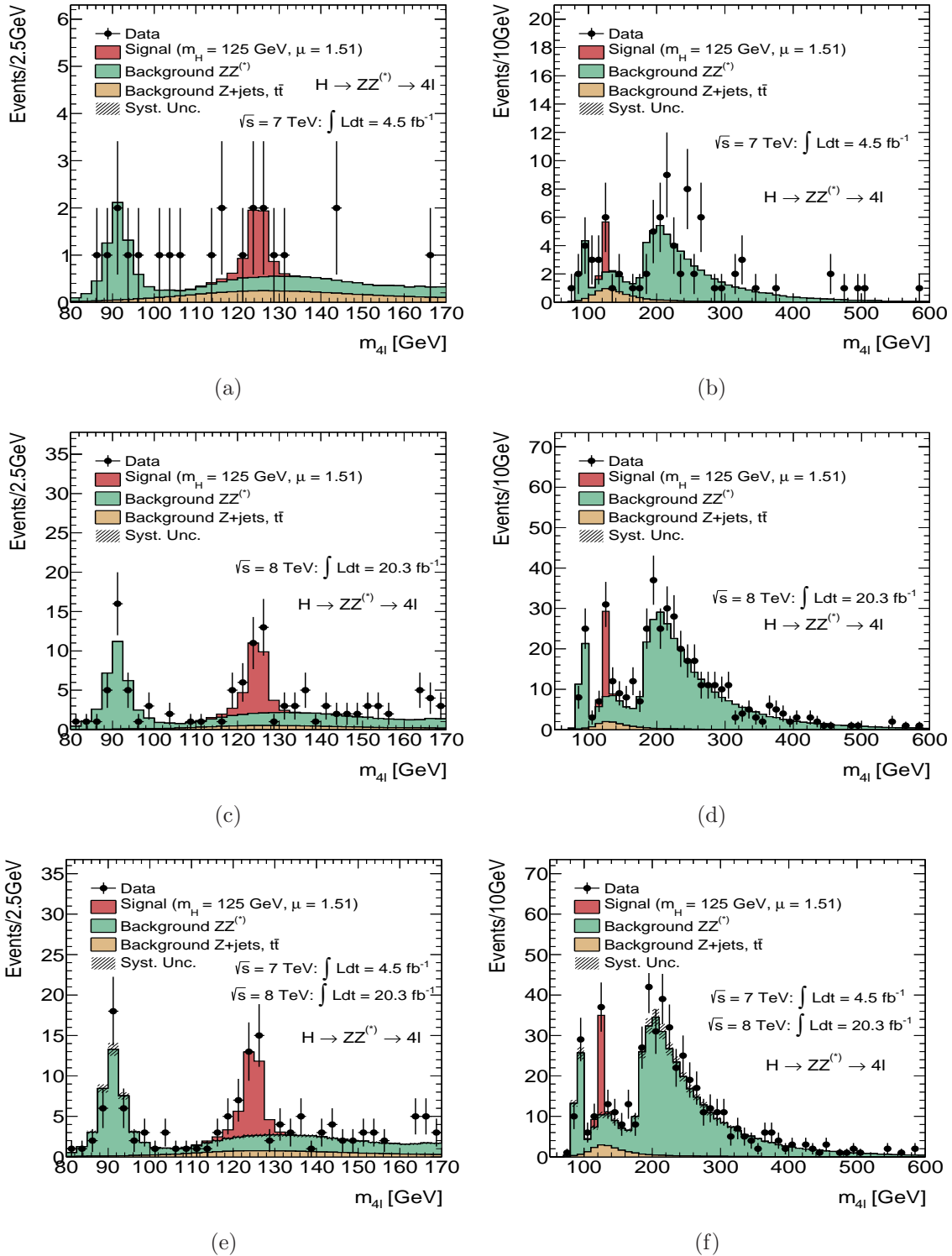
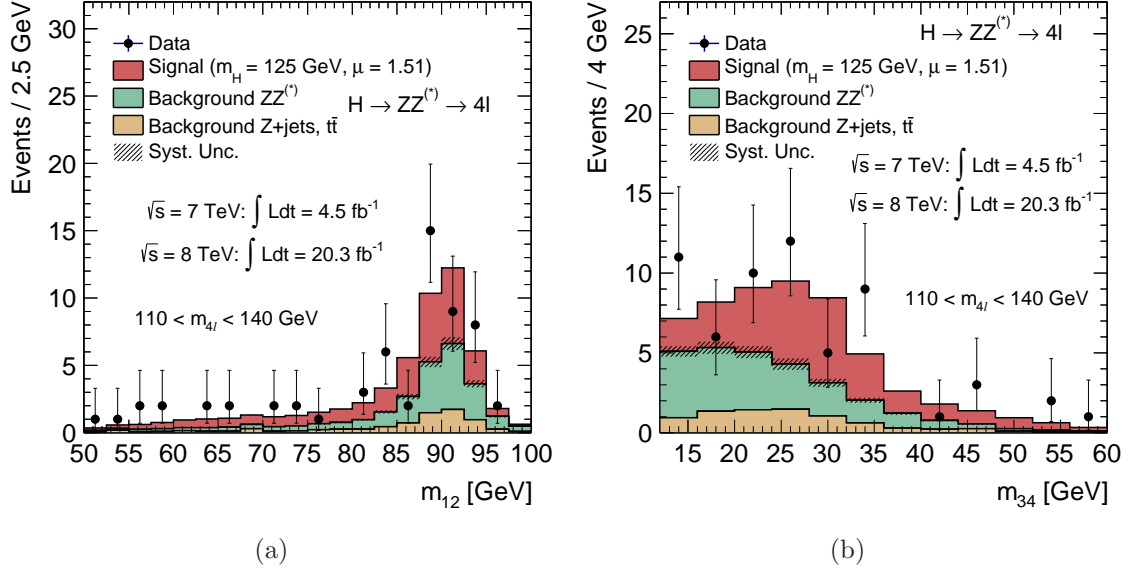


Table 5.34: The number of events expected and observed for a $m_H=125$ GeV hypothesis for the four-lepton final states in a window of $120 < m_{4\ell} < 130$ GeV. The second column shows the number of expected signal events for the full mass range, without a selection on $m_{4\ell}$. The other columns show for the $120 - 130$ GeV mass range the number of expected signal events, the number of expected ZZ background and reducible background events, the signal-to-background ratio (S/B), together with the number of observed events, for 4.5 fb^{-1} at $\sqrt{s} = 7 \text{ TeV}$ and 20.3 fb^{-1} at $\sqrt{s} = 8 \text{ TeV}$ as well as for the combined data sample.

Final state	Signal full mass range	Signal	ZZ	$Z\text{jets}, t\bar{t}$	S/B	Expected	Observed
$\sqrt{s} = 7 \text{ TeV}$							
4μ	1.00 ± 0.10	0.91 ± 0.09	0.46 ± 0.02	0.10 ± 0.04	1.7	1.47 ± 0.10	2
$2e2\mu$	0.66 ± 0.06	0.58 ± 0.06	0.32 ± 0.02	0.09 ± 0.03	1.5	0.99 ± 0.07	2
$2\mu2e$	0.50 ± 0.05	0.44 ± 0.04	0.21 ± 0.01	0.36 ± 0.08	0.8	1.01 ± 0.09	1
$4e$	0.46 ± 0.05	0.39 ± 0.04	0.19 ± 0.01	0.40 ± 0.09	0.7	0.98 ± 0.10	1
Total	2.62 ± 0.26	2.32 ± 0.23	1.17 ± 0.06	0.96 ± 0.18	1.1	4.45 ± 0.30	6
$\sqrt{s} = 8 \text{ TeV}$							
4μ	5.80 ± 0.57	5.28 ± 0.52	2.36 ± 0.12	0.69 ± 0.13	1.7	8.33 ± 0.6	12
$2e2\mu$	3.92 ± 0.39	3.45 ± 0.34	1.67 ± 0.08	0.60 ± 0.10	1.5	5.72 ± 0.37	7
$2\mu2e$	3.06 ± 0.31	2.71 ± 0.28	1.17 ± 0.07	0.36 ± 0.08	1.8	4.23 ± 0.30	5
$4e$	2.79 ± 0.29	2.38 ± 0.25	1.03 ± 0.07	0.35 ± 0.07	1.7	3.77 ± 0.27	7
Total	15.6 ± 1.6	13.8 ± 1.4	6.24 ± 0.34	2.00 ± 0.28	1.7	22.1 ± 1.5	31
$\sqrt{s} = 7 \text{ TeV} \text{ and } \sqrt{s} = 8 \text{ TeV}$							
4μ	6.80 ± 0.67	6.20 ± 0.61	2.82 ± 0.14	0.79 ± 0.13	1.7	9.81 ± 0.64	14
$2e2\mu$	4.58 ± 0.45	4.04 ± 0.40	1.99 ± 0.10	0.69 ± 0.11	1.5	6.72 ± 0.42	9
$2\mu2e$	3.56 ± 0.36	3.15 ± 0.32	1.38 ± 0.08	0.72 ± 0.12	1.5	5.24 ± 0.35	6
$4e$	3.25 ± 0.34	2.77 ± 0.29	1.22 ± 0.08	0.76 ± 0.11	1.4	4.75 ± 0.32	8
Total	18.2 ± 1.8	16.2 ± 1.6	7.41 ± 0.40	2.95 ± 0.33	1.6	26.5 ± 1.7	37

Figure 5.22: Distributions of $\sqrt{s} = 8$ TeV and 7 TeV data and the expected signal and backgrounds events. The m_{12} (a) and m_{34} (b) are shown for $m_{4\ell}$ in the range of $110 - 140$ GeV.



luminosities of 4.5 and 20.3 fb^{-1} at $\sqrt{s} = 7$ TeV and $\sqrt{s} = 8$ TeV respectively recorded with the ATLAS detector at the LHC. The signal and background simulation, the electron and muon reconstruction and identification, the event selection and in particular the method which were developed to measure the reducible background in the case where the secondary dilepton is a muon pair are discussed in detail. The analysis is performed inclusively at this Chapter and in the next Chapter the events are separated into categories for VBF, VH and ggF production modes.

For the inclusive analysis, in the m_H range of $120 - 130$ GeV, 37 events are observed while 26.5 ± 1.7 events are expected, decomposed as 16.2 ± 1.6 events for a SM Higgs signal with $m_H = 125$ GeV, 7.4 ± 0.4 $ZZ^{(*)}$ background events and 2.9 ± 0.3 reducible background events. This excess corresponds to a $H \rightarrow ZZ^{(*)} \rightarrow 4\ell$ signal observed with a significance of 8.1 standard deviations³ at the combined ATLAS measurement of the Higgs boson mass [70].

One 4μ candidate event display is shown in Figure 5.24. All the muons of this events pass through one EndCap of the detector and two of the muons pass through the CSC detector. The quadruplet mass of this events is 123.2 GeV.

³Standard deviation measures the distribution of data points around a mean or average.

Figure 5.23: $m_{4\ell}$ distributions of the selected candidates for $\sqrt{s} = 7$ and 8 TeV for the different subchannels of the analysis, compared to the background expectation in the mass range of 80 – 170 GeV: (a) 4μ , (b) $2\mu 2e$, (c) $2e 2\mu$, (d) $4e$. The $2e 2\mu$ and $2\mu 2e$ channels are differentiated by the pair with a mass closest to the Z boson mass which is listed first. The contribution of the reducible background is also shown separately. The signal expectation for $m_H = 125$ GeV is also shown scaled to 1.51 times the SM prediction.

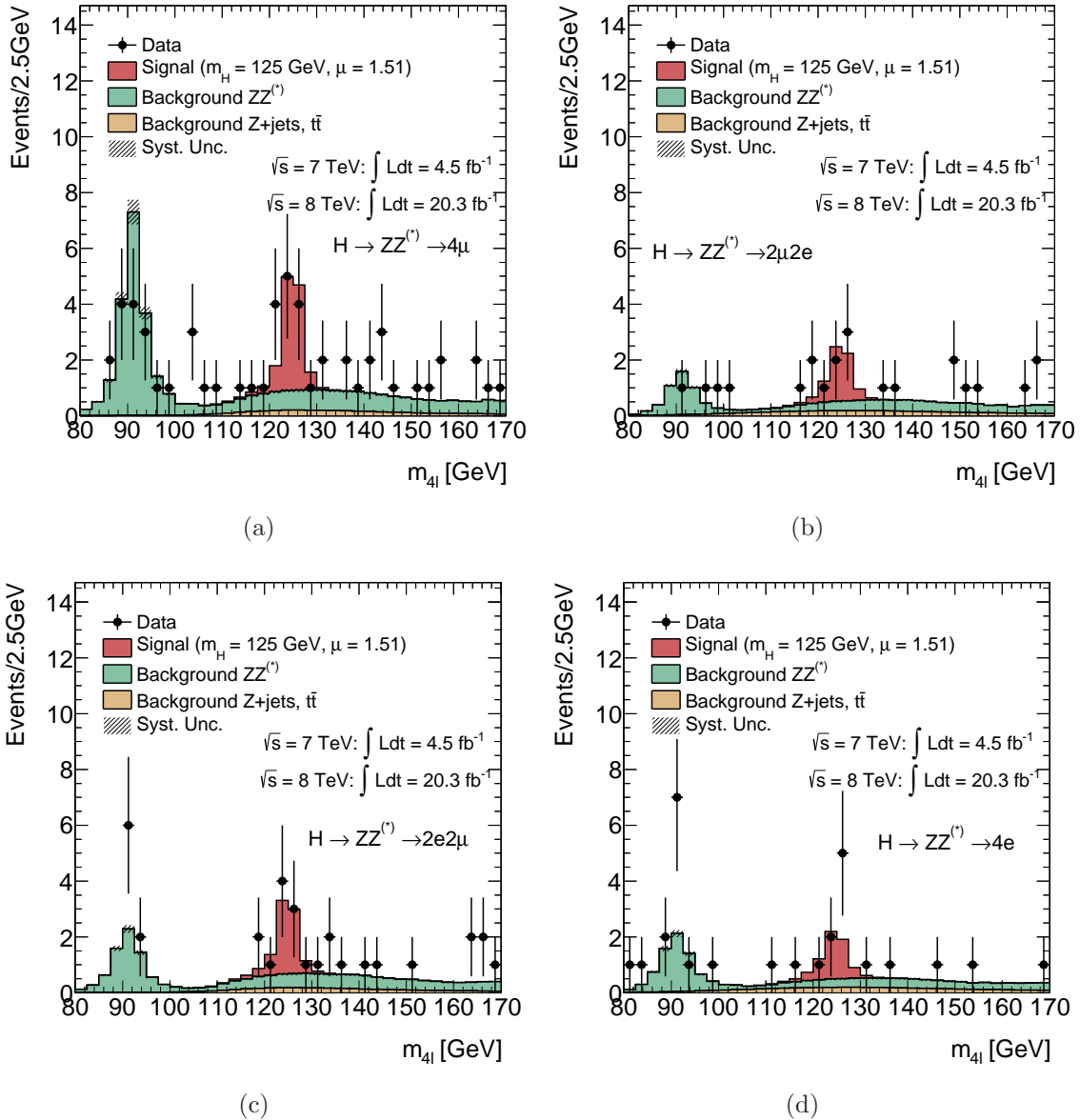
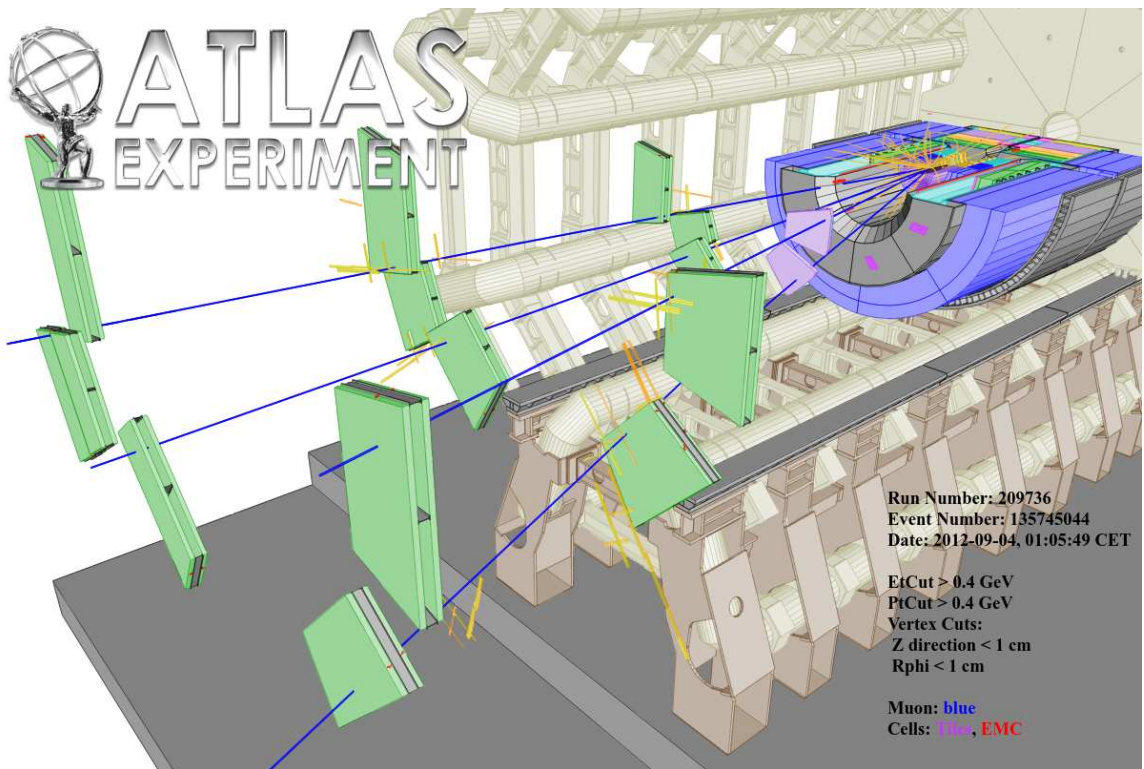


Figure 5.24: Display of a 4μ candidate with mass $m_{4\ell} = 123.2$ GeV. All the muons of this event pass through one EndCap of the detector and two of the muons pass through the CSC detector.



3632 Chapter Bibliography

3633 [1] LEP Working Group for Higgs boson searches, ALEPH, DELPHI, L3 and OPAL
 3634 Collaborations, Search for the standard model Higgs boson at LEP, *Phys. Lett.*,
 3635 B 565:61–75, 2003, hep-ex/0306033.

3636 [2] The T.E.V.N.P.H.. Working Group, Combined CDF and D0 Upper Limits on Stan-
 3637 dard Model Higgs-Boson Production with up to 6.7 fb^{-1} of Data, 2010, 1007.4587.

3638 [3] ATLAS Collaboration, Limits on the production of the Standard Model Higgs
 3639 Boson in pp collisions at $\sqrt{s} = 7 \text{ TeV}$ with the ATLAS detector, *Eur. Phys. J.*,
 3640 C 71:1728, 2011, 1106.2748.

3641 [4] ATLAS Collaboration, ATLAS luminosity public results,
 3642 <https://twiki.cern.ch/twiki/bin/view/AtlasPublic/LuminosityPublicResults>.

3643 [5] ATLAS Collaboration, Data quality information public results,
 3644 <https://twiki.cern.ch/twiki/bin/view/AtlasPublic/RunStatsPublicResults2010>.

3645 [6] Simone Alioli, Paolo Nason, Carlo Oleari, and Emanuele Re, NLO Higgs boson
 3646 production via gluon fusion matched with shower in POWHEG, *JHEP*, 04:002,
 3647 2009, 0812.0578.

3648 [7] Paolo Nason and Carlo Oleari, NLO Higgs boson production via vector-boson
 3649 fusion matched with shower in POWHEG, *JHEP*, 02:037, 2010, 0911.5299.

3650 [8] Daniel de Florian and Massimiliano Grazzini, Higgs production at the LHC: up-
 3651 dated cross sections at $\sqrt{s} = 8 \text{ TeV}$, *Phys. Lett.*, B718:117–120, 2012, 1206.4133.

3652 [9] Torbjorn Sjostrand, Stephen Mrenna, and Peter Z. Skands, PYTHIA 6.4 Physics
 3653 and Manual, *JHEP*, 05:026, 2006, hep-ph/0603175.

3654 [10] Piotr Gononka and Zbigniew Was, PHOTOS Monte Carlo: A Precision tool for
 3655 QED corrections in Z and W decays, *Eur. Phys. J.*, C 45:97–107, 2006, hep-
 3656 ph/0506026.

3657 [11] S. Dittmaier et al., Handbook of LHC Higgs Cross Sections: 1. Inclusive Observ-
 3658 ables, 2011, 1101.0593.

3659 [12] S. Dittmaier, S. Dittmaier, C. Mariotti, G. Passarino, R. Tanaka, et al., Handbook
 3660 of LHC Higgs Cross Sections: 2. Differential Distributions, 2012, 1201.3084.

3661 [13] A. Djouadi, M. Spira, and P. M. Zerwas, Production of Higgs bosons in proton
 3662 colliders: QCD corrections, *Phys. Lett.*, B 264:440–446, 1991.

3663 [14] S. Dawson, Radiative corrections to Higgs boson production, *Nucl. Phys.*,
 3664 B 359:283–300, 1991.

3665 [15] M. Spira, A. Djouadi, D. Graudenz, and P. M. Zerwas, Higgs boson production at
 3666 the LHC, *Nucl. Phys.*, B 453:17–82, 1995, hep-ph/9504378.

3667 [16] Robert V. Harlander and William B. Kilgore, Next-to-next-to-leading order Higgs
 3668 production at hadron colliders, *Phys. Rev. Lett.*, 88:201801, 2002, hep-ph/0201206.

3669 [17] Charalampos Anastasiou and Kirill Melnikov, Higgs boson production at hadron
 3670 colliders in NNLO QCD, *Nucl. Phys.*, B 646:220–256, 2002, hep-ph/0207004.

3671 [18] V. Ravindran, J. Smith, and W. L. van Neerven, NNLO corrections to the total
 3672 cross-section for Higgs boson production in hadron hadron collisions, *Nucl. Phys.*,
 3673 B665:325–366, 2003, hep-ph/0302135.

3674 [19] Stefano Catani, Daniel de Florian, Massimiliano Grazzini, and Paolo Nason,
 3675 Soft gluon resummation for Higgs boson production at hadron colliders, *JHEP*,
 3676 0307:028, 2003, hep-ph/0306211.

3677 [20] U. Aglietti, R. Bonciani, G. Degrassi, and A. Vicini, Two loop light fermion
 3678 contribution to Higgs production and decays, *Phys. Lett.*, B595:432–441, 2004,
 3679 hep-ph/0404071.

3680 [21] Stefano Actis, Giampiero Passarino, Christian Sturm, and Sandro Uccirati,
 3681 NLO Electroweak Corrections to Higgs Boson Production at Hadron Colliders,
 3682 *Phys. Lett.*, B670:12–17, 2008, 0809.1301.

3683 [22] D. de Florian and M. Grazzini, Higgs production at the LHC: updated cross
 3684 sections at $\sqrt{s} = 8 \text{ TeV}$, 2012, 1206.4133.

3685 [23] Charalampos Anastasiou, Stephan Buehler, Franz Herzog, and Achilleas Lazopoulos,
 3686 Inclusive Higgs boson cross-section for the LHC at 8 TeV, *JHEP*, 1204:004,
 3687 2012, 1202.3638.

3688 [24] Julien Baglio and Abdelhak Djouadi, Higgs production at the IHC, *JHEP*,
 3689 1103:055, 2011, 1012.0530.

3690 [25] M. Ciccolini, Ansgar Denner, and S. Dittmaier, Strong and electroweak cor-
 3691 rections to the production of Higgs + 2jets via weak interactions at the LHC,
 3692 *Phys. Rev. Lett.*, 99:161803, 2007, 0707.0381.

3693 [26] Mariano Ciccolini, Ansgar Denner, and Stefan Dittmaier, Electroweak and QCD
 3694 corrections to Higgs production via vector-boson fusion at the LHC, *Phys. Rev.*,
 3695 D77:013002, 2008, 0710.4749.

3696 [27] K. Arnold, M. Bahr, Giuseppe Bozzi, F. Campanario, C. Englert, et al., VBFNLO:
3697 A Parton level Monte Carlo for processes with electroweak bosons, *Comput.Phys.Commun.*, 180:1661–1670, 2009, 0811.4559.

3699 [28] Paolo Bolzoni, Fabio Maltoni, Sven-Olaf Moch, and Marco Zaro, Higgs production
3700 via vector-boson fusion at NNLO in QCD, *Phys.Rev.Lett.*, 105:011801, 2010,
3701 1003.4451.

3702 [29] Tao Han and S. Willenbrock, QCD correction to the $pp \rightarrow WH$ and $Z H$ total
3703 cross-sections, *Phys.Lett.*, B273:167–172, 1991.

3704 [30] Oliver Brein, Abdelhak Djouadi, and Robert Harlander, NNLO QCD corrections
3705 to the Higgs-strahlung processes at hadron colliders, *Phys.Lett.*, B579:149–156,
3706 2004, hep-ph/0307206.

3707 [31] M.L. Ciccolini, S. Dittmaier, and M. Kramer, Electroweak radiative corrections
3708 to associated WH and ZH production at hadron colliders, *Phys.Rev.*, D68:073003,
3709 2003, hep-ph/0306234.

3710 [32] Z. Kunszt, Associated Production of Heavy Higgs Boson with Top Quarks,
3711 *Nucl.Phys.*, B247:339, 1984.

3712 [33] W. Beenakker, S. Dittmaier, M. Kramer, B. Plumper, M. Spira, et al., Higgs
3713 radiation off top quarks at the Tevatron and the LHC, *Phys.Rev.Lett.*, 87:201805,
3714 2001, hep-ph/0107081.

3715 [34] W. Beenakker, S. Dittmaier, M. Kramer, B. Plumper, M. Spira, et al., NLO QCD
3716 corrections to t anti-t H production in hadron collisions, *Nucl.Phys.*, B653:151–203,
3717 2003, hep-ph/0211352.

3718 [35] S. Dawson, L.H. Orr, L. Reina, and D. Wackerlo, Associated top quark Higgs
3719 boson production at the LHC, *Phys.Rev.*, D67:071503, 2003, hep-ph/0211438.

3720 [36] S. Dawson, C. Jackson, L.H. Orr, L. Reina, and D. Wackerlo, Associated Higgs
3721 production with top quarks at the large hadron collider: NLO QCD corrections,
3722 *Phys.Rev.*, D68:034022, 2003, hep-ph/0305087.

3723 [37] A. Djouadi, J. Kalinowski, and M. Spira, HDECAY: A Program for Higgs
3724 boson decays in the standard model and its supersymmetric extension, *Comput.Phys.Commun.*, 108:56–74, 1998, hep-ph/9704448.

3726 [38] A. Bredenstein, Ansgar Denner, S. Dittmaier, and M.M. Weber, Precise predictions
3727 for the Higgs-boson decay $H \rightarrow WW/ZZ \rightarrow to4$ leptons, *Phys.Rev.*, D74:013004,
3728 2006, hep-ph/0604011.

3729 [39] A. Bredenstein, Ansgar Denner, S. Dittmaier, and M.M. Weber, Radiative cor-
 3730 rections to the semileptonic and hadronic Higgs-boson decays $H \rightarrow WW/ZZ \rightarrow 4$
 3731 fermions, *JHEP*, 0702:080, 2007, hep-ph/0611234.

3732 [40] Michiel Botje, Jon Butterworth, Amanda Cooper-Sarkar, Albert de Roeck, Joel
 3733 Feltesse, et al., The PDF4LHC Working Group Interim Recommendations, 2011,
 3734 1101.0538.

3735 [41] Hung-Liang Lai, Marco Guzzi, Joey Huston, Zhao Li, Pavel M. Nadolsky, et al.,
 3736 New parton distributions for collider physics, *Phys.Rev.*, D82:074024, 2010,
 3737 1007.2241.

3738 [42] A.D. Martin, W.J. Stirling, R.S. Thorne, and G. Watt, Parton distributions for
 3739 the LHC, *Eur.Phys.J.*, C63:189–285, 2009, 0901.0002.

3740 [43] Richard D. Ball, Valerio Bertone, Francesco Cerutti, Luigi Del Debbio, Stefano
 3741 Forte, et al., Impact of Heavy Quark Masses on Parton Distributions and LHC
 3742 Phenomenology, *Nucl.Phys.*, B849:296–363, 2011, 1101.1300.

3743 [44] Sergey Alekhin, Simone Alioli, Richard D. Ball, Valerio Bertone, Johannes Blum-
 3744 lein, et al., The PDF4LHC Working Group Interim Report, 2011, 1101.0536.

3745 [45] Tom Melia, Paolo Nason, Raoul Rontsch, and Giulia Zanderighi, W+W-, WZ and
 3746 ZZ production in the POWHEG BOX, *JHEP*, 1111:078, 2011, 1107.5051.

3747 [46] T. Binoth, N. Kauer, and P. Mertsch, Gluon-induced QCD corrections to $pp \rightarrow$
 3748 $ZZ \rightarrow l \bar{l} \bar{l}' l'$ anti- l prime anti- l prime, page 142, 2008, 0807.0024.

3749 [47] Michelangelo L. Mangano, Mauro Moretti, Fulvio Piccinini, Roberto Pittau, and
 3750 Antonio D. Polosa, ALPGEN, a generator for hard multiparton processes in
 3751 hadronic collisions, *JHEP*, 0307:001, 2003, hep-ph/0206293.

3752 [48] Michelangelo L. Mangano, Mauro Moretti, Fulvio Piccinini, and Michele Trec-
 3753 canni, Matching matrix elements and shower evolution for top-quark production in
 3754 hadronic collisions, *JHEP*, 0701:013, 2007, hep-ph/0611129.

3755 [49] Kirill Melnikov and Frank Petriello, Electroweak gauge boson production at hadron
 3756 colliders through $O(\alpha(s)^{**2})$, *Phys.Rev.*, D74:114017, 2006, hep-ph/0609070.

3757 [50] Charalampos Anastasiou, Lance J. Dixon, Kirill Melnikov, and Frank Petriello,
 3758 High precision QCD at hadron colliders: Electroweak gauge boson rapidity distri-
 3759 butions at NNLO, *Phys.Rev.*, D69:094008, 2004, hep-ph/0312266.

3760 [51] John M. Campbell and R.K. Ellis, MCFM for the Tevatron and the LHC,
 3761 *Nucl.Phys.Proc.Suppl.*, 205-206:10–15, 2010, 1007.3492.

3762 [52] S. Jadach, Z. Was, R. Decker, and Johann H. Kuhn, The tau decay library
3763 TAUOLA: Version 2.4, *Comput.Phys.Commun.*, 76:361–380, 1993.

3764 [53] P. Golonka, B. Kersevan, T. Pierzchala, E. Richter-Was, Z. Was, et al., The
3765 Tauola photos F environment for the TAUOLA and PHOTOS packages: Release.
3766 2., *Comput.Phys.Commun.*, 174:818–835, 2006, hep-ph/0312240.

3767 [54] T. Gleisberg, Stefan. Hoeche, F. Krauss, M. Schonherr, S. Schumann, et al., Event
3768 generation with SHERPA 1.1, *JHEP*, 0902:007, 2009, 0811.4622.

3769 [55] G. Aad et al., The ATLAS Simulation Infrastructure, *Eur.Phys.J.*, C70:823–874,
3770 2010, 1005.4568.

3771 [56] S. Agostinelli et al., GEANT4: A Simulation toolkit, *Nucl.Instrum.Meth.*,
3772 A506:250–303, 2003.

3773 [57] Georges Aad et al., Electron reconstruction and identification efficiency measure-
3774 ments with the ATLAS detector using the 2011 LHC proton-proton collision data,
3775 *Eur.Phys.J.*, C74(7):2941, 2014, 1404.2240.

3776 [58] Improved electron reconstruction in ATLAS using the Gaussian Sum Filter-based
3777 model for bremsstrahlung, 2012, ATLAS-CONF-2012-047, ATLAS-COM-CONF-
3778 2012-068.

3779 [59] Georges Aad et al., Electron and photon energy calibration with the ATLAS
3780 detector using LHC Run 1 data, *Eur.Phys.J.*, C74(10):3071, 2014, 1407.5063.

3781 [60] P. Speckmayer, A. Hocker, J. Stelzer, and H. Voss, The toolkit for multivariate
3782 data analysis, TMVA 4, *J.Phys.Conf.Ser.*, 219:032057, 2010.

3783 [61] Georges Aad et al., Measurement of the muon reconstruction performance of
3784 the ATLAS detector using 2011 and 2012 LHC proton-proton collision data,
3785 *Eur.Phys.J.*, C74(11):3130, 2014, 1407.3935.

3786 [62] G. Aad et al., Expected Performance of the ATLAS Experiment - Detector, Trigger
3787 and Physics, 2009, 0901.0512.

3788 [63] Muon Reconstruction Performance, 2010, ATLAS-CONF-2010-064, ATLAS-
3789 COM-CONF-2010-065.

3790 [64] A measurement of the ATLAS muon reconstruction and trigger efficiency using
3791 J/psi decays, 2011, ATLAS-CONF-2011-021, ATLAS-COM-CONF-2011-002.

3792 [65] Reconstruction of collinear final-state-radiation photons in Z decays to muons in
3793 sqrt{s}=7 TeV proton-proton collisions., Technical Report ATLAS-CONF-2012-143,
3794 CERN, Geneva, Nov 2012.

3795 [66] Wouter Verkerke and David P. Kirkby, The RooFit toolkit for data modeling,
 3796 *eConf*, C0303241:MOLT007, 2003, physics/0306116.

3797 [67] The ATLAS collaboration, Electron efficiency measurements with the AT-
 3798 LAS detector using the 2012 LHC proton-proton collision data, 2014,
 3799 ATLAS-CONF-2014-032, ATLAS-COM-CONF-2014-030.

3800 [68] The ATLAS collaboration, Preliminary results on the muon reconstruction effi-
 3801 ciency, momentum resolution, and momentum scale in ATLAS 2012 pp collision
 3802 data, 2013, ATLAS-CONF-2013-088, ATLAS-COM-CONF-2013-096.

3803 [69] Georges Aad et al., Improved luminosity determination in pp collisions at $\sqrt{s} =$
 3804 7 TeV using the ATLAS detector at the LHC, *Eur.Phys.J.*, C73(8):2518, 2013,
 3805 1302.4393.

3806 [70] Georges Aad et al., Measurement of the Higgs boson mass from the $H \rightarrow \gamma\gamma$ and
 3807 $H \rightarrow ZZ^* \rightarrow 4\ell$ channels with the ATLAS detector using 25 fb^{-1} of pp collision
 3808 data, *Phys.Rev.*, D90:052004, 2014, 1406.3827.

3809 [71] ATLAS Collaboration, Luminosity public results - 2011 pp collisions,
 3810 <https://twiki.cern.ch/twiki/bin/view/AtlasPublic/LuminosityPublicResults>.

3811 [72] Muon Momentum Resolution in First Pass Reconstruction of pp Collision Data
 3812 Recorded by ATLAS in 2010, 2011, ATLAS-CONF-2011-046, ATLAS-COM-
 3813 CONF-2011-003.

3814 [73] Muon reconstruction efficiency in reprocessed 2010 LHC proton-proton collision
 3815 data recorded with the ATLAS detector, 2011, ATLAS-CONF-2011-063, ATLAS-
 3816 COM-CONF-2011-068.

3817 [74] R. Frühwirth, Track fitting with nonGaussian noise, *Comput.Phys.Commun.*,
 3818 100:1–16, 1997.

6

3819

3820 Study of the $H \rightarrow ZZ^{(*)} \rightarrow 4\ell$ Production 3821 Mechanisms

3822 **6.1 Introduction**

3823 The Higgs signal candidates identified in the previous Chapter 5 are studied to
3824 reveal the mechanism that generates them. At the LHC, the dominant production
3825 mechanism for a Standard Model Higgs boson is the gluons fusion (denoted as ggF for
3826 simplicity) with an expected cross section of (19.27 ± 2.9) pb for a Higgs boson with
3827 mass $m_H = 125$ GeV at $\sqrt{s} = 8$ TeV. The second biggest contribution to the total cross
3828 section is given by the vector boson fusion (VBF) process, where the Higgs boson is
3829 produced together with two energetic jets with large rapidity gap. The third production
3830 mechanism of interest is the associated production with a vector boson (VH) and the
3831 lowest cross section contributions are the associated production with a $b\bar{b}$ pair (bbH) and
3832 a $t\bar{t}$ pair (ttH). In Table 6.1 the cross sections for the various production mechanisms
3833 of a Higgs boson with mass $m_H = 125$ GeV are reported at both $\sqrt{s} = 7$ TeV and
3834 $\sqrt{s} = 8$ TeV [1]. Measuring the production cross section for each of these processes is
3835 an important test of the Standard Model of the Higgs boson (introduced in Chapter 1).

3836 The events selected as Higgs candidates (Chapter 5) are classified in four different
3837 categories: *VBF-like*, *hadronic VH-like*, *leptonic VH-like* and *ggF-like*. For the Run-I,
3838 the $b\bar{b}H$ and $t\bar{t}H$ productions are not studied because of their small cross section. The
3839 background is measured with data driven techniques in the different categories, with

Table 6.1: Higgs boson ($m_H = 125$ GeV) production cross sections for ggF, VBF, VH, $b\bar{b}H$ and $t\bar{t}H$ processes, for both $\sqrt{s} = 7$ TeV and $\sqrt{s} = 8$ TeV [1].

Production mechanism	$\sqrt{s} = 7$ TeV		$\sqrt{s} = 8$ TeV	
	cross section [pb]	fraction of total [%]	cross section [pb]	fraction of total [%]
$gg \rightarrow H$	15.1	86.4	19.3	86.4
$qq' \rightarrow Hqq'$	1.22	7.0	1.58	7.1
$q\bar{q} \rightarrow WH$	0.579	3.3	0.705	3.2
$q\bar{q} \rightarrow ZH$	0.335	1.9	0.415	1.9
$q\bar{q}/gg \rightarrow t\bar{t}H$	0.086	0.5	0.13	0.6

3840 focus on the muon background. The data driven method is based on the simultaneous fit used for the inclusive analysis. The measured candidates in each category are 3841 compared to the Standard Model expectations stemming from the different production 3842 mechanisms. 3843

3844 Important role of this study play the jets selection and their uncertainties. Jets 3845 selection and the corresponding uncertainties are crucial for this study. Therefore, this 3846 chapter starts with a summary of the jets reconstruction and identification.

3847 6.2 Jet Identification and Reconstruction

3848 Jets are reconstructed from topological clusters [2] using an anti- k_T algorithm [3] 3849 with a distance parameter $R = 0.4$. The topological clusters are then corrected from 3850 the electromagnetic scale to the hadronic energy scale using a p_T - and η -dependent 3851 jet energy scale (JES) determined from Monte Carlo simulation (2011) and from data 3852 (2012). The latter significantly decreases the associated uncertainty.

3853 Dedicated correction methods addressing contributions from in-time and out-of- 3854 time pile-up to jets in the calorimeters have been developed using a MC simulation- 3855 based approach to measure the change of the jet signal as function of the characteristic 3856 variables measuring the pile-up activity, which are the number of reconstructed primary 3857 vertexes NPV (in-time pile-up) and the average number of pile-up interactions per 3858 bunch crossing μ (out-of-time pile-up).

3859 The pile-up correction was also improved for the full 2012 dataset, based on the jet 3860 area and event p_T density, which results in reduced pile-up uncertainties, improves jet 3861 energy resolution at low p_T , and provides higher suppression of fake pile-up jets. Jets 3862 originating from pile-up are removed by requiring that at least 50% (75% for 2011) of

Table 6.2: Summary of jets selection for 7 TeV and 8 TeV data and Monte Carlo.

Selection criteria	Data 2011	Data 2012
Identification	Anti- k_T $R = 0.4$ topological jets	Anti- k_T $R = 0.4$ topological jets
Kinematic cuts	$p_T > 25$ GeV (30 GeV) $ \eta < 2.5 (> 2.5)$	$p_T > 25$ GeV (30 GeV) $ \eta < 2.5 (> 2.5)$
Quality	Looser quality cuts	Looser quality cuts
pile-up	$ JVF > 0.5$	$ JVF > 0.75$

3863 the tracks associated to the jet (within $\Delta R = 0.4$ around the jet axis) must originate
 3864 from the primary vertex. This is implemented as a cut on the absolute value of the "jet
 3865 vertex fraction", respectively $|JVF| > 0.75$ for 7 TeV and $|JVF| > 0.5$ for 8 TeV data
 3866 and Monte Carlo.

3867 As a pre-selection cut, the jets are required to have $p_T > 25$ GeV for $|\eta| < 2.5$ and
 3868 $p_T > 30$ GeV for $2.5 < |\eta| < 4.5$. To avoid double-counting objects in the event, a
 3869 jet is removed if an electron, satisfying the criteria of the Section 5.4, is found within
 3870 $\Delta R < 0.2$ around the jet axis. The jet selection is summarized in Table 6.2 for the 2011
 3871 and 2012 dataset.

3872 6.3 Definition of Categories

3873 6.3.1 VBF-like Section

3874 The classification process starts by testing the event for VBF-like properties. VBF-
 3875 like events are selected by requiring the Higgs candidate to be accompanied by at least
 3876 two energetic jets passing the pre-selection criteria listed in Section 6.2. If more than
 3877 two jets fulfill these requirements, the two highest p_T jets are tagged as VBF jets. In
 3878 order to increase the purity of this category, the di-jet mass is required to be greater than
 3879 130 GeV. The efficiency of the simple requirement of two jets in the event is 62% for
 3880 the VBF production mechanism while the efficiency of the VBF-specific cuts is $\sim 55\%$.
 3881 This category has also a considerable contamination from ggF events, specifically 58% of
 3882 the ggF events pass the VBF selection. To cope with this, a multi-variate discriminant
 3883 is developed to improve the sensitivity of the couplings fit.

3884 The boosted decision tree (BDT) with gradient boost is used to discriminate VBF
 3885 against other production mechanisms, specifically the $ZZ^{(*)}$ background and the ggF
 3886 production. The training is performed using POWHEG+PYTHIA8 ggF and VBF
 3887 samples and the $ZZ^{(*)}$ samples used for the inclusive analysis. The following variables

3888 are used to build the multi-variate discriminant:

3889 • Invariant mass of the di-jet system (after applying $m_{JJ} > 130$ GeV pre-selection)

3890 • pseudo-rapidity separation between the two jets

3891 • transverse momentum of both jets

3892 • pseudo-rapidity of the leading (i.e. the highest p_T) jet.

3893 The separation provided by the variable x , is calculated via the integral:

$$\frac{1}{2} \int \frac{(\hat{x}_S(x) - \hat{x}_B(x))^2}{\hat{x}_S(x) + \hat{x}_B(x)} \quad (6.1)$$

3894 where $\hat{x}_S(x)$ and $\hat{x}_B(x)$ are the signal and background PDFs. Table 6.3 shows the
 3895 separation strength of this variables, together with their importance which is calculated
 3896 by counting how many times this variable has been used in the splitting of a node. Each
 3897 of these counts is then weighted with the number of events belonging to the specific
 3898 node and the separation gain-squared provided by the node. This is a method that
 3899 takes into account correlations between the inputs which are not accounted for by the
 3900 simple ranking based on the separation.

Table 6.3: Results of the variables ranking performed by the VBF BDT for its discrimination against the ggF and the $ZZ^{(*)}$. For each input variable, both the separation and the importance are specified together with their ranking.

Variable	Separation (Rank)	Importance (Rank)
m_{JJ}	0.220 (1)	0.1937 (4)
$\Delta\eta_{JJ}$	0.155 (2)	0.2092 (2)
Leading jet p_T	0.033 (3)	0.1906 (5)
Sub-leading jet p_T	0.032 (4)	0.1955 (3)
Leading jet η	0.027 (5)	0.2110 (1)

3901 The variables used represent the minimal set of variables providing discrimination
 3902 between VBF and the other production mechanisms. They are presented in Figure 6.1
 3903 and their correlations are shown in Figures 6.2, 6.3, 6.4 for the VBF, the ggF and the
 3904 $ZZ^{(*)}$ respectively for the $\sqrt{s} = 8$ TeV data.

Figure 6.1: Distributions of VBF (red), ggF (blue) and $ZZ^{(*)}$ (magenta) events used in the training of the VBF boosted decision tree. The dijet invariant mass (a), the dijet η distance (b), the leading jet p_T (c), the subleading jet p_T (d) and the leading jet η (e) are presented. Histograms are normalized to the same area.

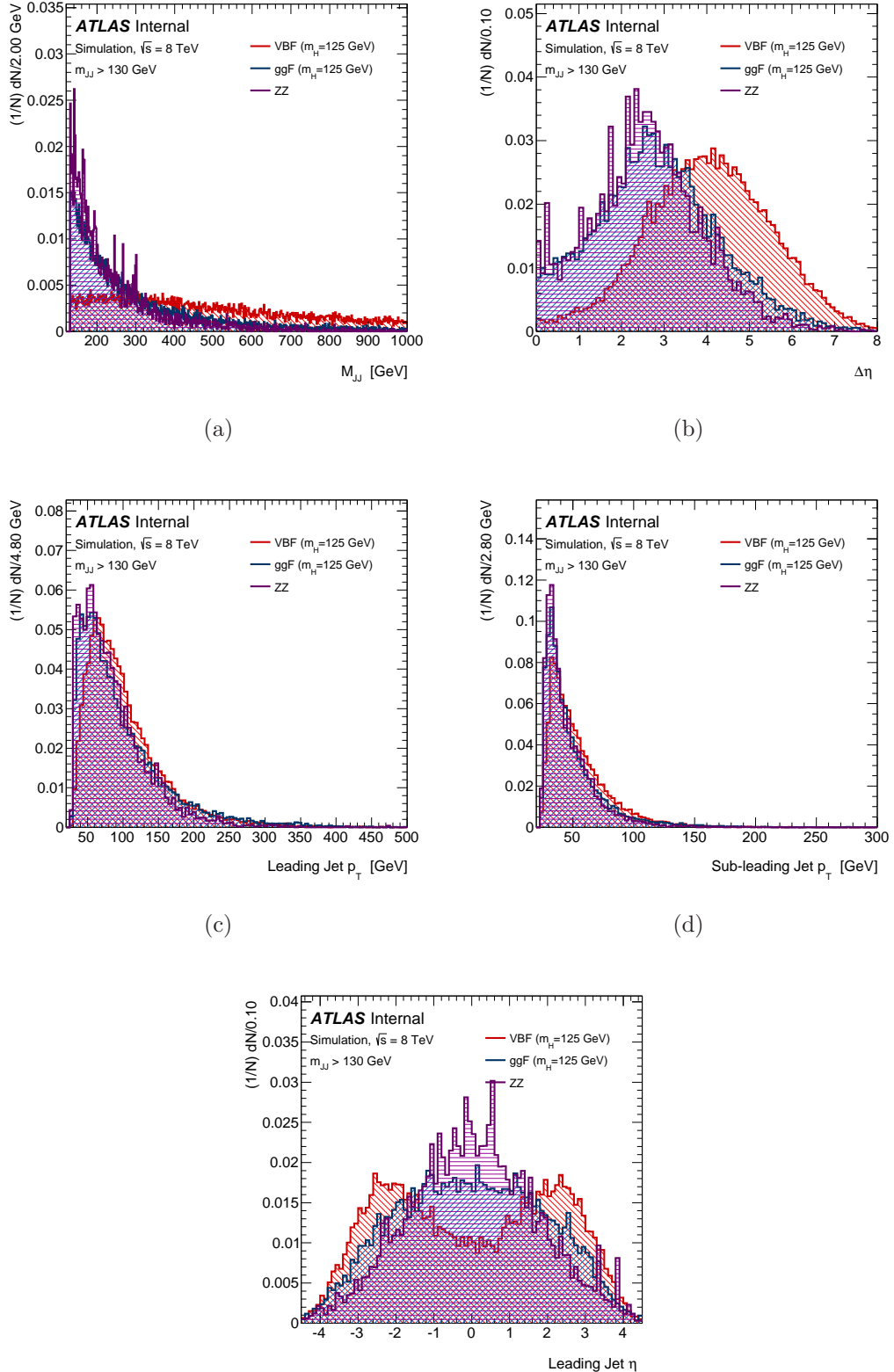


Figure 6.2: Correlations among the input variables used in the BDT for the VBF-like category, for VBF events.

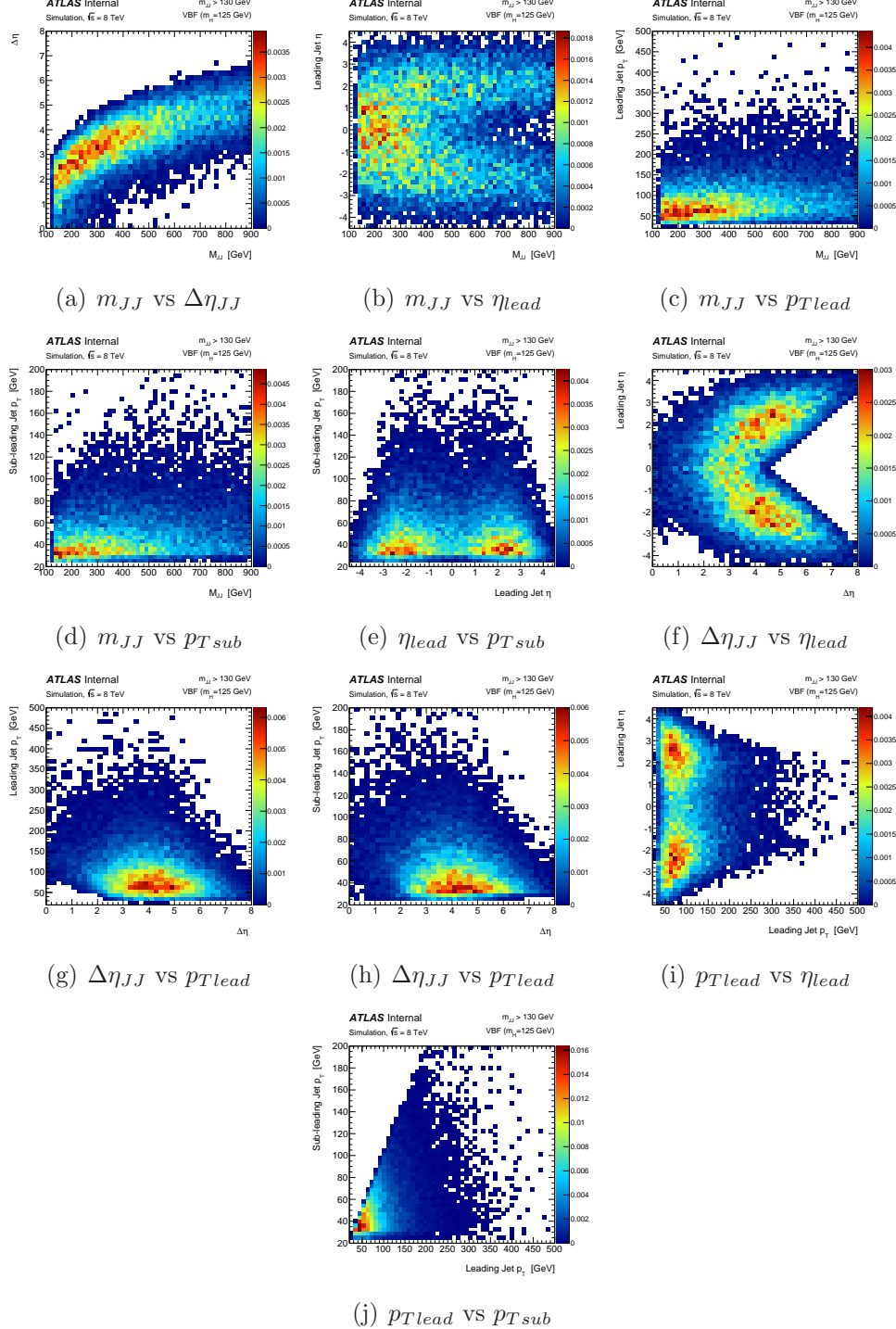


Figure 6.3: Correlations among the input variables used in the BDT for the VBF-like category, for ggF events.

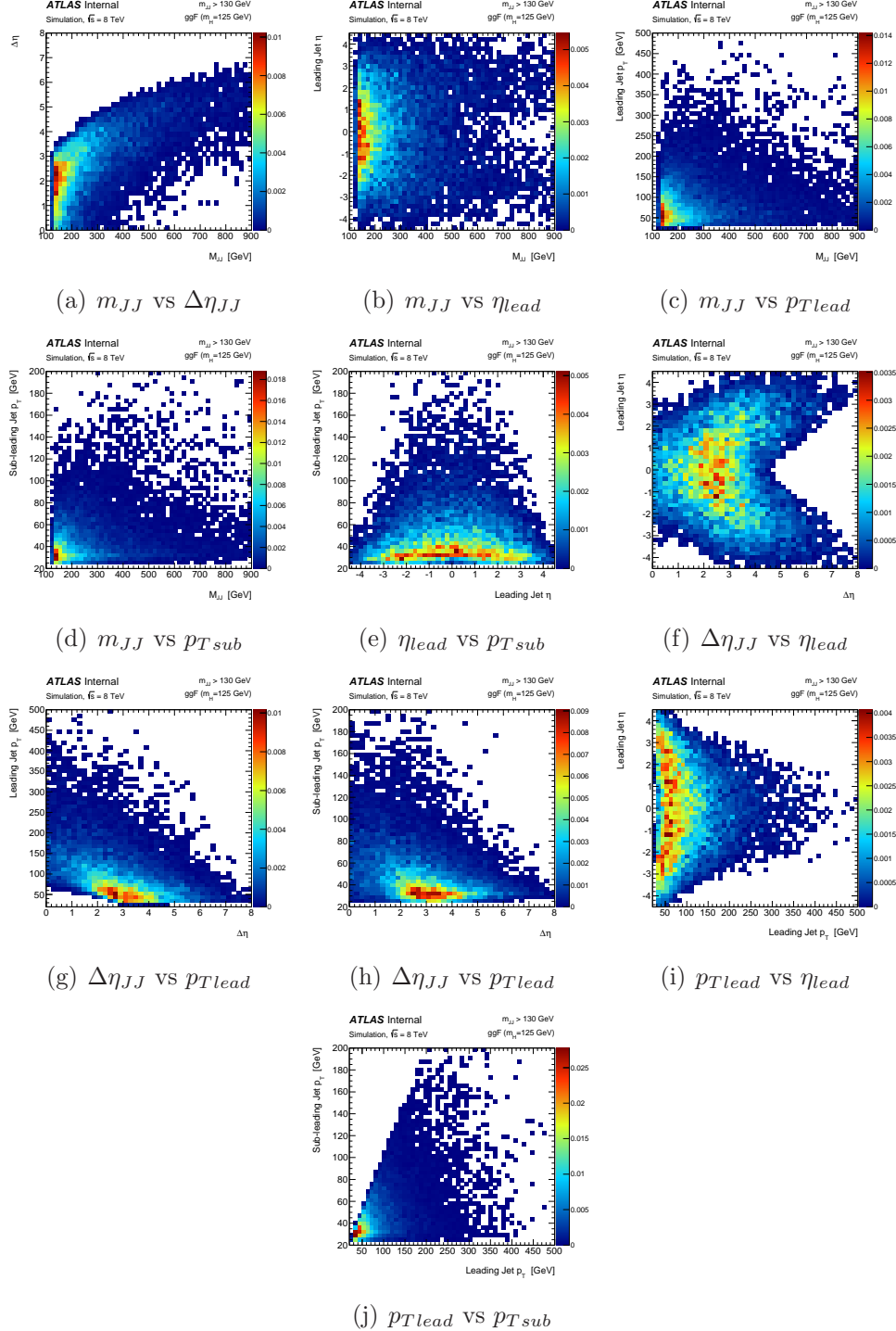
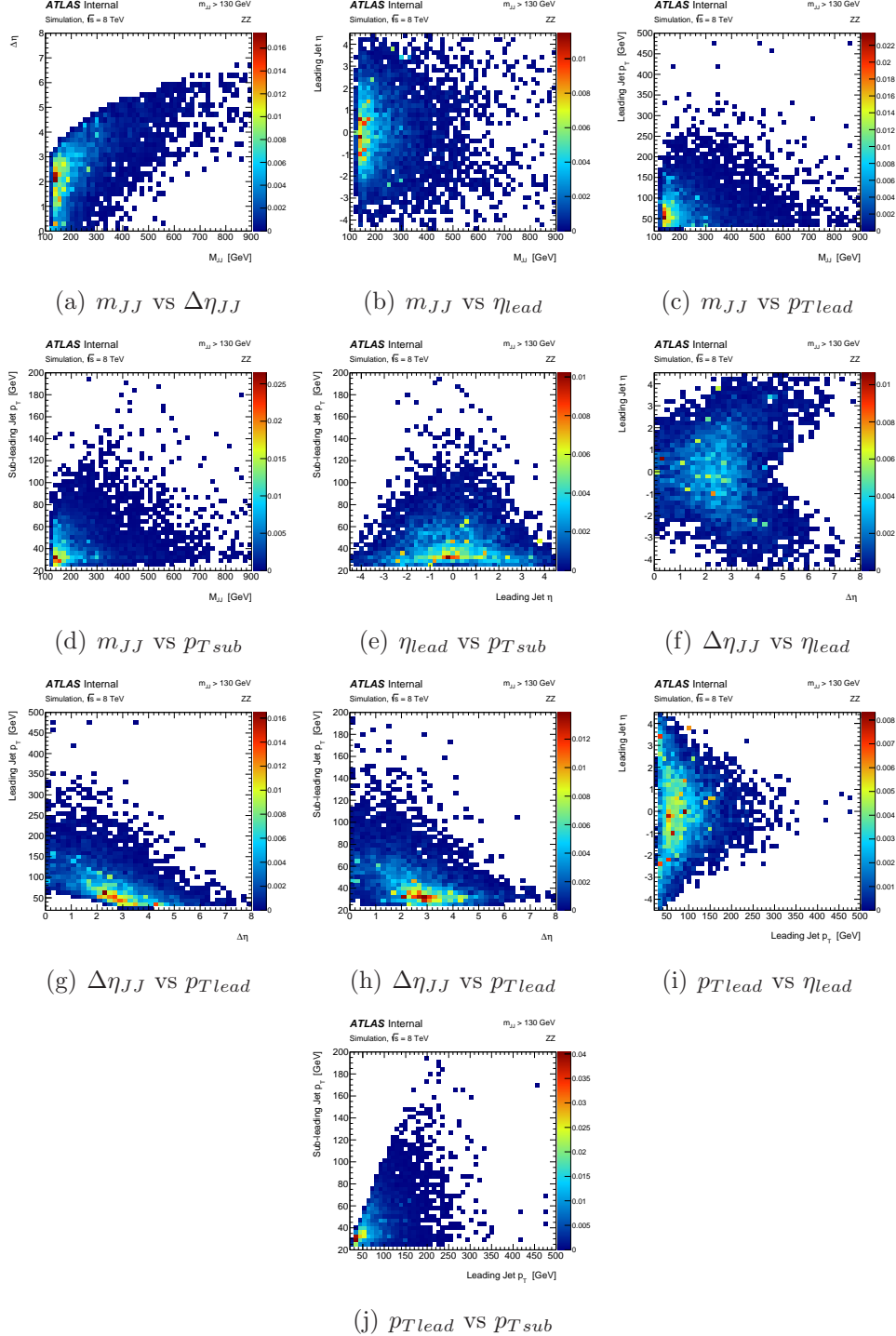
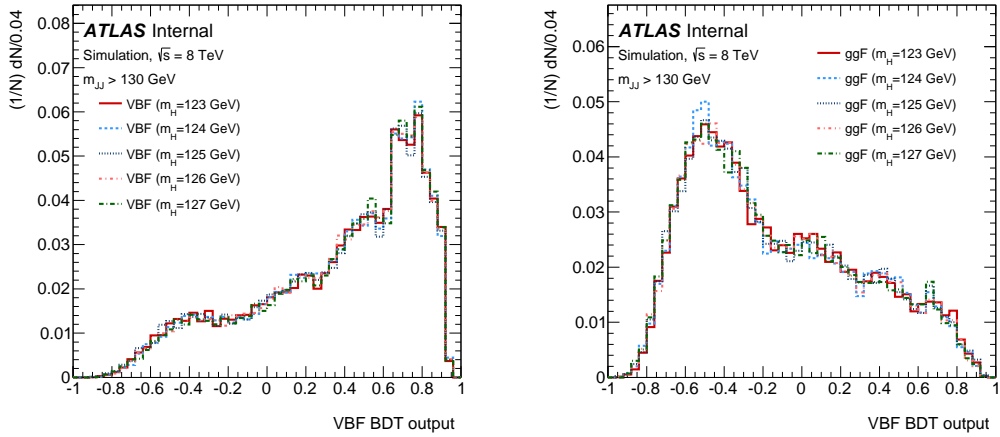


Figure 6.4: Correlations among the input variables used in the BDT for the VBF-like category, for $ZZ^{(*)}$ events.



3905 In these plots the expected features of the vector-boson fusion production of a Higgs
 3906 boson are visible. The di-jet system has a high invariant mass and the two jets are
 3907 emitted in the forward region with a considerable $\Delta\eta$ separation between them. The
 3908 ggF events, on the other hand, are more centrally produced with a smaller invariant
 3909 mass and $\Delta\eta$ separation. The output of the BDT is shown in Figure 6.5 using different
 3910 mass hypotheses, on the left for the vector boson fusion produced Higgs and on the right
 3911 for the gluon fusion produced Higgs. The Figure also shows clearly that the output of
 3912 the BDT discriminant has little dependence on the generated mass of the Higgs boson.
 3913 This is exploited by using in the training all the samples with a Higgs boson generated
 3914 mass between 123 and 127 GeV for the VBF and ggF processes. The direct VBF BDT
 3915 output compared to the ggF and $ZZ^{(*)}$ backgrounds is shown in Figure 6.6.

Figure 6.5: BDT output for Higgs masses between 123 and 127 GeV for the vector boson fusion production mechanism on the left and for the gluon fusion production mechanism on the right.

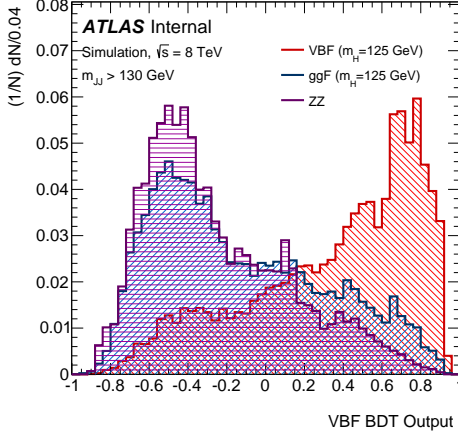


3916 The BDT output is used as an observable together with the quadruplet mass ($m_{4\ell}$)
 3917 in a maximum likelihood fit dedicated for the VBF category. Therefore, no BDT cut
 3918 is chosen and no significance as a function of the BDT is shown.

3919 6.3.2 Hadronic VH-like Selection

3920 If the event does not fulfill the VBF criteria, then is tested for hadronic VH-like
 3921 properties. Hadronic VH events are those where an electroweak boson is produced
 3922 together with a Higgs boson and decays in hadrons. Experimentally, this results to
 3923 the presence of two jets whose invariant mass peaks at either $m_{W^\pm} = 80.4$ GeV or

Figure 6.6: VBF BDT output distributions for the VBF compared to the $ZZ^{(*)}$ irreducible background and the ggF production. Histograms are normalized to the same area.



³⁹²⁴ $m_Z = 91.2$ GeV (as Figure 6.7 shows). For this reason, a preliminary cut is applied on
³⁹²⁵ the invariant mass of the di-jet system and specifically it is required to be in the range of
³⁹²⁶ 40 – 130 GeV. Events surviving the mass cuts are then passed through a multi-variate
³⁹²⁷ analysis (MVA) [4] to discriminate those coming from the associated production with
³⁹²⁸ an electroweak boson. The discriminant is built using a boosted decision tree with
³⁹²⁹ gradient boost, trained with the same variables as the VBF BDT tree.

³⁹³⁰ These variables are presented in Figure 6.8 for the VH and the dominant ggF back-
³⁹³¹ ground. The ranking of these variables is shown in Table 6.4, for a training that
³⁹³² is performed using merged samples with different generated Higgs masses of $m_H =$
³⁹³³ 123, 124, 126, 127 GeV. The correlations of the variables can be seen in Figures 6.9, 6.10
³⁹³⁴ for the signal VH and the ggF background respectively. The BDT response and the
³⁹³⁵ efficiencies are shown in Figure 6.11. The cut used for the BDT is -0.432 for 2011 and
³⁹³⁶ -0.393 for 2012, in order for the ggF contamination to be the same. The VH efficiency
³⁹³⁷ after this selection is estimated to be $\sim 25\%$.

Figure 6.7: Invariant mass distribution of the dijet system for the hadronic WH (red) and ZH (blue) processes.

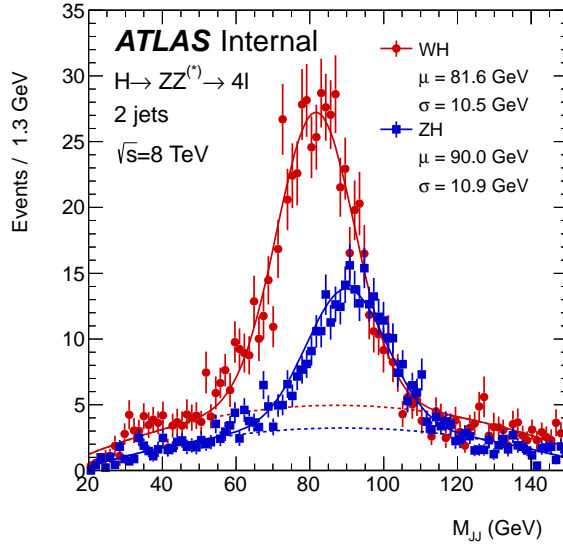


Table 6.4: Results of the variables ranking performed by the MVA for the hadronic VH category. For each input variable both the separation and the importance are specified, together with their ranking.

Variable	Separation (Rank)	Importance (Rank)
m_{JJ}	0.085 (1)	0.235 (1)
Sub-leading jet p_T	0.083 (2)	0.190 (4)
Leading jet p_T	0.055 (3)	0.204 (2)
$\Delta\eta_{JJ}$	0.047 (4)	0.191 (3)
Leading jet η	0.033 (5)	0.180 (5)

Figure 6.8: Distribution of the VH signal, i.e. WH and ZH, and the dominant ggF background at $\sqrt{s} = 8$ TeV used for the BDT discriminant. The figures show the di-jet mass (a), the η separation between the jets (b), the leading jet p_T (c), the subleading jet p_T (d) and the leading jet η (e).

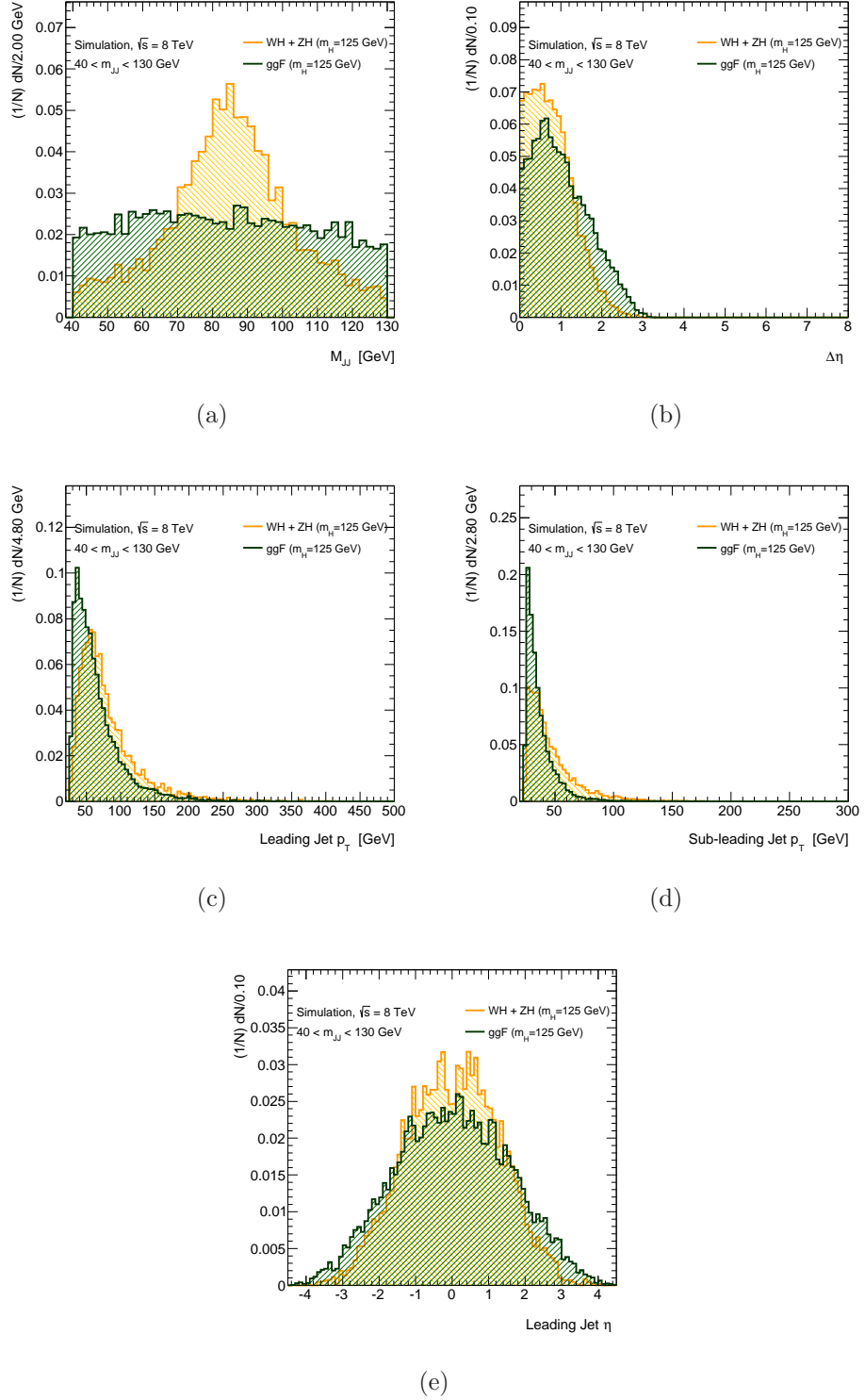


Figure 6.9: Correlations among the input variables used in the BDT for the hadronic-VH-like category, for VH events.

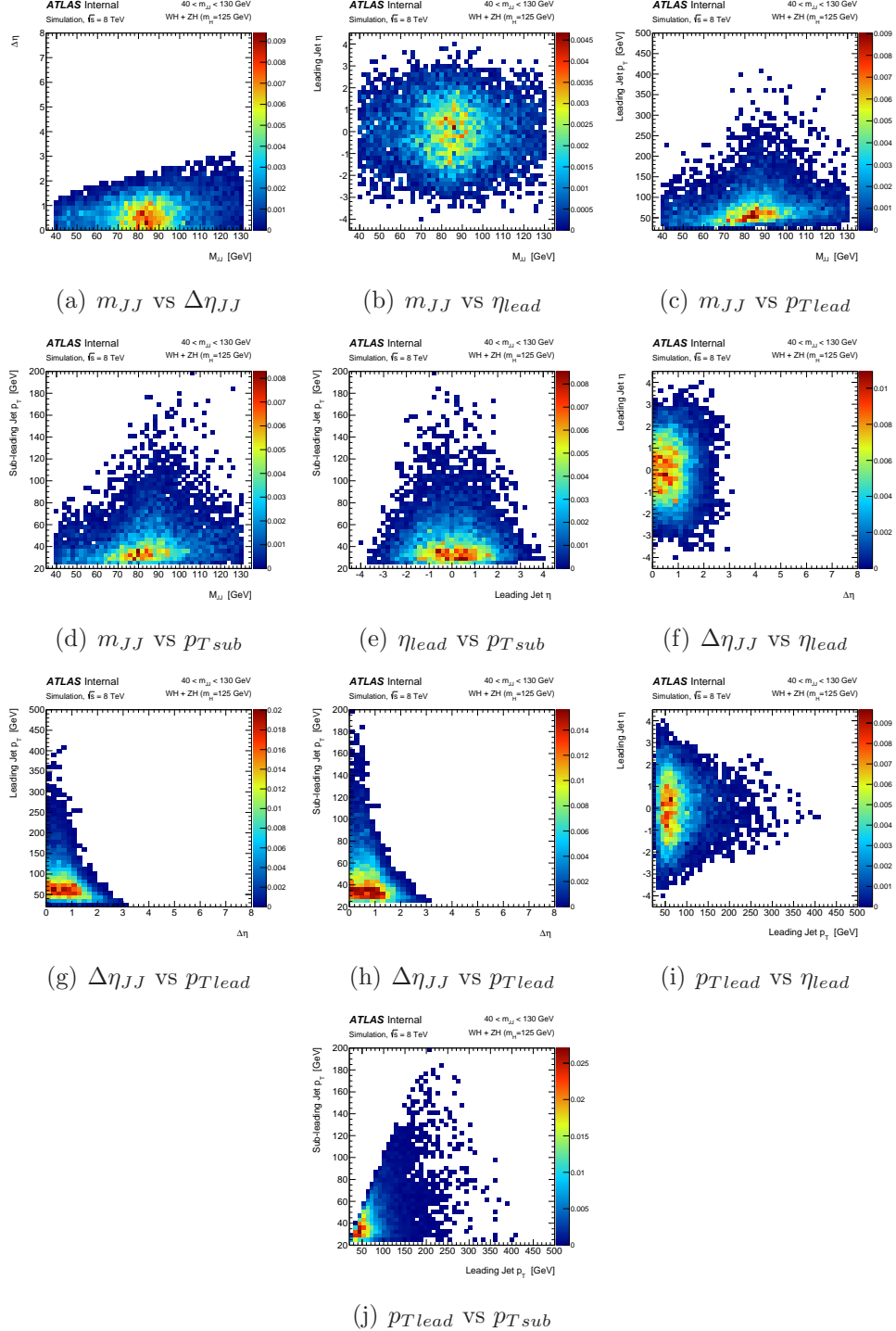
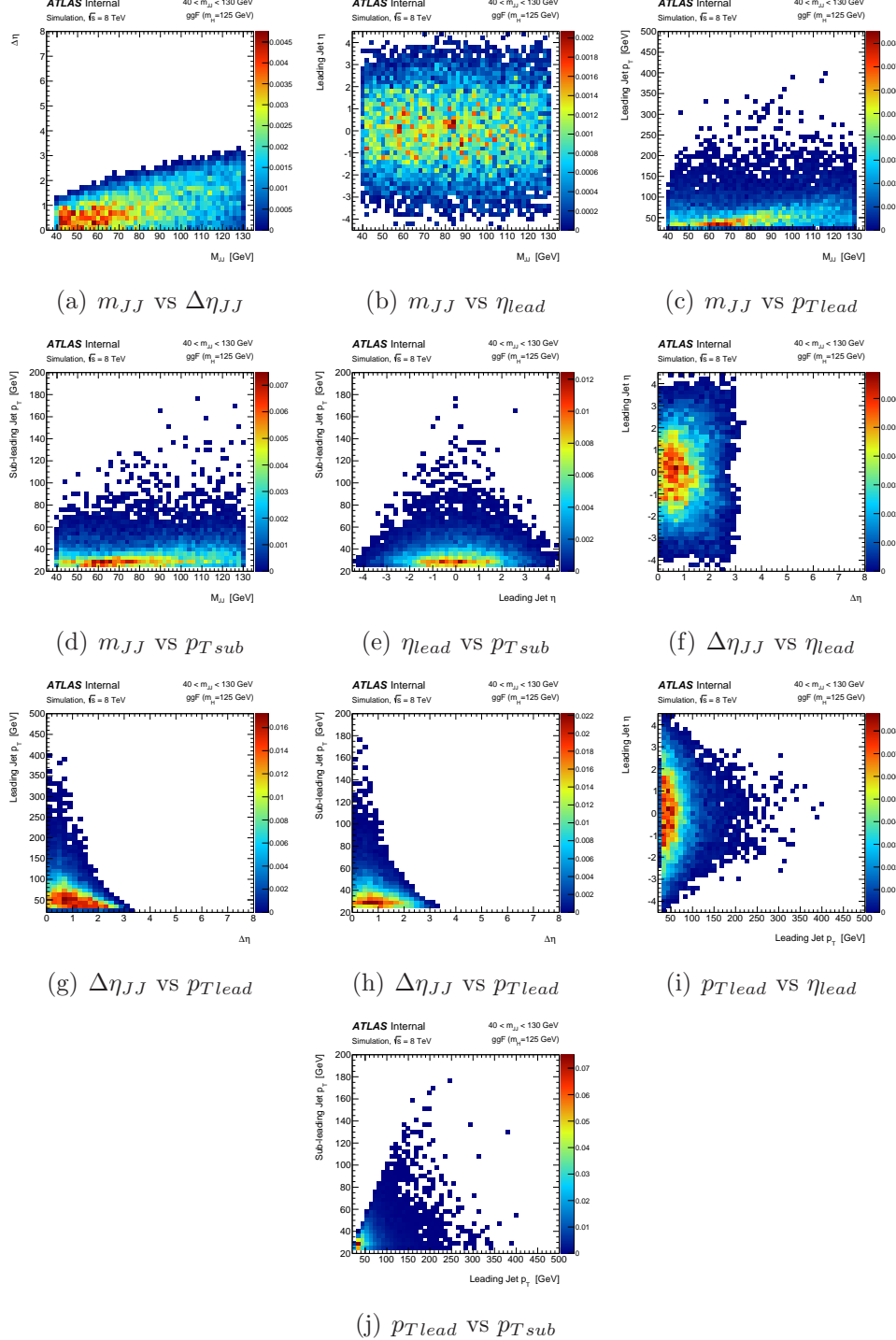


Figure 6.10: Correlations among the input variables used in the BDT for the hadronic-VH-like category, for ggF events.



6.3.3 Leptonic VH-like Selection

Events that are neither VBF nor VH-hadronic like are tested for the leptonic VH categorization. The presence of at least one extra lepton (e or μ) in addition to the four used to reconstruct the Higgs decay is required. To suppress backgrounds, this additional lepton should pass the standard lepton identification, has $p_T > 8$ GeV and satisfy the same isolation, impact parameter significance and ΔR requirements as the leptons from the Higgs decay (presented in Section 5.6). The efficiency of that for VH signal events at $m_H = 125$ GeV is $\sim 15\%$.

6.3.4 ggF-like Selection

If the event does not comply any of the previous selections then it is considered to be a ggF-like event.

6.4 Expected Yields and Signal MC

The efficiency of each selection used in the VBF-like and hadronic VH-like categories are presented in Table 6.5. The expected yields, after following the previously defined categorization, is presented in Table 6.6, in the range of $110 < m_H < 140$ GeV, assuming a Higgs mass of $m_H = 125$ GeV.

Table 6.5: The efficiency table for VBF-like and Hadronic VH-like specific cuts.

Production Mode	> 1 jet	$m_{jj} \in [40, 130]$ GeV	$m_{jj} > 130$ GeV	hadronic VH-like cuts
ggF	16%	6%	8%	2%
VBF	62%	5%	55%	2%
WH	48%	34%	12%	25%
ZH	48%	34%	11%	25%

The irreducible $ZZ^{(*)}$ background also contributes to the production mechanisms. The $ZZ^{(*)}$ continuum is modeled using POWHEG [5] for quark-antiquark annihilation and gg2ZZ [6] for gluon fusion. The mass-dependent PDF and α_s scale uncertainties are parametrized as recommended in Reference [7]. The QCD scale uncertainty has a $\pm 5\%$ effect on the expected $ZZ^{(*)}$ background at 125 GeV, and the effect due to the PDF and α_s uncertainties is $\pm 4\%$ ($\pm 8\%$) at 125 GeV for quark-initiated (gluon-initiated) processes. The EW production of the $ZZ^{(*)}$ with two jets down to $O(\alpha_W^6)$ is generated

Figure 6.11: The VH hadronic BDT response is presented for the $\sqrt{s} = 7$ TeV MC (a) and the 8 TeV (b). The cut values on the output are selected to be the points which give the same significance. The corresponding efficiencies are shown in Figures (c).

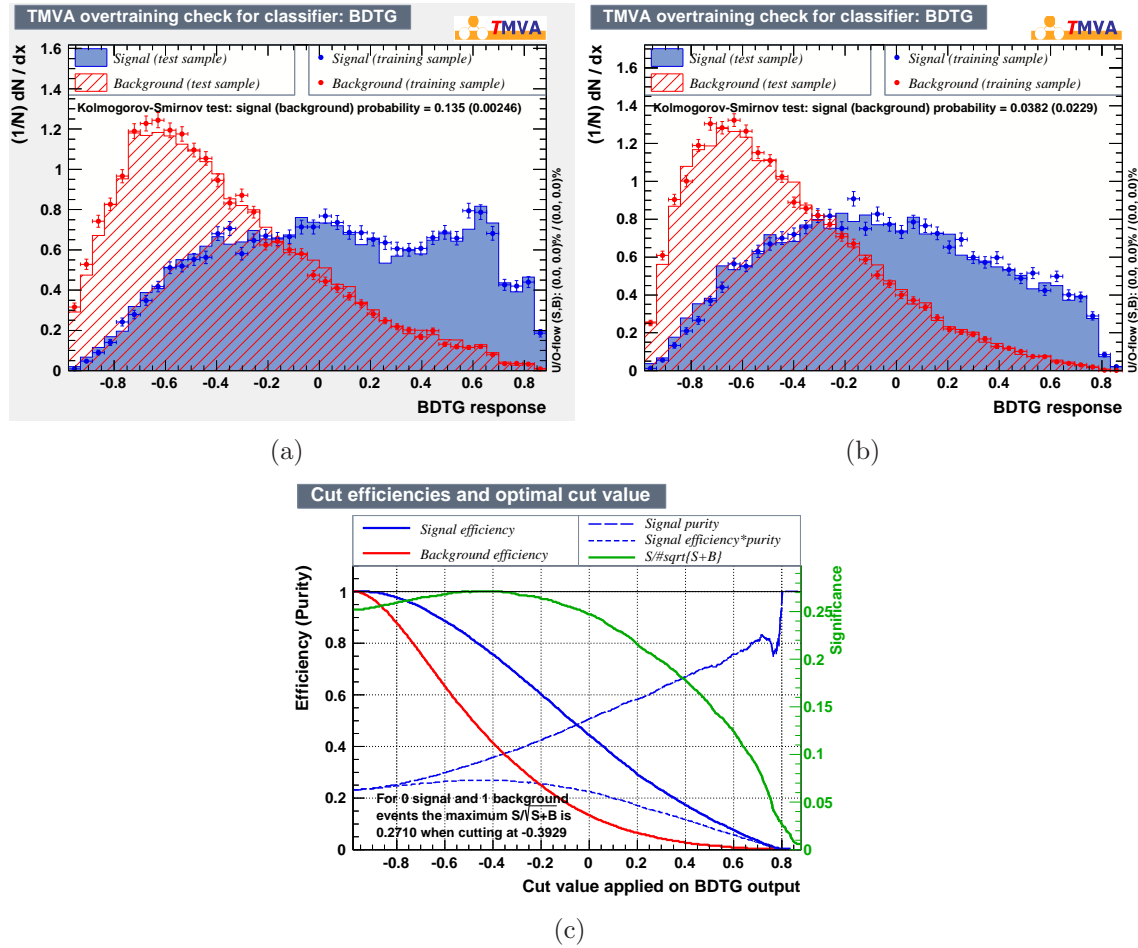


Table 6.6: Expected events in each category (ggF-like, VBF-like, hadronic VH-like, leptonic VH-like) assuming $m_H = 125$ GeV for the 2011 and 2012 data in the range of $110 < m_{4\ell} < 140$ GeV.

True Origin	Category			
	ggF-like	VBF-like	hadronic VH-like	leptonic VH-like
$\sqrt{s} = 7$ TeV				
ggF	2.035	0.107	0.046	0.004
VBF	0.114	0.135	0.007	0.000
WH	0.034	0.009	0.023	0.011
ZH	0.026	0.005	0.014	0.002
$t\bar{t}H$	0.000	0.007	0.002	0.000
$\sqrt{s} = 8$ TeV				
ggF	11.846	1.084	0.367	0.009
VBF	0.508	0.679	0.030	0.001
WH	0.195	0.059	0.124	0.062
ZH	0.148	0.035	0.080	0.010
$t\bar{t}H$	0.002	0.051	0.012	0.002

3961 using SHERPA [8], in which the process $ZZZ \rightarrow 4\ell qq$ is also taken into account. The
 3962 scale uncertainty is obtained by varying the factorization scale and renormalization scale
 3963 by a factor of 4.0. The largest deviation from the nominal value, 6.5%, is considered
 3964 as the corresponding uncertainty. Another source of theoretical uncertainty comes
 3965 from the multi-jet criteria, specified by CKKW parameter, that defines which phase-
 3966 space regions are populated by matrix elements and which ones by parton showers.
 3967 Changing the CKKW from $\sqrt{20/E_{CMS}}$ to $\sqrt{30/E_{CMS}}$ and $\sqrt{10/E_{CMS}}$, leads to a
 3968 largest deviation of $\sim 0.8\%$. Therefore the total uncertainties of ZZqq cross section is
 3969 about 7.3%, which is treated as the theoretical uncertainty in the VBF-like category
 3970 for the ZZ background.

3971 The expected $ZZ^{(*)}$ background in the categories and in the range of $110 < m_H <$
 3972 135 GeV is presented in Table 6.7.

3973 6.5 Reducible Background

3974 The reducible background is estimated using the same methods as for the inclusive
 3975 analysis, described in Section 5.10.2. Specifically the muons background is estimated by
 3976 multiplying the estimated background in the inclusive analysis with the probability of

Table 6.7: Expected $ZZ^{(*)}$ background events in the range $110 < m_{4\ell} < 140$ GeV for the inclusive case (before any categorization selection), the VBF-like category, the VH-like categories and the ggF category for the 2011 data and 2012 data.

Category	2012 Dataset			2011 Dataset		
	$qq \rightarrow ZZ$	$gg \rightarrow ZZ$	SHERPA $ZZqq'$	$qq \rightarrow ZZ$	$gg \rightarrow ZZ$	SHERPA $ZZqq'$
Inclusive	16.51	0.27	0.07	3.169	0.082	0.011
VBF-like	0.398	0.0219	0.043	0.057	0.003	0.007
Hadronic VH-like	0.219	0.004	0.007	0.040	0.000	0.002
Leptonic VH-like	0.037	0.001	0.000	0.017	0.000	0.000
ggF-like	16.001	0.242	0.019	3.055	0.079	0.003

each background type to pass the selection of each category (estimated from the MC):

$$N_{Category}^{SR} = N^{SR} \times \frac{Inclusive\ MC\ Events\ Passing\ the\ Category\ Selection}{Inclusive\ MC\ Events}. \quad (6.2)$$

This fractions are presented in Table 6.8 for the $Zjets$ and $t\bar{t}$ backgrounds. The $Zb\bar{b}$ and $Zlight$ are treated together because of the limited statistics. The uncertainties correspond to the statistical MC uncertainties.

If the statistics allowed, a simultaneous fit could be performed on the reference OS CR which passes the category selection (separately for each category) without the application of the additional selection (isolation and impact parameter criteria). Then the fit estimations could be extrapolated to the SR events by the application of the transfer factors used in Chapter 5.

The estimated reducible background in the 4μ and $2e2\mu$ channels is presented in Table 6.9 for the 2012 and in Table 6.10 for the 2011 data. In summary, the total irreducible backgrounds is given in Table 6.11.

6.6 Systematic Uncertainties

The systematic uncertainties on the expected yields from the different processes contributing to the VBF, hadronic VH, leptonic VH and ggF categories are reported in Table 6.12, expressed as the fractional uncertainties on the yields. The uncertainties on the theoretical predictions for the cross sections for the different processes arise mainly from the requirement on the jet multiplicity used in the event categorization [9, 1]. Because of event migrations, this also affects the leptonic VH and the ggF categories, where no explicit requirement on jets is applied. The uncertainty accounting for a potential mismodeling of the underlying event is conservatively estimated with $Z \rightarrow \mu\mu$

Table 6.8: The expected yield and relative fractions, from the MC, of Z jets and $t\bar{t}$ 4 μ and 2e2 μ backgrounds.

Category	Z+jets	
	4 μ (fraction)	2e2 μ (fraction)
ggF-like	2.18 ± 0.09 (96.42%)	1.87 ± 0.17 (95.36%)
VBF-like	0.07 ± 0.13 (3.10%)	0.07 ± 0.13 (3.57%)
VH-hadronic-like	0.01 ± 0.12 (.44%)	0.02 ± 0.12 (1.02%)
VH-leptonic-like	0.001 ± 0.12 (.04%)	0.001 ± 0.12 (.05%)
Category	$t\bar{t}$	
	4 μ (fraction)	2e2 μ (fraction)
ggF-like	0.13 ± 0.05 (41.94%)	0.35 ± 0.07 (78.65%)
VBF-like	0.14 ± 0.05 (45.16%)	0.031 ± 0.015 (6.97%)
VH-hadronic-like	0.039 ± 0.027 (12.58%)	0.063 ± 0.025 (14.16%)
VH-leptonic-like	0.001 ± 0.014 (.32%)	0.001 ± 0.014 (.22%)

Table 6.9: Reducible background estimates in the signal region after the categories selection, for the 4 μ and 2e2 μ channels in the 2012 data.

4 μ		
Category	Z + jets	$t\bar{t}$
ggF-like	2.98 ± 0.67	0.33 ± 0.06
VBF-like	0.10 ± 0.02	0.14 ± 0.03
VH-hadronic-like	0.02 ± 0.005	0.05 ± 0.01
VH-leptonic-like	0.001 ± 0.001	0.001 ± 0.001
2e2 μ		
Category	Z + jets	$t\bar{t}$
ggF-like	2.47 ± 0.55	0.31 ± 0.06
VBF-like	0.09 ± 0.02	0.13 ± 0.02
VH-hadronic-like	0.02 ± 0.004	0.05 ± 0.01
VH-leptonic-like	0.001 ± 0.001	0.001 ± 0.001

Table 6.10: Reducible background estimates in the signal region after the categories selection, for the 4μ and $2e2\mu$ channels in the 2011 data.

4μ		
Category	$Z + jets$	$t\bar{t}$
ggF-like	0.422 ± 0.243	0.051 ± 0.017
VBF-like	0.015 ± 0.008	0.022 ± 0.007
VH-hadronic-like	0.003 ± 0.002	0.007 ± 0.002
VH-leptonic-like	0.0002 ± 0.0001	~ 0
$2e2\mu$		
Category	$Z + jets$	$t\bar{t}$
ggF-like	0.288 ± 0.170	0.036 ± 0.017
VBF-like	0.010 ± 0.006	0.015 ± 0.005
VH-hadronic-like	0.002 ± 0.001	0.005 ± 0.002
VH-leptonic-like	0.0001 ± 0.0001	~ 0

Table 6.11: Summary of the background estimates in both the 4μ and $2e2\mu$ channels for the 2011 and 2012 years. The uncertainty quoted includes both statistical and systematic errors.

Year	ggF-like	VBF-like	VH-hadronic-like	VH-leptonic-like
2012	0.98 ± 0.32	0.12 ± 0.08	0.04 ± 0.02	0.004 ± 0.004
2011	6.71 ± 1.44	0.63 ± 0.59	0.21 ± 0.13	0.003 ± 0.003

3998 simulated events by applying the selection for the VBF (or hadronic VH) category and
 3999 taking the difference of the efficiencies with and without multiparton interactions.

4000 The main experimental uncertainty is related to the jet energy scale determination,
 4001 including the uncertainties associated with the modeling of the absolute and relative
 4002 *in situ* jet calibrations, as well as the flavor composition of the jet sample. The impact
 4003 on the yields of the various categories is anti-correlated because a variation of the jet
 4004 energy scale results primarily in the migration of events among the categories. The
 4005 impact of the jet energy scale uncertainty results in an uncertainty of about $\pm 10\%$
 4006 for the VBF category, $\pm 8\%$ for the hadronic VH category, $\pm 1.5\%$ for the leptonic VH
 4007 category and $\pm 1.5\%$ for the ggF category.

4008 The uncertainty on the jet energy resolution is also taken into account, even though
 4009 its impact is small compared to that of the jet energy scale uncertainty, as reported
 4010 in Table 6.12. Finally, the uncertainties associated with the additional leptons in the
 4011 leptonic VH category are the same as already described in Chapter 5 for the four leptons
 4012 of the Higgs boson decay.

4013 6.7 Higgs Categorized Candidates

4014 The numbers of expected and observed events in each of the categories previously
 4015 described are summarized in Table 6.13. The expected yield in each enriched category
 4016 is given for each of the production modes, where the ggF, $b\bar{b}H$ and $t\bar{t}H$ yields are
 4017 combined. The expected and observed numbers of events are given for two $m_{4\ell}$ mass
 4018 ranges: 120 – 130 GeV and above 110 GeV. Three of the VBF candidates are found
 4019 in the mass region 120 – 130 GeV with invariant masses of 123.2 GeV, 123.4 GeV and
 4020 125.7 GeV.

4021 Only one VBF candidate ($m_{4\ell} = 123.4$ GeV) has a BDT output value of 0.7. In
 4022 this mass window, the expected number of VBF candidates with BDT output above
 4023 zero is 1.26 ± 0.15 , where half of this is expected to be from a true VBF signal, about
 4024 35% from ggF production and the rest is mostly from $ZZ^{(*)}$ and reducible backgrounds.
 4025 The distributions of $m_{4\ell}$ and the BDT output for the VBF category in the full mass
 4026 range and in the fit range of 110 – 140 GeV are shown in Figure 6.12.

4027 There is no VH candidate in the 120 – 130 GeV mass range for either the hadronic or
 4028 leptonic categories. For the full mass range above 110 GeV all categories are dominated
 4029 by the $ZZ^{(*)}$ background as can be seen in Table 6.13.

Table 6.12: Systematic uncertainties on the yields expected from various processes contributing to the VBF, hadronic VH, leptonic VH and ggF categories expressed as percentages of the yield. The various uncertainties are added in quadrature. Uncertainties that are negligible are omitted in the table.

Process	$gg \rightarrow H, q\bar{q}/gg \rightarrow b\bar{b}H/t\bar{t}H$	$qq' \rightarrow Hqq'$	$q\bar{q} \rightarrow W/ZH$	$ZZ^{(*)}$
VBF category				
Theoretical cross section	20.4%	4%	4%	8%
Underlying event	6.6%	1.4%	—	—
Jet energy scale	9.6%	4.8%	7.8%	9.6%
Jet energy resolution	0.9%	0.2%	1.0%	1.4%
Total	23.5%	6.4%	8.8%	12.6%
Hadronic VH category				
Theoretical cross section	20.4%	4%	4%	2%
Underlying event	7.5%	3.1%	—	—
Jet energy scale	9.4%	9.3%	3.7%	12.6%
Jet energy resolution	1.0%	1.7%	0.6%	1.8%
Total	23.7%	10.7%	5.5%	12.9%
Leptonic VH category				
Theoretical cross section	12%	4%	4%	5%
Leptonic VH-specific cuts	1%	1%	5%	—
Jet energy scale	8.8%	9.9%	1.7%	3.2%
Total	14.9%	10.7%	6.6%	5.9%
ggF category				
Theoretical cross section	12%	4%	4%	4%
Jet energy scale	2.2%	6.6%	4.0%	1.0%
Total	12.2%	7.7%	5.7%	4.1%

Figure 6.12: Distributions of the selected events and expected signal and background yields for the VBF enriched category: $m_{4\ell}$ (a) and the BDT output (b) in the full mass range, the $m_{4\ell}$ (c) and the BDT output (d) in the signal mass of range $110 < m_{4\ell} < 140$ GeV. The expected Higgs signal contributions, assuming $m_H = 125$ GeV, from the ggF, VBF and VH production modes are included. The expected background contributions, $ZZ^{(*)}$ and $Z\text{jets, } t\bar{t}$, are also shown; the systematic uncertainty associated to the total background contribution is represented by the hatched areas. In every case, the combination of 7 TeV and 8 TeV results is shown.

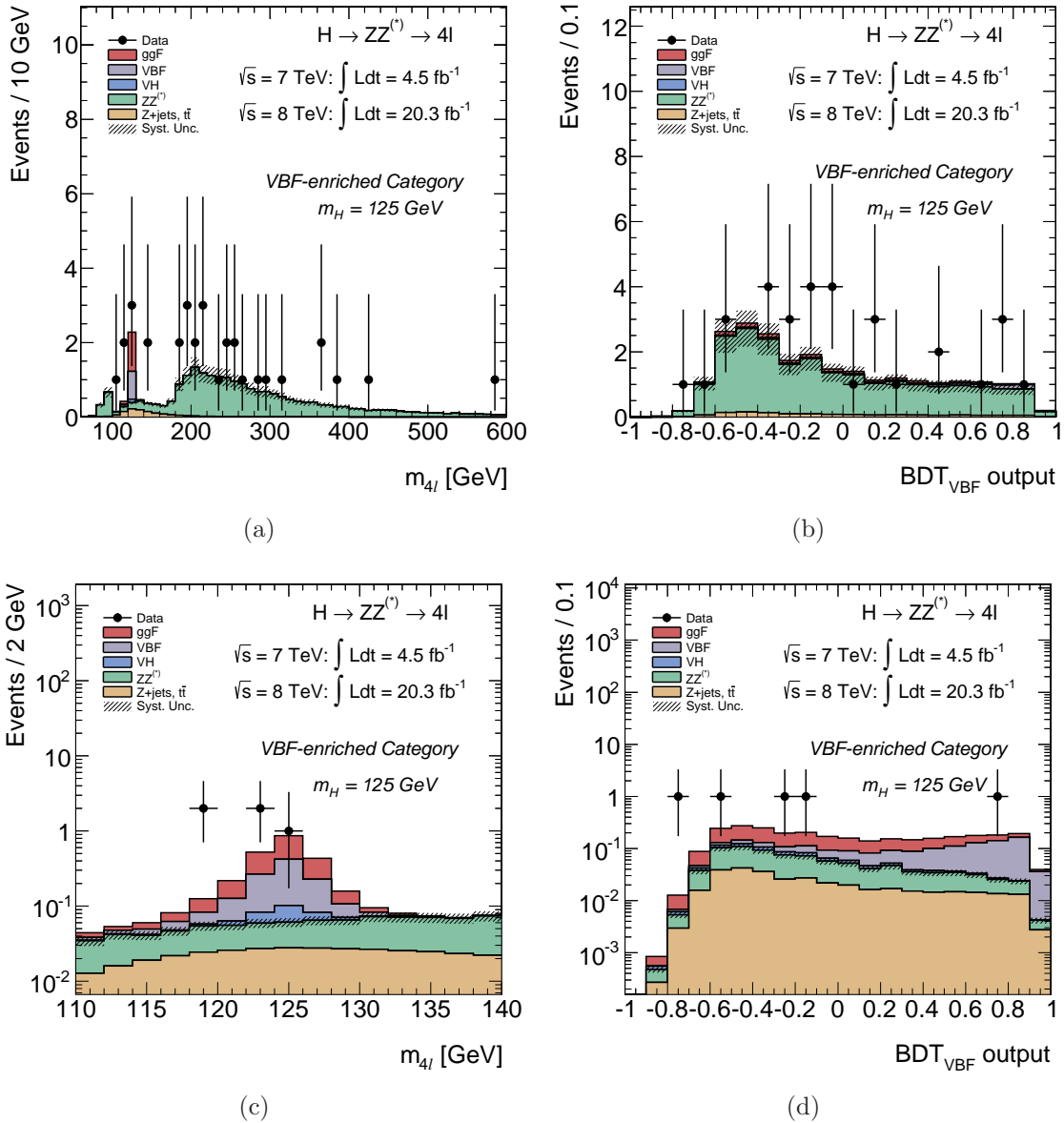


Table 6.13: Expected and observed yields in the VBF-enriched, hadronic VH-enriched, leptonic VH-enriched and ggF-enriched categories. Yields are given for the different production modes and the $ZZ^{(*)}$ and reducible background for 4.5 fb^{-1} at $\sqrt{s} = 7 \text{ TeV}$ and 20.3 fb^{-1} at $\sqrt{s} = 8 \text{ TeV}$. The estimates are given for the both the $m_{4\ell}$ mass range of $120 - 130 \text{ GeV}$ and the full mass range above 110 GeV .

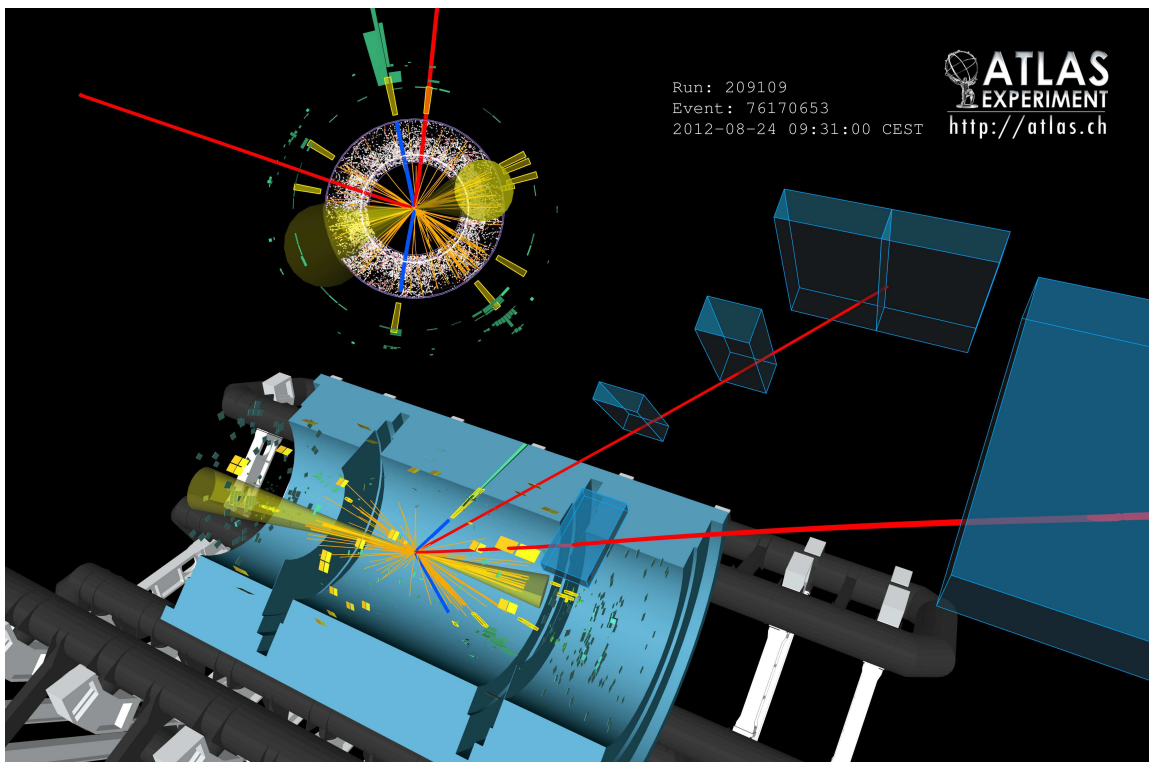
Enriched category	$ggF + b\bar{b}H + t\bar{t}H$	Signal		Background		Total	Observed
	VBF	VH-hadronic	VH-leptonic	$ZZ^{(*)}$	$Z + \text{jets}, t\bar{t}$	expected	
$120 < m_{4\ell} < 130 \text{ GeV}$							
<i>VBF</i>	1.18 ± 0.37	0.75 ± 0.04	0.083 ± 0.006	0.013 ± 0.001	0.17 ± 0.03	0.25 ± 0.14	2.4 ± 0.4
<i>VH-hadronic</i>	0.40 ± 0.12	0.034 ± 0.004	0.20 ± 0.01	0.009 ± 0.001	0.09 ± 0.01	0.09 ± 0.04	0.80 ± 0.12
<i>VH-leptonic</i>	0.013 ± 0.002	< 0.001	< 0.001	0.069 ± 0.004	0.015 ± 0.002	0.016 ± 0.019	0.11 ± 0.02
<i>ggF</i>	12.8 ± 1.3	0.57 ± 0.02	0.24 ± 0.01	0.11 ± 0.01	7.1 ± 0.2	2.7 ± 0.4	23.5 ± 1.4
$110 < m_{4\ell}$ GeV							
<i>VBF</i>	1.4 ± 0.4	0.82 ± 0.05	0.092 ± 0.007	0.022 ± 0.002	$20. \pm 4.$	1.6 ± 0.9	$24. \pm 4.$
<i>VH-hadronic</i>	0.46 ± 0.14	0.038 ± 0.004	0.23 ± 0.01	0.015 ± 0.001	9.0 ± 1.2	0.6 ± 0.2	10.3 ± 1.2
<i>VH-leptonic</i>	0.026 ± 0.004	< 0.002	< 0.002	0.15 ± 0.01	0.63 ± 0.04	0.11 ± 0.14	0.92 ± 0.16
<i>ggF</i>	14.1 ± 1.5	0.63 ± 0.02	0.27 ± 0.01	0.17 ± 0.01	$351. \pm 12.$	16.6 ± 2.2	$383. \pm 12.$
							420

6.8 Summary

The inclusive events identified in Chapter 5 undergo further selection to unveil their production mechanism. The categories explored are the VBF, VH hadronic and leptonic and the dominant ggF production. Due to small cross sections, the $t\bar{t}H$ and $b\bar{b}H$ categories are ignored for the $\sqrt{s} = 7$ and 8 TeV analysis. The selection of each one is described and alternative methods are also studied. The background method of the inclusive analysis is extended in order to measure the reducible background in the categories.

For the VBF category, one event is seen with a high multivariate discriminant value and a mass of 123.4 GeV , the event display of this event is presented in Figure 6.13. No VH candidate is found in the m_H range $120 - 130 \text{ GeV}$ with the W or Z decaying either hadronically or leptonicly. The observed yields for VBF and especially ggF are higher than the expected values. This fact leads to a higher production rate than the one expected from the Standard Model. Thus, one of the most interesting measurements of Run-II would be to verify if this excess persists or it can be classified as a statistical fluctuation.

Figure 6.13: Display of a $2e2\mu$ candidate with $m_{4\ell} = 123.4$ GeV. This is the only VBF candidate with $BDT_{VBF} > 0$, specifically the BDT_{VBF} value is 0.7. There are six jets in total, the two leading jets have $p_T = 180$ and 150 GeV and $\Delta\eta_{jj} = 3.4$, the missing of the event is $E_T = 40$ GeV.



4046 Chapter Bibliography

4047 [1] S. Heinemeyer et al., Handbook of LHC Higgs Cross Sections: 3. Higgs Properties,
4048 2013, arXiv:1307.1347.

4049 [2] W. Lampl, S. Laplace, D. Lelas, P. Loch, H. Ma, et al., Calorimeter clustering
4050 algorithms: Description and performance, 2008.

4051 [3] Matteo Cacciari, Gavin P. Salam, and Gregory Soyez, The Anti-k(t) jet clustering
4052 algorithm, *JHEP*, 0804:063, 2008, 0802.1189.

4053 [4] P. Speckmayer, A. Hocker, J. Stelzer, and H. Voss, The toolkit for multivariate
4054 data analysis, *TMVA 4*, *J.Phys.Conf.Ser.*, 219:032057, 2010.

4055 [5] Tom Melia, Paolo Nason, Raoul Rontsch, and Giulia Zanderighi, W^+W^- , WZ
4056 and ZZ production in the POWHEG BOX, *JHEP*, 1111:078, 2011, 1107.5051.

4057 [6] T. Binoth, N. Kauer, and P. Mertsch, Gluon-induced QCD corrections to $pp \rightarrow$
4058 $ZZ \rightarrow l \text{ anti-}l l \text{ prime anti-}l \text{ prime}$, page 142, 2008, 0807.0024.

4059 [7] S. Dittmaier, S. Dittmaier, C. Mariotti, G. Passarino, R. Tanaka, et al., Handbook
4060 of LHC Higgs Cross Sections: 2. Differential Distributions, 2012, 1201.3084.

4061 [8] T. Gleisberg, Stefan. Hoeche, F. Krauss, M. Schonherr, S. Schumann, et al., Event
4062 generation with SHERPA 1.1, *JHEP*, 0902:007, 2009, 0811.4622.

4063 [9] Iain W. Stewart and Frank J. Tackmann, Theory Uncertainties for Higgs and
4064 Other Searches Using Jet Bins, *Phys.Rev.*, D85:034011, 2012, 1107.2117.

4065 [10] Georges Aad et al., Light-quark and gluon jet discrimination in pp collisions at
4066 $\sqrt{s} = 7$ TeV with the ATLAS detector, 2014, 1405.6583.

7

4067

4068

$H \rightarrow ZZ^{(*)} \rightarrow 4\ell$ Prospect Studies

4069 7.1 Introduction

4070 One of the main motivations for an upgrade of the LHC to deliver high luminosity,
4071 HL-LHC, is to enable precise measurements of the Higgs boson properties. In the
4072 Standard Model, all the properties of the Higgs boson are defined once its mass is known.
4073 However, this model leaves many open questions such as the hierarchy problem or the
4074 nature of dark matter. Many alternative theories addressing these issues make different
4075 predictions for the properties of one or more Higgs bosons. Precise measurements in
4076 the Higgs sector are therefore a priority in the future program of particle physics [1].

4077 The present LHC program is expected to deliver a total integrated luminosity of
4078 about 300 fb^{-1} by the year 2022. The peak instantaneous luminosity will be in the
4079 range $2 - 3 \times 10^{34} \text{ cm}^{-2} \text{ s}^{-1}$. The luminosity will decrease from the peak value during a
4080 fill, though a typical average number of pile-up events per bunch crossing is estimated
4081 to be $\mu = 50 - 60$. The HL-LHC would deliver a total luminosity of about 3000 fb^{-1} ,
4082 at a peak leveled luminosity of $5 \times 10^{34} \text{ cm}^{-2} \text{ s}^{-1}$, with a value of $\mu = 140$.

4083 The detector design for the high luminosity phase is not yet completely defined and
4084 it will take years to adapt and optimize the event reconstruction software to the high-
4085 pile-up conditions. The goal is that the performance of the new detector in the harsh
4086 conditions of the high luminosity phase will not be worse than the performance of the
4087 current detector with $\mu = 20$.

4088 A study is performed based on efficiency and resolution (smearing) functions to

4089 physics objects [2], which were derived from samples using the Run-I ATLAS detector
 4090 with various values of μ , up to a maximum average of $\mu = 69$. Many of these functions
 4091 were updated with the results of full the simulation of the Phase-I detector [2] with μ
 4092 values up to 80, and the Phase-II detector with μ values of 80, 140 and 200.

4093 The rates of tagging b , c and *light* flavor jets have been parametrized using one
 4094 of the more robust tagging algorithms at a 70% efficiency working point for b -jets
 4095 produced in $t\bar{t}$ events. It is expected that more sophisticated algorithms will give even
 4096 better light jet rejection for the same efficiency, but they are not yet optimized for the
 4097 Phase-II detector. A higher efficiency working point would also be preferred for some of
 4098 the statistics limited channels presented here, since the light-jet rejection rate is better
 4099 than with the Run-I detector, despite the high pile-up.

4100 Functions to describe the detector resolution, reconstruction efficiency and trigger
 4101 efficiency were defined by extrapolations from the existing data sample and Monte
 4102 Carlo simulations in the same bunch crossing (in-time pile-up) and in preceding bunch
 4103 crossings (out-of-time pile-up). In defining these parametrizations, it is also considered
 4104 that the Phase-II detector would be designed to retain the performance of the present
 4105 detector for many aspects.

4106 In this chapter, the $H \rightarrow ZZ^{(*)} \rightarrow \ell^+\ell^-\ell^+\ell^-$ channel study is presented for $300\text{ }fb^{-1}$
 4107 and $3000\text{ }fb^{-1}$. This channel offers a very clean final state signature with excellent signal
 4108 to background ratio at the LHC environment. The large number of events expected
 4109 in a $3000\text{ }fb^{-1}$ sample, allows the study of all the Higgs production modes separately
 4110 using this final state, adding important sensitivity to the measurement of the Higgs
 4111 coupling parameters.

4112 The 4ℓ analysis is based on the same selection criteria applied for the Run-I analysis
 4113 (Chapter 5). Track confirmation is required for all candidate jets falling inside the ID
 4114 acceptance and their p_T thresholds are tuned to allow 1% jet fake rate, thus making the
 4115 contribution from pile-up jets marginal. An alternative scenario, allowing 10% fake rate
 4116 is also presented. The main background is the Standard Model is $q\bar{q} \rightarrow ZZ^{(*)}$ di-boson
 4117 production. The relevant reducible background processes which are $Z + \text{jets}$, $Zb\bar{b}$ and $t\bar{t}$,
 4118 are added conservatively as a 50% proportion of the main irreducible background.

4119 Investigation of possible gain from an increased muon acceptance is explored. Specif-
 4120 ically, it is considered that both the inner detector and the muon spectrometer could
 4121 be extended with sectors covering the region of $2.7 < \eta < 4.0$. Expected yields and
 4122 important Higgs properties are reported.

4123 At the end of this chapter, the Run-II expectations are explored through projections
 4124 made from the Run-I (Chapter 6) due to the lack of fully simulated events for the Run-
 4125 II conditions. In Run-II, the expected center of mass collision energy is expected to
 4126 be $\sqrt{s} = 13\text{ TeV}$ and the delivered luminosity will not exceed the $100\text{ }fb^{-1}$. The pile
 4127 up conditions will lie between the Run-I and the Phase-II conditions of $300\text{ }fb^{-1}$, but
 4128 the allowed fake rate will be closer to the Run-I. For the Run-II yields prediction, the
 4129 previously estimated yields are extrapolated to the $\sqrt{s} = 13\text{ TeV}$ and the $100\text{ }fb^{-1}$,

4130 using the theoretical cross sections from Reference [3], already summarized in Chapter 1.

4131 The production theoretical cross sections used for this study have been presented
4132 in Chapter 1 and the MC samples used are mentioned in the Appendix B.

4133 **7.2 Categories Event Selection**

4134 After the $H \rightarrow ZZ^{(*)} \rightarrow \ell^+\ell^-\ell^+\ell^-$ candidates identification, using the selection pre-
4135 sented in Chapter 5, the production mechanisms categorization follows. The selection of
4136 the events in the different categories is chosen in a way to allow the minimal cross talk
4137 between the production mechanisms and hence is different from Chapter 6. Namely,
4138 the order followed aims to tag $t\bar{t}H$, ZH , WH and VBF respectively. The remaining
4139 events are assumed to fall in the gluon-gluon fusion category.

4140 A lepton quadruplet is formed from two pairs of same flavor and opposite sign
4141 leptons. The dilepton pair, with mass closest to the Z nominal mass, is required to
4142 have a mass between 50 and 115 GeV. The mass of the remaining dilepton is required
4143 to be between 12 and 115 GeV. Quadruplets with same flavor opposite sign lepton pairs
4144 with mass less than 5 GeV are excluded to avoid J/ψ contamination. p_T thresholds of
4145 20, 15, 10 and 6 (7 for electrons) GeV are applied to the leptons. At this level, the
4146 agreement between the analysis based on smeared truth quantities and the one obtained
4147 from full simulation is very good.

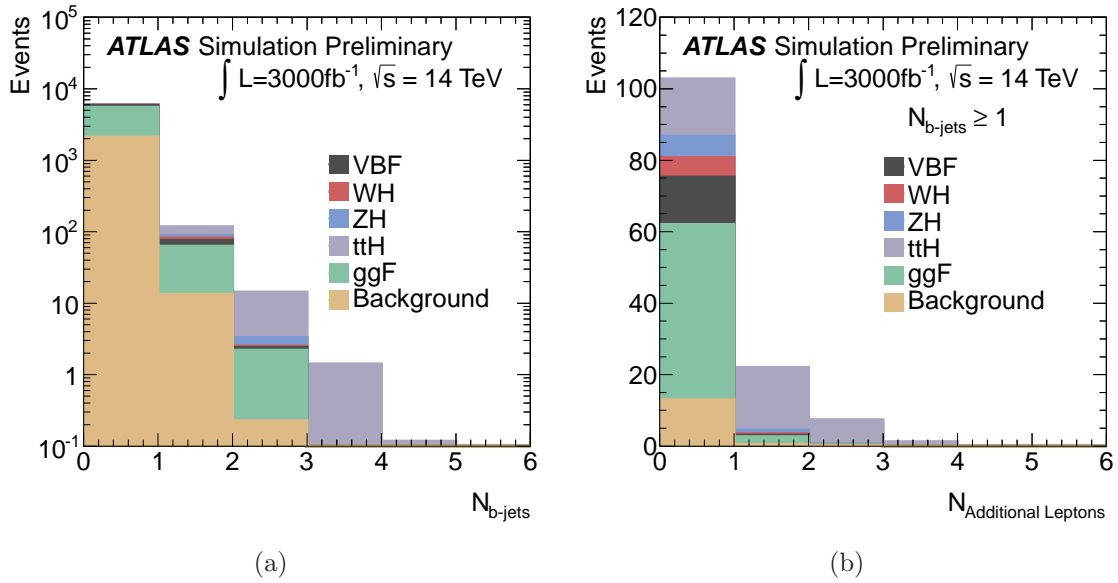
4148 The last requirement in the full analysis is the lepton isolation, which can not be
4149 applied with truth level information. The lepton isolation, however, is very important
4150 for the suppression of the reducible backgrounds. In particular for leptons with $p_T \leq$
4151 10 GeV, for which the pile-up can induce some loss of efficiency with respect to Run-I
4152 (95% at $p_T \simeq 20$ GeV, 90% at $p_T \simeq 10$ GeV). Therefore, in order to maintain similar
4153 suppression of the reducible backgrounds at peak level luminosities of $5 \times 10^{34} \text{ cm}^{-2}\text{s}^{-1}$
4154 compared to the 2012 analysis, a conservative 20% inefficiency, for leptons with $p_T <$
4155 20 GeV, is assumed.

4156 **7.2.1 $t\bar{t}H$, $H \rightarrow ZZ^{(*)}$**

4157 The selection of the $t\bar{t}H$ events exploits the existence of two b-jets stemming from
4158 the decays of the top quarks. Therefore, the presence of at least one b-tagged jet is
4159 required. To account for the leptonic W decays, one additional lepton with $p_T > 8$ GeV
4160 is also required. If the event does not pass this selection, at least four additional jets are
4161 required in order to account for hadronic decays of both W s and classify the event in the
4162 $t\bar{t}H$ category. Figure 7.1 shows the distribution of the number of b-tagged jets, as well

as the distribution of the number of the additional leptons (excluding the ones coming from the Higgs decay) in the events where at least one b-tagged jet is present, for the different Higgs production mechanisms and the background. It is clear that on top of the initial four lepton requirement, the criteria imposed in this analysis are sufficient to produce a very clean $t\bar{t}H$ sample. To reduce the ZH contamination in this category, events with two additional opposite sign same flavor leptons within ± 15 GeV of the nominal Z mass are vetoed. The mispairing effect, between the additional leptons and the quadruplet, is also taken into account for the category decision.

Figure 7.1: The distribution of the number of b-tagged jets (a) and the number of additional leptons in events with at least one b-tagged jet (b), for different Higgs production mechanisms and the background.



7.2.2 VH , $V = Z$ or W , $H \rightarrow ZZ^{(*)}$

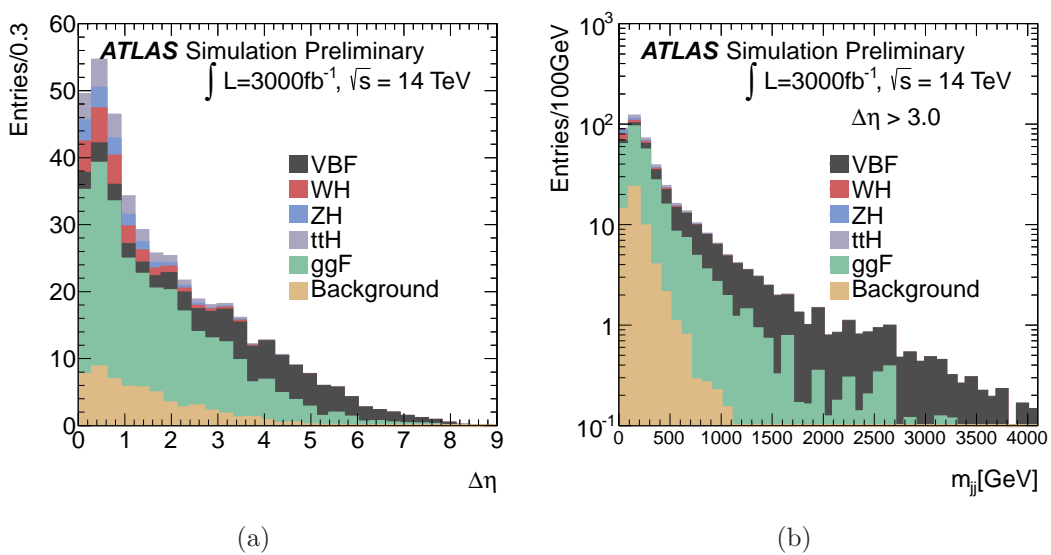
Events that contain two additional same flavor opposite sign leptons and do not fall in the previous category are classified as ZH , $H \rightarrow ZZ^{(*)}$, candidates. In order to reduce that $t\bar{t}H$ events, that failed b-tagging and would populate this category, the additional lepton pair mass is required to be within 15 GeV to the nominal Z boson mass. Events which are not yet selected and contain one additional lepton are classified in the WH category.

⁴¹⁷⁸ **7.2.3 $VBF, H \rightarrow ZZ^{(*)}$**

⁴¹⁷⁹ Events that are not selected in the above categories are supposed to fall either in the
⁴¹⁸⁰ VBF category or the gluon-gluon fusion category. A search for at least two additional
⁴¹⁸¹ jets is then performed in these events. A jet pair is accepted if it has an η difference
⁴¹⁸² above $\Delta\eta > 3$. The invariant mass of the two higher p_T jets is then used as discriminant
⁴¹⁸³ for the VBF category. In this analysis, the event is accepted in the VBF category if
⁴¹⁸⁴ this mass is $m_{jj} > 350$ GeV.

⁴¹⁸⁵ Figure 7.2 shows the distribution of $\Delta\eta$ (a) and the mass m_{jj} (b) of the selected
⁴¹⁸⁶ di-jet pair, for different Higgs production mechanisms and the background.

Figure 7.2: The distribution of $\Delta\eta$ (a) and the mass m_{jj} (b) of the selected di-jet pair,
 for different Higgs production mechanisms and the background.



⁴¹⁸⁷ **7.2.4 $ggF, H \rightarrow ZZ^{(*)}$**

⁴¹⁸⁸ The gluon-gluon fusion category consists of all the events that are not tagged with
⁴¹⁸⁹ the above requirements.

4190 7.3 Simulation Procedure

4191 The code for the selection of the 4ℓ final state performs also the reweighting of
 4192 the event accounting for trigger and lepton reconstruction efficiency, as well as the
 4193 smearing of the lepton momenta and energies. At this level of the analysis, the overall
 4194 efficiencies of the $H \rightarrow ZZ^{(*)} \rightarrow \ell^+\ell^-\ell^+\ell^-$ signature are found to vary between 63%
 4195 (4e) and 74% (4 μ), for the final states containing only electrons and muons. Lepton
 4196 isolation is expected to be less effective in suppressing the reducible backgrounds with
 4197 instantaneous luminosities of $5 \times 10^{34} \text{ cm}^{-2}\text{s}^{-1}$ compared to the Run-I analysis. Due to
 4198 the lack of precise full simulation studies to measure this effect, a conservative approach
 4199 has been adopted, decreasing the lepton efficiency, for leptons with $p_T < 20 \text{ GeV}$, by
 4200 20%. As a result of this assumption the signal efficiency is decreased by approximately
 4201 27%.

4202 The subsequent categorization of events is performed using additional leptons and
 4203 jets. For the additional leptons the same treatment as the ones produced by the Higgs
 4204 boson decay is followed. Figure 7.3 shows the p_T distribution of the additional leptons
 4205 and the dilepton mass in the case where two additional leptons exist. Track confirmation
 4206 is required for all jets in the relevant acceptance in order to be considered as jet
 4207 candidates. The jets are then smeared according to the recommendation. Furthermore
 4208 a p_T threshold allowing for a fake jet rate below 1% is required. Jet truth origin is
 4209 established by ΔR requirement between the jet candidates and truth partons. Then
 4210 b-tagging is applied. The efficiency of the b-tagging in the $t\bar{t}H$ sample is found to be
 4211 $\sim 70\%$, and the rejection of light quark jets close to 100%. The track confirmation effi-
 4212 ciency is found to be $\sim 90\%$. Figure 7.4 shows the p_T distribution of the b-tagged jets
 4213 in the ttH category and the tagged jets in the VBF category, following this procedure.

4214 7.4 Systematic Uncertainties

4215 The theoretical uncertainties on the signal yields assumed in this analysis for the
 4216 different production mechanisms of the Higgs boson, follow Reference [4]. The irre-
 4217 ducible background will be evaluated using the side-band regions around the Higgs
 4218 boson mass peak. Reducible backgrounds are also expected to be evaluated using data
 4219 driven methods similarly to the Run-I (Chapter 5). In the cases where it is not possible
 4220 to constrain it with data driven methods, a 7% (35% for the VBF case) uncertainty on
 4221 the background is introduced.

4222 The detector uncertainties concerning lepton reconstruction and selection, are af-
 4223 fecting all channels in a similar way and are assumed to be equal to the ones measured in
 4224 the Run-I [5]. The uncertainty on the muon identification and reconstruction efficiency
 4225 results in an uncertainty on the yields for the signal and the dominant $ZZ^{(*)}$ back-

Figure 7.3: Distribution of the p_T of additional leptons (a) and the dilepton mass (b) in case there are two additional leptons.

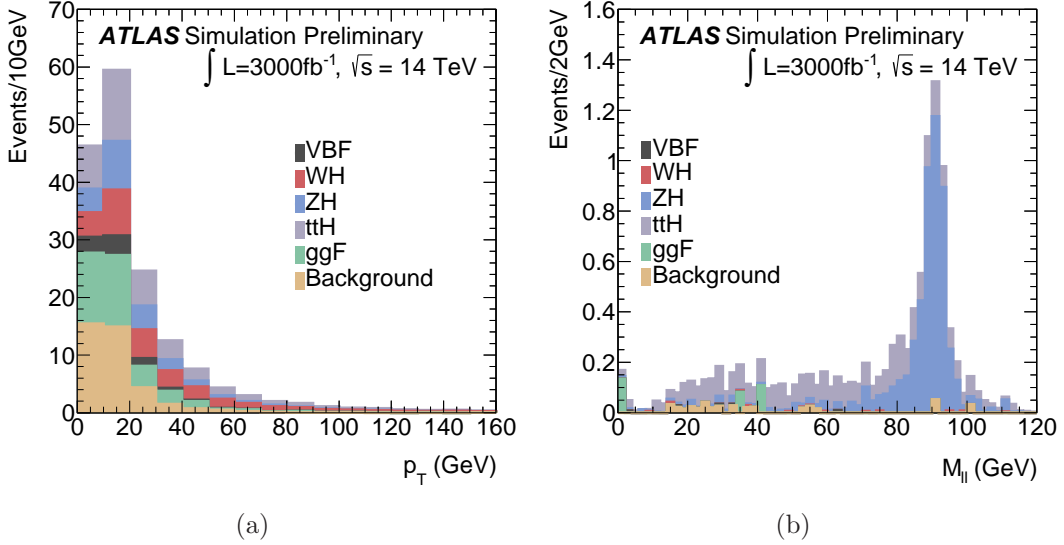
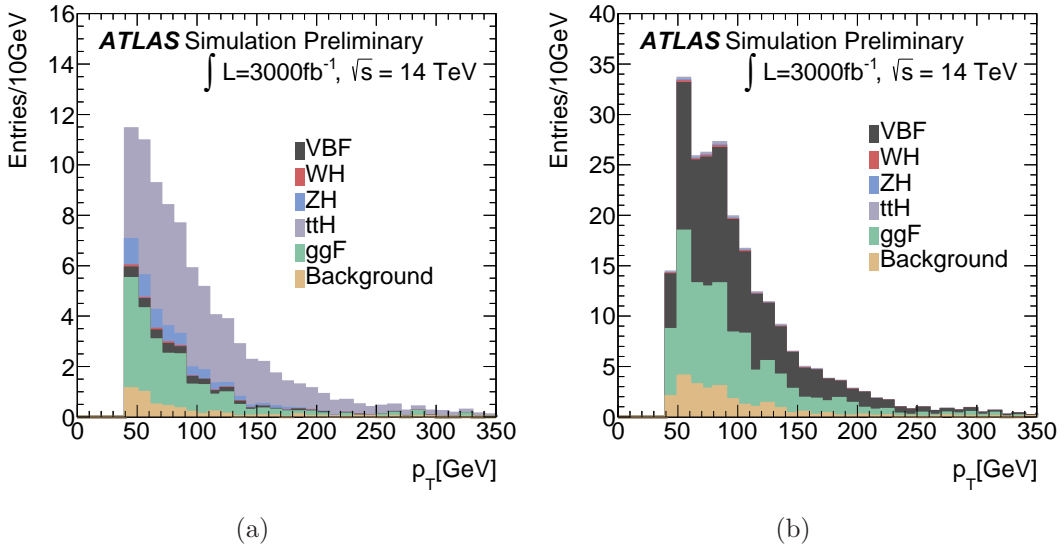


Figure 7.4: Distribution of the p_T of b-tagged jets (a) and tagged jets in VBF analysis (b).



ground which is uniform over the low mass range of interest, and amounts to $\pm 0.8\%$ ($\pm 0.4\% / \pm 0.4\%$) for the 4μ ($2\mu 2e/2e 2\mu$) channel. The uncertainty on the electron identification and reconstruction efficiency results in an uncertainty on the yields for

4229 the signal of $\pm 2.4\%$ ($\pm 1.8\% / \pm 1.6\%$) for the $4e$ ($2\mu 2e / 2e 2\mu$) channel at $m_{4\ell} = 1$ TeV
 4230 and $\pm 9.4\%$ ($\pm 8.7\% / \pm 2.4\%$) at $m_{4\ell} = 125$ GeV.

4231 The selection efficiency of the isolation and impact parameter requirements, studied
 4232 using data from Z decays in Run-I and were found with good accuracy to be in
 4233 good agreement between data and simulation. Similarly in this study, the systematic
 4234 uncertainty from this source is estimated to be small with respect to other systematic
 4235 uncertainties.

4236 The jet energy scale, the jet track confirmation and the b-tagging performance
 4237 are the main jet related uncertainties that affect mostly the $t\bar{t}H$ and VBF categories.
 4238 The main systematic uncertainty for the $t\bar{t}H$ category is due to b-tagging and the
 4239 track confirmation is required for the jets. However these uncertainties are quite small,
 4240 compared to the theory uncertainties. A 5% uncertainty on b-tagging efficiency or the
 4241 track confirmation inefficiency corresponds to 2% uncertainty on the $t\bar{t}H$ efficiency. The
 4242 other Higgs boson production contributions as well as the background are also affected
 4243 by the jet energy scale and resolution below the level of 10%. The dominant sources of
 4244 detector related uncertainties, in the VBF category, are due to the jet energy scale and
 4245 resolution together with uncertainties concerning the underlying events. It is assumed
 4246 that their contribution is similar to the Run-I, i.e. amounts $\sim 10\%$ for the VBF-like
 4247 category, 0.7% for the VH-like category and 0.7% for the ggF-like category.

4248 Finally, a 3% uncertainty on the luminosity is assumed [2].

4249 7.5 $3000\ fb^{-1}$ Results

4250 Following the event selection defined above, the yields of expected events in each
 4251 category from the signal and background events are reported in Table 7.1 for $3000\ fb^{-1}$.
 4252 The yields are reported in the lepton quadruplet mass interval between 115 and 130 GeV.
 4253 The total uncertainties on the corresponding estimates are given. Figure 7.5 shows the
 4254 invariant mass distributions of the lepton quadruplets coming from Higgs production
 4255 mechanisms and background for the different category selections.

4256 7.6 Comparison with the Full Analysis at 8 TeV

4257 In order to verify the validity of the smearing used in this analysis, a comparison
 4258 is made using the full analysis results at 8 TeV normalized to the cross section and
 4259 integrated luminosity of the current analysis. After the application of the trigger and
 4260 lepton efficiencies and resolutions at the truth level, the yields of the events are expected
 4261 to be 5080 from gluon-gluon fusion production and 470 from VBF production compared

Table 7.1: Expected events in each category (ggF-like, VBF-like, WH-like, ZH-like, ttH-like) assuming $m_H = 125$ GeV and 3000 fb^{-1} of data. For each category, the expected events from the various Higgs production mechanisms are specified. Estimates are given in the lepton quadruplet mass interval between 115 and 130 GeV, along with their total uncertainties.

Category	Truth Origin					
	ggF	VBF	WH	ZH	ttH	Background
ttH-like	3.1 ± 1.0	0.6 ± 0.1	0.6 ± 0.1	1.1 ± 0.2	30 ± 6	0.6 ± 0.2
ZH-like	0.0	0.0	0.01 ± 0.02	4.4 ± 0.3	1.3 ± 0.3	0.06 ± 0.06
WH-like	22 ± 7	6.6 ± 0.4	25 ± 2	4.4 ± 0.3	8.8 ± 1.8	13 ± 0.8
VBF-like	41 ± 14	54 ± 6	0.7 ± 0.1	0.4 ± 0.1	1.0 ± 0.2	4.2 ± 1.5
ggF-like	3380 ± 650	274 ± 17	77 ± 5	53 ± 3	25 ± 4	2110 ± 50

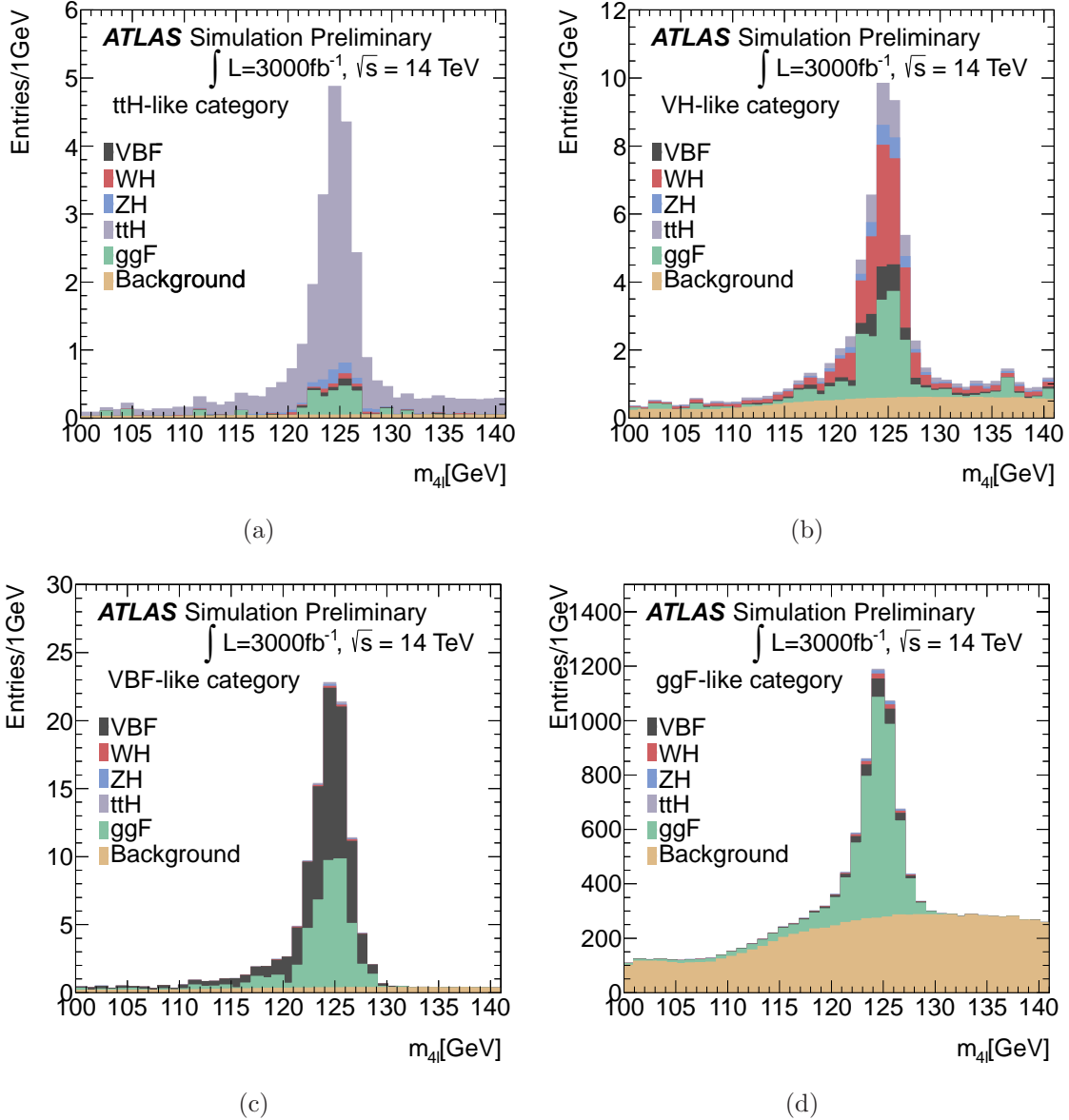
4262 to 5000 and 460 respectively, from the extrapolation of the 8 TeV results. At the VBF
4263 category, using the same criteria, 106 events are expected from gluon-gluon fusion and
4264 167 events from VBF, while the corresponding expectations from 8 TeV are 100 and
4265 165 respectively. The agreement between the extrapolation of the 8 TeV analysis and
4266 the current one is, therefore, considered to be very satisfactory.

4267 Despite the good agreement of the parametrized analysis and the full simulation
4268 analysis at 8 TeV, the pile-up conditions in the current study, require certain changes.
4269 The most important is the 20% decrease of the efficiency of the leptons with $p_T <$
4270 20 GeV. Furthermore, to reduce the fake jets due to pile-up harder jet p_T thresholds
4271 have to be used. In this analysis, a working point of jet fake rate of 1% is used together
4272 with the requirement of track confirmation for the jets falling in the acceptance of the
4273 Inner Detector. This reduced the efficiency in identifying the true VBF events to $\sim 50\%$.
4274 Furthermore, the jet energy resolution allowed the migration of a substantial number
4275 of gluon-gluon fusion events, as well as ZZ background events in the VBF category. In
4276 general the treatment of the VBF category in the current analysis is conservative.

4277 7.7 Study of the VBF Category with Higher Jet 4278 Fake Rate

4279 As an attempt to have higher efficiency in the VBF category, jet thresholds corre-
4280 sponding to 10% fake rate were used. To emulate the effect of pile-up at 14 TeV, extra
4281 jets were inserted according to an extrapolation done from Run-I data. The amount
4282 of these jets corresponds to the fake rate chosen according to the jet p_T thresholds, as

Figure 7.5: Quadruplet mass for the $t\bar{t}H$ -like (a), VH-like (b), VBF-like (c) and ggF-like (d) categories.



described in Reference [2]. These jets follow the rest of the analysis steps as the original jets of the event. Using the working point of 10% jet fake rate for the case of $\mu = 140$, an increase of 8% of the gluon-gluon fusion contribution in the VBF category is observed. For $\mu = 50$, the increase is estimated at the 3% level. Since this effect should be studied in detail with fully simulated samples, an equal amount of uncertainty is

introduced in the background of this category. In the case of 1% jet fake rate the effect contributes below the 1% level and is considered negligible. The analysis based on the 10% jet fake rates, results in a statistical accuracy which is better than the one using 1% fake rates thresholds by $\sim 30\%$. Nevertheless, the systematic error in this case is increased by $\sim 20\%$. Therefore, the gain in accuracy is estimated to be less than 10%.

Results obtained with p_T thresholds corresponding to 10% fake rate are reported in Table 7.2.

Table 7.2: Expected events in each category (ggF-like, VBF-like, WH-like, ZH-like, ttH-like) assuming $m_H = 125\text{ GeV}$ and $3000\text{ }fb^{-1}$ of data. The p_T thresholds used for the jets correspond to 10% fake rate. For each category, the expected events from the various Higgs production mechanisms are specified. Estimates are given in the lepton quadruplet mass interval between 115 and 130 GeV, along with their total uncertainties.

Category	Truth Origin					
	ggF	VBF	WH	ZH	ttH	Background
ttH-like	5.8 ± 1.5	0.9 ± 0.2	0.9 ± 0.1	1.6 ± 0.2	36 ± 7	1.0 ± 0.2
ZH-like	0.0	0.0	0.01 ± 0.01	4.4 ± 0.3	1.2 ± 0.3	0.06 ± 0.06
WH-like	21 ± 7	6.3 ± 0.4	25 ± 2	4.4 ± 0.3	7.3 ± 1.7	12 ± 0.8
VBF-like	102 ± 34	101 ± 11	1.2 ± 0.2	0.9 ± 0.1	1.0 ± 0.2	12.8 ± 4.5
ggF-like	3310 ± 650	227 ± 14	77 ± 5	53 ± 3	20 ± 4	2110 ± 150

7.8 $300\text{ }fb^{-1}$ Results

This study is performed similarly to the one of the $3000\text{ }fb^{-1}$. Concerning lepton reconstruction different parametrizations are used to account for the status of the detector. Furthermore, isolation criteria are expected to behave more similarly to the full simulation analysis of 8 TeV and therefore the 20% inefficiency introduced for leptons with p_T below 20 GeV is changed to 10%. The yields of expected events in each category from signal and background events are reported in Table 7.3. The yields are reported in the lepton quadruplet mass interval between 115 and 130 GeV. The total uncertainties on the corresponding estimates are also provided.

Table 7.3: Expected events in each category (ggF-like, VBF-like, WH-like, ZH-like, ttH-like) assuming $m_H = 125$ GeV and 300 fb^{-1} of data. For each category, the expected events from the various Higgs production mechanisms are specified. Estimates are given in the lepton quadruplet mass interval between 115 and 130 GeV, along with their total uncertainties.

Category	Truth Origin					
	ggF	VBF	WH	ZH	ttH	Background
ttH-like	0.47 ± 0.12	0.07 ± 0.02	0.07 ± 0.01	0.15 ± 0.02	3.9 ± 0.7	0.15 ± 0.04
ZH-like	0.0	0.0	0.0	0.51 ± 0.03	0.15 ± 0.03	0.01 ± 0.01
WH-like	2.8 ± 0.7	0.85 ± 0.06	3.3 ± 0.3	0.6 ± 0.1	1.0 ± 0.2	1.7 ± 0.1
VBF-like	5.0 ± 1.7	6.7 ± 0.7	0.08 ± 0.02	0.05 ± 0.01	0.12 ± 0.04	0.41 ± 0.14
ggF-like	457 ± 41	36 ± 3	10 ± 0.6	7.1 ± 0.4	3.1 ± 0.6	296 ± 20

7.9 Large- η Acceptance Scenario

The possibility of extending the coverage of the muon acceptance for the Phase-II upgrade of the ATLAS detector and its impact on the $H \rightarrow ZZ^{(*)} \rightarrow 4\ell$ channel is investigated in this section.

The muon identification requires tracking, which is more precise if it combines information from the inner detector and the muon chambers, as well as a magnetic field for the charge identification and momentum measurement. In the most optimistic scenario, the tracker is considered to extend up to $\eta = 4.0$ with additional Pixel sensors and the current beam pipe layout, the muon spectrometer is considered to have additional stations covering the region of $2.7 < \eta < 4.5$ and an enhanced magnetic field in this region is assumed. No change in the electrons identification is foreseen in this scenario.

In order to study the effect on the $H \rightarrow ZZ^{(*)} \rightarrow 4\ell$ sensitivity, a study similar to the one conducted in the previous sections of this chapter is performed based on the truth information. The channel that is expected to be affected the most by the extended detector layout is the $H \rightarrow ZZ^{(*)} \rightarrow 4\mu$. The yields of the expected events in this final state are reported in Table 7.4 and for comparison reasons the yields for the current layout ($\eta < 2.7$) are given. Based on these, the gain in the truth and smeared level is calculated. It has to be noted that no production mechanisms categorization applied to extract these yields.

The mass distributions of the 4μ candidates are presented in Figure 7.6 and the muons p_T and η distributions are presented in Figure 7.7. The η as a function of the p_T distributions for the muons that form the quadruplets are shown in Figure 7.8 for the different signals and the background. The formed Higgs candidates p_T and η spectrum appear in Figure 7.9.

Table 7.4: Expected events in the $H \rightarrow ZZ^{(*)} \rightarrow 4\mu$ final state from different Higgs signals and the SM background. It has to be noted that no production mechanisms categorization is applied. For comparison, the yields for the current detector layout are given ($\eta < 2.7$) and the gains are extracted from both the truth level and after the application of the smearing functions.

	Signal Samples					
	ggF	VBF	WH	ZH	ttH	Background
$\eta < 2.7$	1030	101	31	19	19	651
$\eta < 4.0$	1244	117	39	24	20	911
Smeared Gain	20.78%	16.50%	26.69%	25.26%	8.13%	40.00%
Truth Gain	29.66%	23.31%	39.37%	37.98%	9.87%	70.73%

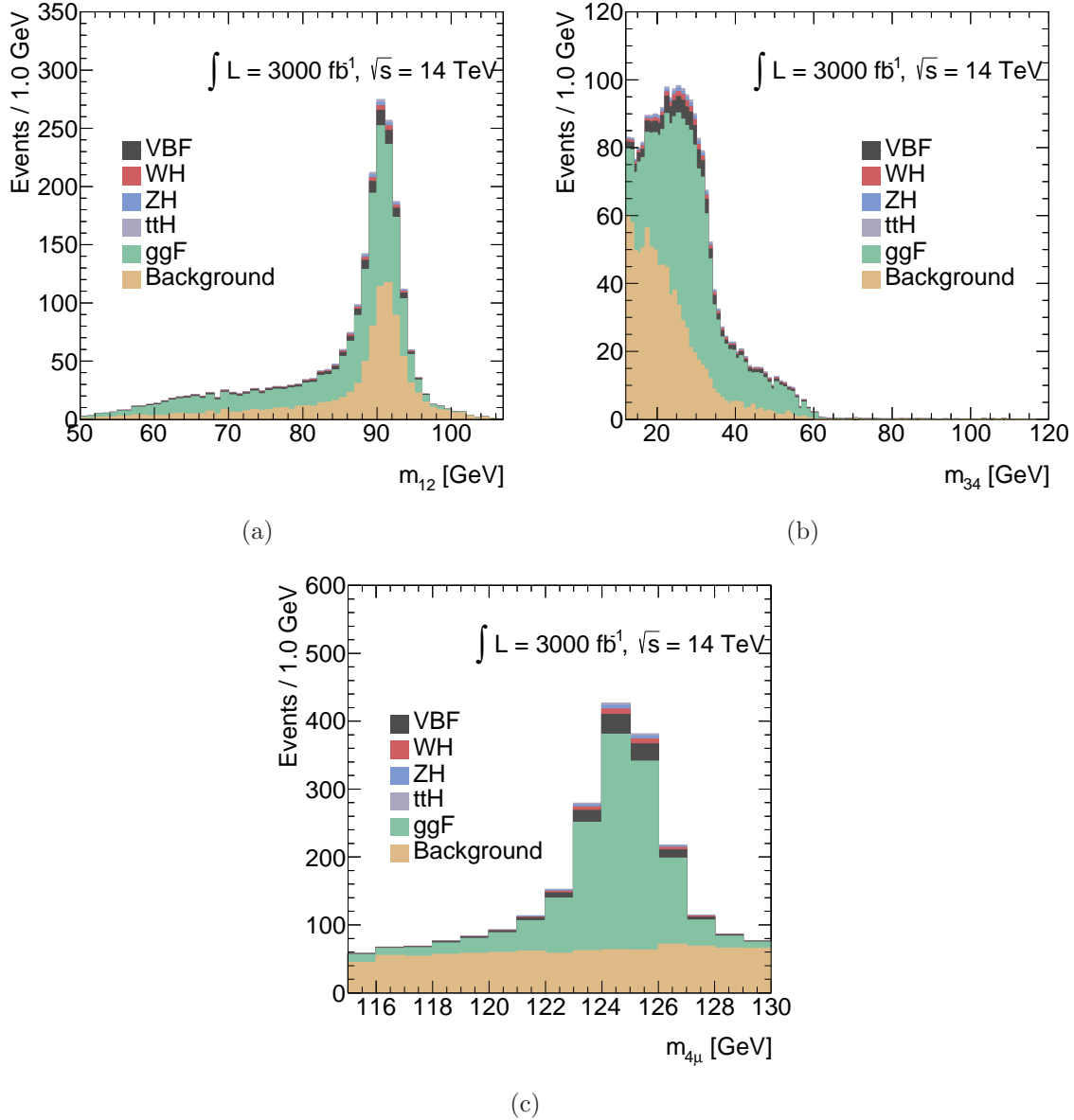
4328 The other channels which include muons, the $2e2\mu$ and $2\mu2e$, are affected less with
 4329 respect to the 4μ final state. Table 7.5 presents the $H \rightarrow ZZ^{(*)} \rightarrow 4\ell$ results for the
 4330 high eta region, where the electrons acceptance is unchanged (hence the $4e$ channel
 4331 is not affected) and the muons acceptance is increased. The gains in the truth and
 4332 smeared levels are also reported.

4333 The observed gain is non-negligible, however the background increase is significant.
 4334 Thus further studies should be made to reach a final decision.

Table 7.5: Expected events in the $H \rightarrow ZZ^{(*)} \rightarrow 4\ell$ final state from different Higgs signals and the SM background. It has to be noted that no production mechanisms categorization is applied. The electrons acceptance is unchanged (therefore the $4e$ channel is not affected) and the muons acceptance is increased. For comparison, the yields for the current detector layout are given ($\eta < 2.7$) and the gains are extracted from both the truth level and after the application of the smearing.

	Signal Samples					
	ggF	VBF	WH	ZH	ttH	Background
$\eta < 2.7$	3439	335	104	64	66	2126
$\eta < 4.0$	3765	361	116	72	68	2493
Smeared Gain	9.49%	7.88%	11.92%	11.88%	3.81%	17.30%
Truth Gain	12.04%	9.85%	15.97%	15.46%	4.31%	26.86%

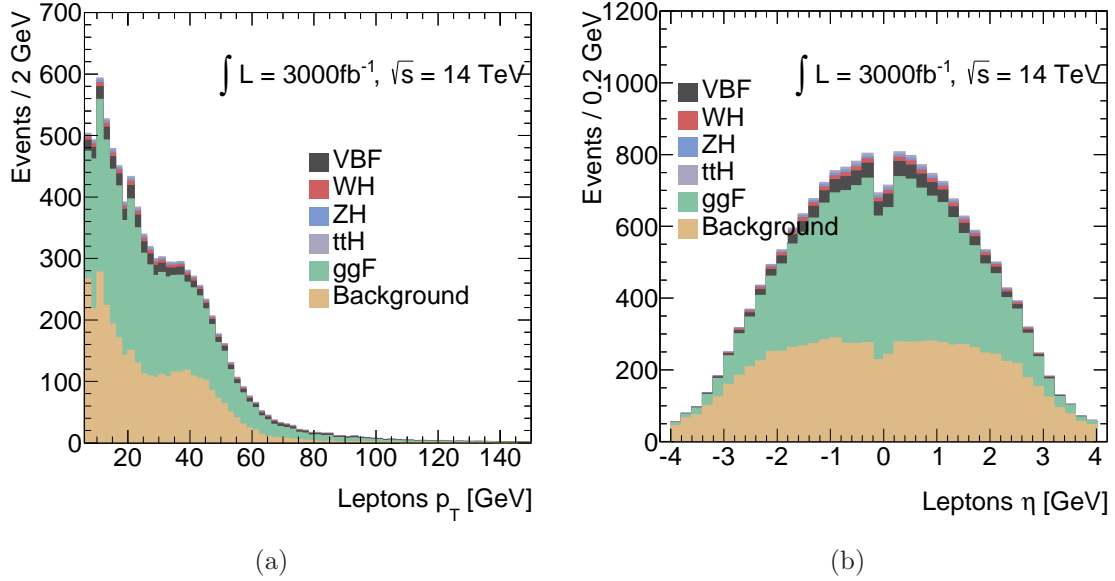
Figure 7.6: The m_{12} (a), m_{34} (b) and $m_{4\ell}$ (c) of the $H \rightarrow ZZ^{(*)} \rightarrow 4\mu$ candidates with η up to 4.0.



4335 7.10 Run-II Projections

4336 In this section projections are made from the Run-I results presented in Chapter 6.
 4337 The summary expectations for the ggF – like, VBF – like, VH – leptonic – like and
 4338 VH – hadronic – like categories are in Table 7.6. The yields are reported in the mass

Figure 7.7: The p_T (a) and η (b) distributions of the muons forming the $H \rightarrow ZZ^{(*)} \rightarrow 4\mu$ candidates. The maximum allowed η is the 4.0.



range of $110 - 140$ GeV and the $ttH - like$ and $bbH - like$ categories are ignored due to marginal cross sections in the Run-I. These numbers are considered to be optimistic given that the pile-up conditions are expected to be harsher.

Table 7.6: Projections are made from the Run-I results (Chapter 6) for the Run-II at $\sqrt{s} = 13$ TeV and $100 fb^{-1}$ considered luminosity. The cross section scaling is taken into account according to the Reference [3]. The reported events are in the mass range of $110 - 140$ GeV and the $ttH - like$ and $bbH - like$ categories are missing due to marginal cross sections in the Run-I. The “Background” corresponds to the ZZ and 50% of the ZZ to account for the reducible background.

Origin	$ggF - like$	$VBF - like$	$VH - hadronic - like$	$VH - leptonic - like$
ggF	134.4	12.4	4.2	0.2
VBF	6.0	8.0	0.4	0.012
WH	1.2	0.6	1.2	0.9
ZH	1.7	0.4	0.9	0.4
ttH	0.04	1.3	0.3	0.06
Background	131.6	3.3	1.8	0.3

Figure 7.8: The distributions of the p_T vs η for the muons forming $H \rightarrow ZZ^{(*)} \rightarrow 4\mu$ candidates for the ggF (a), VBF (b), WH (c), ZH (d), ttH (e) and $ZZ^{(*)}$ background (f) samples. The muons in the high η region tend to populate in low p_T region.

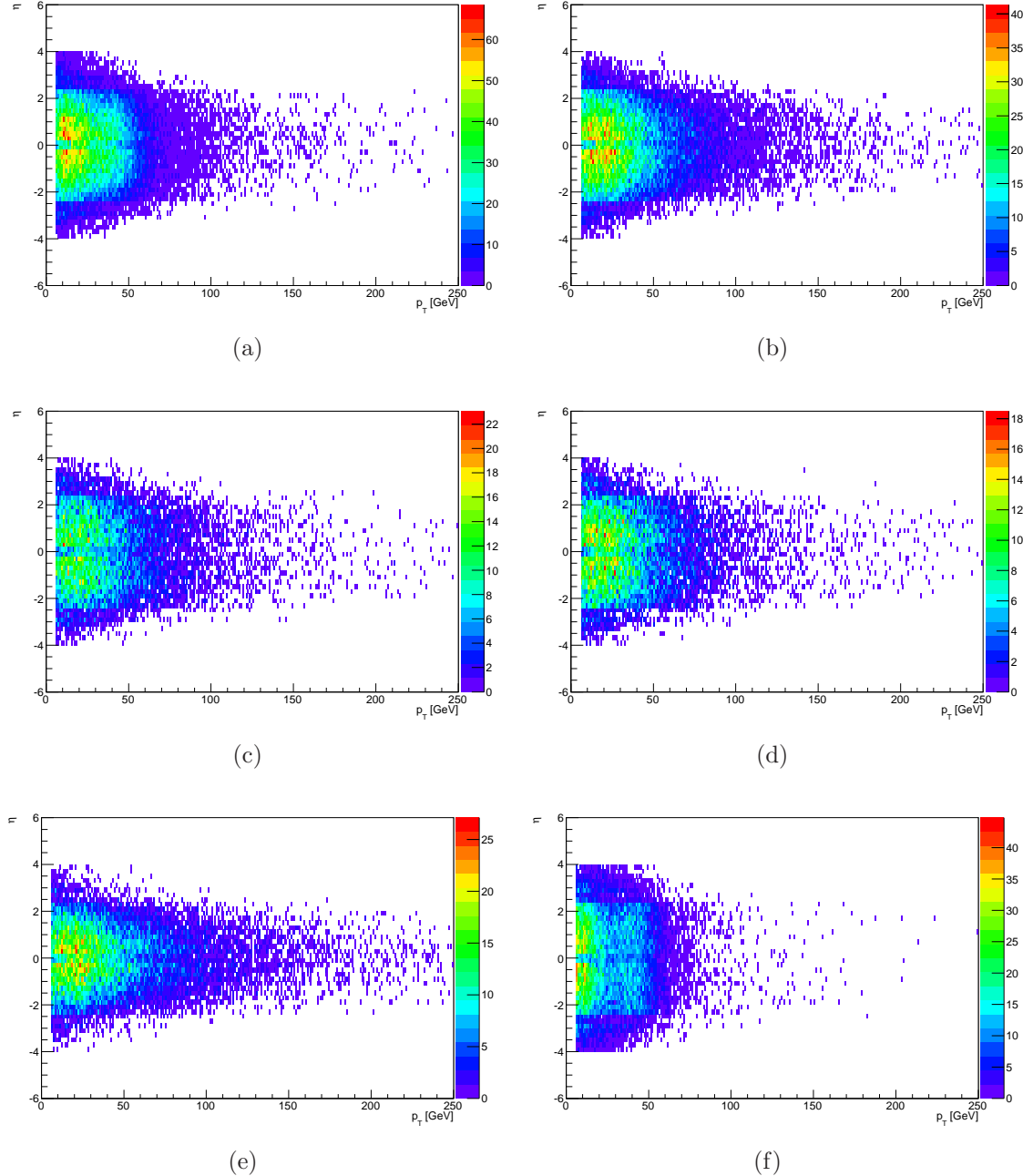
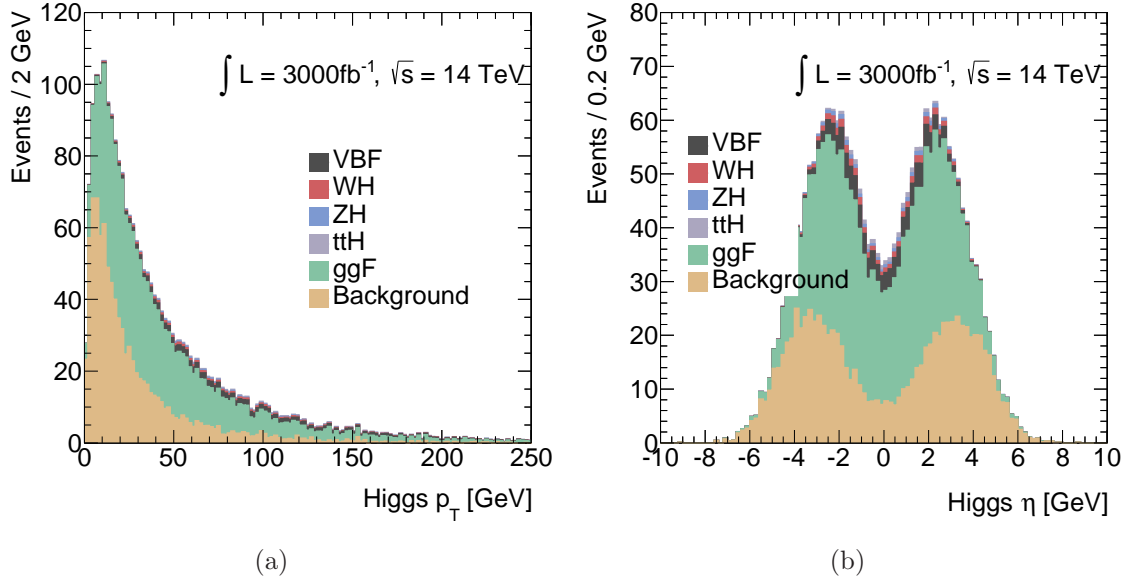


Figure 7.9: The p_T (a) and η (b) distributions of the $H \rightarrow ZZ^{(*)} \rightarrow 4\mu$ candidates. The maximum allowed muons η is the 4.0.



7.11 Summary

The $H \rightarrow ZZ^{(*)} \rightarrow 4\ell$ decay mode presented for the 3000 fb^{-1} at the HL-LHC and for a sample of 300 fb^{-1} that would be accumulated before the Phase-II upgrades at $\sqrt{s} = 14 \text{ TeV}$. The result is compared to the Run-I projections, to verify the validity of the parametrizations, and is found to be in agreement given the different pile-up conditions. At high luminosities, the precision of the channels can be improved and the couplings accuracy will be significant as Tables 7.7 and 7.8 report for 3000 and 300 fb^{-1} respectively. Even rare production such as the ttH will be possible to be measured.

The scenario of the extended muons acceptance coverage with new inner detector sectors, muon spectrometer chambers and magnets in the η region between 2.7 and 4.0 is explored. The 4μ final state is affected the most and the estimated gain is not negligible. However, the study of the properties of the Higgs boson may not benefit because of the background increase.

Projections are made for Run-II based on the Run-I due to lack of fully simulated events. The pile up is expected to be higher compared to the Run-I and lower compared to the Run-II, however the allowed fake rate will be closer to the Run-I. The projections do not include estimations of the bbH and ttH productions because of their negligible production in the Run-I [3].

Table 7.7: Expected uncertainties on the signal strength, with 3000 fb^{-1} of data at peak instantaneous luminosity $5 \times 10^{34} \text{ cm}^{-2} \text{s}^{-1}$, for the various Higgs production mechanisms and their combination.

Production Mode	μ (over all error)	μ (stat error)	μ (exp syst error)	μ (theory error)
ggF	0.128	0.025	0.027	0.124
VBF	0.370	0.187	0.223	0.226
WH	0.389	0.375	0.053	0.085
ZH	0.531	0.526	0.024	0.073
$t\bar{t}H$	0.222	0.184	0.016	0.120
Combined	0.095	0.016	0.019	0.093

Table 7.8: Expected uncertainties on the signal strength, with 300 fb^{-1} of data at peak instantaneous luminosity $2 \times 10^{34} \text{ cm}^{-2} \text{s}^{-1}$, for the various Higgs production mechanisms and their combination.

Production Mode	μ (over all error)	μ (stats error)	μ (syst error)	μ (theory error)
ggF	0.149	0.066	0.044	0.124
VBF	0.624	0.545	0.231	0.226
WH	1.074	1.064	0.053	0.085
$t\bar{t}H$	0.534	0.516	0.023	0.120
Combined	0.121	0.042	0.032	0.108

4360 Chapter Bibliography

4361 [1] Projections for measurements of Higgs boson cross sections, branching ratios and
4362 coupling parameters with the ATLAS detector at a HL-LHC, Technical Report
4363 ATL-PHYS-PUB-2013-014, CERN, Geneva, Oct 2013.

4364 [2] Performance assumptions based on full simulation for an upgraded ATLAS detector
4365 at a High-Luminosity LHC, Technical Report ATL-PHYS-PUB-2013-009, CERN,
4366 Geneva, Sep 2013.

4367 [3] S. Dittmaier, S. Dittmaier, C. Mariotti, G. Passarino, R. Tanaka, et al., Handbook
4368 of LHC Higgs Cross Sections: 2. Differential Distributions, 2012, 1201.3084.

4369 [4] S. Dittmaier, S. Dittmaier, C. Mariotti, G. Passarino, R. Tanaka, et al., Handbook
4370 of LHC Higgs Cross Sections: 2. Differential Distributions, 2012, 1201.3084.

4371 [5] Measurements of the properties of the Higgs-like boson in the four lepton decay
4372 channel with the ATLAS detector using 25 fb⁻¹ of proton-proton collision data,
4373 2013.

Appendices

A

4375

4376

RunI MC Samples List

4377 The MC samples used for the $H \rightarrow ZZ^{(*)} \rightarrow 4\ell$ RunI analysis are summarized
4378 below.

4379 A.0.1 Signal Samples

4380 A.0.1.1 ggF with No tau Decays

4381 These samples are used for the m4l models.

4382 e.g. mc12_8TeV.167895.PowhegPythia8_AU2CT10_ggH120.ZZ4lep_noTau.merge.NTUP_HSG2.e2220_s1771_s1741_r4829_r4540_p1344/

Generators	PDFs	Generator tune	
Powheg+Pythia8+Photospp	CT10	AUET2	CT10

Table A.1: Signal MC ggF with no tau decays.

MC ID	Mass (GeV)	Tags
167895	120	e2220_s1771_s1741_r4829_r4540_p1344
181330	121	e2113_s1771_s1741_r4829_r4540_p1344
181331	122	e2113_s1771_s1741_r4829_r4540_p1344
167890	123	e1622_s1771_s1741_r4829_r4540_p1344
181332	123.5	e2099_s1771_s1741_r4829_r4540_p1344
167891	124	e1622_s1771_s1741_r4829_r4540_p1344
181333	124.5	e2099_s1771_s1741_r4829_r4540_p1344
167892	125	e1622_s1771_s1741_r4829_r4540_p1344
181334	125.5	e2099_s1771_s1741_r4829_r4540_p1344
167893	126	e1622_s1771_s1741_r4829_r4540_p1344
167894	127	e1622_s1771_s1741_r4829_r4540_p1344
181335	128	e2113_s1771_s1741_r4829_r4540_p1344
181336	129	e2113_s1771_s1741_r4829_r4540_p1344
167896	130	e2220_s1771_s1741_r4829_r4540_p1344

⁴³⁸³ **A.0.1.2 ggF with tau decays**

⁴³⁸⁴ e.g. mc12_8TeV.160152.PowhegPythia8_AU2CT10_ggH110_ZZ4lep.merge.NTUP_HSG2.e1191_s1771_s1741_r4829_r4540_p1344/

Generators	PDFs	Generator tune	
Powheg+Pythia8+Photospp	CT10	AUET2	CT10

Table A.2: Signal MC ggF with tau decays.

MC ID	Mass (GeV)	Tags
160152	110	e1191_s1771_s1741_r4829_r4540_p1344
160153	115	e1191_s1771_s1741_r4829_r4540_p1344
160154	120	e1191_s1771_s1741_r4829_r4540_p1344
167220	123	e1437_s1771_s1741_r4829_r4540_p1344
167222	124	e1437_s1771_s1741_r4829_r4540_p1344
160155	125	e1191_s1771_s1741_r4829_r4540_p1344
167225	126	e1437_s1771_s1741_r4829_r4540_p1344
167227	127	e1437_s1771_s1741_r4829_r4540_p1344
160156	130	e1191_s1771_s1741_r4829_r4540_p1344
160157	135	e1191_s1771_s1741_r4829_r4540_p1344
160158	140	e1191_s1771_s1741_r4829_r4540_p1344
160159	145	e1191_s1771_s1741_r4829_r4540_p1344
160160	150	e1191_s1771_s1741_r4829_r4540_p1344
160161	155	e1191_s1771_s1741_r4829_r4540_p1344
160162	160	e1191_s1771_s1741_r4829_r4540_p1344
160163	165	e1191_s1771_s1741_r4829_r4540_p1344
160164	170	e1191_s1771_s1741_r4829_r4540_p1344
160165	175	e1191_s1771_s1741_r4829_r4540_p1344
160166	180	e1191_s1771_s1741_r4829_r4540_p1344
160167	185	e1191_s1771_s1741_r4829_r4540_p1344
160168	190	e1191_s1771_s1741_r4829_r4540_p1344
160169	195	e1191_s1771_s1741_r4829_r4540_p1344
160170	200	e1191_s1771_s1741_r4829_r4540_p1344
160171	220	e1191_s1771_s1741_r4829_r4540_p1344
160172	240	e1191_s1771_s1741_r4829_r4540_p1344
160173	260	e1191_s1771_s1741_r4829_r4540_p1344
160174	280	e1191_s1771_s1741_r4829_r4540_p1344
160175	300	e1191_s1771_s1741_r4829_r4540_p1344
160176	320	e1191_s1771_s1741_r4829_r4540_p1344
160177	340	e1191_s1771_s1741_r4829_r4540_p1344
160178	360	e1191_s1771_s1741_r4829_r4540_p1344
160179	380	e1191_s1771_s1741_r4829_r4540_p1344

4385 **A.0.1.3 VBF with no tau decays**

4386 These samples are not merged with the including-tau ones. They are used for the m4l
 4387 models. e.g. mc12_8TeV.167995.PowhegPythia8_AU2CT10_VBFH120_ZZ4lep_noTau.merge.NTUP_HSG2.e2464_s1831_s1741_r4829_r4540_

Generators	PDFs	Generator tune	
Powheg+Pythia8+Photospp	CT10	AUET2	CT10

Table A.3: Signal MC VBF with no tau decays.

MC ID	Mass (GeV)	Tags
167995	120	e2464_s1831_s1741_r4829_r4540_p1344
181337	121	e2113_s1831_s1741_r4829_r4540_p1344
181338	122	e2113_s1831_s1741_r4829_r4540_p1344
167990	123	e1890_s1771_s1741_r4829_r4540_p1344
181339	123.5	e2099_s1771_s1741_r4829_r4540_p1344
167991	124	e1890_s1771_s1741_r4829_r4540_p1344
181340	124.5	e2099_s1771_s1741_r4829_r4540_p1344
167992	125	e1890_s1771_s1741_r4829_r4540_p1344
181341	125.5	e2099_s1771_s1741_r4829_r4540_p1344
167993	126	e1890_s1771_s1741_r4829_r4540_p1344
167994	127	e1890_s1771_s1741_r4829_r4540_p1344
181342	128	e2113_s1831_s1741_r4829_r4540_p1344
181343	129	e2113_s1771_s1741_r4829_r4540_p1344
167996	130	e2464_s1831_s1741_r4829_r4540_p1344

4388 **A.0.1.4 VBF with tau decays**

4389 e.g. mc12_8TeV.160202.PowhegPythia8_AU2CT10_VBFH110_ZZ4lep.merge.NTUP_HSG2.e1195_s1771_s1741_r4829_r4540_p1344/

Generators	PDFs	Generator tune	
Powheg+Pythia8+Photospp	CT10	AUET2	CT10

Table A.4: Signal MC VBF with tau decays.

MC ID	Mass (GeV)	Tags
160202	110	e1195_s1771_s1741_r4829_r4540_p1344
160203	115	e1195_s1771_s1741_r4829_r4540_p1344
160204	120	e1195_s1771_s1741_r4829_r4540_p1344
167230	123	e1437_s1771_s1741_r4829_r4540_p1344
167232	124	e1437_s1771_s1741_r4829_r4540_p1344
160205	125	e1195_s1771_s1741_r4829_r4540_p1344
167235	126	e1437_s1771_s1741_r4829_r4540_p1344
167237	127	e1437_s1771_s1741_r4829_r4540_p1344
160206	130	e1195_s1771_s1741_r4829_r4540_p1344
160207	135	e1195_s1771_s1741_r4829_r4540_p1344
160208	140	e1195_s1771_s1741_r4829_r4540_p1344
160209	145	e1195_s1771_s1741_r4829_r4540_p1344
160210	150	e1195_s1771_s1741_r4829_r4540_p1344
160211	155	e1195_s1771_s1741_r4829_r4540_p1344
160212	160	e1195_s1771_s1741_r4829_r4540_p1344
160213	165	e1195_s1771_s1741_r4829_r4540_p1344
160214	170	e1195_s1771_s1741_r4829_r4540_p1344
160215	175	e1195_s1771_s1741_r4829_r4540_p1344
160216	180	e1195_s1771_s1741_r4829_r4540_p1344
160217	185	e1195_s1771_s1741_r4829_r4540_p1344
160218	190	e1195_s1771_s1741_r4829_r4540_p1344
160219	195	e1195_s1771_s1741_r4829_r4540_p1344
160220	200	e1195_s1771_s1741_r4829_r4540_p1344
160221	220	e1195_s1771_s1741_r4829_r4540_p1344
160222	240	e1195_s1771_s1741_r4829_r4540_p1344
160223	260	e1195_s1771_s1741_r4829_r4540_p1344
160224	280	e1195_s1771_s1741_r4829_r4540_p1344
160225	300	e1195_s1771_s1741_r4829_r4540_p1344
160226	320	e1195_s1771_s1741_r4829_r4540_p1344
160227	340	e1195_s1771_s1741_r4829_r4540_p1344
160228	360	e1195_s1771_s1741_r4829_r4540_p1344
160229	380	e1195_s1771_s1741_r4829_r4540_p1344

4390 A.0.1.5 WH

4391 e.g. mc12_8TeV.160250.Pythia8_AU2CTEQ6L1_WH100_ZZ4lep.merge.NTUP_HSG2.e1419_s1771_s1741_r4829_r4540_p1344/

Generators		PDFs		Generator tune	
Pythia8+Photospp	CTEQ6L1	LO, LO	a_s	AUET2	CTEQ6L1
MC ID		Mass		Tags	
		(GeV)			
160250	100	e1419_s1771_s1741_r4829_r4540_p1344			
160251	105	e1419_s1771_s1741_r4829_r4540_p1344			
160252	110	e1419_s1771_s1741_r4829_r4540_p1344			
160253	115	e1419_s1771_s1741_r4829_r4540_p1344			
160254	120	e1419_s1771_s1741_r4829_r4540_p1344			
167240	123	e1436_s1771_s1741_r4829_r4540_p1344			
167242	124	e1436_s1771_s1741_r4829_r4540_p1344			
160255	125	e1419_s1771_s1741_r4829_r4540_p1344			
167245	126	e1436_s1771_s1741_r4829_r4540_p1344			
167247	127	e1436_s1771_s1741_r4829_r4540_p1344			
160256	130	e1419_s1771_s1741_r4829_r4540_p1344			
160257	135	e1419_s1771_s1741_r4829_r4540_p1344			
160258	140	e1419_s1771_s1741_r4829_r4540_p1344			
160259	145	e1419_s1771_s1741_r4829_r4540_p1344			
160260	150	e1419_s1771_s1741_r4829_r4540_p1344			
160261	155	e1419_s1771_s1741_r4829_r4540_p1344			
160262	160	e1419_s1771_s1741_r4829_r4540_p1344			
160263	165	e1419_s1771_s1741_r4829_r4540_p1344			
160264	170	e1419_s1771_s1741_r4829_r4540_p1344			
160265	175	e1419_s1771_s1741_r4829_r4540_p1344			
160266	180	e1419_s1771_s1741_r4829_r4540_p1344			
160267	185	e1419_s1771_s1741_r4829_r4540_p1344			
160268	190	e1419_s1771_s1741_r4829_r4540_p1344			
160269	195	e1419_s1771_s1741_r4829_r4540_p1344			
160270	200	e1419_s1771_s1741_r4829_r4540_p1344			
160271	220	e1419_s1771_s1741_r4829_r4540_p1344			
160272	240	e1419_s1771_s1741_r4829_r4540_p1344			
160273	260	e1419_s1771_s1741_r4829_r4540_p1344			
160274	280	e1419_s1771_s1741_r4829_r4540_p1344			
160275	300	e1419_s1771_s1741_r4829_r4540_p1344			
160276	320	e1419_s1771_s1741_r4829_r4540_p1344			
160277	340	e1419_s1771_s1741_r4829_r4540_p1344			
160278	360	e1419_s1771_s1741_r4829_r4540_p1344			
160279	380	e1419_s1771_s1741_r4829_r4540_p1344			
160280	400	e1191_s1771_s1741_r4829_r4540_p1344			

4392 A.0.1.6 ZH

4393 e.g. mc12_8TeV.160300.Pythia8_AU2CTEQ6L1_ZH100_ZZ4lep.merge.NTUP_HSG2.e1217_s1771_s1741_r4829_r4540_p1344/

Generators	PDFs	Generator tune
Pythia8+Photospp	CTEQ6L1 LO, LO a_s	AUET2 CTEQ6L1

MC ID	Mass (GeV)	Tags
160300	100	e1217_s1771_s1741_r4829_r4540_p1344
160301	105	e1217_s1771_s1741_r4829_r4540_p1344
160302	110	e1217_s1771_s1741_r4829_r4540_p1344
160303	115	e1217_s1771_s1741_r4829_r4540_p1344
160304	120	e1217_s1771_s1741_r4829_r4540_p1344
167250	123	e1436_s1771_s1741_r4829_r4540_p1344
167252	124	e1436_s1771_s1741_r4829_r4540_p1344
160305	125	e1217_s1771_s1741_r4829_r4540_p1344
167255	126	e1436_s1771_s1741_r4829_r4540_p1344
167257	127	e1436_s1771_s1741_r4829_r4540_p1344
160306	130	e1217_s1771_s1741_r4829_r4540_p1344
160307	135	e1217_s1771_s1741_r4829_r4540_p1344
160308	140	e1217_s1771_s1741_r4829_r4540_p1344
160309	145	e1217_s1771_s1741_r4829_r4540_p1344
160310	150	e1217_s1771_s1741_r4829_r4540_p1344
160311	155	e1217_s1771_s1741_r4829_r4540_p1344
160312	160	e1217_s1771_s1741_r4829_r4540_p1344
160313	165	e1217_s1771_s1741_r4829_r4540_p1344
160314	170	e1217_s1771_s1741_r4829_r4540_p1344
160315	175	e1217_s1771_s1741_r4829_r4540_p1344
160316	180	e1217_s1771_s1741_r4829_r4540_p1344
160317	185	e1217_s1771_s1741_r4829_r4540_p1344
160318	190	e1217_s1771_s1741_r4829_r4540_p1344
160319	195	e1217_s1771_s1741_r4829_r4540_p1344
160320	200	e1217_s1771_s1741_r4829_r4540_p1344
160321	220	e1217_s1771_s1741_r4829_r4540_p1344
160322	240	e1217_s1771_s1741_r4829_r4540_p1344
160323	260	e1217_s1771_s1741_r4829_r4540_p1344
160324	280	e1217_s1771_s1741_r4829_r4540_p1344
160325	300	e1217_s1771_s1741_r4829_r4540_p1344
160326	320	e1217_s1771_s1741_r4829_r4540_p1344
160327	340	e1217_s1771_s1741_r4829_r4540_p1344
160328	360	e1217_s1771_s1741_r4829_r4540_p1344
160329	380	e1217_s1771_s1741_r4829_r4540_p1344
160330	400	e1217_s1771_s1741_r4829_r4540_p1344

4394 **A.0.2 ZZ background samples**

4395 **A.0.2.1 ZZ Full Mass**

4396 e.g. mc12_8TeV.126937.PowhegPythia8_AU2CT10_ZZ_4e_mll4_2pt5.merge.NTUP_HSG2.e1280_s1771_s1741_r4829_r4540_p1344/

Generators	PDFs	Generator tune
Powheg+Pythia8+Photospp	CT10	AUET2 CT10

Table A.5: ZZ Full Mass.

MC ID	final state	Tags
126937	4e	e1280_s1771_s1741_r4829_r4540_p1344
126938	2e2 μ	e1280_s1771_s1741_r4829_r4540_p1344
126939	2e2 τ	e2372_s1771_s1741_r4829_r4540_p1344
126940	4 μ	e1280_s1771_s1741_r4829_r4540_p1344
126941	2 μ 2 τ	e2372_s1771_s1741_r4829_r4540_p1344
126942	4 τ	e2372_s1771_s1741_r4829_r4540_p1344

4397 **A.0.2.2 ZZ Filter 100-150 GeV**

4398 e.g. mc12_8TeV.167162.PowhegPythia8_AU2CT10_ZZ_4e_m4l100_150_mll4_4pt3.merge.NTUP_HSG2.e1486_s1771_s1741_r4829_r4540
4399 -p1344/

Generators	PDFs	Generator tune
Powheg+Pythia8+Photospp	CT10	AUET2 CT10

4400 **A.0.2.3 ZZ Filter 500-50000 GeV**

4401 e.g. mc12_8TeV.169690.PowhegPythia8_AU2CT10_ZZ_4e_m4l500_50000_mll4_4pt3.merge.NTUP_HSG2.e1776_s1771_s1741_r4829_r4540
4402 -p1344/

4403 **A.0.2.4 gg2ZZ**

4404 e.g. mc12_8TeV.116601.gg2ZZJimmy_AUET2CT10_ZZ4e.merge.NTUP_HSG2.e1525_s1771_s1741_r4829_r4540_p1344/

4405 **A.0.2.5 qq2ZZ Inclusive**

4406 e.g. mc12_8TeV.161988.Sherpa_CT10_llll_ZZ_EW6_noHiggs.merge.NTUP_HSG2.e1434_s1771_s1741_r4829_r4540_p1344/

Table A.6: ZZ Filter $100 - 150 \text{ GeV}$.

MC ID	final state	Tags
167162	$4e$	e1486_s1771_s1741_r4829_r4540_p1344
167163	$2e2\mu$	e1486_s1771_s1741_r4829_r4540_p1344
167164	$2e2\tau$	e2372_s1771_s1741_r4829_r4540_p1344
167165	4μ	e1486_s1771_s1741_r4829_r4540_p1344
167166	$2\mu2\tau$	e2372_s1771_s1741_r4829_r4540_p1344
167167	4τ	e2372_s1771_s1741_r4829_r4540_p1344

Generators	PDFs	Generator tune
Powheg+Pythia8+Photospp	CT10	AUET2 CT10

Table A.7: ZZ Filter $500 - 50000 \text{ GeV}$.

MC ID	final state	Tags
169690	$4e$	e1776_s1771_s1741_r4829_r4540_p1344
169691	$2e2\mu$	e1776_s1771_s1741_r4829_r4540_p1344
169692	4μ	e1776_s1771_s1741_r4829_r4540_p1344

Generators	PDFs	Generator tune
McAtNlo+Herwig+Photos+Tauola	CT10	AUET2 CT10

MC ID	final state	Tags
116601	$4e$	e1525_s1771_s1741_r4829_r4540_p1344
116602	4μ	e1525_s1771_s1741_r4829_r4540_p1344
116603	$2e2\mu$	e1525_s1771_s1741_r4829_r4540_p1344

Generators	PDFs	Generator tune
Sherpa	CT10	CT10

A.0.2.6 Single Z

4407 e.g. mc12_8TeV.147563.PowhegPythia8_AU2CT10_ZZ_4e_mll1_4lpt3_m4l40.merge.NTUP_HSG2.e2111_s1831_s1741_r4829_r4540_p1344/

4408

Generators	PDFs	Generator tune
Powheg+Pythia8+Photospp	CT10	AUET2 CT10

MC ID	final state	Tags
147563	4e	e2111_s1831_s1741_r4829_r4540_p1344
147565	4mu	e2111_s1831_s1741_r4829_r4540_p1344
147564	2e2mu	e2111_s1831_s1741_r4829_r4540_p1344

4409 A.0.3 Reducible Background Samples

4410 A.0.3.1 $t\bar{t}$

4411 mc12_8TeV.181087.PowhegPythia_P2011C_ttbar_dilepton.merge.NTUP_HSG2.e2091_a188_a205_r4540_p1344/

Generators	PDFs	Generator tune
Powheg+Pythia+Photos+Tauola	CTEQ6L1 LO, LO a_s	Perugia2011C

4412 A.0.3.2 $Z+jets$ (light jets), $m_{\ell\ell} > 60\,GeV$

4413 e.g. mc12_8TeV.117650.AlpgenPythia_P2011C_ZeeNp0.merge.NTUP_HSG2.e1477_s1499_s1504_r3658_r3549_p1344/

Generators	PDFs	Generator tune
Alpgen+Pythia+Photos	CTEQ6L1 LO, LO a_s	Perugia2011C

MC ID	Process	Tags
117650	Zee , Np0	e1477_s1499_s1504.r3658_r3549_p1344
117651	Zee , Np1	e1477_s1499_s1504.r3658_r3549_p1344
117652	Zee , Np2	e1477_s1499_s1504.r3658_r3549_p1344
117653	Zee , Np3	e1477_s1499_s1504.r3658_r3549_p1344
117654	Zee , Np4	e1477_s1499_s1504.r3658_r3549_p1344
117655	Zee , Np5	e1477_s1499_s1504.r3658_r3549_p1344
117660	$Z\mu\mu$, Np0	e1477_s1499_s1504.r3658_r3549_p1344
117661	$Z\mu\mu$, Np1	e1477_s1499_s1504.r3658_r3549_p1344
117662	$Z\mu\mu$, Np2	e1477_s1499_s1504.r3658_r3549_p1344
117663	$Z\mu\mu$, Np3	e1477_s1499_s1504.r3658_r3549_p1344
117664	$Z\mu\mu$, Np4	e1477_s1499_s1504.r3658_r3549_p1344
117665	$Z\mu\mu$, Np5	e1477_s1499_s1504.r3658_r3549_p1344
117670	$Z\tau\tau$, Np0	e1711_s1581_s1586.r3658_r3549_p1344
117671	$Z\tau\tau$, Np1	e1711_s1581_s1586.r3658_r3549_p1344
117672	$Z\tau\tau$, Np2	e1711_s1581_s1586.r3658_r3549_p1344
117673	$Z\tau\tau$, Np3	e1711_s1581_s1586.r3658_r3549_p1344
117674	$Z\tau\tau$, Np4	e1711_s1581_s1586.r3658_r3549_p1344
117675	$Z\tau\tau$, Np5	e1711_s1581_s1586.r3658_r3549_p1344
147105	Zee , Np0	e1879_s1581_s1586.r3658_r3549_p1344
147106	Zee , Np1	e1879_s1581_s1586.r3658_r3549_p1344
147107	Zee , Np2	e1879_s1581_s1586.r3658_r3549_p1344
147108	Zee , Np3	e1879_s1581_s1586.r3658_r3549_p1344
147109	Zee , Np4	e1879_s1581_s1586.r3658_r3549_p1344
147110	Zee , Np5incl	e1879_s1581_s1586.r3658_r3549_p1344
147113	$Z\mu\mu$, Np0	e1880_s1581_s1586.r3658_r3549_p1344
147114	$Z\mu\mu$, Np1	e1880_s1581_s1586.r3658_r3549_p1344
147115	$Z\mu\mu$, Np2	e1880_s1581_s1586.r3658_r3549_p1344
147116	$Z\mu\mu$, Np3	e1880_s1581_s1586.r3658_r3549_p1344
147117	$Z\mu\mu$, Np4	e1880_s1581_s1586.r3658_r3549_p1344
147118	$Z\mu\mu$, Np5incl	e1880_s1581_s1586.r3658_r3549_p1344
147121	$Z\tau\tau$, Np0	e1881_s1581_s1586.r3658_r3549_p1344
147122	$Z\tau\tau$, Np1	e1881_s1581_s1586.r3658_r3549_p1344
147123	$Z\tau\tau$, Np2	e1881_s1581_s1586.r3658_r3549_p1344
147124	$Z\tau\tau$, Np3	e1881_s1581_s1586.r3658_r3549_p1344
147125	$Z\tau\tau$, Np4	e1881_s1581_s1586.r3658_r3549_p1344
147126	$Z\tau\tau$, Np5incl	e1881_s1581_s1586.r3658_r3549_p1344

⁴⁴¹⁴ **A.0.3.3 $Z+jets$, $10 \text{ GeV} < m_{\ell\ell} < 40 \text{ GeV}$**

⁴⁴¹⁵ e.g. mc12_8TeV.178354.AlpgenPythia.P2011C_ZeeNp0Excl_Mll10to40_2LeptonFilter5.merge.NTUP_HSG2.e2373_s1581_s1586_r4485
⁴⁴¹⁶ _r4540_p1344/

Generators	PDFs	Generator tune
Alpgen+Pythia+Photos+Tauola	CTEQ6L1 LO, LO a_s	Perugia2011C

Table A.8: $Z+jets$ samples, $10 \text{ GeV} < m_{\ell\ell} < 40 \text{ GeV}$.

MC ID	Process	Tags
178354	Zee , Np0	e2373_s1581_s1586_r4485_r4540_p1344
178355	Zee , Np1	e2371_s1581_s1586_r4485_r4540_p1344
178356	Zee , Np2	e2371_s1581_s1586_r4485_r4540_p1344
178357	Zee , Np3	e2371_s1581_s1586_r4485_r4540_p1344
178358	Zee , Np4	e2371_s1581_s1586_r4485_r4540_p1344
178359	$Z\mu\mu$, Np0	e2373_s1581_s1586_r4485_r4540_p1344
178360	$Z\mu\mu$, Np1	e2371_s1581_s1586_r4485_r4540_p1344
178361	$Z\mu\mu$, Np2	e2371_s1581_s1586_r4485_r4540_p1344
178362	$Z\mu\mu$, Np3	e2371_s1581_s1586_r4485_r4540_p1344
178363	$Z\mu\mu$, Np4	e2371_s1581_s1586_r4485_r4540_p1344
178364	$Z\tau\tau$, Np0	e2373_s1581_s1586_r4485_r4540_p1344
178365	$Z\tau\tau$, Np1	e2371_s1581_s1586_r4485_r4540_p1344
178366	$Z\tau\tau$, Np2	e2371_s1581_s1586_r4485_r4540_p1344
178367	$Z\tau\tau$, Np3	e2371_s1581_s1586_r4485_r4540_p1344
178368	$Z\tau\tau$, Np4	e2371_s1581_s1586_r4485_r4540_p1344

⁴⁴¹⁷ **A.0.3.4 $Z+jets$, $40 \text{ GeV} < m_{\ell\ell} < 60 \text{ GeV}$**

⁴⁴¹⁸ e.g. mc12_8TeV.178369.AlpgenPythia.P2011C_ZeeNp0Excl_Mll40to60_2LeptonFilter5.merge.NTUP_HSG2.e2373_s1581_s1586_r4485_r454

Generators	PDFs	Generator tune
Alpgen+Pythia+Photos+Tauola	CTEQ6L1 LO, LO a_s	Perugia2011C

Table A.9: Z +jets samples, $40 \text{ GeV} < m_{\ell\ell} < 60 \text{ GeV}$.

MC ID	Process	Tags
178369	Zee , Np0	e2373_s1581_s1586_r4485_r4540_p1344
178370	Zee , Np1	e2371_s1581_s1586_r4485_r4540_p1344
178371	Zee , Np2	e2371_s1581_s1586_r4485_r4540_p1344
178372	Zee , Np3	e2371_s1581_s1586_r4485_r4540_p1344
178373	Zee , Np4	e2371_s1581_s1586_r4485_r4540_p1344
178374	$Z\mu\mu$, Np0	e2373_s1581_s1586_r4485_r4540_p1344
178375	$Z\mu\mu$, Np1	e2371_s1581_s1586_r4485_r4540_p1344
178376	$Z\mu\mu$, Np2	e2371_s1581_s1586_r4485_r4540_p1344
178377	$Z\mu\mu$, Np3	e2371_s1581_s1586_r4485_r4540_p1344
178378	$Z\mu\mu$, Np4	e2371_s1581_s1586_r4485_r4540_p1344
178379	$Z\tau\tau$, Np0	e2373_s1581_s1586_r4485_r4540_p1344
178380	$Z\tau\tau$, Np1	e2371_s1581_s1586_r4485_r4540_p1344
178381	$Z\tau\tau$, Np2	e2371_s1581_s1586_r4485_r4540_p1344
178382	$Z\tau\tau$, Np3	e2371_s1581_s1586_r4485_r4540_p1344
178383	$Z\tau\tau$, Np4	e2371_s1581_s1586_r4485_r4540_p1344

4419 A.0.3.5 $Z + bb$

4420 e.g. mc12_8TeV.181435.AlpgenPythia_Auto_P2011C_3lFilter_4lVeto_ZbbmmumuNp0.merge.NTUP_HSG2.e2314_s1581_s1586_r4485

4421 .r4540_p1344/

Generators	PDFs	Generator tune
Alpgen+Pythia+Photos+Tauola	CTEQ6L1 LO, LO a_s	Perugia2011C

MC ID	Filter	Process	Tags
181435	3ℓ	$Zbb\mu\mu$, Np0	e2314_s1581_s1586_r4485_r4540_p1344
181436	3ℓ	$Zbb\mu\mu$, Np1	e2314_s1581_s1586_r4485_r4540_p1344
181437	3ℓ	$Zbb\mu\mu$, Np2	e2314_s1581_s1586_r4485_r4540_p1344
181430	3ℓ	$Zbbee$, Np0	e2314_s1581_s1586_r4485_r4540_p1344
181431	3ℓ	$Zbbee$, Np1	e2314_s1581_s1586_r4485_r4540_p1344
181432	3ℓ	$Zbbee$, Np2	e2314_s1581_s1586_r4485_r4540_p1344
181425	3ℓ	$Zbb\mu\mu$, Np0	e2314_s1581_s1586_r4485_r4540_p1344
181426	3ℓ	$Zbb\mu\mu$, Np1	e2314_s1581_s1586_r4485_r4540_p1344
181427	3ℓ	$Zbb\mu\mu$, Np2	e2314_s1581_s1586_r4485_r4540_p1344
181420	3ℓ	$Zbbee$, Np0	e2314_s1581_s1586_r4485_r4540_p1344
181421	3ℓ	$Zbbee$, Np1	e2314_s1581_s1586_r4485_r4540_p1344
181422	3ℓ	$Zbbee$, Np2	e2314_s1581_s1586_r4485_r4540_p1344

4422 A.0.3.6 WZ

4423 e.g. mc12_8TeV.147194.Sherpa_CT10_lllnjj_WZjj_EW6.merge.NTUP_HSG2.e1613_s1499_s1504_r3658_r3549_p1344/

Generators	PDFs	Generator tune
Sherpa	CT10	CT10

MC ID	Process	Tags
147194	$\ell\ell\ell\nu jj$	e1613_s1499_s1504_r3658_r3549_p1344
147197	$\ell\ell\ell\nu$	e1614_s1499_s1504_r3658_r3549_p1344

B

4424

4425

HL-LHC MC Samples List

4426 The following Monte Carlo samples are used for the Higgs signal:

4427 mc12-14TeV.160155.PowhegPythia8-AU2CT10-ggH125-ZZ4lep.evgen.EVNT.e1337
4428 mc12-14TeV.160205.PowhegPythia8-AU2CT10-VBFH125-ZZ4lep.evgen.EVNT.e1337
4429 mc12-14TeV.160255.Pythia8-AU2CTEQ6L1-WH125-ZZ4lep.evgen.EVNT.e2286
4430 mc12-14TeV.160305.Pythia8-AU2CTEQ6L1-ZH125-ZZ4lep.evgen.EVNT.e1413
4431 mc12-14TeV.167562.Pythia8-AU2CTEQ6L1-ttH125-ZZ4lep.evgen.EVNT.e2211

4432 For the ZZ background a million Monte Carlo events were generated with Mad-
4433 Graph5 V1.5 showered with Pythia 8, in the mass range $100 - 150$ GeV with 4l-filter
4434 with $\eta < 2.8$ and lepton p_T thresholds of 20, 15, 10 and 6 GeV .

C

4435

4436

Test Fit Distributions

4437

The fitted CR of the fits presented in Chapter 5 are available in this appendix.

Figure C.1: The data m_{12} distributions are presented after the test fit, where the shape parameters set free to fluctuate, applied for consistency reasons. The CRs of the inverted $d_0/\sigma d_0$ (a), inverted isolation and nominal $d_0/\sigma d_0$ (b), SS (c) and $e\mu + \mu\mu$ (d) are presented. The test proves no significant deviation with the nominal results.

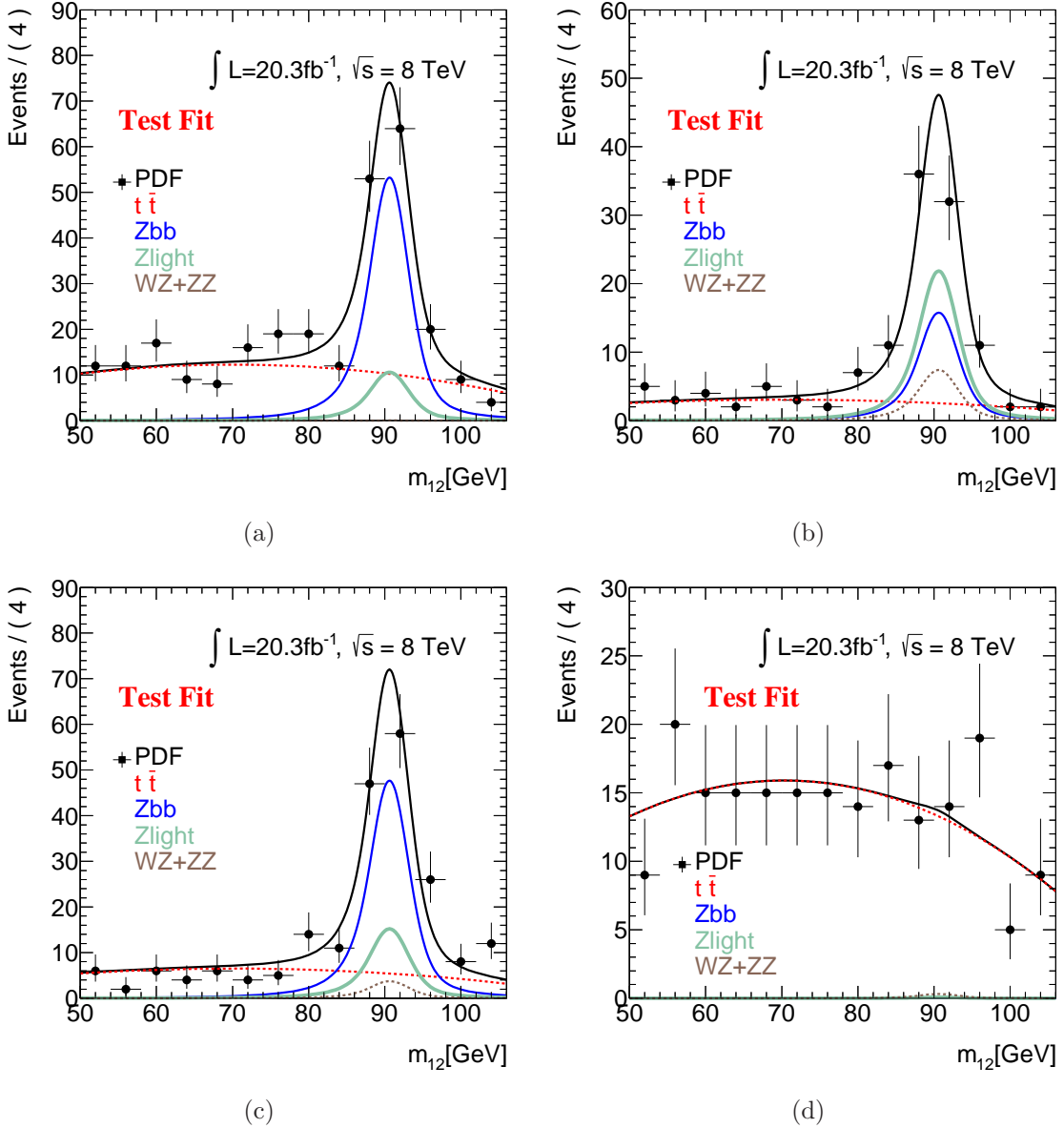


Figure C.2: The data m_{12} distributions are presented after the test fit, where the fractions uncertainties reduced to 0.1 of each value, applied for consistency reasons. The CRs of the inverted $d_0/\sigma d_0$ (a), inverted isolation and nominal $d_0/\sigma d_0$ (b), SS (c) and $e\mu + \mu\mu$ (d) are presented. The test proves no significant deviation with the nominal results.

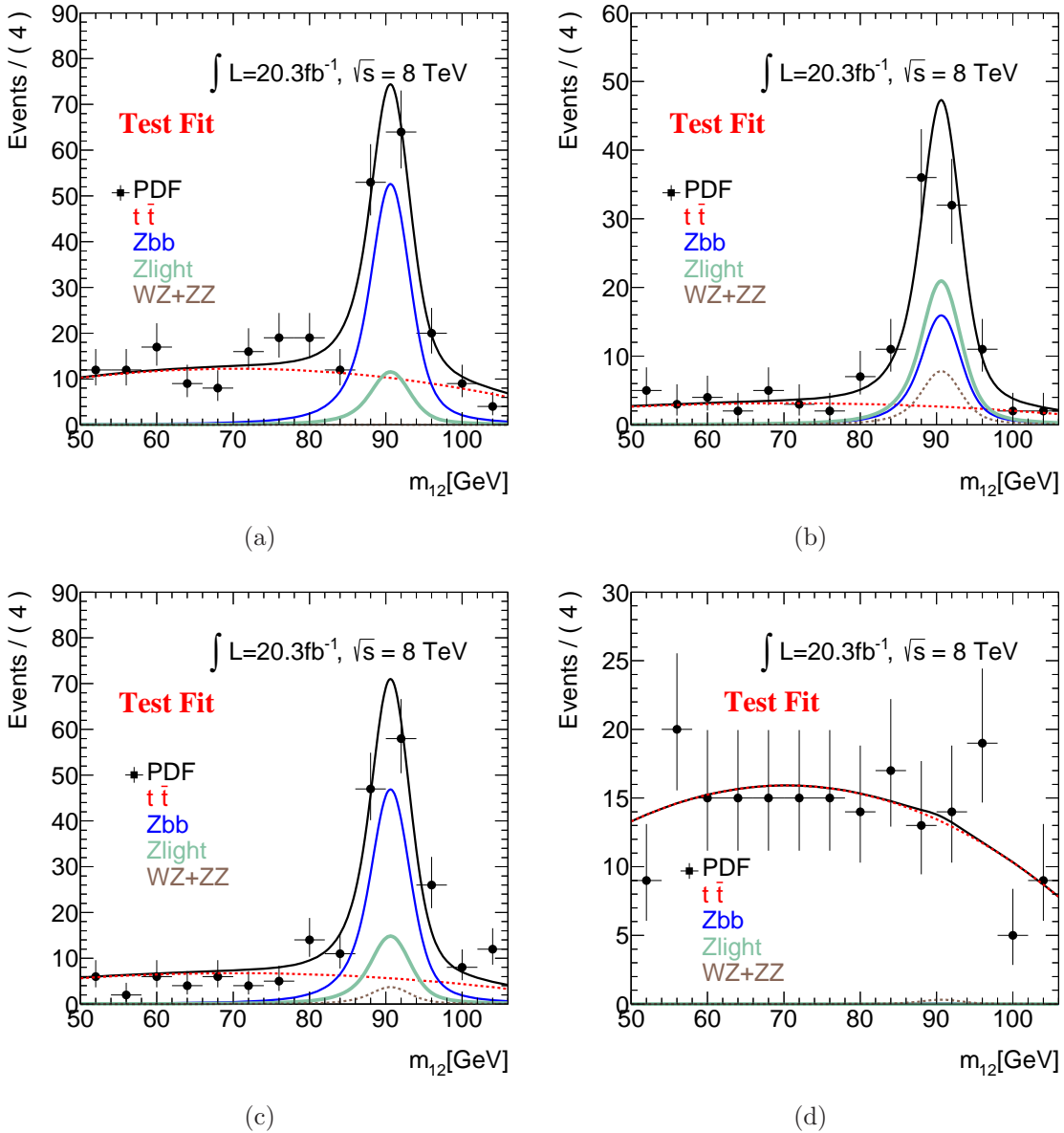


Figure C.3: The data m_{12} distributions are presented after the test fit, where the fractions uncertainties doubled, applied for consistency reasons. The CRs of the inverted $d_0/\sigma d_0$ (a), inverted isolation and nominal $d_0/\sigma d_0$ (b), SS (c) and $e\mu + \mu\mu$ (d) are presented. The test proves no significant deviation with the nominal results.

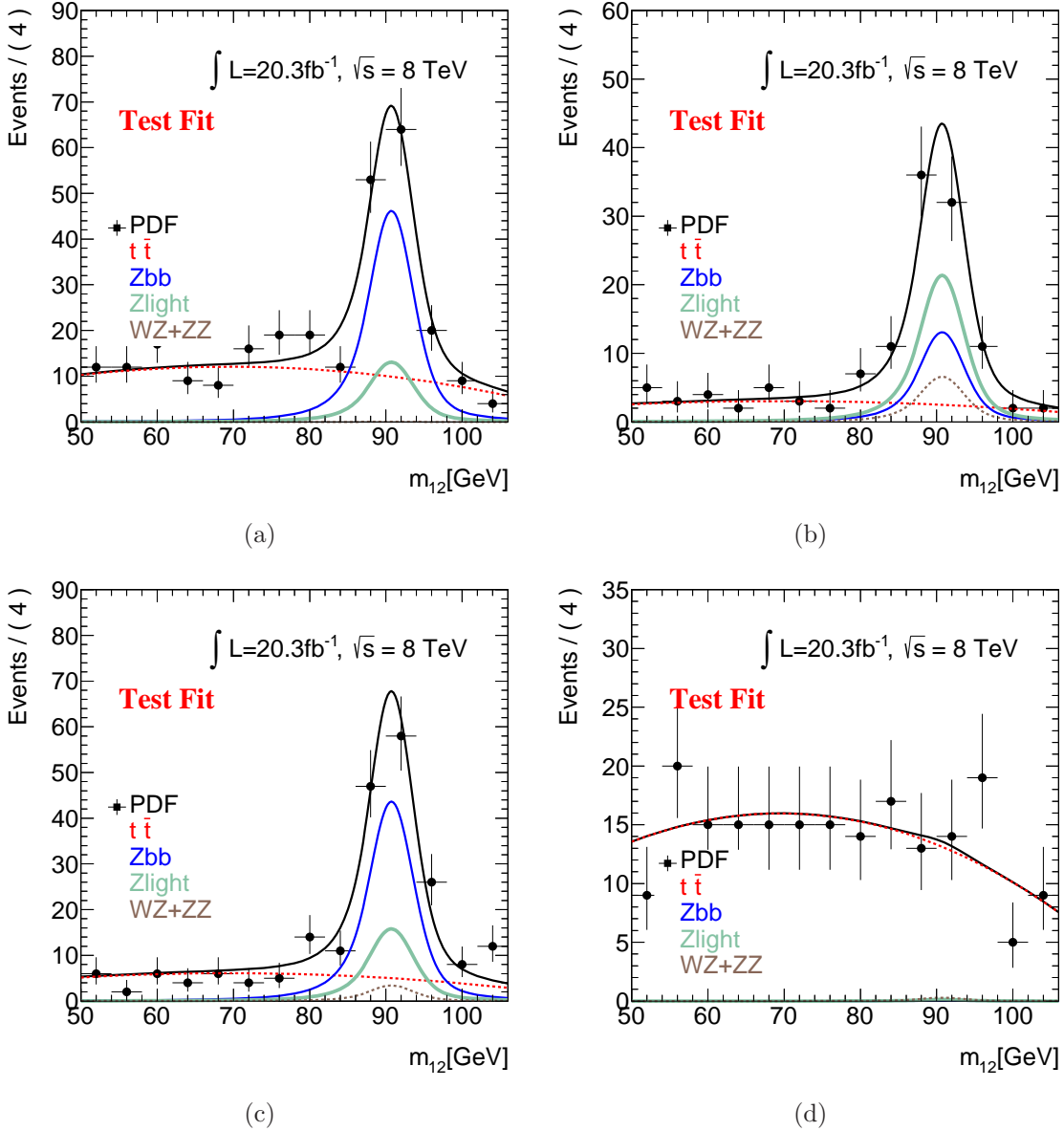
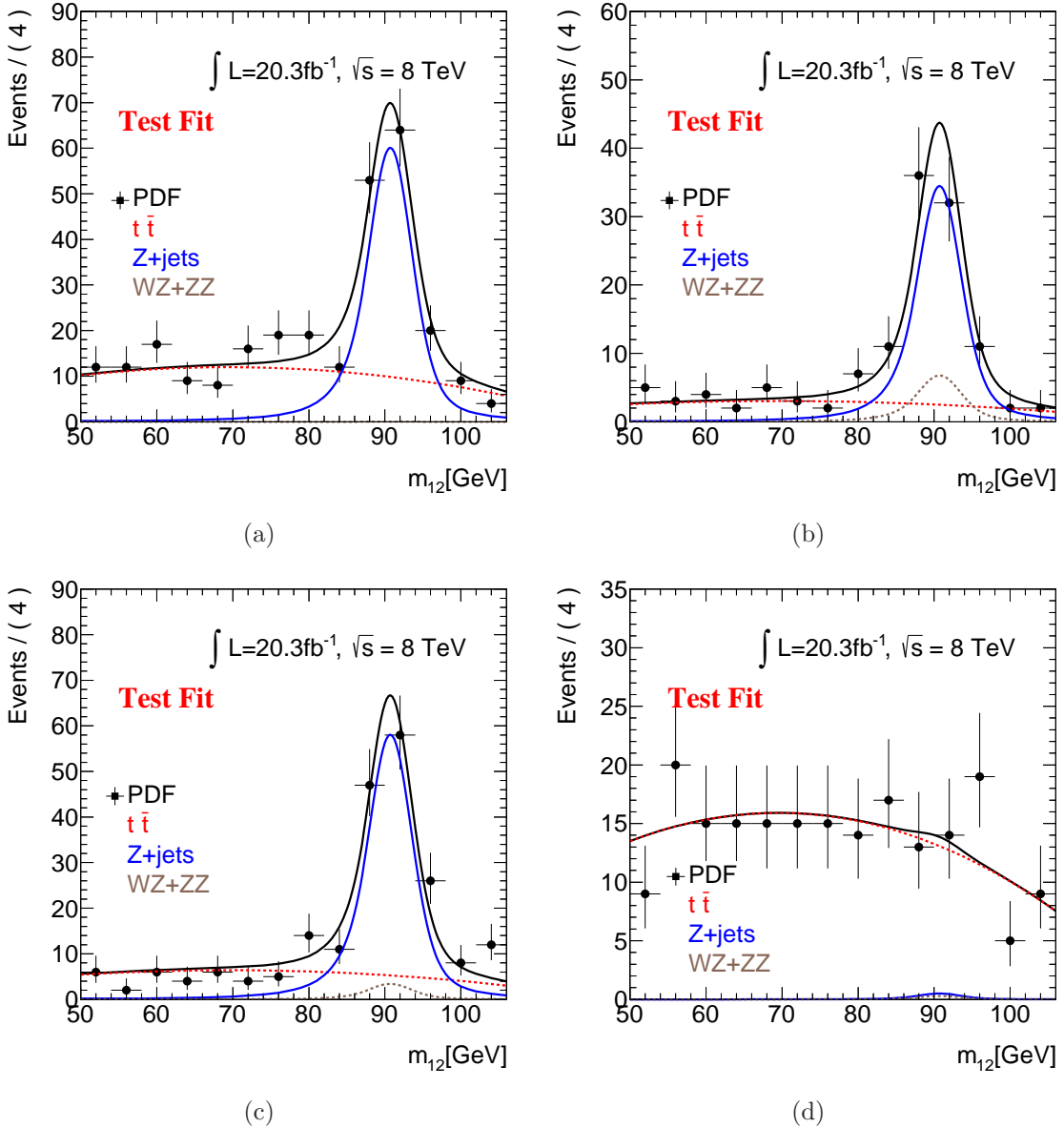


Figure C.4: The data m_{12} distributions are presented after the test fit, where the $Zb\bar{b}$ and $Zlight$ are treated as one background, the $Zjets$, for testing reasons. The CRs of the inverted $d_0/\sigma d_0$ (a), inverted isolation and nominal $d_0/\sigma d_0$ (b), SS (c) and $e\mu + \mu\mu$ (d) are presented. The test proves no significant deviation with the nominal results.



List of Figures

1.1	Matter building blocks	22
1.2	Potential for $\mu^2 > 0$ and $\mu^2 < 0$	34
1.3	Higgs boson Coupling	39
1.4	Higgs Expected Width	40
1.5	Triviality and Vacuum Stability Bounds	41
1.6	Contours of the Fine-Tuning Parameter Δ_{FT}	42
1.7	Higgs Production at Hadron Colliders	45
1.8	Higgs Mechanisms Cross Sections	46
1.9	LEP Gfitter Results	48
1.10	Higgs Branching Ratios	49
2.1	The LHC tunnel	54
2.2	The LHC Collision Points	54
2.3	Hydrogen injection for proton beam creation	57
2.4	The CERN accelerator complex	57
2.5	Particles interaction with detector components	61
2.6	ATLAS Detector	62
2.7	CMS Detector	63
2.8	ALICE Detector	64
2.9	LHCb Detector	65
2.10	TOTEM Detector	66
2.11	LHCf Detector	67
2.12	MoEDAL Detector	68
3.1	Inner Detector	73
3.2	B-layer Extraction for the 2013-2014 Upgrade	74
3.3	Barrel Semiconductor Tracker	76
3.4	TRT detector component	78
3.5	LAr accordion-shaped electrodes	80
3.6	LAr Electromagnetic Calorimeter	81
3.7	Tile Calorimeter Central Barrel Assembly	84
3.8	Muon Spectrometer	85

3.9	MDT Tubes	86
3.10	CSC Cutout View	88
3.11	RPC Chamber	90
3.12	TGC Schematic	91
3.13	Magnetic Field Schematic View	93
3.14	Central Solenoid	94
3.15	Toroid Barrel	95
3.16	EndCap Toroid	97
3.17	Trigger Flow Diagram	98
3.18	Luminosity Measurements	103
3.19	Small Wheel Measured Hit Rate	104
3.20	MicroMegas Sketch of the Operating Principle	105
3.21	sTGC Internal structure	106
3.22	Expected L1 Calorimeter Rates	107
3.23	Particles Identification Through the Detector Components	110
4.1	Small Wheel View	117
4.2	Schematic Diagram of the Cathode Strip Chamber	118
4.3	Illustration of CSC Principle of Operation	119
4.4	Chamber Assembly Sequence	123
4.5	CSC Fiber Connections	125
4.6	CSC Pedestal Pattern	126
4.7	CSC Pedestal Pattern Deviations	127
4.8	CSC 2012 Dead and Hot Channels	128
4.9	CSC Pulse Shape	128
4.10	CSC Run-I Dead-Time	129
4.11	CSC Information Flow Schema	130
4.12	CSC Chamber Numbers Assign	131
4.13	CSC Run-II Readout System	132
4.14	CSC OTDR measurements	135
4.15	CSC Trigger and Timing Unit	136
4.16	CSC Cosmic Track Event Display with the New Readout Complex	137
4.17	CSC <i>2 – samples</i> Time Reconstruction	138
4.18	CSC Strip Charges	139
4.19	CSC Interstrip Position vs Charge Ratio	140
4.20	CSC Interstrip Position	141
4.21	CSC Categorized Hits for the two Reconstruction	142
4.22	CSC Precision Charge with Unspoiled Requirements	142
4.23	CSC η Clusters Width	143
4.24	CSC Cluster Charge	143
4.25	CSC Peak Charge on Segment	144

4.26	CSC η Peak Charge on Segment with Spoil Requirement	145
4.27	CSC Tracks Momentum	146
4.28	CSC Charge Ratio vs Interstrip Position	147
4.29	CSC Number of Hits vs Threshold	150
4.30	CSC ROD Busy Monitoring	150
4.31	CSC Cluster Volume With Reduced Time Window	151
4.32	CSC Residuals for 4 – <i>samples</i> Runs	152
4.33	CSC Segment Angle	153
4.34	CSC Resolution vs Angle	153
4.35	CSC Alignment Checks	154
4.36	CSC Lorentz Effect on the Resolution	155
4.37	CSC 2 – <i>samples</i> Runs η Charge	156
4.38	CSC Residuals for 2 – <i>samples</i> Runs	157
4.39	CSC Pulls for 4 and 2 – <i>samples</i> Runs	157
4.40	CSC Tag and Probe Mass in the High η Region	158
4.41	CSC Tag and Probe Efficiency in the High η Region	160
4.42	CSC Segment Efficiencies in the STACO Algorithm	162
4.43	CSC C01 Pseudo-Segments Charge Correlation	163
4.44	CSC C01 Pseudo-Segments Angle Deviation	163
4.45	CSC C05L1 Observed and Expected Occupancy	164
4.46	CSC C05L1 Current	164
4.47	CSC Run-I Performance	166
4.48	CSC 25 ns Performance	168
4.49	CSC 25 ns η Charge	169
4.50	CSC 25 ns η Charge for Clusters on Segments	170
4.51	CSC 25 ns and 50 ns Peaking Time vs Amplitude	170
4.52	CSC 25 ns and 50 ns Peaking Time	171
4.53	CSC 25 ns and 50 ns Unspoiled Hits on Segments	171
4.54	CSC 25 ns Residuals	172
4.55	CSC Chamber Removal Tool	173
4.56	CSC Chambers Repair	174
4.57	CSC Repaired Chambers Pedestals	175
4.58	ATLAS Official Reports for the Run-I	176
5.1	Higgs Background Productions	183
5.2	Muons Radiation Length	189
5.3	Isolation Background - Signal Discrimination	198
5.4	$d_0/\sigma d_0$ Background - Signal Discrimination	199
5.5	2011 $Z + \mu$ Properties	201
5.6	2012 $Z + \mu$ Properties	202
5.7	Momentum Imbalance	203

5.8	2012 Inverted CRs m_{12} Distributions	206
5.9	Mass Distributions of $e^\pm\mu^\mp + \mu\mu$ CR	207
5.10	2012 Closure Test	210
5.11	2012 Simultaneous Fit	212
5.12	2012 Correlation Matrix	213
5.13	2012 Fit Parameters Pulls	214
5.14	2012 Reference CR Masses	215
5.15	Individual Data Fits Sanity Check	218
5.16	2011 Simultaneous Fit	222
5.17	2011 Reference CR Masses	223
5.18	ZZ Decay Angles	226
5.19	2011 Reference CR Angular Distributions	227
5.20	2012 Reference CR Angular Distributions	228
5.21	Signal Region $m_{4\ell}$ Distributions	231
5.22	m_{12} and m_{34} Distributions of Signal Region events	232
5.23	Channels $m_{4\ell}$, $\sqrt{s} = 7$ and 8 TeV, in the Low Mass Region	235
5.24	4 μ Candidate Event Display	236
6.1	VBF BDT Variables	247
6.2	VBF Correlations Estimated from the VBF BDT	248
6.3	ggF Correlations Estimated from the VBF BDT	249
6.4	$ZZ^{(*)}$ Correlations Estimated from the VBF BDT	250
6.5	VBF BDT Output for Different Masses	251
6.6	VBF BDT Output	252
6.7	Dijet Mass of the VH Production	253
6.8	VH Training Variables	254
6.9	VH Correlations in the VH Hadronic BDT	255
6.10	ggF Correlations in the VH Hadronic BDT	256
6.11	VH Hadronic BDT Response and Efficiencies	258
6.12	VBF Enriched Category Distributions	265
6.13	VBF Candidate Event Display	267
7.1	b-jets and Additional Leptons	272
7.2	$\Delta\eta$ and m_{jj} of Di-jet Pairs	273
7.3	Additional Leptons Distributions	275
7.4	Jets Distributions	275
7.5	Quadruplet Mass In the Categories	278
7.6	$H \rightarrow ZZ^{(*)} \rightarrow 4\mu$ Mass Distributions	282
7.7	$H \rightarrow ZZ^{(*)} \rightarrow 4\mu$ p_T and η Distributions	283
7.8	$H \rightarrow ZZ^{(*)} \rightarrow 4\mu$ Muons p_T vs η Distributions	284
7.9	$H \rightarrow ZZ^{(*)} \rightarrow 4\mu$ p_T and η Distributions	285

C.1	Shape Parameters Data Sanity Check	310
C.2	Reduced Fractions Uncertainties Data Sanity Check	311
C.3	Increased Fractions Uncertainties Data Sanity Check	312
C.4	ZJets Data Sanity Check	313

List of Tables

1.1	Lepton properties summary	22
1.2	Quark quantum numbers	23
1.3	Relative strength of the interacting forces	24
1.4	Higgs Cross Sections at $\sqrt{s} = 7, 8, 13, 14$ TeV	47
2.1	LHC design parameters	56
4.1	CSC Basic Operation and Design Parameters	116
4.2	Data Fibers Light Measurements	134
4.3	CSC Number of Hits vs Threshold	149
4.4	CSC Tag and Probe Selection	159
4.5	CSC Tag and Probe Selection	161
4.6	CSC C05L1 Performance after Occupancy Reduction	165
4.7	CSC Run-I Performance	165
4.8	CSC Run-I Performance for Sectors with Malfunctions	167
4.9	25 ns Runs Conditions	167
5.1	Data Taking in 2011 and 2012	180
5.2	Higgs Production Cross Section	182
5.3	Higgs Backgrounds Cross Sections	184
5.4	Electron Selection Criteria	187
5.5	Muon ID Hits Requirements	190
5.6	Muon Selection Criteria	190
5.7	2011 $H \rightarrow ZZ^{(*)} \rightarrow 4\ell$ Triggers	191
5.8	2012 $H \rightarrow ZZ^{(*)} \rightarrow 4\ell$ Triggers	192
5.9	$H \rightarrow ZZ^{(*)} \rightarrow 4\ell$ Event Selection	193
5.10	$H \rightarrow ZZ^{(*)} \rightarrow 4\ell$ m_{34} Cuts	193
5.11	$Z + \mu$ Selection	200
5.12	$Z + \mu$ Efficiencies	203
5.13	2012 MC Estimated CRs Background	208
5.14	2012 MC Fractions	208
5.15	2012 Closure Test Results	209

5.16	MC Fit Shape Parameters	209
5.17	2012 Simultaneous Fit Results	211
5.18	2012 Background Parameters Correlation	211
5.19	Shape Parameters Data Sanity Check	216
5.20	Reduced Fractions Uncertainties Data Sanity Check	216
5.21	Increased Fractions Uncertainties Data Sanity Check	217
5.22	ZJets Data Sanity Check	217
5.23	Individual CR Fits	219
5.24	$t\bar{t}$ Cross Checks	219
5.25	2012 Transfer Factors	220
5.26	2012 SR Reducible Background Estimations	221
5.27	2011 MC Fractions	221
5.28	2011 Simultaneous Fit Results	224
5.29	2011 Transfer Factors	224
5.30	2011 SR Reducible Background Estimations	225
5.31	Isolation and Impact Parameter Uncertainties on the Signal	229
5.32	$H \rightarrow ZZ^{(*)} \rightarrow 4\ell$ Observed Events and Expected Background	230
5.33	$H \rightarrow ZZ^{(*)} \rightarrow 4\ell$ Observed Events and Expected Background	232
5.34	$H \rightarrow ZZ^{(*)} \rightarrow 4\ell$ Results in the Signal Range	234
6.1	Higgs Production Cross Section	244
6.2	Jets Selection	245
6.3	VBF BDT Separation and Importance	246
6.4	VH Hadronic BDT Variables Ranking	253
6.5	VBF and VH Hadronic Selection Efficiency	257
6.6	Categories Expected Yields	259
6.7	Expected $ZZ^{(*)}$ Background in the Categories	260
6.8	Expected Categories Reducible Background	261
6.9	2012 Measured Reducible Background in the Categories	261
6.10	2011 Measured Reducible Background in the Categories	262
6.11	Reducible Background Summary	262
6.12	Categories Systematic Uncertainties	264
6.13	Expected and Observed Category Yields	266
7.1	3000 fb^{-1} Expected Yields	277
7.2	Yields With Higher Jet Fake Rate	279
7.3	300 fb^{-1} Expected Yields	280
7.4	$H \rightarrow ZZ^{(*)} \rightarrow 4\mu$ Expected Yields for Large Eta Scenario	281
7.5	$H \rightarrow ZZ^{(*)} \rightarrow 4\ell$ Expected Yields for Large Eta Scenario	281
7.6	Run-I Projections for the Run-II	283
7.7	Expected Signal Strength Uncertainties 3000 fb^{-1}	286

7.8	Expected Signal Strength Uncertainties 300 fb^{-1}	286
A.1	Signal MC ggF with no tau decays.	292
A.2	Signal MC ggF with tau decays.	293
A.3	Signal MC VBF with no tau decays.	294
A.4	Signal MC VBF with tau decays.	295
A.5	ZZ Full Mass.	299
A.6	ZZ Filter $100 - 150 \text{ GeV}$.	300
A.7	ZZ Filter $500 - 50000 \text{ GeV}$.	300
A.8	$Z + \text{jets}$ samples, $10 \text{ GeV} < m_{\ell\ell} < 40 \text{ GeV}$.	303
A.9	$Z + \text{jets}$ samples, $40 \text{ GeV} < m_{\ell\ell} < 60 \text{ GeV}$.	304